UNIVERSITY OF SOUTHAMPTON
Faculty of Engineering and Applied Science
Department of Electronics and Computer Science

Antenna Diversity-Assisted Adaptive Wireless Multiuser OFDM Systems

by

Dipl.Ing. Matthias Münster

Supervisor: Prof. Lajos Hanzo

A thesis submitted in partial fulfilment of the requirements for the award of a Doctor of Philosophy at the University of Southampton

June 2002

Dedicated to my academic supervisor and friend Lajos Hanzo.

UNIVERSITY OF SOUTHAMPTON

ABSTRACT

Faculty of Engineering

Department of Electronics and Computer Science

Doctor of Philosophy

Antenna Diversity-Assisted Adaptive Wireless Multiuser OFDM Systems

by Matthias Münster

Single-user decision-directed channel estimation for OFDM is known to deliver potentially more accurate channel transfer factor estimates than pilot-assisted schemes, when benefitting from error-free symbol decisions. However, the estimates' accuracy is degraded in the context of rapidly fluctuating channels, since the channel transfer factor estimates produced during the previous OFDM symbol period are employed for the frequency-domain equalization of the most recently received OFDM symbol. Hence, the employment of Wiener prediction filtering was shown to be an effective countermeasure for mitigating the effects of channel transfer function variations imposed by higher Doppler frequencies. Two techniques were compared against each other, namely a scheme, which was insensitive to the shape of the CIR encountered and an adaptive prediction filtering. Furthermore, the joint effects of employing decision-directed channel prediction and adaptive modulation were demonstrated.

Based on the philosophy of a decision-directed channel estimator designed for single-user scenarios, a parallel interference cancellation assisted channel estimator was proposed for multi-user scenarios, or more generally for OFDM systems employing multiple transmit antennas. This was motivated by the observation that the utilization of the most prominent subspace-based least-squares channel estimator is restricted to scenarios, where the number of users supported is lower than or equal to the number of OFDM subcarriers normalized to the number of significant CIR-related taps to be estimated. An iterative procedure was proposed for the off-line optimization of the estimator's coefficients. Alternatively, an adaptive approach based on the recursive least-squares (RLS) algorithm was proposed for updating the channel estimator coefficients on an OFDM symbol-by-symbol basis.

Furthermore, a suite of detection techniques to be employed in a multi-user SDMA-OFDM scenario was compared against each other. Specifically, least-squares detection (LS), minimum mean-square error (MMSE) detection, sucessive interference cancellation (SIC), parallel interference cancellation (PIC) and maximum likelihood detection (ML) were studied. Detailed investigations were conducted with respect to the effects of error-propagation potentially occuring across the different SIC detection stages. Various strategies designed for improving the standard SIC detector's performance based on tracking multiple symbol decisions from each SIC detection node were compared against each other. An improved soft-bit metric, which takes into account the effects of error propagation was proposed for a system employing both SIC detection and turbo-decoding. Investigations conducted for a system employing PIC-detection and turbo-decoding demonstrated that potentially the same performance as that of the SIC-detection assisted turbo-decoded system can be achieved, although at a lower complexity.

Finally, the performance of the low-complexity MMSE- or PIC detection aided systems was further improved by employing adaptive modulation or Walsh-Hadamard Transform based spreading, with the aim of exploiting the wideband channel's diversity potential in the detection process.

LIST OF PUBLICATIONS

1. M. Münster, T. Keller and L. Hanzo,"Co–Channel Interference Suppression Assisted Adaptive OFDM in Interference Limited Environments", *Proceedings of IEEE Vehicular Technology Conference*, Amsterdam, Netherlands, pp. 284–288, September 19–22, 1999

2. M. Münster and L. Hanzo,"Co–Channel Interference Cancellation Techniques for Antenna Array Assisted Multiuser OFDM Systems", *Proceedings of IEE 3G-'2000 Conference*, London, Great Britain, pp. 256–260, March 27–29, 2000

3. T. Keller, M. Münster and L. Hanzo,"A Wideband Transform-Coded Symbol-by-Symbol Adaptive Speech and Audio Transceiver", *Proceedings of IEEE International Telecommunications Conference ITC'2000*, Acapulco, Mexico, pp. 847–851, May 22–25, 2000

4. M. Münster and L. Hanzo,"MMSE Channel Prediction for Symbol-by-Symbol Adaptive OFDM Systems", *Proceedings of* 5^{th} *International OFDM-Workshop'2000*, Technische Universität Hamburg-Harburg, Germany, pp. 35/1–35/6, September 12–13, 2000

5. T. Keller, M. Münster and L. Hanzo,"Turbo-Coded Burst-by-Burst Adaptive Wideband Speech Transceiver", *Journal on Selected Areas in Communications*, vol.18, no.11, pp. 2363-2372, November 2000

6. B. J. Choi, M. Münster, L. L. Yang and L. Hanzo,"Performance of Rake Receiver Assisted Adaptive-Modulation Based CDMA over Frequency Selective Slowly Rayleigh Fading Channels", *IEE Electronics Letters*, no.37, pp. 247-248, 2001

7. M. Münster and L. Hanzo,"First-Order Channel Parameter Estimation Assisted Cancellation of Channel Variation-Induced Inter-Subcarrier Interference in OFDM Systems", *Proceedings of EUROCON*, Bratislava, Czech, pp.1-5, July 4-7, 2001

8. M. Münster and L. Hanzo,"Parallel Interference Cancellation Assisted Decision-Directed Channel Estimation for Multi-User OFDM", *Proceedings of* 6^{th} *International OFDM-Workshop '2001*, Technische Universität Hamburg-Harburg, Germany, pp. 35/1–35/5, September 18–19, 2001

9. P. J. Cherriman and M. Münster and L. Hanzo,"HIPERLAN like Turbo Coded Multi-User Detection Assisted OFDM Based Interactive Video Telephony", *Proceedings of IEEE Vehicular Technology Conference*, Atlantic City, NJ, pp.87-91, October 7-11, 2001

10. M. Münster and L. Hanzo,"Performance of SDMA Multi-User Detection Techniques for Walsh-Hadamard-Spread OFDM", *Proceedings of IEEE Vehicular Technology Conference*, Atlantic City, NJ, pp.2319-2323, October 7-11, 2001

11. M. Münster and L. Hanzo,"MMSE Channel Prediction Assisted Symbol-by-Symbol Adaptive OFDM", *Proceedings of IEEE International Conference on Communications*, Birmingham, Alabama, April 28 - May 2, 2002

12. M. Münster and L. Hanzo,"Parallel Interference Cancellation Assisted Decision-Directed Channel Estimation for Multi-User OFDM", *Proceedings of IEEE Vehicular Technology Conference*, Vancouver, Canada, September, 2002, *accepted for publication*

13. M. Münster and L. Hanzo,"Parallel Interference Cancellation Assisted Decision-Directed Channel Estimation for Multi-User OFDM", *IEEE Transactions on Wireless Communications, submitted*

ACKNOWLEDGEMENT

First of all I would like to thank Prof. Lajos Hanzo for his outstanding supervision and support of my work. Specifically his fruitful ideas contributed to this project, his investment in terms of time, his continual encouragement and enthusiasm as well as his generous financial support deserve my uttermost acknowledgement and gratitude - but most importantly I would like to thank him for his friendship.

I would also like to thank a number of staff members associated with the Communications Research group, namely Mr. Steve Braithwaite, Dr. Jeff Reeve, Dr. Joe Stefanov, Mr. David Stewart, Dr. Stephan Weiss and our group secretary Denise Harvey. Furthermore, my thanks must also go to Dr. Byoung Jo Choi, Mr. Soon X Ng, Mr. Ahmad Samingan, Dr. Lie Liang Yang, Dr. Bee Leong Yeap, Dr. Spyros Vlahoyiannatos as well as to all other colleagues, to numerous to mention here explicitly.

My personal thanks are specifically due to Hubert Dietl, to Markus Zensen and to our friends from the Optoelectronics Research Centre, namely to Walter Belardi, Dr. Alessandro Buzaka and to Fabio Ghiringheli.

Finally, I am extremely grateful to my parents for their support during my education at school and university.

Contents

List of General Symbols

B_D:	Doppler spread of the channel: $B_D = 2f_D$.
c:	Speed of light.
f_c:	OFDM carrier frequency.
f_d:	Any frequency of the Doppler spectrum.
f_D:	Doppler frequency: maximum frequency in the sense of a limitation of the Doppler spectrum.
f_s:	OFDM sampling frequency: $f_s = 1/T_s$.
F_D:	OFDM symbol duration normalized Doppler frequency: $F_D = f_D T_f$.
$F_{D,K}$:	OFDM symbol duration normalized Doppler frequency used in the context of quantifying the effects of ICI: $F_{D,K} = f_D K T_s$.
$h(t,\tau)$:	Time-variant channel impulse response (CIR) at time instant t and multipath delay τ.
$H(t,f)$:	Time-variant channel transfer function: $H(t,f) = \underset{\tau \to f}{\mathcal{FT}}\{h(t,\tau)\}$.
k:	OFDM subcarrier index.
n:	OFDM symbol index.
K:	Number of OFDM subcarriers.
K_c:	Constraint length of the channel code.
K_g:	Number of OFDM guard interval samples.

$r_h(\Delta t, \tau_1, \tau_2)$: Auto-correlation function of the CIR: $r_h(\Delta t, \tau_1, \tau_2) = E\{h(t, \tau_1)h^*(t-\Delta t, \tau_2)\} = r_h(\Delta t, \tau_1) \cdot \delta(\tau_1 - \tau_2)$.

$r_h(\Delta t, \tau)$: Spaced-time auto-correlation function of the CIR for the multipath delay τ, namely: $r_h(\Delta t, \tau) = r_h(\Delta t, \tau_1, \tau_2)|_{(\tau=\tau_1=\tau_2)}$.

$r_h(\tau)$: Multipath intensity profile or delay power spectrum: $r_h(\tau) = r_h(\Delta t, \tau)|_{(\Delta t=0)}$.

$r_H(\Delta t, \Delta f)$: Spaced-frequency spaced-time correlation function of the channel: $r_H(\Delta t, \Delta f) = \underset{\tau \to \Delta f}{\mathcal{FT}}\{r_h(\Delta t, \tau)\}$. In the context of 'separability' we have: $r_H(\Delta t, \Delta f) = r_H(\Delta t) \cdot r_H(\Delta f)$.

$r_H(\Delta t)$: Spaced-time correlation function in the context of 'separability' of $r_H(\Delta t, \Delta f)$.

$r_H(\Delta f)$: Spaced-frequency correlation function in the context of 'separability' of $r_H(\Delta t, \Delta f)$.

R_c: Coding rate of the channel encoder.

$S_h(f_d, \tau)$: Scattering function of the channel: $S_h(f_d, \tau) = \underset{\Delta t \to f_d}{\mathcal{FT}}\{r_h(\Delta t, \tau)\}$.

$S_H(f_d, \Delta f)$: $S_H(f_d, \Delta f) = \underset{\Delta t \to f_d}{\mathcal{FT}}\{r_H(\Delta t, \Delta f)\}$.

$S_H(f_d)$: Doppler power spectrum of the channel: $S_H(f_d) \equiv S_H(f_d, \Delta f)|_{\Delta f=0}$.

T_m: Multipath spread of the channel.

T_s: OFDM sampling period duration: $T_s = 1/f_s$.

T_f: OFDM symbol duration: $T_f = (K + K_g)T_s$.

v: Vehicular speed.

$\mathbf{W}$: Unitary DFT matrix, where the complex phaser in the i-th row and j-th column is given by $\mathbf{W}|_{i,j} = \frac{1}{\sqrt{K}} e^{-j2\pi \frac{ij}{K}}$: $\mathbf{W} \in \mathbb{C}^{K \times K}$.

$\alpha_n(t)$: Time-variant attenuation factor of the n-th CIR component.

$\delta(t)$: Dirac impulse function.

κ_{ICI}: ICI noise proportionality constant. Note that $\kappa_{\text{ICI}} = f(F_{D,K})$.

ρ: Inverse of the signal to noise ratio: $\rho = \sigma_n^2/\sigma_s^2$.

σ^2_{AWGN}: Variance of the AWGN.

σ_H^2: Variance of the frequency-domain channel transfer factors.

σ^2_{ICI}:	Subcarrier domain ICI noise variance: $\sigma^2_{\text{ICI}} = \kappa_{\text{ICI}}\sigma^2_s$.
σ^2_n:	Total noise variance: $\sigma^2_n = \sigma^2_{\text{AWGN}} + \sigma^2_{\text{ICI}}$.
σ^2_s:	Signal variance.
$\tau_n(t)$:	Time-variant delay of the n-th CIR component.
ω_D:	Doppler angular velocity: $\omega_D = 2\pi f_D$.
ΔF:	Subcarrier spacing of the OFDM symbol: $\Delta F = \frac{1}{KT_s}$.
$(\Delta f)_c$:	Coherence bandwidth of the channel: $(\Delta f)_c \approx \frac{1}{T_m}$.
$(\Delta t)_c$:	Coherence time of the channel: $(\Delta t)_c \approx \frac{1}{B_D}$.
$()\|_{opt}$:	Index used in the context of the vector of estimator coefficients in order to indicate its optimality in the sense of a minimum MSE.
$()\|_{rob}$:	Index used in conjunction with auto-correlation matrices or cross-correlation vectors in order to indicate their 'robustness', which is related to the uniform ideally support-limited scattering function.
$()_{unif}$:	Channel correlation functions related to a uniform ideally support limited scattering function.
$\tilde{()}$:	Index employed to denote variables, vectors and matrices associated with the design of an estimator or predictor. An exception is given by the least-squares channel transfer factor- or CIR-related tap estimates, which are also identified by a superscript of $\tilde{()}$.
$\lfloor\rfloor$:	Largest integer that is not greater than the argument in brackets.
$\lceil\rceil$:	Smallest integer that is not less than the argument in brackets.
$\|\|.\|\|_2^2$:	Euclidean norm of a vector.

Chapter 1

Introduction

1.1 Historic Background

Orthogonal Frequency Division Multiplexing (OFDM) was discovered by Chang in his pioneering paper in 1966 [1]. The basic idea is that dispersive transmission media can be rendered non-dispersive, if the transmission channel is subdivided in a high number of parallel, low-rate, non-dispersive channels [2]. Given the propagation environment, irrespective, whether it is a wire-line, stationary or mobile wireless scenario, the increased dispersion associated with increased transmission rates can always be avoided by increasing the number of subchannels. This is equivalent to increasing the memory of the channel equaliser in conventional equalised serial modems [2]. Since its discovery, this technique has fascinated researchers [1]-[3], but due to its implementational complexity its applications have been scarce until quite recently. Recently, however, it has been adopted as the new European digital audio broadcasting (DAB) standard [4] and it is also a strong favourite for digital terrestrial television broadcast (DTTB) in Europe [5]. Its recent revival was heralded by Hirosaki [6], Schüssler and his colleagues at Erlangen University [7]-[8], Cimini's impressive contribution [9] and Kalet's work [3]. Of particular note are a range of further contributions for example from the impressive state-of-art collection of works edited by Fazel and Fettweis [10], including the research by Fettweis *et al.* at the University of Dresden, Rohling *et al.* at the University of Hamburg, Vandendorp at the University of Loeven, Huber *et al.* at the University of Erlangen, Lindner *et al.* at the University of Ulm, Kammeyer *et al.* at the University of Bremen and Meyr *et al.* [11, 12] at the University of Aachen, but the individual contributions are too numerous to mention. In the USA it has also been advocated for asymmetric digital subscriber loop (ADSL) applications. In Europe it has been proposed for high-rate applications, such as 155 Mbps Wireless Asynchronous Transfer Mode (WATM) local area networks. These wide-ranging applications underline its significance as an alternative technique to conventional, channel equalisation assisted serial modems [2] in order to combat signal dispersion [1]-[3].

1.2 Outline of the Thesis and Novel Contributions

In this section we will provide an overview of the novel contributions presented in the context of this thesis. Specifically, Section 1.2.1 highlights the novel contributions provided in the context of decision-directed single-user channel estimation in Chapter 2. Furthermore, Section 1.2.2 summarizes our novel contributions provided during our discussions of decision-directed multi-user channel estimation in Chapter 3. Finally, a range of advances in the field of multi-user detection techniques designed for SDMA-OFDM in Chapter 4 are summarized in Section 1.2.3.

1.2.1 Chapter 2: "Decision-Directed Channel Estimation for Single-User OFDM"

As it will be argued in the context of our description of the single-user OFDM receiver in Section 1.3.1.4, a prerequisite for performing coherent detection of the different subcarriers' symbols at the receiver is the availability of a reliable estimate of each subcarrier's channel transfer factor. The channel transfer factor estimation strategies known from the literature can be divided into pilot-assisted- and decision-directed approaches. Various frequency-domain interpolation methods applicable to both pilot-assisted and decision-directed approaches, such as linear-, polynomial- and Wiener filter based interpolation techniques have been investigated in the literature. Wiener filtering is regarded as the conceptually most elegant solution. The importance of the Wiener filtering based solution is also manifested by its application in the context of channel transfer factor prediction as well as in the linear multi-user detection techniques to be discussed in Chapter 4.

While the purely pilot-assisted channel transfer factor estimator is known to operate reliably even at low SNRs, its MSE performance suffers in the context of sparse pilot patterns. Furthermore, in the context of the more effecient 2D-pilot patterns - compared to 1D-pilot patterns - the processing at the receiver is performed on a block-by-block basis, where a single block typically contains several OFDM symbols. Besides the increased storage requirement imposed, also the processing delay is increased, which might become unacceptable for example in voice-based communications services. These disadvantages can be addressed with the aid of the decision-directed channel estimator (DDCE), which employs the remodulated subcarrier symbol decisions as pilots.

- Our discussions in Chapter 2 commence by reviewing the concepts of 1D- and 2D-MMSE based DDCE contrived for single-user OFDM, which was analysed for example by Edfors *et al.* [13, 14, 15], Sandell [16] and Li *et al.* [17]. Based on the observation that in the context of DDCE the most recently received OFDM symbol is equalized based on a potentially outdated channel transfer function estimate, which was generated during the previous OFDM symbol period, the CIR-related tap *estimation filters* invoked by the 2D-MMSE DDCE proposed by Li *et al.* [17] are substituted by CIR-related tap *prediction filters*. For this configuration we derive the channel predictor's average *a priori* estimation MSE observed in the

frequency-domain, as it will be shown in Section 2.2.4.6. In the context of our performance assessments provided in Section 2.3 two methods are compared against each other for evaluating the Wiener prediction filter's coefficients, namely the robust approach as advocated by Li *et al.* [17] and the adaptive approach as proposed by Al-Susa and Ormondroyd [18], based on the Burg-algorithm known from speech coding. As a third- and most promising alternative, the RLS algorithm could be employed, as proposed in the context of our discussions in Chapter 3.

- Following our in-depth performance assessment of the CIR-related tap prediction assisted DDCE, both in the context of uncoded and turbo-coded scenarios, combining channel transfer factor prediction-assisted DDCE with AOFDM is proposed in Section 2.4. As a result of the channel transfer factor prediction, AOFDM is rendered attractive also in scenarios having a relatively high OFDM symbol-normalized Doppler frequency. These contributions were published in [19] and [20].

1.2.2 Chapter 3: "Decision-Directed Channel Estimation for Multi-User SDMA-OFDM"

In the context of a single-user OFDM system, where the mobile user is equipped with a single transmit antenna, the generation of initial channel transfer factor estimates is rather simple. More specifically, the signal received in a subcarrier has to be divided by the associated transmitted symbol. The channel transfer factor estimates acquired could then be further enhanced for example by Wiener filtering. By contrast, in the multi-user SDMA-OFDM scenario to be outlined in Section 1.3.2 the signal received by any of the receiver antenna elements in a specific subcarrier is constituted by the superposition of the different users' transmitted - and independently faded - signals. Hence, the task of identifying the different users' associated channel transfer factors is less straightforward.

- Chapter 3 commences in Section 3.3 with an in-depth discussion of Li's Least-Squares (LS) assisted DDCE, which was contrived for space-time coded OFDM systems [21], or more generally for OFDM systems employing multiple transmit antennas encountered in the context of multi-user SDMA-OFDM scenarios. Our contribution in this section is the provision of a sophisticated mathematical description, which provides the standard LS-related solution of the associated estimation problem. In the context of these discussions a necessary condition for the existence of the LS-channel estimates is identified. In contrast to Li's discussions in [21], which provided an expression for the estimation MSE based on sample-spaced CIRs, here we also derived expression for the estimation MSE assuming the more realistic scenario of a non-sample-spaced CIR.

- Motivated by the potentially excessive complexity of the LS-assisted DDCE [21] and by its limitation in terms of the number of users- or transmit antennas supported, we focused our attention in Section 3.4 on the investigation of Parallel Interference Cancellation (PIC) assisted DDCE. We found that the PIC operations can either be performed in the CIR-related domain - as proposed by Li [22] - or in the frequency-domain as proposed by Jeon *et al.* [23]. Specifically the frequency-domain PIC appears more advantageous in terms of its lower complexity. In contrast to the contributions of Li [22] and Jeon *et al.* [23], in Section 3.4 we provide an in-depth mathematical analysis with respect to a number of key points. Based on identifying the estimator's recursive structure, expressions are derived for the *a posteriori*- and *a priori* estimation MSE and conditions are provided for the estimator's stability. Furthermore, an iterative procedure is devised for the off-line calculation of the *a priori* predictor coefficients. In order to provide an improved flexibility for the PIC-assisted DDCE with respect to variations of the channel's statistics and in order to increase its resilience to impulsive noise imposed by the erroneous symbol decisions that may be encountered in the DDCE, the RLS algorithm is adopted for the task of predictor coefficient adaptation. Part of this work was published in [24] or it was accepted for publication [25].

1.2.3 Chapter 4: "Uplink Detection Techniques for Multi-User SDMA-OFDM"

As it will be argued in the context of our portrayal of the multi-user SDMA-OFDM scenario in Section 1.3.2, instead of performing frequency-domain equalization of the channel transfer factors, followed by demodulation as in the single-user OFDM scenario to be outlined in Section 1.3.1, a multi-user detector has to be employed at the receiver for detecting the different users' transmitted symbols.

In Chapter 4 various linear- and non-linear multi-user detection techniques are compared against each other in terms of their applicability to the problem of detecting the subcarrier-based vectors of the L different users' transmitted symbols encountered in a multi-user SDMA-OFDM system. Specifically, the Least-Squares Error (LSE) and Minimum Mean-Square Error (MMSE) schemes are studied in Section 4.2, while the Successive Interference Cancellation (SIC) scheme and its derivatives, such as M-SIC and partial M-SIC, as well as the Parallel Interference Cancellation (PIC) and the Maximum Likelihood (ML) detection algorithms are considered in Section 4.3. These sections include the different techniques' mathematical derivation, as well as their performance and complexity analysis.

- Specifically, in the context of SIC detection our investigations of the effects of error propagation occurring through the different detection stages should be emphasized. Motivated by

the results of these investigations an improved metric is proposed for the generation of soft-bit values suitable for turbo-decoding. Furthermore, our contributions contrived for hard-decision based turbo-decoding assisted PIC for SDMA-OFDM should be mentioned here, which were published in [26].

- Based on the observation that SIC detection as the second-best performing detection approach after ML detection exhibits a potentially high complexity, further investigations are conducted in Section 4.4 for the sake of enhacing the performance of both MMSE- and PIC detection. Specifically, in Section 4.4.1 we discuss the employment of adaptive modulation in the context of an SDMA-OFDM scenario, which is hence termed as SDMA-AOFDM. This scheme will be shown to be effective in the context of an almost 'fully-loaded' system, where the L number of users supported approaches the P number of reception antennas employed at the basestation. This novel scheme was disseminated in [27].

- However, the employment of the SDMA-AOFDM scheme is restricted to duplex transmission scenarios having a reverse link, such as those in Time Division Duplexing (TDD). An enhancement of the MMSE- and PIC-assisted detection schemes' performance was achieved with the aid of orthogonal Walsh-Hadamard spreading codes, which will be investigated in Section 4.4.2. These advances were published in [20].

1.3 Outline of the OFDM System

Our discussions commence in Section 1.3.1 with an overview of the OFDM system and its components in a single-user, single-reception antenna scenario. This scenario is then extended in Section 1.3.2 to the case of multiple users and multiple reception antennas, which follows the concept of an SDMA-OFDM system.

1.3.1 Single-User, Single Reception Antenna Assisted OFDM Scenario

The further structure of this section is as follows. Based on a portrayal of the principles of Frequency Division Multiplexing (FDM) in Section 1.3.1.1, the principles of Orthogonal Frequency Division Multiplexing (OFDM) and its associated advantages are described in Section 1.3.1.2. The structure of the associated OFDM transmitter and receiver is then described in Section 1.3.1.4. Finally, in Section 1.3.1.5 we will outline a range of pivotal OFDM-related topics, which have been the subject of intensive research. For further reading on OFDM we refer to [16, 14, 28, 29, 30, 31, 32, 33, 34].

1.3.1.1 Principles of Frequency Division Multiplexing

Recall that the philosophy of OFDM [1, 3, 9] originates from Frequency Division Multiplexing (FDM) systems, where different modulated symbols are transmitted in parallel on neighbouring subcarriers, which are separated from each other by a frequency guard band. As a consequence of the frequency division, the signalling rate associated with each of the parallel subcarriers is a fraction of the system's total signalling rate. To be more explicit, while in a single-carrier system the individual modulated symbols are transmitted at a rate of $1/T_s$ symbols per second, where T_s denotes the sampling period duration, in the FDM system the signalling rate on each subcarrier is $1/KT_s$ symbols per second, under the simplistic assumption that no frequency guard bands are employed. In other words, the transmission of a single frequency-domain subcarrier symbol is stretched over the entire length of K sampling periods of duration T_s in the time-domain. As a result, a high resilience is achieved against impulsive noise incurred in the time-domain. While a couple of time-domain signal samples might be affected by this impulsive noise, which potentially results in erroneous decisions of the corresponding symbols in the context of conventional single-carrier transmission systems, by contrast in the frequency-domain its effects are spread over the K number of subcarriers thus mitigating the impact on each single transmitted symbol. A typical example of such impulsive noise is the Inter-Symbol Interference (ISI) between consecutive FDM symbols, which is due to receiving delayed replicas of the transmitted symbols over the multipath channel assumed here. A further advantage of the FDM system is that upon neglecting the ISI between consecutive OFDM symbols, the channel equalization can be simply implemented as a division of each received subcarrier symbol by the channel's effective transfer factor at this frequency. This one-tap frequency-domain equalization is typically less complex, than employing Finite Impulse Response (FIR) or Infinite Impulse Response (IIR) filters for time-domain equalization.

1.3.1.2 Principles of Orthogonal Frequency Division Multiplexing

However, the FDM scheme also exhibits a number of disadvantages, namely a relatively low bandwidth efficiency owing to the employment of frequency guard bands, as well as having a relatively cumbersome implementation based on a bank of separate modulators and demodulators assigned to the different subcarriers. Furthermore, the frequency-domain effects of the residual time-domain ISI impose a serious limitation on the system's achievable BER. Potential solutions to these problems will be discussed in the following. Specifically, in Section 1.3.1.2.1 we will discuss the employment of orthogonal subcarrier signalling functions instead of using frequency guard intervals, as in case of FDM. This allows us to perform the modulation of the different subcarriers with the aid of the IFFT, as will be outlined in Section 1.3.1.2.2. Furthermore, the ISI between the consecutive OFDM symbols is avoided even in the context of a multipath channel scenario, with the aid of a guard interval- or cyclic extension, as it will be discussed in Section 1.3.1.3.

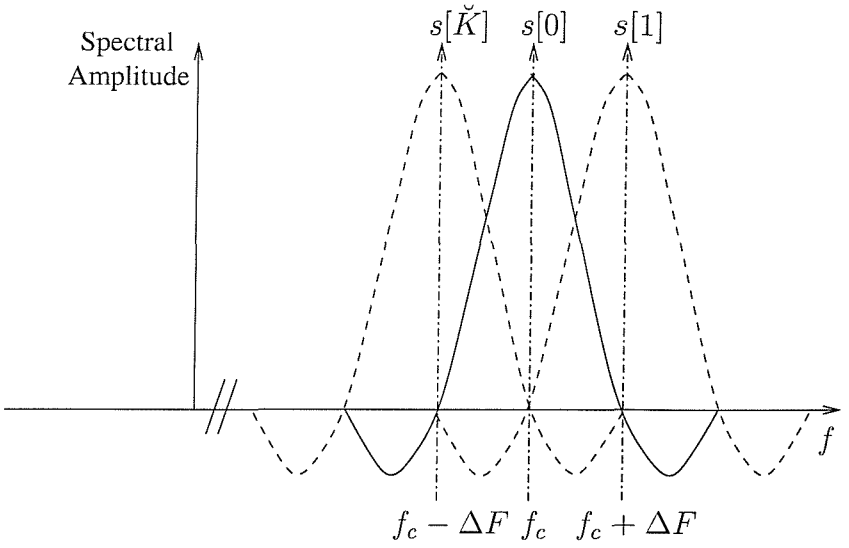

Figure 1.1: Sinc-shaped subcarrier spectra shown here for the subcarrier located at the center of the frequency-band and its nearest neighbours, which are separated by $\Delta F = 1/KT_s$. The entire OFDM spectrum is constituted by the superposition of the sinc-shaped subcarrier spectra, which are modulated by the symbols $s[k]$, $k = 0, \ldots, \breve{K}$ transmitted. Note that for simplicity we have defined $\breve{K} = K - 1$.

1.3.1.2.1 Maintaining a High Bandwidth Efficiency Using Orthogonal Signalling Functions

As suggested by the terminology, in OFDM we employ a set of K orthogonal signalling functions. These signalling functions are constituted by the harmonically related set of complex exponentials given by:

$$s_k(t) = \frac{1}{\sqrt{KT_s}} e^{j2\pi(k\Delta F)t}, \tag{1.1}$$

where we have $k = -\frac{K}{2} + 1, \ldots, \frac{K}{2}$ and $-\infty \leq t \leq \infty$. Corresponding to the set of K number of time-domain signalling functions, we have a series of K number of Dirac impulses in the frequency-domain at frequencies of $k\Delta F$. Note that the different Dirac impulses are spaced apart from each other by $\Delta F = 1/KT_s$. This corresponds to the division of the available frequency band of width $1/T_s$ into K equal-width subbands. However, as a result of the signal's temporal limitation in the time-domain to a number of K sample periods of duration T_s each, which can be described as the multiplication of the complex exponential signalling functions with a rectangular windowing function, the series of frequency-domain Dirac impulses is convolved with the rectangular window's spectrum, namely the sinc-function. This is portrayed in Figure 1.1 for the subcarrier located at the center frequency f_c and for its nearest neighbours, where the individual sinc-shaped subcarrier transfer functions have to be weighted with the complex modulating symbols $s[k]$, $k = 0, \ldots, K-1$ that have been transmitted. Most importantly, we note that the sinc-shaped spectrum of a specific subcarrier intersects the frequency-axis exactly at those frequencies, which are associated with the

remaining subcarriers. This can be directly inferred from the spectral representation $W(f)$ of the rectangular window $w(t)$, namely from:

$$w(t) = \text{rect}(\frac{t}{KT_s}) \quad \Longleftrightarrow \quad W(f) = KT_s \cdot \text{sinc}(\pi KT_s f), \tag{1.2}$$

where $\text{sinc}(x) = \sin(x)/x$. Observe that for the set of frequencies $f = k\Delta F$, $k \in \{-\frac{K}{2} + 1, \ldots, \frac{K}{2}\} \setminus \{0\}$ we have $W(f) = 0$. Hence, no interference occurs between the symbols modulating the different subcarriers in the absence of ISI and upon assuming perfect frequency synchronization. Note that due to the signals' time-frequency duality, the orthogonality of the subcarrier transfer functions observed in Figure 1.1 in the frequency-domain corresponds to the orthogonality of the signalling functions - represented by the complex exponentials of Equation 1.1 - in the time-domain. More specifically, for the complex exponential signal functions of Equation 1.1 it is straightforward to show that we have:

$$\int_{t=-\frac{KT_s}{2}}^{\frac{KT_s}{2}} s_{k_1}(t) s^*_{k_2}(t) dt = \begin{cases} 1, & k_1 = k_2 \\ 0, & k_1 \neq k_2 \end{cases} . \tag{1.3}$$

Note that as a result of the overlapping nature of the sinc-shaped subcarrier transfer functions, the bandwidth efficiency of the OFDM scheme is increased compared to that of non-orthogonal FDM capitalizing on 'wasteful' frequency guard bands.

1.3.1.2.2 Fast Fourier Transform Aided Reduced Complexity Implementation A further significant advantage of OFDM compared FDM is that the modulation of the different subcarriers can be efficiently implemented with the aid of the Discrete Fourier Transform (DFT) or its low complexity implementation, namely the Fast Fourier Transform (FFT). Recall that the OFDM transmitter's output signal during the n-th OFDM symbol period is constituted by the superposition of the K number of modulated subcarrier signalling functions, namely by:

$$tr(n,t) = \frac{1}{\sqrt{KT_s}} \sum_{k=0}^{\frac{K}{2}} s[n,k] e^{j2\pi k \Delta F t} + \frac{1}{\sqrt{KT_s}} \sum_{k=\frac{K}{2}+1}^{K-1} s[n,k] e^{j2\pi (k-K) \Delta F t}, \tag{1.4}$$

where the first term is associated with the positive frequencies, while the second term with negative frequencies in the OFDM signal's baseband representation. In the context of a digital implementation, the time-discrete equivalent of Equation 1.4 is given by:

$$tr[n,\acute{n}] = \frac{1}{\sqrt{K}} \sum_{k=0}^{K-1} s[n,k] e^{j2\pi k \acute{n}}, \tag{1.5}$$

where we have exploited that $e^{j2\pi(k-K)\Delta F t} = e^{j2\pi k \acute{n}}$ for $t = \acute{n} T_s$. Apart from a normalization factor, Equation 1.5 describes the IDFT of the K number of subcarrier symbols to be transmitted. In the context of a digital implementation the signal samples, which are located between the time

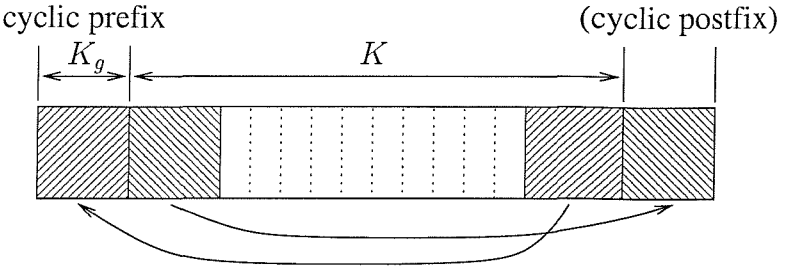

Figure 1.2: Generation of the cyclic prefix- and postfix in the time-domain. The cyclic prefix is generated by replicating the last K_g number of IFFT output samples at the front of the OFDM symbol. By contrast, the cyclic postfix is generated by copying a number of IFFT output samples from the beginning to the end of the OFDM symbol.

instants of $t = \acute{n}T_s$, $\acute{n} = 0, \ldots, K-1$ are generated by lowpass filtering. Similarly, following sampling of the time-continuous signal, demodulation at the receiver can be implemented with the aid of the DFT.

1.3.1.3 Inter-Symbol Interference Reduction Using a Guard Interval

The ISI potentially affects the first few samples of an OFDM symbol in the time-domain[1]. However, as a result of the DFT-based demodulation at the OFDM receiver this problem is mitigated by spreading its effects across the K different subcarriers in the frequency-domain. Nonetheless, a persistent performance degradation is observed, when encountering a multipath channel scenario, opposed to an ISI free pure AWGN channel scenario. This problem is addressed in the context of the OFDM system with the aid of a guard interval or cyclic prefix, which is generated in the time-domain by replicating the last K_g number of IFFT output samples. As illustrated in Figure 1.2, these samples a copied from the back to the beginning of the OFDM symbol. Upon appropriately choosing the number of guard interval samples, namely by ensuring that we have $K_g \geq \lceil T_m/T_s \rceil$([2]), where T_m is the multipath spread of the channel and by assuming furthermore perfect synchronization, namely that the start of the FFT window coincides with the first arriving multipath components, the FFT window will only contain cyclically shifted, but weighted[3] replicas of the original OFDM symbol transmitted. Hence, no ISI is incurred between the consecutive OFDM symbols. As a result of employing the guard interval- or cyclic prefix portrayed in Figure 1.2, effectively the OFDM symbol transmitted is cyclically convolved with the CIR.

Hence, when viewing the corresponding operations in the frequency-domain, after FFT-based

[1]This is correct under the assumption of perfect synchronization with respect to the first arriving multipath component.

[2]The Gauss brackets $\lceil \rceil$ denote the smallest integer, which is not less than the original argument enclosed in brackets.

[3]The weighting is due to the multiplication of each replica with the specific path's time-variant complex transfer factor.

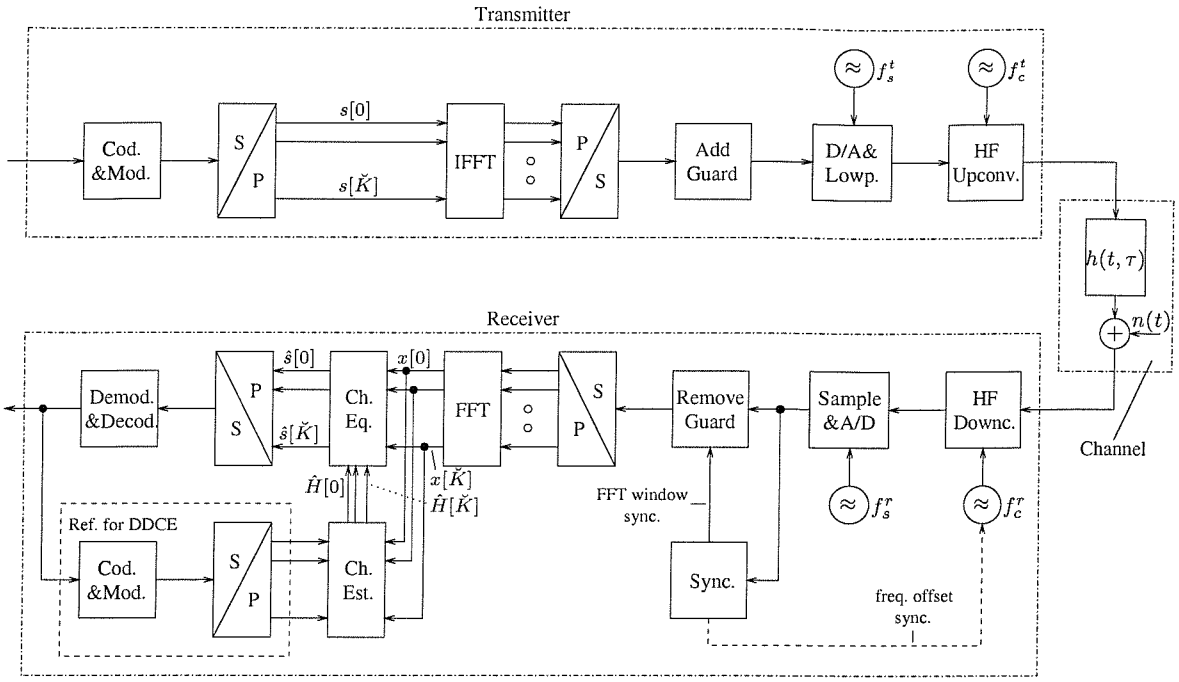

Figure 1.3: Simplified illustration of the OFDM transmitter and receiver, which are linked via the transmission channel. The time-domain signal generated in the OFDM transmitter seen at the top is conveyed over the transmission channel, which is characterized by the time-variant impulse response $h(t, \tau)$ plus the AWGN contribution $n(t)$, to the OFDM receiver.Note that $\breve{K} = K - 1$.

demodulation at the receiver, each subcarrier symbol was multiplied by the complex channel transfer factor encountered at this frequency. This renders the frequency-domain equalization process computationally inexpensive compared to conducting the equalization in the time-domain. In order to render the OFDM system furthermore insensitive against imperfections of the FFT window synchronization, namely against a delayed positioning of the FFT window, also a cyclic postfix can be appended to the OFDM symbol by copying signal samples from the beginning to the end of the OFDM symbol. We note however, that the redundancy introduced by the guard interval implies a decrease of the system's bandwidth efficiency. This bandwidth efficiency reduction can be compensated by increasing the K number of subcarriers, although unfortunately at the same time this results in increasing the system's sensitivity against frequency offsets between the transmitter's and receiver's local oscillator frequencies.

1.3.1.4 Structure of the OFDM Transmitter and Receiver

In this section we will briefly review the typical structure of the OFDM transmitter- and receiver employed in a single-user, single reception antenna scenario. A simplified block diagram of these components is portrayed in Figure 1.3. Specifically, the OFDM transmitter is shown at the top, while

the OFDM receiver at the bottom of Figure 1.3. Furthermore, a simplified model of the transmission channel, constituted by its time-variant impule response $h(t, \tau)$ and the Additive White Gaussian Noise (AWGN) contribution $n(t)$ is shown at the right-hand side of Figure 1.3.

1.3.1.4.1 OFDM Transmitter Specifically, in the OFDM transmitter seen at the top of Figure 1.3 the incoming bit-stream is optionally subjected to channel coding followed by the mapping of blocks of $\log_2 M_c$ number of consecutive bits to one of the M_c number of constellation points associated with the M_c-ary modulation scheme employed ("Cod.&Mod."). The serial stream of symbols is then transformed into blocks of K parallel symbols each ("S/P") for forming the OFDM symbol. Each of the symbols contained in a block then modulates one of the K subcarriers, which is achieved with the aid of the IFFT, as highlighted in Section 1.3.1.2.2. Based on the block of K parallel IFFT output samples, a serial stream of time-domain signal samples is generated ("P/S") and the guard interval ("Add Guard") is concentrated at the beginning of this block in order to render the transmitted OFDM symbol insensitive against the dispersion effects of the multipath channel, as alluded to in Section 1.3.1.3. Then the binary, time-discrete representation of the signal to be transmitted is converted to an analogue, time-continous representation with the aid of a Digital-to-Analogue (D/A) converter followed by lowpass filtering ("D/A&Lowp."). Next the High-Frequency (HF) stage of Figure 1.3 is encountered, which includes up-conversion to the carrier frequency f_c and power-amplification ("HF Upconv.").

The signal is then conveyed over the AWGN-contaminated multipath transmission channel, which can be described as a convolution with the channel's time-variant CIR $h(t, \tau)$, followed by an additive perturbation with the Gaussian noise process $n(t)$.

1.3.1.4.2 OFDM Receiver The OFDM receiver which is illustrated at the bottom of Figure 1.3 exhibits a structure, which is almost symmetric to that of the transmitter depicted at the top of Figure 1.3. After HF down-conversion ("HF downc."), followed by sampling and Analogue-to-Digital (A/D) conversion ("Sample&A/D") the guard interval is removed ("Remove Guard") under the control of the synchronization unit ("Sync."). This implies deciding upon the start of the FFT window. Furthermore, the synchronization unit also generates a signal for performing the correction of the frequency-offset potentially incurred between the transmitter's and receiver's local oscillators. This is necessary, since a frequency offset results in a loss of orthogonality between the sinc-shaped subcarrier transfer functions of Figure 1.1. This is known to inflict inter-subcarrier interference, with the effect of degrading the effective SNR in the different subcarriers. Again, similarly to the processing at the transmitter, based on a serial-to-parallel conversion ("S/P"), blocks of K signal samples are transformed to the frequency-domain with the aid of the FFT, resulting in a set of K subcarrier signals, $x[n, k]$, $k = 0, \ldots, K-1$. As argued in Section 1.3.1.3, in case of an ISI-free scenario, in the frequency-domain the effects of the multipath channel manifest themselves as

the multiplication of each subcarrier symbol with the channel's transfer factor at this frequency-position, plus an AWGN contribution, which can be expressed as:

$$x[n,k] = s[n,k] \cdot H[n,k] + n[n,k], \tag{1.6}$$

where the channel transfer factor $H[n,k]$ is given by:

$$H[n,k] = H(nT_f, k\Delta F) = \underset{\tau->f}{\mathcal{FT}}\Big\{h(nT_f,\tau)\Big\}|_{f=k\Delta F}, \tag{1.7}$$

and $T_f = (K + K_g)T_s$ represents the OFDM symbol duration. Furthermore, $\mathcal{FT}\{\}$ denotes the Fourier Transform. Note that Equation 1.7 is based on the simplified assumption that the CIR is time-invariant for the duration of an OFDM symbol period. For the case of the more realistic scenario of encountering a CIR, which is time-variant during the transmission of a specific OFDM symbol it can be shown that the effective subcarrier channel transfer factors are given as the Fourier transform of the complex CIR tap values, which have been averaged over the duration of the OFDM symbol period. In addition, Inter-Subcarrier Interference (ICI) would be observed as a consequence of the loss of orthogonality between the different subcarrier transfer functions. In order to facilitate the correct detection of the different users' transmitted symbols in the case of coherent detection, the effects of the channel must be removed from the signal $x[n,k]$ associated with the K different subcarriers $k = 0,\ldots,K-1$. This is the task of the equalizer block ("Ch. Eq.") of Figure 1.3, which performs a normalization of the signal received by each subcarrier with its associated channel transfer factor estimate. This results in a linear estimate $\hat{s}[n,k]$ of the symbol transmitted on the k-th subcarrier in the following form:

$$\hat{s}[n,k] = \frac{x[n,k]}{\hat{H}[n,k]}, \tag{1.8}$$

where we have $k = 0,\ldots,K-1$. Following again a parallel-to-serial ("P/S") conversion as seen in Figure 1.3, the linear symbol estimates are demodulated and potentially channel-decoded ("Demod.&Decod."). A prerequisite for obtaining linear symbol estimates according to Equation 1.8 is the availability of the channel transfer factor estimates $\hat{H}[n,k]$, $k = 0,\ldots,K-1$, which are generated within the channel estimation block ("Ch. Est.") of Figure 1.3. Various approaches are known from the literature for performing the channel estimation task, namely pilot-assisted-, decision-directed and blind methods. While in the pilot-assisted case the channel estimation is performed based on a number of dedicated subcarriers, which employ pilot symbols known both to the receiver and the transmitter, in the decision-directed case the symbol decisions are remodulated and then employed as 'pilot symbols'. The process of remodulating the subcarrier symbol-decisions is represented by the box at the bottom of Figure 1.3, which is enclosed in dashed lines. In the next section we will summarize some of the main design aspects of OFDM systems, which have been addressed by researchers.

1.3.1.5 Design Aspects of OFDM Systems Adressed by Research

Before we embark on outlining the structure of multi-user SDMA-OFDM systems in Section 1.3.2, here we summarize some of the main aspects of OFDM systems, which have been addressed by researchers over the past few decades. These are local oscillator frequency- and timing-synchronization, Peak-to-Average Power Ratio (PAPR) reduction, multiple-access concepts, channel estimation, channel coding and adaptive modulation of Sections 1.3.1.5.1, 1.3.1.5.2, 1.3.1.5.3, 1.3.1.5.4, 1.3.1.5.5 and 1.3.1.5.6, respectively.

1.3.1.5.1 Frequency- and Time-Synchronization Recall from Section 1.3.1.4 that two important tasks to be performed at the receiver are the local oscillator frequency- and time-sychronization [35, 36]. A residual frequency offset results in a loss of orthogonality between the different subcarriers' transfer functions with the effect of imposing frequency-domain ICI and consequently reducing the effective subcarrier SNR. Furthermore, accurate timing-synchronization is necessary for correctly determining the start of the FFT window [35, 36]. Again, an inaccurate timing-synchronization potentially results in ISI, with the consequence of reducing the effective subcarrier SNR. These effects can be reduced by increasing the length of the cyclic prefix- and postfix, however, at the cost of also reducing the bandwidth available for data transmissions.

1.3.1.5.2 Peak-to-Average Power Ratio and Power Amplifier Non-Linearities A further aspect of OFDM systems which has to be appropriately dealt with is that of a potentially excessive Peak-to-Average Power Ratio (PAPR) [36] measured at the IFFT output described by Equation 1.5, which is associated with the OFDM transmitter seen at the top of Figure 1.3. Depending on the set of subcarrier symbols to be transmitted, the modulated signal's peak amplitude might become excessive for some time-domain samples due to a constructive superposition of the different subcarriers' associated time-domain signal functions. Hence, the power amplifier employed at the transmitter is required to cater for peak-power values, which might substantially differ from the average power output. A further aspect is that hence the power amplifier is required to be as linear as possible, which is particularly difficult to achieve for the potentially large range of amplitudes to be supported. Hence often linear class-A amplifiers have to be used, which have a low power-efficiency. Otherwise the amplifier non-linearities result in high out-of-band emissions due to the harmonic distortions generated. Therefore, substantial efforts have been made by researchers for reducing the PAPR of OFDM symbols [37, 38, 39, 40, 41, 42, 43, 44, 45, 46, 47, 48, 49, 50].

1.3.1.5.3 Multiple-Access Concepts: TDMA/FDMA/CDMA/SDMA Various multiple-access approaches are known from the literature of single-carrier communications systems for supporting the transmissions of a multiplicity of users in mobile communications environments. The most common schemes are Time-Division Multiple Access (TDMA) [51], where each user is assigned the

entire available bandwidth for a limited time-duration, as well as Frequency-Division Multiple Access (FDMA) [51], where the different users are assigned different portions of the frequency-band, which supports their simultaneous communications. Furthermore, Code-Division Multiple Access (CDMA) [52] may be employed, where the different users share the entire available frequency-band, while their separation at the receiver is facilitated with the aid of unique user-specific spreading codes. Finally, in recent years Space-Division Multiple Access (SDMA) [53], where the different users share the same frequency-band, while their separation at the receiver is facilitated with the aid of their unique spatial signature in the context of employing an array of antennas at the receiver, has gained popularity. The suitability of these techniques for an application in the context of OFDM has been investigated in a variety of publications.

1.3.1.5.4 Channel Estimation As argued in the context of single-user OFDM systems in Section 1.3.1.4 one of the prerequisites for employing coherent subcarrier symbol detection at the receiver is the availability of the different subcarriers' channel transfer factor estimates. The channel estimation strategies can be separated into three categories, namely *pilot-assisted*, *decision-directed* and *blind approaches*.

In the context of pilot-assisted channel estimation [54, 55, 56, 57, 58, 59, 60, 61, 62, 63, 64] the channel's transfer function is estimated based only on the initial transfer factor estimates provided by dedicated pilot subcarriers, whose associated transmitted symbols are known both to the receiver and to the transmitter. By contrast, in the context of decision-directed approaches [65, 66, 13, 67, 68, 17, 15, 18, 69] the sliced symbols available at the receiver's output are remodulated and then employed as 'pilots'. The decision-directed approach will be further elaborated on in the context of our discussions in Section 2. As a third alternative, blind approaches [70, 71, 72, 73] are known from the literature.

1.3.1.5.5 Channel Coding Besides employing standard channel coding schemes, such as convolutional coding and turbo-coding [74, 36] in the context of OFDM, investigations have also been conducted with respect to employing coded modulation, namely Trellis-Coded Modulation (TCM) and Turbo Trellis-Coded Modulation (TTCM). Furthermore, the employment of Residual Number Systems (RNS) based codes has been investigated [75, 76].

1.3.1.5.6 Adaptive Modulation In the context of employing OFDM in a wide-band channel scenario, where the channel transfer function's amplitude is known to fluctuate significantly across the different subcarriers, an effective approach for reducing the BER while keeping the system's throughput constant, or for increasing the throughput while keeping the BER constant, is provided by adaptive modulation [36, 77, 78, 3]. The strategy common to both schemes is to assign a more robust, lower throughput modulation mode to low-quality subcarriers in terms of their SNR, while

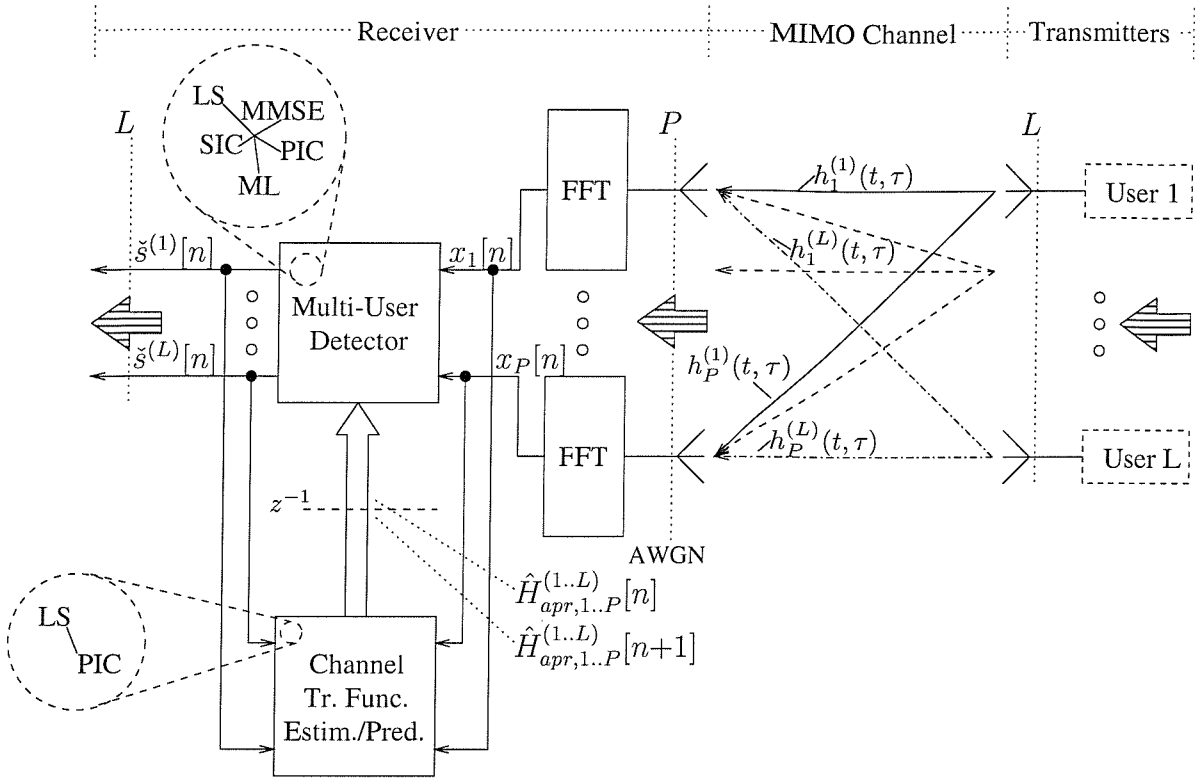

Figure 1.4: Simplified illustration of the SDMA-OFDM scenario. The L different users, each equipped with a single transmit antenna are linked to the BS receiver, which employs P number of antenna elements, via the $L \times P$-dimensional MIMO channel. The output signal of each receiver antenna element is separately subjected to FFT-based demodulation, which results in the subcarrier signals $x_p[n,k]$, $p = 1,\ldots,P$, $k = 0,\ldots,K-1$. This is followed by subcarrier-based multi-user detection with the aim of obtaining the sliced symbols $\check{s}^{(l)}[n,k]$, $l = 1,\ldots,L$, $k = 0,\ldots,K-1$. Based on these sliced symbols and on the received subcarrier signals, *a priori* estimates $\hat{H}^{(l)}_{apr,p}[n,k]$ of the channel transfer factors encountered during the next OFDM symbol period are generated.

a less robust, higher throughput modulation mode to higher-quality subcarriers. A prerequisite for the employment of AOFDM is the knowledge of the channel's transfer function associated with the following transmission timeslot, for which the modulation mode assignment has to be performed. This can be efficiently provided with the aid of channel transfer function prediction approaches, as it will be demonstrated in the context of our discussions in Chapter 2.

1.3.2 Multi-User Multiple Reception Antenna OFDM Scenario

In Section 1.3.1 we have outlined the basic principles of OFDM and the associated transmitter- and receiver structure in the context of a single-user single-reception antenna assisted scenario. Specifically, in Section 1.3.1.5.3 we argued that employing Space-Division Multiple Access (SDMA) is a

viable approach for supporting the transmissions of multiple users in a mobile OFDM-based communications environment. More specifically, the L different users' transmitted signals are separated at the receiver with the aid of their spatial signature, namely based on the knowledge of their unique set of channel impulse responses or transfer functions associated with each user's transmit antenna and the P different BS receiver antenna elements. This SDMA-MIMO channel scenario is shown at the right-hand side of Figure 1.4.

While in the multi-user SDMA-OFDM scenario the same OFDM transmitter design can be employed as in the single-user scenario, the SDMA-OFDM receiver shown at the left-hand side of Figure 1.4 exhibits important changes compared to the single-user, single-reception antenna based receiver of Figure 1.3. Besides the simplifications, namely that of removing the time-domain HF down-conversion-, analogue-to-digital conversion-, synchronization-, serial-to-parallel and parallel-to-serial conversion- as well as the demodulation and decoding blocks explicitly shown in the single-user receiver of Figure 1.3, we have substituted the single FFT block by separate FFT blocks for the different receiver branches. At the FFT blocks' outputs the different reception branches' frequency-domain subcarrier signals $x_p[n,k],\ p = 1,\ldots,P,\ k = 0,\ldots,K-1$ become available.

Furthermore, the channel equalizer- and demodulator blocks of Figure 1.3 have been substituted by the multi-user detector block as seen in Figure 1.4. At the output of the multi-user detector each of the L different users' sliced symbols $\check{s}^{(l)}[n,k],\ l = 1,\ldots,L,\ k = 0,\ldots,K-1$ become available. As it will be shown in Section 4 for the case of the so-called linear detectors, namely the Least-Squares (LS)- and the Minimum Mean-Square (MMSE) based detectors, the detection process constituted by the signal combining- and classification process is sequentially performed, which is equivalent to the channel equalization- and demodulation processes performed in the context of the single-user receiver of Figure 1.3. By contrast, in the context of the more effective detectors, namely Successive Interference Cancellation (SIC), Parallel Interference Cancellation (PIC) and Maximum Likelihood (ML) detection, *a priori* knowledge of the other users' transmitted symbols is required at each subcarrier position for the identification of a specific user's transmitted subcarrier symbol.

The multi-user detection process is based on estimates $\hat{H}_p^{(l)}[n,k]$ of the channel transfer factors $H_p^{(l)}[n,k]$, $l = 1,\ldots,L$, $p = 1,\ldots,P$, $k = 0,\ldots,K-1$, associated with the K different subcarriers of the $L \cdot P$ number of MIMO channels. Hence, the channel estimator of Figure 1.3 designed for estimating a single set of K number of channel transfer factors has to be substituted by a multi-channel estimator, as shown in Figure 1.4. While in general both pilot-assisted- as well as decision-directed approaches could be employed as in the single-user scenario of Figure 1.3, in Figure 1.4 we have portrayed the scenario of decision-directed channel estimation. More specifically, the channel transfer factor estimates generated during the current OFDM symbol period - after detection of the different users' symbols - are employed in the detection stage during the next OFDM symbol period. Two of the most promising estimation approaches are the LS-assisted DDCE and

the PIC-assisted DDCE, which will be detailed in Section 3.

Chapter 2

Decision-Directed Channel Estimation for Single-User OFDM

2.1 Introduction

In recent years numerous research contributions have appeared on the topic of channel transfer function estimation techniques designed for employment in single-user, single transmit antenna assisted OFDM scenarios, since the availability of an accurate channel transfer function estimate is one of the prerequisites for coherent symbol detection at an OFDM receiver. The techniques proposed in the literature can be classified as *pilot-assisted*, *decision-directed* (DD) and *blind* channel estimation (CE) methods.

In the context of pilot-assisted channel transfer function estimation a subset of the available subcarriers is dedicated to the transmission of specific pilot symbols known to the receiver, which are used for 'sampling' the desired channel transfer function. Based on these samples of the frequency domain transfer function, the well-known process of interpolation is used for generating a transfer function estimate for each subcarrier residing between the pilots. This is achieved at the cost of a reduction of the number of useful subcarriers available for data transmission. The family of *pilot-assisted* channel estimation techniques was investigated for example by Chang and Su [64], Höher [54, 56, 57], Itami *et al.* [58], Li [60], Tufvesson and Maseng [55], Wang and Liu [62], as well as Yang *et al.* [59, 61, 63].

By contrast, in the context of Decision-Directed Channel Estimation (DDCE) all the sliced and remodulated subcarrier data symbols are considered as pilots. In the absence of symbol errors and also depending on the rate of channel fluctuation, it was found that accurate channel transfer function estimates can be obtained, which are often of better quality in terms of the channel transfer function estimator's mean-square error (MSE), than the estimates offered by pilot-assisted schemes. This is because the latter arrangements usually invoke relatively sparse pilot patterns.

Year	Author	Contribution
'91	Höher [54]	Cascaded 1D-FIR channel transfer factor interpolation was carried out in the frequency- and time-direction for frequency-domain PSAM.
'93	Chow, Cioffi and Bingham [79]	Subcarrier-by-subcarrier based LMS related channel transfer factor equalization techniques were employed.
'94	Wilson, Khayata and Cioffi [65]	Linear channel transfer factor filtering was invoked in the time-direction for DDCE.
'95	van de Beek, Edfors, Sandell, Wilson and Börjesson [66]	DFT-aided CIR-related domain Wiener-filter based noise-reduction was advocated for DDCE. The effects of leakage in the context of non-sample-spaced CIRs were analysed.
'96	Edfors, Sandell, van de Beek, Wilson and Börjesson[13]	SVD-aided CIR-related domain Wiener-filter based noise-reduction was introduced for DDCE.
	Frenger and Svensson [67]	MMSE-based frequency-domain channel transfer factor prediction was proposed for DDCE.
	Mignone and Morello [68]	FEC was invoked for improving the DDCE's remodulated reference.
'97	Tufvesson and Maseng [55]	An analysis of various pilot patterns employed in frequency-domain PSAM was provided in terms of the system's BER for different Doppler frequencies. Kalman filter-aided channel transfer factor estimation was used.
	Höher, Kaiser and Robertson [56, 57]	Cascaded 1D-FIR Wiener filter channel interpolation was utilized in the context of 2D-pilot pattern aided PSAM
'98	Li, Cimini and Sollenberger [17]	An SVD-aided CIR-related domain Wiener filter based noise-reduction was achieved by employing CIR-related tap estimation filtering in the time-direction.
	Edfors, Sandell, van de Beek, Wilson and Börjesson [15]	A detailed analysis of SVD-aided CIR-related domain Wiener-filter based noise-reduction was provided for DDCE, which expanded the results of [13].
	Tufvesson, Faulkner and Maseng [80]	Wiener filter-aided frequency-domain channel transfer factor prediction assisted pre-equalization was studied.
	Itami, Kuwabara, Yamashita, Ohta and Itoh [58]	Parametric finite-tap CIR model based channel estimation was employed for frequency-domain PSAM.

Table 2.1: Contributions on channel transfer factor estimation for single-transmit antenna assisted OFDM.

Year	Author	Contribution
'99	Al-Susa and Ormondroyd [18]	DFT-aided Burg-algorithm assisted adaptive CIR-related tap prediction filtering was employed for DDCE.
	Yang, Letaief, Cheng and Cao [59]	Parametric, ESPRIT-assisted channel estimation was employed for frequency-domain PSAM.
'00	Li [60]	Robust 2D frequency-domain Wiener filtering was suggested for employment in frequency-domain PSAM using 2D pilot patterns.
'01	Yang, Letaief, Cheng and Cao [81]	Detailed discussions of parametric, ESPRIT-assisted channel estimation were provided in the context of frequency-domain PSAM [59].
	Zhou and Giannakis [70]	Finite alphabet-based channel transfer factor estimation was proposed.
	Wang and Liu [62]	Polynomial frequency-domain channel transfer factor interpolation was contrived.
	Yang, Cao, and Letaief [63]	DFT-aided CIR-related domain one-tap Wiener-filter based noise-reduction was investigated, which is supported by variable frequency-domain Hanning windowing.
	Lu and Wang [71]	A Bayesian blind turbo receiver was contrived for coded OFDM systems.
	Li and Sollenberger [69]	Various transforms were suggested for CIR-related tap estimation filtering assisted DDCE.
	Morelli and Mengali [82]	LS- and MMSE based channel transfer factor estimators were compared in the context of frequency-domain PSAM.
'02	Chang and Su [64]	Parametric quadrature surface based frequency-domain channel transfer factor interpolation was studied for PSAM.
	Necker and Stüber [73]	Totally blind channel transfer factor estimation based on the finite alphabet property of PSK signals was investigated.

Table 2.2: Contributions on channel transfer factor estimation for single-transmit antenna assisted OFDM.

The family of *decision-directed* channel estimation techniques was investigated for example by van de Beek *et al.* [66], Edfors *et al.* [13, 15], Li *et al.* [17], Li [69], Mignone and Morello [68], Al-Susa and Ormondroyd [18], Frenger and Svensson [67], as well as Wilson *et al.* [65].

Furthermore, the family of *blind* channnel estimation techniques was studied by Lu and Wang [71], Necker *et al.* [73], as well as by Zhou and Giannakis [70]. The various contributions have been summarized in Tables 2.1 and 2.2.

In order to render the various DDCE techniques more amenable to employment in scenarios associated with a relatively high rate of channel variation expressed in terms of the OFDM symbol normalized Doppler frequency, linear prediction techniques well-known from the speech coding literature [83, 84] can be invoked. To elaborate a little further, we will substitute the CIR-related tap

estimation filter - which is part of the two-dimensional channel transfer function estimator proposed in [17] - by a CIR-related tap prediction filter. The employment of this CIR-related tap prediction filter enables a more accurate estimation of the channel transfer function encountered during the forthcoming transmission timeslot and thus potentially enhances the performance of the channel estimator. We will be following the general concepts described by Duel-Hallen *et al.* [85] and the ideas presented by Frenger and Svensson [67], where frequency-domain prediction filter assisted DDCE was proposed. Furthermore, we should mention the contributions of Tufvesson *et al.* [80, 29], where a prediction filter assisted frequency domain pre-equalization scheme was discussed in the context of OFDM. In a further contribution by Al-Susa and Ormondroyd [18], adaptive prediction filter assisted DDCE designed for OFDM has been proposed upon invoking techniques known from speech-coding, such as the Levinson-Durbin algorithm or the Burg algorithm [83, 86, 87] in order to determine the predictor coefficients.

Chapter 2 has the following structure. In Section 2.2 the philosophy of the CIR-tap prediction filter assisted DDCE will be described, while its performance will be studied in Section 2.3, in the context of both the MSE and the BER. In Section 2.4 a system will be described and characterized, which combines decision-directed channel prediction[1] with adaptive modulation since the efficiency of adaptive modulation critically depends on the quality of channel prediction. Our conclusions will be offered in Section 2.5.

2.2 Description

Let us commence our discourse by outlining the structure of Section 2.2. In Section 2.2.1 the concepts of DDCE are outlined with an emphasis on generating the initial *a posteriori* least-squares channel transfer function estimate on the basis of the sliced and remodulated subcarrier symbols. Furthermore, in an effort to improve the initial *a posteriori* least-squares channel estimate, in Section 2.2.2 the concepts of the Karhunen-Loeve Transform (KLT) based 1D-MMSE estimator proposed by Sandell and Edfors *et al.* [13, 16, 14, 15] will be discussed. Based on the structure of this estimator, a 2D-MMSE estimator was proposed by Li *et al.* [17], which potentially capitalizes on the availability of an infinite number of previous initial *a posteriori* channel estimates associated with past OFDM symbols. These concepts will discussed in Section 2.2.3. The improved *a posteriori* channel transfer function estimate calculated for the current OFDM symbol is employed as an *a priori* channel estimate during the demodulation of the OFDM symbol received in the next timeslot. Due to the potentially considerable decorrelation of the channel transfer function incurred between consecutive OFDM symbols, which critically depends on the OFDM symbol normalized Doppler frequency, it was found beneficial to directly obtain an *a priori* estimate of the channel transfer

[1] In the following we will refer to channel transfer function prediction simply as channel prediction. Furthermore, note that the set of K different subcarriers' channel transfer factors is referred to here as the channel transfer function.

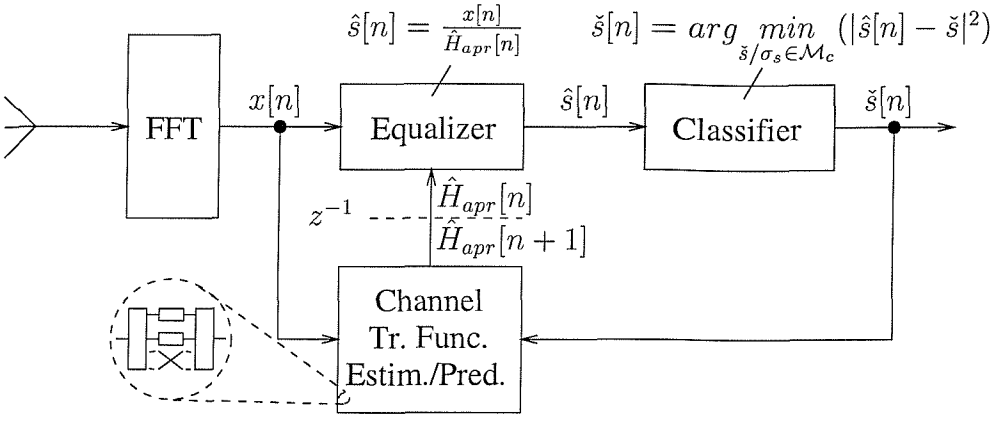

Figure 2.1: Stylized illustration of the OFDM receiver employing decision-directed channel estimation- or prediction. Following FFT processing, the complex frequency-domain signal $x[n, k]$ associated with each of the K subcarriers $k = 0, \ldots, K-1$ is equalized based on the *a priori* channel transfer factor estimates generated during the previous OFDM symbol period for employment during the current period. As a result, the linear estimates $\hat{s}[n, k]$ of the transmitted signals $s[n, k]$ are obtained. These estimates are classified with the aid of the Maximum Likelihood (ML) approach, yielding the complex symbols $\check{s}[n, k]$ that are most likely to have been transmitted. These classified symbols $\check{s}[n, k]$ are then employed together with the received subcarrier signals $x[n, k]$ for generating *a priori* channel transfer factor estimates for employment during the $(n+1)$-th OFDM symbol period. The specific structure of the channel transfer function estimator- or predictor, which is indicated by the stylized illustration at the bottom left corner, will be detailed in the context of Section 2.2. Note that in the above illustration the subcarrier index k has been omitted from the different variables for the sake of visual clarity.

function for the next OFDM symbol upon invoking the MMSE *prediction* techniques to be detailed in Section 2.2.4 instead of the related MMSE *estimation* techniques of Section 2.2.3. Hence, in Section 2.2.4 we will explicitly compare the Finite Impulse Response (FIR) Wiener filter based estimation- and prediction techniques. A prerequisite for the application of Wiener filtering [87] in the context of channel transfer function estimation or prediction along the time-direction is the availability of an estimate of the channel's statistics in form of the spaced-time correlation function. Note that the various representations of the channel's statistics are outlined in Figure 6.2. In Section 2.2.5 two different approaches are invoked for providing these estimates. Specifically, robust Wiener filtering employing a uniform, ideally support-limited scattering function will be contrasted to a block-adaptive estimation of the channel's statistics, which is combined with the calculation of the Wiener filter coefficients. Numerous techniques are known in the literature for solving the latter problem, such as the Levinson-Durbin algorithm [84] or the Burg algorithm [86, 83]. We will use the latter one.

2.2.1 Decision-Directed *A Posteriori* Least-Squares Channel Estimation

The following discussions are with reference to the decision-directed channel transfer function estimation- or prediction block seen at the bottom of Figure 2.1, which is the stylized illustration of an OFDM receiver.

An *a posteriori* least-squares estimate $\tilde{H}_{apt}[n,k]$ of the actual channel transfer factor $H[n,k]$ of the k-th subcarrier in the n-th OFDM symbol is obtained upon dividing the complex received OFDM symbol $x[n,k]$ by the subcarrier's sliced symbol $\check{s}[n,k]$ [17], yielding:

$$\begin{aligned}\tilde{H}_{apt}[n,k] &= \frac{x[n,k]}{\check{s}[n,k]},\ k=0,\ldots,K-1 \\ &= H[n,k]\cdot\frac{s[n,k]}{\check{s}[n,k]}+\frac{n[n,k]}{\check{s}[n,k]},\end{aligned} \tag{2.1}$$

where $H[n,k]$ denotes the complex Gaussian-distributed channel transfer factor having a variance of σ_H^2, which is unity. Furthermore, $s[n,k]$ represents the complex OFDM symbol transmitted, which exhibits zero mean and a variance of σ_s^2, and finally $n[n,k]$ is the additive noise contribution having a mean value of zero and variance of σ_n^2. The total noise variance σ_n^2 is constituted by the sum of the AWGN process' variance σ_{AWGN}^2 plus the variance of the Gaussian noise-like inter-subcarrier interference (ICI) contribution σ_{ICI}^2 [88]. The latter component can be neglected in fading channels exhibiting a low OFDM symbol normalized Doppler frequency $F_{D,K}$[2]. However, under high-mobility channel conditions - which may be encountered in worst-case scenarios - an estimate of σ_{ICI}^2 has to be provided [88]. Upon assuming error-free symbol decisions, where we have $\check{s}[n,k]=s[n,k]$, the *a posteriori* least-squares channel transfer factor estimate of Equation 2.1 is simplified to:

$$\tilde{H}_{apt}[n,k]=H[n,k]+\frac{n[n,k]}{s[n,k]}, \tag{2.2}$$

which has a mean-square estimation error of:

$$\begin{aligned}\text{MSE}_{apt}[n,k] &= E\{|H[n,k]-\tilde{H}_{apt}[n,k]|^2\} \\ &= \alpha\cdot\frac{\sigma_n^2}{\sigma_s^2}.\end{aligned} \tag{2.3}$$

In Equation 2.3 the so-called "modulation-noise enhancement factor" $\alpha = E\{|1/s[n,k]|^2\}$ [89] depends on the modulation mode employed in the k-th subcarrier. For M-PSK modulation for example, we have $\alpha_{\text{M-PSK}}=1$, while for 16-QAM $\alpha_{\text{16-QAM}}=17/9$ [89, 15].

In order to further reduce the *a posteriori* channel transfer factor estimation error, a one-dimensional (1D) minimum mean-square error (MMSE) channel estimator, which capitalizes on the *a posteriori*

[2]In the context of quantifying the effects of ICI a definition of the OFDM symbol normalized Doppler frequency according to $F_{D,K}=f_D K T_s$ - which is related to the FFT window's duration denoted by KT_s - is more appropriate, than its conventional definition expressed as $F_D=f_D(K+K_g)T_s$ [88]. This conventional definition is rather used for characterizing the channel's correlation in the context of investigating channel transfer function estimation schemes.

least-squares channel transfer factor estimates extracted from each OFDM symbol was proposed by Edfors *et al.* [13, 14, 15] as well as Sandell [16]. Its concepts will be outlined in Section 2.2.2. This channel estimation approach was later extended by Li *et al.* [17] to two dimensions, where the *a posteriori* least-squares channel transfer factor estimates of both the current and the previous OFDM symbols are invoked for obtaining an *improved a posteriori* channel transfer function estimate for the current OFDM symbol. The concepts of this estimator will be outlined in Section 2.2.3.

2.2.2 Enhancement of the *A Posteriori* Least-Squares Channel Transfer Factor Estimates by One-Dimensional MMSE Estimation

A one-dimensional (1D) minimum mean-square error (MMSE) channel estimator, which exploits the channel's correlation in the frequency direction was proposed by Edfors *et al.* [13, 14, 15] and Sandell [16], for inferring improved *a posteriori* channel transfer factor estimates $\hat{H}_{apt}[n,k]$ from the initial *a posteriori* least-squares channel transfer factor estimates $\tilde{H}_{apt}[n,\acute{k}]$, $\{k,\acute{k}\} = 0,\ldots,K-1$. Note that this estimator - in the absence of a rank-reduction, which will be further explained in Section 2.2.2.1 - is the time-domain related dual of a 1D-FIR Wiener filter, which invokes all the K least-squares channel transfer factor estimates available in a specific OFDM symbol.

The specific structure of this estimator is outlined in Section 2.2.2.1 with reference to Figure 2.2, where the 'Channel Estimator' block of Figure 1.3 is replaced by this schematic. Furthermore, an expression for the estimator's MSE valid under mismatched channel conditions is provided in Section 2.2.2.2.

2.2.2.1 Structure of the 1D-MMSE Channel Estimator

In a first step the vector $\tilde{\mathbf{H}}_{apt}[n] \in \mathbb{C}^{K\times 1}$ of K correlated *a posteriori* subcarrier channel transfer factor estimates $\tilde{H}_{apt}[n,k]$, $k = 0,\ldots,K-1$ associated with the K subcarriers of the n-th OFDM symbol is subjected to a unitary linear inverse transform $\mathbf{U}^{[f]H}$, specifically the Karhunen-Loeve Transform (KLT) [16, 15], where the matrix $\mathbf{U}^{[f]H}$ used by the KLT is determined from the channel's spaced-frequency correlation matrix $\mathbf{R}^{[f]}$.[3] This transforms the frequency domain least-squares channel transfer factor estimates to a time-domain related domain. As a result, the vector $\tilde{\mathbf{h}}_{apt}[n] \in \mathbb{C}^{K\times 1}$ of K uncorrelated CIR-related taps, $\tilde{h}_{apt}[n,l]$, $l = 0,\ldots,K-1$ is obtained. In matrix notation this can be expressed as:

$$\tilde{\mathbf{h}}_{apt}[n] = \mathbf{U}^{[f]H}\tilde{\mathbf{H}}_{apt}[n]. \tag{2.4}$$

[3]The EigenValue Decomposition (EVD) of the Hermitian spaced-frequency correlation matrix $\mathbf{R}^{[f]} = E\{\mathbf{H}\mathbf{H}^H\} \in \mathbb{C}^{K\times K}$, where $\mathbf{H} \in \mathbb{C}^{K\times 1}$ is the vector of the different subcarriers' channel transfer factors, is given by $\mathbf{R}^{[f]} = \mathbf{U}^{[f]}\Lambda^{[f]}\mathbf{U}^{[f]H}$, where $\mathbf{U}^{[f]} \in \mathbb{C}^{K\times K}$ is unitary, and $\Lambda^{[f]} \in \mathbb{R}^{K\times K}$ exhibits the form of $\Lambda^{[f]} = diag(\lambda_0^{[f]},\ldots,\lambda_{K-1}^{[f]})$. The diagonal elements of $\Lambda^{[f]}$ are referred to as the *eigenvalues* of $\mathbf{R}^{[f]}$ [87].

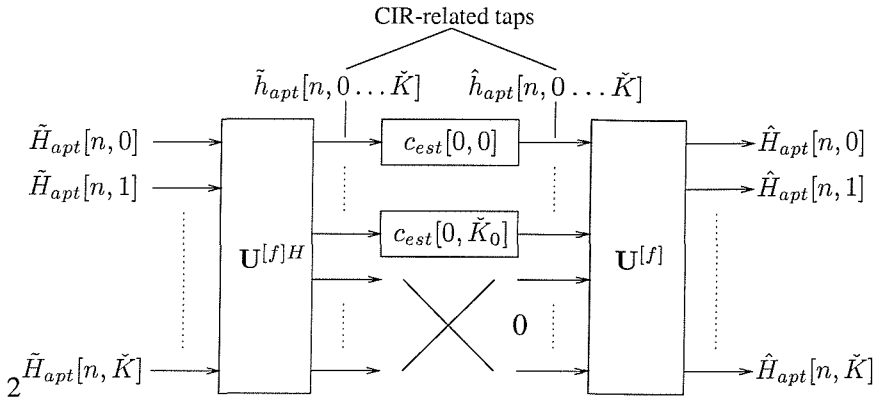

Figure 2.2: 1D-MMSE channel estimator design proposed by Edfors *et al.* [13, 14, 15] replacing the 'Channel Estimator' block of Figure 2.1. The set of *a posteriori* least-squares channel transfer factor estimates $\tilde{H}_{apt}[n,k]$, $k = 0,\ldots,K-1$ of Equation 2.1 is subjected to an inverse unitary linear transform $\mathbf{U}^{[f]H}$ which generates a set of uncorrelated CIR-related taps $\tilde{h}_{apt}[n,l], l = 0,\ldots,K-1$. Only the first K_0 coefficients are retained, the rest of them are set to zero. Each of the K_0 coefficients is subjected to time-direction one-tap Wiener filtering using the coefficients $c_{est}[0,l]$, $l = 0,\ldots,K-1$ given by Equation 2.5. Finally, a unitary transform $\mathbf{U}^{[f]}$ is applied for conveying the filtered CIR-related taps $\hat{h}_{apt}[n,l], l = 0,\ldots,K-1$ back to the frequency-domain, which yields the set of improved *a posteriori* channel transfer factor estimates $\hat{H}_{apt}[n,k]$, $k = 0,\ldots,K-1$. Note that the unitary transform matrix $\mathbf{U}^{[f]}$ is associated with the EVD of the channel's spaced-frequency correlation matrix $\mathbf{R}^{[f]} = \mathbf{U}^{[f]}\Lambda^{[f]}\mathbf{U}^{[f]H}$. For notational simplicity we have defined in the schematic $\check{K}_0 = K_0 - 1$ and $\check{K} = K - 1$.

In a second step linear *one-tap* Wiener filtering is performed separately for those CIR-related taps $\tilde{h}_{apt}[n,l]$, for which the variance is significant. The specific value of the l-th CIR-related tap's filter coefficient is given by [15]:

$$c_{est}[0,l] = \begin{cases} \frac{\lambda_l^{[f]}}{\lambda_l^{[f]}+\frac{\alpha}{\mathrm{SNR}}} & l = 0,\ldots,K_0-1 \\ 0 & l = K_0,\ldots,K-1 \end{cases}, \tag{2.5}$$

where $\lambda_l^{[f]}$ is the l-th eigenvalue associated with the EigenValue Decomposition (EVD) of the channel's spaced-frequency correlation matrix $\mathbf{R}^{[f]}$. Since for the set of practical multipath intensity profiles considered the variance $E\{|\tilde{h}_{apt}[n,l]|^2\}$ usually decreases along with increasing the delay index l, a standard complexity reduction procedure [89, 15] is to perform time-direction filtering individually for each of the CIR-related taps associated with the K_0 number of lowest values of l, while setting the CIR-related taps associated with higher delay or dispersion indices to zero. Again, this reduces the estimator's complexity at the cost of a certain MSE performance degradation due to removing some of the CIR-related taps conveying useful signal components. The filter operation can also be expressed in matrix notation, namely as:

$$\hat{\mathbf{h}}_{apt}[n] = \mathbf{C}_{est}[0]\tilde{\mathbf{h}}_{apt}[n], \tag{2.6}$$

where $\hat{\mathbf{h}}_{apt}[n] \in \mathbb{C}^{K\times 1}$ is the vector of filtered CIR-related tap values and the diagonal-shaped filter matrix $\mathbf{C}_{est}[0] \in \mathbb{R}^{K\times K}$ is given by:

$$\mathbf{C}_{est}[0] = diag(c_{est}[0,0], \ldots, c_{est}[0,K-1]). \tag{2.7}$$

In a last step the vector $\hat{\mathbf{h}}_{apt}[n]$ of filtered CIR-related tap values $\hat{h}_{apt}[n,l], l = 0,\ldots,K-1$ is transformed back to the OFDM symbol's frequency-domain representation with the aid of the unitary linear transform $\mathbf{U}^{[f]}$, yielding the vector $\hat{\mathbf{H}}_{apt}[n] \in \mathbb{C}^{K\times 1}$ of MMSE channel transfer factor estimates. Again, this can be formulated in matrix notation as:

$$\hat{\mathbf{H}}_{apt}[n] = \mathbf{U}^{[f]}\hat{\mathbf{h}}_{apt}[n]. \tag{2.8}$$

The 1D-MMSE channel estimator's structure is further illustrated in Figure 2.2.

2.2.2.2 Estimator MSE for Mismatched Channel Conditions

In practice the estimator's spaced-frequency correlation matrix $\tilde{\mathbf{R}}^{[f]}$ and its associated EVD, $\tilde{\mathbf{R}}^{[f]} = \tilde{\mathbf{U}}^{[f]}\tilde{\Lambda}^{[f]}\tilde{\mathbf{U}}^{[f]H}$, as well as the EVD of the channel's spaced-frequency correlation matrix $\mathbf{R}^{[f]}$, namely $\mathbf{R}^{[f]} = \mathbf{U}^{[f]}\Lambda^{[f]}\mathbf{U}^{[f]H}$, are typically different. We often refer to this scenario as a mismatch between the channel statistics assumed and those encountered. For this scenario Edfors *et al.* [15] derived an expression for the MSE of the rank-K_0 estimator seen in Figure 2.2:

$$\overline{\mathrm{MSE}}_{apt}|_{K_0}^{N_{tap}^{[t]}=1} = \frac{1}{K}\sum_{l=0}^{K_0-1}\left[v_l^{[f]}(1-\tilde{c}_{est}[0,l])^2 + \frac{\alpha}{\mathrm{SNR}}\tilde{c}_{est}^2[0,l]\right] + \frac{1}{K}\sum_{l=K_0}^{K-1} v_l^{[f]}, \tag{2.9}$$

where $\tilde{c}_{est}[0,l]$, $l = 0,\ldots,K_0-1$ is the set of filter coefficients following the philosophy of Equation 2.5. We note that the coefficients $\tilde{c}_{est}[0,l]$, $l = 0,\ldots,K_0-1$ are based on the potentially imperfect estimate $\tilde{\mathbf{R}}^{[f]}$ of the channel's spaced-frequency correlation matrix $\mathbf{R}^{[f]}$ and on the estimate $\tilde{\mathrm{SNR}}$ of the true SNR measured at the reception antenna. Furthermore, in Equation 2.9 the variable $v_l^{[f]}$ denotes the l-th diagonal element of the decomposition associated with the channel's spaced-frequency correlation matrix $\mathbf{R}^{[f]}$ with respect to the unitary transform matrix $\tilde{\mathbf{U}}^{[f]}$ instead of $\mathbf{U}^{[f]}$, which is formulated as $v_l^{[f]} = (\tilde{\mathbf{U}}^{[f]H}\mathbf{R}^{[f]}\tilde{\mathbf{U}}^{[f]})_{[l,l]}$. Also note that if $\tilde{\mathbf{U}}^{[f]} = \mathbf{U}^{[f]}$ holds, we have $v_l^{[f]} = \lambda_l^{[f]}$.

2.2.3 Enhancement of the *A Posteriori* Least-Squares Channel Transfer Factor Estimates by Two-Dimensional MMSE Estimation

Based on the 1D-MMSE channel estimator proposed by Edfors *et al.* [13, 14, 15], which was outlined in Section 2.2.2, a two-dimensional (2D) MMSE channel estimator exploiting the channel's correlation both in the frequency direction as well as in the time direction was proposed by Li *et al.* in [17]. The objective of Li's design was to infer improved *a posteriori* channel transfer factor estimates $\hat{H}_{apt}[n,k]$ from the initial *a posteriori* least-squares channel transfer factor estimates

$\tilde{H}_{apt}[n,\acute{k}]$, $\{k,\acute{k}\} = 0,\ldots,K-1$. This can be achieved by capitalizing not only on the most recent *a posteriori* estimates $\tilde{H}_{apt}[n,\acute{k}]$, $\acute{k} = 0,\ldots,K-1$, but also on the *a posteriori* least-squares channel transfer factor estimates $\tilde{H}_{apt}[n-\acute{n},\acute{k}]$, $\acute{n} = 1,\ldots,N_{tap}^{[t]}-1$, $\acute{k} = 0,\ldots,K-1$ of the $(N_{tap}^{[t]}-1)$ number of past OFDM symbols, where $(N_{tap}^{[t]}-1)$ denotes the order of the associated estimation filter. Note that in the absence of a rank-reduction, such as conducted by the scheme portrayed in Figure 2.2, this estimator is the time-domain related dual of a frequency-domain 2D-FIR Wiener filter, which invokes all least-squares channel transfer factor estimates available in a specific block of $N_{tap}^{[t]}$ number of OFDM symbols.

Our further discourse in Section 2.2.3 evolves as follows. In Section 2.2.3.1 we outline the difference between Li's 2D-MMSE estimator [17] and Edfors's 1D-MMSE estimator, which was the topic of Section 2.2.2. Furthermore, Section 2.2.3.2 highlights Li's discussions on the 2D-MMSE estimator's MSE performance under mismatched channel conditions, with an emphasis on the concepts of robustness or resilience against mismatched channel conditions. Finally, the idea of employing time-direction prediction filtering instead of time-direction estimation filtering[4], as advocated by Li *et al.* [17], will be augmented in Section 2.2.3.3.

2.2.3.1 Structure of the 2D-MMSE Estimator

As it was demonstrated by Li *et al.* [17], the two-dimensional channel transfer factor estimation problem can be readily separated into two one-dimensional estimation tasks, which is motivated by the separability of the channel's spaced-time spaced-frequency correlation function originally introduced in Figure 6.2. As noted before, instead of carrying out the channel transfer factor estimation in the frequency domain, the philosophy of rank-reduction in the CIR-related domain, portrayed in Figure 2.2 is used, which results in a reduced complexity.

The structure of Li's 2D-MMSE channel estimator shown in Figure 2.4 is identical to that of the 1D-MMSE channel estimator proposed by Edfors *et al.* [13, 14, 15], as outlined in Section 2.2.2, with the sole difference that $N_{tap}^{[t]}$-tap estimation filters are invoked in the CIR-related domain instead of one-tap filters. More explicitly, filtering of the specific l-th CIR-related tap in the time-direction is performed by capitalizing on the current value $\tilde{h}_{apt}[n,l]$ and on the $(N_{tap}^{[t]}-1)$ previous values $\tilde{h}_{apt}[n-\acute{n},l]$. This process is illustrated in Figure 2.3. As a result, in the case of estimation filtering [17] an improved *a posteriori* estimate $\hat{h}_{apt}[n,l]$ of $h[n,l]$ is obtained. By contrast, in case of prediction filtering, which will be the topic of Section 2.2.4 an *a priori* estimate $\hat{h}_{apr}[n+1,l]$ of $h[n+1,l]$ is obtained.

[4]The basic difference of time-direction channel prediction- and estimation filtering is that in the former an *a priori* channel transfer function estimate for the next OFDM symbol is obtained, while in the latter an improved *a posteriori* channel estimate for the current OFDM symbol.

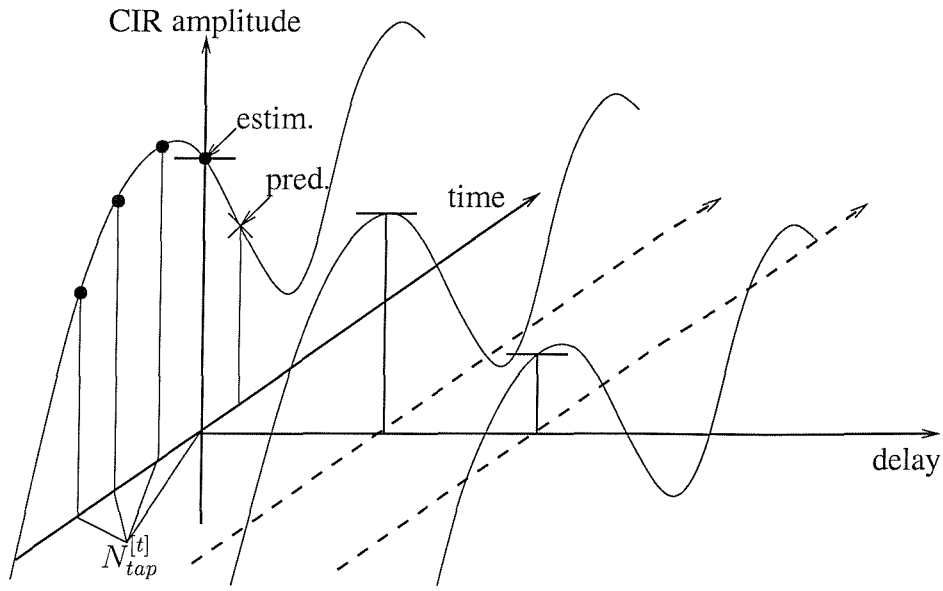

Figure 2.3: Stylized illustration of the estimation and prediction filter, both operating in the CIR-related domain using $N_{tap}^{[t]}$ number of previous *a posteriori* CIR-related tap estimates. In the context of *estimation filtering* improved *a posteriori* tap estimates are generated for the current OFDM symbol period, while in the context *prediction filtering a priori* tap estimates are computed for the next OFDM symbol period.

2.2.3.2 Estimator MSE for Mismatched Channel Statistics

The salient contribution of Li *et al.* [17] was the investigation of the channel estimator's MSE under mismatched channel conditions, where the spaced-time- spaced-frequency correlation function defined in Figure 6.2 and assumed in the calculation of the channel estimator coefficients actually differed from those of the transmission channel. Note that these investigations were conducted under the assumption of employing the *a posteriori* least-squares channel transfer factor estimates $\tilde{H}_{apt}[n - \acute{n}, \acute{k}]$, $\acute{n} = 1, \ldots, \infty$, $\acute{k} = 0, \ldots, K-1$ associated with an infinite number of past OFDM symbols in the 2D-MMSE estimation process. Let us summarize now the most significant associated aspects:

1. *MMSE Upper Bound for Channels Band-Limited to* $\omega_D = 2\pi f_D$ [17]. From the set of all possible channels band-limited to f_D the channel estimator exhibits the worst MSE for transmission over a channel having an ideally band-limited spaced-time correlation function, with associated Doppler-power spectral density function of:

$$S_{H,unif}(f_d) = \begin{cases} \frac{1}{2f_D}, & \text{if } |f_d| \leq f_D \\ 0, & \text{otherwise.} \end{cases} \tag{2.10}$$

In this case the MMSE averaged over the K subcarriers is given by [17]:

$$\overline{\mathrm{MMSE}}_{apt}|^{N_{tap}^{[t]}\to\infty} = \frac{\rho}{K}\sum_{l=0}^{K-1}\left(1 - \frac{1}{\left(1+\frac{\pi\lambda_l^{[f]}}{\omega_D\rho}\right)^{\frac{\omega_D}{\pi}}}\right). \tag{2.11}$$

In Equation 2.11 ω_D is defined as $\omega_D = 2\pi F_D$, where F_D is the OFDM symbol normalized Doppler frequency. Furthermore, the variable ρ is defined as the reciprocal of the average SNR, namely as $\rho = 1/\mathrm{SNR}$, and $\lambda_l^{[f]}$, $l \in \{0,\ldots,K-1\}$ denotes the l-th eigenvalue[5] of the EVD of the spaced-frequency channel correlation matrix $\mathbf{R}^{[f]}$. Please also note that in contrast to [17] here the first subcarrier is denoted by the index zero.

2. *Spaced-Time Correlation Function Mismatch* [17]. Let us assume that the spaced-frequency correlation function $\tilde{r}_H^{[f]}[\Delta k]$ of the channel estimator matches that of the channel $r_H^{[f]}[\Delta k]$ and that the spaced-time correlation function $\tilde{r}_H^{[t]}[\Delta n]$ of the channel estimator is ideally band-limited to f_D having a PSD function of $S_{H,unif}(f_d)$. Assume furthermore that the spaced-time correlation function $r_H^{[t]}[\Delta n]$ of the channel is associated with an arbitrary PSD function band-limited to f_D. Then the estimator's MSE is given by $\overline{\mathrm{MMSE}}_{apt}|^{N_{tap}^{[t]}\to\infty}$.

3. *Spaced-Frequency Correlation Function Mismatch* [17]. Let us assume that the spaced-time correlation function $\tilde{r}_H^{[t]}[\Delta n]$ of the channel estimator matches that of the channel, namely $r_H^{[t]}[\Delta n]$. Assume furthermore that the eigenvectors of the channel estimator's spaced-frequency correlation matrix $\tilde{\mathbf{R}}^{[f]}$ - which constitute the column vectors of the unitary transform matrix $\tilde{\mathbf{U}}^{[f]}$ - are identical to those of the channel's spaced-frequency correlation matrix $\mathbf{R}^{[f]}$ - which constitute the column vectors of the unitary transform matrix $\mathbf{U}^{[f]}$. Under these assumptions for a channel estimator having spaced-frequency correlation matrix related eigenvalues of [17]:

$$\tilde{\lambda}_l^{[f]} = \begin{cases} \frac{K}{K_0}, & \text{for } 0 \le l \le K_0 - 1 \\ 0, & \text{for } K_0 \le l \le K-1 \end{cases} \tag{2.12}$$

the estimator's MSE is identical for all channels having spaced-frequency correlation matrix related eigenvalues of $\lambda_l^{[f]} = 0$ for $K_0 \le l \le K-1$ and $\sum_{l=0}^{K_0-1}\lambda_l^{[f]} = K$.Note that these conditions can be directly derived from Equation 2.9 associated with the 1D-MMSE channel estimator. As shown in [15, 17], the assumption of $\tilde{\mathbf{U}}^{[f]} \approx \mathbf{U}^{[f]}$ is reasonable, since both the

[5]Note that in contrast to Li's discussions [17], where the l-th eigenvalue is denoted by d_l, here we follow the conventional notation and denote the l-th eigenvalue by $\lambda_l^{[f]}$.

transform matrices $\tilde{\mathbf{U}}^{[f]}$ and $\mathbf{U}^{[f]}$ can be approximated by the DFT matrix $\mathbf{W}$ given by [17]:

$$\mathbf{W} = \frac{1}{\sqrt{K}} \begin{pmatrix} 1 & 1 & \cdots & 1 \\ 1 & e^{-j(2\pi/K)} & \cdots & e^{-j(2\pi(K-1)/K)} \\ \vdots & \cdots & \cdots & \vdots \\ 1 & e^{-j(2\pi(K-1)/K)} & \cdots & e^{-j(2\pi(K-1)(K-1)/K)} \end{pmatrix}. \quad (2.13)$$

The average MSE of the robust estimator is hence given upon substituting the associated eigenvalues $\tilde{\lambda}_l^{[f]}$, $0 \leq l \leq K-1$ given by Equation 2.12 into Equation 2.11, yielding [17]:

$$\overline{\text{MMSE}}_{apt}|_{rob}^{N_{tap}^{[t]} \to \infty} = \frac{K_0 \rho}{K} \left(1 - \frac{1}{\left(1 + \frac{\pi K}{K_0 \omega_D \rho}\right)^{\frac{\omega_D}{\pi}}} \right). \quad (2.14)$$

The implications of the above assumptions on the estimator's design are illustrated more explicitly in Figure 2.4.

Li *et al.* [17] demonstrated furthermore that the MSE degradation incurred by a robust estimator having a spaced-time spaced-frequency correlation function (seen in Figure 6.2) associated with a uniform, ideally support-limited scattering function as stated in paragraphs 2) and 3) above is marginal compared to a relaxed-specification estimator, which only assumes a spaced-frequency correlation function associated with an ideally support-limited multipath intensity profile, as outlined in paragraph 3) while exactly matching the actual Doppler PSD of the channel.

We emphasize that in the context of the above-mentioned robust estimator design identical CIR-related domain filters are employed for filtering all the different K_0 number of CIR-related taps. We note that the associated estimation filtering could also be performed in the frequency-domain by capitalizing on the same set of filter coefficients. Hence again, the disadvantage of performing K individual time-direction filtering operations related to the different subcarriers, instead of K_0 number of time-direction filtering operations for the first K_0 CIR-related taps is the associated higher complexity. The assumption of employing an infinite number of previous *a posteriori* channel transfer function estimates in order to obtain an improved *a posteriori* channel transfer function estimate for the current OFDM symbol is unrealistic. Hence, Li *et al.* [17] also proposed a time-domain filter estimator, employing a finite number of previous CIR-related tap estimates. As expected, the MSE of this scheme is lower-bounded by the MSE of an estimator using an infinite number of previous CIR-related tap estimates, which was given in Equation 2.11.

2.2.3.3 Motivation of Time-Direction Channel Prediction Filtering

In [17] the improved *a posteriori* channel transfer factor estimates $\hat{H}_{apt}[n,k]$, $k = 0, \ldots, K-1$ were employed as *a priori* decision-directed channel transfer factor estimates for the demodulation process during the $(n+1)$-th transmission timeslot. More explicitly, we have $\hat{H}_{apr}[n+1,k] =$

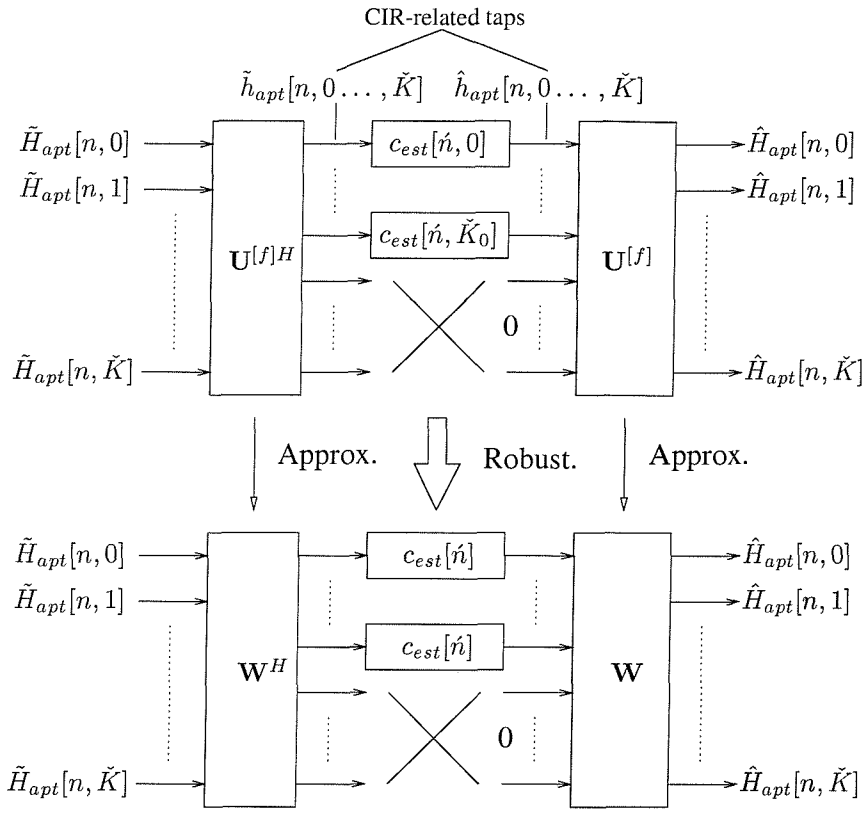

Figure 2.4: 2D-MMSE channel estimator design proposed by Li *et al.* [17] replacing the 'Channel Estimator' block of Figure 2.1. In contrast to the 1D-MMSE channel estimator design of Edfors *et al.* [14, 15], portrayed in Figure 2.2, the 2D-MMSE channel estimator employs CIR-domain related estimation filters having a filter order higher than zero, potentially capitalizing on the *a posteriori* least-squares channel transfer factor estimates of several previously received OFDM symbols. In the lower half of this figure, the implications of the assumptions of robustness on the estimator design are illustrated. Specifically, the unitary matrix $\mathbf{U}^{[f]}$ associated with the KLT and hosting the eigenvectors associated with the channel's spaced-frequency correlation matrix $\mathbf{R}^{[f]}$ is substituted by the DFT matrix $\mathbf{W}$ of Equation 2.13. Furthermore identical filters having an impulse response $c[\acute{n}]$, $\acute{n} = 0,\ldots,N_{tap}^{[t]} - 1$ are employed in the context of the identical eigenvalues $\tilde{\lambda}_l^{[f]} = \frac{K}{K_0}$, $l = 0,\ldots,\check{K}_0$ associated with the robust design instead of individual CIR-related tap-specific filters having different impulse responses $c_{est}[\acute{n},l]$, $\acute{n} = 0,\ldots,N_{tap}^{[t]}-1$, $l = 0,\ldots,\check{K}_0$ in the context of the individual eigenvalues $\lambda_l^{[f]}$, $l = 0,\ldots,\check{K}_0$ associated with the optimum design. For notational simplicity we have defined in the schematic $\check{K}_0 = K_0 - 1$ and $\check{K} = K - 1$.

F_D	0.007	0.01	0.05	0.1
$\text{MSE}_{dec,J}\|_{dB}$	-30.14	-27.05	-13.07	-7.05

Table 2.3: Approximate MSE according to Equation 2.19 induced by the channel's decorrelation observed between two successive OFDM symbols in the context of Jakes' model - as a function of the OFDM symbol normalized Doppler frequency $F_D = f_D T_f$.

$\hat{H}_{apt}[n,k]$, $k = 0,\ldots,K-1$, which implies the assumption that the channel transfer function has not changed between the n-th and the $(n+1)-th$ transmission timeslot. The associated decorrelation-related mean-square channel transfer factor estimation error incurred by this assumption can be quantified for any of the K subcarriers as:

$$\begin{aligned}\text{MSE}_{dec}[n,k] &= E\left\{|H[n+1,k]-H[n,k]|^2\right\} \\ &= 2\left(E\{|H[n+1,k]|^2\} - \Re\mathrm{e}\{E\{H[n+1,k]H^*[n,k]\}\}\right) \quad (2.15) \\ &= 2\left(r_H^{[t]}[0] - \Re\mathrm{e}\{r_H^{[t]}[1]\}\right). \quad (2.16)\end{aligned}$$

Assuming that the channel's Doppler power spectrum obeys Jakes' model [90], the spaced-time channel correlation function is given by $r_{H,J}^{[t]}[\Delta n] = J_0(\Delta n \omega_D)$ [17], where $J_0(x)$ is the zero-order Bessel function of its first kind, which can be approximated by [86, 91]:

$$J_0(x) \approx 1 - \frac{1}{4}x^2,\ x \ll 1. \quad (2.17)$$

Hence, in the context of Jakes' model we obtain for the channel decorrelation-related estimation error:

$$\begin{aligned}\text{MSE}_{dec,J}[n,k] &= 2(1 - J_0(\omega_D)) \quad (2.18) \\ &\approx \frac{1}{2}\omega_D^2. \quad (2.19)\end{aligned}$$

Equation 2.19 has been evaluated for different values of the OFDM symbol normalized Doppler frequency of $F_D = f_D T_f$, which is related to ω_D by $\omega_D = 2\pi F_D$. The corresponding results are summarized in Table 2.3. We observe from Table 2.3 that depending on the value of F_D the channel-decorrelation-related estimation error associated with the assumption of $\hat{H}_{apr}[n+1,k] = \hat{H}_{apt}[n,k]$, $k = 0,\ldots,K-1$, may become excessive. This was the motivation for Tufvesson [80, 29] as well as Al-Susa and Ormondroyd [18] to employ prediction filtering instead of estimation filtering along the time-direction. The specific structure of the time-direction prediction filter will be contrasted against that of the time-direction estimation filter of [17] in the next section, namely in Section 2.2.4. The stylised estimation and prediction process was portrayed in Figure 2.3.

2.2.4 MMSE *A Priori* Time-Direction Channel Prediction Filtering

In the previous section estimation filtering of the CIR-related taps was employed for enhancing the performance of the decision-directed channel transfer function estimator using the schematic of Figure 2.4. By contrast, in this section we will highlight the structure of the MMSE *a priori* channel predictor, which operates along the time-direction [92, 18, 85, 87]. Initially we will *not* impose any of the robustness-related constraints, which were proposed in [17] and summarized in Section 2.2.3 in the context of the two-dimensional channel estimator. Hence, the optimum design in the sense of a minimum channel prediction MSE obeys again the structure seen at the top of Figure 2.4. Most notably, different CIR-related tap prediction filters having coefficients of $c[\acute{n}, l], \acute{n} = 0, \ldots, N_{tap}^{[t]} - 1$ for each of the l-th CIR-related taps, $l \in \{0, \ldots, K_0 - 1\}$ are invoked for exploiting the correlation of the CIR-related taps along the time-direction. In contrast to the discussions of Section 2.2.3, the filters considered here are of finite order. We note that in the context of an optimum channel transfer function predictor design based on the unitary transform matrix $\mathbf{U}^{[f]}$ seen in Figure 2.4, which hosts the eigenvectors of the spaced-frequency correlation matrix $\mathbf{R}^{[f]}$ it would be incorrect to refer to the filtering along the time-direction as CIR tap filtering, since by definition the CIR is related to the 'frequency-continuous' channel transfer function by the Fourier Transform (FT). By contrast, in the context of the estimator considered here, a finite set of channel transfer function samples is transferred to a CIR-related domain by means of the unitary transform matrix $\mathbf{U}^{[f]}$. However, there is an exceptional case, where the CIR is obtained by subjecting the set of K number of channel transfer factors to the unitary matrix $\mathbf{U}^{[f]}$. This is when the CIR is sample-spaced[6]. Here we will employ the more general terminology of *CIR-related* tap prediction filtering, rather than CIR tap prediction filtering.

The structure of Section 2.2.4 is as follows. In Section 2.2.4.1 the predicted *a priori* value for a specific CIR-related tap is expressed as a linear combination of past *a posteriori* CIR-related tap values. In Section 2.2.4.2 we define the *a posteriori* CIR-related tap values' auto-correlation matrix and cross-correlation vector, which are then employed in the context of Section 2.2.4.3 for deriving the Wiener equation with the aid of two different methods, namely the gradient approach [87] and the orthogonality principle [87]. The Wiener equation allows for a direct solution with respect to the desired vector of predictor coefficients, which will be outlined in Section 2.2.4.4. In the same section we also present an expression for the predictor MSE in the CIR-related domain under perfectly matched channel conditions, where the channel statistics invoked in the calculation of the predictor coefficients are identical to those of the channel encountered. Furthermore, in Section 2.2.4.5 the predictor's MSE under mismatched channel conditions will be considered. Finally in Section 2.2.4.6 an expression for the average channel prediction MSE in the frequency-domain will be derived.

[6]Note that in this case the unitary KLT matrix $\mathbf{U}^{[f]}$ is identical to the DFT matrix $\mathbf{W}$.

2.2.4.1 Linear Prediction of the CIR-Related Taps

An *a priori* estimate $\hat{h}_{apr}[n+1,l]$ of the l-th CIR-related tap for the $(n+1)$-th timeslot is given by:

$$\hat{h}_{apr}[n+1,l] = \sum_{\acute{n}=0}^{N_{tap}^{[t]}-1} c_{pre}[\acute{n},l] \cdot \tilde{h}_{apt}[n-\acute{n},l], \tag{2.20}$$

where $l = 0,\ldots,K_0-1$. In Equation 2.20 the variable $c_{pre}[\acute{n},l]$ denotes the $\acute{n}$-th coefficient of the $N_{tap}^{[t]}$-tap CIR-related tap predictor and $\tilde{h}_{apt}[n-\acute{n},l]$ represents the *a posteriori* estimate of the l-th CIR-related tap in the $(n-\acute{n})$-th timeslot, which is related to the *a posteriori* least-squares estimates $\tilde{H}_{apt}[n-\acute{n},k]$, $k = 0,\ldots,K-1$ of the channel transfer factors by the unitary transform matrix $\mathbf{U}^{[f]}$, as shown in Equation 2.4. Equation 2.20 can also be expressed in vector notation as:

$$\hat{h}_{apr}[n+1,l] = \mathbf{c}_{pre}^{H}[l]\tilde{\mathbf{h}}_{apt}[n,l], \tag{2.21}$$

where $\mathbf{c}_{pre}[l] \in \mathbb{C}^{N_{tap}^{[t]}\times 1}$ is the vector of CIR-related tap predictor coefficients:

$$\mathbf{c}_{pre}[l] = \left(c_{pre}^{*}[0,l], c_{pre}^{*}[1,l], \ldots, c_{pre}^{*}[N_{tap}^{[t]}-1,l]\right)^{T}, \tag{2.22}$$

and $\tilde{\mathbf{h}}_{apt}[n,l] \in \mathbb{C}^{N_{tap}^{[t]}\times 1}$ is the sample vector containing the current and the previous $(N_{tap}^{[t]}-1)$ *a posteriori* tap estimates at the l-th tap position:

$$\tilde{\mathbf{h}}_{apt}[n,l] = \left(\tilde{h}_{apt}[n,l], \tilde{h}_{apt}[n-1,l], \ldots, \tilde{h}_{apt}[N_{tap}^{[t]}-1,l]\right)^{T}. \tag{2.23}$$

The complex error between the true value $h[n+1,l]$ of the l-th CIR-related tap with respect to the unitary transform matrix $\mathbf{U}^{[f]}$ and its predicted value $\hat{h}_{apr}[n+1,l]$ can be expressed as:

$$e_{pre}[n+1,l] = h[n+1,l] - \hat{h}_{apr}[n+1,l]. \tag{2.24}$$

The two most prominent methods of inferring the vector of optimum CIR-related tap predictor coefficients [7] are constituted by the *gradient approach* [92, 87] and the application of the *orthogonality principle* [92, 87].

2.2.4.2 Definition of the CIR-related Taps' Auto-Correlation Matrix and Cross-Correlation Vector

It is convenient to define the auto-correlation matrix $\mathbf{R}_{apt}^{[t]}[l] \in \mathbb{C}^{N_{tap}^{[t]}\times N_{tap}^{[t]}}$ of the CIR-related *a posteriori* tap estimates as well as the cross-correlation vector $\mathbf{r}_{apt}^{[t]}[l] \in \mathbb{C}^{N_{tap}^{[t]}\times 1}$ between the 'true'

[7] Unless otherwise stated, for the sake of conciseness we will refer to the CIR-related tap predictor coefficients simply as predictor coefficients.

CIR-related tap in the $(n+1)$-th timeslot and the CIR-related *a posteriori* tap estimates of the $N_{tap}^{[t]}$ number of previous timeslots at the l-th tap position in advance. More specifically, we have:

$$\mathbf{R}_{apt}^{[t]}[l] = E\left\{\tilde{\mathbf{h}}_{apt}[n,l]\tilde{\mathbf{h}}_{apt}^{H}[n,l]\right\} \quad (2.25)$$

$$= \mathbf{R}_{h}^{[t]}[l] + \rho\mathbf{I} \quad (2.26)$$

$$= \lambda_{l}^{[f]}\mathbf{R}^{[t]}[l] + \rho\mathbf{I}. \quad (2.27)$$

In Equation 2.26 $\mathbf{R}_{h}^{[t]}[l] = E\{\mathbf{h}[n,l]\mathbf{h}^{H}[n,l]\} \in \mathbb{C}^{N_{tap}^{[t]} \times N_{tap}^{[t]}}$ denotes the l-th CIR-related tap's spaced-time auto-correlation matrix of the 'true' CIR-related taps as hosted by the vector $\mathbf{h}[l] \in \mathbb{C}^{N_{tap}^{[t]} \times 1}$. By contrast, $\mathbf{R}^{[t]}[l]$ of Equation 2.27 denotes the normalized spaced-time auto-correlation matrix[8], where the normalization has been performed with respect to the l-th eigenvalue $\lambda_{l}^{[f]}$ of the spaced-frequency correlation matrix $\mathbf{R}^{[f]}$. Furthermore, the cross-correlation vector $\mathbf{r}_{apt}^{[t]}[l] \in \mathbb{C}^{N_{tap}^{[t]} \times 1}$ is defined as:

$$\mathbf{r}_{apt}^{[t]}[l] = E\left\{h^{*}[n+1,l]\tilde{\mathbf{h}}_{apt}[n,l]\right\} \quad (2.28)$$

$$= \mathbf{r}_{h}^{[t]}[l] \quad (2.29)$$

$$= \lambda_{l}^{[f]}\mathbf{r}^{[t]}[l]. \quad (2.30)$$

In Equation 2.29 $\mathbf{r}_{h}^{[f]}[l] = E\{h^{*}[n+1,l]\mathbf{h}[l]\} \in \mathbb{C}^{N_{tap}^{[t]} \times 1}$ denotes the l-th CIR-related tap's spaced-time cross-correlation vector. By contrast, in Equation 2.30 $\mathbf{r}^{[t]}[l] \in \mathbb{C}^{N_{tap}^{[t]} \times 1}$ denotes the l-th CIR-related tap's normalized spaced-time cross-correlation vector[9].

The difference between the CIR-related tap *predictor* considered here and the CIR-related tap *estimator* advocated by Li *et al.* [17] resides in the structure of the cross-correlation vector. Specifically, as seen in Equation 2.28, the *a priori* predictor for the l-th CIR-related tap of the $(n+1)$-th transmission timeslot capitalizes on an estimate of the cross-correlation between the CIR-related tap expected during the $(n+1)$-th transmission time-slot and that of the current, namely the n-th, as well as the $(N_{tap}^{[t]}-1)$ previous transmission time-slots. By contrast, the improved *a posteriori* estimator for the l-th CIR-related tap of the current, namely the n-th, transmission time-slot capitalizes on the cross-correlation between the CIR-related tap expected during the n-th transmission time-slot and that of the n-th as well as the $(N_{tap}^{[t]}-1)$ previous transmission time-slots. In the next paragraph Equations 2.27 and 2.30 will be invoked for deriving the optimum predictor coefficients with the aid of the gradient approach and by applying the orthogonality principle.

[8]Note that $\mathbf{R}^{[t]}[l] = (1/\lambda_{l}^{[f]})\mathbf{R}_{h}^{[t]}[l]$. As a result of the normalization the main diagonal elements of $\mathbf{R}^{[t]}[l]$ are unity. In case of channels having a separable spaced-time spaced-frequency correlation function $r_H(\Delta t, \Delta f) = r_H(\Delta t) \cdot r_H(\Delta f)$ as outlined in Section 6.2.6, the different CIR-related taps' normalized spaced-time correlation matrices are identical, namely $\mathbf{R}^{[t]} = \mathbf{R}^{[t]}[0] = \ldots = \mathbf{R}^{[t]}[K-1]$ and specifically they contain the samples of the normalized spaced-time correlation function $r_H(\Delta t)$. Specifically we have $\mathbf{R}^{[t]}|_{n_1,n_2} = r_H^{[t]*}(\Delta n T_f)$, $\Delta n = n_1 - n_2$.

[9]In case of channels having a separable spaced-time spaced-frequency correlation function $r_H(\Delta t, \Delta f) = r_H(\Delta t) \cdot r_H(\Delta f)$ as outlined in Section 6.2.6, the different CIR-related taps' normalized spaced-time cross-correlation vectors are identical, namely $\mathbf{r}^{[t]} = \mathbf{r}^{[t]}[0] = \ldots = \mathbf{r}^{[t]}[K-1]$ and specifically they contain the samples of the normalized spaced-time correlation function $r_H(\Delta t)$. Specifically we have $\mathbf{r}^{[t]}|_{n_1} = r_H^{[t]*}((1+n_1)T_f)$.

2.2.4.3 Derivation of the Wiener Equation using the Gradient Approach or the Orthogonality Principle

2.2.4.3.1 Gradient Approach Upon invoking the complex estimation error expression $e[n+1,l]$ of Equation 2.24 the squared estimation error is formed, and its mean value is given by:

$$\begin{aligned} J(\mathbf{c}_{pre}[l]) &= \mathrm{MSE}(\mathbf{c}_{pre}[l]) && (2.31)\\ &= E\{|e_{pre}[n+1,l]|^2\} && (2.32)\\ &= \lambda_l^{[f]} - \mathbf{c}_{pre}^T[l]\mathbf{r}_{apt}^{[t]*}[l] - \mathbf{c}_{pre}^H[l]\mathbf{r}_{apt}^{[t]}[l] + \\ &\quad + \mathbf{c}_{pre}^H[l]\mathbf{R}_{apt}^{[t]}[l]\mathbf{c}_{pre}[l]. && (2.33) \end{aligned}$$

Recall that the auto-correlation matrix $\mathbf{R}_{apt}^{[t]}[l]$ and the cross-correlation vector $\mathbf{r}_{apt}^{[t]}[l]$ were defined by Equations 2.25 and 2.28. Furthermore note that $\lambda_l^{[f]} = E\{|h[n+1,l]|^2\}$.

The vector $\mathbf{c}_{pre}[l]|_{opt}$ of optimum predictor coefficients is identified by minimizing the value of the cost-function $J(\mathbf{c}_{pre}[l])$. Hence the gradient of $J(\mathbf{c}_{pre}[l])$ given by Equation 2.33 with respect to the conjugate complex vector $\mathbf{c}_{pred}^*[l]$ of predictor coefficients is set to zero, which is expressed as:

$$\mathbf{c}_{pre}[l]|_{opt} = \underset{\mathbf{c}_{pre}[l]}{arg\,min}\,(J(\mathbf{c}_{pre}[l])) \quad \longleftrightarrow \quad \left.\frac{\partial J(\mathbf{c}_{pre}[l])}{\partial \mathbf{c}_{pre}^*[l])}\right|_{\mathbf{c}_{pre}[l]|_{opt}} \stackrel{!}{=} 0. \qquad (2.34)$$

Hence, upon invoking Equation 2.34 together with Equation 2.33 the set of $N_{tap}^{[t]}$ number of Wiener-Hopf equations [92, 93, 87] is obtained in vector notation as:

$$\left.\frac{\partial J(\mathbf{c}_{pre}[l])}{\partial \mathbf{c}_{pre}^*[l]}\right|_{\mathbf{c}_{pre}[l]|_{opt}} = -\mathbf{r}_{apt}^{[t]}[l] + \mathbf{R}_{apt}^{[t]}[l]\mathbf{c}_{pre}[l]|_{opt} \stackrel{!}{=} 0, \qquad (2.35)$$

from which the vector $\mathbf{c}_{pre}[l]|_{opt}$ of optimum predictor coefficients can be inferred.

2.2.4.3.2 Orthogonality Principle The orthogonality principle of MMSE optimization implies that the inner product related norm of the difference- or error vector between any vector contained in a vector space S and its projection onto a sub-space spanned by a specific number of data vectors is minimized in the sense of the expectation value, provided that the error vector is orthogonal to the above-mentioned sub-space [87]. Hence, in the context of the optimization problem considered here we obtain a set of $N_{tap}^{[t]}$ equations:

$$E\left\{e_{pre}[n+1,l]\tilde{h}_{apt}^*[n+\acute{n},l]\right\} = 0, \quad \acute{n} = -N_{tap}^{[t]}+1,\ldots,0. \qquad (2.36)$$

Equation 2.36 can be readily transferred into the form of Equation 2.35 by capitalizing on the definition of the tap prediction error signal $e_{pre}[n+1,l]$ given by Equation 2.24 as well as on that of the predicted signal given by Equation 2.20 while invoking the definition of the auto-correlation

matrix $\mathbf{R}_{apt}^{[t]}[l]$ and that of the cross-correlation matrix $\mathbf{r}_{apt}^{[t]}[l]$ given by Equations 2.27 and 2.30, respectively, yielding:

$$-\mathbf{r}_{apt}^{[t]}[l] + \mathbf{R}_{apt}^{[t]}[l]\mathbf{c}_{pre}[l]|_{opt} \stackrel{!}{=} 0. \tag{2.37}$$

2.2.4.4 Optimum Predictor Coefficients and Minimum CIR-Related Domain Predictor MSE

Provided that the inverse of the auto-correlation matrix $\mathbf{R}_{apt}^{[t]}[l]$ exists, which requires that $\mathbf{R}_{apt}^{[t]}[l]$ is of full rank [87], Equations 2.35 or 2.37 can be uniquely solved with respect to the vector $\mathbf{c}_{pre}[l]|_{opt}$ of optimum predictor coefficients associated with the l-th CIR-related tap:

$$\mathbf{c}_{pre}[l]|_{opt} = \mathbf{R}_{apt}^{[t]-1}[l]\mathbf{r}_{apt}^{[t]}[l]. \tag{2.38}$$

Hence by substituting the vector $\mathbf{c}_{pre}[l]|_{opt}$ of optimum predictor coefficients into the MSE expression of Equation 2.33, an equation is obtained for the minimum MSE (MMSE):

$$\begin{aligned} \text{MMSE}_{apr}[l] &= \text{MSE}_{apr}[l]|_{(\mathbf{c}_{pre}[l]|_{opt})} & (2.39)\\ &= \lambda_l^{[f]} - \mathbf{c}_{pre}^H[l]|_{opt}\mathbf{r}_{apt}^{[t]}[l]. & (2.40) \end{aligned}$$

2.2.4.5 Optimum Predictor Coefficients for Mismatched Channel Statistics

In the context of deriving the vector $\mathbf{c}_{pre}[l]|_{opt}$ of optimum predictor coefficients given by Equation 2.38 we have implicitly assumed perfect knowledge of the specific spaced-time correlation function associated with the l-th CIR-related tap, which appeared in the form of the auto-correlation matrix $\mathbf{R}^{[t]}[l]$ in Equation 2.27 and in the form of the cross-correlation vector $\mathbf{r}^{[t]}[l]$ in Equation 2.30. We also assumed perfect knowledge of the spaced-frequency correlation matrix $\mathbf{R}^{[f]}$, namely the knowledge of its EVD-related representation $\mathbf{R}^{[f]} = \mathbf{U}^{[f]}\Lambda^{[f]}\mathbf{U}^{[f]H}$ associated with the unitary transform matrix $\mathbf{U}^{[f]}$ and the diagonal matrix $\Lambda^{[f]}$ hosting the eigenvalues $\lambda_l^{[f]}, l = 0, \ldots, K-1$. Normally this knowledge is not explicitly available and hence the optimum coefficients are based on the corresponding "estimates" $\tilde{\mathbf{R}}^{[t]}[l]$, $\tilde{\mathbf{r}}^{[t]}[l]$ and $\tilde{\mathbf{R}}^{[f]}$, where $\tilde{\mathbf{R}}^{[f]}$ can be decomposed according to $\tilde{\mathbf{R}}^{[f]} = \tilde{\mathbf{U}}^{[f]}\tilde{\Lambda}^{[f]}\tilde{\mathbf{U}}^{[f]H}$. We also need the *estimates* of the auto-correlation matrix $\tilde{\mathbf{R}}_{apt}^{[t]}[l]$ of the *a posteriori* CIR-related taps, which can be formulated by following the philosophy of Equation 2.27, yielding:

$$\tilde{\mathbf{R}}_{apt}^{[t]}[l] = \tilde{\lambda}_l^{[f]}\tilde{\mathbf{R}}^{[t]}[l] + \tilde{\rho}\mathbf{I}, \tag{2.41}$$

where also a potentially imperfect estimate $\tilde{\rho}$ of the reciprocal value $\rho = 1/\text{SNR}$ of the SNR measured at the reception antenna has been invoked. Similarly, the cross-correlation vector $\tilde{\mathbf{r}}_{apt}^{[t]}[l]$ of *a posteriori* CIR-related tap estimates can be expressed following the philosophy of Equation 2.30:

$$\tilde{\mathbf{r}}_{apt}^{[t]}[l] = \tilde{\lambda}_l^{[f]}\tilde{\mathbf{r}}^{[t]}[l]. \tag{2.42}$$

According to Equation 2.38 the vector $\tilde{\mathbf{c}}_{pre}[l]|_{opt}$ of sub-optimum predictor coefficients is hence given by:

$$\tilde{\mathbf{c}}_{pre}[l]|_{opt} = \tilde{\mathbf{R}}_{apt}^{[t]-1}[l]\tilde{\mathbf{r}}_{apt}^{[t]}[l]. \tag{2.43}$$

Furthermore, the CIR-related domain MSE achieved by this predictor in the context of an arbitrary vector $\tilde{\mathbf{c}}_{pre}[l]$ of coefficients is given similarly to Equation 2.33 by:

$$\begin{aligned} \mathrm{MSE}_{apr}[l]|_{(\tilde{\mathbf{c}}_{pre}[l])} &= v_l^{[f]} - \tilde{\mathbf{c}}_{pre}^T[l]\mathbf{r}_{apt}^{[t]*}[l]|_{\tilde{\mathbf{U}}^{[f]}} - \tilde{\mathbf{c}}_{pre}^H[l]\mathbf{r}_{apt}^{[t]}[l]|_{\tilde{\mathbf{U}}^{[f]}} + \\ &\quad + \tilde{\mathbf{c}}_{pre}^H[l]\mathbf{R}_{apt}^{[t]}[l]|_{\tilde{\mathbf{U}}^{[f]}}\tilde{\mathbf{c}}_{pre}[l], \end{aligned} \tag{2.44}$$

where the auto-correlation matrix $\mathbf{R}_{apt}^{[t]}[l]|_{\tilde{\mathbf{U}}^{[f]}}$ of the l-th CIR-related tap conditioned on employing the unitary transform matrix $\tilde{\mathbf{U}}^{[f]}$ is defined similarly to Equation 2.27 by:

$$\mathbf{R}_{apt}^{[t]}[l]|_{\tilde{\mathbf{U}}^{[f]}} = v_l^{[f]}\mathbf{R}^{[t]}[l]|_{\tilde{\mathbf{U}}^{[f]}} + \rho\mathbf{I}. \tag{2.45}$$

By the same token the cross-correlation vector $\mathbf{r}_{apt}^{[t]}[l]|_{\tilde{\mathbf{U}}^{[f]}}$ is defined similarly to Equation 2.30 by:

$$\mathbf{r}_{apt}^{[t]}[l]|_{\tilde{\mathbf{U}}^{[f]}} = v_l^{[f]}\mathbf{r}^{[t]}[l]|_{\tilde{\mathbf{U}}^{[f]}}. \tag{2.46}$$

The variable $v_l^{[f]}$ was defined earlier in Section 2.2.2.2 as the variance of the l-th CIR-related tap, which can be expressed as the l-th diagonal element of the decomposition of $\mathbf{R}^{[f]}$ with respect to the unitary transform matrix $\tilde{\mathbf{U}}^{[f]}$, namely as $v_l^{[f]} = (\tilde{\mathbf{U}}^{[f]H}\mathbf{R}^{[f]}\tilde{\mathbf{U}}^{[f]})_{[l,l]}$. Again, note that if $\tilde{\mathbf{U}}^{[f]} = \mathbf{U}^{[f]}$ holds, we have $v_l^{[f]} = \lambda_l^{[f]}$. Clearly, the predictor's MSE in Equation 2.44 is equal to or higher than the MMSE of Equation 2.40, since the latter assumes perfect knowledge of the channel statistics in the calculation of the predictor coefficients, yielding:

$$\mathrm{MSE}_{apr}[l]|_{(\tilde{\mathbf{c}}_{pre}[l]|_{opt})} \geq \mathrm{MMSE}_{apr}[l]. \tag{2.47}$$

Note again that the predictor MSE values delivered by Equations 2.40 and 2.44 for the cases of matched- and mismatched channel statistics, respectively, are valid for the CIR-related domain, observed on a per tap basis. In practice, the average predictor MSE evaluated in the frequency domain is however of more importance for the system's BER performance.

2.2.4.6 Average Channel Predictor MSE in the Frequency-Domain

Following the notation of [15], below we will characterize the OFDM system's symbol-averaged frequency-domain *a priori* estimation MSE. A rank-K_0 predictor is used, where only the first K_0 CIR-related tap values are retained as shown in Figures 2.2 and 2.4, while the CIR-related tap values associated with a higher index are set to zero for the sake of reducing the predictor's computational complexity. The corresponding MSE is given by:

$$\overline{\mathrm{MSE}}_{apr}|_{K_0} = \frac{1}{K}\mathrm{Trace}\left(E\{\mathbf{E}_{pre}[n+1]|_{K_0}\mathbf{E}_{pre}^H[n+1]|_{K_0}\}\right), \tag{2.48}$$

where the vector $\mathbf{E}_{pre}[n+1]|_{K_0} \in \mathbb{C}^{K\times 1}$ of frequency-domain transfer factor error signals was generated with the aid of the KLT-matrix $\tilde{\mathbf{U}}^{[f]}$ from the vector $\mathbf{e}_{pre}[n+1]|_{K_0} \in \mathbb{C}^{K\times 1}$ of CIR-related domain error signals as follows:

$$\mathbf{E}_{pre}[n+1]|_{K_0} = \tilde{\mathbf{U}}^{[f]}\mathbf{e}_{pre}[n+1]|_{K_0}. \tag{2.49}$$

Recall that $\tilde{\mathbf{U}}^{[f]} \in \mathbb{C}^{K\times K}$ is the matrix of eigenvectors associated with the EVD of the spaced-frequency correlation matrix $\tilde{\mathbf{R}}^{[f]} = \tilde{\mathbf{U}}^{[f]}\tilde{\Lambda}^{[f]}\tilde{\mathbf{U}}^{[f]H}$, invoked in the calculation of the predictor coefficients. The individual components of the vector $\mathbf{e}_{pre}[n+1]|_{K_0}$ of CIR-related domain error signals were given in Equation 2.24, as the difference between the 'true' CIR-related tap values with respect to the transform $\tilde{\mathbf{U}}^{[f]}$ and its predictions, where again, in the context of a rank-K_0 predictor, the predicted CIR-related taps for $l = K_0, \ldots, K-1$ are set to zero. Upon substituting Equation 2.49 into Equation 2.48 we obtain:

$$\overline{\text{MSE}}_{apr}|_{K_0} = \frac{1}{K}\text{Trace}\left(\tilde{\mathbf{U}}^{[f]}E\{\mathbf{e}_{pre}[n+1]|_{K_0}\mathbf{e}^H_{pre}[n+1]|_{K_0}\}\tilde{\mathbf{U}}^{[f]H}\right) \tag{2.50}$$

$$= \frac{1}{K}\text{Trace}\left(E\{\mathbf{e}_{pre}[n+1]|_{K_0}\mathbf{e}^H_{pre}[n+1]|_{K_0}\}\right), \tag{2.51}$$

where in Equation 2.51 we have exploited that $\text{Trace}\left(\mathbf{UAU}^H\right) = \text{Trace}(\mathbf{A})$ for any unitary matrix $\mathbf{U}$ [15, 94]. Note that the first K_0 diagonal elements of the matrix $E\{\mathbf{e}_{pre}[n+1]|_{K_0}\mathbf{e}^H_{pre}[n+1]|_{K_0}\}$ are equal to the CIR-related tap predictors' MSE values given by Equation 2.44, while the diagonal elements associated with a higher index are equal to the CIR-related tap values' variances - conditioned on employing the unitary transform matrix $\tilde{\mathbf{U}}^{[f]}$. This is, because for these taps associated with indices $l = K_0 \ldots, K-1$ the *a priori* predictions $\hat{h}_{apr}[n+1, l]$ are not available and therefore we have $E\{|e_{pre}[n+1, l]|^2\} = E\{|h[n+1, l]|^2\} = v_l^{[f]}$. Hence, Equation 2.51 can be reformulated as:

$$\overline{\text{MSE}}_{apr}|_{K_0} = \frac{1}{K}\sum_{l=0}^{K_0-1}\text{MSE}_{apr}[l]|_{(\tilde{c}_{pre}[l]|_{opt})} + \frac{1}{K}\sum_{l=K_0}^{K-1} v_l^{[f]}. \tag{2.52}$$

Since in general perfect knowledge of the channel statistics is not available, we will highlight in Section 2.2.5 the philosophy of a number of potential strategies that can be invoked for providing estimates of the channel statistics, including Li's approach [17] for rendering the predictor as robust as possible.

2.2.5 Channel Statistics for *A Priori* Time-Direction Channel Prediction Filtering

As we observed in Equation 2.43, evaluating the l-th CIR-related tap's prediction filter coefficients requires estimates $\tilde{\mathbf{R}}^{[t]}_{apt}[l]$ and $\tilde{\mathbf{r}}^{[t]}_{apt}[l]$ of this tap's auto-correlation matrix and cross-correlation vector, respectively. To elaborate a little further, these correlation-related quantities could be calculated according to Equations 2.27 and 2.30 upon stipulating the availability of an estimate of the spaced-frequency correlation matrix's l-th eigenvalue $\tilde{\lambda}_l^{[f]}$, of the reciprocal of the SNR $\tilde{\rho} = 1/\tilde{\text{SNR}}$ at the

reception antenna, and that of the channel's spaced-time correlation function, $\tilde{r}_H^{[t]}[\Delta n]$. These estimates will be provided in Section 2.2.5.1 upon invoking again the concepts of robustness to channel statistics variations, as discussed by Li *et al.* [17] in the context of DDCE. On the other hand, the l-th CIR-related tap's auto-correlation matrix and cross-correlation vector could also be assembled from the auto-correlation function of this tap, which can be estimated on the basis of M_s number of CIR-related tap values. Before continuing our discourse we note that these issues will be further detailed in Section 2.2.5.2.

2.2.5.1 Robust *A Priori* Time-Direction Channel Prediction Filtering

While in Section 2.2.5.1.1 we will briefly revisit the fundamental concepts of a robust channel estimator introduced by Li *et al.* in [17], in Section 2.2.5.1.2 we will offer a number of conclusions assisting in the design of a robust channel predictor.

2.2.5.1.1 Review of Robust Channel Estimation In Section 2.2.4 we highlighted the concept of a robust channel estimator as proposed by Li *et al.* [17]. The conclusion was that an improved *a posteriori* channel transfer function estimator, which capitalizes on an *infinite number* of previous initial *a posteriori* channel transfer function estimates can be rendered insensitive to the exact channel statistics. Arriving at such a robust design requires first of all that the spaced-time correlation function $\tilde{r}_H^{[t]}[\Delta n]$ assumed in the calculation of the channel transfer function estimator's coefficients derived for the time-direction filter is ideally limited to the frequency-band of ω_D. Secondly, it was required that the spaced-frequency correlation matrix $\tilde{\mathbf{R}}^{[f]}$ of the channel transfer function estimator can be eigen-decomposed, such that $\tilde{\mathbf{R}}^{[f]} = \tilde{\mathbf{U}}^{[f]}\tilde{\Lambda}^{[f]}\tilde{\mathbf{U}}^{[f]H}$, where the matrix $\tilde{\mathbf{U}}^{[f]}$ of eigenvectors is identical - with tolerable leakage [17] - to the exact matrix $\mathbf{U}^{[f]}$ of eigenvectors associated with the "true" spaced-frequency correlation matrix $\mathbf{R}^{[f]}$ of the channel. We note here that both of the matrices $\tilde{\mathbf{U}}^{[f]}$ and $\mathbf{U}^{[f]}$ are unitary and can in turn be approximated by the DFT matrix $\mathbf{W}$ as we already argued in the context of Section 2.2.3.2. Furthermore, it is assumed that the diagonal matrix $\tilde{\Lambda}^{[f]}$ hosts K_0 identical eigenvalues of $\tilde{\lambda}_l^{[f]} = K/K_0$ found in the first K_0 diagonal positions of the matrix, while the remaining $(K - K_0)$ number of eigenvalues are equal to zero. Under these conditions the channel estimator's MSE performance is invariant for all channels, which have a spaced-time correlation function $r_H^{[t]}[\Delta n]$ that is limited to the frequency-band of ω_D but not necessarily ideally low-pass shaped and with an arbitrary spaced-frequency correlation function $r_H^{[f]}[\Delta k]$, provided that the related spaced-frequency correlation matrix $\mathbf{R}^{[f]}$ can be eigen-decomposed such that the energy conveyed by the channel is mapped to the K_0 lowest eigenvalues[10]. In this case the *a posteriori* channel estimator's MSE is given by Equation 2.11. It was furthermore demonstrated in

[10]Note that in the context of employing the DFT matrix $\mathbf{W}$ of Equation 2.13 as the unitary transform matrix $\tilde{\mathbf{U}}^{[f]}$, this is only true for sample-spaced CIRs

[17] and also argued in Section 2.2.4 that in a robust estimator design identical sets of predictor coefficients[11] are associated with the different CIR-related taps' time-direction filters. The schematic of the corresponding channel estimator was shown at the bottom of Figure 2.4. This also implies that the estimation filter associated with each CIR-related tap is designed for the same maximum Doppler frequency.

2.2.5.1.2 Design of the Auto-Correlation Matrix and Cross-Correlation Vector of a Robust Channel Predictor The same concepts of robustness can also be applied to the *a priori* channel predictor advocated here, although in contrast to the *a posteriori* channel estimator of [17] an estimate of the channel transfer function is obtained for the $(n+1)$-th timeslot instead of generating an improved estimate for the current timeslot, namely for the n-th timeslot. More specifically, as highlighted above, identical eigenvalues of $\tilde{\lambda}_l^{[f]} = K/K_0$, $l = 0, \ldots, K_0 - 1$ are employed in the calculation of the K_0 number of CIR-related taps' predictor coefficients. Furthermore, the maximum Doppler frequency associated with each of the CIR-related taps' spaced-time correlation functions $\tilde{r}_H^{[t]}[\Delta n]$ is assumed to be identical. Hence identical sets of predictor coefficients are obtained for the different CIR-related taps, which allows us to drop the index l of the specific CIR-related tap considered. Based on Equation 2.41 the auto-correlation matrix $\tilde{\mathbf{R}}_{apt}^{[t]}|_{rob}$ of *a posteriori* CIR-related tap estimates is thus given by:

$$\tilde{\mathbf{R}}_{apt}^{[t]}|_{rob} = \frac{K}{K_0}\tilde{\mathbf{R}}^{[t]}|_{rob} + \tilde{\rho}\mathbf{I}. \tag{2.53}$$

In Equation 2.53 the auto-correlation matrix $\tilde{\mathbf{R}}^{[t]}|_{rob}$ of CIR-related tap estimates is defined in the absence of noise on the basis of the spaced-time correlation function $r_H^{[t]}[\Delta n]|_{rob}$ associated with an ideal low-pass shaped PSD having a cut-off frequency of ω_D, which results in the sinc-shaped correlation function of:

$$\begin{aligned} \tilde{r}_H^{[t]}[\Delta n]|_{rob} &= E\left\{H[n-n_1]H^*[n-n_2]\right\} &(2.54)\\ &= \mathrm{sinc}(\Delta n \cdot \omega_D), &(2.55)\end{aligned}$$

where $\Delta n = n_2 - n_1$ and $\omega_D = 2\pi F_D$. We note that in the case of a slot-by-slot TDD system each downlink transmission timeslot is followed by an uplink transmission timeslot and vice versa. Hence the effective temporal distance between consecutive OFDM symbols is doubled in comparison to that of a scheme having bursts of multiple consecutive downlink timeslots. This has to be considered in the evaluation of the predictor-related correlation matrices with the aid of Equation 2.55. Upon substituting $\tilde{\mathbf{R}}_{apt}^{[t]}|_{rob}$ and $\tilde{\mathbf{r}}_{apt}^{[t]}|_{rob} = \tilde{\mathbf{r}}^{[t]}|_{rob}$ into Equation 2.43 the set of $N_{tap}^{[t]}$ predictor coefficients associated with the robust CIR-related tap predictor is obtained.

[11] A prerequisite was the separability of the channel's spaced-time spaced-frequency correlation function, which was discussed in Section 6.2.6.

We note furthermore that in case of the finite-order predictors as considered here, the properties of robustness with respect to the specific shape of the channel's Doppler power density spectrum - as highlighted for the case of an infinite-order estimator - are only approximately valid. This will be further elaborated on during our performance assessment of the various techniques in Section 2.3.

2.2.5.2 Adaptive *A Priori* Time-Direction Channel Prediction Filtering

In the absence of any *a priori* knowledge concerning the channel's statistics, such as for example the maximum Doppler frequency of the channel, the CIR-related tap predictors' coefficients must be calculated on the basis of a finite set of for example M_s number of past OFDM symbols' *a posteriori* CIR-related tap estimates $\tilde{h}_{apt}[n-\acute{n}, l]$, $\acute{n} = 0, \ldots, M_s - 1$, $l = 0, \ldots, K-1$. An intuitive method of determining the l-th CIR-related tap's correlation values $\tilde{r}^{[t]}_{\tilde{h}_{apt}}[\Delta n, l]$ constituting the auto-correlation matrix $\tilde{\mathbf{R}}^{[t]}_{apt}[n, l]$ and the cross-correlation vector $\tilde{\mathbf{r}}^{[t]}_{apt}[n, l]$ defined in Equations 2.25 and 2.28, respectively, is given by [86]:

$$\tilde{r}^{[t]}_{\tilde{h}_{apt}}[\Delta n, l] = \frac{1}{M_s - \Delta n} \sum_{\acute{n}=0}^{M_s-\Delta n} \tilde{h}_{apt}[n-\acute{n}, l]\tilde{h}^*_{apt}[(n-\Delta n)-\acute{n}, l], \tag{2.56}$$

where the calculation is performed for the n-th transmission timeslot on the basis of the *a posteriori* CIR-related tap samples of the current plus the previous $M_s - 1$ timeslots.

From the literature of predictive speech coding [83] for example, its known that the accuracy of linear prediction is extremely sensitive to the method of estimating the correlation values $\tilde{r}^{[t]}_{H}[\Delta n, l]$. A number of algorithms have been proposed in the literature for determining the predictor coefficients, such as the Levinson-Durbin algorithm and the related Burg algorithm [86, 83]. The employment of these algorithms in the context of channel transfer function prediction for OFDM has also been investigated by Al-Susa and Ormondroyd in [18]. In the context of employing an adaptive predictor instead of updating the CIR-related tap predictors' coefficients on a block basis, they could also be updated on an OFDM symbol-by-symbol basis with the aid of the RLS-algorithm [87]. This approach will be investigated in the context of PIC-assisted DDCE designed for multi-user OFDM systems in Section 3.5. Let us now embark in the next section on the characterization of both the robust- and the adaptive channel transfer function predictor in terms of their MSE performance.

2.3 Performance Assessment of Decision-Directed Channel Prediction Assisted OFDM with Fixed Modulation

In the context of our performance assessment presented here the indoor WATM channel- and system model of Section 6.1.1 is invoked. Specifically, due to the sample-spaced nature of the indoor WATM channel's associated CIR, the DFT can be employed for perfectly decorrelating the least-squares channel transfer factor estimates with respect to the frequency-direction. To elaborate a little

K_0, $\tilde{K}_0$	Sampling period duration normalized multipath spread
F_D, $\tilde{F}_D$	OFDM symbol normalized Doppler frequency
ρ,$\tilde{\rho}$	Reciprocal of the SNR
$N_{tap}^{[t]}$	Length- or range of the CIR-related tap prediction filter
K	Number of subcarriers per OFDM symbol

Table 2.4: Summary of the parameters influencing the MSE performance of the *robust* decision-directed channel predictor, which follows the concepts of the *robust* decision-directed channel estimator of Figure 2.4. Error-free symbol decisions and the absence of ICI is assumed in the corresponding experiments. The parameters associated with the channel predictor are distinguished from those of the channel by $\tilde{()}$.

further, the EigenValue Decomposition (EVD) of the sample-spaced channel's spaced-frequency correlation matrix given by $\mathbf{R}^{[f]} = \mathbf{U}^{[f]}\Lambda^{[f]}\mathbf{U}^{[f]H}$ is such that the EVD-related unitary transform matrix $\mathbf{U}^{[f]}$ is identical to the DFT matrix $\mathbf{W}$ of Equation 2.13 and the eigenvalues found on the main diagonal of $\Lambda^{[f]}$ are given by the CIR tap variances.

The structure of Section 2.3 is as follows. In Section 2.3.1 we will assess the MSE performance of a decision-directed channel predictor, which adopted the philosophy of the robust approach proposed by Li *et al.* in [17], while in Section 2.3.2 its MSE is contrasted to that of the adaptive decision-directed channel predictor proposed by Al-Susa and Ormondroyd in [18]. Furthermore, in Sections 2.3.3 and 2.3.4 the robust channel predictor's MSE performance, as well as the associated BER performance will be evaluated in the context of a system using no channel coding, upon invoking sliced and hence potentially error-prone symbol decisions in the process of decision-directed channel prediction. By contrast, in Section 2.3.5 we will evaluate the BER performance of a turbo-coded system, which employs robust decision-directed channel channel prediction.

2.3.1 MSE Performance of a Robust Decision-Directed Channel Predictor in the Context of Error-Free Symbol Decisions

As a consequence of the sample-spaced nature of the indoor WATM channel model's associated CIR employed here, according to our arguments presented concerning the robust channel estimator in Sections 2.2.3.2 and 2.2.5.1.1, an identical MSE performance is expected for any other sample-spaced CIR, provided that the multipath delay spread of the CIR normalized to the sampling period duration, namely $K_0 = T_m/T_s$ is lower than that employed in our simulations. This is because for a sample-spaced CIR all of the channel's energy is mapped to the K_0 number of significant CIR-related taps' output by the inverse unitary linear transform employed for generating these taps from the frame of frequency domain channel transfer function samples. By contrast, this is only approximately valid for non-sample-spaced channels, as will be demonstrated in the context of our investigations of DDCE for multi-user OFDM in Section 3.

In the context of the simulation results presented in Section 2.3.1 a spaced-time correlation function $r_H^{[t]}[\Delta n]$ as given by Equation 2.55, which follows the concepts of robustness outlined in Section 2.2.5.1.2 was associated with the channel predictor, while a spaced-time correlation function obeying Jakes' model [90] was associated with the specific transmission channel actually encountered.

The further structure of Section 2.3.1 is as follows. Our MSE performance assessment commences in Section 2.3.1.1 by considering a scenario, where the normalized multipath spread $\tilde{K}_0 = \tilde{T}_m/T_s$ and the OFDM symbol normalized Doppler frequency $\tilde{F}_D$, as well as the inverse of the SNR at the reception antenna, namely $\tilde{\rho}$, associated with the channel predictor are identical to that of the channel, namely to K_0, F_D and ρ, respectively. By contrast, in the context of our investigations to be outlined in Section 2.3.1.2 the OFDM symbol normalized Doppler frequency $\tilde{F}_D$ associated with the channel predictor, was fixed, while that associated with the specific channel encountered, namely, F_D, was varied across a range of values. Furthermore, in Section 2.3.1.3 the effects of a mismatch between the inverse of the SNR, $\tilde{\rho}$, associated with the channel predictor, and that of the channel, namely ρ are investigated. In Section 2.3.1.4 we continue our discourse by studying the effects of a misadjustment between the normalized multipath spread, $\tilde{K}_0$, which is associated with the channel predictor, and K_0, associated with the specific channel encountered. Finally, in Section 2.3.1.5 we offer some conclusions.

In Table 2.4 we have summarized again the specific parameters, which influence the MSE performance of the robust decision-directed channel predictor in the context of idealized error-free symbol decisions and in the absence of ICI. Our results related to potentially erroneous, sliced symbol decisions will be presented at a later stage in Section 2.3.3.

2.3.1.1 MSE Performance under Matched Channel Conditions

Initially we will assume employing "robust" prediction filter coefficients, which are perfectly matched to the specific channel conditions encountered. More specifically, the SNR experienced at the reception antenna is identical to that assumed in the calculation of the predictor coefficients, expressed in terms of the effective noise variance as $\rho = \tilde{\rho}$. Furthermore, the OFDM symbol normalized Doppler frequency assumed in the coefficients' calculation was identical to that of the channel, namely we had $F_D = \tilde{F}_D$.

In Figure 2.5 we have portrayed the MSE exhibited by the *a priori* channel predictor as a function of the SNR recorded at the reception antenna and experienced in different propagation scenarios characterized by their specific OFDM symbol normalized Doppler frequency denoted by F_D. Various CIR-related tap prediction filter lengths ranging between one and 64 taps were invoked. We observe that with the aid of a modest prediction filter length of approximately four to eight taps already most of the channel's correlation in the time-direction can be exploited. Hence, an even

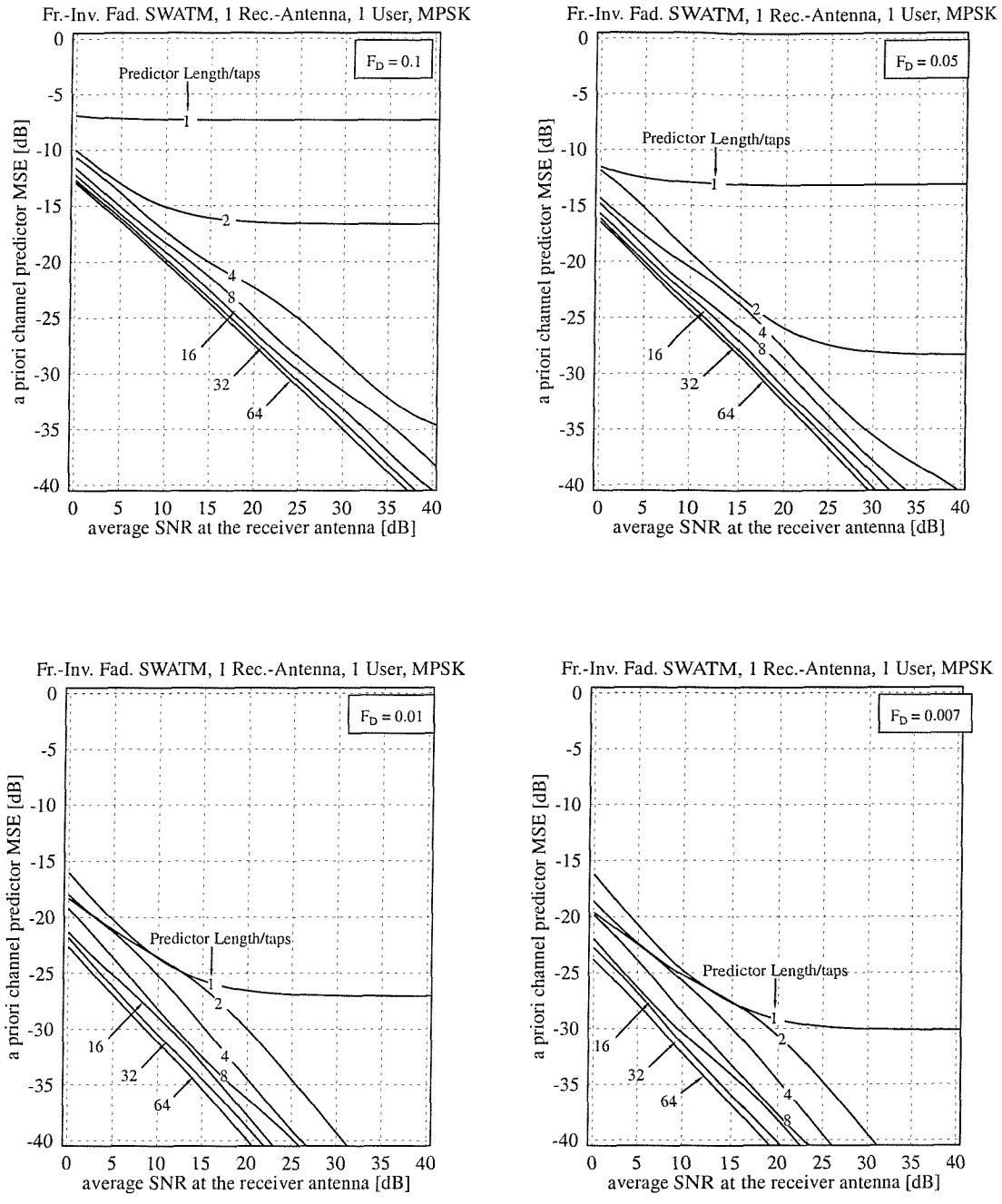

Figure 2.5: Mean-Square Error (MSE) exhibited by the **robust decision-directed *a priori* channel predictor**, which follows the philosophy of Figure 2.4, as a function of the Signal-to-Noise Ratio (SNR) at the reception antenna. **Error-free symbol decisions** and prediction filter lengths of up to 64 taps were used in the **"frame-invariant"** fading **indoor WATM channel** environment of Figure 6.1 at OFDM symbol-normalized Doppler frequencies of $F_D = 0.1$ (**top left**), 0.05 (**top right**), 0.01 (**bottom left**) and 0.007 (**bottom right**); the variance of the AWGN was $\sigma_n^2 = 2$; the CIR window size was $K_0 = 12$ taps. The results were evaluated from Equation 2.52.

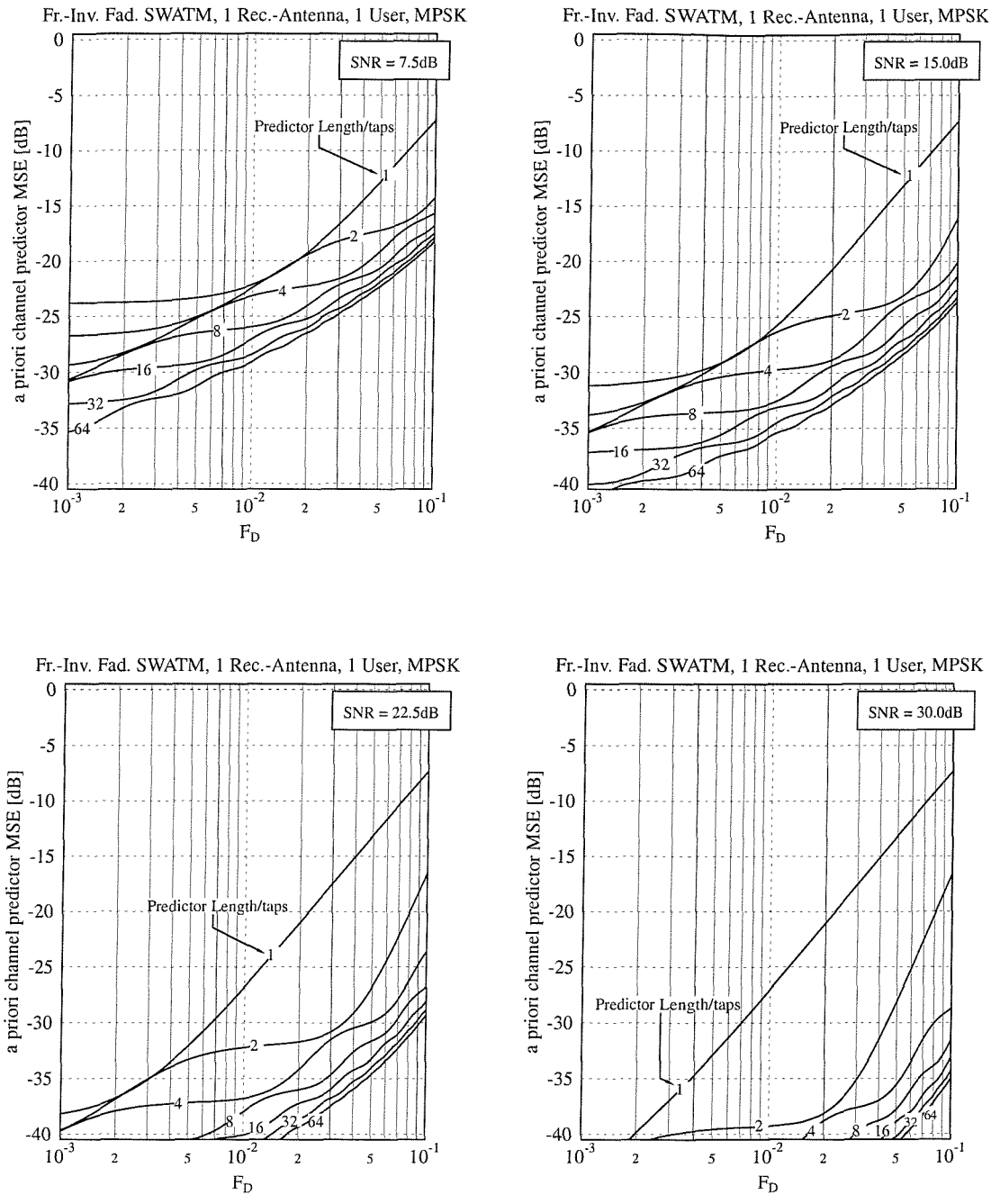

Figure 2.6: Mean-Square Error (MSE) exhibited by the **robust decision-directed *a priori* channel predictor**, which follows the philosophy of Figure 2.4, as a function of the OFDM symbol normalized Doppler frequency F_D. **Error-free symbol decisions** and prediction filter lengths of up to 64 taps were used in the **"frame-invariant"** fading **indoor WATM channel** environment of Figure 6.1 at Signal-to-Noise Ratios (SNRs) of $7.5dB$ (**top left**), $15.0dB$ (**top right**), $22.5dB$ (**bottom left**) and $30.0dB$ (**bottom right**); the variance of the AWGN was $\sigma_n^2 = 2$; the CIR window size was $K_0 = 12$ taps. The results were evaluated from Equation 2.52.

further increase of the prediction filter's length results in no substantial additional channel prediction gain, only in further noise mitigation. This is because a higher-order prediction filter produces its output based on a higher number of input samples and hence averages the additive noise samples more efficiently, which results in a reduced noise variance. This phenomenon is reflected by the parallel nature of the MSE curves corresponding to a relatively high number of CIR-related tap prediction filter coefficients.

Similar conclusions can be drawn from Figure 2.6, where we have portrayed the MSE exhibited by the predictor as a function of the OFDM symbol normalized Doppler frequency for specific values of the SNR. Again, CIR-related tap prediction filter lengths ranging between one and 64 coefficients were invoked. At higher SNRs, where the Wiener filter based predictor is only required to compensate for the decorrelation of the channel, rather than mitigating the receiver's residual AWGN, a tremendous beneficial impact is observed even in conjunction with prediction filters of a relatively low number of coefficients.

2.3.1.2 MSE Performance under Mismatched Channel Conditions with Respect to the Doppler Frequency

So far the robust channel predictor's *a priori* MSE performance has been investigated in the specific scenario, where its design parameters have been perfectly matched to the channel conditions encountered, as outlined at the beginning of this section. Let us now investigate the impact of a mismatch between the OFDM symbol normalized Doppler frequency F_D observed on the channel and that assumed in the calculation of the predictor coefficients, namely $F_{D,filter} = \tilde{F}_D$. Hence in Figure 2.7 we have portrayed the MSE of the channel predictor as a function of the OFDM symbol normalized Doppler frequency of the channel, while employing predictor coefficients optimized for a specific OFDM symbol normalized Doppler frequency $\tilde{F}_D$, that was potentially different from that of the channel encountered. For comparison we have also plotted the MSE performance in the context of employing the optimum "robust" CIR-related tap prediction filter coefficients, which match the channel conditions in terms of both the OFDM symbol normalized Doppler frequency and the SNR measured at the receiver antenna. A fixed CIR-related tap prediction filter length of four taps was assumed. The simulation results have additionally been parameterized with the SNR measured at the receiver antenna, which was assumed to match the SNR employed in the CIR-related tap's prediction filter coefficient calculation. As expected, in Figure 2.7 an MSE degradation is observed in case of encountering mismatched channel Doppler frequencies. An important characteristic of these MSE curves, which motivated the introduction of the terminology of "robust" estimator by Li *et al.* [17] in the context of infinite-order channel estimators is that only a marginal MSE degradation is observed under channel conditions, where the associated OFDM symbol normalized Doppler frequency F_D is lower, than the Doppler frequency $\tilde{F}_D$ assumed in the CIR-related tap prediction

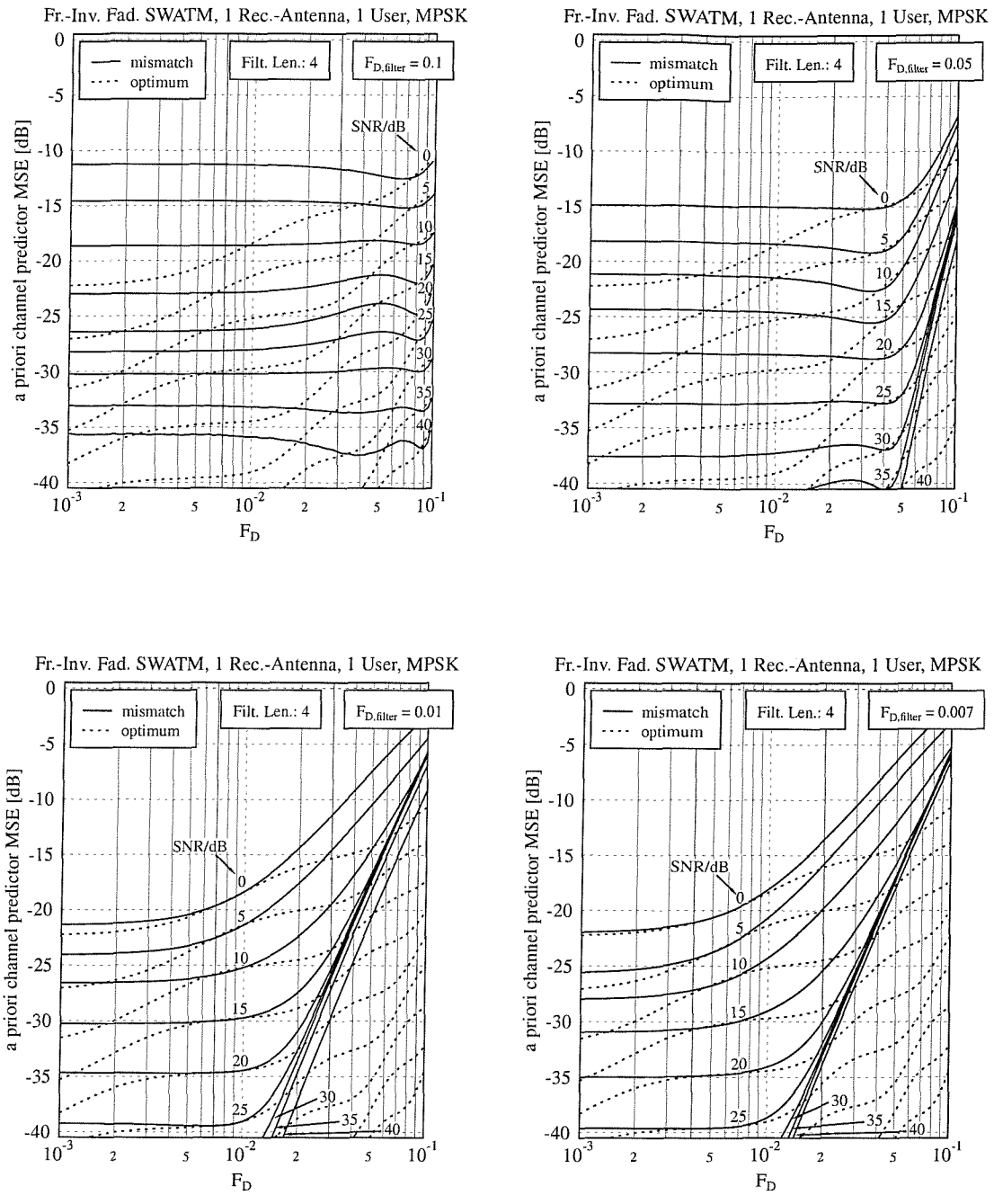

Figure 2.7: Mean-Square Error (MSE) exhibited by the **robust decision-directed *a priori* channel predictor**, which follows the philosophy of Figure 2.4, as a function of the channel's OFDM symbol normalized Doppler frequency F_D. The results were recorded for different values of the Signal-to-Noise Ratio (SNR) at the reception antenna, using **error-free symbol decisions** and a CIR-related tap prediction filter length of 4 taps in the **"frame-invariant"** fading **indoor WATM channel** environment of Figure 6.1. Fixed OFDM symbol normalized Doppler frequencies of $F_{D,filter} = \tilde{F}_D$ of 0.1 (**top left**), 0.05 (**top right**), 0.01 (**bottom left**) and 0.007 (**bottom right**) were assumed in the calculation of the CIR-related tap predictor's coefficients; the variance of the AWGN was $\sigma_n^2 = 2$; the CIR window size was $K_0 = 12$ taps. The results were evaluated from Equation 2.52.

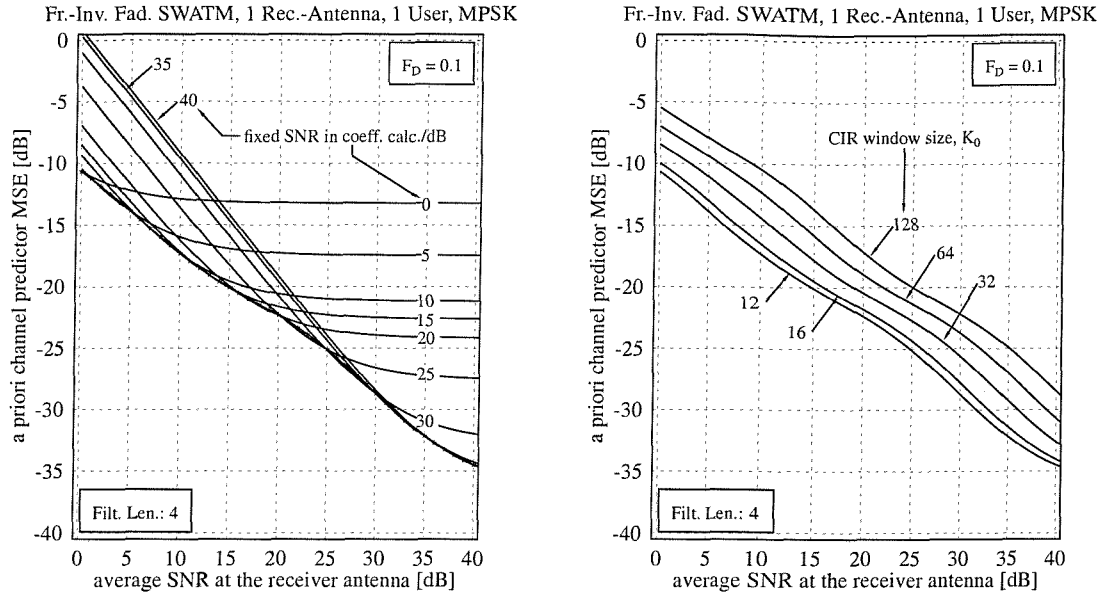

Figure 2.8: Mean-Square Error (MSE) exhibited by the **robust decision-directed *a priori* channel predictor**, which follows the concepts of Figure 2.4, as a function of the Signal-to-Noise Ratio (SNR) at the reception antenna. A fixed OFDM symbol normalized Doppler frequency of $F_D = 0.1$, **error-free symbol decisions** and a CIR-related tap prediction filter length of 4 taps was used in the **"frame-invariant"** fading **indoor WATM channel** environment of Figure 6.1. Fixed SNRs were assumed in the calculation of the predictor coefficients, regardless of the SNR encountered on the channel (**left**) and for perfectly matched conditions as a function of the CIR window size K_0 (**right**); the variance of the AWGN was $\sigma_n^2 = 2$; in the former case characterized in the left-hand-side illustration the CIR window size was $K_0 = 12$ taps. The results were evaluated from Equation 2.52.

filter's coefficient calculation, compared to the ideal case, when F_D matches $\tilde{F}_D$. We note that in the context of the finite-order prediction filters considered here, the insensitivity of the MSE to the Doppler frequency encountered is only approximate due to the filters' imperfections imposed by their finite order, which manifests itself in terms of a less selective frequency domain representation. By contrast, if the Doppler value F_D associated with the channel encountered exceeds the specific $\tilde{F}_D$ value associated with the predictor design, an MSE degradation is observed in comparison to the case, when both values are identical. This is, because significant spectral components are removed from the fading signal's frequency domain representation associated with each of the CIR-related taps.

2.3.1.3 MSE Performance under Mismatched Channel SNR Conditions

In the previous paragraph we investigated the influence of a mismatch between the Doppler frequency $\tilde{F}_D$ assumed in the calculation of the CIR-related tap prediction filter's coefficients and the actual Doppler frequency F_D observed on the channel. Similarly, an MSE degradation is observed,

if the SNR assumed in the coefficient calculation differs from that measured at the reception antenna. As an example, the MSE degradation incurred has been analytically evaluated for a scenario associated with an OFDM symbol normalized Doppler frequency of $F_D = 0.1$ observed on the channel, which was also assumed in the filter calculation. A filter length of 4 taps was used. The SNR at the reception antenna was varied between 0dB and 40dB, while the SNR invoked in the filter calculation was fixed to specific values. The corresponding results are portrayed in the left graph of Figure 2.8. In order to justify and interpret the evolution of the different curves please recall from Section 2.2.4 the mechanisms associated with the operation of the Wiener prediction filter. More specifically, a trade-off has to be found between the mitigation of the AWGN and the error incurred as a result of the decorrelation of the channel between the transmission of two consecutive OFDM symbols. If the SNR actually measured at the reception antenna is lower than the SNR assumed in the CIR-related tap prediction filter's calculation, an MSE degradation is incurred, since the mitigation of the channel decorrelation is over-weighted, while that of the noise is underestimated. By contrast, if the SNR at the reception antenna is higher than the SNR assumed in the filter calculation, the channel's correlation along the time-direction is not optimally exploited and the AWGN mitigation is over-emphasized. As a result a residual MSE is observed even at high channel SNRs.

2.3.1.4 MSE Performance under Mismatched Multipath Spread Conditions

So far we have assumed a fixed CIR window size - or sampling period duration normalized multipath spread - of $K_0 = 12$ CIR-related taps in our analytical evaluations, which - in conjunction with $K = 512$ subcarriers associated with the indoor WATM system model of Section 6.1.1 - resulted in a "filter noise reduction factor" [89] of $K_0/K \approx 0.0234$ or equivalently $K_0/K|_{dB} \approx -16.3dB$ as a consequence of setting the remaining CIR-related taps to zero. In other systems the maximum CIR-induced delay spread will be potentially different from that of the 12 taps of the indoor WATM channel model and hence K_0 would have to be adjusted accordingly. At this stage we recall that it was demonstrated for example in Equation 2.11 for an idealized channel estimator, which capitalizes on an infinite number of previous initial least-squares channel transfer factor estimates that the estimator's MSE achieved is a function of the product $(K_0/K)\rho$, where $\rho = 1/\text{SNR}$. Furthermore, this is also the case for the channel predictor considered here, where an increase of the factor K_0/K due to considering a longer CIR can be compensated by increasing the SNR i.e the transmitted signal's power, if this is deemed acceptable in the system considered. Hence, varying the factor K_0/K results in a horizontal shift of the MSE versus SNR curves, where the SNR is associated with the abscissa axis. This is illustrated in the right graph of Figure 2.8 for values of K_0 ranging from 16 to 128 in comparison to $K_0 = 12$ used as a reference and for a fixed number of $K = 512$ subcarriers.

2.3.1.5 Conclusions on the MSE Performance of Robust Decision-Directed Channel Prediction in the Context of Error-Free Symbol Decisions

In Section 2.3.1 the robust decision-directed channel predictor's MSE performance was assessed in the context of error-free symbol decisions as a function of a variety of system parameters. Specifically, in Section 2.3.1.1 we investigated the influence of the number of predictor coefficients and that of the channel's OFDM symbol normalized Doppler frequency on the predictor's MSE versus SNR performance. We found that using four predictor taps was sufficient for exploiting most of the channel's correlation in the time-direction. This was concluded on the basis of the quasi-parallel nature of the MSE curves recorded for a higher number of prediction filter taps. Our further investigations in Section 2.3.1.2 were focused on the effects of a misadjustment between the OFDM symbol normalized Doppler frequency of the channel - associated with the Jakes' spectrum [90] - and that associated with the robust channel predictor's uniform Doppler power spectrum invoked in the calculation of the CIR-related tap prediction filter coefficients. We observed even for a relatively modest number of four prediction filter taps that the channel predictor's MSE was relatively insensitive to the OFDM symbol normalized Doppler frequency of the channel, provided that the Doppler frequency encountered was lower than that assumed in the design of the predictor. Furthermore, in Section 2.3.1.3 we evaluated the predictor's sensitivity with respect to a misadjustment of the SNR encountered at the reception antenna and that employed in the calculation of the predictor's coefficients. We found that at SNRs lower than that associated with the design of the predictor, the MSE was degraded, while for SNRs higher than that assumed in the calculation of the predictor, an MSE floor was experienced. This MSE floor was encountered, because the channel's correlation was not optimally exploited. Our investigations were concluded in Section 2.3.1.4 by assessing the influence of the number of significant CIR-related taps on the predictor's MSE performance. We found that for a higher number of taps the MSE versus SNR curves were shifted towards higher SNRs, since more of the AWGN was retained.

2.3.2 MSE Performance of an Adaptive Decision-Directed Channel Predictor in the Context of Error-Free Symbol Decisions

In this section we will assess the MSE performance of the adaptive decision-directed channel predictor briefly addressed in Section 2.2.5.2, where the different CIR-related taps' predictor coefficients are obtained with the aid of the Burg algorithm [86, 83] on the basis of the statistics estimated from actual CIR-related tap samples, as advocated by Al-Susa *et al.* [18]. We have listed the relevant system parameters in Table 2.5. Recall that in our investigations of the robust channel predictor in Section 2.3.1, we had to explicitly specify the SNR and the OFDM symbol normalized Doppler frequency assumed in the CIR-related tap predictor's calculation as additional parameters, which are potentially different from those actually observed on the channel encountered. By contrast, both

K_0	Sampling period duration normalized multipath spread
F_D	OFDM symbol normalized Doppler frequency
ρ	Reciprocal of the SNR
$N_{tap}^{[t]}$	Length- or range of the CIR-related tap prediction filter
M_s	Number of samples involved in the predictor coefficient calculation
K	Number of subcarriers per OFDM symbol

Table 2.5: Summary of the parameters influencing the MSE performance of the *adaptive* decision-directed CIR-related tap predictor in the context of error-free symbol decisions and in the absence of ICI.

of these parameters are implicitly specified in the context of the adaptive channel prediction process investigated here by the number M_s of the CIR-related tap samples involved in the estimation of the channel's statistics. In addition to the parameters listed in Table 2.5 the particular shape of the power-delay profile will also affect the channel predictor's MSE performance. Please note that during our forthcoming MSE investigations of this section we have neglected the boundary effects related to the predictor's potentially impaired performance during the algorithm's startup phase, when the required M_s number of channel samples is not yet available.

The further structure of Section 2.3.2 is as follows. In Section 2.3.2.1 we portray the adaptive channel predictor's MSE performance as a function of the SNR encountered at the reception antenna in the context of various OFDM symbol normalized Doppler frequencies, F_D, and additionally parameterized with the number of samples M_s invoked in the Burg algorithm assisted evaluation of the CIR-related tap predictor's coefficients. Based on these MSE performance results, in Section 2.3.2.2 the MSE performance results of Section 2.3.1.1 associated with the robust channel predictor recorded in the context of perfectly matched channel conditions of $K_0 = \tilde{K}_0$ as well as $F_D = \tilde{F}_D$ and $\rho = \tilde{\rho}$ will be compared to those of the adaptive channel predictor. Furthermore, in Section 2.3.2.3 the adaptive channel predictor's MSE performance achieved in conjunction with various sample-spaced negative exponentially decaying multipath intensity profiles will be compared to that associated with a sample-spaced uniform multipath intensity profile. Finally, in Section 2.3.2.4 we will offer our conclusions with respect to the comparison of the robust- and adaptive decision-directed channel predictors.

2.3.2.1 MSE Performance under Matched Channel Conditions as a Function of the Number of Samples invoked in the Predictor Design

In Figure 2.9 we have evaluated the MSE exhibited by the Burg algorithm assisted decision-directed channel predictor as a function of the SNR recorded at the reception antenna in the context of the indoor WATM channel model of Figure 6.1 using various OFDM symbol normalized Doppler frequencies F_D and a fixed predictor length of 4 taps. The predictor's MSE has been parameterized

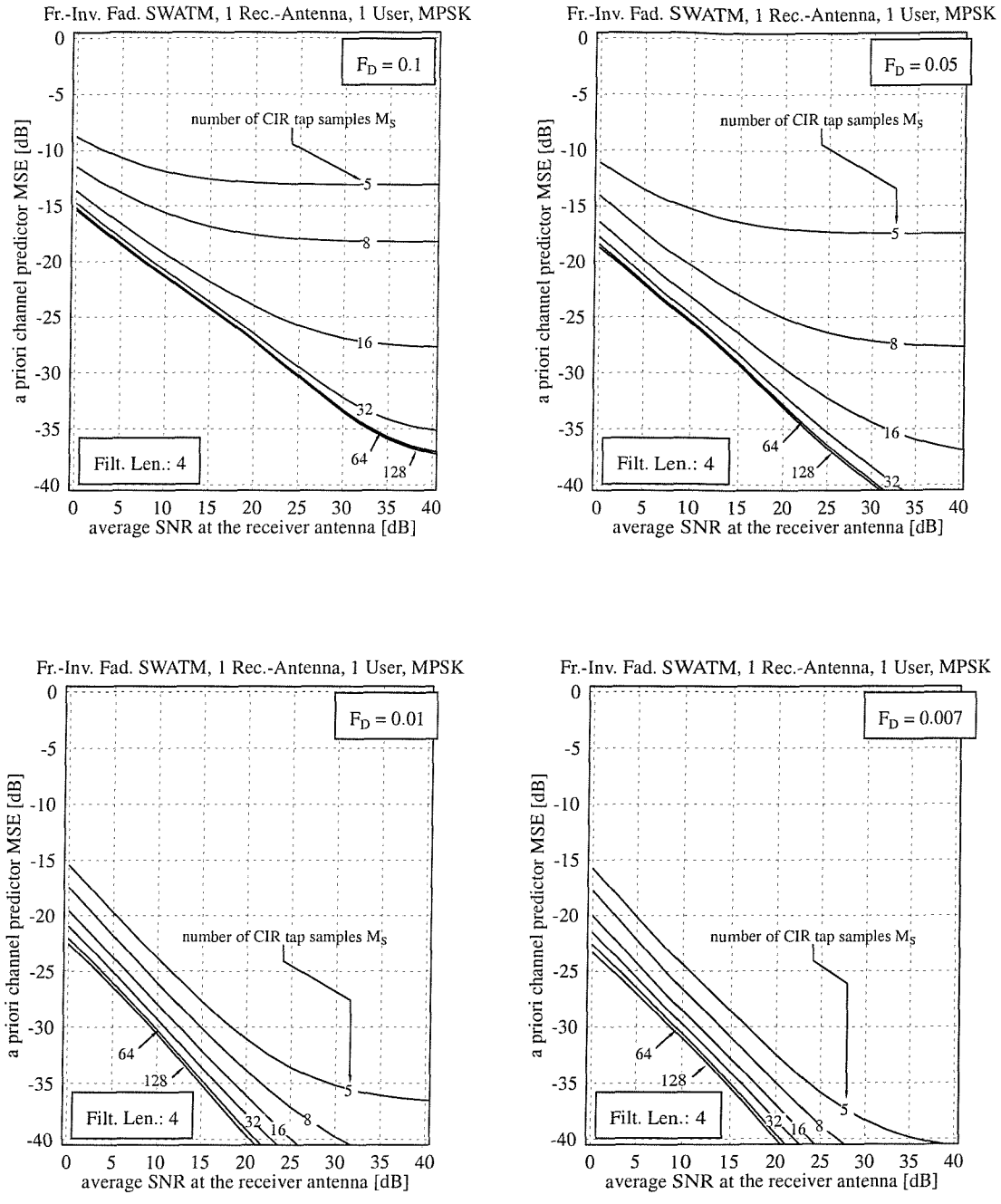

Figure 2.9: Mean-Square Error (MSE) exhibited by the **Burg algorithm assisted decision-directed *a priori* channel predictor** as a function of the Signal-to-Noise Ratio (SNR) at the reception antenna. The results are parameterized with the number of samples M_s invoked in the Burg algorithm. **Error-free symbol decisions** were used and a prediction filter length of 4 taps was employed in the **"frame-invariant"** fading **indoor WATM channel** environment of Figure 6.1. The OFDM symbol-normalized Doppler frequencies used were F_D of 0.1 (**top left**), 0.05 (**top right**), 0.01 (**bottom left**) and 0.007 (**bottom right**). The variance of the AWGN was $\sigma_n^2 = 2$. The CIR window size was $K_0 = 12$ taps.

with the number of time-direction CIR-related tap samples M_s considered in the estimation of the individual CIR-related taps' correlation inherent in the Burg algorithm, in form of the spaced-time correlation function associated with each CIR tap's fading process. We observe a reduction of the MSE along with an increasing number of samples M_s invoked. This is due to the increased accuracy of the estimated channel statistics. However, when the number of channel samples is in excess of about $M_s = 64$, only a marginal further MSE reduction can be observed.

2.3.2.2 MSE Performance in Comparison to that of the Robust Channel Transfer Function Predictor

Upon comparing the MSE curves of Figure 2.9 for a sufficiently high number of time-direction CIR-related tap samples M_s to the MSE curves of Figure 2.5, which were associated with the robust channel predictor and were recorded for a prediction filter length of 4 taps, we observe furthermore that the adaptive Burg-algorithm based predictor outperforms the robust approach in terms of the achievable MSE by about 6dB, also depending on the specific channel SNR encountered. The mechanisms responsible for this improvement will be highlighted during our forthcoming discourse in this section. In the context of the simulation results presented here we employed the indoor WATM system model of Section 6.1.1, having a 3-path sample-spaced CIR. The non-zero CIR tap values are associated with the tap indices of 0, 6 and 11. While the robust channel predictor assessed in Section 2.3.1 applied the same CIR-related tap prediction filter coefficients to the different CIR taps, regardless of the power level associated with the specific CIR-related tap, the adaptive predictor performed a more effective suppression of the undesired additive noise associated with the specific estimated CIR-related taps that have a near-zero magnitude. This is a consequence of the spectrally white distribution of the AWGN. As a result, the components of the specific CIR-related tap's estimated cross-correlation vector tend to zero in the absence of a correlated channel signal, provided that a sufficiently high number of samples associated with $M_s \rightarrow \infty$ is used. Hence, for the specific indoor WATM channel model used and for a sufficiently high number of channel samples M_s invoked in the prediction process, the noise reduction factor becomes $3/512$. By contrast, for the same channel model in the context of the robust prediction based approach and for a CIR-related window size of $K_0 = 12$ taps the noise reduction factor is $12/512$. This corresponds to an MSE reduction by a factor of 4, or on a logarithmic scale by 6.02dB. The same sparse nature of the CIR can also be exploited in the context of the robust channel predictor characterized in Section 2.3.1 upon applying a threshold to the estimated CIR-related tap values, below which the corresponding CIR-related taps are forced to zero. This technique was referred to as "significant tap catching" (STC) by Li *et al.* [21] in the context of channel estimation contrived for space-time coded OFDM systems. It should be noted that not only the estimates of the insignificant, low-energy CIR-related taps, but also the estimates of the significant CIR-related taps benefit from the more efficient adaptation of

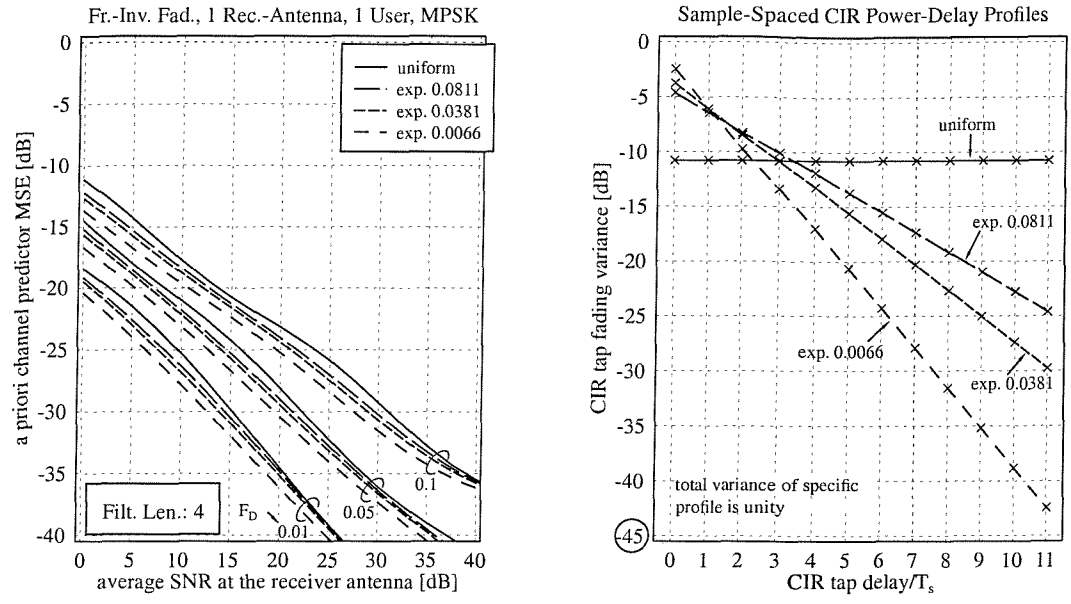

Figure 2.10: (**left**): **Mean-Square Error (MSE)** exhibited by the **Burg algorithm assisted decision-directed *a priori* channel predictor** upon invoking a near-infinite number of CIR samples, namely $M_s \rightarrow \infty$ as a function of the Signal-to-Noise Ratio (SNR) recorded at the reception antenna. **Error-free symbol decisions** and a prediction filter length of 4 taps were used for a **"frame-invariant"** fading channel having OFDM symbol-normalized Doppler frequencies of $F_D = 0.1, 0.05$ and 0.01, as well as different power delay profiles. The variance of the AWGN was $\sigma_n^2 = 2$. The CIR window size was $K_0 = 12$ taps. (**right**): Characterization of the various power delay profiles; the numerical value, which constitutes part of a specific delay profile's identifier is identical to the ratio r defined in Equation 2.58.

the CIR-related tap prediction filter to the actual channel statistics encountered. From Equation 2.27 it became explicit that in the context of the optimum two-dimensional channel predictor each CIR-related tap is associated with a specific eigenvalue of the channel's spaced-frequency correlation matrix, while in the context of the potentially sub-optimum robust channel predictor an identical eigenvalue of $\tilde{\lambda}_l^{[f]} = K/K_0$ was associated with each CIR-related tap. As a result, the robust channel predictor was rendered insensitive against the specific shape of the channel's multipath intensity profile, while at the same time exhibiting the worst MSE performance of all predictors operating on channels having power-delay profiles confined to a limited CIR window dimension of K_0 taps.

2.3.2.3 MSE Performance for Various Multipath Intensity Profiles

The influence of the specific shape of the channel's multipath intensity profile on the adaptive channel predictor's MSE performance has been further illustrated in Figure 2.10. Four different sample-spaced multipath intensity profiles are invoked in our comparisons. The specific multipath intensity trajectories are portrayed in the right-hand side graph of Figure 2.10. The uniform multipath intensity profile serves as a benchmarker, while with the aid of the different negative exponentially

decaying multipath intensity profiles the influence of a 'power compaction' to a few CIR-related taps on the estimator's MSE can conveniently be demonstrated. Here the static negative exponentially decaying amplitude delay profile is defined as:

$$h_{expo}[l] = \beta_{expo} e^{-\alpha_{expo} l}, \qquad 0 \leq l \leq K_0 - 1, \tag{2.57}$$

The specific values of the decay factor α_{expo} and the amplitude scaling factor β_{expo} are determined here by the ratio r of the CIR tap amplitude in the K_0-th CIR tap, versus that in the zero-th CIR tap, which is formulated as:

$$r = \frac{h_{expo}[K_0]}{h_{expo}[0]}, \tag{2.58}$$

and by the condition that the sum of the squared CIR tap amplitudes is unity, which implies that no power loss or gain is imposed by the channel, yielding:

$$\sum_{l=0}^{K_0-1} |h_{expo}[l]|^2 \stackrel{!}{=} 1. \tag{2.59}$$

From Equations 2.58 and 2.57 the value of the decay factor α_{expo} can be determined as:

$$\alpha_{expo} = -\frac{1}{K_0} \ln(r), \tag{2.60}$$

while upon invoking Equations 2.59 and 2.57 the amplitude scaling factor β_{expo} is given by:

$$\beta_{expo} = \sqrt{\frac{1 - e^{-2\alpha_{expo}}}{1 - e^{-2\alpha_{expo} K_0}}}. \tag{2.61}$$

In Figure 2.10 the numerical value, which is part of a specific exponential profile's identifier is identical to the factor r defined by Equation 2.58. As illustrated in the left-hand side graph of Figure 2.10, the worst MSE performance is exhibited by the adaptive channel predictor on a channel having a uniform multipath intensity profile. In this case identical CIR-related tap prediction filters are invoked in the different CIR taps' prediction processes and hence the prediction could also be performed using the same channel transfer factor prediction filter on a subcarrier by subcarrier basis in the frequency domain instead of on a CIR-related tap-by-tap basis in the time-domain. By contrast, for the specific negative exponential multipath intensity profiles, which exhibit a non-uniform power distribution across the different CIR taps a reduced MSE is observed. More specifically, the highest performance improvement is achieved for a negative exponentially decaying multipath intensity profile associated with a ratio of $r = 0.0066$, where the highest energy compaction into the first few taps is observed.

2.3.2.4 Conclusions on Adaptive Decision-Directed Channel Prediction in the Context of Error-Free Symbol Decisions

In Section 2.3.2 Burg algorithm assisted block-adaptive decision-directed channel prediction was investigated in the idealistic scenario of error-free symbol decisions. Our discussions commenced

in Section 2.3.2.1 by portraying the effects of the specific number of M_s past time-direction CIR-related tap samples invoked in the Burg algorithm on the predictor's MSE. We found that in the context of a four-tap CIR-related tap prediction filter increasing the number M_s of the past time-direction CIR-related tap samples beyond $M_s = 64$ does not result in any significant performance improvement. Furthermore, in Section 2.3.2.2 the adaptive channel predictor's MSE was compared against that of the robust predictor on the basis of the results portrayed in Section 2.3.1. These comparisons were further expanded in Section 2.3.2.3 upon invoking various sample-spaced multipath intensity profiles. Recall that the uniform profile is the one associated with the robust CIR-related tap predictor.

In order to elaborate a little further, based on the simulation results presented in Section 2.3.2.3 we conclude that in scenarios associated with a uniform channel multipath intensity profile, where identical prediction filters are applied to the different CIR-related taps, the task of two-dimensional channel transfer function prediction in the frequency domain can be split into that of one-dimensional CIR-related tap windowing in the time-domain followed by one-dimensional subcarrier-by-subcarrier based channel transfer factor prediction in the time-direction using the same channel transfer factor prediction filter for all subcarriers. However, in order to reduce the computational complexity of the actual implementation, the filtering along the time-direction is performed in the time-domain, since the number of filtering operations is reduced by filtering K_0 CIR-related taps, rather than K frequency-domain channel transfer factors. In this case the MSE of the adaptive channel predictor characterized in Section 2.3.2, while employing the Burg algorithm [86, 83] is identical to that of the robust channel predictor assessed in Section 2.3.1, provided that the Doppler frequency assumed in the design of the robust predictor's time-direction filter matches that of the channel encountered and the SNR assumed in the filter's calculation is identical to that experienced at the reception antenna. Otherwise a further MSE degradation is observed for the robust predictor in comparison to the adaptive Burg-algorithm assisted predictor, as it was illustrated in Figures 2.7 and 2.8, respectively. By contrast, in cases where the channel's multipath intensity profile is sharply decaying, an MSE degradation is observed in conjunction with the robust predictor of Section 2.3.1 compared to the adaptive predictor of Section 2.3.2. Recall that the "robust" channel predictor, where the prediction is performed individually for each tap, i.e on a tap-by-tap basis in the CIR-related domain, is actually identical to two cascaded 1D frequency-domain filters, where one of them interpolates the subcarrier channel transfer factors across a given frequency-domain OFDM symbol, while the other one provides a predicted channel transfer function for the next OFDM symbol. By contrast, the adaptive channel predictor investigated in Section 2.3.2, where different prediction filters are employed for the different CIR-related taps is actually equivalent to a true $2D$ channel predictor operating in the frequency domain.

2.3.3 MSE Performance of a Robust Decision-Directed Channel Predictor in the Context of an Uncoded System

In Sections 2.3.1 and 2.3.2 we evaluated the MSE of the robust channel predictor and that of the Burg algorithm assisted adaptive channel predictor in the context of the idealistic scenario of error-free symbol decisions at the receiver. We demonstrated that for transmissions over the channels investigated, which had a sample-spaced impulse response of a maximum dispersion of K_0 samples, the robust channel predictor's MSE upper-bounds the MSE exhibited by the adaptive channel predictor upon invoking a sufficiently high number of time-direction CIR samples in the CIR-related tap prediction process. For the OFDM symbol normalized Doppler frequencies considered no significant further *a priori* MSE reduction was observed upon increasing the number of time-direction CIR-related tap samples invoked beyond about $M_s = 64$. Motivated by the fact that the MSE performance of the robust channel predictor constitutes the worst-case MSE performance of the adaptive channel predictor provided that a sufficiently high number of error-free CIR-related tap samples is available, in this section we will focus our attention on studying the robust channel predictor further, again, in the context of a continuous transmission mode, where the predictor's boundary effects were avoided by always providing a sufficiently high number of least-squares channel transfer factor estimates based on past OFDM symbols. Although the simulation results were obtained in the context of the indoor WATM channel model of Figure 6.1, no specific assumptions were stipulated concerning the shape of the channel's impulse response in the context of the robust channel predictor design. Hence the same performance results would be obtained in the context of any other sample-spaced CIR profile having a maximum dispersion of 11 taps.

The further structure of Section 2.3.3 is as follows. Based on Monte-Carlo simulations in Section 2.3.3.1 we will evaluate the MSE performance of the robust channel predictor under frame-invariant fading channel conditions upon assuming error-free symbol decisions. In Section 2.3.3.2 our performance assessments are rendered more realistically by allowing transmission errors to occur in the demodulation process at the receiver. Furthermore, in Section 2.3.3.3 the idealistic assumption of frame-invariant fading is removed in favour of the more realistic frame-variant fading scenario. As a result, inter-subcarrier interference (ICI) [88] is encountered. Again, our conclusions will be outlined in Section 2.3.3.4. In contrast to our investigations in Section 2.3.3, where we have employed the predictor MSE as our performance measure, in Section 2.3.4 the system BER will be assessed in both uncoded- and coded scenarios in conjunction with various modulation schemes.

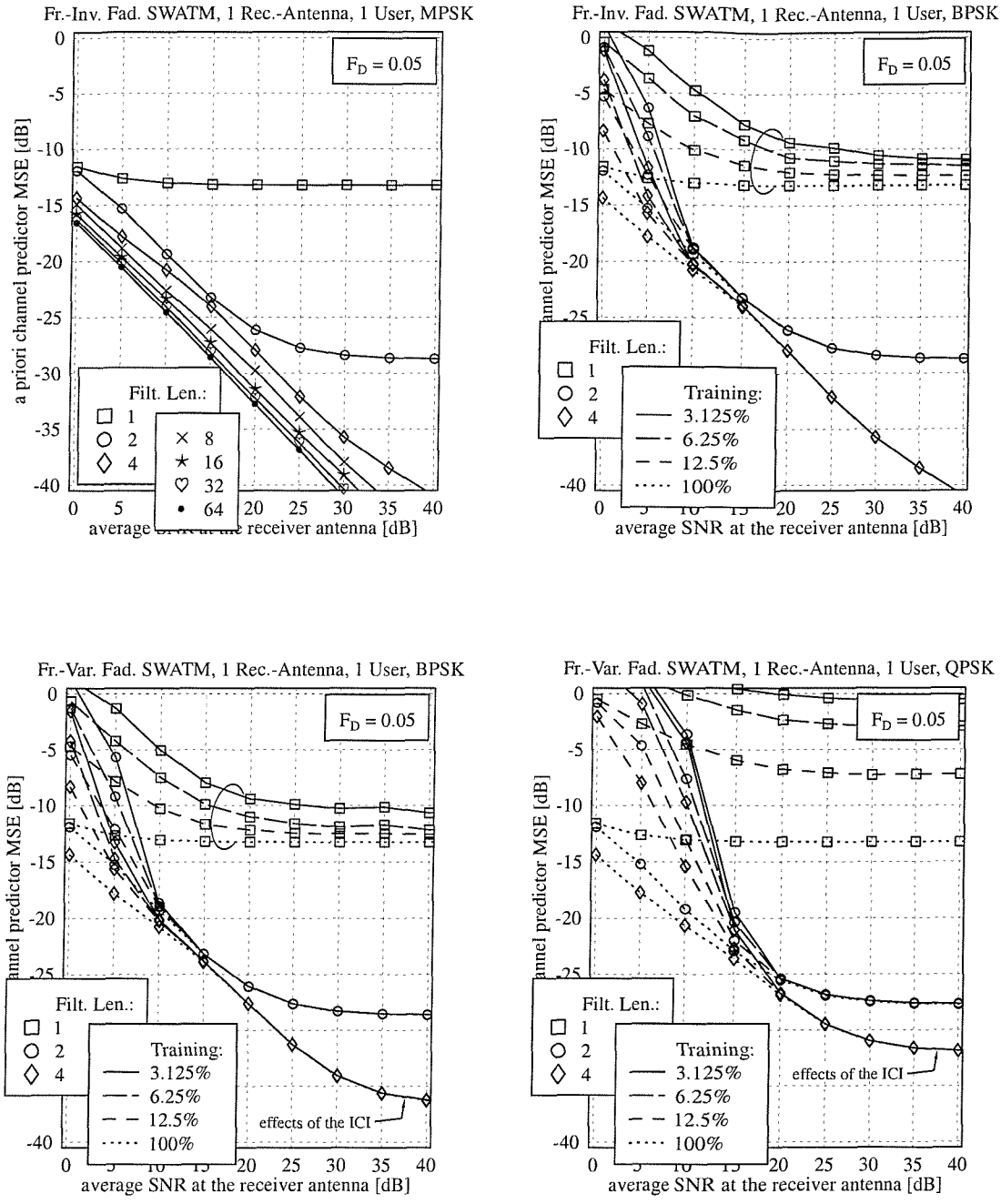

Figure 2.11: Mean-Square Error (MSE) exhibited by the **robust decision-directed *a priori* channel predictor** as a function of the SNR encountered at the reception antenna. The results are additionally parameterized with the prediction filter length used. The fading **indoor WATM channel** environment of Figure 6.1 was encountered at an OFDM symbol-normalized Doppler frequency F_D of 0.05; (**top left**): MSE for various prediction filter lengths of up to 64 taps and for error-free symbol decisions in the context of a frame-invariant fading channel; (**top right**): MSE for prediction filter lengths of up to 4 taps and potentially error contaminated BPSK symbol decisions in the context of a frame-invariant fading channel; (**bottom left**): same conditions as in the top right figure, but transmitting over a frame-variant fading channel; (**bottom right**): same conditions as in bottom left figure, but for QPSK symbol decisions; the variance of the AWGN was $\sigma_n^2 = 2$; the CIR window size was $K_0 = 12$ taps.

2.3.3.1 MSE Performance for a Frame-Invariant Fading Channel and for Error-Free Symbol Decisions

We commence our investigations based on the idealistic assumption of encountering a "frame-invariant" fading channel, where the fading channel's magnitude and phase was kept constant during the OFDM symbol's period, so as to avoid obfuscating the results of channel prediction by the effects of Inter-subCarrier Interference (ICI) [88]. Furthermore, we assumed the availability of *error-free symbol decisions*. During our discourse we will gradually relax these constraints in favour of more realistic operating conditions. The corresponding MSE simulation results obtained for an OFDM symbol normalized Doppler frequency of $F_D = 0.05$ are portrayed in the top left graph of Figure 2.11, where we have fixed the CIR dispersion to $K_0 = 12$ taps, which is equal to the normalized multipath spread of the CIR associated with the indoor WATM channel model of Figure 6.1. We observe that as expected, upon increasing the prediction filter length from 1 to 64 taps, the MSE performance improves. On the basis of the slope of the MSE curves we also infer - as alluded to in Section 2.3.1 - that most of the channel transfer function's correlation observed in the time-direction for consecutive frequency-domain OFDM symbols can be exploited with the aid of a prediction filter length of 4 taps. Further increasing the CIR-related tap prediction filter length has the beneficial but modest effect of reducing the influence of the channel noise due to averaging a higher number of additive noise components during the filtering process. As argued before in the context of Figure 2.5, this noise averaging or mitigation process manifests itself in the parallel nature of the MSE curves observed for filter lengths in excess of 4 taps in Figure 2.11.

2.3.3.2 MSE Performance for a Frame-Invariant Fading Channel and Sliced Symbol Decisions

In practice, error-free symbol decisions are normally not available, even if the system is designed for operating at a low BER of say 10^{-5}. To be more realistic, let us now consider the case of potentially error contaminated, *sliced symbol decisions*, where the reference signal is generated by simply re-modulating the sliced symbols. Channel coding is not considered at the moment. The corresponding simulation results recorded for the "frame-invariant" fading WATM channel of Figure 6.1 in the context of BPSK modulated OFDM transmissions over a channel that is fading at a rate of $F_D = 0.05$ are illustrated in the top right-hand side graph of Figure 2.11. Observe that we have specified the proportion of pilot-based channel measurement or training information as an additional parameter. More explicitly, training information is employed in form of dedicated OFDM pilot symbols, where all the subcarriers host randomly BPSK-modulated pilot symbols, which are known to the receiver. Thus error propagation extending over a duration longer than the time between consecutive pure pilot-based training OFDM symbols is reduced. It should be noted that a channel sounding training overhead of 3.125% corresponds to assigning pure pilot-based training information to every 32-nd

OFDM symbol. Similarly, 6.25% overhead corresponds to a pure pilot-based training period of 16 OFDM symbols and 12.5% corresponds to an 8 OFDM symbol training period, respectively, when assuming the transmission of single, rather than multiple consecutive pure pilot-based training OFDM symbols. In the top right graph of Figure 2.11 the impact of the different training OFDM symbol densities becomes explicit for the case of first-order i.e 1-tap CIR-related tap filtering, which provides relatively inaccurate channel estimates in the context of propagation scenarios having a high OFDM symbol normalized Doppler frequency, such as $F_D = 0.05$. For the more accurate 2- and 4-tap CIR-related tap prediction arrangements, transmitting training OFDM symbols shows the highest impact at SNRs below 10dB, while for higher SNRs the MSE performance curves merge as a result of the increasingly high-probability of error-free symbol decisions.

2.3.3.3 MSE Performance for a Frame-Variant Fading Channel and for Sliced Symbol Decisions

In order to further improve the degree of realism in our simulations, let us now focus our attention on the case of a "frame-variant" fading channel. The corresponding simulation results acquired for BPSK modulation are illustrated in the bottom left graph of Figure 2.11. In comparison to the performance exhibited by the decision-directed channel predictor in the idealistic environment of a "frame-invariant" fading channel, the MSE performance becomes more limited, particularly at relatively high SNRs. This is a result of the noise-like ICI contributions [88] induced by the frame-variant fading channel.[12] In order to further illustrate the impact of erroneous symbol decisions on the quality of the predicted channel transfer functions, the *a priori* channel predictor MSE has also been evaluated in the context of the QPSK modulation scheme used. The corresponding simulation results are portrayed in the bottom right graph of Figure 2.11. In contrast to the corresponding simulation results acquired for BPSK modulation and shown in the bottom left graph of Figure 2.11, the merging point of the two sets of curves associated with the erroneous symbol decisions and the error-free symbol decisions is found at higher SNRs, namely between 15 and 20dB. Furthermore, we note that the residual MSE inflicted by the ICI at SNRs in excess of about 20dB is increased in the context of QPSK modulation in comparison to BPSK modulation, as it was shown in the bottom left graph of Figure 2.11. Although the variance of the ICI is independent of the specific choice of the modulation scheme used, our results not included here for reasons of space economy suggest that differences can be observed between the subcarrier-based ICI power distributions for the different modulation modes employed. For modulation schemes, which transmit two orthogonal

[12]Note that while the predictor's performance is related to the OFDM symbol normalized Doppler frequency of the channel, namely to $F_D = (K + K_g)T_s f_D$, the variance of the ICI is related to the 'FFT window duration normalized' Doppler frequency, namely to $F_{D,K} = KT_s f_D$. The quotient of these normalized Doppler frequencies is given by $\frac{F_D}{F_{D,K}} = 1 + \frac{K_g}{K}$. Hence, upon neglecting the effects of error propagation, and for all simulation setups using the same modulation scheme, identical OFDM symbol normalized Doppler frequencies F_D and identical quotients K_g/K the performance will be the same, provided that the noise reduction factor K_0/K is also identical.

signal components, such as for example QPSK or higher-order MPSK modulation schemes, the probability of encountering ICI contributions of a high power is higher than for BPSK. Again, the exact impact of various modulation schemes on the predictor's MSE has not been investigated further, but the existence of a correlation between these two phenomena is conjectured.

At this stage of our discussions it is worth noting that in channel scenarios associated with a high Doppler frequency the specific design of the pilot-based training OFDM symbols has a major influence on the estimator's performance. More specifically, transmitting the same constellation point in each of the subcarriers of the pilot-based training OFDM symbol would result in an excessive amount of ICI as well as in a high crest-factor. Hence, in line with standard practice [95], we opted for assigning a randomly BPSK modulated symbol sequence, to each training OFDM symbol, which is also known to the receiver.

On the basis of the simulation results presented so far, we conclude that with the aid of an MMSE CIR-related tap predictor, decision-directed channel estimation can be successfully employed even in channel scenarios exhibiting relatively high OFDM symbol normalized Doppler frequencies. After providing our conclusions in the next section, in Section 2.3.4 we will characterize the system's performance in terms of the achievable BER in the context of robust decision-directed channel prediction.

2.3.3.4 Conclusions on the MSE Performance of a Robust Decision-Directed Channel Predictor in the Context of an Uncoded System

In Section 2.3.3 the robust decision-directed channel predictor's MSE performance has been evaluated in the context of an uncoded system upon invoking sliced and hence potentially error-contaminated symbol decisions. In order to reduce the number of different MSE versus SNR curves we employed an OFDM symbol normalized Doppler frequency having a mediocre value of $F_D = 0.05$. From our simulation results portrayed in Figure 2.11 we inferred that for medium SNRs up to about 15dB the predictor's MSE performance was deteriorated due to the effects of error propagation. These effects can be mitigated with the aid of dedicated pure pilot-based training OFDM symbols transmitted periodically. We have seen in Figure 2.11, that for the frame-variant fading channel scenario and a number of four CIR-related prediction filters taps the channel predictor's *a priori* MSE was limited due to the Gaussian noise like influence of the ICI, rather than as a result of the predictor's imperfections.

2.3.4 BER Performance of an Uncoded System Employing Robust Decision-Directed Channel Prediction

In Figure 2.12 we have plotted the BER performance curves corresponding to the "frame-variant" fading channel scenario associated with OFDM symbol normalized Doppler frequencies of $F_D =$

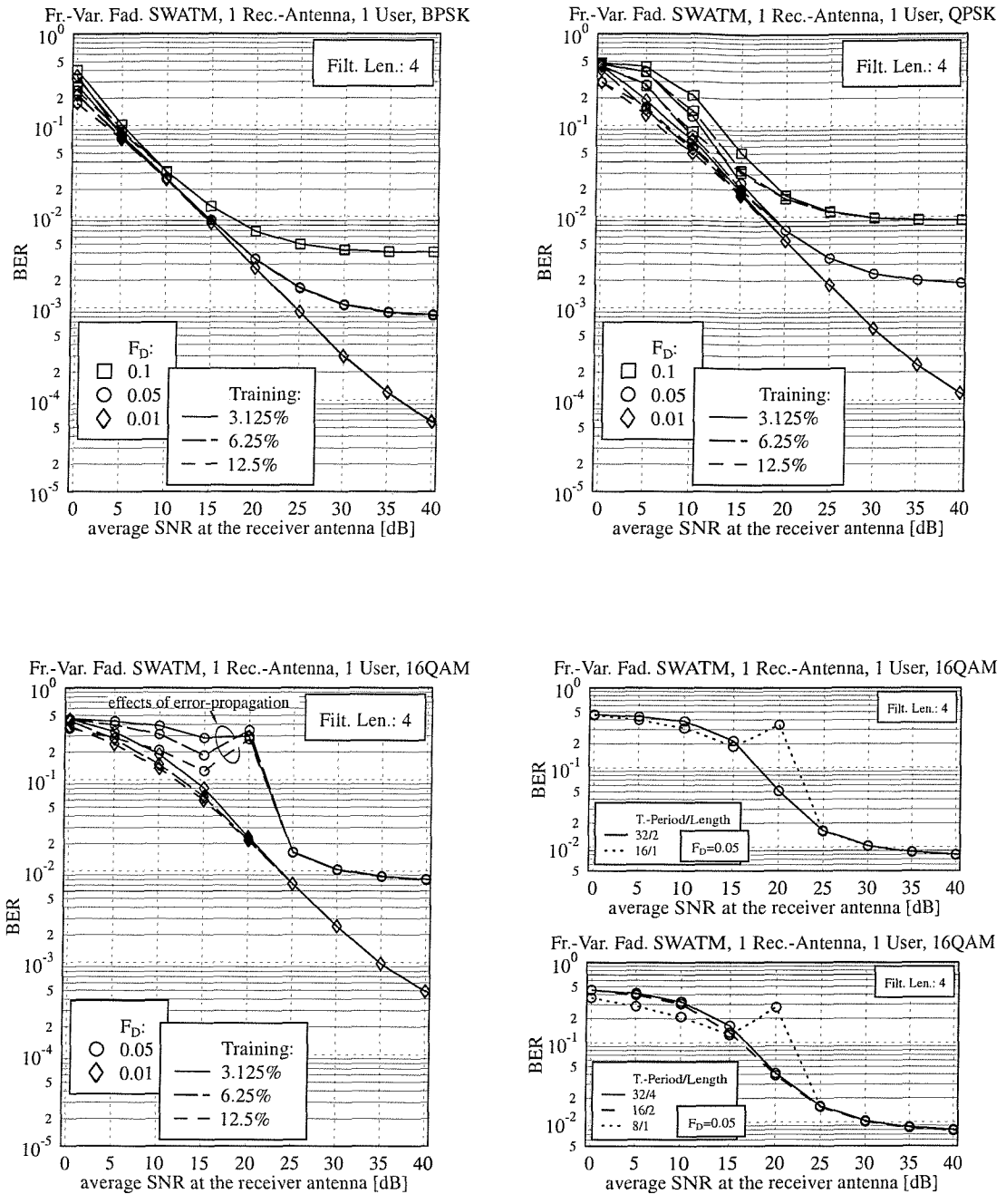

Figure 2.12: Bit Error Ratio (BER) exhibited by a system employing **robust decision-directed *a priori* channel prediction** as a function of the SNR encountered at the reception antenna. A fixed CIR-related tap prediction filter length of 4 taps was used and the results were additionally parameterized with the percentage of pure pilot-based OFDM symbol training overhead in a single reception antenna, single user scenario. The **"frame-variant"** fading **indoor WATM channel** environment of Figure 6.1 was encountered at OFDM symbol-normalized Doppler frequencies F_D of 0.1, 0.05 and 0.01 and (**top left**) BPSK, (**top right**) QPSK and (**bottom**) 16QAM modulation schemes were used. The CIR window size was $K_0 = 12$ taps.

$f_D T_f = 0.1$, 0.05 and 0.01. Different modulation schemes were considered. Specifically, the curves associated with BPSK modulation are shown in the top left graph of Figure 2.12, while those recorded for QPSK modulation and 16QAM are found in the top right graph and in the graph at the bottom of Figure 2.12, respectively. An imperfect reference signal based on sliced and remodulated symbol decisions was assumed in the process of robust decision-directed channel estimation and the CIR-related tap prediction filter length was fixed to four taps. According to our discussions in Section 2.3.3 using four taps was sufficient for exploiting most of the channel's correlation in the time-direction in the specific propagation environment considered.

The structure of the remaining part of Section 2.3.4 is as follows. The system's BER is analysed in Section 2.3.4.1 in conjunction with BPSK and QPSK. The corresponding BER results related to the more vulnerable 16QAM scheme will be provided in Section 2.3.4.2, where we will specifically focus our attention on the influence of the number of consecutive pure pilot-based training OFDM symbols transmitted periodically. Our preliminary conclusions will be offered in Section 2.3.4.3.

2.3.4.1 BER Performance for BPSK and QPSK

In conjunction with BPSK and QPSK modulation we observe in Figure 2.12 that for propagation scenarios, which exhibit relatively high OFDM symbol normalized Doppler frequencies, such as $F_D = 0.05$ and $F_D = 0.1$, the BER performance is rather limited. This is a result of the ICI imposed by the frame-variant fading. The specific choice of the pure pilot-based OFDM training symbol period plays a more dominant role in the relatively low SNR range below 15dB, where the error propagation encountered deteriorates the performance, also depending on the OFDM symbol normalized Doppler frequency F_D of the channel. As expected, the scenarios associated with a higher Doppler frequency are particularly vulnerable. From our further investigations - which are not explicitly described here for reasons of space economy - we inferred that for relatively modest values of F_D associated with SNRs close to 0dB the arrangements employing higher order CIR-related tap prediction filters are more susceptible to error propagation, than those employing a lower-order prediction filter. A plausible explanation of this phenomenon is that for higher-order CIR-related tap prediction filters the probability of invoking previous channel estimates potentially based on erroneous symbol decisions is increased. By contrast, in propagation scenarios of relatively high Doppler frequencies, such as $F_D = 0.05$ and $F_D = 0.1$, this effect is compensated by the more accurate channel estimates offered by the higher-order prediction filter. As outlined in Section 2.3.3, this is the result of a better exploitation of the channel's correlation and that of a more efficient noise mitigation due to averaging a higher number of noise components.

2.3.4.2 BER Performance for 16QAM

As shown in the bottom left graph of Figure 2.12, investigations were also conducted employing 16QAM in a system capitalizing on robust decision-directed channel estimation. In the context of the hostile, rapidly fading scenario of $F_D = 0.1$ maintaining high-integrity communication without inflicting excessive BERs became virtually impossible and hence the associated curves have not been plotted in Figure 2.12. This was attributed to the severe error propagation encountered between successive OFDM symbols, despite periodically transmitting dedicated pure pilot-based training OFDM symbols. More specifically, the effect of erroneous symbol decisions is that an inaccurate *a posteriori* channel estimate is generated for the current OFDM symbol, which in turn degrades the quality of the *a priori* channel estimate derived for the next OFDM symbol and thus the associated BER is also degraded. As a result, a potential system instability is observed with the consequence of excessive BERs. Even when benefitting from high SNRs and additionally imposing error-free OFDM symbol decisions in the remodulated DDCE-related reference, a residual BER of $3 \cdot 10^{-2}$ was observed in the context of the rapidly fading propagation scenario of $F_D = 0.1$ as a result of the excessive ICI inflicted by the frame-variant fading channel. In the more benign scenario of $F_D = 0.05$, where the associated BER results are portrayed together with those of the $F_D = 0.01$ scenario in the bottom left graph of Figure 2.12 - after an initial BER improvement recorded for SNRs up to about 15dB - a BER degradation is observed for SNRs up to 20dB. This is followed by a rapid, avalanche-like reduction of the BER to a value of around $8 \cdot 10^{-3}$, within an SNR interval of 5dB. Upon closer inspection we found that two specific mechanisms are responsible for the performance degradation incurred at these intermediate SNRs, which will be outlined below.

Firstly, the AWGN plus ICI related SNR assumed in the calculation of the CIR-related tap predictor coefficients did not account for the additional impairments resulting in an increased level of "noise" inflicted by erroneous symbol decisions and hence a noise-amplification - also known from zero-forcing (ZF) equalizers - occurred, which resulted in the performance degradation observed. The second design aspect, which influences the system's performance is the specific structure of the block of pure pilot-based training OFDM symbols transmitted. So far, each training block consisted of a single OFDM symbol. Hence, even if the most recently received OFDM symbol was a training symbol, previous erroneously demodulated OFDM symbols within the range of the prediction filter might have deteriorated the MSE of the *a priori* channel estimate for the next OFDM symbol. However, in our previous investigations of Section 2.3.3 this effect was neglected. Our related experiments revealed that this problem requires attention in the context of transmissions employing the relatively vulnerable 16QAM scheme.

In order to further illustrate this effect, we have portrayed in the bottom right graph of Figure 2.12 the BER of a 16QAM assisted OFDM scheme invoking 4-tap CIR-related tap prediction filtering in the context of an OFDM symbol normalized Doppler frequency of $F_D = 0.05$. The results are

parameterized with the number of immediately adjacent pure pilot-based OFDM symbols hosted by a training block, referred to as the training length, as well as with the training period duration between consecutive training blocks, which is assumed to be 32, 16 or, alternatively 8 OFDM symbols long. In the upper graph the training overhead was 6.25%, while in the lower graph it was twice as high, namely 12.5%. From Figure 2.12 we observe that for SNRs of up to about $15dB$ decreasing the training period duration is a more effective measure, than increasing the training block length, while for SNRs between 15- and $25dB$ we encounter the reverse mechanism. More specifically, a training block length of at least two OFDM symbol was required for avoiding the channel predictor instability.

2.3.4.3 Conclusions on the BER Performance of an Uncoded System employing Robust Decision-Directed Channel Prediction

In Section 2.3.4 we have assessed the uncoded system's BER performance in the context of robust decision-directed channel prediction. Our observation was that with the beneficial assistance of prediction filtering, decision-directed channel estimation can also be supported under rapidly fading channel conditions in conjunction with OFDM symbol normalized Doppler frequencies as high as $F_D = 0.1$. Again, as shown in Section 2.3.4.1 for BPSK and QPSK modulation, the system's BER was limited due to the effects of ICI, rather than as a result of the imperfections of the decision-directed channel predictor. By contrast, it was demonstrated in Section 2.3.4.2 for the more vulnerable 16QAM modulation scheme upon invoking four-tap prediction filtering that the system's stability could only be guaranteed for the lowest Doppler frequency of $F_D = 0.01$ used in our investigations. For a higher Doppler frequency of $F_D = 0.05$ the system became unstable at intermediate SNRs, which was a consequence of the noise amplification problem incurred. More specifically, the impairments resulting in an increased level of 'noise' inflicted by erroneous symbol decisions were not considered in the calculation of the predictor's coefficients. We found that these effects could be mitigated upon increasing the pure pilot-based training block length to two consecutive OFDM symbols per training block. This had the beneficial effect that the error-propagation effects extending beyond the training blocks were mitigated. By contrast, for a Doppler frequency of $F_D = 0.1$ the system's BER was excessive.

In the next section the performance of a system employing both decision-directed channel estimation and turbo channel coding will be investigated, where the process of channel estimation potentially benefits from the more reliable, lower-BER symbol decisions.

coding rate	$R_c = 1/2$
constraint length	$K_c = 3$
generator polynomial	$(7,5)_8$
number of iterations	4

Table 2.6: Turbo coding parameters

F_D	0.01	0.05	0.1
κ_{ICI}	0.000105	0.00445	0.01635

Table 2.7: Approximate proportionality constants κ_{ICI} for the indoor WATM system model detailed in Table 6.1 parameterized with the OFDM symbol-normalized Doppler frequency F_D.

2.3.5 BER Performance of a Turbo-Coded System employing Robust Decision-Directed Channel Prediction

In order to further reduce the BER of the system arrangements studied, invoking turbo channel coding [96, 97] is an attractive option. The turbo coding parameters are listed in Table 2.6.

The structure of the rest of this section is as follows. In Section 2.3.5.1 we will argue that an accurate estimate of the channel's ICI noise variance is required, which is incorporated into the calculation of the subcarrier based SNR. Our investigations of the system's BER performance commence in Section 2.3.5.2 using BPSK modulation, while in Section 2.3.5.3 both QPSK modulation as well as 16QAM are invoked in the context of various OFDM symbol normalized Doppler frequencies. In these investigations the BER performance is presented for a specific configuration employing sliced and remodulated data symbols as a reference in the process of decision-directed channel prediction, but refraining from involving the turbo channel decoder in the CIR-related tap prediction process. By contrast, in Section 2.3.5.4 we will discuss the impact of a turbo channel decoded reference signal, where the 'source'-related soft-output bits of the turbo decoder were sliced, re-encoded and remodulated. Our conclusions will be offered in Section 2.3.5.5.

2.3.5.1 Influence of the ICI Variance on the Subcarrier SNR

A prerequisite for minimizing the BER is the availability of a reliable subcarrier by subcarrier based SNR estimate, which is employed in the process of soft-bit generation for the turbo channel codec. In propagation scenarios exhibiting a relatively high OFDM symbol normalized Doppler frequency F_D as considered here, the effective additive noise experienced by the complex modulated symbol received in each OFDM subcarrier is constituted by the superposition of the AWGN and the Gaussian noise-like ICI induced by the frame-variant fading channel. Note that the average ICI-induced noise variance σ^2_{ICI} can be expressed as a function of the signal variance σ^2_s by means of

the proportionality relationship $\sigma_{\text{ICI}}^2 = \kappa_{\text{ICI}}\sigma_s^2$. Hence estimates of the proportionality constants κ_{ICI} have been obtained with the aid of computer simulations for different values of F_D. The results are listed in Table 2.7.

2.3.5.2 BER Performance for BPSK Modulation in the Context of an Undecoded Reference

The BER results are portrayed in Figure 2.13 assuming BPSK modulation and a training overhead of 3.125% due to transmitting a pure pilot-based training OFDM symbol in every block of 32 OFDM symbols. Here we will characterize the performance observed in the context of a 4-tap CIR-related tap prediction filter, which is capable of exploiting most of the channel's correlation. Hence, it was already highlighted in Section 2.3.3, the effect of a further increase of the predictor's length in the context of error-free symbol decisions would be limited to improving the *a priori* channel estimator's MSE in terms of mitigating the influence of the additive noise due to the weighted averaging of a higher number of noise samples.

We observe that in the context of the more rapidly fluctuating propagation scenarios associated with $F_D = 0.05$ and $F_D = 0.1$ sufficiently low BERs can only be achieved upon invoking prediction filter lengths of at least 2 or 4 taps. For a scenario of $F_D = 0.1$ even in conjunction with a 4-tap CIR-related tap prediction filter a residual BER is observed. This is a consequence of the potentially excessive BER at the input of the turbo decoder, as well as a ramification of the limited accuracy associated with the effective SNR's estimate, which leads to relatively inaccurate soft-bit values to be passed to the turbo-decoder. It should be underlined that the proportionality relationship between the average ICI-induced noise variance σ_{ICI}^2 and the signal variance σ_s^2 is valid only in terms of their long-term statistics. The instantaneous or short-term ICI variance might substantially differ from its long-term value, since the ICI incurred is strongly dependent on the speed of channel variation experienced during a specific OFDM symbol period. We also note from the BER results not portrayed here due to a lack of space that the BER performance degradation incurred as a result of employing potentially error-contaminated demodulated symbols for channel prediction compared to the case of an ideal reference in terms of error-free symbol decisions is relatively limited even at low SNRs. This is due to the BPSK modulation scheme's relative robustness.

2.3.5.3 BER Performance for QPSK Modulation and 16QAM in the Context of an Undecoded Reference

In the top-left corner of Figure 2.14 we have summarized once again our simulation results associated with a BPSK modulation assisted turbo-coded system. By contrast, the simulation results associated with a QPSK modulation- and 16QAM assisted turbo-coded system are portrayed at the top-right corner and at the bottom of Figure 2.14, respectively. Again, we have provided simulation results for the case of both an imperfect, potentially error-contaminated reference associated with a

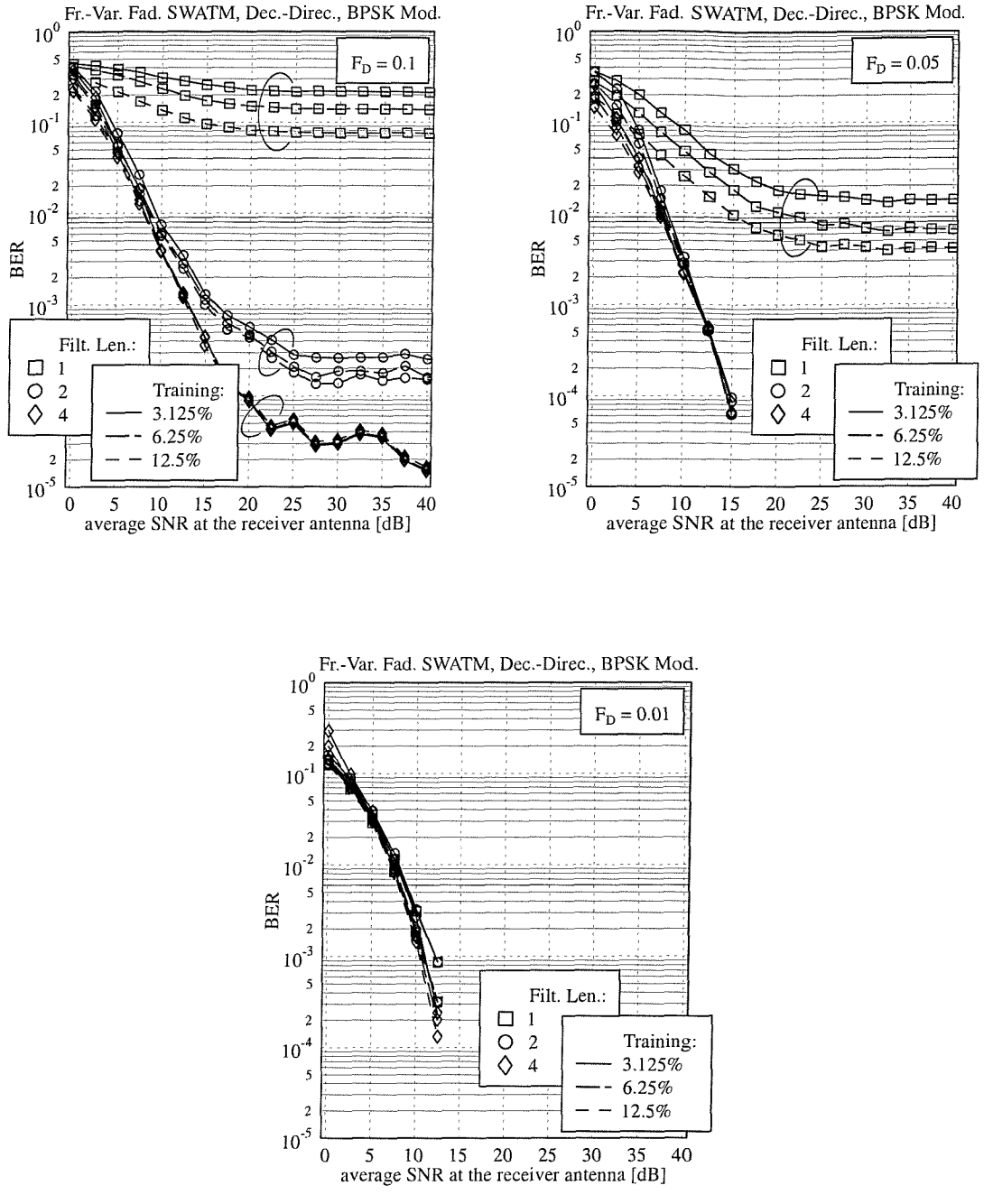

Figure 2.13: Bit Error Ratio (BER) exhibited by a **turbo-coded system** employing **robust decision-directed *a priori* channel prediction** with prediction filter lengths of up to 4 taps upon capitalizing on potentially error-contaminated, **undecoded symbol decisions**. The **"frame-variant"** fading **indoor WATM channel** environment of Section 6.1.1 was encountered at OFDM symbol-normalized Doppler frequencies F_D of 0.1 (**top left**), 0.05 (**top right**) and 0.01 (**bottom**) and **BPSK modulation** was used. The CIR window size was $K_0 = 12$ taps.

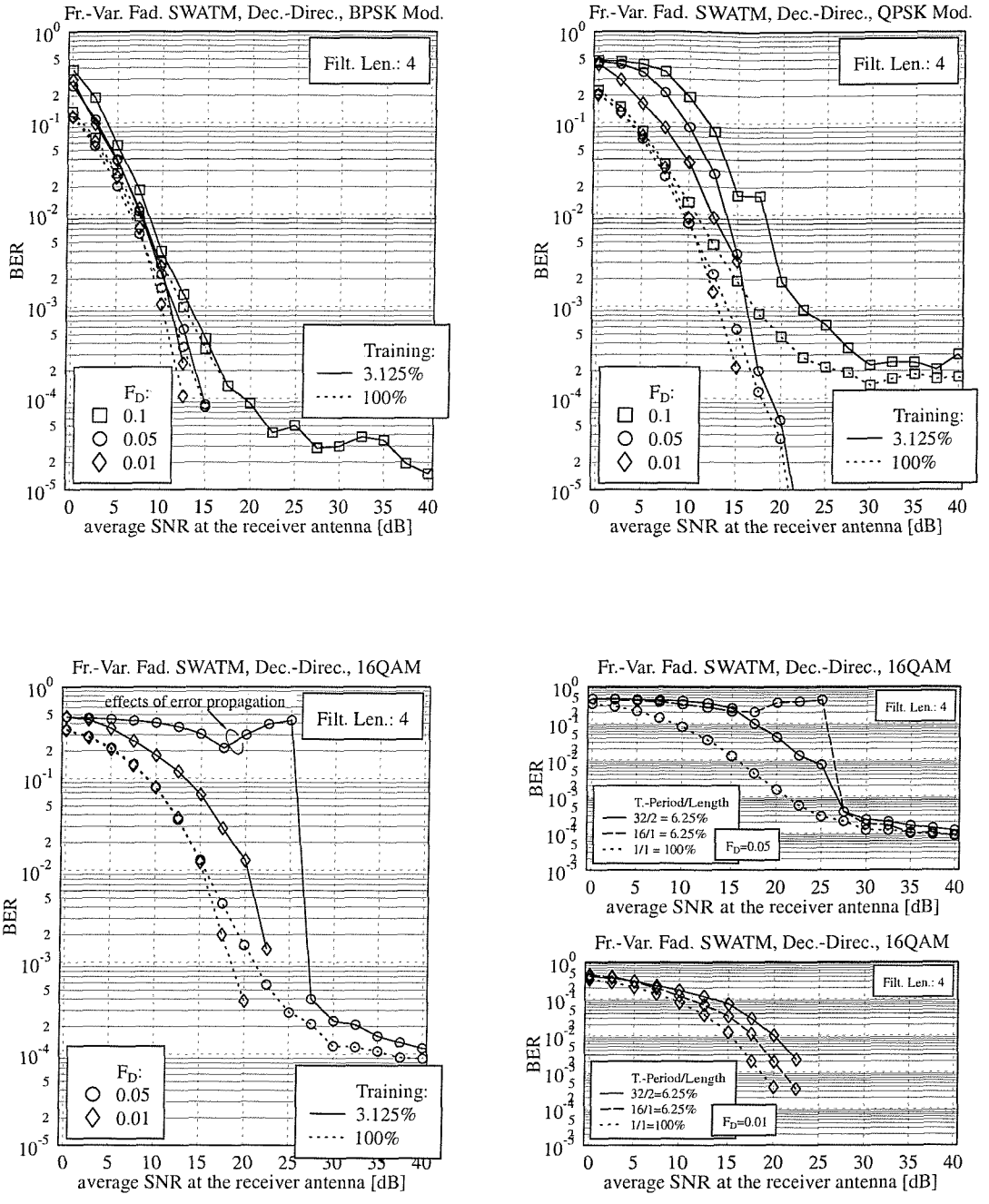

Figure 2.14: Bit Error Ratio (BER) exhibited by a **turbo-coded system** employing **robust decision-directed a priori channel prediction** using a prediction filter length of 4 taps upon capitalizing on potentially error-contaminated, **undecoded symbol decisions**. The **"frame-variant"** fading **indoor WATM channel** environment of Figure 6.1 was encountered at OFDM symbol-normalized Doppler frequencies of $F_D = 0.1$, 0.05 and 0.01 and (**top left**) BPSK, (**top right**) QPSK and (**bottom**) 16QAM modulation schemes were used. The CIR window size was $K_0 = 12$ taps.

pilot-based training overhead of 3.125%, as well as for the idealistic benchmarker of an error-free reference, which would be generated by receiving error-free training information in every OFDM symbol.

In the context of QPSK modulation and OFDM symbol-normalized Doppler frequencies of $F_D = 0.01$ and $F_D = 0.05$ we infer that turbo coding is capable of eliminating virtually all transmission errors. By contrast, for the more rapidly fluctuating and hence more ICI-contaminated scenario of $F_D = 0.1$ the BER recorded at the input of the turbo decoder is significantly increased, as illustrated in Figure 2.12. However, compared to the case of BPSK modulation, which was discussed in Section 2.3.5.2, a significant BER performance degradation is incurred due to employing an imperfect reference compared to the idealistic scenario of employing an error-free reference. This is particularly true for the case of the more rapidly fading scenarios of $F_D = 0.05$ and $F_D = 0.1$.

In case of employing 16QAM further restrictions are imposed with respect to the tolerable Doppler frequency. Specifically, in our investigations only the slowly-fading scenario of $F_D = 0.01$ allows for virtually error-free transmissions at sufficiently high SNRs. By contrast, for $F_D = 0.05$ a BER floor is observed, which is again attributed to the effects of ICI. The rapidly-fading scenario of $F_D = 0.1$ was not considered in the context of 16QAM, since in the uncoded case excessive BERs were observed as a result of the severe error propagation between successive OFDM symbols. Note again in Figure 2.14 the significant BER performance degradation incurred compared to the case of employing an error-free ideal reference.

Similarly to the BER performance results presented in Figure 2.12 for a 16QAM assisted system using no channel coding, investigations were also conducted for the turbo coded system with respect to the specific required pilot-based training period duration and to the training block length necessitated for avoiding the effects of the DDCE's instability at SNRs between 15 and $25dB$. The associated results are illustrated in the graph seen at the bottom right corner of Figure 2.14. Again, for the more rapidly-fading scenario of $F_D = 0.05$, the training block is required to be at least two OFDM symbols long for the sake of avoiding an instability. By contrast, for the more slowly-fading scenario of $F_D = 0.01$, where the effects of an instability are not explicitly observed, a comparison between the curves in the bottom-left- and right graph of Figure 2.14 shows that increasing the training block length is not an appropriate measure for improving the system's BER. In this case Figure 2.14 suggests that decreasing the training period duration with the aim of reducing the mean distance between the training OFDM symbols is a more effective measure.

It should also be noted that the systems employing QPSK modulation or 16QAM potentially benefitted from the increased channel interleaver length compared to the case of BPSK modulation, since the increased number of bits per modulated subcarrier symbol proportionately increased the number of bits mapped to an OFDM symbol without increasing the system's effective interleaving delay. This was achieved at the cost of an increased decoding complexity at the receiver.

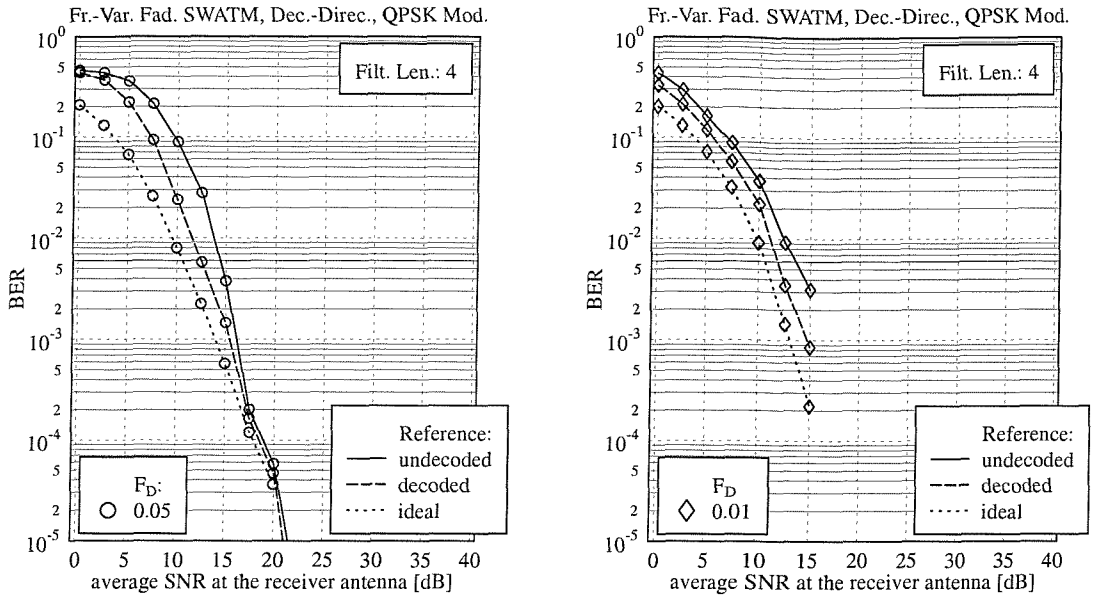

Figure 2.15: Bit Error Ratio (BER) exhibited by a **turbo-coded system** employing **robust decision-directed a priori channel prediction** using a prediction filter length of 4 taps upon capitalizing on an **ideal, undecoded or decoded reference**, respectively. The **"frame-variant"** fading **indoor WATM channel** environment of Figure 6.1 was encountered at OFDM symbol-normalized Doppler frequencies of (**left**) $F_D = 0.05$ and (**right**) $F_D = 0.01$, where QPSK modulation was used. The CIR window size was $K_0 = 12$ taps.

2.3.5.4 BER Performance for QPSK Modulation in the Context of a Decoded Reference

Investigations have also been conducted with respect to employing a turbo decoded reference in the process of decision-directed channel prediction, where the 'source'-related soft-output bits of the turbo decoder were sliced, re-encoded and remodulated. In the context of BPSK modulation, which exhibits the highest robustness among the three modulation schemes employed in our simulations, namely BPSK, QPSK and 16QAM, no significant performance advantage was observed when employing a turbo decoded reference instead of an undecoded reference. By contrast, for the more vulnerable QPSK modulation employed in conjunction with a relatively modest training overhead due to transmitting only one training OFDM symbol within every block of 32 OFDM symbols, a notable performance advantage in favour of the turbo decoded reference is observed for intermediate SNRs up to 15dB, where the effects of error propagation are significant. The associated BER performance curves in conjunction with three different scenarios, namely an ideal-, an undecoded- and a turbo decoded reference are portrayed in Figure 2.15 at the left-hand side for an OFDM symbol normalized Doppler frequency of $F_D = 0.05$ and at the right-hand side for $F_D = 0.01$. Again in contrast, upon invoking 16QAM no BER performance improvement was observed at low OFDM symbol normalized Doppler frequencies, such as $F_D = 0.01$ due to employing a 'source'-related

soft-output bit based reference. However, for the higher Doppler frequency of $F_D = 0.05$ an excessive BER was incurred, which was caused by the instability of the channel estimator. This is because for some OFDM symbols the turbo decoded reference contained significantly more erroneous subcarrier symbols, than the undecoded- or sliced reference, potentially aggravating the effects of error propagation. However, in the context of employing a 'source- plus parity'-related soft-output bit based reference, where both the source- and the parity-related soft-output bits of the turbo decoder are sliced and remodulated, a significantly improved performance is expected for all scenarios.

2.3.5.5 Conclusions on the BER Performance of a Turbo-Coded System employing Robust Decision-Directed Channel Prediction

In Section 2.3.5 the BER of a turbo-coded system employing robust decision-directed channel prediction has been evaluated. In our initial simulations conducted with respect to a BPSK-modulated system in Section 2.3.5.2 and with respect to a QPSK- or 16QAM modulated system in Section 2.3.5.3, an undecoded reference was assumed, where the symbols received in different subcarriers were sliced and remodulated without involving turbo decoding- or encoding. More specifically, for the BPSK- and QPSK-modulated systems - given sufficiently high SNRs - error-free transmissions were observed at OFDM symbol normalized Doppler frequencies of $F_D = 0.01$ and $F_D = 0.05$, while for $F_D = 0.1$ the BER curves exhibited a residual value of $2 \cdot 10^{-5}$ and $2 \cdot 10^{-4}$, respectively, which was attributed to the effects of ICI. This was achieved in conjunction with four-tap CIR-related tap prediction filtering. By contrast, for a 16QAM-assisted system error-free transmissions were only observed for the lowest Doppler frequency of $F_D = 0.01$, while for $F_D = 0.05$ a residual BER of 10^{-4} was incurred together with error-propagation and noise-amplification, which were induced by stability problems. Again, these phenomena could potentially be mitigated upon transmitting blocks of training OFDM symbols, rather than a single OFDM symbol. Our further investigations in Section 2.3.5.4 were concerned with the employment of a decoded reference, where the 'source'-related soft-output bits of the turbo-decoder were sliced, re-encoded and re-modulated. While the employment of a turbo-decoded reference had no significant impact on the performance of BPSK-assisted transmissions due to the modulation scheme's relative robustness, in the context of QPSK-assisted transmissions a notable BER advantage was observed, when employing only a modest training overhead. Finally, for 16QAM-assisted systems the employment of a turbo-decoded reference was not beneficial, particularly in the context of rapidly fading channel scenarios of e.g. $F_D = 0.05$. Our interpretation of this phenomenon was that due to generating the DDCE-related reference based on slicing, re-encoding and re-modulating the 'source'-related soft-output bits of the turbo-decoder only, the detrimental effects of low-SNR subcarriers were smeared over a wider range of subcarriers. A significant further performance improvement can be achieved upon employing a 'source- plus parity'-related soft-output bit based reference, where the source- and parity

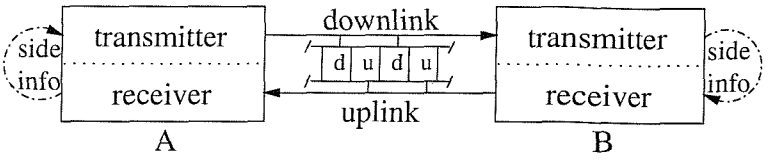

Figure 2.16: Illustration of the Time-Division Duplexing (TDD) assisted AOFDM scenario.

bits at the output of the turbo-decoder are sliced and remodulated. These beneficial effects will be demonstrated in the context of our investigations on PIC detection assisted SDMA-OFDM in Section 4.3.2.

2.4 A Robust Decision-Directed Channel Prediction Assisted Adaptive OFDM Transceiver

Subband Adaptive OFDM (AOFDM) has been shown to be an effective method of improving the system's performance in mobile environments, where the subbands least affected by frequency-selective fading are assigned more bits per subcarrier, than the severely faded subbands [98, 77, 99]. The modulation mode assignment to be employed by the remote transmitter A seen in Figure 2.16 in the next downlink timeslot is determined by the local receiver B upon invoking an estimate of the short-term channel quality experienced by the most recently received OFDM symbol. Due to the channel's variation with time, there is a mismatch between the channel quality estimated by receiver B and that actually experienced by the following OFDM symbol transmitted by transmitter A. This potentially limits the achievable performance gain of AOFDM compared to employing a single fixed modulation mode. Hence the application of AOFDM is confined to channel environments exhibiting relatively low Doppler frequencies, if no channel prediction is used. In order to support AOFDM in a broader range of mobility conditions, signal prediction techniques - which are well-known from the field of speech-coding [83, 84] for example - can be employed for obtaining a more accurate estimate of the channel quality experienced in the next transmission timeslot on the basis of a weighted sum of that in previous slots. A channel predictor assisted OFDM pre-equalization scheme was discussed in [80], while prediction assisted decision-directed channel estimation has been proposed in [18]. In our contribution we will study the performance of an AOFDM transceiver, which employs the decision-directed 2D-MMSE channel prediction technique of Sections 2.2.3 and 2.2.4 and AOFDM modulation mode adaptation. It will be demonstrated that this arrangement is advantageous, since potentially both components, namely the process of channel transfer function estimation as well as that of the modulation mode adaptation benefit from the more accurate channel transfer function estimates provided by the predictor.

In Section 2.4.1 we will commence our discussions with an outline of the adaptive transceiver's

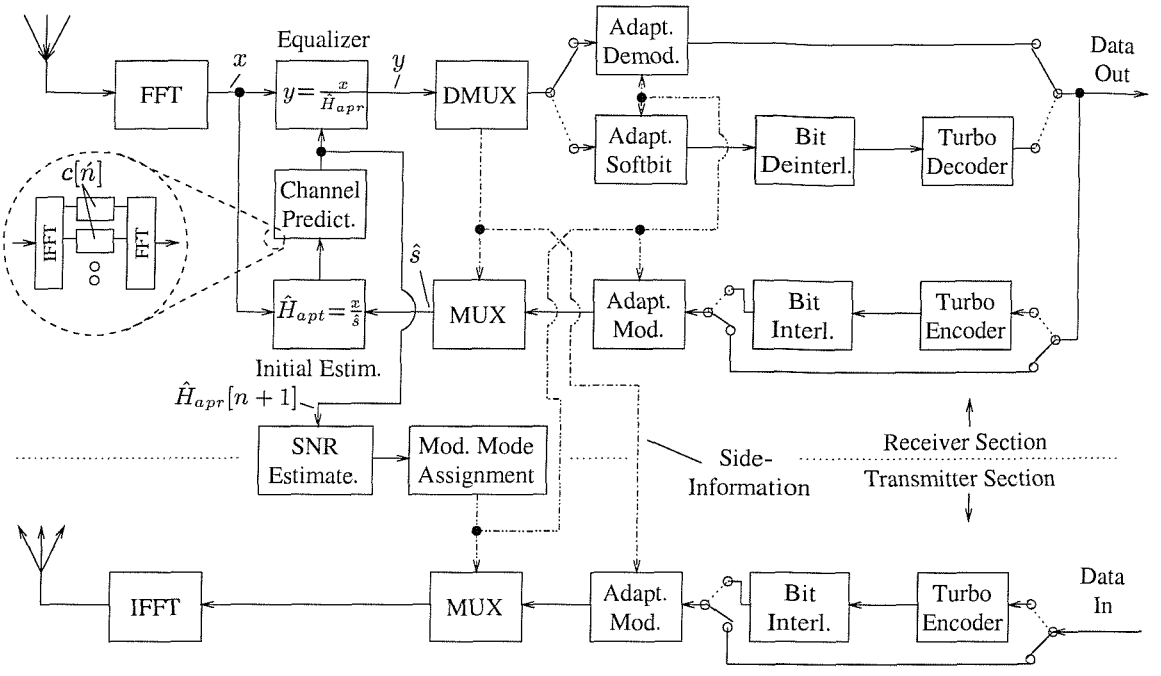

Figure 2.17: Schematic of the subband adaptive transceiver employing robust [17] decision-directed channel transfer function *prediction*. For simplicity the modulation and demodulation of the AOFDM modulation mode related side-information and its associated error protection coding is not shown here. Furthermore, the joint OFDM symbol- and subcarrier index $[n, k]$ has been omitted from the different variables associated with the n-th downlink timeslot, with the exception of $\hat{H}_{apr}[n+1]$, which refers to the set of *a priori* subcarrier channel transfer factor estimates for the OFDM symbol received during the $(n+1)$-th downlink timeslot.

structure, while in Section 2.4.2 its BER performance is assessed under a variety of channel conditions. Our discussions will be concluded in Section 2.4.3.

2.4.1 Transceiver Structure

The schematic of the adaptive Time Division Duplexing (TDD) OFDM transceiver employed in our simulations is shown in Figure 2.17. The signal received by receiver B of Figure 2.17 from the remote transmitter A in the n-th downlink timeslot is forwarded to a Fast Fourier Transform (FFT) block, followed by the frequency-domain equalization of the complex symbols associated with each of the K subcarriers. Equalization ensues using the *a priori* channel transfer factor estimates $\hat{H}_{apr}[n,k]$, $k = 0,\ldots,K-1$ predicted during the $(n-1)$-th downlink timeslot on the basis of the *a posteriori* channel transfer factor estimates $\tilde{H}_{apt}[n-\acute{n},\acute{k}]$, $\acute{n} = 1,\ldots,N_{tap}^{[t]}$, $\acute{k} = 0,\ldots,K-1$ of the OFDM symbols transmitted in the previous $N_{tap}^{[t]}$ number of downlink timeslots, where each TDD timeslot hosts one OFDM symbol. The subband modulation mode assignment to be employed by transmitter B of Figure 2.16 for the OFDM symbol transmitted during the next

uplink timeslot to receiver A is explicitly embedded into the data stream as side-information. As seen in Figure 2.17, the primary data and the AOFDM modem mode signalling streams are separated from each other in the demultiplexer (DMUX) stage of Figure 2.17, followed by adaptive OFDM demodulation of the primary user data. Additionally, turbo coding can be employed in the system, which requires adaptive soft-bit generation at the receiver instead of direct hard-decision based adaptive demodulation, followed by channel-deinterleaving and turbo decoding. The demodulated and turbo decoded data stream is conveyed to the adaptive receiver's output.

Furthermore, the sliced bits are invoked for reconstructing the transmitted OFDM symbol to be used as a reference signal, which allows generating an *a priori* channel estimate for the OFDM symbol received during the $(n+1)$-th downlink timeslot. Hence the output bit stream has to be optionally re-encoded and re-modulated.

In the proposed arrangement the advantage of employing the 2D-MMSE channel transfer function prediction technique of Section 2.2.4 instead of the 2D-MMSE channel transfer function estimation process of Section 2.2.3 as proposed by Li *et al.* [17] is two-fold. Firstly, more accurate *a priori* channel estimates are provided for the frequency-domain OFDM equalization at the receiver. Secondly, the channel quality expressed in terms of the signal-to-noise ratio (SNR) and potentially experienced by an OFDM symbol during the next downlink timeslot can be estimated more reliably. This potentially enhances the performance of our AOFDM scheme in terms of a more accurate modulation mode assignment and more accurate soft-bit values employed in the process of turbo-decoding.

2.4.1.1 Modulation Mode Adaptation

The AOFDM modulation mode adaptation performed by the modem is based on the choice between a set of four modulation modes, namely 4, 2, 1 and 0 bit/subcarrier, where the latter mode corresponds to 'no transmission'.[13] The AOFDM modulation mode could be in theory assigned on a subcarrier-by-subcarrier basis, but the signalling overhead of such a system would be prohibitive, without significant performance advantages [98]. Hence, we have grouped the adjacent AOFDM subcarriers into 'subbands' and assigned the same modulation mode to all subcarriers in a subband [98, 77]. Note that the frequency domain channel transfer function is typically not constant across the subcarriers of a subband, hence the modem mode adaptation will be sub-optimal for some of the subcarriers. The modem mode adaptation is achieved on the basis of the *a priori* SNR, SNR_{apr} estimated in each of the K subcarriers for the OFDM symbol hosted by the $(n+1)$-th downlink

[13]Note that in order to support the process of decision-directed channel prediction, BPSK modulated random sequences - known to the receiver - were also assigned to those subbands to which zero bits were mapped by the modulation mode adaptation procedure.

timeslot, which is formulated as:

$$\hat{\text{SNR}}_{apr}[n+1,k] = |\hat{H}_{apr}[n+1,k]|^2 \frac{\sigma_s^2}{\sigma_n^2}, \tag{2.62}$$

where σ_n^2 is the total noise variance in a subcarrier, given as the sum of the AWGN and the ICI-induced noise variances, expressed as $\sigma_n^2 = \sigma_{\text{AWGN}}^2 + \sigma_{\text{ICI}}^2$. The iterative AOFDM mode assignment commences by calculating in the first step for each subband and for all four modulation modes the expected overall subband BER by means of averaging the estimated individual subcarrier BERs [98]. Throughout the second step of the algorithm - commencing with the lowest-throughput but most robust modulation mode in all subbands - in each iteration the number of bits/subcarrier of that particular subband is increased, which provides the best compromise in terms of increasing the number of expected bit errors and the number of additional data bits accommodated. This process continues, until the target number of bits to be transmitted by the OFDM symbol is reached. This algorithm originates from the philosophy of the Hughes-Harthogs algorithm [100]. As a result of intensive research in the area recently several computationally efficient versions of the algorithm have emerged [98]. Again, the computed AOFDM mode assignment is explicitly signalled to the remote transmitter A of Figure 2.17 on the next uplink OFDM symbol transmitted by transmitter B and it is also stored locally in receiver B for employment during the forthcoming downlink timeslot. In the next section we will embark on the performance assessment of the proposed system.

2.4.2 BER Performance

In this section the performance of the decision-directed channel prediction assisted subband adaptive OFDM transceiver will be assessed in the context of the indoor WATM system- and channel environment of Section 6.1.1. The structure of this section is as follows. In Section 2.4.2.1 we motivate the employment of channel prediction techniques in the context of AOFDM systems by highlighting the impact of the channel's decorrelation as a function of time on the accuracy of the modulation mode assignment. In Section 2.4.2.2 we characterize the performance of the AOFDM system without channel coding in the context of decision-directed channel prediction. By contrast, in Section 2.4.2.3 the performance of the decision-directed channel prediction assisted AOFDM system is assessed in conjunction with turbo coding.

2.4.2.1 Motivation of Channel Transfer Function Prediction Assisted AOFDM

It has been demonstrated in various publications [98, 77] that the employment of the constant-throughput adaptive modulation technique is a viable approach for exploiting the different subband qualities imposed by a wideband channel. In the context of OFDM it would be best to adapt the modulation mode assignment on a subcarrier-by-subcarrier basis, but as outlined in Section 2.4.1.1, the associated signalling overhead would be prohibitive. Hence, sets of adjacent similar quality

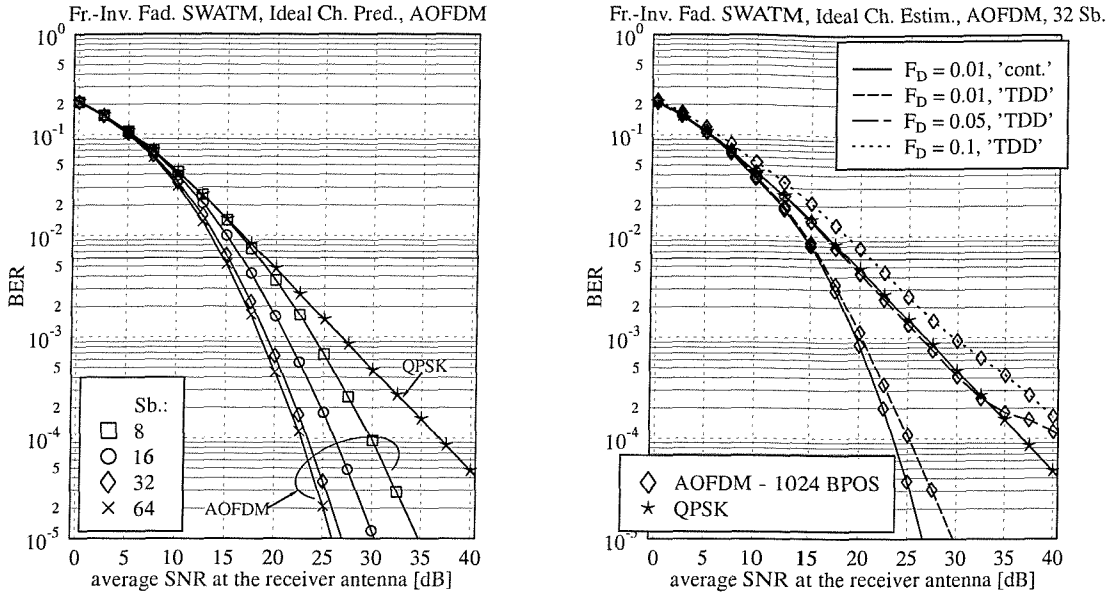

Figure 2.18: (Left): Bit Error Ratio (BER) exhibited by an AOFDM system employing perfect channel prediction as a function of the SNR at the reception antenna and further parameterized with the number of subbands invoked in the modulation mode adaptation. **(Right): Bit Error Ratio (BER)** exhibited by a 32 subband AOFDM system employing perfect channel estimation as a function of the SNR at the reception antenna and further parameterized with the OFDM symbol normalized Doppler frequency of the channel. The simulations were conducted in the **"frame-invariant"** fading **indoor WATM channel** environment of Section 6.1.1. The throughput of the AOFDM modem was equivalent to that of an AOFDM system employing fixed QPSK modulation, namely 1024 Bit per OFDM Symbol (BPOS).

subcarriers are usually grouped into subbands, and an identical modulation mode is assigned to each subband by the adaptation procedure. The maximum bandwidth of each subband is related to the channel's coherence bandwidth, namely to the bandwidth over which the fading of adjacent subcarriers can be considered correlated, as it was argued in Section 6.2.

In order to highlight the influence of the subband width on the performance of the AOFDM modem and to motivate our specific choice of the subband width employed in the context of the simulation results presented throughout this section at the left-hand side of Figure 2.18 we have plotted the BER performance of the AOFDM modem as a function of the SNR encountered at the reception antenna, parameterized with the number of subbands per OFDM symbol. These results were generated upon invoking the indoor WATM system- and channel model of Section 6.1.1. The throughput of the AOFDM modem was assumed to be identical to that of an OFDM modem employing QPSK modulation, which was 1024 bits per OFDM symbol (BPOS), given indoor WATM system parameters. The modulation mode adaptation performed during the n-th OFDM symbol period for the $(n+1)$-th OFDM symbol period was based on perfect knowledge of the channel

transfer function experienced during the $(n+1)$-th OFDM symbol period. We observe that by increasing the number of subbands per OFDM symbol beyond 32, no significant further performance improvement is attained in the context of the specific indoor WATM channel model. Compared to the BER performance of the fixed-mode QPSK modulation assisted OFDM modem, which has also been plotted in Figure 2.18, the BER of the AOFDM modem is substantially improved.

Our previous investigations were conducted under the idealistic assumption of employing perfect knowledge of the channel transfer function experienced by the OFDM symbol during the $(n+1)$-th OFDM symbol period, which was used for the AOFDM modulation mode adaptation performed in the n-th OFDM symbol period. To be more realistic and in order to motivate the employment of channel transfer function prediction techniques in the AOFDM modem, let us now stipulate the availability of perfect channel transfer function knowledge only for the n-th OFDM symbol period, which is again invoked in the adaptation of the modulation mode assignment to be used during the $(n+1)$-th OFDM symbol period. The associated BER simulation results are portrayed at the right-hand side of Figure 2.18. Again, we have plotted both the performance of the fixed-mode QPSK modulation assisted OFDM system, as well as that of the AOFDM modem of the same throughput, namely 1024 bits per OFDM symbol (BPOS). A total of 32 subbands per OFDM symbol was used. As described in Section 2.4.1, the modulation mode assignment for the $(n+1)$-th downlink timeslot was transmitted to the remote transmitter A of Figure 2.17 on the previous uplink timeslot, assuming a slot-by-slot uplink/downlink TDD scenario. Furthermore, we have also considered the rather idealistic scenario of a continuous transmission of downlink timeslots only, where the AOFDM modulation mode assignment for the $(n+1)$-th downlink timeslot is instantaneously signalled to the remote transmitter A of Figure 2.17 after the n-th downlink timeslot. Note that in the context of the above TDD scenario the effective Doppler frequency with respect to the channel's decorrelation incurred between two consecutive downlink timeslots is actually doubled compared to the scenario of a continuous transmission. In the graph on the right-hand side of Figure 2.18 we observe that as a result of the channel's decorrelation experienced at the relatively high OFDM symbol normalized Doppler frequencies of $F_D = 0.05$ and $F_D = 0.1$, the AOFDM modem performs in fact worse, than the fixed-mode QPSK modulation assisted OFDM system. This is because the receiver is expected to perform the modulation mode adaptation virtually based on near-uncorrelated channel estimates. As it will be demonstrated in the following paragraphs, this problem can be mitigated upon invoking channel transfer function prediction techniques.

2.4.2.2 BER Performance of the Uncoded System

While in the context of our investigations presented in Section 2.4.2.1 we capitalized on the idealistic assumption of benefitting from perfect channel transfer function knowledge, here we will investigate the more realistic environment where the channel transfer function estimates for the

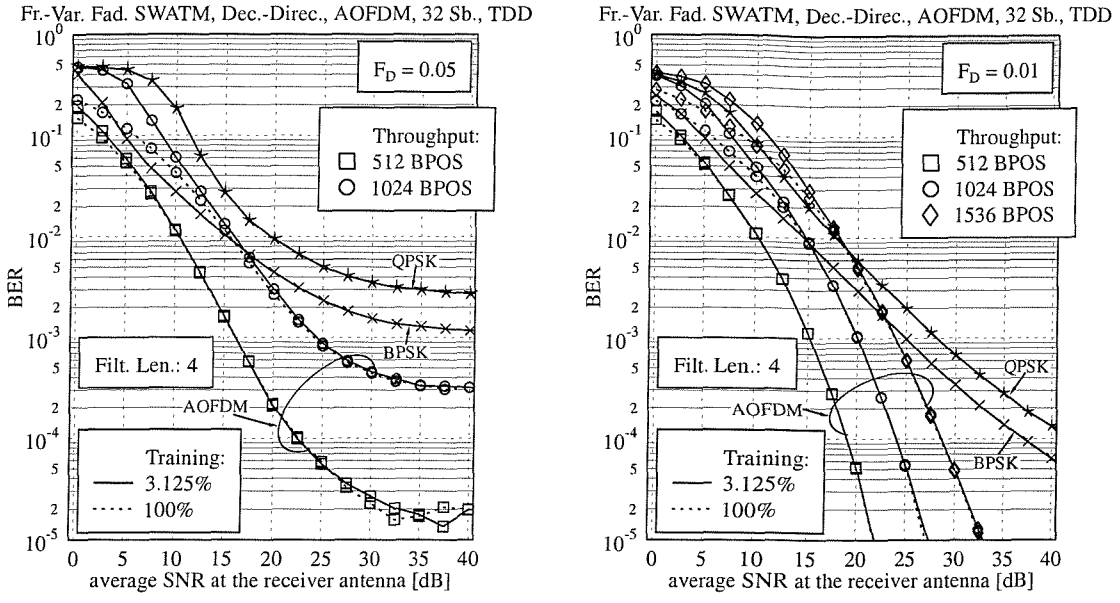

Figure 2.19: Bit Error Ratio (BER) exhibited by an AOFDM system employing **robust decision-directed *a priori* channel prediction** using a prediction filter length of 4 taps as a function of the SNR at the reception antenna, and parameterized with the throughput in terms of the number of bits transmitted per OFDM symbol. Both an ideal error-free- and a sliced potentially error-contaminated reference were employed in the process of decision-directed channel prediction. The **"frame-variant"** fading **indoor WATM channel** environment of Figure 6.1 was encountered at OFDM symbol-normalized Doppler frequencies F_D of (**left:**) 0.05 and (**right:**) 0.01. The BER performance curves associated with fixed BPSK and QPSK modulation are also plotted as a reference. The CIR window size was $K_0 = 12$ taps.

$(n+1)$-th OFDM symbol period are generated during the n-th OFDM symbol period with the aid of a decision-directed channel predictor. Both the demodulation of the transmitted subcarrier symbols performed during the $(n+1)$-th OFDM symbol period, as well as the accuracy of the AOFDM modulation mode assignment computed during the n-th OFDM symbol period for use during the $(n+1)$-th OFDM symbol period will benefit from the more accurate estimates provided by the channel transfer function predictor of Section 2.2.4 instead of the estimator of Section 2.2.3 originally proposed in [17].

Furthermore, we have dropped the idealistic assumption of encountering a frame-invariant fading channel in favour of the more realistic frame-variant fading channel scenario, with the consequence of incurring an ICI-induced limitation of the effective SNR in the demodulation process, regardless of the SNR at the reception antenna.

The corresponding BER simulation results are portrayed in Figure 2.19 at the left-hand side for an OFDM symbol normalized Doppler frequency of $F_D = 0.05$, while at the right-hand side for $F_D = 0.01$. Simulation results are provided both for the case of a sliced potentially error-contaminated reference, where the received symbols are demodulated, sliced and remodulated, as

well as for an idealistic error-free reference due to stipulating perfect knowledge of the transmitted symbols at the receiver. In the scenario of employing a sliced reference a relatively modest pilot-based training overhead due to transmitting one dedicated training OFDM symbol in every block of 32 OFDM symbols was imposed. Furthermore, the BER curves corresponding to the fixed-mode BPSK- or QPSK modulation assisted scenarios have been plotted as a reference. Again, a CIR-related tap prediction filter length of four taps was invoked in our simulations.

Note that for the more rapidly fading scenario of $F_D = 0.05$ no BER curve is provided for a throughput of 1536 bits per OFDM symbol (BPOS). This is, because as outlined in Section 2.3.4.2 in the context of the fixed modulation mode based scenarios, the channel predictor tends to become unstable due to error propagation effects, when employing the relatively vulnerable 16QAM modulation scheme in rapidly fading channel environments.

We observe that the AOFDM scheme is capable of significantly outperforming the fixed modulation assisted OFDM scheme. More specifically, for an OFDM symbol normalized Doppler frequency of $F_D = 0.01$ the channel SNR gain due to employing adaptive modulation is in excess of 15dB at a BER of 10^{-4} for both a BPSK- and a QPSK based fixed-mode equivalent throughput system. Similar advantages are observed under the more rapidly fading channel conditions of $F_D = 0.05$, where a comparison to the performance results of Figure 2.18 reveals that the employment of adaptive modulation is facilitated by the four-tap channel prediction filter. In contrast to the case of $F_D = 0.01$ a BER floor is observed at higher SNRs, which is due to the effects of the ICI. At these SNRs the BER reduction attained with the advent of adaptive modulation compared to fixed modulation was about two orders of magnitude in the context of a throughput of 512 bits per OFDM symbol. At the higher throughput of 1024 bits per OFDM symbol the performance advantage of adaptive modulation was still about an order of magnitude.[14] We also note that not only the modulation mode adaptation benefitted from the enhanced channel transfer function accuracy due to employing prediction filtering in the process of decision-directed channel estimation, but also the process of decision-directed channel estimation itself gained from the more reliable symbol decisions delivered by adaptive modulation.

In conclusion, our discussions in this section demonstrated that with the aid of channel prediction filtering constant bitrate adaptive modulation techniques can be supported even at relatively high OFDM symbol normalized Doppler frequencies.

[14]Note that here we have not taken into account the AOFDM mode signalling overhead imposed by explicitly signalling the modulation mode assignment to the remote transmitter. This is necessary, unless blind modulation mode detection techniques [101] are employed, which are known to be relatively inaccurate at low SNRs. Hence, for the sake of a more fair comparison to the fixed modulation mode assisted system, the number of subbands available to the procedure of modulation mode adaptation for data transmissions would have to be reduced appropriately. To be more explicit, in case of 32 subbands per OFDM symbol and four available modulation modes per subband to be encoded in groups of two bits, the total number of signalling bits per OFDM symbol would be 64. Furthermore, upon invoking halfrate channel coding for providing error protection to the signalling bits, the total overhead is increased to 128 bits per OFDM symbol.

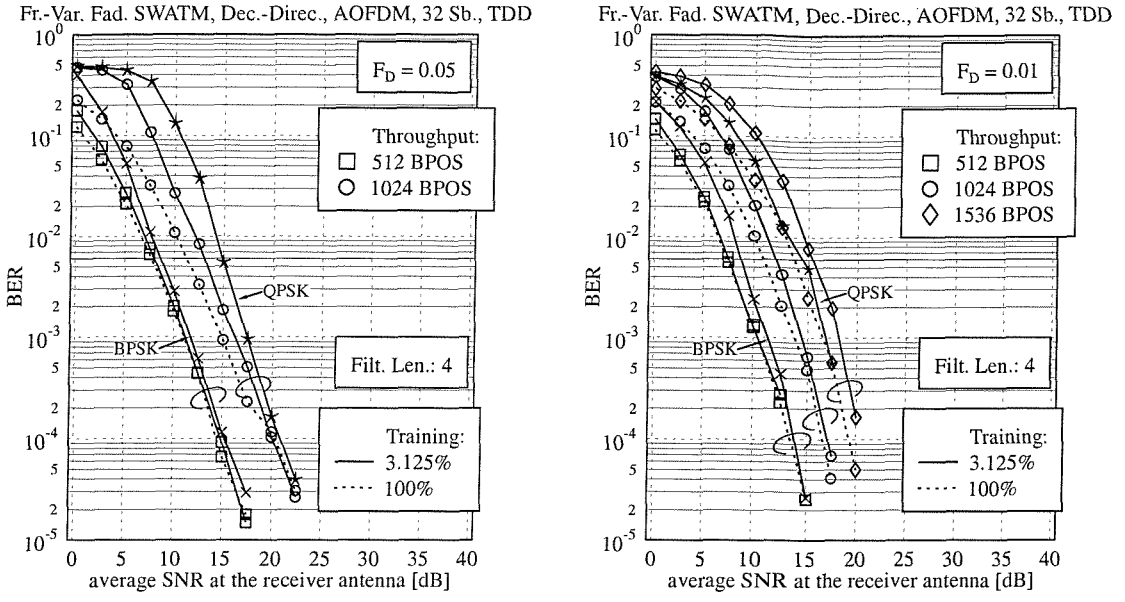

Figure 2.20: Bit Error Ratio (BER) exhibited by a turbo-coded AOFDM system employing **robust decision-directed *a priori* channel prediction** using a prediction filter length of 4 taps as a function of the SNR encountered at the reception antenna, and parameterized with the throughput in terms of the number of bits transmitted per OFDM symbol. The turbo-coding parameters were given in Table 2.6. Both an ideal and a sliced reference were employed in the process of decision-directed channel prediction. The **"frame-variant"** fading **indoor WATM channel** environment of Figure 6.1 was encountered at OFDM symbol-normalized Doppler frequencies of (**left:**) $F_D = 0.05$ and (**right:**) $F_D = 0.01$. The BER performance curves associated with fixed mode BPSK and QPSK modulation are also plotted as a reference. The CIR window size was $K_0 = 12$ taps.

2.4.2.3 BER Performance of the Turbo-Coded System

Having portrayed the BER versus SNR performance of the uncoded decision-directed channel prediction assisted AOFDM system in Section 2.4.2.2, we will now investigate the achievable performance with the aid of turbo-coding. The associated turbo coding specific parameters were summarized in Table 2.6. Again, we employ a sliced reference, generated upon performing hard decisions to the received subcarrier symbols, followed by remodulation. We demonstrated earlier in Section 2.3.5.4 that employing a turbo-decoded reference based on the 'source'-related soft-output bits of the turbo-decoder provides a relatively modest performance advantage compared to a sliced reference, in conjunction with QPSK modulation, while in the context of BPSK modulation and 16QAM no performance advantage was observed.

The simulation results are portrayed in Figure 2.20, at the left-hand side for an OFDM symbol normalized Doppler frequency of $F_D = 0.05$, while at the right-hand side for $F_D = 0.01$. In contrast to the system using no turbo-coding, which was characterized in terms of its BER in Section 2.4.2.2, the performance advantage of the AOFDM system in comparison to a system having

the same throughput, but using a fixed modulation mode is significantly reduced. A slight advantage in favour of the AOFDM system is observed at relatively low SNRs, where the decision-directed channel predictor is sensitive to the effects of error propagation. This advantage is further eroded upon invoking a potentially error-contaminated decoded reference signal in the process of decision-directed channel prediction. The reason for the similar performance exhibited by the turbo-coded AOFDM- and fixed-mode BPSK- or QPSK modulation assisted OFDM systems is that both adaptive modulation and turbo-coding attempt to mitigate the same channel impairments, namely the time- and frequency-dependent channel quality offered by the wideband channel.

We concluded that although we were unable to demonstrate a significant advantage of turbo-coded AOFDM compared to turbo coded fixed-mode BPSK- or QPSK modulation assisted OFDM at high Doppler frequencies, we have shown that adaptive modulation assisted OFDM can in fact be invoked even in channel scenarios having relatively high OFDM symbol normalized Doppler frequencies with the advent of capitalizing on FIR Wiener filter prediction techniques.

2.4.3 Conclusions on Robust Decision-Directed Channel Prediction Assisted AOFDM

In Section 2.4 we have highlighted that with the aid of channel transfer function prediction techniques constant throughput AOFDM systems can be operated in the context of relatively rapidly fluctuating channel conditions, characterized by high OFDM symbol normalized Doppler frequencies. In our simulations AOFDM transmissions were successfully demonstrated for Doppler frequencies of $F_D = 0.01$ and 0.05. For the more rapidly fading channel associated with $F_D = 0.05$ the range of throughputs supported was restricted to values below 1536 bits per OFDM symbol. At higher throughputs the decision-directed channel predictor became unstable due to the excessive activation of the relatively vulnerable 16QAM modulation mode. A similar behaviour was also observed in Section 2.3.4.2 for fixed-mode 16QAM assisted OFDM transmissions. In the context of an uncoded system not only the modulation mode adaptation conducted during the n-th OFDM symbol period for the transmission of the OFDM symbol associated with the $(n + 1)$-th downlink period benefitted from the accurate channel estimates provided by the predictor, but also the decision-directed channel predictor gained from the less error-contaminated reference with the advent of the modulation mode adaptation. Furthermore, a turbo coded AOFDM system was also considered. A slight performance advantage was observed for the turbo-coded AOFDM scheme at a given throughput compared to a turbo coded BPSK or QPSK modulation assisted OFDM system. In the turbo coded cases the main advantage of adaptive modulation remains its flexibility with respect to the desired throughput, since fixed-mode transmission is only capable of conveying 512, 1024 or 2048 bits per OFDM symbol.

2.5 Conclusions

2.5.1 Description

In Chapter 2 decision-directed channel estimation (DDCE) and prediction (DDCP) has been investigated in the context of single-user single-transmit antenna based OFDM systems. The corresponding OFDM receiver's associated structure was shown in Figure 2.1.

Our specific discussions commenced in Section 2.2.1 with an outline of the procedure of generating *a posteriori* least-squares channel transfer factor estimates based on the received subcarrier signals $x[n,k]$ and based on the classified symbols $\check{s}[n,k]$ that are most likely to have been transmitted in the different subcarriers $k = 0, \ldots, K-1$. Furthermore, in Section 2.2.2 the 1D-MMSE channel transfer function estimator proposed by Edfors *et al.* [13, 14, 15] and Sandell [16] for inferring improved *a posteriori* channel transfer factor estimates from the initial least-squares channel transfer factor estimates of Section 2.2.1 was described. Based on these ideas Li *et al.* [17] proposed a 2D-MMSE channel transfer function estimator, which additionally capitalizes on the least-squares channel transfer factor estimates of past OFDM symbols. This approach was outlined in Section 2.2.3 with an emphasis on the aspects of 'robustness' as advocated by Li *et al.* [17].

As a result of the potentially excessive decorrelation of the channel transfer function experienced by consecutive OFDM symbols as demonstrated in Section 2.2.3.3, we found that it is more beneficial to employ a CIR-related tap prediction filter, which operates in the time-direction instead of the CIR-related tap estimation filter as in Li's contribution [17]. More explicitly, instead of generating improved *a posteriori* channel transfer factor estimates for the n-th OFDM symbol period, which are then used - upon neglecting the channel's decorrelation - as *a priori* channel transfer factor estimates for demodulation during the $(n+1)$-th OFDM symbol period, we directly generate *a priori* channel transfer factor predictions for the $(n+1)$-th OFDM symbol period during the n-th OFDM symbol period. The specific structure of the MMSE CIR-related tap prediction filter was discussed in Section 2.2.4. This included the derivation of an expression for the subcarrier-averaged *a priori* prediction MSE in Section 2.2.4.6.

During our performance study provided in Section 2.3 two approaches were considered for evaluating the CIR-related tap predictor coefficients based on the Wiener solution of Equation 2.38. These were the robust approach advocated by Li *et al.* [17], which was also discussed in Section 2.2.3 and the block-adaptive approach proposed by Al-Susa and Ormondroyd [18], which is based on the Burg algorithm [83].

Specifically, in the context of the robust approach of Section 2.2.3, a uniform, ideally support-limited Doppler power spectrum was employed, which is related to a sinc-shaped spaced-time correlation function $\tilde{r}_H^{[f]}[\Delta n]$, as given by Equation 2.55. Furthermore, the different CIR-related tap variances were assumed to be identical, which is related to imposing a uniform, ideally support-limited multipath intensity profile in the design of the estimator. Recall from our discussions in

Section 2.2.3.2 that the estimator's MSE can be rendered insensitive with respect to the specific shape of the channel's scattering function, provided that we can capitalize on an infinite number of previous OFDM symbols in the time-direction and on an infinite number of subcarriers in the frequency-direction. However, there is an exceptional case, when perfect robustness can be achieved with respect to the channel scattering function's associated multipath intensity profile, namely in the context of a sample-spaced CIR.

In contrast to the robust approach, the block-adaptive approach employs estimates of the CIR-related taps' correlation in the time-direction, which are periodically generated from blocks of consecutive OFDM symbols. Note however that these estimates do not become explicitly available, since the Burg algorithm of [83] directly produces the optimum predictor weights. In order to avoid the inconvenience of storing a potentially large number of previous OFDM symbols, which may exceed the $N_{tap}^{[t]}$ number of OFDM symbols employed in the actual prediction process, an attractive alternative to the block-adaptive approach is an OFDM symbol-by-symbol adaptive approach, which could be based on the RLS algorithm. This will be demonstrated in Section 3.5 in the context of our investigations on DDCP designed for multi-user OFDM systems.

2.5.2 Performance Assessment

The performance investigations conducted in Section 2.3 commenced with a portrayal of both the robust- and that of the adaptive decision-directed channel predictor's MSE in Sections 2.3.1 and 2.3.2, respectively, upon assuming error-free symbol decisions. We found that as a result of the CIR-related tap-by-tap adaptation of the predictor coefficients, the *a priori* estimation MSE performance achieved with the aid of the block-adaptive predictor - assuming the availability of a sufficiently high number of previous OFDM symbols' CIR-related *a posteriori* tap estimates - is potentially lower than that of the robust predictor. However, in the specific case of encountering a uniform multipath intensity profile, both predictors are expected to exhibit the same MSE performance. Our detailed conclusions for these investigations were offered in Sections 2.3.1.5 and 2.3.2.4, respectively. Furthermore, in Section 2.3.3 we assessed the robust predictor's MSE in the context of an uncoded system, based on Monte-Carlo simulations. Again, the related detailed conclusions were offered in Section 2.3.3.4. The uncoded system's corresponding BER performance in conjunction with various modulation schemes, namely BPSK, QPSK and 16QAM was studied in Section 2.3.4 and our detailed conclusions were provided in Section 2.3.4.3. In order to even further reduce the DDCE assisted system's BER, additionally turbo-coding was invoked, which was the topic of Section 2.3.5. Our detailed conclusions were offered in Section 2.3.5.5.

In order to summarize, from the investigations of Section 2.3 we conclude that upon invoking 2D-MMSE channel transfer function prediction filtering, decision-directed channel estimation is rendered attractive even in the context of high-mobility channel scenarios associated with OFDM

symbol-normalized Doppler frequencies ranging up to $F_D = 0.1$. We found that already in conjunction with a relatively short linear prediction filter length of four taps, most of the channel's time-direction correlation can be exploited, while a further increase of the predictor's length results in a further reduction of the channel noise. At higher values of F_D, the BER performance was rather limited due to the effects of ICI. Even in conjunction with turbo coding for example, only the most robust BPSK modulation was capable of facilitating near error-free OFDM transmissions in the worst-case scenario of $F_D = 0.1$. For the less error-resilient QPSK modulation scheme the $F_D = 0.05$ scenario was found to be the highest-speed environment, where reliable operation was feasible and for 16QAM even less time-variant channel conditions were required. This was a result of the instability observed for the robust predictor - specifically at higher OFDM symbol normalized Doppler frequencies - which was mainly due to the increased amount of ICI. This caused an increased number of subcarrier symbol decisions, which were then propagated to the following OFDM symbols with the effects of a 'noise amplification problem' due to the robust estimator's inflexibility to react to the degraded channel conditions caused by the subcarrier symbol errors. In this context the employment of the adaptive predictor would be advantageous, with the disadvantage of having a higher complexity as a result of the coefficient adaptation.

2.5.3 Adaptive OFDM Transceiver

Our further investigations conducted in Section 2.4 concentrated on employing robust decision-directed channel prediction in the context of a constant-throughput AOFDM TDD system. After a description of the transceiver's structure in Section 2.4.1 the associated performance assessments of Section 2.4.2 considered both an uncoded as well as a turbo-coded scenario. Our more detailed conclusions concerning these investigations were offered in Section 2.4.3. In order to summarize, we found that with the aid of channel transfer function prediction techniques constant throughput AOFDM TDD systems can be reliably supported in the context of even relatively rapidly fluctuating channel conditions. In our simulations AOFDM transmissions were successfully demonstrated for Doppler frequencies of $F_D = 0.01$ and 0.05. For the more rapidly fading channel associated with $F_D = 0.05$ the range of throughputs supported was restricted to values below 1536 bits per OFDM symbol. Having characterized the family of single-user decision-directed channel estimation- and prediction techniques in this chapter, in the next chapter we will study multi-user channel estimation techniques.

Special Symbols - Decision-Directed Channel Estimation for Single-User OFDM

$c_{\{est/pre\}}[\acute{n}, l]$: Estimator/predictor coefficient associated with the l-th CIR-related tap of the OFDM symbol having an offset of $-\acute{n}$, where $\acute{n} \in \{0, \ldots, N_{tap}^{[t]} - 1\}$, relative to the current OFDM symbol.

$\mathbf{c}_{\{est/pre\}}[l]$: Vector of estimator/predictor coefficients $c_{\{est/pre\}}[\acute{n}, l]$, $\acute{n} = 0, \ldots, N_{tap}^{[t]} - 1$ associated with the l-th CIR-related tap: $\mathbf{c}_{\{est/pre\}}[l] \in \mathbb{C}^{N_{tap}^{[t]} \times 1}$.

$\mathbf{C}_{est}[\acute{n}]$: Diagonal matrix of CIR-related tap estimator coefficients associated with the OFDM symbol having an offset of $-\acute{n}$, where $\acute{n} \in \{0, \ldots, N_{tap}^{[t]} - 1\}$, relative to the current OFDM symbol: $\mathbf{C}_{est}[\acute{n}] \in \mathbb{C}^{K \times K}$.

$e_{pre}[n+1, l]$: Prediction error of the l-th CIR-related tap observed during the $(n+1)$-th OFDM symbol period, when using the prediction generated during the n-th OFDM symbol period.

$\mathbf{e}_{pre}[n+1]|_{K_0}$: Vector of the K CIR-related taps' prediction errors observed during the $(n+1)$-th OFDM symbol period when using the predictions generated during the n-th OFDM symbol period, upon assuming a rank-K_0 predictor: $\mathbf{e}_{pre}[n+1]|_{K_0} \in \mathbb{C}^{K \times 1}$.

$\mathbf{E}_{pre}[n+1]|_{K_0}$: Frequency-domain representation of the vector $\mathbf{e}_{pre}[n+1]|_{K_0}$ of the K CIR-related taps' prediction errors observed during the $(n+1)$-th OFDM symbol period when using the predictions generated during the n-th OFDM symbol period, upon assuming a rank-K_0 predictor: $\mathbf{E}_{pre}[n+1]|_{K_0} = \tilde{\mathbf{U}}^{[f]}\mathbf{e}_{pre}[n+1]|_{K_0} \in \mathbb{C}^{K \times 1}$.

$h_{expo}[l]$: Sample-spaced negative exponentially decaying CIR: $h_{expo}[l] = \beta_{expo}e^{-\alpha_{expo}l}$, $l = 0, \ldots, K_0 - 1$.

$h[n, l]$: l-th CIR-related tap associated with the n-th OFDM symbol period.

$\tilde{h}_{apt}[n, l]$: CIR-related *a posteriori* least-squares tap estimate.

$\hat{h}_{apt}[n, l]$: Improved CIR-related *a posteriori* tap estimate.

$\hat{h}_{apr}[n+1, l]$: CIR-related *a priori* tap estimate generated during the n-th OFDM symbol period for employment during the $(n+1)$-th OFDM symbol period.

$\mathbf{h}[n]$: Vector of the K different CIR-related taps $h[n,l]$, $l = 0,\ldots,K-1$: $\mathbf{h}[n] = \tilde{\mathbf{U}}^{[f]H}\mathbf{H}[n] \in \mathbb{C}^{K\times 1}$. ([15])

$\tilde{\mathbf{h}}_{apt}[n]$: Vector of the K different CIR-related *a posteriori* least-squares tap estimates $\tilde{h}_{apt}[n,l]$, $l = 0,\ldots,K-1$: $\tilde{\mathbf{h}}_{apt}[n] = \tilde{\mathbf{U}}^{[f]H}\tilde{\mathbf{H}}_{apt}[n] \in \mathbb{C}^{K\times 1}$. ([16])

$\hat{\mathbf{h}}_{apt}[n]$: Vector of the K different improved CIR-related *a posteriori* tap estimates, namely $\hat{h}_{apt}[n,l]$, $l = 0,\ldots,K-1$: $\hat{\mathbf{h}}_{apt}[n] = \tilde{\mathbf{U}}^{[f]H}\hat{\mathbf{H}}_{apt}[n] \in \mathbb{C}^{K\times 1}$. ([17])

$\mathbf{h}[n,l]$: Vector of the l-th CIR-related tap's current plus the $N_{tap}^{[t]}-1$ number of past values, namely $h[n+\acute{n},l]$, $\acute{n} = -N_{tap}^{[t]}+1,\ldots,0$ each associated with either the current or one of the past $N_{tap}^{[t]}-1$ number of OFDM symbols: $\mathbf{h}[n,l] \in \mathbb{C}^{N_{tap}^{[t]}\times 1}$.

$\tilde{\mathbf{h}}_{apt}[n,l]$: Vector of the l-th CIR-related tap's current plus the $N_{tap}^{[t]}-1$ number of past OFDM symbols' *a posteriori* least-squares estimates, namely $\tilde{h}_{apt}[n+\acute{n},l]$, $\acute{n} = -N_{tap}^{[t]}+1,\ldots,0$ each associated with either the current or one of the $N_{tap}^{[t]}-1$ number of past OFDM symbols: $\tilde{\mathbf{h}}_{apt}[n,l] \in \mathbb{C}^{N_{tap}^{[t]}\times 1}$.

$H[n,k]$: Cannel transfer factor associated with the k-th subcarrier of the n-th OFDM symbol.

$\tilde{H}_{apt}[n,k]$: *A posteriori* least-squares channel transfer factor estimate.

$\hat{H}_{apt}[n,k]$: Improved *a posteriori* channel transfer factor estimate.

$\hat{H}_{apr}[n+1,k]$: *A priori* channel transfer factor estimate generated during the n-th OFDM symbol period for the $(n+1)$-th OFDM symbol duration.

$\mathbf{H}[n]$: Vector of the K different subcarriers' channel transfer factors $H[n,k]$, $k = 0,\ldots,K-1$: $\mathbf{H}[n] \in \mathbb{C}^{K\times 1}$.

$\tilde{\mathbf{H}}_{apt}[n]$: Vector of the K different subcarriers' *a posteriori* least-squares channel transfer factor estimates $\tilde{H}_{apt}[n,k]$, $k = 0,\ldots,K-1$: $\tilde{\mathbf{H}}_{apt}[n] \in \mathbb{C}^{K\times 1}$.

$\hat{\mathbf{H}}_{apt}[n]$: Vector of the K different subcarriers' improved *a posteriori* channel transfer factor estimates $\hat{H}_{apt}[n,k]$, $k = 0,\ldots,K-1$: $\hat{\mathbf{H}}_{apt}[n] \in \mathbb{C}^{K\times 1}$.

$\hat{\mathbf{H}}_{apr}[n+1]$: Vector of the K different subcarriers' *a priori* channel transfer factor estimates $\hat{H}_{apr}[n+1,k]$, $k = 0,\ldots,K-1$: $\hat{\mathbf{H}}_{apr}[n+1] \in \mathbb{C}^{K\times 1}$.

[15] Note that the choice of $\tilde{\mathbf{U}}^{[f]}$ is arbitrary, as long as the matrix is unitary. However, the optimum choice is $\tilde{\mathbf{U}}^{[f]} = \mathbf{U}^{[f]}$. In this case the CIR-related taps are uncorrelated.

[16] See Footnote 15.

[17] See Footnote 15.

$J_0(x)$: Zero-order Bessel function of the first kind.

$J(\mathbf{c}_{pre}[l])$: MSE-related cost-function used for deriving the l-th CIR-related tap's vector of optimum predictor coefficients.

K_0: Number of significant CIR-related taps.

$\mathcal{M}_c$: Set of M_c number of constellation points associated with the modulation scheme employed.

M_s: Number of OFDM symbols contained in the input block of the Burg algorithm assisted predictor. Note that we have $M_s \geq N_{tap}^{[t]}$.

$\text{MSE}_{dec}[n,k]$: Subcarrier-based MSE imposed by the channel's time-variance in the absence of prediction filtering, when using the channel transfer factors of the current OFDM symbol for the equalization conducted during the next OFDM symbol period. In the context of Jakes' Doppler spectrum the decorrelation-induced MSE is denoted as $\text{MSE}_{dec,J}[n,k]$.

$\text{MSE}_{apr}[l]|_{(\mathbf{c}_{pre}[l])}$: MSE associated with the linear prediction of the l-th CIR-related tap in the context of using the arbitrary vector $\mathbf{c}_{pre}[l]$ of predictor coefficients.

$\text{MMSE}_{apr}[l]$: Minimum MSE associated with the linear prediction of the l-th CIR-related tap in the context of using the vector $\mathbf{c}_{pre}[l]|_{opt}$ of optimum predictor coefficients.

$\overline{\text{MSE}}_{apr}|_{K_0}$: Subcarrier-averaged *a priori* estimation MSE of the rank-K_0 2D-MMSE based channel predictor in the context of arbitrary estimator coefficients.

$\overline{\text{MSE}}_{apt}|_{K_0}^{N_{tap}^{[t]}=1}$: Subcarrier-averaged *a posteriori* estimation MSE of the rank-K_0 1D-MMSE based channel estimator in the context of arbitrary estimator coefficients.

$\overline{\text{MMSE}}_{apt}|^{N_{tap}^{[t]}\to\infty}$: Subcarrier-averaged *a posteriori* estimation MSE of the 2D-MMSE based channel estimator employing no rank-reduction in the context of the optimum estimator coefficients, when using infinite-length CIR-related tap estimation filters.

$\overline{\text{MMSE}}_{apt}|_{rob}^{N_{tap}^{[t]}\to\infty}$: Subcarrier-averaged *a posteriori* estimation MSE of the 2D-MMSE based channel estimator employing no rank-reduction in the context of the sub-optimum estimator coefficients based on the assumptions of 'robustness' with respect to the channel's multipath intensity profile, when using infinite-length CIR-related tap estimation filters.

$n[n,k]$: AWGN contribution having a variance of σ_n^2.

$N_{tap}^{[t]}$: Number of filter taps associated with the CIR-related tap estimator- or predictor.

r_{expo}: Amplitude ratio of the sample-spaced exponential CIR: $r_{expo} = \frac{h_{expo}[K_0-1]}{h_{expo}[0]}$.

$r_H^{[f]}[\Delta k]$: Spaced-frequency correlation function in the context of the OFDM system: $r_H^{[f]}[\Delta k] = r_H^{[f]}(\Delta k \Delta F) = r_H(\Delta k \Delta F)$.

$r_H^{[t]}[\Delta n]$: Spaced-time correlation function in the context of the OFDM system: $r_H^{[t]}[\Delta n] = r_H^{[t]}(\Delta n T_f) = r_H(\Delta n T_f)$. Upon assuming Jakes Doppler spectrum whose associated correlation function is given by the zero-order Bessel function of the first kind, we have $r_{H,J}^{[t]}[\Delta n] = J_0(\Delta n \cdot \omega_D)$.

$\mathbf{R}^{[f]}$: Spaced-frequency correlation matrix: $\mathbf{R}^{[f]} = E\{\mathbf{H}[n]\mathbf{H}^H[n]\} \in \mathbb{C}^{K \times K}$. The Eigen-Value Decomposition (EVD) of the correlation matrix $\mathbf{R}^{[f]}$ is given by $\mathbf{R}^{[f]} = \mathbf{U}^{[f]}\Lambda^{[f]}\mathbf{U}^{[f]H}$.

$\mathbf{r}_h^{[t]}[l]$: Spaced-time cross-correlation vector of the l-th CIR-related taps, which is given by: $\mathbf{r}_h^{[t]}[l] = E\{h^*[n+1,l]\mathbf{h}[n,l]\} \in \mathbb{C}^{N_{tap}^{[t]} \times 1}$.

$\mathbf{r}^{[t]}[l]$: Normalized spaced-time cross-correlation vector of the l-th CIR-related taps: $\mathbf{r}^{[t]}[l] = \frac{1}{\lambda_l^{[f]}}\mathbf{r}_h^{[t]}[l] \in \mathbb{C}^{N_{tap}^{[t]} \times 1}$.

$\mathbf{r}_{apt}^{[t]}[l]$: Spaced-time cross-correlation vector of the l-th CIR-related *a posteriori* least-squares tap estimates: $\mathbf{r}_{apt}^{[t]}[l] = E\{h^*[n+1,l]\tilde{\mathbf{h}}_{apt}[n,l]\} = \mathbf{r}_h^{[t]}[l] \in \mathbb{C}^{N_{tap}^{[t]} \times 1}$.

$\mathbf{R}_h^{[t]}[l]$: Spaced-time auto-correlation matrix of the l-th CIR-related taps: $\mathbf{R}_h^{[t]}[l] = E\{\mathbf{h}[n,l]\mathbf{h}^H[n,l]\} \in \mathbb{C}^{N_{tap}^{[t]} \times N_{tap}^{[t]}}$.

$\mathbf{R}^{[t]}[l]$: Normalized spaced-time auto-correlation matrix of the l-th CIR-related taps: $\mathbf{R}^{[t]}[l] = \frac{1}{\lambda_l^{[f]}}\mathbf{R}_h^{[t]}[l] \in \mathbb{C}^{N_{tap}^{[t]} \times N_{tap}^{[t]}}$.

$\mathbf{R}_{apt}^{[t]}[l]$: Spaced-time auto-correlation matrix of the l-th CIR-related *a posteriori* least-squares tap estimates: $\mathbf{R}_{apt}^{[t]}[l] = E\{\tilde{\mathbf{h}}_{apt}[n,l]\tilde{\mathbf{h}}_{apt}^H[n,l]\} = \mathbf{R}_h^{[t]}[l] + \rho\mathbf{I} \in \mathbb{C}^{N_{tap}^{[t]} \times N_{tap}^{[t]}}$.

$s[n,k]$: Transmitted subcarrier symbol having a variance of σ_s^2.

$\hat{s}[n,k]$: Linear estimate of the transmitted subcarrier symbol.

$\check{s}[n,k]$: Classified transmitted subcarrier symbol.

$\hat{\text{SNR}}_{apr}[n+1,k]$: SNR predicted for the k-th subcarrier of the $(n+1)$-th OFDM symbol to be used in the modulation mode assignment during the n-th OFDM symbol period: $\hat{\text{SNR}}_{apr}[n+1,k] = |\hat{H}_{apr}[n+1,k]|^2 \frac{\sigma_s^2}{\sigma_n^2}$.

$\mathbf{U}^{[f]}$: Unitary KLT matrix associated with the EVD of the spaced-frequency correlation matrix $\mathbf{R}^{[f]}$: $\mathbf{U}^{[f]} \in \mathbb{C}^{K \times K}$.

$x[n,k]$: Received subcarrier signal.

α: Modulation-noise enhancement factor $\alpha = E\{\frac{1}{|s[n,k]|^2}\}$ [89, 15], where for the specific case of using M-PSK modulation we have $\alpha_{\text{M-PSK}} = 1$, while for 16-QAM we have $\alpha_{\text{16-QAM}} = \frac{17}{9}$ [15].

α_{expo}: Decay factor of the sample-spaced exponential CIR.

β_{expo}: Amplitude scaling factor of the sample-spaced exponential CIR.

$\lambda_l^{[f]}$: l-th eigenvalue associated with the EVD of the spaced-frequency correlation matrix $\mathbf{R}^{[f]}$: $\lambda_l^{[f]} = (\mathbf{U}^{[f]H}\mathbf{R}^{[f]}\mathbf{U}^{[f]})_{[l,l]}$.

$\upsilon_l^{[f]}$: l-th eigenvalue associated with the decomposition of the spaced-frequency correlation matrix $\mathbf{R}^{[f]}$ with respect to the unitary matrix $\tilde{\mathbf{U}}^{[f]}$ employed in the estimator design: $\upsilon_l^{[f]} = (\tilde{\mathbf{U}}^{[f]H}\mathbf{R}^{[f]}\tilde{\mathbf{U}}^{[f]})_{[l,l]}$. Note that for $\tilde{\mathbf{U}}^{[f]} = \mathbf{U}^{[f]}$ we have $\upsilon_l^{[f]} = \lambda_l^{[f]}$.

$\Lambda^{[f]}$: Diagonal matrix of eigenvalues $\lambda_l^{[f]}$, $l = 0, \ldots, K-1$ associated with the EVD of the spaced-frequency correlation matrix $\mathbf{R}^{[f]}$: $\Lambda^{[f]} \in \mathbb{R}^{K \times K}$.

$()|_{\tilde{\mathbf{U}}^{[f]}}$: Index used in conjunction with the CIR-related taps' spaced-time cross-correlation vector and auto-correlation matrix in order to indicate that the transform of the channel transfer factors to the CIR-related domain was carried out with the aid of the unitary matrix $\tilde{\mathbf{U}}^{[f]}$ associated with the design of the estimator, where potentially $\tilde{\mathbf{U}}^{[f]} = \mathbf{U}^{[f]}$.

Chapter 3

Channel Transfer Function Estimation for Multi-User OFDM

3.1 Motivation

The topic of decision-directed channel estimation has been addressed in a variety of contributions, notably for example in the detailed discussions of Li *et al.* [17] in the context of *single-user single-transmit antenna* OFDM environments. As it was outlined in great detail in Chapter 2 the basic idea is to equalize the channel transfer function experienced by an OFDM symbol during the current transmission period by capitalizing on that encountered during the previous OFDM symbol period. This implies assuming quasi-invariance of the channel's transfer function between the two consecutive OFDM symbols' transmission intervals. An improved channel transfer function estimate can then be obtained for detecting the most recently received OFDM symbol upon dividing the complex symbol received in each subcarrier by the sliced and remodulated information symbol hosted by a subcarrier. The updated channel estimate is then employed again as an initial channel estimate during the next OFDM symbol's transmission period.

By contrast, in the multi-user OFDM scenario to be outlined in Section 3.2 the signal received by each antenna is constituted by the superposition of the signal contributions associated with the different users- or transmit antennas. Note that in terms of the multiple-input multiple-output (MIMO) structure of the channel the multi-user single-transmit antenna scenario is equivalent for example to a single-user space-time coded (STC) scenario using multiple transmit antennas. For the latter a Least-Squares (LS) error channel estimator was proposed by Li *et al.* [21], which aims at recovering the different transmit antennas' channel transfer functions on the basis of the output signal of a specific reception antenna element and by also capitalizing on the remodulated received symbols associated with the different users. The performance of this estimator was found to be limited in

Year	Author	Contribution
'99	Li, Seshadri and Ariyavisitakul [21]	The LS-assisted DDCE proposed exploits the independence of the transmitted subcarrier symbol sequences.
'00	Jeon, Paik and Cho [23]	Frequency-domain PIC-assisted DDCE is studied, which exploits the channel's slow variation versus time.
	Li [22]	Time-domain PIC-assisted DDCE is investigated as a simplification of the LS-assisted DDCE of [21]. Optimum training sequences are proposed for the LS-assisted DDCE of [21].
'01	Mody and Stüber [102]	Channel transfer factor estimation designed for frequency-domain PSAM based on CIR-related domain filtering is studied.
	Gong and Letaief [103]	MMSE-assisted DDCE is advocated which represents an extension of the LS-assisted DDCE of [103]. The MMSE-assisted DDCE is shown to be practical in the context of transmitting consecutive training blocks. Additionally, a low-rank approximation of the MMSE-assisted DDCE is considered.
	Jeon, Paik and Cho [104]	2D MMSE based channel estimation is proposed for frequency-domain PSAM.
	Vook and Thomas [105]	2D MMSE based channel estimation is invoked for frequency-domain PSAM. A complexity reduction is achieved by CIR-related domain based processing.
	Xie and Georghiades [106]	Expectation maximization (EM) based channel transfer factor estimation approach for DDCE.
'02	Li [107]	A more detailed discussion on time-domain PIC-assisted DDCE is provided and optimum training sequences are proposed [22].
	Bölcskei, Heath Jr. and Paulray [72]	Blind channel indentification and equalization using second-order cyclostationary statistics as well as antenna precoding was studied.
	Minn, Kim and Bhargava [108]	A reduced-complexity version of the LS-assisted DDCE of [21] is introduced, based on exploiting the channel's correlation in the frequency-direction, as opposed to invoking the simplified scheme of [107], which exploits the channel's correlation in the time-direction. A similar approach was suggested by Slimane [109] for the specific case of two transmit antennas.
	Komninakis, Fragouli, Sayed and Wesel [110]	Fading channel tracking and equalization was proposed for employment in MIMO systems assisted by Kalman estimation and channel prediction.

Table 3.1: Contributions on channel transfer factor estimation for multiple-transmit antenna assisted OFDM.

terms of the mean-square estimation error in scenarios, where the product of the number of transmit antennas and the number of CIR taps to be estimated per transmit antenna approaches the total number of subcarriers hosted by an OFDM symbol.

In [23] a DDCE was proposed by Jeon *et al.* for a space-time coded OFDM scenario of two transmit antennas and two receive antennas. Specifically, the channel transfer function[1] associated with each transmit-receive antenna pair was estimated on the basis of the output signal of the specific receive antenna upon *subtracting* the interfering signal contributions associated with the remaining transmit antennas. These interference contributions were estimated by capitalizing on the knowledge of the channel transfer functions of all interfering transmit antennas predicted during the $(n-1)$-th OFDM symbol period for the n-th OFDM symbol, also invoking the corresponding remodulated symbols associated with the n-th OFDM symbol. To elaborate further, the difference between the subtraction based channel transfer function estimator of [23] and the LS estimator proposed by Li *et al.* in [21] is that in the former the channel transfer functions predicted during the previous, i.e. the $(n-1)$-th OFDM symbol period for the current, i.e. the n-th OFDM symbol are employed for both symbol detection *as well as* for obtaining an updated channel estimate for employment during the $(n+1)$-th OFDM symbol period. In the approach advocated in [23] the subtraction of the different transmit antennas' interfering signals is performed in the frequency-domain.

By contrast, in [22] a similar technique was proposed by Li with the aim of simplifying the DDCE approach of [21], which operates in the time-domain. A prerequisite for the operation of this parallel interference cancellation (PIC)-assisted DDCE is the availability of a reliable estimate of the various channel transfer functions for the current OFDM symbol, which are employed in the cancellation process in order to obtain updated channel transfer function estimates for the demodulation of the next OFDM symbol. In order to compensate for the channel's variation as a function of the OFDM symbol index, linear prediction techniques can be employed, as it was also proposed for example in [22]. However, due to the estimator's recursive structure, determining the optimum predictor coefficients is not as straightforward as for the transversal FIR filter-assisted predictor as described in Section 2.2.4 for the single-user DDCE.

A comprehensive overview of further publications on channel transfer factor estimation for OFDM systems supported by multiple transmit antennas is provided in Table 3.1.

Our further discourse in Chapter 3 evolves as follows. In Section 3.2 we portray the signal model associated with the SDMA uplink transmission scenario. Note again that in terms of the MIMO structure of the channel this SDMA system is equivalent for example to a single-user STC scenario employing multiple transmit antennas. Hence, the algorithms discussed here are amenable to a wide range of applications involving multiple transmit antennas. Our discussion of specific channel estimation techniques commences in Section 3.3 with a portrayal of the least-squares error assisted

[1] In the context of the OFDM system the set of K different subcarriers' channel transfer factors is referred to as the channel transfer function, or simply as the channel.

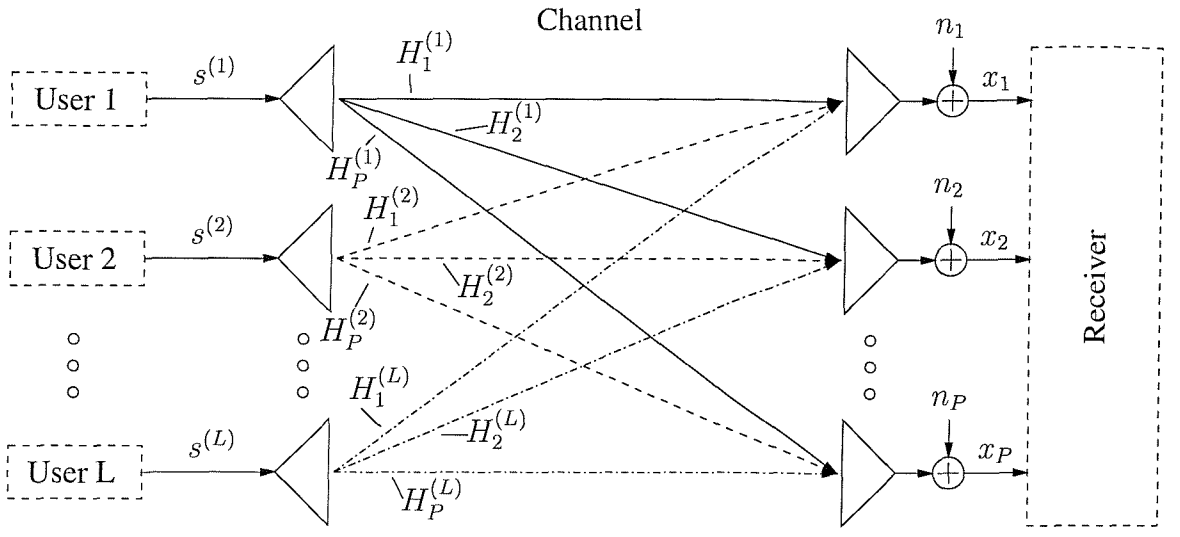

Figure 3.1: Schematic of an SDMA *uplink* scenario as observed on an OFDM subcarrier basis, where each of the L users is equipped with a single transmit antenna and the basestation's receiver is assisted by a P-element antenna front-end. For comparison, in an STC scenario the L transmit antennas are used for providing L-th order transmit diversity for a single user.

estimator proposed by Li *et al.* [21]. In this section we will derive a necessary condition for channel identification and the equations describing the estimator's MSE in the context of both sample-spaced- as well as non-sample-spaced CIRs. The estimator's potentially high complexity provides a further motivation for devising alternative approaches. Specifically, in Section 3.4 we will focus on the far less complex PIC-assisted DDCE employing prediction filtering along the time-axis in the CIR-related domain. Then expressions are derived for the estimator's MSE and an iteration-based novel approach is devised for evaluating the optimum CIR-related tap predictor coefficients. This is followed by an extensive performance assessment under both sample-spaced and non-sample-spaced CIR conditions. In order to avoid the off-line optimization of the predictor coefficients based on certain assumptions about the channel's statistics, the CIR-related tap predictors can be rendered adaptive with the aid of the RLS algorithm. This has the potential of significantly further improving the performance, while maintaining the system's stability under time-variant channel conditions. Our conclusions will be offered in Section 3.6.

3.2 The SDMA Signal Model on a Subcarrier Basis

In Figure 3.1 we have portrayed an SDMA uplink transmission scenario, where each of the P simultaneous users is equipped with a single transmission antenna, while the receiver capitalizes on a P-element antenna front-end. The set of complex signals, $x_p[n,k]$, $p = 1,\ldots,P$ received by the P-element antenna array in the k-th subcarrier of the n-th OFDM symbol is constituted by

the superposition of the independently faded frequency-domain signals associated with the L users sharing the same space-frequency resource. The received signal was corrupted by the Gaussian noise at the array elements. Regarding the statistical properties of the different signal components depicted in Figure 3.1, we assume that the complex data signal $s^{(l)}$ transmitted by the l-th user has zero-mean and a variance of σ_l^2. The AWGN noise process n_p at any antenna array element p exhibits also zero-mean and a variance of σ_n^2, which is identical for all array elements. The frequency-domain channel transfer factors $H_p^{(l)}$ of the different array elements $p = 1, \ldots, P$ or users $l = 1, \ldots, L$ are independent, stationary, complex Gaussian distributed random variables with zero-mean and unit variance.

3.3 Least-Squares Error Assisted Decision-Directed Channel Transfer Function Estimation

In [21] the Least-Squares Error (LSE) approach was proposed by Li *et al.* for estimating the vector of channel transfer factors associated with each specific transmit-receive antenna pair in the context of the multi-user scenario outlined in Section 3.1. In contrast to [21] our derivation is based on a more compact matrix notation. The outline of Section 3.3 is as follows. In Section 3.3.1 the estimator's specific structure is derived, while in Section 3.3.2 the equations describing its MSE are developed for channel scenarios associated with both sample-spaced and *non-sample-spaced* CIRs. The method of further enhancing the estimator's MSE performance with the aid of CIR-related tap prediction filtering is briefly addressed in Section 3.3.3. Furthermore, in Section 3.3.4 Li's simplified - parallel interference cancellation assisted - approach [22] is outlined, which is then further developed in Section 3.4. The analysis of the estimator's complexity is provided in Section 3.3.5. Our conclusions will be offered in Section 3.3.6.

3.3.1 Derivation of the LS-Estimator

Let us commence by providing a brief outline of Section 3.3.1. In Section 3.3.1.1 the signal recorded for a specific receiver antenna element is described using vector notations, while in Section 3.3.1.2 we embark on the characterization of the LS estimator based on a simplified, noise-free version of the received signal's model outlined in Section 3.3.1.1.

3.3.1.1 The SDMA Signal Model on a Receiver Antenna Basis

Recall from Section 3.2 that the complex signal $x_p[n,k]$ associated with the p-th receiver antenna element in the k-th subcarrier of the n-th OFDM symbol is given as the superposition of the different

users' channel-impaired received signal contributions plus the AWGN, which is expressed as:

$$x_p[n,k] = \sum_{i=1}^{L} H_p^{(i)}[n,k]s^{(i)}[n,k] + n_p[n,k], \tag{3.1}$$

where again, the different variables have been defined in Section 3.2. Upon invoking vector notations, the set of equations constituted by Equation 3.1 for $k = 0,\ldots,K-1$ can be rewritten as:

$$\mathbf{x}_p[n] = \sum_{i=1}^{L} \mathbf{S}^{(i)}[n]\mathbf{H}_p^{(i)}[n] + \mathbf{n}_p[n] \tag{3.2}$$

$$= \mathbf{S}^T[n]\mathbf{H}_p[n] + \mathbf{n}_p[n], \tag{3.3}$$

where in Equation 3.2 $\mathbf{x}_p[n] \in \mathbb{C}^{K\times 1}$, $\mathbf{H}_p^{(i)}[n] \in \mathbb{C}^{K\times 1}$ and $\mathbf{n}_p[n] \in \mathbb{C}^{K\times 1}$ are column vectors hosting the subcarrier-related variables $x_p[n,k]$, $H_p^{(i)}[n,k]$ and $n_p[n,k]$, respectively, and $\mathbf{S}^{(i)}[n] \in \mathbb{C}^{K\times K}$ is a diagonal matrix with elements given by $s^{(i)}[n,k]$, where $k = 0,\ldots,K-1$. Furthermore, for the inner-product based representation of Equation 3.3 we have defined $\mathbf{S}[n] \in \mathbb{C}^{LK\times K}$ and $\mathbf{H}_p[n] \in \mathbb{C}^{LK\times 1}$ ([2]):

$$\mathbf{S}[n] = \left(\mathbf{S}^{(1)}[n]\ldots\mathbf{S}^{(L)}[n]\right)^T, \quad \mathbf{H}_p[n] = \left(\mathbf{H}_p^{(1)T}[n]\ldots\mathbf{H}_p^{(L)T}[n]\right)^T. \tag{3.4}$$

From now on we will omit the receiver antenna's index p. The dimension of the estimation task, namely that of determining the L users' vectors of channel transfer factors $\mathbf{H}_p^{(i)}[n], i = 1,\ldots,L$ containing K entries each - separately for each receiver antenna element $p = 1,\ldots,P$ - can be significantly reduced with the aid of a sub-space approach, which is the topic of the next section.

3.3.1.2 Sub-Space Based Approach

The key idea of sub-space-based techniques is to project the received signal on the basis of which the desired signal is to be estimated, onto the desired signal's vector sub-space, which is potentially spanned by only a fraction of the number of basis vectors which span the received signal's vector space. Thus the contributions outside the desired signal's sub-space, which should ideally only be the undesired AWGN, are removed. Unfortunately, however, in the context of non-sample-spaced CIRs the desired signal's space has potentially the same dimension as the received signal's space. Hence, the projection of the received signal onto the lower-dimensional- or lower-rank sub-space implies an imperfect representation of the desired signal.

The further structure of this section is as follows. The low-rank approximation of the i-th user's vector $\mathbf{H}^{(i)}[n]$ of channel transfer factors across the K different subcarriers is outlined in

[2] In order to avoid conflicts with the previous definition of $\mathbf{H}[n]$ cast in the context of single-user OFDM systems it would be useful to add a superscript of $()^{[L]}$ to this variable. However, this superscript has been omitted here for reasons of notational simplicity.

Section 3.3.1.2.1 and the associated coefficients- or CIR-related taps are then determined in Section 3.3.1.2.2. A necessary condition for the unambiguous identification of the different user's CIR-related taps will be outlined in Section 3.3.1.2.3. Our discussions in Section 3.3.1.2 will be concluded in Section 3.3.1.2.4 upon portraying an alternative approach capitalizing on the QR matrix factorization [87] for evaluating the vector $\tilde{\mathbf{h}}_{apt,K_0}[n]$ of CIR-related tap estimates instead of directly performing the inversion of matrix $\mathbf{Q}[n]$ as suggested by Equation 3.22.

3.3.1.2.1 Low-Rank Approximation of the i-th User's Vector of Different Subcarriers' Channel Transfer Factors Let us commence our detailed discourse by stating that Li *et al.* [21] assumed that upon neglecting the effects of leakage[3] due to the potentially non-sample-spaced nature of the "true" CIR of practical channels, the i-th user's vector $\mathbf{H}^{(i)}[n]$ of channel transfer factors can be approximated by the Discrete Fourier Transform (DFT) vector $\hat{\mathbf{H}}^{(i)}[n] \in \mathbb{C}^{K\times 1}$ of the vector $\hat{\mathbf{h}}^{(i)}_{K_0}[n] \in \mathbb{C}^{K_0\times 1}$ of $K_0 < K$ number of significant CIR-related *a posteriori* tap estimates as follows:

$$\hat{\mathbf{H}}^{(i)}[n] = \mathbf{W}\mathbf{J}^{(i)}_{K_0}\hat{\mathbf{h}}^{(i)}_{K_0}[n] \tag{3.5}$$

$$= \mathbf{W}^{(i)}_{J}\hat{\mathbf{h}}^{(i)}_{K_0}[n], \tag{3.6}$$

where $\mathbf{W}$ denotes the unitary DFT matrix [87] and $\mathbf{J}^{(i)}_{K_0} \in \mathbb{C}^{K\times K_0}$ has the role of mapping the K_0 CIR-related *a posteriori* tap estimates contained in the vector $\hat{\mathbf{h}}^{(i)}_{K_0}[n]$ to their "true" positions in terms of an OFDM time-domain sample-spaced delay, as it will be augmented below. The product of these matrices is denoted here as $\mathbf{W}^{(i)}_{J} \in \mathbb{C}^{K\times K_0}$, namely:

$$\mathbf{W}^{(i)}_{J} = \mathbf{W}\mathbf{J}^{(i)}_{K_0}. \tag{3.7}$$

More specifically, if the $\acute{m}$-th component of the estimated CIR-related tap vector $\hat{\mathbf{h}}^{(i)}_{K_0}[n]$ is associated with the $\acute{n}$-th integer delay tap raster position, then matrix $\mathbf{J}^{(i)}_{K_0}$ will have a numerical value of unity at the position given by the $\acute{n}$-th row and $\acute{m}$-th column. Since the mapping has to be unambiguous, we note that each column of $\mathbf{J}^{(i)}_{K_0}$ contains one and only one unity entry, while the remaining $K-1$ entries are zero. Hence, the total number of unity entries contained in $\mathbf{J}^{(i)}_{K_0}$ is equal to K_0. A more compact form of Equation 3.6 for the different users $i = 1, \ldots, L$ is given by:

$$\hat{\mathbf{H}}[n] = \mathbf{W}_J\hat{\mathbf{h}}_{K_0}[n], \tag{3.8}$$

where $\hat{\mathbf{H}}[n] \in \mathbb{C}^{LK\times 1}$ and $\hat{\mathbf{h}}_{K_0}[n] \in \mathbb{C}^{LK_0\times 1}$ are defined as:

$$\hat{\mathbf{H}}[n] = \left(\hat{\mathbf{H}}^{(1)T}[n]\ldots\hat{\mathbf{H}}^{(L)T}[n]\right)^T, \quad \hat{\mathbf{h}}_{K_0}[n] = \left(\hat{\mathbf{h}}^{(1)T}_{K_0}[n]\ldots\hat{\mathbf{h}}^{(L)T}_{K_0}[n]\right)^T, \tag{3.9}$$

[3]Consider the case of a non-sample-spaced CIR when the set of K frequency-domain channel transfer factor samples is transferred to the CIR-related domain with the aid of a unitary transform, which could be e.g. the DFT matrix $\mathbf{W}$. Although the original CIR might consist of a single non-sample-spaced tap only, its effects are potentially spread across all the K taps in the output of the unitary transform. This effect is known as leakage.

and the block-diagonal matrix $\mathbf{W}_J \in \mathbb{C}^{LK \times LK_0}$ is defined as:

$$\mathbf{W}_J = diag(\mathbf{W}_J^{(1)} \dots \mathbf{W}_J^{(L)}). \tag{3.10}$$

Then following the philosophy of Equation 3.2 the vector $\mathbf{x}[n]$ of received subcarrier signals can be approximated by:

$$\begin{aligned} \hat{\mathbf{x}}[n] &= \sum_{i=1}^{L} \check{\mathbf{S}}^{(i)}[n]\hat{\mathbf{H}}^{(i)}[n] && (3.11)\\ &= \check{\mathbf{S}}^{T}[n]\hat{\mathbf{H}}[n] && (3.12)\\ &= \mathbf{A}[n]\hat{\mathbf{h}}_{K_0}[n], && (3.13) \end{aligned}$$

where Equation 3.13 was obtained upon substituting Equation 3.8 into Equation 3.12 and by introducing the short-hand of $\mathbf{A}[n] \in \mathbb{C}^{K \times LK_0}$, namely:

$$\mathbf{A}[n] = \check{\mathbf{S}}^{T}[n]\mathbf{W}_J. \tag{3.14}$$

Hence, the initial estimation task is reduced to that of determining the L users' associated vectors $\hat{\mathbf{h}}_{K_0}^{(i)}[n]$, $i = 1, \dots, L$, constituting $\hat{\mathbf{h}}_{K_0}[n]$, each hosting K_0 number of significant CIR-related taps. Note that in Equation 3.11 $\check{\mathbf{S}}^{(i)}[n] \in \mathbb{C}^{K \times K}$ denotes the i-th user's matrix of sliced symbol decisions, while $\check{\mathbf{S}}[n] \in \mathbb{C}^{LK \times LK}$ is the L different users' matrix of sliced symbol decisions, which is defined similarly to the matrix $\mathbf{S}[n]$ of transmitted symbols given by Equation 3.4.

3.3.1.2.2 Determination of the LS-DDCE Coefficients Using the Gradient Approach The model-mismatch related error vector $\Delta\hat{\mathbf{x}}[n] \in \mathbb{C}^{K \times 1}$ between the vector $\mathbf{x}$ of received channel-impaired signals of the K different subcarriers, and the vector $\hat{\mathbf{x}}$ of estimated subcarrier signals given by Equation 3.13 can be defined as:

$$\begin{aligned} \Delta\hat{\mathbf{x}}[n] &= \mathbf{x}[n] - \hat{\mathbf{x}}[n] && (3.15)\\ &= \mathbf{x}[n] - \mathbf{A}\hat{\mathbf{h}}_{K_0}[n]. && (3.16) \end{aligned}$$

Furthermore, the total squared error of all the subcarriers of an OFDM symbol is given by the inner product of the vector of subcarrier errors as stated by Equation 3.16, yielding:

$$\begin{aligned} ||\Delta\hat{\mathbf{x}}[n]||_2^2 &= \Delta\hat{\mathbf{x}}^{H}[n]\Delta\hat{\mathbf{x}}[n] && (3.17)\\ &= \mathbf{x}^{H}[n]\mathbf{x}[n] - 2\Re\mathfrak{e}\left(\hat{\mathbf{h}}_{K_0}^{H}[n]\mathbf{p}[n]\right) + \\ &\quad + \hat{\mathbf{h}}_{K_0}^{H}[n]\mathbf{Q}[n]\hat{\mathbf{h}}_{K_0}[n], && (3.18) \end{aligned}$$

where the 'cross-correlation' vector $\mathbf{p}[n] \in \mathbb{C}^{LK_0 \times 1}$ is given by:

$$\mathbf{p}[n] = \mathbf{A}^{H}[n]\mathbf{x}[n], \tag{3.19}$$

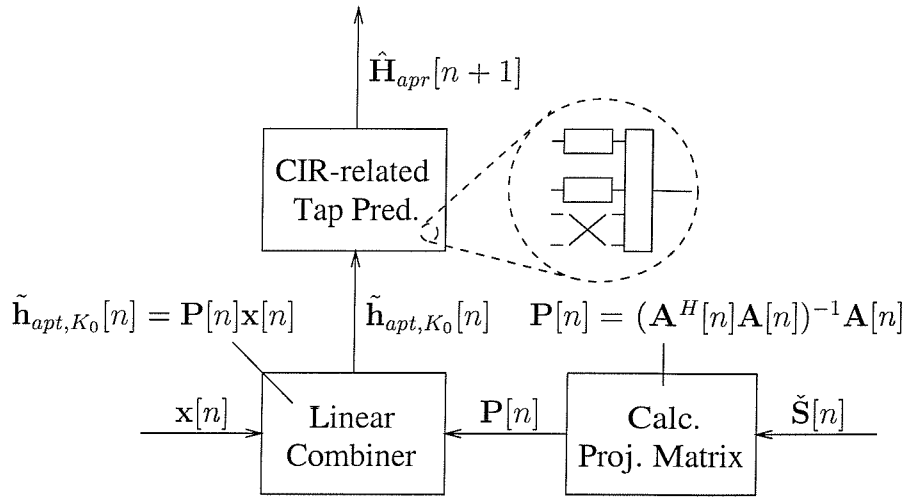

Figure 3.2: Stylized illustration of the LS-assisted DDCE as associated with the p-th receiver antenna. Based on the matrix $\check{\mathbf{S}}[n]$ of tentative symbol decisions, which follows the formulation of $\mathbf{S}[n]$ in Equation 3.4, the projection matrix $\mathbf{P}[n]$ is calculated as shown in Equation 3.24. By multiplication with the vector $\mathbf{x}[n]$ of received subcarrier signals during the combiner stage, the vector $\tilde{\mathbf{h}}_{apt,K_0}[n] \in \mathbb{C}^{LK_0 \times 1}$ of the L different users' CIR-related least-squares *a posteriori* tap estimates is obtained. In the simplest case the vector $\hat{\mathbf{H}}_{apr}[n+1] \in \mathbb{C}^{LK \times 1}$ of channel transfer factor estimates is generated upon invoking Equation 3.8 and by assuming that we have $\hat{\mathbf{H}}_{apr}[n+1] = \tilde{\mathbf{H}}_{apt}[n]$. However, a further reduction of the estimation MSE can be achieved with the aid of the CIR-related tap prediction filtering techniques discussed in Section 2.2.4 for single-user scenarios.

and the 'auto-correlation' matrix[4] $\mathbf{Q}[n] \in \mathbb{C}^{LK_0 \times LK_0}$ is given by:

$$\mathbf{Q}[n] = \mathbf{A}^H[n]\mathbf{A}[n]. \tag{3.20}$$

Following the philosophy of the least-squares (LS) error criterion, a standard approach for determining the optimum vector $\tilde{\mathbf{h}}_{apt,K_0}[n] \in \mathbb{C}^{LK_0 \times 1}$ of CIR-related *a posteriori* tap estimates[5] is to minimize the model-mismatch related squared error given by Equation 3.18. Note that in the optimum point the conjugate gradient $\nabla^* = \frac{\partial}{\partial \hat{\mathbf{h}}^*_{K_0}[n]}$ of the error term of Equation 3.18 $||\Delta\hat{\mathbf{x}}[n]||_2^2$ with respect to the vector $\hat{\mathbf{h}}_{K_0}[n]$ of CIR-related tap estimates is zero [21], which can be formulated as:

$$||\Delta\hat{\mathbf{x}}[n]||_2^2 = \text{Min.} \quad \Longleftrightarrow \quad \nabla^* ||\Delta\hat{\mathbf{x}}[n]||_2^2 \stackrel{!}{=} \mathbf{0}. \tag{3.21}$$

Upon substituting Equation 3.18 into Equation 3.21 and using a number of mathematical manipulations, we obtain the following expression [21]:

$$\mathbf{Q}[n]\tilde{\mathbf{h}}_{apt,K_0}[n] = \mathbf{p}[n] \quad \Longleftrightarrow \quad \tilde{\mathbf{h}}_{apt,K_0}[n] = \mathbf{Q}^{-1}[n]\mathbf{p}[n]. \tag{3.22}$$

[4]Note that according to standard definition evaluating the auto-correlation- or cross-correlation involves using the expectation operator, which is not the case in the context of the LS-approach. However, these expressions have still been used in inverted commas, in order to highlight the similarities to a potential MMSE solution.

[5]In accordance with the notation used for DDCE in single-user scenarios, which was discussed in Section 2.2, the least-squares solution is denoted by a superscript of $\tilde{()}$.

Here we have specifically exploited that the gradient with respect to the constant first term of Equation 3.18 is equal to zero, while the gradient with respect to the second term was evaluated by capitalizing on $\frac{\partial}{\partial \mathbf{z}^*}\Re\mathfrak{e}(\mathbf{z}^H\mathbf{a}) = \frac{1}{2}\mathbf{a}$ [87], which is valid for complex valued column vectors $\mathbf{z}$ and $\mathbf{a}$. The gradient of the last term in Equation 3.18 was evaluated upon exploiting that $\frac{\partial}{\partial \mathbf{z}^*}\mathbf{z}^H\mathbf{R}\mathbf{z} = \mathbf{R}\mathbf{z}$ [87] for a Hermitian matrix $\mathbf{R}$.

Note that we could have also directly obtained the solution for this CIR-related tap estimation problem by recognizing the characteristic shape of Equation 3.16, for which the least-squares solution is given by [87]:

$$\tilde{\mathbf{h}}_{apt,K_0}[n] = \mathbf{P}[n]\mathbf{x}[n], \tag{3.23}$$

where:

$$\mathbf{P}[n] = (\mathbf{A}^H[n]\mathbf{A}[n])^{-1}\mathbf{A}^H[n]. \tag{3.24}$$

The matrix $\mathbf{P}[n] \in \mathbb{C}^{LK_0 \times K}$ of Equation 3.24 is also known from the literature [87] as a matrix, which projects - when multiplied from the right with $\mathbf{x}[n]$ - on the column vectors of $\mathbf{A}[n]$. These span the signal's sub-space [87]. Alternatively, $\mathbf{P}[n]$ can be interpreted as the pseudo-inverse- or so-called Moore-Penrose inverse [87] of $\mathbf{A}[n]$, denoted by $\mathbf{A}^\dagger[n]$. The representation of the LS-assisted DDCE by means of Equations 3.23 and 3.24 is further illustrated in Figure 3.2. Note that based on Equation 3.8 the vector $\tilde{\mathbf{H}}_{apt}[n] \in \mathbb{C}^{LK\times 1}$ of *a posteriori* channel transfer factor estimates is given by:

$$\tilde{\mathbf{H}}_{apt}[n] = \mathbf{W}_J\tilde{\mathbf{h}}_{apt,K_0}[n]. \tag{3.25}$$

Upon resubstituting the vector $\tilde{\mathbf{h}}_{apt,K_0}[n]$ of LS-optimum CIR-related tap estimates given by Equations 3.22 or 3.23 into the model-mismatch related cost-function of Equation 3.18 we obtain:

$$(||\Delta\hat{\mathbf{x}}[n]||_2^2)|_{\tilde{\mathbf{h}}_{apt,K_0}[n]} = \mathbf{x}^H[n]\mathbf{x}[n] - \mathbf{p}^H[n]\tilde{\mathbf{h}}_{apt,K_0}[n], \tag{3.26}$$

which is the minimum mismatch error.

3.3.1.2.3 Necessary Condition for Identification of the LS-DDCE Coefficients As mentioned in Section 3.3.1.2.2, the solution of the estimation problem according to Equation 3.23 requires computation of the Moore-Penrose- or left-inverse of the matrix $\mathbf{A}[n] \in \mathbb{C}^{K\times LK_0}$ given in Equation 3.24. A necessary and sufficient condition for its existence is that the LK_0 number of columns of the matrix $\mathbf{A}$ are linearly independent [87]. This implies that we have $rank(\mathbf{A}[n]) = LK_0$, where a *necessary condition* for this to be the case is that the number of rows of $\mathbf{A}[n]$, namely K is higher than the number of columns, namely LK_0, which is formulated as:

$$LK_0 \leq K \quad \Longleftrightarrow \quad L \leq \frac{K}{K_0}. \tag{3.27}$$

Equation 3.27 imposes a constraint with respect to the L number of simultaneous users- or the number of transmit antennas. Avoiding this limitation is a further motivation for devising alternative channel transfer function estimation approaches.

3.3.1.2.4 Implementation by QR Decomposition It is well-known from the literature that the matrix $\mathbf{Q}[n] = \mathbf{A}^H[n]\mathbf{A}[n]$ associated with the projection matrix $\mathbf{P}[n]$ of Equation 3.24, which is also known as the Moore-Penrose- or pseudo-inverse $\mathbf{A}^\dagger[n]$ of $\mathbf{A}[n]$ [87] exhibits a potentially high condition number $\kappa(\mathbf{A}[n])$, which reflects the degree of ill-conditioning or proximity to rank-deficiency [87]. Hence, a direct inversion of $\mathbf{Q}[n]$ is likely to be inaccurate, specifically for $L \lessapprox \frac{K}{K_0}$, as already mentioned in Section 3.3.1.2.3. These effects can be mitigated with the aid of the procedure of QR matrix factorization or decomposition, as demonstrated for example in [87]. The QR factorization implies that the matrix $\mathbf{A}[n]$ can be factored as:

$$\mathbf{A}[n] = \mathbf{QR} = \mathbf{Q}\begin{pmatrix} \mathbf{R}_1 \\ \mathbf{0} \end{pmatrix}, \tag{3.28}$$

where $\mathbf{Q} \in \mathbb{C}^{K \times K}$ is a unitary matrix - which intentionally lacks the index $[n]$ in order to distinguish it from $\mathbf{Q}[n]$ of Equation 3.20 and $\mathbf{R} \in \mathbb{C}^{K \times LK_0}$ is an upper triangular matrix which can be expressed as $\mathbf{R} = (\mathbf{R}_1\ \mathbf{0})^T$ since $K \geq LK_0$, with $\mathbf{R}_1 \in \mathbb{C}^{LK_0 \times LK_0}$ and $\mathbf{0}$ being a $(K - LK_0) \times LK_0$-dimensional zero-matrix. Upon substituting Equation 3.28 into Equation 3.16 and by substituting the result into Equation 3.17 we obtain for $||\Delta\hat{\mathbf{x}}[n]||_2^2$ [87]:

$$\begin{aligned}
||\Delta\hat{\mathbf{x}}[n]||_2^2 &= ||\mathbf{x}[n] - \mathbf{QR}\hat{\mathbf{h}}[n]||_2^2 && (3.29)\\
&= ||\mathbf{Q}(\mathbf{Q}^H\mathbf{x}[n] - \mathbf{R}\hat{\mathbf{h}}[n])||_2^2 && (3.30)\\
&= ||\mathbf{Q}^H\mathbf{x}[n] - \mathbf{R}\hat{\mathbf{h}}[n])||_2^2 && (3.31)\\
&= \left|\left|\begin{pmatrix} \mathbf{c} \\ \mathbf{d} \end{pmatrix} - \begin{pmatrix} \mathbf{R}_1 \\ \mathbf{0} \end{pmatrix}\hat{\mathbf{h}}[n]\right|\right|_2^2 && (3.32)\\
&= ||\mathbf{c} - \mathbf{R}_1\hat{\mathbf{h}}[n]||_2^2 + ||\mathbf{d}||_2^2, && (3.33)
\end{aligned}$$

where all variables are defined below. The solution in the sense of minimizing $||\Delta\hat{\mathbf{x}}[n]||_2^2$ is given by [87]:

$$\hat{\mathbf{R}}_1\tilde{\mathbf{h}}[n] = \mathbf{c}, \tag{3.34}$$

which can be directly solved for the vector $\tilde{\mathbf{h}}[n]$ of the L different users' CIR-related tap estimates by back-substitution, since $\mathbf{R}_1[n]$ is an upper triangular matrix. Note that in the context of Equation 3.30 we have exploited the unitarity nature of the matrix $\mathbf{Q}$, namely, that we have $\mathbf{QQ}^H = \mathbf{I}$, while in the context of Equation 3.31 that the Euclidean norm of a matrix or vector remains unchanged, when subjected to a unitary transform [87]. Furthermore, we have exploited in Equation 3.32 that $\mathbf{Q}^H\mathbf{x}[n] = (\mathbf{c}\ \mathbf{d})^T$, where $\mathbf{c} \in \mathbb{C}^{LK_0 \times LK_0}$ and $\mathbf{d} \in \mathbb{C}^{(K-LK_0)\times(K-LK_0)}$. Note that

other matrix factorizations or decompositions can also be applied to the LS estimation problem, but the solution acquired with the aid of the QR factorization is the most prominent one [87].

3.3.2 Least-Squares Channel Estimation MSE in the Context of Both Sample-Spaced and Non-Sample-Spaced CIRs

Our analysis commences in Section 3.3.2.1 with the derivation of the channel transfer factor estimation errors' auto-correlation matrix, where more specifically, the average of its main-diagonal elements determines the average channel estimation MSE. In this section we impose no specific assumptions on the CIRs or the transmitted subcarrier symbol sequences. By contrast, in Section 3.3.2.2 we will focus our attention on the idealistic case of sample-spaced CIRs. However, in order to render our investigations more realistic, non-sample-spaced CIRs will be considered in Section 3.3.2.3. In characterizing the estimator's performance, we will capitalize on the properties of optimum training sequences, as proposed by Li [22].

3.3.2.1 Correlation Matrix of the Channel Transfer Factor Estimates

Upon substituting Equation 3.3 into Equation 3.23 and by further substituting the result into Equation 3.8 the vector $\tilde{\mathbf{H}}_{apt}[n]$([6]) of least-squares channel transfer factor estimates is obtained as a function of the vector $\mathbf{H}[n]$ of "true" channel transfer factors associated with the specific channel encountered and as a function of the vector of different subcarrier noise processes $\mathbf{n}[n]$, which is formulated as[7]:

$$\tilde{\mathbf{H}}_{apt}[n] = \mathbf{W}_J\mathbf{P}[n](\mathbf{S}^T[n]\mathbf{H}[n] + \mathbf{n}[n]). \tag{3.35}$$

Furthermore, the vector $\Delta\tilde{\mathbf{H}}_{apt}[n] \in \mathbb{C}^{LK\times 1}$ of the L different users' channel transfer factor estimation errors is defined as:

$$\Delta\tilde{\mathbf{H}}_{apt}[n] = \mathbf{H}[n] - \tilde{\mathbf{H}}_{apt}[n], \tag{3.36}$$

while its auto-correlation matrix $\mathbf{R}_{\Delta\tilde{\mathbf{H}}_{apt}[n]} \in \mathbb{C}^{LK\times LK}$ is given by:

$$\begin{aligned}\mathbf{R}_{\Delta\tilde{\mathbf{H}}_{apt}[n]} &= E\{\Delta\tilde{\mathbf{H}}_{apt}[n]\Delta\tilde{\mathbf{H}}^H_{apt}[n]\} &(3.37)\\ &= \mathbf{R}^{[f]} - 2\Re\mathfrak{e}\left\{\mathbf{R}^{[f]}_c\right\} + \mathbf{R}^{[f]}_a. &(3.38)\end{aligned}$$

More specifically, the first term in Equation 3.38, namely the block-diagonal matrix $\mathbf{R}^{[f]} \in \mathbb{C}^{LK\times LK}$ hosting the different users' spaced-frequency correlation matrices $\mathbf{R}^{[f](i)}, i = 1,\ldots,L$ is given by:

$$\begin{aligned}\mathbf{R}^{[f]} &= E\{\mathbf{H}[n]\mathbf{H}^H[n]\} &(3.39)\\ &= diag(\mathbf{R}^{[f](1)}\ldots\mathbf{R}^{[f](L)}). &(3.40)\end{aligned}$$

[6]Note that here we have again omitted the receiver antenna index p.

[7]In the context of a sample-spaced CIR it can be shown that we have $\mathbf{W}_J\mathbf{P}[n]\mathbf{S}^T[n] = \mathbf{I}$, conditioned on an appropriate selection of $\mathbf{J}^{(i)}_{K_0}$, $i = 1,\ldots,L$, such that all of the non-zero taps' energy is retained. In this case $\tilde{\mathbf{H}}_{apt}[n]$ is an unbiased estimate [87] of $\mathbf{H}[n]$, which implies that we have $\tilde{\mathbf{H}}[n] = \mathbf{H}[n] + \mathbf{W}_J\mathbf{P}[n]\mathbf{n}[n]$.

Here we have exploited that the channel transfer functions associated with different transmit antennas are uncorrelated. Again, in Equation 3.40 $\mathbf{R}^{[f](i)} \in \mathbb{C}^{K \times K}$ denotes the i-th user's channel's spaced-frequency correlation matrix, which is defined as:

$$\mathbf{R}^{[f](i)} = E\{\mathbf{H}^{(i)}[n]\mathbf{H}^{(i)H}[n]\}. \tag{3.41}$$

Similarly, for the second term of Equation 3.38, namely the channel transfer factor estimates' cross-correlation matrix $\mathbf{R}_c^{[f]} \in \mathbb{C}^{LK \times LK}$ we obtain:

$$\begin{aligned} \mathbf{R}_c^{[f]} &= E\{\mathbf{H}[n]\tilde{\mathbf{H}}_{apt}^H[n]\} & (3.42)\\ &= \mathbf{R}^{[f]}\mathbf{S}^*[n]\mathbf{P}^H[n]\mathbf{W}_J^H, & (3.43) \end{aligned}$$

while the last term of Equation 3.38, namely the channel transfer factor estimates' auto-correlation matrix $\mathbf{R}_a^{[f]} \in \mathbb{C}^{LK \times LK}$ is given by:

$$\begin{aligned} \mathbf{R}_a^{[f]} &= E\{\tilde{\mathbf{H}}_{apt}[n]\tilde{\mathbf{H}}_{apt}^H[n]\} & (3.44)\\ &= \mathbf{W}_J\mathbf{P}[n](\mathbf{S}^T[n]\mathbf{R}^{[f]}\mathbf{S}^*[n] + \sigma_n^2\mathbf{I})\mathbf{P}^H[n]\mathbf{W}_J^H. & (3.45) \end{aligned}$$

Note that $\mathbf{R}_a^{[f]}$ can be split into a channel- and a noise-related matrix contribution $\mathbf{R}_{a,\text{Channel}}^{[f]} \in \mathbb{C}^{LK \times LK}$ and $\mathbf{R}_{a,\text{AWGN}}^{[f]} \in \mathbb{C}^{LK \times LK}$, respectively, yielding:

$$\mathbf{R}_a^{[f]} = \mathbf{R}_{a,\text{Channel}}^{[f]} + \mathbf{R}_{a,\text{AWGN}}^{[f]}, \tag{3.46}$$

where the two components are given by:

$$\begin{aligned} \mathbf{R}_{a,\text{Channel}}^{[f]} &= \mathbf{W}_J\mathbf{P}[n]\mathbf{S}^T[n]\mathbf{R}^{[f]}\mathbf{S}^*[n]\mathbf{P}^H[n]\mathbf{W}_J^H & (3.47)\\ \mathbf{R}_{a,\text{AWGN}}^{[f]} &= \sigma_n^2\mathbf{W}_J\mathbf{P}[n]\mathbf{P}^H[n]\mathbf{W}_J^H. & (3.48) \end{aligned}$$

While in Section 3.3.2.2 we will further elaborate on the specific structure of the auto-correlation matrix $\mathbf{R}_{\Delta\tilde{\mathbf{H}}_{apt}[n]}$ in the context of the idealistic scenario of a sample-spaced CIR, in Section 3.3.2.3 we will consider its specific structure in the context of a more realistic scenario of a non-sample-spaced CIR, with the ultimate aim of determining the *a posteriori* estimation MSEs.

3.3.2.2 Sample-Spaced CIRs

The discussions in this section are structured as follows. The specific effects of a sample-spaced CIR on the channel transfer factor estimation error's auto-correlation matrix are discussed in Section 3.3.2.2.1. In order to further characterize the estimator's MSE performance, the properties of the optimum training sequences proposed by Li [22] are reviewed in Section 3.3.2.2.2, while their impact on the estimator's performance is elaborated on in Section 3.3.2.2.3.

3.3.2.2.1 Auto-Correlation Matrix of the Channel Transfer Factor Estimation Errors The decomposition of the i-th user's channel's spaced-frequency correlation matrix $\mathbf{R}^{[f](i)}$, $i = 1, \ldots, L$ with respect to the DFT matrix $\mathbf{W}$ can be expressed as:

$$\mathbf{R}^{[f](i)} = \mathbf{W}\Lambda_W^{[f](i)}\mathbf{W}^H, \tag{3.49}$$

where the matrix $\Lambda_W^{[f](i)} \in \mathbb{C}^{K\times K}$ has a diagonal structure with real-valued elements only in the context of a sample-spaced CIR. This is, because in this specific case the Karhunen-Loeve Transform (KLT) matrix [87] of $\mathbf{R}^{[f](i)}$ is identical to the DFT matrix $\mathbf{W}$. Hence the diagonal elements of $\Lambda_W^{[f](i)}$ are the real-valued eigenvalues of the matrix $\mathbf{R}^{[f](i)}$, while the eigenvectors of $\mathbf{R}^{[f](i)}$ are identical to the column vectors of the DFT matrix $\mathbf{W}$. Upon retaining all of the CIR-related taps having a non-zero energy, which is achieved by appropriately designing the matrix $\mathbf{J}_{K_0}^{(i)}$ defined in the context of Equation 3.7, Equation 3.49 can be also formulated as:

$$\begin{aligned}\mathbf{R}^{[f](i)} &= \mathbf{W}\left(\mathbf{J}_{K_0}^{(i)}\mathbf{J}_{K_0}^{(i)H}\right)\Lambda_W^{[f](i)}\left(\mathbf{J}_{K_0}^{(i)}\mathbf{J}_{K_0}^{(i)H}\right)\mathbf{W}^H &(3.50)\\ &= \mathbf{W}_J^{(i)}\Lambda_{W,J}^{[f](i)}\mathbf{W}_J^{(i)H}, &(3.51)\end{aligned}$$

where $\mathbf{W}_J^{(i)}$ was defined in Equation 3.7 and $\Lambda_{W,J}^{[f](i)} = \mathbf{J}_{K_0}^{(i)H}\Lambda_W^{[f](i)}\mathbf{J}_{K_0}^{(i)} \in \mathbb{C}^{K_0\times K_0}$. Recall the definition of the matrix $\mathbf{A}[n]$ from Equation 3.14, namely that we have $\mathbf{A}[n] = \mathbf{S}^T[n]\mathbf{W}_J$ and that the Hermitian transpose of $\mathbf{A}[n]$ is given by $\mathbf{A}^H[n] = \mathbf{W}_J^H\mathbf{S}^*[n]$. Then, upon substituting Equation 3.51 into the formulae of the channel transfer factor estimates' cross-correlation matrix- and auto-correlation matrix given in Equations 3.43 and 3.45, respectively, and upon resubstituting the results into Equation 3.38 we obtain the following expression for the auto-correlation matrix of the channel transfer factor estimation errors:

$$\mathbf{R}_{\Delta\tilde{\mathbf{H}}_{apt}[n]} = \mathbf{R}_{a,\text{AWGN}}^{[f]} = \sigma_n^2\mathbf{W}_J\mathbf{P}[n]\mathbf{P}^H[n]\mathbf{W}_J^H, \tag{3.52}$$

which results from the noise-related contribution of the matrix $\mathbf{R}_a^{[f]}$ in Equation 3.46, namely from its second term. Upon recalling from Equation 3.24 that the projection matrix was defined as $\mathbf{P}[n] = (\mathbf{A}^H[n]\mathbf{A}[n])^{-1}\mathbf{A}^H[n]$, Equation 3.52 is transformed into:

$$\mathbf{R}_{\Delta\tilde{\mathbf{H}}_{apt}[n]} = \sigma_n^2\mathbf{W}_J\mathbf{Q}^{-1}[n]\mathbf{W}_J^H, \tag{3.53}$$

where according to Equation 3.20 we have $\mathbf{Q}[n] = \mathbf{A}^H[n]\mathbf{A}[n]$. Note from Equation 3.53, that since $\mathbf{A}[n] = \mathbf{S}^T[n]\mathbf{W}_J$ according to Equation 3.14, the matrix $\mathbf{R}_{\Delta\tilde{\mathbf{H}}_{apt}[n]}$ and consequently also the average estimation MSE depends on the specific subcarrier symbols transmitted.

3.3.2.2.2 Properties of Optimum Training Sequences In order to draw further conclusions with respect to the estimator's MSE, let us consider the choice of channel sounding or training

subcarrier symbol sequences, as proposed by Li [22], which are given for the i-th user- or transmit antenna by:

$$t^{(i)}[n,k] = \sigma_i t_p[n,k] W_K^{-\overline{K}_0(i-1)k}, \tag{3.54}$$

where $\sigma_i = \sqrt{\sigma_i^2}$ is the i-th user's signal standard deviation, $t_p[n,k],\ k = 0,\ldots,K-1$ denotes an arbitrary training sequence having potentially complex subcarrier symbols of unit variance, $W_K = e^{-j\frac{2\pi}{K}}$ is the complex Fourier kernel, while $\overline{K}_0$ is defined as $\overline{K}_0 = \lfloor \frac{K}{L} \rfloor$. In [22] it was argued that in the context of these training sequences for identical matrices of $\mathbf{J}_{K_0} = \mathbf{J}_{K_0}^{(1)} = \ldots = \mathbf{J}_{K_0}^{(L)}$, where the K_0 number of unity elements in $\mathbf{J}_{K_0}$ are arranged on a diagonal, such that K_0 number of significant adjacent taps are extracted in the CIR-related domain, the matrix $\mathbf{Q}[n]$ is of diagonal shape. This can be demonstrated by recalling the definition of $\mathbf{Q}[n]$ in Equation 3.20, and substituting $\mathbf{A}[n]$ of Equation 3.14 into Equation 3.20 yields:

$$\begin{aligned} \mathbf{Q}[n] &= \mathbf{A}^H[n]\mathbf{A}[n] & (3.55)\\ &= \mathbf{W}_J^H \mathbf{S}^*[n]\mathbf{S}^T[n]\mathbf{W}_J. & (3.56) \end{aligned}$$

By further capitalizing on the expressions of $\mathbf{W}_J$ and $\mathbf{S}[n]$ given in Equations 3.10 and 3.4, respectively, the sub-matrix $\mathbf{Q}^{(i,j)}[n] \in \mathbb{C}^{K_0 \times K_0}$ of the block-matrix $\mathbf{Q}[n] \in \mathbb{C}^{LK_0 \times LK_0}$, which is associated with the i-th "row" and j-th "column" of $\mathbf{Q}[n]$, where $i,j \in \{1,\ldots,L\}$ is given by:

$$\begin{aligned} \mathbf{Q}^{(i,j)}[n] &= \mathbf{W}_J^{(i)H} \mathbf{S}^{(i)*}[n]\mathbf{S}^{(j)}[n]\mathbf{W}_J^{(j)} & (3.57)\\ &= \mathbf{J}_{K_0}^{(i)H} \acute{\mathbf{Q}}^{(i,j)}[n]\mathbf{J}_{K_0}^{(j)}, & (3.58) \end{aligned}$$

where $\acute{\mathbf{Q}}^{(i,j)}[n] \in \mathbb{C}^{K \times K}$ is defined as:

$$\acute{\mathbf{Q}}^{(i,j)}[n] = \mathbf{W}^H \mathbf{S}^{(i)*}[n]\mathbf{S}^{(j)}[n]\mathbf{W}. \tag{3.59}$$

More explicitly, Equation 3.58 was obtained by substituting $\mathbf{W}_J^{(i)}$ given in Equation 3.7 into Equation 3.57. When employing channel sounding or training sequences obeying Equation 3.54 as proposed in [22], the elements of the matrix $\mathbf{S}^{(i)*}[n]\mathbf{S}^{(j)T}[n]$, which is the key component of Equation 3.59, are given by:

$$t^{(i)*}[n,k]t^{(j)}[n,k] = \sigma_i\sigma_j W_K^{\overline{K}_0(i-j)k}. \tag{3.60}$$

By further noting that the elements of the DFT matrix $\mathbf{W}$ are given by $\frac{1}{\sqrt{K}} W_K^{i_1 j_1}$ and that of its Hermitian transpose by $\frac{1}{\sqrt{K}} W_K^{-i_1 j_1}$, where $i_1, j_1 \in \{0,\ldots,K-1\}$, it can be readily shown that the element (i_1, j_1) of the product matrix $\acute{\mathbf{Q}}^{(i,j)}[n]$ defined in Equation 3.59 is given by:

$$\begin{aligned} \acute{\mathbf{Q}}^{(i,j)}[n]|_{i_1,j_1} &= \frac{1}{K} \sum_{k=0}^{K-1} \sigma_i\sigma_j e^{j\frac{2\pi}{K}k[(i_1-j_1)-\overline{K}_0(i-j)]} & (3.61)\\ &= \sigma_i\sigma_j \delta\left[(i_1-j_1) - \overline{K}_0(i-j) - xK\right], & (3.62) \end{aligned}$$

where:

$$x = \begin{cases} -1 & \wedge \quad (i > j \ \wedge \ i_1 < j_1) \\ 0 & \wedge \quad (i > j \ \wedge \ i_1 > j_1) \vee (i < j \ \wedge \ i_1 < j_1) \\ 1 & \wedge \quad (i < j \ \wedge \ i_1 > j_1) \end{cases} . \tag{3.63}$$

In the derivation of Equation 3.62 we have exploited that the summation of the complex exponentials in Equation 3.61 yields a non-zero contribution, if the exponential argument in square brackets is equal to an integer multiple of K, namely, if we have $(i_1 - j_1) - \overline{K}_0(i-j) = xK$. When taking into account the constraint of $i_1, j_1 \in \{0, \ldots, K-1\}$, we have $x \in \{-1, 0, 1\}$. Observe furthermore from Equation 3.62 that when we have $(i = j)$, the matrix $\acute{\mathbf{Q}}^{(i,j)}[n]$ is a diagonal matrix having identical elements of σ_i^2, while for $(i > j)$ the matrix is a diagonal matrix, *cyclically* shifted to the left. Finally, for $(i < j)$ the diagonal matrix $\acute{\mathbf{Q}}^{(i,j)}[n]$ is *cyclically* shifted to the right, exhibiting in both cases the form of:

$$\acute{\mathbf{Q}}^{(i,j)}[n] = \sigma_i \sigma_j \mathbf{I}_{cyc}^{(i,j)}, \text{ where } \mathbf{I}_{cyc}^{(i,j)} = \begin{pmatrix} \mathbf{0} & \mathbf{I}_B \\ \mathbf{I}_A & \mathbf{0} \end{pmatrix} \in \mathbb{C}^{K \times K}, \tag{3.64}$$

and where $\mathbf{I}_A \in \mathbb{R}^{K_A \times K_A}$ with $K_A = [K - \overline{K}_0(i-j)] \bmod K$, while $\mathbf{I}_B \in \mathbb{R}^{K_B \times K_B}$ with $K_B = [K - \overline{K}_0(j-i)] \bmod K$. Note that the matrix $\acute{\mathbf{Q}}^{(i,j)}[n]$ multiplied from the right with a column vector performs a cyclic rotation of the column vector's elements.

Upon also taking into account the 'masking' effects imposed by the matrix $\mathbf{J}_{K_0} = \mathbf{J}_{K_0}^{(1)} = \ldots = \mathbf{J}_{K_0}^{(L)}$ as seen in Equation 3.58, it follows that for CIRs having K_0 adjacent significant CIR-related taps we have $\mathbf{Q}^{(i,i)}[n] = \sigma_i^2 \mathbf{I}$ and $\mathbf{Q}^{(i,j)}[n] = \mathbf{0}$, $i \neq j$.

3.3.2.2.3 *A Posteriori* Estimation MSE Using Optimum Training Sequences By capitalizing on the specific properties of $\mathbf{Q}[n]$ in the context of optimum training sequences, namely that $\mathbf{Q}^{(i,i)}[n] = \sigma_i^2 \mathbf{I}$ and $\mathbf{Q}^{(i,j)}[n] = \mathbf{0}, i \neq j$, Equation 3.53 can be rewritten as:

$$\mathbf{R}_{\Delta \tilde{\mathbf{H}}_{apt}[n]} = \sigma_n^2 diag(\frac{1}{\sigma_1^2} \mathbf{T}_{W,K_0}^{(1)} \cdots \frac{1}{\sigma_L^2} \mathbf{T}_{W,K_0}^{(L)}), \tag{3.65}$$

where the matrix $\mathbf{T}_{W,K_0}^{(i)} \in \mathbb{C}^{K \times K}$ is given by:

$$\mathbf{T}_{W,K_0}^{(i)} = \mathbf{W}_J^{(i)} \mathbf{W}_J^{(i)H} \tag{3.66}$$

$$= \mathbf{W} \mathbf{J}_{K_0}^{(i)} \mathbf{J}_{K_0}^{(i)H} \mathbf{W}^H \tag{3.67}$$

$$= \mathbf{W} \mathbf{I}_{K_0}^{(i)} \mathbf{W}^H, \tag{3.68}$$

with $\mathbf{W}_J^{(i)}$ according to Equation 3.10 and $\mathbf{I}_{K_0}^{(i)} = \mathbf{J}_{K_0}^{(i)} \mathbf{J}_{K_0}^{(i)H} \in \mathbb{R}^{K \times K}$. The latter formula will specifically draw our attention in the context of PIC-assisted DDCE in Section 3.4. The estimation

MSE averaged over the subcarriers of the i-th user is then given by [21]:

$$\overline{\mathrm{MSE}}_{apt}^{(i)}[n] = \frac{1}{K}\mathrm{Trace}(\mathbf{R}_{\Delta\tilde{\mathbf{H}}_{apt}[n]}^{(i,i)}) \quad (3.69)$$

$$= \frac{K_0}{K}\frac{\sigma_n^2}{\sigma_i^2}, \quad (3.70)$$

while by further averaging over the L different users the total average MSE becomes:

$$\overline{\mathrm{MSE}}_{apt}[n] = \frac{1}{L}\sum_{i=1}^{L}\overline{\mathrm{MSE}}_{apt}^{(i)}[n] \quad (3.71)$$

$$= \frac{K_0}{LK}(\sum_{i=1}^{L}\frac{1}{\sigma_i^2})\sigma_n^2. \quad (3.72)$$

Note that the i-th user's *a posteriori* estimation MSE given by Equation 3.70 is equivalent to that of the single-user scenario, when performing CIR-related tap windowing of the initial least-squares *a posteriori* channel transfer factor estimates $\tilde{H}_{apt}[n,k], k = 0,\ldots,K-1$, which were defined in Equation 2.2. Note however, that when transmitting random symbols the estimation MSE is potentially degraded compared to the scenario of transmitting optimum training sequences. This is since the different channels' CIRs are imperfectly separated from each other.

In the next section we will analyse the estimator's performance in the context of the more realistic environment of a non-sample-spaced CIR.

3.3.2.3 Non-Sample-Spaced CIRs

In contrast to the sample-spaced CIR of the previous section, for a non-sample-spaced CIR the decomposition $\Lambda_W^{[f](i)}$ seen in Equation 3.49 for the i-th user's channel's spaced-frequency correlation matrix $\mathbf{R}^{[f](i)}$ with respect to the DFT matrix $\mathbf{W}$ is not a diagonal matrix and does not have a reduced number of $K_0 \ll K$ non-zero elements. In fact, potentially all of the decomposition's taps may become non-zero.

In order to further characterize the estimator's MSE performance, we will commence our elaborations again by considering the channel transfer factor estimation errors' auto-correlation matrix $\mathbf{R}_{\Delta\tilde{\mathbf{H}}_{apt}[n]}$, which was given by Equation 3.38. We note furthermore that the associated components of $\mathbf{R}_{\Delta\tilde{\mathbf{H}}_{apt}[n]}$, namely the block-diagonal matrix $\mathbf{R}^{[f]}$ of the different users' channels' spaced-frequency correlation matrices, as well as the channel transfer factor estimates' cross-correlation as well as auto-correlation matrix, namely $\mathbf{R}_c^{[f]}$ and $\mathbf{R}_a^{[f]}$ were formulated in Equations 3.40, 3.43 and 3.45. In order to simplify $\mathbf{R}_c^{[f]}$ and $\mathbf{R}_a^{[f]}$ of Equations 3.43 and 3.45, we will again capitalize on the properties of the optimum training sequences proposed by Li [22], which also constituted the basis of our derivations in Section 3.3.2.2.

Hence, our further proceedings are as follows. In Section 3.3.2.3.1 the channel transfer factor estimates' cross-correlation matrix is derived, while the estimates' auto-correlation matrix is derived in Section 3.3.2.3.2, both in the context of the optimum training sequences [22] described

in Section 3.3.2.2.2. With the aid of these matrices the average channel transfer factor estimation MSE is then derived in Section 3.3.2.3.3, based on the averaged sum of the main diagonal elements associated with the subcarrier estimation errors' auto-correlation matrix of Equation 3.38.

3.3.2.3.1 Cross-Correlation Matrix of the Channel Transfer Factor Estimates in the Context of Optimum Training Sequences Let us commence by studying the estimates' cross-correlation matrix, which was given by Equation 3.43. Upon substituting $\mathbf{P}[n]$ of Equation 3.24 and $\mathbf{A}[n]$ of Equation 3.14 into Equation 3.43 we arrive at:

$$\mathbf{R}_c^{[f]} = diag(\mathbf{R}^{[f](1)} \dots \mathbf{R}^{[f](L)}) \cdot \mathbf{S}^*[n]\mathbf{S}^T[n] \cdot diag(\frac{1}{\sigma_1^2}\mathbf{T}_{W,K_0}^{(1)} \dots \frac{1}{\sigma_L^2}\mathbf{T}_{W,K_0}^{(L)}), \tag{3.73}$$

where the diagonal matrix at the right-hand side of the product in Equation 3.73 was obtained upon exploiting the specific properties of the training sequences [21] outlined in Section 3.3.2.2.2, implying that $\mathbf{Q}^{(i,i)}[n] = \sigma_i^2\mathbf{I}$ and $\mathbf{Q}^{(i,j)}[n] = \mathbf{0}$, $i \neq j$, as argued in the context of deriving Equation 3.65. From Equation 3.73 we infer that the sub-matrix $\mathbf{R}_c^{[f](i,i)} \in \mathbb{C}^{K \times K}$, located on the diagonal of the matrix $\mathbf{R}_c^{[f]}$, which is associated with the i-th user is given by:

$$\mathbf{R}_c^{[f](i,i)} = \mathbf{R}^{[f](i)}\mathbf{T}_{W,K_0}^{(i)}, \tag{3.74}$$

where we have also exploited that the i-th sub-matrix on the diagonal of $\mathbf{S}^*[n]\mathbf{S}^T[n]$ is given by $\sigma_i^2\mathbf{I}$.

3.3.2.3.2 Auto-Correlation Matrix of the Channel Transfer Factor Estimates in the Context of Optimum Training Sequences The AWGN-related contribution of the estimates' auto-correlation matrix $\mathbf{R}_a^{[f]}$ given by Equation 3.43 was elaborated on in Section 3.3.2.2, and the same derivation is also valid for the case of the non-sample-spaced CIR discussed here. Specifically, from Equations 3.52 and 3.65 we recall that:

$$\mathbf{R}_{a,\text{AWGN}}^{[f]} = \sigma_n^2 diag(\frac{1}{\sigma_1^2}\mathbf{T}_{W,K_0}^{(1)} \dots \frac{1}{\sigma_L^2}\mathbf{T}_{W,K_0}^{(L)}), \tag{3.75}$$

and hence, the i-th user's associated sub-matrix in the matrix of Equation 3.75 is given by:

$$\mathbf{R}_{a,\text{AWGN}}^{[f](i,i)} = \frac{\sigma_n^2}{\sigma_i^2}\mathbf{T}_{W,K_0}^{(i)}. \tag{3.76}$$

By contrast, the channel-related component $\mathbf{R}_{a,\text{Channel}}^{[f]}$ of $\mathbf{R}_a^{[f]}$ defined in Equation 3.46, requires some further elaborations. Specifically, from Equation 3.47 we infer that:

$$\mathbf{R}_{a,\text{Channel}}^{[f]} = \mathbf{W}_J\mathbf{P}[n]\mathbf{S}^T[n]\mathbf{R}^{[f]}\mathbf{S}^*[n]\mathbf{P}^H[n]\mathbf{W}_J^H, \tag{3.77}$$

which can be transformed into:

$$\begin{aligned}\mathbf{R}_{a,\text{Channel}}^{[f]} &= diag(\frac{1}{\sigma_1^2}\mathbf{T}_{W,K_0}^{(1)} \dots \frac{1}{\sigma_L^2}\mathbf{T}_{W,K_0}^{(L)}) \cdot \\ &\cdot \mathbf{S}^*[n]\mathbf{S}^T[n] \cdot diag(\mathbf{R}^{[f](1)} \dots \mathbf{R}^{[f](L)}) \cdot \mathbf{S}^*[n]\mathbf{S}^T[n] \cdot \\ &\cdot diag(\frac{1}{\sigma_1^2}\mathbf{T}_{W,K_0}^{(1)} \dots \frac{1}{\sigma_L^2}\mathbf{T}_{W,K_0}^{(L)}) \end{aligned} \tag{3.78}$$

by substituting $\mathbf{P}[n]$ of Equation 3.24, $\mathbf{A}[n]$ of Equation 3.14 and $\mathbf{R}^{[f]}$ of Equation 3.40 into Equation 3.77. Here we have exploited again the effects of the optimum training sequences on the specific structure of the matrix $\mathbf{Q}[n] = \mathbf{A}^H[n]\mathbf{A}[n]$, similarly to the procedure employed in the context of deriving Equation 3.73. From Equation 3.78 we infer that the sub-matrix $\mathbf{R}_{a,\text{Channel}}^{[f](i,i)} \in \mathbb{C}^{K\times K}$, located on the diagonal of matrix $\mathbf{R}_a^{[f]}$, which is associated with the i-th user is given by:

$$\mathbf{R}_{a,\text{Channel}}^{[f](i,i)} = \frac{1}{\sigma_i^4}\mathbf{T}_{W,K_0}^{(i)} \left(\sum_{j=1}^{L} \mathbf{S}^{(i)*}\mathbf{S}^{(j)}\mathbf{R}^{[f](j)}\mathbf{S}^{(j)*}\mathbf{S}^{(i)} \right) \mathbf{T}_{W,K_0}^{(i)}. \tag{3.79}$$

In order to proceed further let us again recall the decomposition of the i-th user's channel's spaced-frequency correlation matrix $\mathbf{R}^{[f](i)}$ with respect to the DFT matrix $\mathbf{W}$, which was formulated in Equation 3.49. Recall furthermore the decomposition of $\mathbf{T}_{W,K_0}^{(i)}$ from Equation 3.68. Then Equation 3.79 can be reformulated as:

$$\mathbf{R}_{a,\text{Channel}}^{[f](i,i)} = \frac{1}{\sigma_i^4}\mathbf{W}\mathbf{I}_{K_0}^{(i)} \left(\sum_{j=1}^{L} \acute{\mathbf{Q}}^{(i,j)}[n]\Lambda_W^{[f](j)}\acute{\mathbf{Q}}^{(i,j)H}[n] \right) \mathbf{I}_{K_0}^{(i)}\mathbf{W}^H, \tag{3.80}$$

where $\acute{\mathbf{Q}}^{(i,j)}[n]$ was defined in Equation 3.59. Recall also that the specific structure of $\acute{\mathbf{Q}}^{(i,j)}[n]$ in the context of employing optimum training sequences was outlined in Section 3.3.2.3. While for $(i = j)$ we have $\acute{\mathbf{Q}}^{(i,j)}[n] = \sigma_i^2\mathbf{I}$, for $(i \neq j)$ we obtain $\acute{\mathbf{Q}}^{(i,j)}[n] = \sigma_i\sigma_j\mathbf{I}_{cyc}^{(i,j)}$, which was further detailed in Equation 3.64. Upon taking into account these specific properties in Equation 3.80, we obtain:

$$\mathbf{R}_{a,\text{Channel}}^{[f](i,i)} = \frac{1}{\sigma_i^2}\mathbf{W}\mathbf{I}_{K_0}^{(i)} \left(\sigma_i^2\Lambda_W^{[f](i)} + \sum_{\substack{j=1 \\ j\neq i}}^{L} \sigma_j^2\mathbf{I}_{cyc}^{(i,j)}\Lambda_W^{[f](j)}\mathbf{I}_{cyc}^{(i,j)T} \right) \mathbf{I}_{K_0}^{(i)}\mathbf{W}^H. \tag{3.81}$$

Note in Equation 3.81 that the matrix $\mathbf{I}_{cyc}^{(i,j)}$ performs a rotation of the matrix $\Lambda_W^{[f](i)}$ with respect to its rows, while its transpose, namely $\mathbf{I}_{cyc}^{(i,j)T}$, performs a rotation of the matrix $\Lambda_W^{[f](i)}$ with respect to its columns. The effect of the two rotations within the sum of Equation 3.81 is that different parts of the decomposition $\Lambda_W^{[f](i)}$ become visible to the 'masking window' defined by the matrix $\mathbf{I}_{K_0}^{(i)}$.

3.3.2.3.3 Channel Estimation MSE in the Context of Optimum Training Sequences Hence by following the philosophy of Equation 3.38 the i-th user's associated sub-matrix $\mathbf{R}_{\Delta\hat{\mathbf{H}}_{apt}[n]}^{(i,i)}$ of the

channel transfer factor estimation error correlation matrix $\mathbf{R}_{\Delta\tilde{\mathbf{H}}_{apt}[n]}$ is given by:

$$\mathbf{R}^{(i,i)}_{\Delta\tilde{\mathbf{H}}_{apt}[n]} = \mathbf{R}^{[f](i)} - 2\Re\mathrm{e}\{\mathbf{R}^{[f](i,i)}_{c}\} + \mathbf{R}^{[f](i,i)}_{a}, \tag{3.82}$$

where according to Equation 3.46 we have $\mathbf{R}^{[f](i,i)}_{a} = \mathbf{R}^{[f](i,i)}_{a,\text{Channel}} + \mathbf{R}^{[f](i,i)}_{a,\text{AWGN}}$ and $\mathbf{R}^{[f](i,i)}_{c}$, $\mathbf{R}^{[f](i,i)}_{a,\text{Channel}}$ and $\mathbf{R}^{[f](i,i)}_{a,\text{AWGN}}$ were given by Equations 3.74, 3.81 and 3.76. The *a posteriori* estimation MSE averaged over all subcarriers of the i-th user is then given by:

$$\begin{aligned}
\text{MSE}^{(i)}_{apt}[n] &= \frac{1}{K}\text{Trace}(\mathbf{R}^{(i,i)}_{\Delta\tilde{\mathbf{H}}_{apt}[n]}) &(3.83)\\
&= \sigma^2_H - \frac{1}{K}\text{Trace}(\Lambda^{[f](i)}_{W}\mathbf{I}^{(i)}_{K_0}) + \frac{K_0}{K}\frac{\sigma^2_n}{\sigma^2_i} + \\
&\quad + \sum_{\substack{j=1\\ j\neq i}}^{L}\frac{\sigma^2_j}{\sigma^2_i}\frac{1}{K}\text{Trace}(\mathbf{I}^{(i,j)}_{cyc}\Lambda^{[f](j)}_{W}\mathbf{I}^{(i,j)T}_{cyc}\mathbf{I}^{(i)}_{K_0}), &(3.84)
\end{aligned}$$

where we have exploited that $\text{Trace}(\mathbf{UAU}^H) = \text{Trace}(\mathbf{A})$ for a unitary matrix $\mathbf{U}$. Note that in Equation 3.84 the sum of the first three terms is identical to the MSE, which would be achieved in a single-user scenario in the context of a non-sample-spaced CIR. However, as a result of the multi-user interference experienced in the CIR-related domain, the MSE is further degraded in the multi-user scenario by the contribution constituted by the last term of Equation 3.84. Furthermore, we note again that the MSE of Equation 3.84 is only achieved upon employing optimum channel sounding or training sequences [22] of Section 3.3.2.2.2, while for random subcarrier symbol sequences the MSE is potentially further degraded.

3.3.3 *A Priori* Channel Transfer Function Estimation MSE Enhancement by Linear Prediction of the *A Posteriori* CIR-Related Tap Estimates

The vector of CIR-related tap estimates obtained with the aid of Equation 3.22 or 3.23 and its associated vector of channel transfer factor estimates given by Equation 3.8 are actually the *a posteriori* estimates generated for the current OFDM symbol after the detection of the transmitted subcarrier symbols. These estimates could for example be employed again following an iterative approach for obtaining potentially enhanced symbol decisions, since the channel transfer factor estimates employed during the initial symbol detection were imperfect. In the conventional decision-directed channel estimator, however, these *a posteriori* estimates are employed as *a priori* estimates for the demodulation of the next OFDM symbol, assuming that the channel's transfer function remained constant. However, as proposed by Li *et al.* [22], enhanced *a priori* channel transfer function estimates can be obtained for the next OFDM symbol period upon invoking linear prediction techniques, which could operate for example in the context of the estimator structures discussed here, on a time-direction tap-by-tap basis in the CIR-related domain. This was alluded to by the CIR-related tap prediction block shown at the top of Figure 3.2. Recall that linear CIR-related tap prediction

was also used in the context of single-user channel estimation techniques in Chapter 2.2.4. We will make extensive use of these techniques in the context of PIC-assisted DDCE discussed in Section 3.4. Note that Li's LS-assisted DDCE [21] allows for a purely transversal FIR filter-related implementation of the linear predictor operating along the time-direction. Thus, the optimum predictor coefficients can be determined with the aid of the Wiener equation. We note, however, that this approach is different from incorporating a channel transfer function predictor in the context of the PIC-assisted DDCE, a technique, which will be outlined in Section 3.3.4. The evaluation of the associated predictor coefficients is not as straightforward as for the LS-assisted DDCE and will be the topic of our discussions in Section 3.4.

3.3.4 Simplified Approach LS-Assisted DDCE

A disadvantage of the LS estimation approach discussed in Section 3.3.1 is the potentially significant computational complexity imposed by the calculation of the inverse of the correlation matrix $\mathbf{Q}[n]$, which is required for computing the different users' CIR-related tap estimates, as shown in Equation 3.22. As a potential means of reducing the complexity, it was suggested by Li [22] to perform a parallel cancellation of the users' CIR-related contributions. More explicitly, upon invoking Equation 3.22 and by exploiting its specific block structure, the j-th user's vector of CIR-related *a posteriori* tap estimates can be expressed as a function of the $(L-1)$ remaining users' vectors of CIR-related *a posteriori* tap estimates by 'removing' their effect with the aid of the Parallel Interference Cancellation (PIC) step constituted by the second bracketed term in:

$$\tilde{\mathbf{h}}^{(j)}_{apt,K_0}[n] = \mathbf{Q}^{(j,j)-1}[n] \left(\mathbf{p}^{(j)}[n] - \sum_{\substack{i=1 \\ i \neq j}}^{L} \mathbf{Q}^{(j,i)}[n] \hat{\mathbf{h}}^{(i)}_{apr,K_0}[n] \right), \tag{3.85}$$

where $\mathbf{p}^{(j)}[n] \in \mathbb{C}^{K_0 \times 1}$ is the j-th sub-vector of the vector $\mathbf{p}[n]$ of cross-correlations defined in Equation 3.19:

$$\mathbf{p}^{(j)}[n] = \mathbf{W}_j^{(j)H} \mathbf{S}^{(i)*}[n] \mathbf{x}[n], \tag{3.86}$$

and $\mathbf{Q}^{(j,i)}[n] \in \mathbb{C}^{LK_0 \times LK_0}$ is the sub-matrix associated with the j-th "row" and i-th "column" of the auto-correlation matrix $\mathbf{Q}[n]$ defined in Equation 3.20, which is expressed as:

$$\mathbf{Q}^{(j,i)}[n] = \mathbf{W}_j^{(j)H} \mathbf{S}^{(j)*}[n] \mathbf{S}^{(i)} \mathbf{W}_j^{(i)}. \tag{3.87}$$

In the simplest case tentative estimates of the $(L-1)$ remaining users' vectors of CIR-related taps - which are required for the cancellation process outlined in Equation 3.85 could be provided upon assuming that $\hat{\mathbf{h}}^{(j)}_{apr,K_0}[n] \approx \tilde{\mathbf{h}}^{(j)}_{apt,K_0}[n-1]$ for reasonably slowly varying channels [22]. A further improvement of the estimator's MSE can be achieved with the aid of an $N^{[t]}_{tap}$-tap prediction filter,

K_0	number of significant CIR-related taps
K	number of subcarriers
L	number of simultaneous users
P	number of receiver antennas

Table 3.2: Summary of the parameters influencing the LS-assisted DDCE's complexity.

which operates individually on each CIR-related tap in the time-direction. This solution will be the topic of Section 3.4, where the optimum predictor coefficients are determined.

Before concluding this section, we emphasize again, that the difference between the scheme alluded to here and that to be presented in Section 3.4 is essentially the employment of the parallel interference cancellation, which is once conducted in the CIR-related domain and then once again in the frequency-domain. However, it can be readily demonstrated that the scheme proposed in this section and that of Section 3.4 produce identical results.

3.3.5 Complexity Analysis of the Original- and Simplified LS-Assisted DDCE

In this section we will analyse the computational complexity imposed by the LS-assisted DDCE. The relevant system parameters are summarized in Table 3.2. More specifically in Section 3.3.5.1 we will characterize the complexity of the original approach of Section 3.3.1.2 capitalizing on the inversion of the correlation matrix $\mathbf{Q}[n]$, while in Section 3.3.5.2 the complexity of the simplified approach of Section 3.3.4 will be assessed.

3.3.5.1 Complexity of the Original LS-Assisted DDCE

The complexity of the original LS-assisted DDCE technique of [21], which was described in Section 3.3.1, is attributed to three different operations. The first operation is the calculation of the correlation matrix $\mathbf{Q}[n]$ defined in Equation 3.20, which will be considered in Section 3.3.5.1.1. This operation is independent of the specific antenna element considered. The second operation is that of evaluating $\mathbf{p}[n]$ of Equation 3.19, which has to be carried out separately for each of the P receiver antenna elements. The associated complexity will be quantified in Section 3.3.5.1.2. Finally, the system of LS-related equations has to be solved for the vector $\tilde{\mathbf{h}}_{apt}[n]$ of the different users' CIR-related *a posteriori* tap estimates according Equation 3.22, which is transferred to the frequency-domain with the aid of the FFT in order to obtain the channel transfer factor estimates. These steps will be further analysed in terms of their computational complexity in Section 3.3.5.1.3. Based on the analysis of the individual components a formula will then be presented in Section 3.3.5.1.4 for the LS-assisted DDCE's total complexity.

3.3.5.1.1 Complexity Associated with Assembling Matrix $\mathbf{Q}[n]$ More specifically, for the calculation of the sub-matrix $\mathbf{Q}^{(i,j)}[n]$ of the correlation matrix $\mathbf{Q}[n]$ we have relied on the mathematical discourse of [21][8] and found that the normalized number of complex multiplications and additions is given by:

$$C^{(\mathbb{C}*\mathbb{C})}_{\mathbf{Q}^{(i,j)}[n]}|_{\text{norm}} = \frac{1}{LP}(\frac{1}{2}\log_2 K + 1) \quad (3.88)$$

$$C^{(\mathbb{C}+\mathbb{C})}_{\mathbf{Q}^{(ij)}[n]}|_{\text{norm}} = \frac{1}{LP}\log_2 K, \quad (3.89)$$

where the number of operations was normalized to the K number of subcarriers, L number of users and P number of receiver antenna elements. Note that the additive unity contribution enclosed in brackets seen in the expression of the $C^{(\mathbb{C}*\mathbb{C})}_{\mathbf{Q}^{(i,j)}[n]}|_{\text{norm}}$ number of complex multiplications in Equation 3.88 is due to calculating the correlation between the i-th and the j-th user's transmitted symbols on a subcarrier basis, which is explicitly visible for example in the representation of the correlation matrix $\mathbf{Q}^{(i,j)}[n]$ given by Equation 3.87. The entire correlation matrix $\mathbf{Q}[n]$ consists of L^2 sub-matrices and correspondingly the total computational complexity imposed is increased by the same factor of L^2 compared to the complexity of calculating a single sub-matrix. A reduction of this factor of L^2 can be achieved by exploiting the Hermitian structure of the correlation matrix $\mathbf{Q}[n]$, which implies that $\mathbf{Q}^{(i,j)}[n] = \mathbf{Q}^{(j,i)H}[n]$. Hence, the number of off-diagonal sub-matrices to be evaluated is $\binom{L}{2} = \frac{1}{2}L(L-1)$. Furthermore in the context of MPSK modulation schemes the sub-matrices $\mathbf{Q}^{(i,i)}[n]$, $i = 1, \ldots, L$ along the main diagonal of the matrix $\mathbf{Q}[n]$ are weighted unity matrices and therefore no additional complexity is imposed by their computation. Upon incorporating the factor of $\binom{L}{2}$ into Equations 3.88 and 3.89, the total normalized complexity associated with assembling $\mathbf{Q}[n]$ becomes:

$$C^{(\mathbb{C}*\mathbb{C})}_{\mathbf{Q}[n]}|_{\text{norm}} = \frac{1}{2P}(L-1)(\frac{1}{2}\log_2 K + 1) \quad (3.90)$$

$$C^{(\mathbb{C}+\mathbb{C})}_{\mathbf{Q}[n]}|_{\text{norm}} = \frac{1}{2P}(L-1)\log_2 K. \quad (3.91)$$

3.3.5.1.2 Complexity Associated with Assembling Vector $\mathbf{p}[n]$ The computational complexity imposed by evaluating $\mathbf{p}_p[n]$ of Equation 3.19 for $p = 1, \ldots, P$, follows similar considerations, which results in a normalized number of complex multiplications and additions as given by:

$$C^{(\mathbb{C}*\mathbb{C})}_{\mathbf{p}[n]}|_{\text{norm}} = \frac{1}{2}\log_2 K + 1 \quad (3.92)$$

$$C^{(\mathbb{C}+\mathbb{C})}_{\mathbf{p}[n]}|_{\text{norm}} = \log_2 K. \quad (3.93)$$

Here we have taken into account that $\mathbf{p}[n]$ has to be calculated separately for each antenna element. Again, the unity contribution observed in the expression of the $C^{(\mathbb{C}*\mathbb{C})}_{\mathbf{p}[n]}|_{\text{norm}}$ number of complex

[8]Note however that in terms of the scheme's actual implementation it is not advisable to directly employ the representation suggested by Equations 3.19 and 3.20. It is more efficient to implement the associated multiplication involving the DFT matrix $\mathbf{W}$, with the aid of an FFT, which requires $\frac{K}{2}\log_2 K$ number of complex multiplications and twice the number of complex additions.

multiplications is required, because evaluating $\mathbf{p}[n]$ involves calculating the correlation between the received signal and the transmitted symbols, which are assumed to have been correctly detected, on a subcarrier basis, as observed with the i-th user's block-matrix of $\mathbf{p}[n]$, shown in Equation 3.86.

3.3.5.1.3 Complexity Associated with Solving the LS System Equations for the Vector of CIR-Related Tap Estimates $\tilde{\mathbf{h}}_{apt,K_0}[n]$ Once the auto-correlation matrix $\mathbf{Q}[n]$ of Equation 3.20 and the different reception antennas' associated cross-correlation vectors $\mathbf{p}_p[n]$, $p = 1, \ldots, P$ are available, the vector $\tilde{\mathbf{h}}_{apt,K_0,p}[n]$ can be evaluated for each reception antenna separately upon solving Equation 3.22. However, the associated processing can be significantly accelerated by noting that only the right-hand side of Equation 3.22 is changed for the different reception antenna elements. Specifically, we can employ a decomposition-based solution of Equation 3.22 with respect to the matrix $\mathbf{Q}[n]$, such as the LU decomposition [87], for example, or the QR decomposition as described in Section 3.3.1.2.4. This decomposition has to be performed only once, requiring approximately $\frac{1}{3}(LK_0)^3$ complex multiplications and the same number of additions [86]. Then the solution of Equation 3.22 can be carried out by forward- and backward substitutions as outlined in [87]. These operations impose a computational complexity of approximately $(LK_0)^2$ complex multiplications and additions per reception antenna element. Hence, we have a total normalized complexity of:

$$C^{(\mathbb{C}*\mathbb{C})}_{\tilde{\mathbf{h}}_{apt,K_0}[n]}|_{\text{norm}} = C^{(\mathbb{C}+\mathbb{C})}_{\tilde{\mathbf{h}}_{apt,K_0}[n]}|_{\text{norm}} = \frac{(LK_0)^2}{KL}\left[\frac{1}{3}(LK_0)+1\right]. \tag{3.94}$$

3.3.5.1.4 Total Complexity Finally, we have to account for the complexity imposed by transforming the different receiver antennas' and users' CIR-related tap estimates to the frequency-domain with the aid of the DFT matrix $\mathbf{W}$. This operation can also be implemented with the computationally more efficient FFT. It can be shown that the corresponding normalized number of complex multiplications and additions is given by:

$$C^{(\mathbb{C}*\mathbb{C})}_{\tilde{\mathbf{h}}_{apt,K_0}[n]->\tilde{\mathbf{H}}_{apt}[n]}|_{\text{norm}} = \frac{1}{2}\log_2 K \tag{3.95}$$

$$C^{(\mathbb{C}+\mathbb{C})}_{\tilde{\mathbf{h}}_{apt,K_0}[n]->\tilde{\mathbf{H}}_{apt}[n]}|_{\text{norm}} = \log_2 K. \tag{3.96}$$

Hence, the total normalized number of complex multiplications and additions is given by:

$$\begin{aligned} C^{()}_{\text{MU-CE,LS}}|_{\text{norm}} &= C^{()}_{\mathbf{Q}[n]}|_{\text{norm}} + C^{()}_{\mathbf{p}[n]}|_{\text{norm}} + \\ &\quad + C^{()}_{\tilde{\mathbf{h}}_{apt,K_0}[n]}|_{\text{norm}} + C^{()}_{\tilde{\mathbf{h}}_{apt,K_0}[n]->\tilde{\mathbf{H}}_{apt}[n]}|_{\text{norm}}. \end{aligned} \tag{3.97}$$

Specifically, upon assuming that $L = P$, we obtain:

$$C^{(\mathbb{C}*\mathbb{C})}_{\text{MU-CE,LS}}|_{\text{norm}} = \frac{1}{4}\left(5-\frac{1}{L}\right)\log_2 K + \frac{1}{2}\left(3-\frac{1}{L}\right) + \frac{K_0^2}{K}\left[\frac{1}{3}(LK_0)+1\right] \tag{3.98}$$

$$C^{(\mathbb{C}+\mathbb{C})}_{\text{MU-CE,LS}}|_{\text{norm}} = \frac{1}{2}\left(5-\frac{1}{L}\right)\log_2 K + \frac{K_0^2}{K}\left[\frac{1}{3}(LK_0)+1\right], \tag{3.99}$$

	$K_0 = 8/K = 64$	$K_0 = 8/K = 512$	$K_0 = 64/K = 512$
$C^{(\mathbb{C}*\mathbb{C})}_{\text{MU-CE,LS}}\|_{\text{norm}}$	$8.50 + 11.66\dot{6}$	$12.06 + 1.46\dot{6}$	$12.06 + 690.66\dot{6}$
$C^{(\mathbb{C}+\mathbb{C})}_{\text{MU-CE,LS}}\|_{\text{norm}}$	$14.25 + 11.66\dot{6}$	$21.38 + 1.46\dot{6}$	$21.38 + 690.66\dot{6}$

Table 3.3: Computational complexity of the LS-assisted DDCE [21] in terms of the number of complex multiplications and additions normalized to the K number of subcarriers, L number of users and P number of receiver antennas. Here we have assumed that $L = P = 4$.

where a normalization to $KLP = KL^2$ has been performed. Observe that upon increasing the number of simultaneous users L, the normalized complexity increases linearly. We have evaluated the normalized complexity for a number of configurations and the corresponding results are listed in Table 3.3. Note that the second additive term associated with the complexity entries of Table 3.3 is related to the last additive term in Equations 3.98 and 3.99, which originates from the solution of Equation 3.22 for the vectors $\tilde{\mathbf{h}}_{apt,K_0,p}[n]$, $p = 1,\ldots,P$ of CIR-related taps using the LU decomposition. Observe for example, that for $K_0 = 64$ CIR-related taps the contribution due to the matrix inversion is excessive.

3.3.5.2 Complexity of the Simplified LS-Assisted DDCE

For the sake of comparison, in this section let us consider the normalized computational complexity associated with the simplified DDCE approach of Section 3.3.4. Recall from Section 3.3.4 that the difference with respect to the original DDCE approach of Section 3.3.1.2 resides in performing the parallel cancellation of the interfering users' CIR-related tap contributions according to Equation 3.85 instead of carrying out matrix multiplication with the inverse of the correlation matrix $\mathbf{Q}[n]$ of Equation 3.20 as suggested by Equation 3.22. It can be readily shown that the normalized computational complexity of the PIC operations of Equation 3.85 for $p = 1,\ldots,P$ is given by:

$$C^{(\mathbb{C}*\mathbb{C})}_{\tilde{\mathbf{h}}_{apt,K_0,\text{PIC}}[n]}|_{\text{norm}} = C^{(\mathbb{C}+\mathbb{C})}_{\tilde{\mathbf{h}}_{apt,K_0,\text{PIC}}[n]}|_{\text{norm}} = \frac{1}{K}(L-1)K_0^2. \tag{3.100}$$

Hence, following the philosophy of Equation 3.97, the total normalized complexity becomes:

$$\begin{aligned} C^{()}_{\text{MU-CE,PIC-LS}}|_{\text{norm}} &= C^{()}_{\mathbf{Q}[n]}|_{\text{norm}} + C^{()}_{\mathbf{p}[n]}|_{\text{norm}} + \\ &\quad + C^{()}_{\tilde{\mathbf{h}}_{apt,K_0,\text{PIC}}[n]}|_{\text{norm}} + C^{()}_{\tilde{\mathbf{h}}_{apt,K_0}[n]->\tilde{\mathbf{H}}_{apt}[n]}|_{\text{norm}}. \end{aligned} \tag{3.101}$$

With the aid of Equation 3.101 in the specific scenario of $L = P$ we arrive at the following expressions:

$$C^{(\mathbb{C}*\mathbb{C})}_{\text{MU-CE,PIC-LS}}|_{\text{norm}} = \frac{1}{4}\left(5 - \frac{1}{L}\right)\log_2 K + \frac{1}{2}\left(3 - \frac{1}{L}\right) + \frac{1}{K}(L-1)K_0^2 \tag{3.102}$$

$$C^{(\mathbb{C}+\mathbb{C})}_{\text{MU-CE,PIC-LS}}|_{\text{norm}} = \frac{1}{2}\left(5 - \frac{1}{L}\right)\log_2 K + \frac{1}{K}(L-1)K_0^2, \tag{3.103}$$

	$K_0 = 8/K = 64$	$K_0 = 8/K = 512$	$K_0 = 64/K = 512$
$C^{(\mathbb{C}*\mathbb{C})}_{\text{MU-CE,PIC-LS}}\|_{\text{norm}}$	$8.50 + 3.0$	$12.06 + 0.38$	$12.06 + 24.0$
$C^{(\mathbb{C}+\mathbb{C})}_{\text{MU-CE,PIC-LS}}\|_{\text{norm}}$	$14.25 + 3.0$	$21.38 + 0.38$	$21.38 + 24.0$

Table 3.4: Computational complexity of the simplified LS-assisted DDCE [22] in terms of the number of complex multiplications and additions normalized to the K number of subcarriers, L number of users and P number of receiver antennas. Here we have assumed that $L = P = 4$.

where again a normalization to $KLP = KL^2$ has been performed. Note in Equations 3.102 and 3.103 that the complexity is a function of the second power of the number of significant CIR-related taps K_0. This has to be contrasted to the cubical dependency observed in Equations 3.98 and 3.99 in the context of the original approach, as it was discussed in Section 3.3.5.1. In Table 3.4 we have exemplified the complexity of the simplified LS-assisted DDCE, again, for the specific parameters of $L = P = 4$. We observe a significant complexity reduction compared to that of the original estimator, which was characterized for the same parameters in Table 3.3.

3.3.6 Conclusions on the Original- and Simplified LS-Assisted DDCE

As an introduction to the topic of channel transfer factor estimation for multi-user OFDM systems in Section 3.3 we have portrayed Li's sub-space based estimation approach [21]. The corresponding equations, specifically that of the vector of optimum CIR-related tap estimates of Equation 3.22 were derived in Section 3.3.1 using a more compact matrix notation rather than the original notation of Li *et al.* [21]. The matrix notation had the advantage that the standard form of this solution, namely that of minimizing the squared estimation error as formulated in Equation 3.17 became visible. We also highlighted in Equation 3.27 that a necessary condition for the identification of the L different users' CIR-related taps - where each user has a total of K_0 significant taps - is that $L \leq \frac{K}{K_0}$, which is an additional motivation for identifying alternative channel transfer function estimation approaches. In an effort to further characterize the estimation approach proposed by Li *et al.* [21], its associated channel transfer factor estimation MSE was derived in Section 3.3.2, in the context of both sample-spaced and non-sample-spaced CIRs. Our discussions commenced by deriving the channel transfer factor estimation errors' auto-correlation matrix in Section 3.3.2.1. It was evident that the estimation errors' correlation matrix of Equation 3.38 and hence also the estimation MSE are dependent on the transmitted subcarrier symbol sequences. Li demonstrated in [21] that the LS-DDCE's MSE is minimized, if the sub-matrices on the "side-diagonals" of the correlation matrix $\mathbf{Q}[n]$ of Equation 3.22 are zero-matrices and thus no interference occurs between the different users' CIR-related tap estimation processes. For this to be the case, the constraints proposed by Li in [22] have to be imposed on the subcarrier symbol sequences transmitted by the different antennas of the different users, which is only applicable during the transmission of the

training OFDM symbols. However, in order to simplify our analysis, in Section 3.3.2 we have exploited the specific properties of the training sequences. Hence, Equations 3.70 and 3.84 derived in Sections 3.3.2.2 and 3.3.2.3 for describing the LS-DDCE's MSE in the context of both sample-spaced- and non-sample-spaced CIRs, respectively, represent the lowest possible estimation MSE achieved in the presence of random subcarrier symbol sequences. Furthermore, in Section 3.3.3 the strategy of an estimation MSE enhancement by transversal linear prediction was alluded to, while in Section 3.3.4 a simplified approach to DDCE based on parallel interference cancellation in the CIR-related domain, as suggested by Li [22] was outlined, which will be the basis of our further detailed discussions of PIC-assisted DDCE in Section 3.4. In this context it was also argued that as a result of the linear signal processing operations applied prior to extracting the most significant CIR-related taps, the PIC can be conducted both in the CIR-related domain upon invoking the correlation matrix $\mathbf{Q}[n]$ as shown in Equation 3.85, or in the frequency-domain by direct subtraction of the subcarriers' channel transfer factors after weighting them by the transmitted symbols, as it will be demonstrated in Section 3.4. Our complexity analysis conducted in Section 3.3.5 revealed that in the context of the original DDCE approach of Section 3.3.1 the computational complexity imposed by solving Equation 3.22 for generating the different reception antennas' associated vectors of CIR-related tap estimates is potentially excessive due to its cubical dependence on the product of the number of users L and the number of significant CIR-related taps K_0. This is a further motivation for identifying alternative ways of performing the estimation of the different channels' transfer functions.

3.4 Frequency-Domain Parallel Interference Cancellation Assisted Decision-Directed Channel Estimation

In this section a PIC-assisted DDCE scheme will be introduced and characterized. Specifically, its analytical description is provided in Section 3.4.1, while in Section 3.4.2 its performance is assessed in terms of the achievable *a priori* channel estimation[9] MSE as well as the system's BER in the context of both sample-spaced- and non-sample-spaced channel scenarios. The computational complexity of the PIC-assisted DDCE will be analysed in Section 3.4.3. Finally conclusions will be offered in Section 3.4.4. Let us commence our discussions in the next section by considering the recursive estimator's structure.

3.4.1 The Recursive Channel Estimator

The specific structure of Section 3.4.1 is as follows. Our portrayal of the frequency-domain PIC-assisted DDCE commences in Section 3.4.1.1, where we provide expressions both for the *a posteriori* channel transfer factor estimates arrived at after the parallel interference cancellation as well

[9]Unless otherwise stated the channel transfer function estimator is simply referred to as the channel estimator.

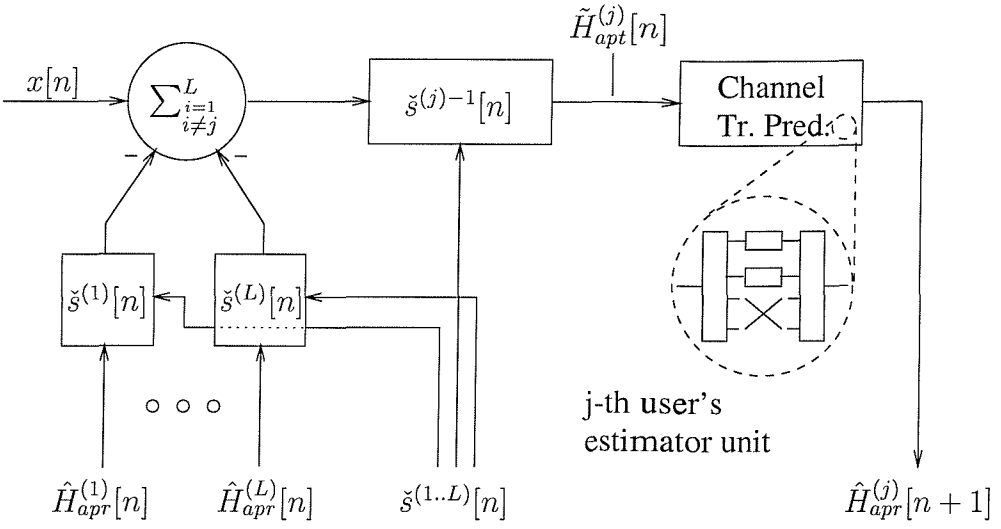

Figure 3.3: Illustration of the PIC-assisted channel transfer function estimation- or prediction block, associated with the j-th user and any of the P receiver antenna elements. The PIC process is described by Equation 3.106. The structure of the channel transfer function predictor follows that described in Section 2.2 for the single-user scenario.

as for the *a priori* channel transfer factor estimates upon taking into account the effects of the CIR-related tap prediction filter. The specific structure of the predictor arrangement is detailed in Section 3.4.1.2. Furthermore, in Section 3.4.1.3 we derived an expression for the average *a priori* channel estimation MSE, while in Section 3.4.1.4 an expression of the average *a posteriori* channel estimation MSE for the current OFDM symbol as a function of the corresponding estimation MSEs associated with the previous $N^{[t]}_{tap}$ number of OFDM symbols. After an analysis of the estimator's stability conditions in Section 3.4.1.5, the expression derived for the *a priori* estimation MSE is then employed in Section 3.4.1.6 - under the assumption that the system is in its steady-state condition - for generating the different users' vectors of optimum predictor coefficients, again, as a function of the predictor coefficient-dependent *a priori* estimation MSEs. Since the recursive structure of the channel transfer function estimator does not allow for an algebraic solution to be generated for the desired predictor coefficients, an iterative approach is applied, which exploits the contractive properties of the system equations. This approach was proposed earlier by Rashid-Farrokhi *et al.* [111] in the context of simultaneously optimizing the transmit power allocation and basestation antenna array weights in wireless networks. Since normally the exact knowledge of the channel's statistics in the form of the spaced-time spaced-frequency correlation function is not available, in Section 3.4.1.7 we discuss potential strategies for providing estimates of the statistics required.

3.4.1.1 *A Priori* and *A Posteriori* Channel Estimates

Recall from Equation 3.1 that the complex output signal $x_p[n,k]$ of the p-th receiver antenna element in the k-th subcarrier of the n-th OFDM symbol is given by:

$$x_p[n,k] = \sum_{i=1}^{L} H_p^{(i)}[n,k]s^{(i)}[n,k] + n_p[n,k], \tag{3.104}$$

where the different variables have been defined in Section 3.2. Upon invoking vector notation, Equation 3.104 can be rewritten as:

$$\mathbf{x}_p[n] = \sum_{i=1}^{L} \mathbf{S}^{(i)}[n]\mathbf{H}_p^{(i)}[n] + \mathbf{n}_p[n], \tag{3.105}$$

where $\mathbf{x}_p[n] \in \mathbb{C}^{K\times 1}$, $\mathbf{H}_p^{(i)}[n] \in \mathbb{C}^{K\times 1}$ and $\mathbf{n}_p[n] \in \mathbb{C}^{K\times 1}$ are column vectors hosting the subcarrier-related variables $x_p[n,k]$, $H_p^{(i)}[n,k]$ and $n_p[n,k]$, respectively, and $\mathbf{S}^{(i)}[n] \in \mathbb{C}^{K\times K}$ is a diagonal matrix having elements given by $s^{(i)}[n,k]$, where $k = 0,\ldots,K-1$. An *a posteriori* (**apt**) estimate $\tilde{\mathbf{H}}_{apt}^{(j)}[n] \in \mathbb{C}^{K\times 1}$ of the vector $\mathbf{H}^{(j)}[n]$ of 'true' channel transfer factors between the j-th user's single transmit antenna and the p-th receiver antenna can be obtained by subtracting all the $(L-1)$ vectors of interfering users' estimated signal contributions from the vector $\mathbf{x}_p[n]$ of composite received signals of the L users, followed by normalization with the j-th user's diagonal matrix of detected complex symbols $\check{\mathbf{S}}^{(j)}[n]$, yielding:

$$\tilde{\mathbf{H}}_{apt}^{(j)}[n] = \check{\mathbf{S}}^{(j)-1}[n]\left(\mathbf{x}[n] - \sum_{\substack{i=1\\ i\neq j}}^{L} \check{\mathbf{S}}^{(i)}[n]\hat{\mathbf{H}}_{apr}^{(i)}[n]\right), \tag{3.106}$$

where for simplicity's sake we have omitted the receiver antenna's index p. The PIC process based on Equation 3.106, has been further illustrated in Figure 3.3. In Equation 3.106, $\hat{\mathbf{H}}_{apr}^{(i)}[n] \in \mathbb{C}^{K\times 1}$ denotes the i-th user's vector of complex *a priori* (**apr**) channel transfer factor estimates predicted during the $(n-1)$-th OFDM symbol period for the n-th OFDM symbol, as a function of the vectors of *a posteriori* channel transfer factor estimates $\tilde{\mathbf{H}}_{apt}^{(i)}[n-\acute{n}]$ associated with the previous $N_{tap}^{[t]}$ number of OFDM symbols, which is formulated as:

$$\hat{\mathbf{H}}_{apr}^{(i)}[n] = f\left(\tilde{\mathbf{H}}_{apt}^{(i)}[n-1],\ldots,\tilde{\mathbf{H}}_{apt}^{(i)}[n-N_{tap}^{[t]}]\right). \tag{3.107}$$

We will further elaborate on the specific structure of the predictor in the next section.

3.4.1.2 *A Priori* Channel Prediction Filtering

The channel transfer function prediction along the time-direction follows the philosophy of the 2D-MMSE channel transfer function estimation approach proposed by Li *et al.* [17], which in turn is based on the rank-reduction assisted 1D-MMSE channel estimation scheme proposed by Edfors and

Sandell *et al.* [13, 15]. These schemes were described in Section 2.2 in the context of single-user OFDM systems. Specifically recall Figure 2.3, which illustrated the process of 2D-MMSE based channel estimation- or prediction.

- **In a first step**, in order to obtain the i-th user's vector of *a priori* channel transfer factor estimates for the n-th OFDM symbol period during the $(n-1)$-th OFDM symbol period, which is denoted by $\hat{\mathbf{H}}_{apr}^{(i)}[n]$, the vector of *a posteriori* channel transfer factor estimates $\tilde{\mathbf{H}}_{apt}^{(i)}[n-1]$ is subjected to a unitary linear inverse transform $\tilde{\mathbf{U}}^{[f](i)H} \in \mathbb{C}^{K\times K}$, yielding the vector $\tilde{\mathbf{h}}_{apt}^{(i)}[n-1] \in \mathbb{C}^{K\times 1}$ of CIR-related *a posteriori* tap values:

$$\tilde{\mathbf{h}}_{apt}^{(i)}[n-1] = \tilde{\mathbf{U}}^{[f](i)H}\tilde{\mathbf{H}}_{apt}^{(i)}[n-1]. \tag{3.108}$$

  From a statistical point of view the optimum unitary transform to be employed is the Karhunen-Loeve Transform (KLT) [16, 15] with respect to the Hermitian spaced-frequency correlation matrix of *a posteriori* channel transfer factor estimates, which is given by $\mathbf{R}_{apt}^{[f](i)} = E\{\tilde{\mathbf{H}}_{apt}^{(i)}\tilde{\mathbf{H}}_{apt}^{(i)H}\}$, when assuming the wide-sense stationarity of $\tilde{\mathbf{H}}_{apt}^{(i)}[n]$. The matrix $\mathbf{R}_{apt}^{[f](i)} \in \mathbb{C}^{K\times K}$ can be decomposed as $\mathbf{R}_{apt}^{[f](i)} = \mathbf{U}_{apt}^{[f](i)}\Lambda_{apt}^{[f](i)}\mathbf{U}_{apt}^{[f](i)H}$, where $\mathbf{U}_{apt}^{[f](i)} \in \mathbb{C}^{K\times K}$ is the unitary KLT matrix of *eigenvectors*, and $\Lambda_{apt}^{[f](i)} \in \mathbb{R}^{K\times K}$ exhibits the diagonal form of $\Lambda_{apt}^{[f](i)} = diag(\lambda_{apt,0}^{[f](i)}, \ldots, \lambda_{apt,K-1}^{[f](i)})$. The diagonal elements of $\Lambda_{apt}^{[f](i)}$ are referred to as the *eigenvalues* of $\mathbf{R}_{apt}^{[f](i)}$ [87]. Similarly, the desired channel's 'true' spaced-frequency correlation matrix $\mathbf{R}^{[f](i)} = E\{\mathbf{H}^{[i]}\mathbf{H}^{[i]H}\}$ can be decomposed as $\mathbf{R}^{[f](i)} = \mathbf{U}^{[f](i)}\Lambda^{[f](i)}\mathbf{U}^{[f](i)H}$. At this stage we note that the error components contaminating the vector $\tilde{\mathbf{H}}_{apt}^{(i)}[n-1]$ estimating the vector $\mathbf{H}^{(i)}[n-1]$ of "true" channel transfer factors are uncorrelated due to the statistical independence of the AWGN and that of the modulated symbols transmitted in the different subcarriers. Hence both $\mathbf{R}_{apt}^{[f](i)}$ and $\mathbf{R}^{[f](i)}$ share the same eigenvectors [16], which implies that we have $\mathbf{U}_{apt}^{[f](i)} = \mathbf{U}^{[f](i)}$. In reality however, the explicit knowledge of the channel's spaced-frequency correlation matrix $\mathbf{R}^{[f](i)}$ and that of its unitary KLT matrix $\mathbf{U}^{[f](i)}$ is typically unavailable. Instead, an estimate $\tilde{\mathbf{R}}^{[f](i)}$ and its associated unitary KLT matrix $\tilde{\mathbf{U}}^{[f](i)}$ has to be employed, which - in contrast to the optimum KLT matrix $\mathbf{U}^{[f](i)}$ - results in an imperfect decorrelation of the *a posteriori* channel transfer factor estimates.

- **In a second step** linear $N_{tap}^{[t]}$-tap filtering is performed in the time-direction separately for those K_0 number of CIR-related components of $\tilde{\mathbf{h}}_{apt}^{(i)}$, for which the variance is significant. This is achieved by capitalizing on the current vector $\tilde{\mathbf{h}}_{apt}^{(i)}[n-1]$ and the vectors $\tilde{\mathbf{h}}_{apt}^{(i)}[n-\acute{n}]$, $\acute{n} = 2, \ldots, N_{tap}^{[t]}$ of the previous $(N_{tap}^{[t]}-1)$ number of OFDM symbols. As a result, in the case of *estimation filtering* [17] an improved estimate $\hat{\mathbf{h}}_{apt}^{(i)}[n-1]$ of $\mathbf{h}^{(i)}[n-1]$ is obtained, although this technique was not employed here. By contrast, in case of the *prediction filtering* employed here, an *a priori* estimate $\hat{\mathbf{h}}_{apr}^{(i)}[n] \in \mathbb{C}^{K\times 1}$ of $\mathbf{h}^{(i)}[n]$ is obtained. In mathematical

terms this can be formulated as:

$$\hat{\mathbf{h}}_{apr}^{(i)}[n] = \mathbf{I}_{K_0}^{(i)} \sum_{\acute{n}=1}^{N_{tap}^{[t]}} \tilde{c}_{pre}^{(i)}[\acute{n}-1]\tilde{\mathbf{h}}_{apt}^{(i)}[n-\acute{n}], \tag{3.109}$$

where $\mathbf{I}_{K_0}^{(i)} \in \mathbb{C}^{K\times K}$ denotes a sparse unity matrix having unity entries only at those K_0 number of diagonal positions, for which the variance of the associated components of $\tilde{\mathbf{h}}_{apt}^{(i)}$ is significant. Furthermore, in Equation 3.109 the variable $\tilde{c}_{pre}^{(i)}[\acute{n}-1] \in \mathbb{C}$ denotes the $(\acute{n}-1)$-th CIR-related tap prediction filter coefficient. Note that for simplicity here we employ the same coefficient $\tilde{c}_{pre}^{(i)}[\acute{n}-1]$ for filtering each of the different K_0 number of taps of the specific $\acute{n}$-th CIR-related vector $\tilde{\mathbf{h}}_{apt}^{(i)}[n-\acute{n}]$, which follows the concepts of robust channel estimation advocated by Li *et al.* [17]. These concepts were outlined in Section 2.2.3.1.

- **In a last step** the vector of CIR-related *a priori* tap estimates $\hat{\mathbf{h}}_{apr}^{(i)}[n]$ is transformed back to the OFDM frequency-domain with the aid of the unitary KLT matrix $\tilde{\mathbf{U}}^{[f](i)}$, yielding the vector of *a priori* channel transfer factor estimates $\hat{\mathbf{H}}_{apr}^{(i)}[n]$ for the n-th OFDM symbol period:

$$\hat{\mathbf{H}}_{apr}^{(i)}[n] = \tilde{\mathbf{U}}^{[f](i)}\hat{\mathbf{h}}_{apr}^{(i)}[n]. \tag{3.110}$$

This vector of *a priori* channel transfer factor estimates is in turn employed in the detection stage during the n-th OFDM symbol period. Upon substituting Equation 3.108 into Equation 3.109 and by substituting the result into Equation 3.110 we obtain the following relation between the vector of *a priori* channel transfer factor estimates derived for the n-th OFDM symbol and the vectors of *a posteriori* channel transfer factor estimates of the past $N_{tap}^{[t]}$ number of OFDM symbols:

$$\hat{\mathbf{H}}_{apr}^{(i)}[n] = \mathbf{T}_{K_0}^{(i)} \sum_{\acute{n}=1}^{N_{tap}^{[t]}} \tilde{c}_{pre}^{(i)}[\acute{n}-1]\tilde{\mathbf{H}}_{apt}^{(i)}[n-\acute{n}], \tag{3.111}$$

where $\mathbf{T}_{K_0,p}^{(i)} \in \mathbb{C}^{K\times K}$ is given by:

$$\mathbf{T}_{K_0}^{(i)} = \tilde{\mathbf{U}}^{[f](i)}\mathbf{I}_{K_0}^{(i)}\tilde{\mathbf{U}}^{[f](i)H}. \tag{3.112}$$

After having described the process of generating the vectors of *a posteriori* and *a priori* channel transfer factor estimates in Sections 3.4.1.1 and 3.4.1.2, we will embark in Section 3.4.1.3 on an evaluation of the associated *a priori* estimation MSE.

3.4.1.3 *A Priori* Channel Estimation MSE

Let us commence our discussions in this section by developing an expression for the vector of *a priori* channel transfer factor estimation errors associated with the j-th user during the n-th

OFDM symbol period as a function of the vectors of *a priori* channel transfer factor estimation errors of the $(L-1)$ remaining users during the $N_{tap}^{[t]}$ number of previous OFDM symbol periods. Assuming error-free symbol decisions we have $\check{\mathbf{S}}^{(j)}[n-\acute{n}] = \mathbf{S}^{(j)}[n-\acute{n}]$, $j = 1,\ldots,L$, $\acute{n} = 1,\ldots,N_{tap}^{[t]}$. Upon substituting Equation 3.105 into Equation 3.106 and then substituting the result into Equation 3.111, yields an expression for the vector of channel transfer factor estimation errors $\Delta\hat{\mathbf{H}}_{apr}^{(j)}[n] \in \mathbb{C}^{K\times 1}$ in the following form:

$$\begin{aligned}\Delta\hat{\mathbf{H}}_{apr}^{(j)}[n] &= -\mathbf{T}_{K_0}^{(j)}\sum_{\acute{n}=1}^{N_{tap}^{[t]}}\tilde{c}_{pre}^{(j)}[\acute{n}-1]\mathbf{S}^{(j)-1}[n-\acute{n}]\sum_{\substack{i=1\\ i\neq j}}^{L}\mathbf{S}^{(i)}[n-\acute{n}]\Delta\hat{\mathbf{H}}_{apr}^{(i)}[n-\acute{n}] - \\ &\quad - \mathbf{T}_{K_0}^{(j)}\sum_{\acute{n}=1}^{N_{tap}^{[t]}}\tilde{c}_{pre}^{(j)}[\acute{n}-1]\mathbf{S}^{(j)-1}[n-\acute{n}]\mathbf{n}[n-\acute{n}] + \\ &\quad + \mathbf{H}^{(j)}[n] - \mathbf{T}_{K_0}^{(j)}\sum_{\acute{n}=1}^{N_{tap}^{[t]}}\tilde{c}_{pre}^{(j)}[\acute{n}-1]\mathbf{H}^{(j)}[n-\acute{n}],\end{aligned} \tag{3.113}$$

where

$$\Delta\hat{\mathbf{H}}_{apr}^{(j)}[n] = \mathbf{H}^{(j)}[n] - \hat{\mathbf{H}}_{apr}^{(j)}[n]. \tag{3.114}$$

Please observe that for the sake of avoiding notational confusion the variable i of Equation 3.111 has been substituted by the variable j. The vector of *a priori* channel transfer factor estimation errors given by Equation 3.113 is constituted by three components. Specifically, the first term of Equation 3.113 is due to the effects of the *a priori* prediction errors of the $N_{tap}^{[t]}$ number of past OFDM symbols, the second term is attributed to the contaminating effect of the AWGN and the third term is due to the lack of 'perfect predictability' of the channel transfer factors by the $(N_{tap}^{[t]}-1)$-order predictor. In other words, the last term is due to the channel transfer function's decorrelation with time.

The average variance of the j-th user's vector of *a priori* channel transfer factor estimation errors or in other words the average mean-square *a priori* estimation error can be expressed in mathematical terms as:

$$\overline{\mathrm{MSE}}_{apr}^{(j)}[n] = \frac{1}{K}\mathrm{Trace}(\mathbf{R}_{\Delta\hat{\mathbf{H}}_{apr}^{(j)}}[n]), \tag{3.115}$$

where $\mathbf{R}_{\Delta\hat{\mathbf{H}}_{apr}^{(j)}}[n] \in \mathbb{C}^{K\times K}$ denotes the auto-correlation matrix of the vector $\Delta\hat{\mathbf{H}}_{apr}^{(j)}[n]$ of *a priori* channel transfer factor estimation errors. The computation of $\overline{\mathrm{MSE}}_{apr}^{(j)}[n]$ of the j-th user's vector of *a priori* estimation errors associated with the n-th OFDM symbol period as given by Equation 3.113 will be carried out in two steps.

In a first step let us evaluate the auto-correlation matrix $\mathbf{R}_{\Delta\hat{\mathbf{H}}^{(j)}_{apr}}[n]$. This is achieved by substituting Equation 3.113 into:

$$\mathbf{R}_{\Delta\hat{\mathbf{H}}^{(j)}_{apr}}[n] = E\left\{\Delta\hat{\mathbf{H}}^{(j)}_{apr}[n]\Delta\hat{\mathbf{H}}^{(j)H}_{apr}[n]\right\} \tag{3.116}$$

$$= \frac{\alpha_j}{\sigma_j^2}\mathbf{T}^{(j)}_{K_0}\left(\sum_{\acute{n}=1}^{N^{[t]}_{tap}}|\tilde{c}^{(j)}_{pre}[\acute{n}-1]|^2\sum_{\substack{i=1\\ i\neq j}}^{L}\sigma_i^2\mathbf{R}_{\Delta\hat{\mathbf{H}}^{(i)}_{apr}}[n-\acute{n}]|_{Diag}\right)\mathbf{T}^{(j)H}_{K_0} +$$

$$+\frac{\alpha_j}{\sigma_j^2}\sigma_n^2\sum_{\acute{n}=1}^{N^{[t]}_{tap}}|\tilde{c}^{(j)}_{pre}[\acute{n}-1]|^2\mathbf{T}^{(j)}_{K_0}\mathbf{T}^{(j)H}_{K_0} + \mathbf{R}_{\mathbf{H}^{(j)}_{dec}}, \tag{3.117}$$

where we introduced a new definition, namely that of the channel transfer function decorrelation-related matrix $\mathbf{R}_{\mathbf{H}^{(j)}_{dec}} \in \mathbb{C}^{K\times K}$, which is given by:

$$\mathbf{R}_{\mathbf{H}^{(j)}_{dec}} = \mathbf{R}^{[f](j)} - \mathbf{T}^{(j)}_{K_0}\mathbf{R}^{[f](j)H}\cdot(\tilde{\mathbf{c}}^{(j)H}_{pre}\mathbf{r}^{[t](j)}) - \mathbf{R}^{[f](j)}\mathbf{T}^{(j)H}_{K_0}\cdot(\tilde{\mathbf{c}}^{(j)T}_{pre}\mathbf{r}^{[t](j)*}) +$$

$$+\mathbf{T}^{(j)}_{K_0}\mathbf{R}^{[f](j)}\mathbf{T}^{(j)H}_{K_0}\cdot(\tilde{\mathbf{c}}^{(j)H}_{pre}\mathbf{R}^{[t](j)}\tilde{\mathbf{c}}^{(j)}_{pre}). \tag{3.118}$$

In the context of Equation 3.117 we have exploited that the three additive components of the vector $\Delta\hat{\mathbf{H}}^{(j)}_{apr}[n]$ of *a priori* channel transfer factor estimation errors in Equation 3.113 are uncorrelated. The uncorrelated nature of these three terms accrues from the statistical independence of the complex AWGN process and that of the complex valued process describing the channel transfer function's evolution versus frequency and time. We have also exploited that the complex symbols transmitted in different subcarriers of a specific user's signal during a specific OFDM symbol period, as well as the symbols transmitted by the same user in different OFDM symbol periods and the symbols transmitted by different users are statistically independent, which also implies that they are uncorrelated. Still considering Equation 3.117, the variable α_j denotes the so-called "modulation noise enhancement factor" [89, 15], defined as $\alpha_j = E\{|s^{(j)}[n,k]|^2\}E\{|1/s^{(j)}[n,k]|^2\}$. For M-ary Phase Shift Keying (MPSK) based modulation schemes, such as for example QPSK we have $\alpha = 1$, while for higher-order Quadrature Amplitude Modulation (QAM) schemes we have $\alpha > 1$ [89, 15]. Note that here we have implicitly assumed that the same modulation scheme is employed on different subcarriers of a specific user's transmitted signal. To elaborate further, the variables to be defined in Equation 3.118 are the spaced-time correlation function related auto-correlation vector $\mathbf{r}^{[t](j)} \in \mathbb{C}^{N^{[t]}_{tap}\times 1}$, of the channel transfer function, where the $\acute{n}$-th element is given by $\mathbf{r}^{[t](j)}|_{\acute{n}} = E\{H^{(j)*}[n,k]H^{(j)}[n-\acute{n},k]\}$, and the spaced-time correlation function related auto-correlation matrix $\mathbf{R}^{[t](j)} \in \mathbb{C}^{N^{[t]}_{tap}\times N^{[t]}_{tap}}$, of the channel transfer function, with the element $(\acute{n}_1,\acute{n}_2)$ given by $\mathbf{R}^{[t](j)}|_{\acute{n}_1,\acute{n}_2} = E\{H^{(j)}[n-\acute{n}_1,k]H^{(j)*}[n-\acute{n}_2,k]\}$. Furthermore, $\tilde{\mathbf{c}}^{(j)}_{pre} \in \mathbb{C}^{N^{[t]}_{tap}\times 1}$ is the vector of conjugate complex CIR-related tap prediction filter coefficients with its $\acute{n}$-th element given by $\tilde{\mathbf{c}}^{(j)}_{pre}|_{\acute{n}} = \tilde{c}^{(j)*}_{pre}[\acute{n}]$. The channel's spaced-frequency correlation matrix $\mathbf{R}^{[f](j)}$ was defined earlier in Section 3.4.1.2. Let us now return to our original objective, namely that of developing an

expression for the average *a priori* channel transfer factor estimation MSE during the n-th OFDM symbol period.

In a second step Equation 3.117 is invoked in conjunction with Equation 3.115 for obtaining an expression for the j-th user's average *a priori* channel transfer factor estimation MSE as a function of the remaining users' *a priori* estimation MSEs associated with the $N_{tap}^{[t]}$ number of previous OFDM symbol periods:

$$\begin{aligned}\overline{\mathrm{MSE}}_{apr}^{(j)}[n] &= \frac{K_0}{K}\frac{\alpha_j}{\sigma_j^2}\sum_{\acute{n}=1}^{N_{tap}^{[t]}}|\tilde{c}_{pre}^{(j)}[\acute{n}-1]|^2\sum_{\substack{i=1\\ i\neq j}}^{L}\sigma_i^2\overline{\mathrm{MSE}}_{apr}^{(i)}[n-\acute{n}]+\\ &+\frac{K_0}{K}\frac{\alpha_j}{\sigma_j^2}\sigma_n^2\tilde{\mathbf{c}}_{pre}^{(j)H}\tilde{\mathbf{c}}_{pre}^{(j)}+\overline{\mathrm{MSE}}_{dec}^{(j)}, \end{aligned} \tag{3.119}$$

where we have:

$$\overline{\mathrm{MSE}}_{dec}^{(j)} = \frac{1}{K}\mathrm{Trace}(\mathbf{R}_{\mathbf{H}_{dec}^{(j)}}) \tag{3.120}$$

$$\begin{aligned}&= \sigma_H^2-\frac{1}{K}\mathrm{Trace}(\Upsilon^{[f](j)}\mathbf{I}_{K_0}^{(j)})\cdot\\ &\quad\cdot\left(\tilde{\mathbf{c}}_{pre}^{(j)H}\mathbf{r}^{[t](j)}+\tilde{\mathbf{c}}_{pre}^{(j)T}\mathbf{r}^{[t](j)*}-\tilde{\mathbf{c}}_{pre}^{(j)H}\mathbf{R}^{[t](j)}\tilde{\mathbf{c}}_{pre}^{(j)}\right).\end{aligned} \tag{3.121}$$

In the context of deriving Equation 3.119 we have capitalized on the relations $\mathrm{Trace}(\mathbf{A}+\mathbf{B}) = \mathrm{Trace}(\mathbf{A})+\mathrm{Trace}(\mathbf{B})$, as well as on $\mathrm{Trace}(\mathbf{UAU}^H) = \mathrm{Trace}(\mathbf{A})$, which are valid for a unitary matrix $\mathbf{U}$ [16, 94]. Furthermore, in the context of deriving the first additive term in Equation 3.119 we exploited that $\frac{1}{K}\mathrm{Trace}(\mathbf{T}_{K_0}^{(j)}\mathbf{R}_{\Delta\hat{\mathbf{H}}_{apr}^{(i)}}[n-\acute{n}]|_{Diag}\mathbf{T}_{K_0}^{(j)H}) = \frac{K_0}{K}\overline{\mathrm{MSE}}_{apr}^{(i)}[n-\acute{n}]$, which is only valid for a unitary transform matrix $\tilde{\mathbf{U}}^{[f](j)}$ having elements of unity magnitude. This is the case for example, when employing the DFT matrix $\mathbf{W}$ as the unitary transform matrix. The second additive term in Equation 3.119 is based on exploiting the relationship of $\frac{1}{K}\mathrm{Trace}(\mathbf{T}_{K_0}^{(j)}\mathbf{T}_{K_0}^{(j)H}) = \frac{K_0}{K}$. We also note in this context that $\mathbf{T}_{K_0}^{(j)H} = \mathbf{T}_{K_0}^{(j)}$ and that $\mathbf{T}_{K_0}^{(j)}\mathbf{T}_{K_0}^{(j)H} = \mathbf{T}_{K_0}^{(j)}$.

Furthermore, in Equation 3.121, the matrix $\Upsilon^{[f](j)} \in \mathbb{C}^{K\times K}$ denotes the decomposition of the j-th user's channel's spaced-frequency correlation matrix $\mathbf{R}^{[f](j)}$ with respect to the unitary transform matrix $\tilde{\mathbf{U}}^{[f](j)}$, which is expressed as $\Upsilon^{[f](j)} = \tilde{\mathbf{U}}^{[f](j)H}\mathbf{R}^{[f](j)}\tilde{\mathbf{U}}^{[f](j)}$. Note that in contrast to $\Lambda^{[f](j)}$ associated with the decomposition of $\mathbf{R}^{[f](j)}$ with respect to $\mathbf{U}^{[f](j)}$, the matrix $\Upsilon^{[f](j)}$ is not necessarily of diagonal shape constrained to having real-valued elements only.

3.4.1.4 *A Posteriori* Channel Estimation MSE

Following the philosophy of Section 3.4.1.3 related to our derivation of an expression describing the j-th user's average *a priori* channel estimation MSE as a function of the remaining $(L-1)$ users' *a priori* channel estimation MSEs associated with the previous $N_{tap}^{[t]}$ number of OFDM symbol periods, in this section a similar expression is derived for the average *a posteriori* channel transfer

factor estimation MSE. This is achieved in a first step upon substituting Equations 3.105 and 3.111 into Equation 3.106. Similarly to the definition of the vector of *a priori* estimation errors in Equation 3.114, the j-th user's vector of *a posteriori* estimation errors $\Delta\tilde{\mathbf{H}}^{(j)}_{apt}[n] \in \mathbb{C}^{K\times 1}$ can be defined as:

$$\Delta\tilde{\mathbf{H}}^{(j)}_{apt}[n] = \mathbf{H}^{(j)}[n] - \tilde{\mathbf{H}}^{(j)}_{apt}[n]. \tag{3.122}$$

In accordance with the definition of the average *a priori* channel transfer factor estimation MSE in Equation 3.115, we can also define the average *a posteriori* estimation MSE as:

$$\overline{\mathrm{MSE}}^{(j)}_{apt}[n] = \frac{1}{K}\mathrm{Trace}(\mathbf{R}_{\Delta\tilde{\mathbf{H}}^{(j)}_{apt}}[n]), \tag{3.123}$$

where $\mathbf{R}_{\Delta\tilde{\mathbf{H}}^{(j)}_{apt}}[n] \in \mathbb{C}^{K\times K}$ denotes the auto-correlation matrix of the vector $\Delta\tilde{\mathbf{H}}^{(j)}_{apt}[n]$ of *a posteriori* estimation errors. Our further mathematical manipulations, which are not detailed here for reasons of space economy yield the following expression for the j-th user's average *a posteriori* estimation MSE during the n-th OFDM symbol period:

$$\begin{aligned}\overline{\mathrm{MSE}}^{(j)}_{apt}[n] &= \frac{K_0}{K}\frac{\alpha_j}{\sigma_j^2}\sum_{\substack{i=1\\ i\neq j}}^{L}\sigma_i^2\sum_{\acute{n}=1}^{N^{[t]}_{tap}}|\tilde{c}^{(i)}_{pre}[\acute{n}-1]|^2\overline{\mathrm{MSE}}^{(i)}_{apt}[n-\acute{n}] + \\ &\quad + \frac{\alpha_j}{\sigma_j^2}\sigma_n^2 + \frac{\alpha_j}{\sigma_j^2}\sum_{\substack{i=1\\ i\neq j}}^{L}\sigma_i^2\overline{\mathrm{MSE}}^{(i)}_{dec}.\end{aligned} \tag{3.124}$$

Finally, the channel decorrelation-related MSE, namely $\overline{\mathrm{MSE}}^{(i)}_{dec}$ of Equation 3.124 is given by Equation 3.121, which is identical for the *a priori* and *a posteriori* estimates.

3.4.1.5 Stability Analysis of the Recursive Channel Estimator

In the steady-state condition we can assume that the specific user's *a priori*- and *a posteriori* estimation MSEs are identical for different OFDM symbols, which is expressed as:

$$\overline{\mathrm{MSE}}^{(i)}_{ap(t/r)} = \overline{\mathrm{MSE}}^{(i)}_{ap(t/r)}[n-\acute{n}], \tag{3.125}$$

where $i = 1,\ldots,L$ and $\acute{n} = 0,\ldots,N^{[t]}_{tap}$. Hence, Equation 3.119 simplifies to:

$$\begin{aligned}\overline{\mathrm{MSE}}^{(j)}_{apr} &= \frac{K_0}{K}\frac{\alpha_j}{\sigma_j^2}\tilde{\mathbf{c}}^{(j)H}_{pre}\tilde{\mathbf{c}}^{(j)}_{pre}\sum_{\substack{i=1\\ i\neq j}}^{L}\sigma_i^2\overline{\mathrm{MSE}}^{(i)}_{apr} + \\ &\quad + \frac{K_0}{K}\frac{\alpha_j}{\sigma_j^2}\tilde{\mathbf{c}}^{(j)H}_{pre}\tilde{\mathbf{c}}^{(j)}_{pre}\sigma_n^2 + \overline{\mathrm{MSE}}^{(j)}_{dec}.\end{aligned} \tag{3.126}$$

Note that Equation 3.126 can be viewed as a system of equations for different values of $j = 1, \ldots, L$, namely for the different users. It can be shown that Equation 3.126 can be represented in a compact vectorial notation as:

$$\mathbf{MSE}_{apr} = \mathbf{C}_{pre} \cdot \mathbf{P}_s^{-1} \cdot \mathbf{F} \cdot \mathbf{P}_s \cdot \mathbf{MSE}_{apr} + \mathbf{C}_{pre} \cdot \mathbf{P}_s^{-1} \cdot \mathbf{p}_n + \mathbf{MSE}_{dec}, \tag{3.127}$$

where $\mathbf{MSE}_{apr} \in \mathbb{R}^{L \times 1}$ hosts the different users' *a priori* estimation MSEs denoted by $\overline{\mathrm{MSE}}_{apr}^{(j)}$, $j = 1, \ldots, L$, and the diagonal matrix $\mathbf{C}_{pre} \in \mathbb{R}^{L \times L}$ hosts the different users' CIR-related tap prediction coefficient related terms of $\frac{K_0}{K} \alpha_j \tilde{\mathbf{c}}_{pre}^{(j)H} \tilde{\mathbf{c}}_{pre}^{(j)}$, $j = 1, \ldots, L$. A characteristic component is the feedback matrix $\mathbf{F} \in \mathbb{R}^{L \times L}$, which exhibits the following structure:

$$\mathbf{F} = \begin{pmatrix} 0 & 1 & \ldots & 1 \\ 1 & \ddots & \ddots & \vdots \\ \vdots & \ddots & \ddots & 1 \\ 1 & \ldots & 1 & 0 \end{pmatrix}, \tag{3.128}$$

where the elements on the side diagonals are of unit value except for the main diagonal, whose elements are zero. The relation to the PIC process is that for the estimation of the j-th user's channel transfer function, the co-channel interference imposed by the $L-1$ remaining users has to be removed. Note in this context that the j-th row of matrix $\mathbf{F}$ is associated with the estimation process of the j-th user's channel. Furthermore, the diagonal matrix $\mathbf{P}_s \in \mathbb{R}^{L \times L}$ hosts the different users' signal variances σ_i^2, $i = 1, \ldots, L$, while the vector $\mathbf{p}_n \in \mathbb{R}^{L \times 1}$ exhibits identical elements equal to the AWGN noise variance σ_n^2. Finally, the matrix $\mathbf{MSE}_{dec} \in \mathbb{R}^{L \times 1}$ hosts the different users' residual channel decorrelation-related MSEs values, given by $\frac{1}{K}\mathrm{Trace}(\mathbf{R}_{\mathbf{H}_{dec}^{(j)}})$, $j = 1, \ldots, L$, which are also a function of the individual users' CIR-related tap predictor coefficients, as evidenced by Equation 3.121. In order to proceed further, Equation 3.127 can be solved for the vector of *a priori* estimation MSEs, conditioned on the knowledge of the vectors $\tilde{\mathbf{c}}_{pre}^{(j)}$, $j = 1, \ldots, L$ of predictor coefficients, yielding:

$$\mathbf{MSE}_{apr} = \left(\mathbf{I} - \mathbf{C}_{pre} \cdot \mathbf{P}_s^{-1} \cdot \mathbf{F} \cdot \mathbf{P}_s\right)^{-1} \cdot \left(\mathbf{C}_{pre} \cdot \mathbf{P}_s^{-1} \cdot \mathbf{p}_n + \mathbf{MSE}_{dec}\right). \tag{3.129}$$

Per definition, the elements of $\mathbf{MSE}_{apr}$ or, equivalently, the different users' *a priori* estimation MSEs must have a finite positive value. This is coupled to the following conditions:

1. existence of $(\mathbf{I} - \acute{\mathbf{F}})^{-1}$, where $\acute{\mathbf{F}} = \mathbf{C}_{pre} \cdot \mathbf{P}_s^{-1} \cdot \mathbf{F} \cdot \mathbf{P}_s$
2. all elements of $(\mathbf{I} - \acute{\mathbf{F}})^{-1}$ must be positive.

It can be demonstrated that these two conditions are fulfilled, if the spectral radius $\rho(\acute{\mathbf{F}})$ [10] of the matrix $\acute{\mathbf{F}} = \mathbf{C}_{pre} \cdot \mathbf{P}_s^{-1} \cdot \mathbf{F} \cdot \mathbf{P}_s$ is less than unity [112]. An *upper-bound* estimate of the spectral

[10] Recall that the spectral radius of a matrix is the smallest radius of a circle centered around the origin of $\mathbb{C}$ that contains all the matrix's eigenvalues [87].

radius is given by the largest Euclidean distance measured from the origin in $\mathbb{C}$, exhibited by a point contained in the union $G(\acute{\mathbf{F}})$ of Gershgorin disks [11] of $\acute{\mathbf{F}}$. Hence, provided that we have:

$$\max_{j=1...L}\left(\frac{K_0}{K}\alpha_j \tilde{\mathbf{c}}_{pre}^{H(j)}\tilde{\mathbf{c}}_{pre}^{(j)}\sum_{\substack{i=1\\ i\neq j}}^{L}\frac{\sigma_i^2}{\sigma_j^2}\right) < 1, \tag{3.130}$$

it can be shown that $\acute{\mathbf{F}}$ is invertible. By contrast, if this condition is not fulfilled, no immediate conclusion can be drawn with respect to the invertibility of $\acute{\mathbf{F}}$.

A further criterion for the existence of the matrix inverse $(\mathbf{I}-\acute{\mathbf{F}})^{-1}$ is coupled to the condition that the determinant of $(\mathbf{I}-\acute{\mathbf{F}})$ is non-zero, namely that we have $\det(\mathbf{I}-\acute{\mathbf{F}}) \neq 0$. Furthermore, it can be shown that for all elements of this specific matrix inverse to be positive as stipulated in (2), we have to satisfy the condition of $\det(\mathbf{I}-\acute{\mathbf{F}}) > 0$. It can be shown that $\det(\mathbf{I}-\acute{\mathbf{F}}) = \det(\mathbf{I}-\mathbf{C}_{pre}\cdot\mathbf{F})$, which implies that the channel estimator's stability is only a function of the estimator coefficients to be determined. Even if the channel conditions are subjected to variations, the estimator remains stable for a "stable" set of coefficients - provided that correct symbol decisions are performed.

3.4.1.6 Iterative Calculation of the CIR-Related Tap Predictor Coefficients

Upon invoking Equation 3.126 the j-th user's vector of CIR-related tap predictor coefficients $\tilde{\mathbf{c}}_{pre}^{(j)}$ can be evaluated conditioned on the remaining $(L-1)$ number of users' *a priori* estimation MSEs, namely on $\overline{\text{MSE}}_{apr}^{(i)}$, $i = 1,\ldots,L$, $i \neq j$, which ensues by calculating the gradient of $\overline{\text{MSE}}_{apr}^{(j)}$ with respect to the j-th user's coefficients, yielding:

$$\begin{aligned}\nabla^{(j)}\overline{\text{MSE}}_{apr}^{(j)} &= \frac{K_0}{K}\frac{\alpha_j}{\sigma_j^2}\tilde{\mathbf{c}}_{pre}^{(j)}\left(\sum_{\substack{i=1\\ i\neq j}}^{L}\sigma_i^2\overline{\text{MSE}}_{apr}^{(i)}+\sigma_n^2\right)+\\ &\quad -\frac{1}{K}\text{Trace}(\Upsilon^{[f](j)}\mathbf{I}_{K_0}^{(j)})\cdot(\mathbf{r}^{[t](j)}-\mathbf{R}^{[t](j)}\tilde{\mathbf{c}}_{pre}^{(j)}),\end{aligned} \tag{3.131}$$

where $\mathbf{R}^{[t](j)}$ and $\mathbf{r}^{[t](j)}$ were defined in the context of Equation 3.118. The gradient vector with respect to the j-th user's coefficients is defined here as $\nabla^{(j)} = \frac{\partial}{\partial \tilde{\mathbf{c}}_{pre}^{(j)*}}$, with individual components given by the Wirtinger calculus $\frac{\partial}{\partial \tilde{c}_{pre}^{(j)*}} = \frac{1}{2}(\frac{\partial}{\partial \tilde{c}_r^{(j)}} + j\frac{\partial}{\partial \tilde{c}_i^{(j)}})$ [113], where $\tilde{c}_r^{(j)}$ and $\tilde{c}_i^{(j)}$ are the real and imaginary parts of $\tilde{c}_{pre}^{(j)}$. In the context of Equation 3.131 we have exploited that $\nabla^{(j)}\tilde{\mathbf{c}}_{pre}^{(j)H} = \mathbf{I}$, as well as that $\nabla^{(j)}\tilde{\mathbf{c}}_{pre}^{(j)T} = \mathbf{0}$ and $\nabla^{(j)}(\tilde{\mathbf{c}}_{pre}^{(j)H}\tilde{\mathbf{c}}_{pre}^{(j)}) = \tilde{\mathbf{c}}_{pre}^{(j)}$.

[11] With the aid of the Gershgorin circle theorem [87] explicit bounds can be placed on the regions in $\mathbb{C}$, which host the eigenvalues of a matrix $\mathbf{A} \in \mathbb{C}^{m\times m}$. The i-th Gershgorin disk is defined as: $R_i(\mathbf{A}) = \{x \in \mathbb{C} : |x-a_{ii}| \leq \sum_{\substack{j=1\\ j\neq i}}^{m}|a_{ij}|\}$, where a_{ij} is the element of the matrix $\mathbf{A}$ associated with its i-th row and j-th column. The eigenvalues of the matrix $\mathbf{A}$ reside within the union of Gershgorin disks of $\mathbf{A}$, which is formulated in a compact form as $\lambda(\mathbf{A}) \subset \bigcup_{i=1}^{m} R_i(\mathbf{A}) = G(\mathbf{A})$ [87].

In the optimum point of operation we have $\nabla^{(j)}\overline{\text{MSE}}^{(j)}_{apr} = \mathbf{0}$ and hence Equation 3.131 can be solved for the j-th user's vector of predictor coefficients, resulting in the Wiener filter related solution of:

$$\tilde{\mathbf{c}}^{(j)}_{pre}|_{opt} = \left[\mathbf{R}^{[t](j)} + \frac{K_0}{\text{Trace}(\Upsilon^{[f](j)}\mathbf{I}^{(j)}_{K_0})}\frac{\alpha_j}{\sigma_j^2}\left(\sum_{\substack{i=1\\ i\neq j}}^{L}\sigma_i^2\overline{\text{MSE}}^{(i)}_{apr} + \sigma_n^2\right)\mathbf{I}\right]^{-1}\cdot\mathbf{r}^{[t](j)}. \quad (3.132)$$

Based on Equations 3.126 and 3.132 a fixed-point iteration algorithm [87] can be devised for obtaining the different users' vectors of predictor coefficients under the constraint of minimizing the sum of the different users' *a priori* estimation MSEs. This approach was proposed earlier by Rashid-Farrokhi *et al.* [111] in the context of simultaneously optimizing both the transmit power allocation and the basestation antenna array weights in wireless networks, leading to formulae similar to Equations 3.126 and 3.132. In our forthcoming discourse we will briefly present the steps of the algorithm with respect to our specific optimization problem, but for a formal proof of the algorithm's convergence and that of the uniqueness of the solution, we refer to [111]. Note that in the context of our description of the algorithm, the iteration index - and not the OFDM symbol index - is given in the square brackets.

1. Initialize the different users' *a priori* estimation MSEs, for example by setting $\overline{\text{MSE}}^{(j)}_{apr}[0] = 0$ for $j = 1, \ldots, L$.

2. *For the n-th iteration*: Conditioned on the *a priori* estimation MSE values obtained during the $(n-1)$-th iteration, namely on $\overline{\text{MSE}}^{(j)}_{apr}[n-1]$, $j = 1, \ldots, L$ calculate the different users' vectors of optimum predictor coefficients for the n-th iteration, namely $\tilde{\mathbf{c}}^{(j)}_{pre}[n]|_{opt}$, $j = 1, \ldots, L$, with the aid of Equation 3.132.

3. Conditioned on the n-th iteration's predictor coefficient vectors $\tilde{\mathbf{c}}^{(j)}_{pre}[n]|_{opt}$, $j = 1, \ldots, L$ obtained in step (2) and also conditioned on the $(n-1)$-th iteration's *a priori* estimation MSE values, namely on $\overline{\text{MSE}}^{(j)}_{apr}[n-1]$, $j = 1, \ldots, L$ calculate the n-th iteration's *a priori* estimation MSE values of $\overline{\text{MSE}}^{(j)}_{apr}[n]$, $j = 1, \ldots, L$ with the aid of Equation 3.126.

4. Start a new iteration by returning to step (2).

Note that instead of invoking Equation 3.126 separately for each user, the different users' *a priori* estimation MSEs can also be calculated in parallel with the aid of Equation 3.129, as a result of which an even faster convergence is achieved. The price to be paid is a higher computational complexity, since an explicit matrix inversion is required in Equation 3.129.

3.4.1.6.1 Simplified Approach for Identical User Statistics A simplification of Equations 3.126 and 3.132, which we will sometimes invoke during our performance assessment in Section 3.4.2 is

achieved by imposing a number of assumptions. Specifically, we will assume perfect power control, implying that $\sigma_s^2 = \sigma_1^2 = \ldots = \sigma_L^2$ and that the same modulation mode is employed by all the L users, yielding $\alpha = \alpha_1 = \ldots = \alpha_L$. Additionally, identical spaced-time correlation functions and hence identical auto-correlation matrices $\mathbf{R}^{[t]} = \mathbf{R}^{[t](1)} = \ldots = \mathbf{R}^{[t](L)}$ and auto-correlation vectors $\mathbf{r}^{[t]} = \mathbf{r}^{[t](1)} = \ldots = \mathbf{r}^{[t](L)}$ are associated with the different users. As a result of these assumptions the same *a priori* estimation MSE, namely $\overline{\text{MSE}}_{apr} = \overline{\text{MSE}}_{apr}^{(1)} = \ldots = \overline{\text{MSE}}_{apr}^{(L)}$ and the same CIR-related tap predictor coefficient vector $\tilde{\mathbf{c}}_{pre} = \tilde{\mathbf{c}}_{pre}^{(1)} = \ldots = \tilde{\mathbf{c}}_{pre}^{(L)}$ is associated with the different users. Hence, Equation 3.126 can be directly solved for $\overline{\text{MSE}}_{apr}$ conditioned on a specific vector $\tilde{\mathbf{c}}_{pre}$ of predictor coefficients, yielding:

$$\overline{\text{MSE}}_{apr}|^{\text{SIMPLE}} = \frac{\chi \frac{\sigma_n^2}{\sigma_s^2} \tilde{\mathbf{c}}_{pre}^H \tilde{\mathbf{c}}_{pre} + \frac{1}{K} \text{Trace}(\mathbf{R}_{\mathbf{H}_{dec}})}{1 - \chi(L-1)\tilde{\mathbf{c}}_{pre}^H \tilde{\mathbf{c}}_{pre}}, \tag{3.133}$$

where $\chi = \frac{K_0}{K}\alpha$. The denominator of the fraction on the right-hand side of Equation 3.133 suggests a particularly simple form of the steady-state stability condition, namely that of:

$$\chi(L-1)\tilde{\mathbf{c}}_{pre}^H \tilde{\mathbf{c}}_{pre} < 1, \tag{3.134}$$

which follows from Equation 3.130 upon invoking the above assumptions. Furthermore, Equation 3.132, which delivers the vector of optimum predictor coefficients as a function of the *a priori* estimation MSE simplifies to:

$$\tilde{\mathbf{c}}_{pre}|_{opt}^{\text{SIMPLE}} = \left[\mathbf{R}^{[t]} + \frac{K_0}{\text{Trace}(\Upsilon^{[f]}\mathbf{I}_{K_0})}\alpha \left((L-1)\overline{\text{MSE}}_{apr}|^{\text{SIMPLE}} + \frac{\sigma_n^2}{\sigma_s^2}\right)\mathbf{I}\right]^{-1} \cdot \mathbf{r}^{[t]}. \tag{3.135}$$

Note that upon removing the $(L-1)$ number of contributions in Equations 3.133 and 3.135, which are related to the PIC process, we obtain the expressions for the estimation MSE and the vector of coefficients associated with a transversal predictor, which can be expressed as:

$$\tilde{\mathbf{c}}_{pre,\text{FIR}}|_{opt}^{\text{SIMPLE}} = \left[\mathbf{R}^{[t]} + \frac{K_0}{\text{Trace}(\Upsilon^{[f]}\mathbf{I}_{K_0})}\alpha\frac{\sigma_n^2}{\sigma_s^2}\mathbf{I}\right]^{-1} \cdot \mathbf{r}^{[t]}. \tag{3.136}$$

By stipulating a sample-spaced CIR hosting K_0 number of non-zero taps and upon appropriately designing the matrix $\mathbf{I}_{K_0}$, namely by assigning a numerical value of unity to those diagonal elements, which are related to the different CIR taps' sample-spaced delays, we obtain $\text{Trace}(\Upsilon^{[f]}\mathbf{I}_{K_0}) = K\sigma_H^2$. This further simplifies Equation 3.136.

In the next section a closed-form solution is presented for the optimum "predictor" coefficient in the context of one-tap *a priori* channel estimation.

3.4.1.6.2 Closed Form Solution for Identical User Statistics and One-Tap CIR-Related Tap Prediction Filtering For the case of simple zero-order CIR-related tap prediction a closed form

solution can be derived from Equations 3.136 and 3.133 for the optimum predictor coefficient in the context of a sample-spaced CIR, which is given by:

$$\tilde{c}_{pre}[0]|_{opt}^{\text{SIMPLE}} = -\sqrt{\nu^2 - \frac{1}{\chi \cdot (L-1)}} + \nu, \tag{3.137}$$

where

$$\nu = \frac{\chi \cdot \frac{\sigma_n^2}{\sigma_s^2} + \chi \cdot (L-1) + 1}{2 \cdot \chi \cdot (L-1) \cdot r_H^{[t]}[1]}. \tag{3.138}$$

By contrast, the optimum predictor coefficient for the case of a transversal one-tap predictor is given by:

$$\tilde{c}_{pre,\text{FIR}}[0]|_{opt}^{\text{SIMPLE}} = \frac{r_H^{[t]}[1]}{1 + \chi \frac{\sigma_n^2}{\sigma_s^2}}, \tag{3.139}$$

which directly follows from Equation 3.136. In Equations 3.138 and 3.139, $r_H^{[t]}[1]$ denotes the channel transfer factor correlation coefficient for a time-lag of one OFDM symbol. Physically this equation simply states that if the channel transfer function varies slowly, $r_H^{[t]}[1] \approx 1$ and hence the predictor coefficient has a high value. By contrast, if the channel correlation is low, the predictor coefficient has to be low.

In the next section we will address the problem of a potential lack of knowledge about the channel's exact statistics namely that of the spaced-time spaced-frequency correlation function.

3.4.1.7 Channel Statistics

As it was observed in Equations 3.126 and 3.132, a prerequisite for determining the different users' vectors of optimum CIR-related tap predictor coefficients is the knowledge of the users' spaced-time channel transfer factor correlation functions $r_H^{[t](j)}[\Delta n]$, $j = 1, \ldots, L$, defined by:

$$r_H^{[t](j)}[\Delta n] = E\{H^{(j)}[n,k] \cdot H^{(j)*}[n - \Delta n, k]\}. \tag{3.140}$$

These are required for evaluating the auto-correlation matrices $\mathbf{R}^{[t](j)}$ and cross-correlation vectors $\mathbf{r}^{[t](j)}$ for $j = 1, \ldots, L$. Assuming Jakes' fading model [90] for example, the channel correlation along the time-direction is given by [17]:

$$r_{H,J}^{[t](j)}[\Delta n] = J_0(\Delta n \cdot \omega_D^{(j)}), \tag{3.141}$$

$$\approx 1 - \frac{1}{4}(\Delta n \cdot \omega_D^{(j)})^2, \quad \Delta n \cdot \omega_D^{(j)} \ll 1, \tag{3.142}$$

where $J_0()$ denotes the zero-order Bessel function of the first kind and $\omega_D^{(j)} = 2\pi T_f f_D^{(j)}$, and T_f being the OFDM symbol duration including the guard period time, while $f_D^{(j)}$ denotes the channel's

Doppler frequency. Since usually the exact Doppler frequency $f_D^{(j)}$ is not known, it was demonstrated in [17] in the context of a transversal-type estimator, that the MSE performance degradation incurred due to a mismatch of the channel statistics is only marginal, if a uniform, ideally support-limited Doppler power spectrum associated with $\tilde{f}_D^{(j)} \geq f_D^{(j)}$ is assumed for the calculation of the correlation coefficients of Equation 3.140. The associated spaced-time correlation function is given as the inverse Fourier Transform (FT) of the uniform Doppler power spectrum, which leads to:

$$\tilde{r}_{H,\text{unif}}^{[t](j)}[\Delta n] = \frac{sin(\Delta n \cdot \tilde{\omega}_D^{(j)})}{\Delta n \cdot \tilde{\omega}_D^{(j)}}. \tag{3.143}$$

Furthermore, the calculation of the vectors of CIR-related tap predictor coefficients according to Equation 3.132 also requires the evaluation of the expression $\text{Trace}(\Upsilon^{[f](j)}\mathbf{I}_{K_0}^{(j)})$. More explicitly we recall from Section 3.4.1.2 that $\Upsilon^{[f](j)}$ is the decomposition of the j-th user's channel's spaced-frequency correlation matrix $\mathbf{R}^{[f](j)}$ with respect to the unitary transform matrix $\tilde{\mathbf{U}}^{[f](j)}$, which is formulated as $\Upsilon^{[f](j)} = \tilde{\mathbf{U}}^{[f](j)H}\mathbf{R}^{[f](j)}\tilde{\mathbf{U}}^{[f](j)}$, and $\mathbf{I}_{K_0}^{(j)}$ is a sparse identity matrix having unity entries only at those K_0 number of positions, which are associated with a significant value of $\Upsilon^{[f](j)}$. Hence, we note that the evaluation of $\text{Trace}(\Upsilon^{[f](j)}\mathbf{I}_{K_0}^{(j)})$ requires the knowledge of $\mathbf{R}^{[f](j)}$, which is not directly available in practice. Below we have listed several potential approaches which can be pursued for addressing this problem:

1. Periodically estimate the diagonal elements of $\Upsilon^{[f](j)}$ upon evaluating the variance of the components associated with the vector $\tilde{\mathbf{h}}_{apt}^{(j)}[n]$, as it was formulated in Equation 3.108. For the l-th component the variance can be approximated by averaging this component's squared magnitude over the past N_{apt} number of OFDM symbols' contributions, which is expressed as:

$$\hat{\sigma}^2_{\tilde{h}_{apt}^{(j)}[n,l]} = \frac{1}{N_{apt}} \sum_{\acute{n}=0}^{N_{apt}-1} |\tilde{h}_{apt}^{(j)}[n-\acute{n}, l]|^2. \tag{3.144}$$

   Note that for $N_{apt} \to \infty$ the accuracy of the estimates provided by Equation 3.144 is determined by the variance of the *a posteriori* estimation error signals. In a second step the sum of those K_0 number of CIR-related tap estimates is calculated, which exhibit the highest variance. This value constitutes the desired estimate of $\text{Trace}(\Upsilon^{[f](j)}\mathbf{I}_{K_0}^{(j)})$. Note that the corresponding positions in the matrix $\mathbf{I}_{K_0}^{(j)}$ associated with the K_0 highest values are set to unity, in order to perform the masking based activation of significant CIR-related taps during the following OFDM symbol periods. A similar strategy of selecting the significant CIR-related taps was also advocated by Li *et al.* [21] with the aim of reducing the complexity of a transversal filter-type channel estimator employed in Space-Time Coded (STC) OFDM systems.

2. The second alternative is that of obtaining an "average" value of Trace($\Upsilon^{[f](j)}\mathbf{I}_{K_0}^{(j)}$) by employing the spaced-frequency correlation matrix $\tilde{\mathbf{R}}^{[f](j)}$ based on the spaced-frequency correlation function associated with a uniform ideally support limited multipath intensity profile. The sparse identity matrix $\mathbf{I}_{K_0}^{(j)}$ could be designed for retaining the *first* K_0 CIR-related coefficients of $\Upsilon^{[f](j)}$ - rather than the K_0 largest one - or alternatively, for retaining the first K_0^I and the last K_0^{II} CIR-related coefficients of $\Upsilon^{[f](j)}$, where $K_0 = K_0^I + K_0^{II}$. This was suggested by van de Beek *et al.* [66] in the context of DFT-based channel transfer function estimation employed for single-user OFDM systems.

In the next section we will embark on the performance assessment of the various channel estimation techniques studied.

3.4.2 Performance Assessment

With the exception of the results to be presented in Section 3.4.2.2.3 our investigations were conducted for an SDMA uplink scenario supporting four simultaneous OFDM users each equipped with one transmit antenna. At the basestation (BS) four reception antennas were assumed. Unless otherwise stated, we impose an OFDM symbol normalized Doppler frequency of $F_D = 0.007$, which corresponds to a vehicular speed of 50km/h, or equivalently, 31.25mph in the context of the indoor WATM system's parameters, as outlined in Section 6.1.1.

Our assessment commences in Section 3.4.2.2 with a study of the average *a priori* channel transfer factor estimation MSE evaluated in the context of the idealistic scenario of a sample-spaced CIR and upon assuming error-free symbol decisions. Specifically, in the simplified scenario of a sample-spaced CIR the exact shape of the multipath intensity profile does not influence the performance of the PIC-assisted DDCE when employing the same vector of predictor coefficients for the different CIR-related taps. This is as outlined in Section 3.4.1.6.1 the case when the channel's entire energy is conveyed by the K_0 number of significant CIR-related taps. By contrast, in Section 3.4.2.3 in the context of our more realistic investigations of the *a priori* estimation MSE involving non-sample-spaced CIRs, three types of multipath intensity profiles, namely, sparse profiles, uniform profiles and exponential profiles are invoked. The analytical MSE performance results of Sections 3.4.2.2 and 3.4.2.3 were generated upon invoking the iterative approach described in Section 3.4.1.6 for simultaneously optimizing the CIR-related tap predictor coefficients and evaluating the different users' *a priori* estimation MSEs.

By contrast, at a later stage, namely in Section 3.4.2.4 we will consider the more realistic case of encountering imperfect, error-contaminated symbol decisions at the detection stage. Both uncoded as well as turbo-coded arrangements will be studied in terms of their *a priori* estimation MSE and system BER. These performance results were generated with the aid of Monte-Carlo simulations upon invoking the indoor WATM system- and channel parameters of Section 6.1.1. Since the indoor

WATM channel's CIR is composed of sample-spaced taps the performance curves presented in this context characterize the system's best possible performance.

Let us commence our discussions in the next section by studying the effects of the specific choice of the CIR-related tap predictor coefficients on the average *a priori* channel transfer factor estimation MSE.

3.4.2.1 Evolution of the *A Priori* Channel Estimation MSE in a Simplified 2-Tap CIR-Related Tap Prediction Scenario

In Figure 3.4 we have exemplified the evolution of the average *a priori* channel transfer factor estimation MSE according to Equation 3.133 as a function of the CIR-related tap predictor coefficients' associated values, where we employed a 2-tap predictor, since for a higher number of predictor taps a visualization is less convenient. Also note that the predictor coefficients are real-valued due to employing the real-valued spaced-time channel correlation function of Equation 3.141. In our particular example the *a priori* channel estimation MSE evaluated from Equation 3.133 is minimized for a coefficient vector of $\tilde{\mathbf{c}}_{pre}|_{opt} \approx (1,771, -0.898)^T$. By contrast, for coefficient pairs outside the circle having a radius of $\sqrt{\frac{K}{K_0\alpha(L-1)}} \approx 3.27$, centered around the origin of the $\mathbb{R}^2$ space, the channel estimator is instable, which is evidenced by the excessive MSEs.

3.4.2.2 *A Priori* Channel Estimation MSE in the Context of Ideal, Error-Free Symbol Decisions Assuming a Sample-Spaced CIR

The simulation results to be presented in this section characterize the average *a priori* channel transfer factor estimation MSE, which is a by-product of the iterative optimization of the CIR-related tap predictor coefficients with the aid of the algorithm outlined in Section 3.4.1.6.

In order to reduce the number of different parameter combinations to be investigated, we stipulate here a simplified scenario, as described in Section 3.4.1.6.1, where identical transmit powers, modulation modes and channel statistics are associated with the different users. More specifically, all users are assumed to employ MPSK modulation which renders the so-called modulation-mode enhancement factor equal to $\alpha_{\text{M-PSK}} = 1$. Unless otherwise stated, the specific channel statistics invoked were that of the channel's spaced-time correlation function provided by Jakes model, as given by Equation 3.141.

Furthermore, we considered 'frame-invariant' fading, where the fading envelope of each CIR-related tap has been kept constant during each OFDM symbol's transmission period. This avoided the obfuscating effects of inter-subcarrier interference and hence enabled us to study the various channel transfer function estimation effects in isolation.

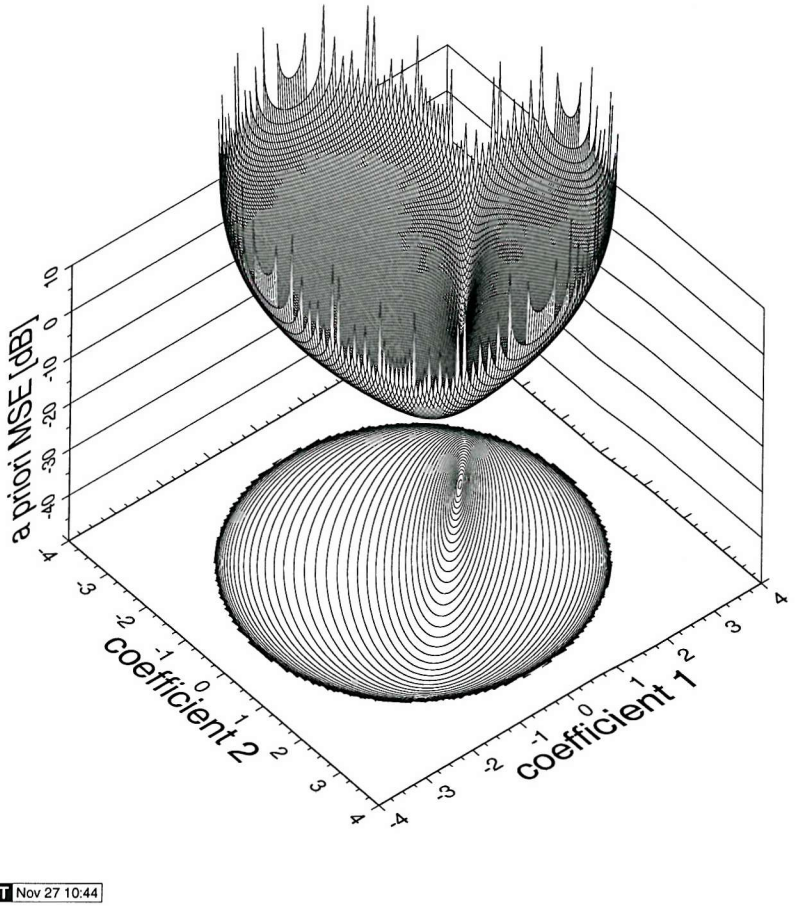

Figure 3.4: Evolution of the *a priori* channel estimation MSE according to Equation 3.133 associated with the simplified scenario of Section 3.4.1.6.1 as a function of the real-valued coefficients of the 2-tap CIR-related tap predictor employed in this particular example. The number of subcarriers was $K = 512$, while the number of significant CIR-related taps was $K_0 = 16$ in the context of a sample-spaced CIR. Furthermore, the number of users was $L = 4$ and the OFDM symbol normalized Doppler frequency was $F_D = 0.1$. The spaced-time channel correlation function of Equation 3.143, associated with a uniform, ideally support limited Doppler power spectrum was invoked. The SNR at the reception antenna was equal to 20dB.

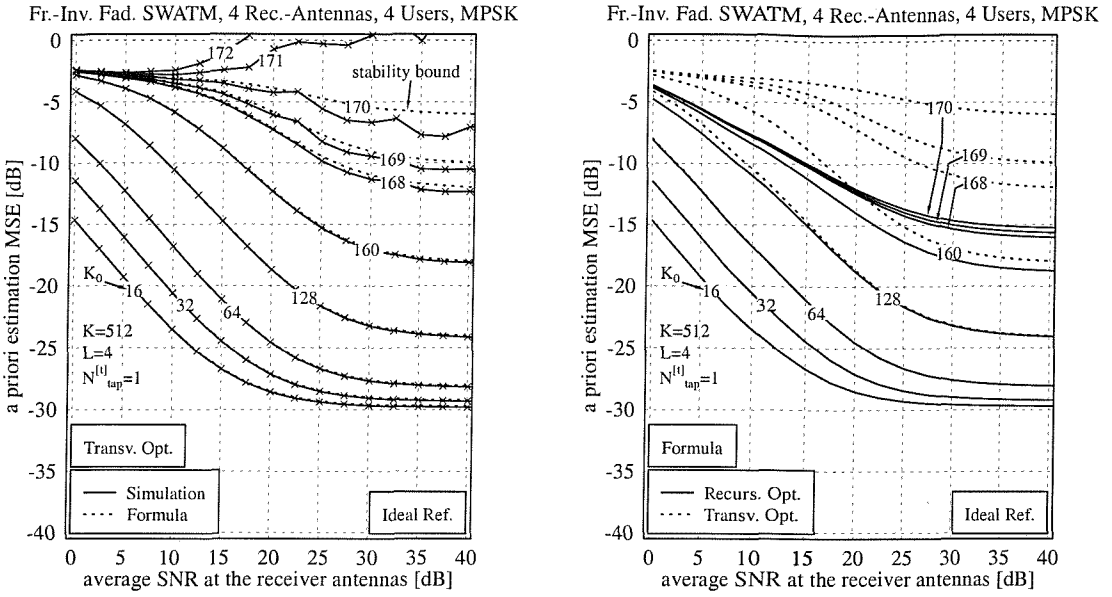

Figure 3.5: (Left:) Comparison between the *a priori* channel estimation MSE versus SNR performance, generated by an analytical evaluation of Equation 3.133 as well as that obtained by Monte-Carlo simulations for the PIC-assisted DDCE of Figure 3.3 in the context of one-tap CIR-related tap prediction filtering invoking the *sub-optimum transversal predictor coefficient* according to Equation 3.139. (Right:) Comparison between the *a priori* channel estimation MSE versus SNR performance exhibited by the PIC-assisted DDCE in the context of one-tap prediction filtering, again, upon invoking the sub-optimum transversal predictor coefficient according to Equation 3.139 or alternatively the *optimum recursive predictor coefficient* according to Equation 3.137. The curves are parameterized with the number of significant CIR-related taps K_0. Each of the SDMA scenario's independently faded channels is characterized by the indoor WATM channel parameters of Section 6.1.1.

The further structure of Section 3.4.2.2 is as follows: In Sections 3.4.2.2.1 and 3.4.2.2.2 a comparison in terms of the *a priori* estimation MSE between employing the optimum recursive predictor coefficients and the sub-optimum transversal predictor coefficients - obtained upon setting the $(L-1)$ number of feedback signals in Equations 3.133 and 3.135 equal to zero. In Section 3.4.2.2.1 we will use a one-tap predictor while in Section 3.4.2.2.2 higher-order predictors. While furthermore in Section 3.4.2.2.3 the influence of the number of simultaneous users on the *a priori* estimation MSE is investigated, in Sections 3.4.2.2.4 and 3.4.2.2.5 the influence of the OFDM symbol normalized Doppler frequency under matched and mismatched channel conditions is portrayed, respectively. Finally, in Section 3.4.2.2.6 a performance comparison to Li's LS-assisted DDCE of Section 3.3 is conducted.

3.4.2.2.1 Optimum Recursive versus Sub-Optimum Transversal CIR-Related Tap Predictor Coefficients - One Tap In the left-hand graph of Figure 3.5 we have portrayed the average *a priori* channel transfer factor estimation MSE exhibited by the PIC-assisted DDCE in the context of

one-tap CIR-related tap prediction filtering. The single predictor coefficient was calculated with the aid of the - in this context sub-optimum transversal filter related Wiener solution of Equation 3.139, while the associated MSE was evaluated with the aid of Monte-Carlo simulations (labelled as "Simulation") as well as by direct evaluation of Equation 3.133 (labelled as "Formula"). We observe that both our analytical evaluations, as well as the simulations result in a similar MSE performance, thus supporting the validity of our derivations. When increasing the K_0 number of significant CIR taps, the *a priori* estimation MSE degrades, since the effects of the AWGN and of the additional noise due to channel variations are less mitigated. Note from Equation 3.139 that for sufficiently high SNRs the sub-optimum transversal filter related coefficient approaches the value of the channel's spaced-time correlation function for a unity time-lag, which is in turn close to unity for the relatively slowly fading channels of $f_D = 0.007$ considered here. Hence, following from Equation 3.134, the maximum value of K_0, which guarantees a stable operation in the absence of symbol errors in the context of a scenario having $K = 512$ MPSK modulated ($\alpha = 1$) subcarriers and $L = 4$ simultaneous users each equipped with a single transmit antenna is $\lceil K_0 \rceil = 170$. This is also reflected by the curves in the left-hand graph of Figure 3.5.

By contrast, in the right-hand graph of Figure 3.5 we have compared - for the same scenario - the average *a priori* channel transfer factor estimation MSE achieved with the aid of the optimum CIR-related tap predictor coefficient given by Equation 3.137, which takes into account the recursive structure of the PIC-assisted DDCE, against the *a priori* estimation MSE offered by a system employing the suboptimum transversal filter based predictor coefficient of Equation 3.139. Both sets of curves have been obtained by direct evaluation of Equation 3.133 ("Formula"), upon assuming error-free symbol decisions. The results suggest that upon employing the optimum recursive predictor coefficient, the system's stability is increased for relatively high values of $\chi \cdot (L-1)$ in the sense of Equation 3.134.

3.4.2.2.2 Optimum Recursive- versus Sub-Optimum Transversal CIR-related Tap Predictor Coefficients - Higher Order Following the approach of Figure 3.5, in Figure 3.6 we have compared the average *a priori* channel transfer factor estimation MSE achieved using the optimum recursive CIR-related tap predictor coefficients which were evaluated with the aid of the iterative approach of Section 3.4.1.6 upon capitalizing on the simplified Equations of Section 3.4.1.6.1 against the - in this context suboptimum - transversal filter coefficients provided by Equation 3.136. Two different predictor lengths, namely four- and eight taps are employed and the curves are additionally parameterized with the number of significant CIR-related taps. Again, we observe that the optimum recursive predictor coefficients allow us to avoid the problem of instability, which was potentially incurred in conjunction with the sub-optimum transversal predictor coefficients.

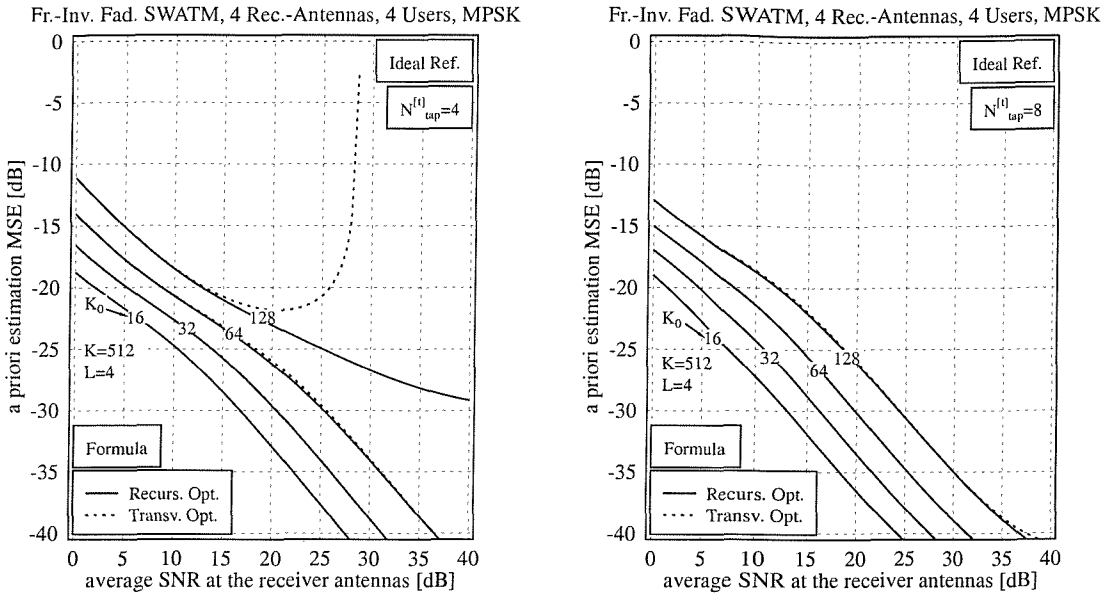

Figure 3.6: *A priori* channel estimation MSE versus SNR performance exhibited by the PIC-assisted DDCE of Figure 3.3 in the context of (Left:) four-tap- and (Right:) eight-tap CIR-related tap prediction filtering upon invoking the *optimum recursive predictor coefficients* evaluated with the aid of the iterative approach of Section 3.4.1.6 on the basis of the simplified equations of Section 3.4.1.6.1. Again, we have plotted the *a priori* channel estimation MSE performance achieved with the aid of the - in this case - sub-optimum transversal predictor coefficients of Equation 3.136 as a reference. The curves are parameterized with the number of significant CIR-related taps K_0. Each of the SDMA scenario's independently faded channels is characterized by the indoor WATM channel parameters of Section 6.1.1.

3.4.2.2.3 Influence of the Number of Simultaneous Users in the Context of the Optimum Recursive CIR-Related Tap Predictor Coefficients So far we considered the scenario of four simultaneous users, each equipped with a single transmit antenna. From the perspective of the number of channels to be estimated this is equivalent to a space-time coded (STC) scenario of two simultaneous users each employing two transmit antennas or to an STC scenario of a single user employing four transmit antennas. Based on this analogy, it is worth investigating, whether the PIC-assisted DDCE approach advocated here is capable of supporting scenarios of a higher complexity in terms of the $L \times P$ number of channels involved. In Figure 3.7 we have plotted the average *a priori* channel transfer factor estimation MSE as a function of the L number of simultaneous users, assuming a four- or eight-tap CIR-related tap prediction filter and a fixed number of $K_0 = 64$ significant CIR-related taps. This associated CIR duration corresponds to 12.5% of the duration of a 512-subcarrier OFDM symbol's time-domain representation. This may be viewed as the relative upper bound of the CIR length in a well-designed OFDM system. Here we capitalized again on the idealistic assumption of error-free symbol decisions. We observe in Figure 3.7 that the *a priori* channel estimation MSE performance is degraded upon increasing the number of users supported.

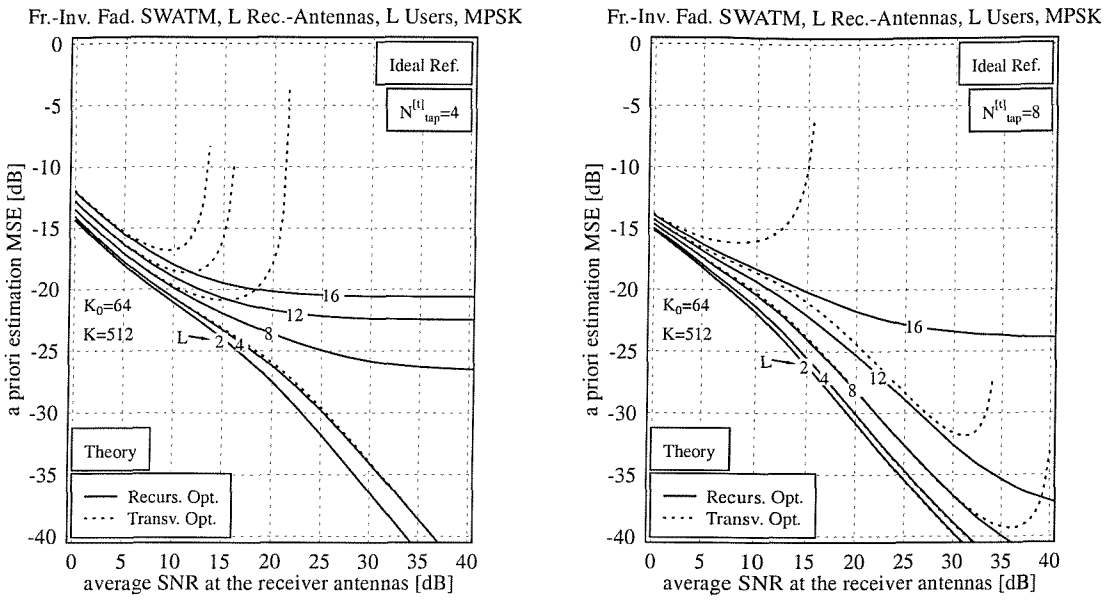

Figure 3.7: *A priori* channel estimation MSE versus SNR performance exhibited by the PIC-assisted DDCE of Figure 3.3 in the context of (Left:) four-tap- and (Right:) eight-tap CIR-related tap prediction filtering upon invoking the *optimum recursive predictor coefficients* evaluated with the aid of the iterative approach of Section 3.4.1.6 on the basis of the simplified equations of Section 3.4.1.6.1. Again, we have plotted the *a priori* channel estimation MSE performance achieved with the aid of the - in this case - sub-optimum transversal predictor coefficients of Equation 3.136 as a reference. The curves are parameterized with the L number of simultaneous users, while the K_0 number of significant CIR taps was kept constant. Each of the SDMA scenario's independently faded channels is characterized by the indoor WATM channel parameters of Section 6.1.1.

This is, because more multiuser interference related noise is inflicted by the *a posteriori* channel estimates during the PIC process, which is then injected into the *a priori* channel estimates' prediction process. As a comparison between the MSE curves corresponding to the four-tap and eight-tap prediction arrangements suggests, these effects can be mitigated by increasing the predictor's range. Again, we observe that in the context of the sub-optimum transversal predictor coefficients the PIC-assisted DDCE tends to become unstable at higher SNRs.

3.4.2.2.4 Influence of the OFDM Symbol Normalized Doppler Frequency In the context of our previous assessment a fixed OFDM symbol-normalized Doppler frequency of $F_D = 0.007$ was assumed. By contrast, in this section we will investigate the influence of the OFDM symbol normalized Doppler frequency on the average *a priori* channel transfer factor estimation MSE for different CIR-related tap predictor lengths of $N_{tap}^{[t]}$. The results of our analytical evaluations are portrayed in Figure 3.8, both for an SNR of 20dB measured at the reception antennas and for an SNR of 40dB. For both SNRs we observe that the *a priori* channel estimation MSE recorded at a given OFDM symbol normalized Doppler frequency improves only marginally upon increasing

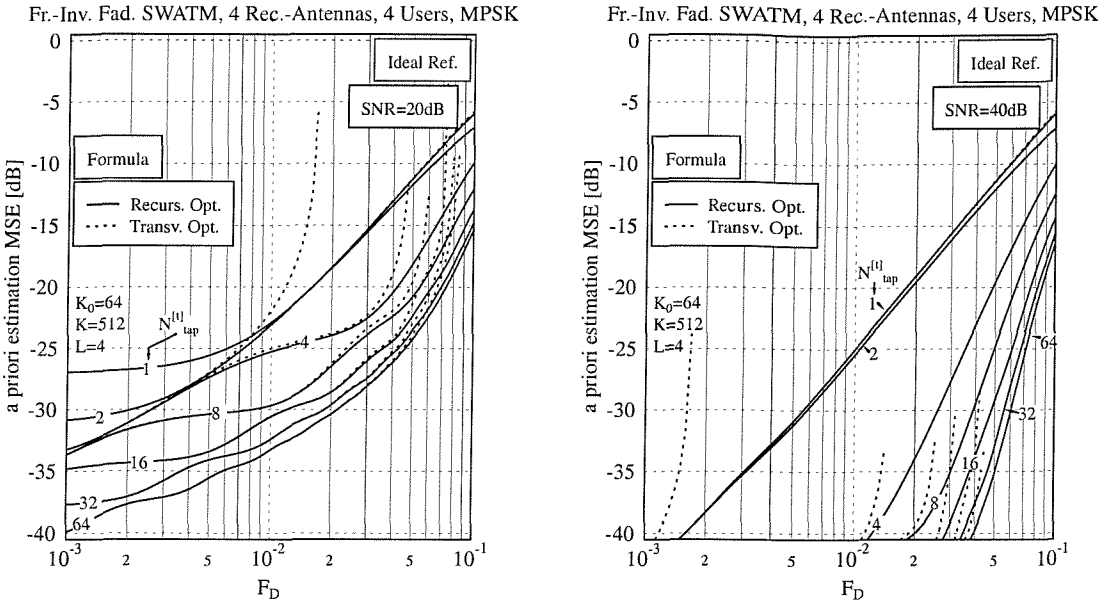

Figure 3.8: *A priori* channel estimation MSE versus OFDM symbol normalized Doppler frequency performance exhibited by the PIC-assisted DDCE of Figure 3.3 in the context of an SNR of (Left:) 20dB and (Right:) 40dB at the reception antennas upon invoking the *optimum recursive CIR-related tap predictor coefficients* evaluated with the aid of the iterative approach of Section 3.4.1.6 on the basis of the simplified equations of Section 3.4.1.6.1. Again, we have plotted the *a priori* channel estimation MSE performance achieved with the aid of the - in this case - sub-optimum transversal predictor coefficients of Equation 3.136 as a reference. The curves are parameterized with the $N_{tap}^{[t]}$ number of predictor taps, while the K_0 number of significant CIR-related taps was kept constant. Each of the SDMA scenario's independently faded channels is characterized by the indoor WATM channel parameters of Section 6.1.1.

the predictor length beyond a value of about 32 taps, for which most of the channel's correlation is exploited. Furthermore, we infer that the predictor's length should be at least four taps, in order to achieve a significant reduction of the *a priori* channel estimation MSE compared to the case of one-tap filtering. Note furthermore in Figure 3.8 that in the higher-SNR scenario of 40dB the MSE reduction due to employing a higher number of CIR-related predictor taps is even more dramatic than in the lower SNR scenario. This is, because the MMSE predictor strikes a trade-off between the mitigation of the AWGN and the exploitation of the channel's correlation between the channel transfer functions experienced by successive OFDM symbols.

So far we have assumed a perfect matching between the channel statistics invoked in the calculation of the predictor coefficients and that of the channel. By contrast, in the next section we investigate the effects of a mismatch with respect to the maximum Doppler frequencies.

3.4.2.2.5 Influence of a Mismatch of the OFDM Symbol Normalized Doppler Frequency In our previous investigations we employed a Doppler power spectrum according to Jakes' model

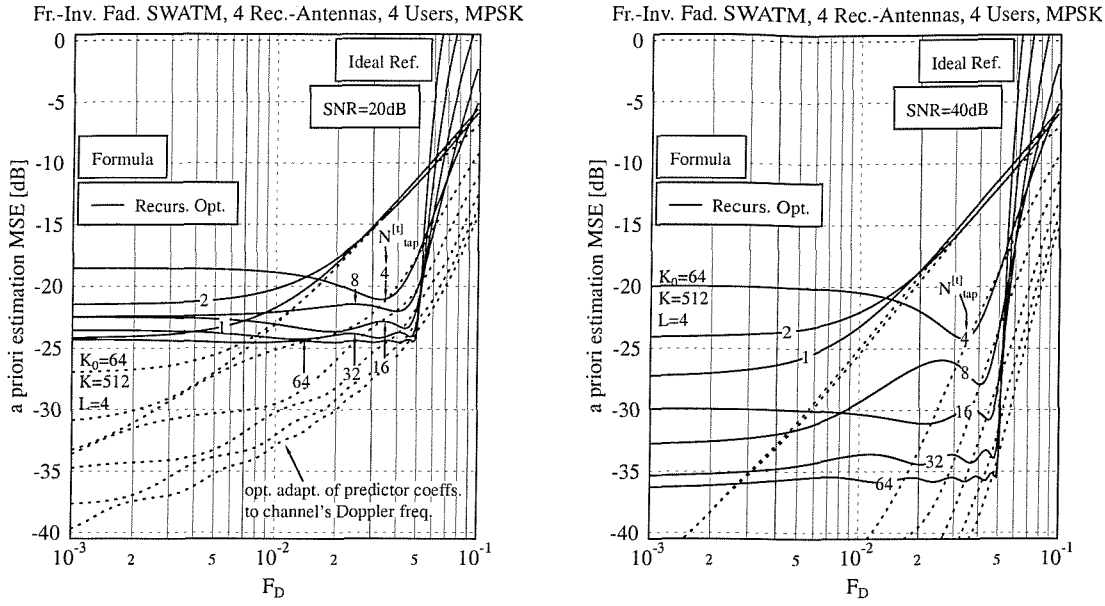

Figure 3.9: *A priori* channel estimation MSE versus OFDM symbol normalized Doppler frequency performance exhibited by the PIC-assisted DDCE of Figure 3.3 in the context of an SNR of (Left:) 20dB and (Right:) 40dB at the reception antennas upon invoking a fixed vector of recursive CIR-related tap predictor coefficients optimized for an OFDM symbol normalized Doppler frequency of $\tilde{F}_D = 0.05$ with the aid of the iterative approach of Section 3.4.1.6 on the basis of the simplified equations of Section 3.4.1.6.1. As in previous graphs, a Jakes spectrum-related spaced-time correlation function obeying Equation 3.141 was associated with the channel. The predictor coefficients were calculated on the basis of the spaced-time correlation function of Equation 3.143 associated with a uniform, ideally support-limited Doppler power spectrum. Furthermore, we have also plotted the MSE curves corresponding to predictor coefficients optimized for the channel's Doppler frequency as a reference. The MSE curves are parameterized with the $N^{[t]}_{tap}$ number of prediction filter taps, while K_0, namely the number of significant CIR-related taps was fixed. Each of the SDMA scenario's independently faded channels is characterized by the indoor WATM channel parameters of Section 6.1.1.

[90] which is related to a spaced-time channel correlation function given by the zero-order Bessel function of its first kind, as shown in Equation 3.141. Jakes' model was employed both for the derivation of the CIR-related tap predictor coefficients as well as in the "simulated" channel used for evaluating the *a priori* channel estimation MSE. The maximum Doppler frequency used for the calculation of the predictor coefficients as well as for the simulated channel was identical.

In order to render a transversal filter-assisted channel estimator insensitive against the variations of the maximum OFDM symbol normalized Doppler frequency associated with the channel, compared to that imposed in the calculation of the filter coefficients, it was proposed in [57, 17] to invoke a uniform, ideally support-limited Doppler power spectrum in the calculation of the filter coefficients, having a maximum OFDM symbol normalized Doppler frequency higher than that of the channel. Recall that the same 'robust' DDCE was also used in Section 2.3 for single-user

channel estimation. It was argued in [17] that in this case, regardless of the specific shape of the "true" Doppler power spectrum associated with the channel, the channel estimator would exhibit the same channel estimation MSE performance, as if a uniform, ideally support-limited Doppler spectrum was assumed *both* in the evaluation of the filter coefficients, as well as for the channel encountered. Also note that in this case the channel estimator's MSE performance represented the worst-case MSE performance that might be encountered when communicating over channels having non-uniform Doppler power spectra, but using optimally adapted filter coefficients. Furthermore, note from [17] that the MSE performance difference observed between the scenario, where Jakes' Doppler spectrum is associated both with the channel encountered as well as with the computation of the filter coefficients and the case, where a uniform, ideally support-limited Doppler power spectrum is associated with both the channel encountered and with the computation of the filter coefficients, is marginal.

As it will be highlighted in the context of our forthcoming discussions, the channel estimator's insensitivity with respect to the channel's Doppler power spectral shape is valid only upon employing an infinite number of predictor taps. Naturally, in practical situations this is not the case.

In Figure 3.9 we have portrayed the average *a priori* channel transfer factor estimation MSE versus OFDM symbol normalized Doppler frequency performance of the recursive estimator of Figure 3.3 in the context of employing a uniform, ideally support-limited Doppler power spectrum having a spaced-time correlation function obeying Equation 3.143 in the calculation of the CIR-related tap predictor coefficients. Furthermore, as in our previous investigations of Section 3.4.2.2 a Doppler power spectrum obeying Jakes' model [90] and having a spaced-time correlation function given by Equation 3.141 was associated with the channel. In our particular example the predictor coefficients were calculated upon invoking once again, the iterative approach of Section 3.4.1.6 for an OFDM symbol normalized Doppler frequency of $\tilde{F}_D = 0.05$. Furthermore, as a reference we have also plotted the *a priori* channel estimation MSE performance in the context of predictor coefficients, which were optimized for the channel's specific Doppler frequency. As reported in [17] and also observed in Figure 3.9 upon increasing the number of predictor taps the *a priori* channel estimation MSE is rendered quasi-invariant for OFDM symbol normalized Doppler frequencies on the channel, which are lower than that assumed in the calculation of the CIR-related tap predictor coefficients, namely $\tilde{F}_D = 0.05$. By contrast, for higher Doppler frequencies a rapid degradation of the MSE is observed in Figure 3.9. This 'robustness' is achieved at the cost of a potentially significant loss in performance compared to the case of optimally adapted predictor coefficients. To give an example, for an SNR of 20dB and for 64 predictor coefficients the *a priori* channel estimation MSE performance loss is as high as 10dB at an OFDM symbol normalized Doppler frequency of $F_D = 0.007$, when the predictor coefficients were designed for $\tilde{F}_D = 0.05$.

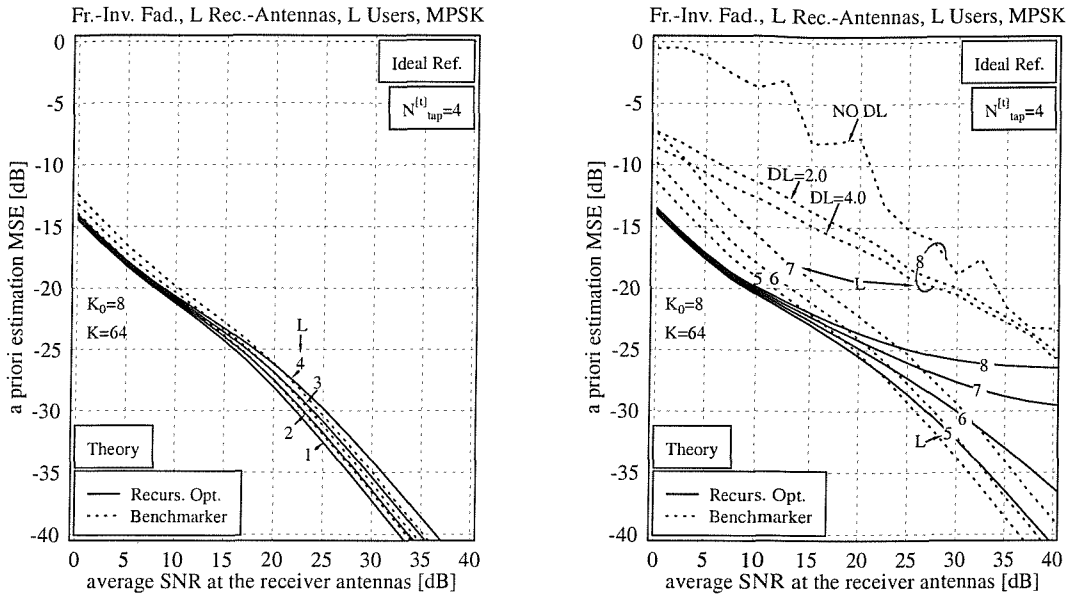

Figure 3.10: *A priori* channel estimation MSE versus SNR at the reception antennas exhibited by the LS-assisted DDCE [21] of Figure 3.2 outlined in Section 3.3 and by the PIC-assisted DDCE of Figure 3.3 seen in Section 3.4, for a number of users L ranging between (left:) one to four and (right:) five to eight, in the context of $N_{tap}^{[t]}$ = 4-tap *a priori* CIR-related tap prediction filtering for an OFDM symbol normalized Doppler frequency of $F_D = 0.007$. A Jakes spectrum-related spaced-time correlation function was associated with both the channel encountered as well as with the calculation of the predictor coefficients. Note that in contrast to our previous discussions we have assumed here $K = 64$ and $K_0 = 8$. 'DL' indicates Diagonal Loading of the matrix $\mathbf{Q}[n]$ defined in Equation 3.20 in order to support its invertibility.

3.4.2.2.6 Performance Comparison to Li's LS-Assisted DDCE In this section we will evaluate the *a priori* channel estimation MSE exhibited by the LS-assisted DDCE of Figure 3.2 proposed by Li *et al.* [21] capitalizing on a direct inversion of the correlation matrix $\mathbf{Q}[n]$ of the different users' transmitted subcarrier symbol sequences' as outlined in Section 3.3. We will then compare the performance of Li's LS-assisted DDCE against the MSE performance achieved by the PIC-assisted DDCE of Figure 3.3. In both cases we have employed a $N_{tap}^{[t]}$ = 4-tap CIR-related tap predictor, where in the context of the LS-assisted DDCE of Figure 3.2 the optimum predictor coefficients were obtained by direct solution of the Wiener equation, while for the PIC-assisted DDCE of Figure 3.3 the predictor coefficients were optimized with the aid of the iterative approach portrayed in Section 3.4.1.6. Note that in contrast to our performance results presented in previous sections for $K = 512$, here we have assumed $K = 64$ subcarriers and $K_0 = 8$ significant CIR-related taps. It can be argued that from the perspective of an AWGN reduction in the context of the sample-spaced CIRs considered here, this system is equivalent to the scenario of $K = 512$ and $K_0 = 64$. However, in the latter case the correlation matrix $\mathbf{Q}[n]$ of Equation 3.20 employed in the LS-assisted DDCE would be of potentially excessive dimension, depending on the number of users

L. Hence $K = 512$ and $K_0 = 64$ would result in a complexity, which would be impractical in terms of our simulations. More specifically, our aim in this section is also to demonstrate the deficiencies associated with the direct inversion of the correlation matrix $\mathbf{Q}[n]$, namely that error amplification may be encountered, when the matrix becomes rank deficient[12]. This is observed upon increasing the L number of simultaneous users supported in conjunction with a fixed value of K_0.

Our corresponding simulation results are portrayed in Figure 3.10. On the left-hand side we presented results for a number of simultaneous users ranging between one and four while on the right hand side for five to eight users. For a lower number of users we observe in the left illustration of Figure 3.10 that up to SNRs of about 15dB measured at the reception antennas the PIC-assisted DDCE of Figure 3.3 performs slightly better, while at higher SNRs the LS-assisted DDCE of Figure 3.2 exhibits a slight performance advantage. The reason for these performance trends is that at lower SNRs the multi-user interference (MUI) imposed, when the matrix $\mathbf{Q}[n]$ has non-zero off-diagonal elements results in a degradation of the MSE of the LS-assisted DDCE shown in Figure 3.2, while at higher SNRs the effects of imperfect CIR-related tap prediction yield an increased MUI in the PIC-assisted DDCE, again, as seen in Figure 3.10. This effect becomes more obvious upon further increasing the number of simultaneous users L, as shown in the right-hand side illustration of Figure 3.10. Note that the less attractive performance exhibited by the LS-assisted DDCE is due to two effects. First of all the effects of MUI are more pronounced due to the higher number of users supported and secondly, the imperfections of the direct numerical inversion of the correlation matrix $\mathbf{Q}[n]$ of Equation 3.20 carried out here in the context of our *simulations* contributes to the significant MSE degradation. This is, because matrices of the form - $\mathbf{Q}[n] = \mathbf{A}^H[n]\mathbf{A}[n]$ as encountered in the context of calculating the Moore-Penrose inverse [87] $\mathbf{A}^\dagger[n]$ of $\mathbf{A}[n]$ - exhibit a potentially high condition number $\kappa(\mathbf{A}[n])$, where the condition number indicates the degree to which a matrix is ill-conditioned- or close to rank-deficiency [87]. Note again that specifically in the context of least-squares estimation problems the direct inversion of the correlation matrix $\mathbf{Q}[n] = \mathbf{A}^H[n]\mathbf{A}[n]$ and the associated deficiencies can be mitigated with the aid of the QR matrix factorization [87].

3.4.2.3 Effects of a Non-Sample Spaced CIR in the Context of Ideal, Error-Free Symbol Decisions

In Equations 3.126 and 3.132 as well as correspondingly also in Equations 3.133 and 3.135 associated with the simplified scenario of identical transmit powers and identical channel statistics, we observe that the evaluation of the optimum CIR-related tap predictor coefficients with the aid of the iterative approach described in Section 3.4.1.6 relies on the *a priori* knowledge of the term $\text{Trace}(\Upsilon^{[f](j)}\mathbf{I}_{K_0}^{(j)})$ associated with the j-th user, where $j = 1, \ldots, L$.

Our analytical evaluations in Section 3.4.2 were conducted so far under the assumption of a

[12]A square matrix is referred to as rank deficient, if the number of linearly independent rows or columns is lower than the number of rows or columns.

sample-spaced CIR. Using a sample-spaced CIR facilitates the recovery of almost all the energy of the channel's output, upon invoking a finite number of K_0 significant taps, despite the fact that K_0 is potentially smaller than the total number of K available CIR-related taps. In this case we have $\text{Trace}(\Upsilon^{[f](j)}\mathbf{I}_{K_0}^{(j)}) = K\sigma_H^2$. By contrast, in the context of the more realistic scenario of a non-sample-spaced CIR the energy conveyed by the channel is distributed over a higher number of CIR-related taps, i.e. it potentially 'leaks' to all CIR-related taps. This is particularly the case when employing the DFT matrix $\mathbf{W}$ as the unitary transform matrix. While $\text{Trace}(\Upsilon^{[f](j)}) = K\sigma_H^2$ still holds, we potentially incur $\text{Trace}(\Upsilon^{[f](j)}\mathbf{I}_{K_0}^{(j)}) < K\sigma_H^2$ for $K_0 < K$. The motivation for choosing $K_0 < K$ is twofold, namely that of reducing the predictor's complexity, but also for further reducing the noise in the context of the *simplified predictor design* of Section 3.4.1.6.1 employed here, relying on identical predictor coefficients for each of the different CIR-related taps.

Our further efforts in characterizing the *a priori* channel estimation MSE performance in the context of non-sample-spaced CIRs will concentrate on three different types of power-delay profiles, namely, what we refer to as sparse profiles, uniform profiles and exponential profiles. These profiles will be outlined in Sections 3.4.2.3.1, 3.4.2.3.2 and 3.4.2.3.3. On the basis of these profiles we will then assess the PIC-assisted DDCE's average - as well as the subcarrier based - *a priori* channel transfer factor estimation MSE in Sections 3.4.2.3.4 and Section 3.4.2.3.5, respectively.

3.4.2.3.1 Sparse Profiles Here we define as a sparse multipath intensity profile a finite number of Dirac impulses, each characterized by its delay τ_i and variance $\sigma_{h,i}^2$, which is formulated as:

$$r_{h,\text{spar}}(\tau) = \sum_i \sigma_{h,i}^2 \delta(\tau - \tau_i). \tag{3.145}$$

We impose the condition that the sum of the multipath intensity profile's different tap variances is unity:

$$\sum_i \sigma_{h,i}^2 = 1, \tag{3.146}$$

which implies that no energy is lost or gained during the signal's transmission over the channel. By applying the Fourier transform to Equation 3.145, the spaced-frequency correlation function of the associated multipath intensity profile is obtained:

$$r_{H,\text{spar}}(\Delta f) = \sum_i \sigma_{h,i}^2 e^{-j2\pi\tau_i\Delta f}. \tag{3.147}$$

In the context of employing the DFT matrix $\mathbf{W}$ as the unitary transform matrix $\tilde{\mathbf{U}}^{[f]}$ it can be shown that the element $[n_1, n_2]$ of the matrix $\Upsilon_{\text{spar}}^{[f]}$, which is the result of the decomposition of the spaced-frequency correlation matrix $\mathbf{R}_{\text{spar}}^{[f]}$ with respect to $\tilde{\mathbf{U}}^{[f]}$, which is formulated as $\Upsilon_{\text{spar}}^{[f]} = \tilde{\mathbf{U}}^{[f]H}\mathbf{R}_{\text{spar}}^{[f]}\tilde{\mathbf{U}}^{[f]}$, is given by [66]:

$$\Upsilon_{\text{spar}}^{[f]}[n_1, n_2] = \frac{1}{K}\sum_i \sigma_{h,i}^2 e^{-j\frac{K-1}{K}\pi(n_1-n_2)} \frac{\sin(\pi\acute{n}_1)\cdot\sin(\pi\acute{n}_2)}{\sin(\pi\frac{\acute{n}_1}{K})\cdot\sin(\pi\frac{\acute{n}_2}{K})}, \tag{3.148}$$

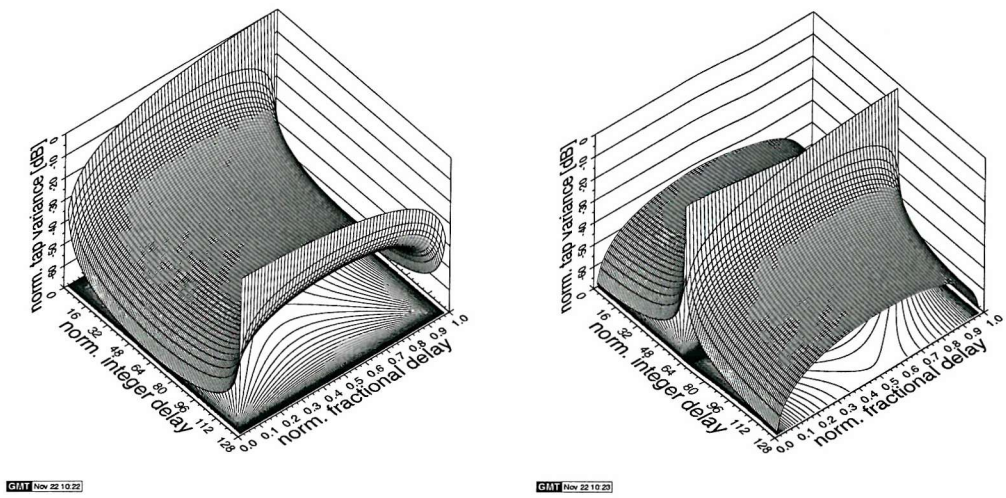

(a) norm. integer delay: -1 **(b)** norm. integer delay: 64

Figure 3.11: Illustration of the normalized leakage across the diagonal elements of the decomposition $\Upsilon_{\text{spar}}^{[f]}$ of $\mathbf{R}_{\text{spar}}^{[f]}$ with respect to $\tilde{\mathbf{U}}^{[f]} = \mathbf{W}$ in the context of a CIR exhibiting a single tap of unit variance, characterized by its normalized integer- and fractional delay. The normalization of the diagonal elements of $\Upsilon_{\text{spar}}^{[f]}$ was carried out with respect to the $K = 128$ number of subcarriers, while the normalization of the single CIR tap's integer- and fractional delay was performed with respect to the sampling period duration T_s.

where $\acute{n}_1 = \frac{\tau_i}{T_s} - n_1$ and $\acute{n}_2 = \frac{\tau_i}{T_s} - n_2$ and T_s is the sampling period duration. For the diagonal elements of $\Upsilon_{\text{spar}}^{[f]}$, identified by the condition of $n_1 = n_2$, Equation 3.148 simplifies to:

$$\Upsilon_{\text{spar}}^{[f]}[n_1, n_1] = \frac{1}{K} \sum_i \sigma_{h,i}^2 \frac{\sin^2(\pi \acute{n}_1)}{\sin^2(\pi \frac{\acute{n}_1}{K})}. \tag{3.149}$$

With the aid of Equation 3.149 we have evaluated the influence of the fractional component of a single CIR tap's delay with respect to the sampling period duration T_s on the leakage[13] experienced by neighbouring integer delay taps in the context of employing the DFT matrix $\mathbf{W}$ as the unitary transform matrix $\tilde{\mathbf{U}}^{[f]}$ in the sense of Equation 3.108. Recall that Equation 3.149 reflects the n_1-th CIR-related tap's variance, where $n_1 = 0, \ldots, K-1$. The results - normalized to the K number of subcarriers - are portrayed in Figure 3.11 on the left-hand side for a normalized integer delay of -1 tap or, equivalently, 127 taps and on the right-hand side for a normalized integer delay of 64 taps. Let us concentrate here on the second figure, namely that of a normalized integer delay of 64 taps associated with the single CIR tap employed. For an additional fractional delay of 0 all of the

[13] Although as in our experiments the CIR might consist of a single non-sample-spaced tap only, after transforming the associated set of K different subcarriers' channel transfer factors to the CIR-related domain with the aid of the unitary transform $\tilde{\mathbf{U}}^{[f]}$ as shown in Equation 3.108, all of the transform's output taps are potentially non-zero. This effect is referred to as leakage.

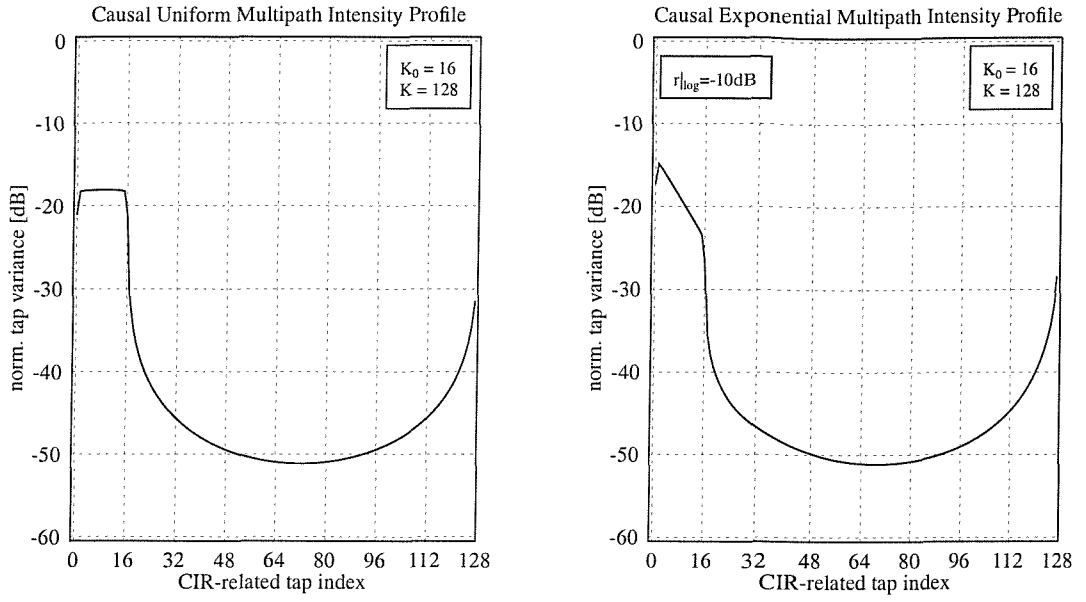

Figure 3.12: Illustration of the normalized leakage among the diagonal elements of the decomposition $\Upsilon^{[f]}$ of $\mathbf{R}^{[f]}$ with respect to $\tilde{\mathbf{U}}^{[f]} = \mathbf{W}$ in the context of a (left:) uniform multipath intensity profile or (right:) exponential multipath intensity profile. Both profiles exhibited the same total sampling period duration normalized multipath spread of $T_m/T_s = 16$. The normalization of the diagonal elements of $\Upsilon^{[f]}$ was carried out with respect to the $K = 128$ number of subcarriers.

single CIR tap's energy is projected onto the diagonal element of the matrix $\Upsilon^{[f]}_{\text{spar}}$ at index 64, or on the equivalent tap in the output of the unitary inverse linear transform following the philosophy of Equation 3.108. Upon increasing the additional normalized fractional delay, more of the CIR-tap's energy is conveyed to the tap at the index 65 and the other surrounding taps. Specifically, for a normalized fractional delay of 0.5 both contributions, namely that of the 64-th and 65-th tap are identical. Upon further increasing the normalized fractional delay to unity, all of the single CIR tap's energy is projected onto the 65-th CIR-related tap. Also note the cyclic symmetry of the figures with respect to the integer delay.

3.4.2.3.2 Uniform Profiles While in the previous section we considered sparse profiles having discrete delay taps, let us now focus on a continuous uniform power delay profile, which is characterized by the following equation:

$$r_{h,\text{unif}}(\tau) = \frac{1}{T_m}\text{rect}\left(\frac{\tau - \tau_{shift}}{T_m}\right), \tag{3.150}$$

where T_m is the associated delay spread of the channel and τ_{shift} denotes the average delay with respect to the origin of the time-axis. Normalization to the multipath spread T_m ensures that the energy transfer factor of the CIR, which is the integral of the multipath intensity profile across its region of support, where it exhibits non-zero values, is equal to unity. This implies that no

energy is gained or lost during transmission over the channel. Also note that for an average delay of $\tau_{shift} = T_m/2$ an "ideally causal" delay profile is obtained. The spaced-frequency correlation function is given as the Fourier Transform (FT) of the power delay profile, yielding the expected sinc-shaped function of:

$$r_{H,\text{unif}}(\Delta f) = si(\pi T_m \Delta f) \cdot e^{-j2\pi\tau_{shift}\Delta f}. \tag{3.151}$$

Observe in Equation 3.151 that the higher the delay-spread, the more rapid the frequency-domain fading envelope fluctuation and hence the correlation function decays more rapidly, as a function of the frequency spacing. Similarly to our investigations of the leakage effects due to the CIR's non-sample-spaced nature in the context of a sparse profile, which were conducted in Section 3.4.2.3.1, at the left-hand side of Figure 3.12 we have plotted the normalized variance of the diagonal elements of the decomposition of $\mathbf{R}_{\text{unif}}^{[f]}$ based on $r_{H,\text{unif}}(\Delta f)$ with respect to employing the DFT matrix $\mathbf{W}$ as the unitary transform matrix $\tilde{\mathbf{U}}^{[f]}$, which is expressed mathematically as $\Upsilon_{\text{unif}}^{[f]} = \tilde{\mathbf{U}}^{[f]H}\mathbf{R}_{\text{unif}}^{[f]}\tilde{\mathbf{U}}^{[f]}$. The normalized multipath spread was assumed to be $T_m/T_s = 16$, which corresponds to 16 time-domain OFDM sample durations and the number of subcarriers was $K = 128$. The "u"-shaped evolution of the tap variances seen on the left-hand side of Figure 3.12 for tap indices in excess of $T_m/T_s = 16$ is again a result of the leakage incurred. Note that in contrast to the leakage floor observed in conjunction with the sparse multipath intensity profile hosting in the particular example of Figure 3.11 a single tap only, the leakage floor incurred here is reduced by more than 10dB. This is, because as demonstrated in Figure 3.11 of Section 3.4.2.3.1 for a single Dirac impulse-like CIR, the maximum leakage is observed at a normalized fractional delay of 0.5. By contrast, in the context of the continuous delay profiles considered here we encounter fractional delay components ranging between the values of zero and one. Note that Equation 3.149 suggests an alternative way of obtaining the diagonal elements of $\Upsilon^{[f]}$ for different power delay profiles, namely that of directly integrating the right-hand side of Equation 3.149 with respect to the specific power delay profile, instead of performing the decomposition of the spaced-frequency correlation matrix.

3.4.2.3.3 Exponential Profiles The exponential multipath intensity delay profile is characterized by:

$$r_{h,\text{expo}}(\tau) = \begin{cases} \beta_{\text{expo}} e^{-\alpha_{\text{expo}}\tau} & \text{for } \tau = 0 \leq \tau \leq T_m \\ 0 & \text{otherwise} \end{cases}, \tag{3.152}$$

where the decay factor α_{expo} is determined on the basis of the value of the quotient of $r_{h,\text{expo}}(\tau)$ at a delay of $\tau = 0$ and at $\tau = T_m$, namely:

$$r_{\text{expo}} = \frac{r_{h,\text{expo}}(T_m)}{r_{h,\text{expo}}(0)}, \tag{3.153}$$

yielding:

$$\alpha_{\text{expo}} = -\frac{1}{T_m} ln(r_{\text{expo}}). \tag{3.154}$$

Furthermore the amplitude scaling factor β_{expo} can be determined as a function of α_{expo}, again, based on the condition that the integral of the multipath intensity profile across its region of support is unity, resulting in:

$$\beta_{\text{expo}} = \frac{\alpha_{\text{expo}}}{1 - e^{-\alpha_{\text{expo}} T_m}}. \tag{3.155}$$

The exponential multipath intensity profile's spaced-frequency correlation function is given by the Fourier transform of the multipath intensity profile of Equation 3.152, yielding:

$$r_{H,\text{expo}}(\Delta f) = \frac{\beta_{\text{expo}}}{\alpha_{\text{expo}} + j2\pi\Delta f}[1 - e^{-(\alpha_{\text{expo}} + j2\pi\Delta f)T_m}]. \tag{3.156}$$

Once again, at the right of Figure 3.12 we have plotted the normalized diagonal elements of the decomposition $\Upsilon^{[f]}_{\text{expo}} = \tilde{\mathbf{U}}^{[f]H}\mathbf{R}^{[f]}_{\text{expo}}\tilde{\mathbf{U}}^{[f]}$ of the spaced-frequency correlation matrix $\mathbf{R}^{[f]}_{\text{expo}}$ based on $r_{H,\text{expo}}(\Delta f)$ with respect to $\tilde{\mathbf{U}}^{[f]} = \mathbf{W}$. The normalization was performed with respect to the $K = 128$ number of subcarriers. Furthermore, as in our previous example of a uniform multipath intensity profile discussed in Section 3.4.2.3.2, the normalized delay spread was $T_m/T_s = 16$. Again, the result of our evaluations is portrayed at the right-hand side of Figure 3.12. For a higher number of subcarriers than $K = 128$, the leakage floor observed in Figure 3.12 is expected to be found at lower variance values, which can be demonstrated with the aid of Equation 3.149.

Having demonstrated the effects of non-sample-spaced multipath intensity profiles on the decomposition $\Upsilon^{[f]} = \tilde{\mathbf{U}}^{[f]H}\mathbf{R}^{[f]}\tilde{\mathbf{U}}^{[f]}$ of the associated spaced-frequency correlation matrix $\mathbf{R}^{[f]}$ with respect to the unitary transform matrix $\tilde{\mathbf{U}}^{[f]} = \mathbf{W}$, we will now embark in the next section on a performance assessment of the PIC-assisted DDCE in the context of non-sample-spaced multipath intensity profiles.

3.4.2.3.4 *A Priori* Channel Estimation MSE for a Non-Sample Spaced CIR The PIC-assisted DDCE's average *a priori* channel transfer factor estimation MSE performance was evaluated with the aid of the iterative approach proposed in Section 3.4.1.6. The spaced-frequency correlation matrix $\mathbf{R}^{[f]}$ was calculated on the basis of the spaced-frequency correlation function of Equation 3.147 associated with a sparse multipath intensity profile consisting of only a single non-sample-spaced tap having a normalized integer delay of zero and a normalized fractional delay of 0.5. Following from our discussions in Section 3.4.2.3.1, this particular choice of the CIR ensures that the maximum amount of leakage is generated and hence our performance results constitute the worst-case performance. Alternatively, a spaced-frequency correlation function obeying Equation 3.151, associated with a uniform multipath intensity profile was employed. The normalized multipath spread was set equal to one eighth of the $K = 512$ subcarriers assumed here, namely to $T_m/T_s = 64$.

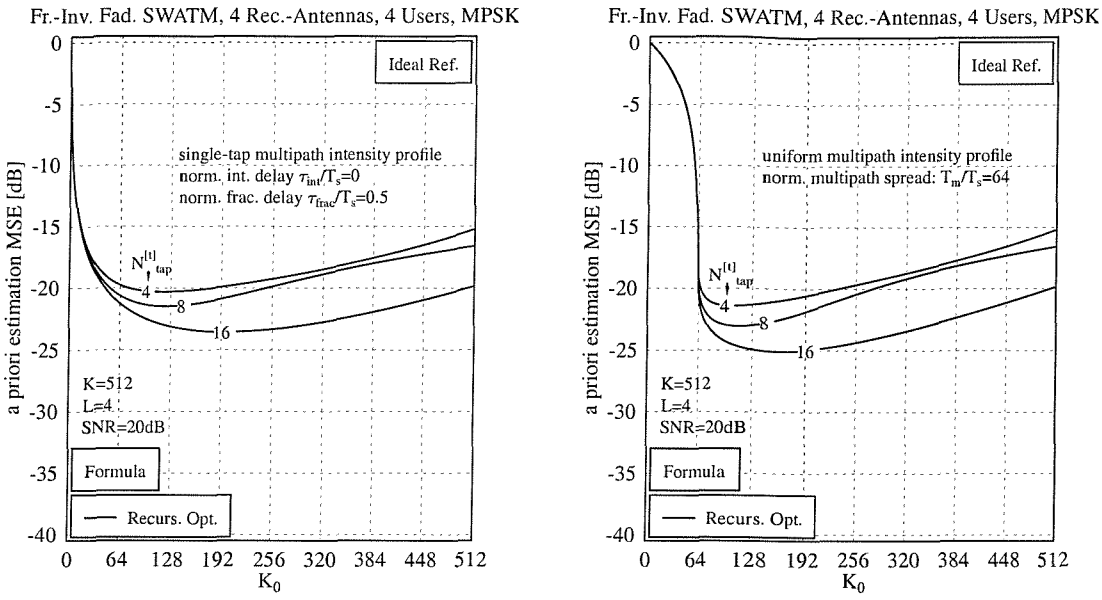

Figure 3.13: *A priori* channel estimation MSE performance of the PIC-assisted DDCE of Figure 3.3 versus the K_0 number of significant CIR-related taps retained in the context of (left:) a single-tap multipath intensity profile having a normalized integer delay of $\tau_{int}/T_s = 0$ and a normalized fractional delay of $\tau_{frac}/T_s = 0.5$ and (right:) a uniform multipath intensity profile having a normalized multipath spread of $T_m/T_s = 64$. The curves are furthermore parameterized with the $N^{[t]}_{tap}$ number of CIR predictor taps. The number of subcarriers was equal to $K = 512$ and the SNR at the reception antennas was assumed to be 20dB.

The knowledge of the factor $\frac{K_0}{\text{Trace}(\Upsilon^{[f](j)}\mathbf{I}^{(j)}_{K0})}$ is a prerequisite for determining both the optimum CIR-related tap predictor coefficients and the *a priori* channel estimation MSE as outlined in Section 3.4.1.6. The factor $\frac{K_0}{\text{Trace}(\Upsilon^{[f](j)}\mathbf{I}^{(j)}_{K0})}$ was evaluated upon selecting the K_0 largest tap variances from the decomposition $\Upsilon^{[f]} = \tilde{\mathbf{U}}^{[f]H}\mathbf{R}^{[f]}\tilde{\mathbf{U}}^{[f]}$ of the specific spaced-frequency correlation matrices of the channel with respect to $\tilde{\mathbf{U}}^{[f](j)} = \mathbf{W}$.

The corresponding *a priori* channel estimation MSE curves are plotted in Figure 3.13 as a function of the K_0 number of significant CIR-related taps. The curves are also parameterized with the $N^{[t]}_{tap}$ number of predictor taps. For both the single-tap and for the uniform multipath intensity profile channel scenarios a rapid improvement of the estimator's MSE is observed upon increasing the K_0 number of significant CIR-related taps up to a certain optimum K_0 value, which is a consequence of retaining more of the channel's energy. At the same time more of the undesired noise is retained since a gradually decreasing fraction of the CIR-related taps are discarded. Upon increasing the K_0 number of significant taps beyond the optimum point seen in Figure 3.13, the opposite behaviour is observed, namely that the MSE is degraded again. This is, because for these taps the benefit of extracting more of the channel's energy is lower, than the penalty incurred due to retaining more

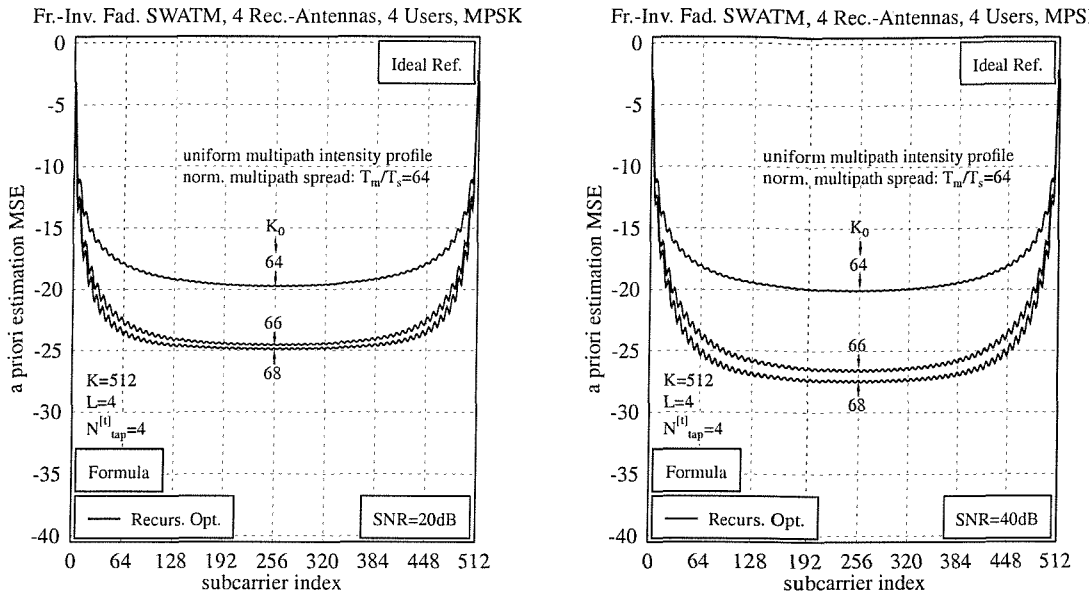

Figure 3.14: *A priori* channel estimation MSE performance versus the subcarrier index exhibited by the PIC-assisted DDCE of Figure 3.3 in the context of a uniform multipath intensity profile with a normalized multipath spread of $T_m/T_s = 64$, at an SNR of (left:) 20dB and (right:) 40dB. The curves are further parameterized with the K_0 number of significant CIR-related taps retained. The number of predictor taps employed was $N_{tap}^{[t]} = 4$ and the number of subcarriers was equal to $K = 512$.

of the undesired noise. Note that this behaviour is a result of employing the same set of predictor coefficients for filtering each of the different CIR-related taps. By contrast, in the context of a predictor arrangement employing individually optimized sets of coefficients for the prediction of each of the different CIR-related taps, a "levelling out" of the *a priori* estimation MSE performance would be observed, instead of the explicit degradation seen in Figure 3.13. This is, because for the low-energy CIR-related taps suffering from a low channel-related signal component-to-noise ratio the noise would be more mitigated. As expected, in the context of the channel associated with a uniform multipath intensity profile on the right-hand side of Figure 3.13 an improved MSE performance is observed compared to the case of a single-tap multipath intensity profile, where the tap's normalized fractional delay had been intentionally adjusted to 0.5 in order to maximize the leakage.

Our previous investigations only delivered the *a priori* channel transfer factor estimation MSE averaged over the K subcarriers hosted by each OFDM symbol. By contrast, for the process of multi-user detection the quality of the channel transfer factor estimates recorded on a subcarrier-by-subcarrier basis is of relevance. Hence, our further aim is to characterize the *a priori* channel transfer factor estimation MSE distribution across the various subcarriers, which is the topic of the next section.

3.4.2.3.5 *A Priori* Channel Transfer Factor Estimation MSE for a Non-Sample Spaced CIR on a Subcarrier Basis The specific distribution of the *a priori* channel transfer factor estimation MSE across the different subcarriers can also be obtained using the approach outlined in Section 3.4.1.6 for jointly optimizing the average *a priori* channel estimation MSE and the predictor coefficients. This procedure involved updating the average *a priori* channel estimation MSE of the j-th user, where $j = 1, \ldots, L$, based on the average *a priori* channel estimation MSEs of the remaining users, employing the j-th user's specific vector of predictor coefficients determined with the aid of Equation 3.126. In a second step the j-th user's vector of predictor coefficients was then recomputed based on the updated *a priori* channel estimation MSEs of the remaining users with the aid of Equation 3.132.

By contrast, here we are interested in the exact distribution of the *a priori* channel transfer factor estimation MSE across the different subcarriers. This can be obtained upon invoking Equation 3.117 instead of Equation 3.126 in the algorithm outlined above. Again, in the context of a stable operation as defined in Section 3.4.1.5 we assume that the estimator's statistics recorded in form of the *a priori* channel transfer factor estimation errors' correlation matrix $\mathbf{R}_{\Delta\hat{\mathbf{H}}_{apr}^{(j)}}[n] = \mathbf{R}_{\Delta\hat{\mathbf{H}}_{apr}^{(j)}}[n - \acute{n}]$ is invariant for $\acute{n} = 1, \ldots, N_{tap}^{[t]}$, yielding:

$$\begin{aligned}\mathbf{R}_{\Delta\hat{\mathbf{H}}_{apr}^{(j)}}[n] &= \frac{\alpha_j}{\sigma_j^2}\tilde{\mathbf{c}}_{pre}^{(j)H}\tilde{\mathbf{c}}_{pre}^{(j)}\mathbf{T}_{K_0}^{(j)}\left(\sum_{\substack{i=1\\ i\neq j}}^{L}\sigma_i^2\mathbf{R}_{\Delta\hat{\mathbf{H}}_{apr}^{(i)}}[n]|_{Diag}\right)\mathbf{T}_{K_0}^{(j)H} + \\ &+ \frac{\alpha_j}{\sigma_j^2}\sigma_n^2\tilde{\mathbf{c}}_{pre}^{(j)H}\tilde{\mathbf{c}}_{pre}^{(j)}\mathbf{T}_{K_0}^{(j)}\mathbf{T}_{K_0}^{(j)H} + \mathbf{R}_{\mathbf{H}_{dec}^{(j)}}. \end{aligned} \tag{3.157}$$

Recall that the desired subcarrier-based *a priori* channel transfer factor estimation MSE variances are found on the main-diagonal of the matrix $\mathbf{R}_{\Delta\hat{\mathbf{H}}_{apr}^{(j)}}[n]$ of Equation 3.157. The iteration commences with an initial assignment for the matrices $\mathbf{R}_{\Delta\hat{\mathbf{H}}_{apr}^{(j)}}[n]$, $j = 1, \ldots, L$, potentially constrained by the condition that the matrices are supposed to be Hermitian. The j-th user's *a priori* channel transfer factor estimation error correlation matrix is then updated with the aid of Equation 3.157 on the basis of the remaining users' error correlation matrices' diagonals denoted by $\mathbf{R}_{\Delta\hat{\mathbf{H}}_{apr}^{(i)}}[n]|_{Diag}$, employing the remaining users' associated current vectors of predictor coefficients. After updating all users' error correlation matrices the vectors of predictor coefficients are updated with the aid of Equation 3.132. This involves evaluating first the average *a priori* channel transfer factor estimation MSEs with the aid of Equation 3.115 on the basis of the updated error correlation matrices. The iteration continues by updating the error correlation matrices again upon invoking the updated vectors of predictor coefficients.

Our analytical performance evaluations have been carried out for the uniform multipath intensity profile, again, in conjunction with a normalized multipath spread of $T_m/T_s = 64$ and for $K = 512$ subcarriers. The number of predictor taps was $N_{tap}^{[t]} = 4$. Our simulation results are portrayed in

Figure 3.14, on the left-hand side for an SNR of 20dB at the reception antenna and on the right-hand side for 40dB. The curves are further parameterized with the K_0 number of significant CIR-related taps. As also evidenced by the simulation results of Figure 3.13 the number K_0 should be in excess of $T_m/T_s = 64$ in order to be able to extract all the significant taps and hence to prevent an excessive degradation of the MSE. The most important observation drawn from Figure 3.14 is that as a result of the effects of leakage imposed by the uniform multipath intensity profile the estimation MSE is substantially degraded for the subcarriers near the beginning and the end of the frequency-domain OFDM symbol. Estimation MSEs as high as -5dB are observed. Furthermore, upon increasing the SNR measured at the reception antenna to 40dB, the MSE remains relatively high. This is, because the variance of the leakage as defined in Section 3.4.2.3 is independent from the SNR measured at the reception antenna. The somewhat lower MSE observed at the right-hand side of Figure 3.14 for the higher SNR of 40dB is achieved, because the Wiener filter-based CIR-related tap predictor becomes capable of more efficiently exploiting the channel's correlation. Note that at relatively high SNRs, such as for example 40dB, the MSE could be further improved upon employing a more beneficial, smooth window function, such as for example the Hamming window, instead of a rectangular window as employed here for windowing the *a posteriori* channel transfer factor estimates. Naturally, this would have to be appropriately considered in the calculation of the predictor coefficients. Based on the relatively high MSE associated with the outer subcarriers, we also expect for these subcarriers a significantly deteriorated BER performance, compared to the subcarriers at the center of the OFDM symbol.

3.4.2.4 *A Priori* Channel Estimation MSE and System BER in the Context of Imperfect, Error-Contaminated Symbol Decisions Assuming a Sample-Spaced CIR

So far in this section we have capitalized on the idealistic assumption of error-free symbol decisions. By contrast, in a realistic scenario the channel estimation process is impaired by erroneous symbol decisions. These effects will be further highlighted during our forthcoming discussions. While a qualitative description of the associated effects is given in Section 3.4.2.4.1 a more quantitative analysis will be provided in Section 3.4.2.4.2, where the *a priori* channel estimation MSE performance and the system's BER performance will be assessed for the uncoded case. Furthermore, in Section 3.4.2.4.3 the impact of employing turbo coding will be highlighted.

3.4.2.4.1 Effects of Error-Contaminated Symbol Decisions The effect of erroneous symbol decisions can be viewed as an additional source of noise associated with statistical properties that are different from those of the AWGN. As expected, the variance of the impairment induced by erroneous symbol decisions in the DDCE process is a function of the channel SNR. If any of the multiuser channel transfer functions encountered during the current OFDM symbol exhibits a deep fade, potentially causing multiple symbol errors in the corresponding subcarriers, the quality of

the associated *a priori* channel transfer factor estimates derived for the next OFDM symbol will be degraded. This will in turn increase the subcarrier symbol error probability at the output of the demodulator during the next OFDM symbol period. In this context the extraction of the K_0 number of significant *a posteriori* CIR-related taps has an adverse effect. This is, because the time-domain multiplication of the rectangular window-based extraction mask defined by the sparse diagonal matrix $\mathbf{I}_{K_0}$ exhibiting K_0 non-zero entries with the output of the unitary inverse transform $\tilde{\mathbf{U}}^{[f]H}$ given by Equation 3.108 corresponds to the cyclic convolution of the associated transfer functions in the subcarrier domain. Thus, after time-domain CIR-related tap windowing even a single subcarrier symbol error will affect the *a priori* channel transfer factor estimates of multiple adjacent subcarriers. As a result, an error-propagation effect may be observed, where the channel estimation quality is gradually degraded over a period of several consecutive OFDM symbols, also depending on the depth and width of the channel fades. In order to curtail these error propagation effects, a standard technique is to periodically transmit dedicated training OFDM symbols [17].

The effect of symbol errors can potentially be further mitigated upon increasing the *a priori* channel predictor's range, thus reducing the relative influence of each individual OFDM symbol's *a posteriori* estimated channel on the *a priori* channel predictor's output. On the other hand, as a result of using an increased number of OFDM symbols, at the same time the probability of incurring erroneous subcarrier symbol decisions during the estimation process is also increased. A less obvious effect related to the role of erroneous symbol decisions yet acting as an additional source of noise is that the system can be rendered unstable. This is, because correct symbol decisions were assumed in the calculation of the predictor coefficients as outlined in Section 3.4.1, and hence a noise amplification problem classically known from the behaviour of conventional zero-forcing channel equalizers might occur. Since it is difficult to quantify the symbol-error-induced noise contribution, the best strategy for avoiding these effects is to employ an a priori CIR-related tap predictor having a sufficient range such as for example four- or eight taps. The probability of incurring the adverse effects of erroneous symbol decision is of course also reduced upon employing more effective symbol detection schemes at the receiver, such as for example Successive Interference Cancellation (SIC) [114, 115, 116, 53, 117, 118, 119, 120, 121, 122] instead of MMSE detection [114, 123, 124, 125, 53, 126, 127, 128, 117, 118, 129] and additionally by capitalizing on powerful channel coding techniques such as turbo coding [96, 97]. The essence of the SIC and MMSE detection techniques was highlighted in Sections 4.2.3 and 4.3.1.

3.4.2.4.2 MSE and BER Performance in an Uncoded Scenario In Figure 3.15 we have plotted at the left-hand side the average *a priori* channel transfer factor estimation MSE, while at the right-hand side the system's BER as a function of the SNR measured at the receiver antennas upon invoking both MMSE detection and the more effective, but also more complex M-SIC (M=2) detection technique, which are discussed in Sections 4.2.3 and 4.3.1, respectively. The curves are further

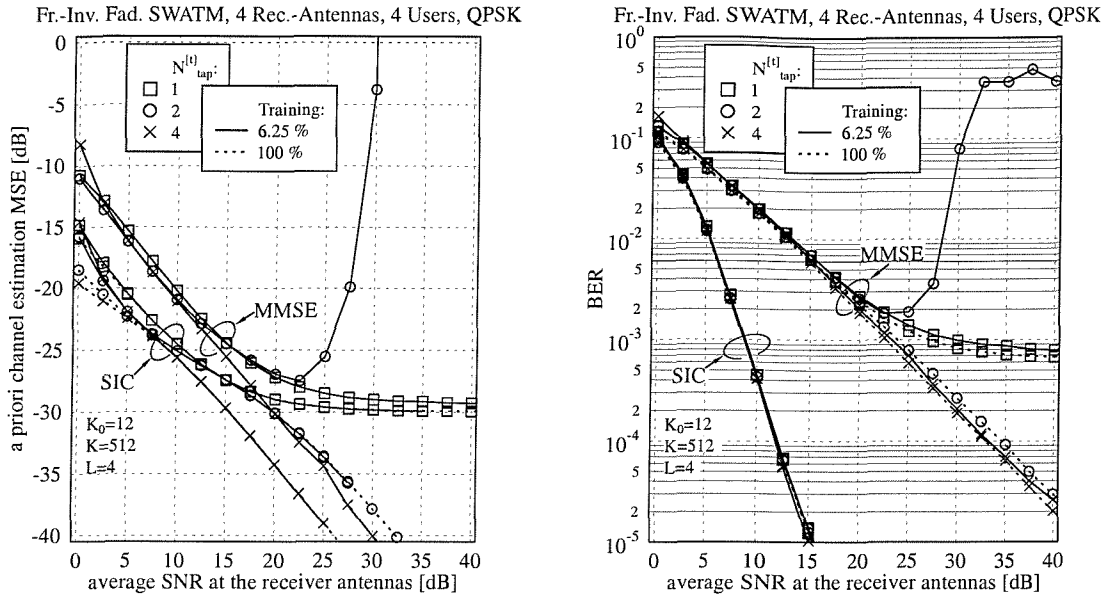

Figure 3.15: (left:) *A priori* channel estimation MSE versus SNR performance and (right:) BER versus SNR performance of an *uncoded system* employing the PIC-assisted DDCE of Figure 3.3 in conjunction with both MMSE and M-SIC (M=2) based detection at the receiver. The curves are further parameterized with the number of predictor taps $N_{tap}^{[t]}$ - ranging from one to four - and with the fraction of training overhead imposed, where 6.25% overhead corresponds to transmitting one dedicated training OFDM symbol per every block of 16 OFDM symbols, and 100% overhead denotes the idealistic case of an error-free reference. QPSK was employed as the modulation scheme.

parameterized with the number of CIR-related predictor taps and the fraction of training overhead incorporated. While a training overhead of 6.25% corresponds to transmitting one dedicated training OFDM symbol in every block of 16 OFDM symbols, a training overhead of 100% indicates here the scenario, where an error-free reference was made available to the DDCE for benchmarking. In terms of the *a priori* channel estimation MSE we observe at the left of Figure 3.15 that as a result of the M-SIC detector's lower error probability - compared to a system employing MMSE detection - the remodulated reference employed in the PIC-assisted DDCE is of better quality and hence the DDCE's MSE is significantly improved. By comparing the corresponding dashed and continuous curves in Figure 3.15 we observe that for SNRs up to about 7.5dB an MSE degradation is observed with respect to the scenario benefitting from an error-free reference. An interesting phenomenon is observed in the context of MMSE detection, when using two predictor taps. Due to an "excessive" number of erroneous subcarrier symbol decisions encountered in a specific OFDM symbol - which may be potentially induced by a deep fade on one of the channels of the multiple users - the *a priori* channel estimation MSE encountered during the next OFDM symbol is severely degraded, which in turn may trigger an avalanche of errors, which may lead to the system's instability. In the context of

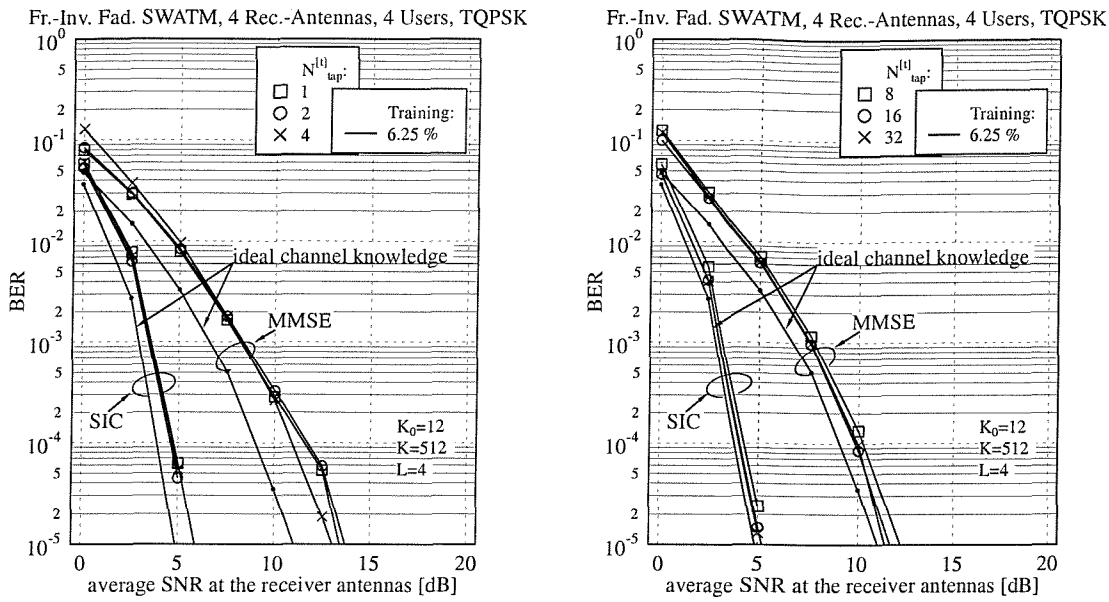

Figure 3.16: BER versus SNR performance of a *turbo coded system* employing the PIC-assisted DDCE of Figure 3.3 in conjunction with MMSE or M-SIC (M=2) detection at the receiver. The curves are parameterized with the number of CIR predictor taps - (left:) ranging from one to four - and - (right:) ranging from eight to 32. A training overhead of 6.25% was incorporated by transmitting one dedicated training OFDM symbol in every block of 16 OFDM symbols. As a reference, we have also plotted the BER performance curves associated with the case of ideal channel parameter knowledge. QPSK was employed as the modulation scheme.

one-tap CIR-related tap prediction filtering error-propagation events exceeding the length of a training period duration are prevented by periodically transmitting dedicated training OFDM symbols. By contrast, in the case of a higher number of predictor taps the OFDM training block length should ideally be identical to the number of predictor taps in order to eliminate the possibility of error propagation across the training OFDM symbols. Note furthermore that these effects are not observed for the four-tap predictor - at least not in the range of SNRs considered - since the effects of errors imposed by a single OFDM symbol are more efficiently mitigated. The graph on the right-hand side of Figure 3.15 is again an evidence of the SIC combiner's more powerful detection capability.

3.4.2.4.3 BER Performance in the Turbo Coded Scenario In addition to our discussions of Section 3.4.2.4.2, which were cast in the context of uncoded systems, here we consider a turbo-coded system[14]. Instead of plotting the performance of a system capitalizing on an error-free reference in the context of PIC-assisted DDCE, as a benchmarker, the case of ideal channel parameter knowledge was considered for our further comparisons. Our BER performance results are portrayed at the left-hand side of Figure 3.16 for various numbers of CIR-related predictor taps ranging

[14]The SIC-related soft-bits were generated with the aid of the simplified method of Section 4.3.1.3.1 rather than with the weighted soft-bit method of Section 4.3.1.3.2. Hence there is still some potential for a performance improvement

K_0	number of significant CIR-related taps
K	number of subcarriers
L	number of simultaneous users
$N_{tap}^{[t]}$	number of CIR predictor taps
P	number of receiver antennas

Table 3.5: Summary of the parameters influencing the PIC-assisted DDCE's complexity.

from one to four, while at the right-hand side the number of predictor taps was between eight and 32. Apart from noticing the M-SIC detector's more effective operation compared to MMSE detection, we observe that upon increasing the number of predictor taps to a sufficiently high value, the system's BER is within a fraction of a dB in comparison to that exhibited by a system capitalizing on perfect channel knowledge. By contrast, for the MMSE detector of Section 4.2.3 - even in conjunction with the predictor spanning the highest $N_{tap}^{[t]}$ number of CIR-related taps - a significant performance difference is observed in comparison to the perfect-reference scenario. This phenomenon is attributed to the imperfect error-contaminated remodulated reference.

Note that in the context of the simulations conducted in this section we have employed an "undecoded" reference, where the output signal of the combiner was sliced and remodulated. As a more complex design alternative, one could also employ a channel decoded reference, where the 'source'-related soft-output bits of the turbo-decoder are sliced, reencoded and remodulated. A further improvement can be achieved by generating the reference based on slicing the 'source- plus parity'-related soft-output bits of the turbo-decoder.

3.4.3 Computational Complexity

In this section we will estimate the complexity of the proposed PIC-assisted DDCE scheme of Figure 3.3 in terms of the number of complex multiplications and additions required during the estimation phase. We will consider two specific cases. In the first scenario PIC was carried out in the frequency-domain, which was based on the concept of Section 3.4, while in the second case PIC was invoked in the time-domain, as proposed by Li [22]. The latter approach was outlined in Section 3.3.4. Note again that these schemes are equivalent in terms of their system equations and performance. Hence the decision, as to which domain to perform the PIC in, should be made on the basis of the computational complexity imposed.

In Table 3.5 we have once again summarized the system parameters, which will influence the achievable performance. Our further discourse is divided into two parts. While in Section 3.4.3.1 we will focus on the complexity imposed by the frequency-domain *a posteriori* channel estimation, in Section 3.4.3.2 we will focus on the estimation of the complexity associated with the *a priori* channel estimation conducted in the CIR-related domain.

3.4.3.1 *A Posteriori* Channel Estimation Complexity

Following our discussions outlined in Section 3.4.1.1 an *a posteriori* channel transfer function estimate can be obtained for the j-th user and the p-th receiver antenna element during the n-th OFDM symbol period upon subtracting all the $(L-1)$ remaining users' estimated signal contributions from the frequency-domain representation of the signal received by the p-th antenna element. The schematic of this arrangement was shown in Figure 3.3. According to Equation 3.106 this implies multiplying the *a priori* channel transfer factor estimates of the $(L-1)$ users with the users' associated sliced and remodulated subcarrier symbols, followed by the subtraction of these components from the received signal and by its normalization with respect to the desired user's sliced and remodulated subcarrier symbols. Upon neglecting the specific properties of the modulated signal constellations employed, such as for example the constant modulus property of the various MPSK modulation schemes, the complexity imposed in terms of the number of complex multiplications and additions - normalized to the K number of subcarriers, L number of users and P number of receiver antenna elements is given by[15]:

$$C_{apt}^{(\mathbb{C}*\mathbb{C})}|_{\text{norm}} = 2 \tag{3.158}$$

$$C_{apt}^{(\mathbb{C}+\mathbb{C})}|_{\text{norm}} = L-1, \tag{3.159}$$

where the computational complexity of the division-based normalization has been accounted for as a complex multiplication. Note in this context that $1/\check{s}^{(j)}[n,k] = \check{s}^{(j)*}[n,k]/|\check{s}^{(j)}[n,k]|^2$, where $|\check{s}^{(j)}[n,k]|^2 = \sigma_j^2$ for constant-modulus MPSK modulation schemes.

3.4.3.2 *A Priori* Channel Estimation Complexity

Calculating the i-th user's *a priori* channel transfer factor estimates for the next OFDM symbol period involves transforming the user's current set of *a posteriori* channel transfer factor estimates to the CIR-related domain with the aid of the inverse unitary linear transform $\tilde{\mathbf{U}}^{[f](i)H}$ according to Equation 3.108. In our specific case this unitary transform is implemented with the aid of the inverse DFT matrix $\mathbf{W}^H$. Instead of directly multiplying the vector of *a posteriori* channel transfer factor estimates with the inverse DFT matrix $\mathbf{W}^H$ according to Equation 3.108, we rather employ here the IFFT. Employing the IFFT requires a $\frac{K}{2}\log_2 K$ number of complex multiplications and twice the number of additions. Hence, the corresponding normalized complexity contribution in the sense of Equations 3.158 and 3.159 is given by:

$$C_{\text{IFFT}}^{(\mathbb{C}*\mathbb{C})}|_{\text{norm}} = \frac{1}{2}\log_2 K \tag{3.160}$$

$$C_{\text{IFFT}}^{(\mathbb{C}+\mathbb{C})}|_{\text{norm}} = \log_2 K. \tag{3.161}$$

[15]For reasons of space economy in the rest of this section we refrain from spelling out always that normalization was carried out with respect to K, L and P. For the sake of brevity we will simply refer to 'normalized' complexity.

	$K_0 = 8/K = 64$	$K_0 = 8/K = 512$	$K_0 = 64/K = 512$
$C^{(\mathbb{C}*\mathbb{C})}_{\text{MU-CE,PIC}}\|_{\text{norm}}$	8.13	11.02	11.13
$C^{(\mathbb{C}+\mathbb{C})}_{\text{MU-CE,PIC}}\|_{\text{norm}}$	15.13	21.02	21.13

Table 3.6: Computational complexity of the frequency-domain PIC-assisted DDCE of Figure 3.3 in terms of the number of complex multiplications and additions normalized to the K number of subcarriers, L number of users and P number of receiver antennas. Here we have assumed that $L = P = 4$ and furthermore we had $N_{tap}^{[t]} = 1$.

Furthermore, filtering each of the K_0 number of most significant CIR-related taps along the time-direction according to Equation 3.109 using an N-tap prediction filter results in a normalized complexity contribution of:

$$C_{apr}^{(\mathbb{C}*\mathbb{C})}|_{\text{norm}} = \frac{K_0}{K} N_{tap}^{[t]} \tag{3.162}$$

$$C_{apr}^{(\mathbb{C}+\mathbb{C})}|_{\text{norm}} = \frac{K_0}{K} N_{tap}^{[t]}. \tag{3.163}$$

Upon invoking Equation 3.110, the predicted CIR-related taps are transformed back to the frequency-domain, where again, for the specific case of $\tilde{\mathbf{U}}^{[f](i)} = \mathbf{W}$ the FFT is employed. The FFT requires the same number of operations, as the IFFT, namely those given by Equations 3.160 and 3.161.

Hence, the total number of complex multiplications and additions, normalized to the product of the K number of subcarriers, L number of users and P number of transmit antennas is given by:

$$C_{\text{MU-CE,PIC}}^{(\mathbb{C}*\mathbb{C})}|_{\text{norm}} = 2 + \log_2 K + \frac{K_0}{K} N_{tap}^{[t]} \tag{3.164}$$

$$C_{\text{MU-CE,PIC}}^{(\mathbb{C}+\mathbb{C})}|_{\text{norm}} = L - 1 + 2\log_2 K + \frac{K_0}{K} N_{tap}^{[t]}. \tag{3.165}$$

We conclude that in most scenarios the computational complexity imposed will be dominated by the contribution associated with performing the IFFT and FFT operations. In order to provide an illustrative example, we have evaluated the computational complexity of the frequency-domain (FD) PIC-assisted DDCE of Figure 3.3 again, for the standard configurations as employed in the context of our rudimentary complexity analysis of Li's original approach and for the simplified, time-domain (TD)-PIC-assisted DDCE in Tables 3.3 and 3.4. Specifically, compared to the TD-PIC-assisted DDCE's complexity summarized in Table 3.4, we observe that the FD-PIC's complexity is lower in terms of the number of complex multiplications and additions required. While this applies to the number of complex multiplications regardless of the specific choice of the system parameters, the number of complex additions imposed has to be considered in more detail. Upon comparing Equations 3.99 and 3.165 - which reflect the complexity of the TD-PIC and FD-PIC in terms of the number of complex additions we conclude that if we have $K \geq 2^{2(L-1)}$, then the TD-PIC is more complex for any choice of K_0. By contrast, for the case of $K < 2^{2(L-1)}$ it depends on the

specific choice of K_0 whether the TD- or the FD-PIC is more complex. It can be readily shown that the 'complexity cross-over point' is given by $\acute{K}_0 = \sqrt{K(1 - \frac{1}{2(L-1)} \log_2 K)}$. More explicitly, for $K_0 < \acute{K}_0$ the TD-PIC is less complex, while for $K_0 > \acute{K}_0$ the FD-PIC is less complex. Note that in formulating these considerations we have assumed in Equation 3.99 that we have $\frac{1}{L} \approx 0$ and furthermore that the term of $\frac{K_0}{K} N_{tap}^{[t]}$ was neglected in Equation 3.165. In order to provide an example, for $L = 8$ and $K = 64$ we have $\acute{K}_0 = 6.04$, while for $K = 512$ we obtain $\acute{K}_0 = 13.52$.

3.4.4 Summary and Conclusions

In summary, in Section 3.4 we have discussed frequency-domain PIC-assisted DDCE employed in the context of multi-user OFDM systems- or phrased in more general terms, used in OFDM systems relying on multiple transmit antennas. The outline of this section is as follows. In Section 3.4.4.1 a summary and conclusions will be provided for the specific structure of the PIC-assisted DDCE. Furthermore, in Section 3.4.4.2 our summary and conclusions will be offered for the performance assessment of the PIC-assisted DDCE. Finally, in Section 3.4.4.3 the results of our complexity analysis conducted with respect to the PIC-assisted DDCE will be summarized.

3.4.4.1 Summary and Conclusion on the PIC-Assisted DDCE's Structure

After an introduction of the vectors of *a priori* and *a posteriori* channel transfer factor estimates and their associated expressions in Section 3.4.1.1, the employment of *a priori* CIR-related tap prediction filtering was discussed in Section 3.4.1.2 for the sake of obtaining improved channel transfer factor estimates for the next OFDM symbol period. On the basis of the associated system equations an expression, namely, Equation 3.113 was derived for the vector of different subcarriers' *a priori* channel transfer factor estimation errors associated with the j-th user and p-th receiver antenna element during the current OFDM symbol period as a function of the vectors of *a priori* channel transfer factor estimation errors of the remaining $(L-1)$ users during the past $N_{tap}^{[t]}$ number of OFDM symbol periods, where $N_{tap}^{[t]}$ denotes the predictor's range. This expression was then employed for deriving the j-th user's *a priori* channel transfer factor estimation error correlation matrix of Equation 3.117. Furthermore, the j-th user's average channel transfer factor- or simply channel estimation MSE given by Equation 3.119 was derived, again, as a function of the remaining users' corresponding magnitudes associated with the past $N_{tap}^{[t]}$ number of OFDM symbol periods. A similar expression, namely, Equation 3.124 was also derived for the j-th user's *a posteriori* channel estimation MSE. Our discussions continued in Section 3.4.1.5 upon further considering the channel estimator's operation in the steady-state condition, implying that the estimator's MSE has reached its steady-state value and hence it was time-invariant for the consecutive OFDM symbols. Upon employing a more compact matrix notation a closed form solution, namely Equation 3.129 was derived for the vector of the different users' *a priori* channel estimation MSEs as a function of the

different users' transmit powers as well as that of the AWGN noise variance, that of the CIR-related predictor coefficients, that of the channel statistics expressed in form of the channels' spaced-time spaced-frequency correlation functions, and finally that of the specific unitary transforms employed. The criteria to be satisfied for the existence of the equation's solution were provided, which also ensure the system's stability. Furthermore, in Section 3.4.1.6 an expression, namely Equation 3.132 was derived, for the j-th user's vector of CIR-related predictor coefficients as a function of the $(L-1)$ remaining users' *a priori* channel estimation MSEs. This equation was then employed in conjunction with Equation 3.126 in the context of a fixed-point iteration based approach for jointly optimizing the expected *a priori* channel estimation MSE and the predictor coefficients, following a similar strategy to that proposed by Rashid-Farrokhi *et al.* [111] for jointly optimizing the transmit power allocation and basestation antenna array weights in wireless networks. Furthermore, in Section 3.4.1.6.1 simplified expressions were presented for the *a priori* channel estimation MSE, the stability condition and for the vector of optimum predictor coefficients, namely, which were given by Equations 3.133, 3.134 and 3.135, respectively. These equations were valid in the context of a scenario of identical transmit powers- and channel statistics associated with the different users. For this specific scenario, while employing single-tap prediction filtering a closed form solution was presented in Section 3.4.1.6.2 for the predictor's optimum coefficient, which was given by Equation 3.137. Finally, in Section 3.4.1.7 various strategies were discussed for providing estimates of the channel statistics, which constitute the prerequisites for obtaining the optimum predictor coefficients, as it was highlighted in Section 3.4.1.6.

3.4.4.2 Summary and Conclusions on the Performance Assessment of the PIC-Assisted DDCE

The further structure of this section is as follows. The PIC-assisted DDCE's performance in the context of sample-spaced- as well as non-sample-spaced CIRs and error-free symbol decisions is summarized in Sections 3.4.4.2.1 and 3.4.4.2.2, respectively. In contrast, in Section 3.4.4.2.3 our findings for the scenario of a sample-spaced CIR and imperfect, potentially error-contaminated symbol decisions are summarized.

3.4.4.2.1 Performance of the PIC-Assisted DDCE in the Context of Sample-Spaced CIRs and Error-Free Symbol Decisions Our performance assessment of the various techniques studied commenced with Figure 3.4 of Section 3.4.2.1, portraying the *a priori* channel estimation MSE's evolution as a function of the CIR-related tap predictor coefficients in the context of two-tap CIR prediction filtering. Figure 3.4 highlighted the estimator's sensitivity with respect to the choice of the predictor coefficients. Our further investigations in Section 3.4.2.2.1 then concentrated on the average *a priori* channel estimation MSE in the idealistic scenario of a sample-spaced CIR and error-free symbol decisions, which provided us with a useful benchmarker. Specifically the investigations conducted in Sections 3.4.2.2.1 and 3.4.2.2.2 demonstrated that without exploiting the

system's recursive structure characterized by our derivations presented in Sections 3.4.1.3, 3.4.1.4 and 3.4.1.5 the system may potentially become unstable as observed in Figures 3.5 and 3.6. This is the case for example, when calculating the predictor coefficients associated with a specific user with the aid of the conventional Wiener solution, while neglecting the remaining users' *a priori* channel estimation MSEs. Our further investigations in Sections 3.4.2.2.1, 3.4.2.2.2 as well as 3.4.2.2.3, 3.4.2.2.4 and 3.4.2.2.5, respectively, which were associated with Figures 3.5, 3.6 as well as 3.7, 3.8 and 3.9, respectively, concentrated on portraying the influence of the various system parameters on the *a priori* channel estimation MSE. More explicitly, we studied the effects of the $N_{tap}^{[t]}$ number of predictor coefficients, that of the K_0 number of significant CIR-related taps, that of the L number of simultaneous users, that of the impact of the OFDM symbol normalized Doppler frequency denoted by F_D, and finally, that of the potential mismatch between the channel statistics assumed in the derivation of the predictor coefficients and that of the channel encountered. Specifically, the investigations conducted in Section 3.4.2.2.5 with respect to the mismatch of the channel statistics supported the arguments of Li *et al.* [17] that if an ideally support-limited Doppler power spectrum having a maximum OFDM symbol normalized Doppler frequency of $\tilde{F}_D$ is assumed in the calculation of the predictor coefficients, then for channels obeying $F_D \leq \tilde{F}_D$ no further *a priori* channel estimation MSE performance degradation is observed. Our illustrations in Figure 3.9 demonstrated that this is only true in the strict sense, when increasing the CIR-related tap predictor's order towards infinity. In more practical terms however, a number of 64 predictor taps appeared to be sufficient for rendering the evolution of the MSE almost flat as a function of the channel's OFDM symbol normalized Doppler frequency. On the other hand, a moderate number of predictor taps, which was as low as four, was found sufficient for exploiting much of the channel transfer function's correlation in the time-direction. Furthermore, we observed that if the difference between the target OFDM symbol normalized Doppler frequency for which the predictor coefficients were designed, and that of the channel encountered is too high, then the channel's correlation cannot be optimally exploited. *The conclusion that transpired was that of rendering the channel transfer function estimator adaptive, which will be the topic of our discussions in Section 3.5.* Our investigations conducted in the context of a sample-spaced CIR and error-free symbol decisions were concluded in Section 3.4.2.2.6 by comparing the *a priori* channel estimation MSE performance of PIC-assisted DDCE to that of the LS-assisted DDCE proposed by Li *et al.* [21], which was characterized in Section 3.3. As shown in Figure 3.10 the general tendency is that for lower SNRs, namely for SNR values up to about 15dB, the PIC-assisted DDCE outperforms the LS-assisted DDCE, while for higher SNRs the opposite trend is observed. The reason is that the LS-assisted DDCE suffers from the MUI imposed due to the imperfect cross-correlation properties of the different users' transmitted subcarrier symbol sequences. By contrast, the PIC-assisted DDCE of Figure 3.3 suffers from MUI due to the imperfections of the *a priori* channel estimates imposed on the PIC process, which becomes more obvious

for higher SNRs. It was observed furthermore in conjunction with the LS-assisted DDCE of Figure 3.2 that when the L number of simultaneous SDMA users approaches the maximum tolerable number of users given by the ratio $\frac{K}{K_0}$, as outlined in Section 3.3.1.2.3, then the *a priori* channel estimation MSE is further degraded. This was explained by the increased MUI due to supporting more users, but also due to the numerical imperfections associated with a potentially excessive condition number of the subcarrier symbol sequences' auto-correlation matrix $\mathbf{Q}[n]$, which was defined earlier in Equation 3.20 of Section 3.3.1.2.1. These imperfections were mitigated for example with the aid of the QR matrix factorization based approach outlined in Section 3.3.1.2.4.

3.4.4.2.2 Performance of the PIC-Assisted DDCE in the Context of Non-Sample-Spaced CIRs and Error-Free Symbol Decisions In order to render our investigations more realistic, in Section 3.4.2.3 we considered the estimator's MSE performance in the context of non-sample-spaced CIRs. More specifically, we introduced three multipath intensity profiles, namely the sparse-, the uniform- and the exponential multipath intensity profile. Their associated spaced-frequency channel correlation functions were reviewed in Sections 3.4.2.3.1, 3.4.2.3.2 and 3.4.2.3.3, respectively. Further investigations were conducted with respect to the leakage effects incurred upon decomposing the associated spaced-frequency correlation matrices with respect to the DFT matrix $\mathbf{W}$. Specifically, in case of a sparse multipath intensity profile, using a single tap in the most basic scenario, it was found in Figure 3.11 that the leakage was maximal for a fractional delay of 0.5. The effects of leakage observed when using the uniform- and exponential multipath intensity profiles were portrayed in Figure 3.12. Our more specific investigations of the *a priori* channel estimation MSE exhibited by the PIC-assisted DDCE in the context of non-sample-spaced CIRs focussed further on the specific influence of the K_0 number of significant CIR-related taps. The corresponding simulation results were presented in Figure 3.13 for a single-tap- and for a uniform multipath intensity profile. In both scenarios the estimation MSE exhibited the same tendencies, namely that of having an MSE floor between -20- and -25dB, even for an optimum choice of the number K_0 of significant CIR-related taps. This was attributed to the leakage effects associated with employing the DFT matrix $\mathbf{W}$ instead of the optimum KLT matrix for transforming the *a posteriori* channel transfer factor estimates to the CIR-related domain in the sense of Equation 3.108. Upon further increasing the number of significant CIR-related taps K_0 beyond its optimum point, the *a priori* channel estimation MSE was degraded. This was related to employing the same set of tap predictor coefficients in the different CIR-related taps and hence the AWGN was not optimally suppressed. Our more detailed investigations conducted in Section 3.4.2.3.5, which were quantified in Figure 3.14, focussed on the distribution of the *a priori* channel transfer factor estimation MSE across the various subcarriers of the OFDM symbol. For evaluating the MSE distribution an iterative algorithm following the philosophy of that in Section 3.4.1.6 was devised. We observed in Figure 3.14 that the *a priori* channel transfer factor estimation MSEs at the boundaries of the OFDM symbol interpreted in the

sense of the DFT-index based notation or at the center of the OFDM symbol with respect to the frequency may potentially become excessive, again, as a result of the effects of leakage. *Hence, in order to optimize the entire system's performance, the value of the* a priori *channel estimation MSE to be expected in the different subcarriers should be passed on to the combining- or detection stage.*

3.4.4.2.3 Performance of the PIC-Assisted DDCE in the Context of Sample-Spaced CIRs and Imperfect, Error-Contaminated Symbol Decisions Our performance assessment was concluded in Section 3.4.2.4 upon considering sample-spaced CIRs and potentially erroneous symbol decisions, as encountered in practical physical implementations. While a qualitative assessment of the associated effects was provided in Section 3.4.2.4.1, the corresponding MSE- and BER simulation results recorded for the uncoded scenario were portrayed in Figure 3.15 of Section 3.4.2.4.2. Two MUD detection schemes, namely the MMSE- and SIC detection schemes of Sections 4.2.3 and 4.3.1 were compared against each other. It was found on the basis of the MSE curves of Figure 3.15 that the impact of erroneous symbol decisions was distinctively visible. From the further evolution of the different MMSE detection-related performance curves of Figure 3.15 it can be concluded that a relatively powerful MUD scheme, such as SIC or M-SIC is necessary for avoiding the PIC-assisted DDCE's instability induced as a result of erroneous symbol decisions. Upon employing a further enhanced turbo-decoding assisted system, which was the topic of Section 3.4.2.4.3, the associated BER performance curves provided in Figure 3.16, suggested that the entire system's BER performance was significantly enhanced. More specifically, it was observed in Figure 3.16 that in the context of SIC assisted detection, while employing CIR predictor lengths in excess of four taps, the system's BER performance may approach that exhibited in the context of perfect channel transfer function knowledge.

3.4.4.3 Summary and Conclusion on the PIC-Assisted DDCE's Computational Complexity

Our discussions in Section 3.4 were concluded by a complexity study. It was argued on the basis of the associated complexity under which conditions should the PIC be performed in the CIR-related domain- and in the frequency-domain, respectively, while noting that both schemes exhibit the same MSE performance. As our comparisons revealed earlier in Section 3.3, the PIC-assisted DDCE - regardless of whether the PIC is performed in the time- or in the frequency-domain - is significantly less complex, than the LS-assisted DDCE, particularly for a high number of significant CIR-related taps.

The advantages in favour of PIC-assisted DDCE compared to LS-assisted DDCE, namely that of a significantly reduced complexity and the potential support of a higher number of simultaneous users or transmit antennas have to be considered in the light of the disadvantage of requiring a less straightforward procedure for evaluating the CIR-related tap predictor coefficients, while also suffering from a slight performance disadvantage at higher SNRs. Furthermore, common to both

approaches was the MSE floor observed at higher SNRs in the context of non-sample-spaced CIRs, which was attributed to the imperfections of the DFT matrix $\mathbf{W}$ in the context of transforming the *a posteriori* channel transfer factor estimates to the CIR-related domain. From these observations we conclude that an improved channel transfer function estimation scheme should perform all filtering operations in the frequency-domain, and thus potentially avoiding the effects of transform-related leakage. Furthermore the filtering process should be adaptive with respect to the filters' coefficients. Alternatively, the previous design could be improved upon employing an adaptive unitary transform - such as the KLT - which takes into account the channel's statistics, and again to render the estimator adaptive with respect to the CIR-related tap prediction coefficients. In the next section we will focus on rendering the PIC-assisted DDCE of Figure 3.3 adaptive with respect to the channel's statistics, which is achieved with the aid of employing the Recursive Least Squares (RLS) algorithm.

3.5 RLS-Adaptive Parallel Interference Cancellation Assisted Decision-Directed Channel Estimation

In an effort to further improve the PIC-assisted DDCE's MSE performance under time-varying conditions with respect to the channel's specific multipath intensity profile and Doppler power spectrum, a viable approach is to adaptively adjust the CIR-related tap predictors' coefficients. A number of rudimentary approaches for rendering the predictor adaptive were outlined in Section 3.4.1.7. A common feature of these techniques was that the adaptation was assumed to be performed on a training block-by-block basis, possibly during training OFDM symbol periods. However, from a computational perspective it might be more advantageous to perform the adaptation on an OFDM symbol-by-symbol basis, once the new *a posteriori* channel transfer factor samples or CIR-related tap estimates become available. Furthermore, it was assumed in Section 3.4.1.2 that in order to simplify the task of determining the predictor coefficients, the same set of predictor coefficients would be employed for each of the K_0 number of different CIR-related taps, regardless of the specific tap's variance. This followed the philosophy of "robust" channel transfer function estimation, which was originally proposed by Li *et al.* [17] with respect to the specific shape of the channel's associated multipath intensity profile. This robustness was achieved at the cost of a sub-optimum MSE performance. As a result, the predictor's complexity was found to be relatively low, which was attributed to the off-line optimization of the predictor coefficients.

An approach for providing block-adaptivity for the CIR-related tap predictor's coefficients was outlined in Section 2.2.5.2 in form of the Burg algorithm assisted predictor proposed by Al-Susa and Ormondroyd [18] for single-user OFDM systems. Although the Burg algorithm, which has been initially proposed in the context of speech processing [83] is known to achieve a low MSE due to its strategy of simultaneously minimizing both the forward- and backward prediction errors, its main

disadvantage follows from the necessity of storing a potentially large number of past OFDM symbols' channel transfer factor estimates beyond the prediction filter's range. This can be avoided by performing the CIR-related tap prediction coefficient adaptation on an OFDM symbol-by-symbol. Here we opted for employing the RLS algorithm [87], which is known to converge relatively rapidly.

The further structure of Section 3.5 is as follows. In Section 3.5.1 the application of the RLS algorithm to the problem of CIR-related tap prediction is discussed, including the assessment of the *a priori* channel estimation MSE and the estimation of the computational complexity imposed. Without any modifications, we then employ the RLS-based CIR-related tap predictor in the context of the PIC-assisted DDCE for multi-user OFDM communications, which is the topic of Section 3.5.2. We also characterize the BER- and MSE performance of the RLS-based PIC-assisted DDCE in the context of sample-spaced CIRs. Our conclusions will then be offered in Section 3.5.3.

3.5.1 Single-User RLS-Adaptive CIR-Related Tap Prediction

As an introduction, we will consider in this section the application of RLS-adaptive CIR-related tap prediction filtering in the context of a single-user scenario. The specific structure of Section 3.5.1 is as follows. While in Section 3.5.1.1 the standard RLS algorithm is reviewed with respect to its potential application in CIR-related tap prediction filtering, a simplified scheme based on ensemble averaging is outlined in Section 3.5.1.2. Furthermore, in Section 3.5.1.3 a rudimentary MSE performance assessment is provided concerning the influence of the RLS-specific forgetting factor α_{RLS} and of the OFDM symbol normalized Doppler frequency F_D on the *a priori* channel estimation MSE. Finally, in Section 3.5.1.4 we will evaluate the complexity imposed by the RLS-assisted "on-line" adaptation of the CIR-related tap predictor coefficients.

3.5.1.1 Review of the RLS Algorithm

For the single-user scenario we recall from Section 2.2.4.4, more specifically from Equation 2.38, that the l-th CIR-related tap's vector $\tilde{\mathbf{c}}_{pre}[n,l]|_{opt} \in \mathbb{C}^{N_{tap}^{[t]} \times 1}$ of optimum predictor coefficients[16] is determined by the Wiener equation [87], namely:

$$\tilde{\mathbf{c}}_{pre}[n,l]|_{opt} = \tilde{\mathbf{R}}_{apt}^{[t]-1}[n,l]\tilde{\mathbf{r}}_{apt}^{[t]}[n,l], \tag{3.166}$$

where $\tilde{\mathbf{R}}_{apt}^{[t]}[n,l] \in \mathbb{C}^{N_{tap}^{[t]} \times N_{tap}^{[t]}}$ is the l-th CIR-related tap's *estimated* auto-correlation matrix and $\tilde{\mathbf{r}}_{apt}^{[t]}[n,l] \in \mathbb{C}^{N_{tap}^{[t]} \times 1}$ is the *estimated* cross-correlation vector, both of which are valid for the n-th OFDM symbol period. The estimate $\tilde{\mathbf{R}}_{apt}^{[t]}[n,l]$ for the n-th OFDM symbol period could be obtained on the basis of the estimate $\tilde{\mathbf{R}}_{apt}^{[t]}[n-1,l]$ associated with the $(n-1)$-th OFDM symbol period by

[16]Note that in contrast to our simplified analysis of PIC-assisted DDCE in Section 3.4 different CIR-related taps are potentially associated with individual vectors of predictor coefficients.

evaluating [87]:

$$\tilde{\mathbf{R}}_{apt}^{[t]}[n,l] = \alpha_{\text{RLS}}\tilde{\mathbf{R}}_{apt}^{[t]}[n-1,l] + (1-\alpha_{\text{RLS}})\tilde{\mathbf{h}}_{apt}[n-1,l]\tilde{\mathbf{h}}_{apt}^{H}[n-1,l], \tag{3.167}$$

where $\tilde{\mathbf{h}}_{apt}[n-1,l]$ is defined in correspondence with Equation 2.23 as the vector of $N_{tap}^{[t]}$ number of past CIR-related tap estimates starting with the tap index $(n-1)$. Furthermore, the "update-term" of Equation 3.167 is identical to that of Equation 2.25 upon removing the expectation operator. Furthermore, in Equation 3.167 the variable $\alpha_{\text{RLS}} \in \mathbb{R}$ denotes the so-called *forgetting factor* [87]. Similarly, the estimate $\tilde{\mathbf{r}}_{apt}^{[t]}[n,l]$ for the n-th OFDM symbol period can be obtained following the philosophy of Equation 3.167, yielding [87]:

$$\tilde{\mathbf{r}}_{apt}^{[t]}[n,l] = \alpha_{\text{RLS}}\tilde{\mathbf{r}}^{[t]}[n-1,l] + (1-\alpha_{\text{RLS}})\tilde{h}_{apt}^{*}[n,l]\tilde{\mathbf{h}}_{apt}[n-1,l], \tag{3.168}$$

where again, the "update-term" of Equation 3.168 is identical to that of Equation 2.28 upon removing the expectation operator. Instead of explicitly inverting the estimated auto-correlation matrix $\tilde{\mathbf{R}}_{apt}^{[t]}[n]$ associated with the n-th OFDM symbol period, an iterative update strategy based on the matrix inversion lemma - also known as the Sherman-Morrison formula - or Woodbury's identity [87] can be invoked, which is known from the literature as the RLS algorithm [87]. In the context of our specific CIR-related tap prediction problem the RLS-algorithm is summarized below. Specifically, the so-called Kalman gain vector $\mathbf{k}[n,l] \in \mathbb{C}^{N_{tap}^{[t]}\times 1}$ for the n-th OFDM symbol period is given by [87]:

$$\mathbf{k}[n,l] = \frac{(1-\alpha_{\text{RLS}})\tilde{\mathbf{R}}_{apt}^{[t]-1}[n-1,l]\tilde{\mathbf{h}}_{apt}[n-1,l]}{\alpha_{\text{RLS}} + (1-\alpha_{\text{RLS}})\tilde{\mathbf{h}}_{apt}^{H}[n-1,l]\tilde{\mathbf{R}}_{apt}^{[t]-1}[n-1]\tilde{\mathbf{h}}_{apt}[n-1,l]}, \tag{3.169}$$

which is then employed in the process of updating the inverse of the CIR-related taps' auto-correlation matrix, namely [87]:

$$\tilde{\mathbf{R}}_{apt}^{[t]-1}[n,l] = \frac{1}{\alpha_{\text{RLS}}}\left[\tilde{\mathbf{R}}_{apt}^{[t]-1}[n-1,l] - \mathbf{k}[n,l]\tilde{\mathbf{h}}_{apt}^{H}[n-1,l]\tilde{\mathbf{R}}_{apt}^{[t]-1}[n-1,l]\right]. \tag{3.170}$$

Furthermore, the CIR-related tap predictor coefficient vector for the n-th OFDM symbol period is given by [87]:

$$\tilde{\mathbf{c}}_{pre}[n,l]|_{opt} = \tilde{\mathbf{c}}_{pre}[n-1,l]|_{opt} + \mathbf{k}[n,l]\left[\tilde{h}_{apt}[n,l] - \tilde{\mathbf{c}}_{pre}^{H}[n-1,l]\tilde{\mathbf{h}}_{apt}[n-1,l]\right]^{*}, \tag{3.171}$$

where the term in brackets denotes the prediction error associated with the n-th OFDM symbol period. A standard approach for initializing the RLS algorithm [87] is that of assuming an inverse correlation matrix having a diagonal shape defined as:

$$\tilde{\mathbf{R}}_{apt}^{[t]-1}[0,l] = \frac{1}{\varepsilon_{\text{RLS},0}}\mathbf{I}, \tag{3.172}$$

where the specific choice of $\varepsilon_{\text{RLS},0} \in \mathbb{R}$ is less critical in our application, than the specific value of the forgetting-factor α_{RLS}. A plausible choice for $\tilde{\mathbf{c}}_{pre}[0,l]$ is for example $(1,0,\ldots,0)^T$, which corresponds to the case of zero-forcing based one-tap prediction.

3.5.1.2 Potential Simplification by Ensemble Averaging

According to the formulae presented in the previous section, the RLS adaptation has to be performed separately for each of the K_0 number of significant CIR-related taps. A simplification in terms of the computational complexity can potentially be achieved upon invoking the concepts of 'robustness' with respect to the channel's specific spaced-frequency correlation function, as proposed by Li *et al.* [17]. These were discussed in Section 2.2.3 in the context of a single-user OFDM scenario. An implication was that the same set of CIR-related tap predictor coefficients was invoked in the process of predicting the different CIR-related tap values - at the cost of an MSE performance degradation. More specifically, in each OFDM symbol period the auto-correlation matrix of the CIR-related *a posteriori* tap estimates is updated according to Equation 3.167 but upon substituting the tap-specific update term by its ensemble average:

$$\tilde{\mathbf{R}}_{apt}^{[t]}[n] = \alpha_{\text{RLS}}\tilde{\mathbf{R}}_{apt}^{[t]}[n-1] + (1-\alpha_{\text{RLS}})\frac{1}{K_0}\sum_{l\in S_{tap}}\tilde{\mathbf{h}}_{apt}[n-1,l]\tilde{\mathbf{h}}_{apt}^{H}[n-1,l], \tag{3.173}$$

where S_{tap} denotes the set of indices associated with the K_0 number of significant CIR-related taps. Following the same concepts instead of Equation 3.168 we obtain the following cross-correlation vector update expression:

$$\tilde{\mathbf{r}}_{apt}^{[t]}[n] = \alpha_{\text{RLS}}\tilde{\mathbf{r}}^{[t]}[n-1] + (1-\alpha_{\text{RLS}})\frac{1}{K_0}\sum_{l\in S_{tap}}\tilde{h}_{apt}^{*}[n,l]\tilde{\mathbf{h}}_{apt}[n-1,l]. \tag{3.174}$$

Note that as a result of the ensemble averaging, as seen in Equation 3.173 the innovation-related term of the auto-correlation matrix $\tilde{\mathbf{R}}_{apt}^{[t]}[n]$ may exhibit a rank, which is potentially higher than unity. This precludes the application of the Sherman-Morrison formula [87]. Consequently, the vector of CIR-related tap predictor coefficients has to be evaluated with the aid of Equation 3.166, namely:

$$\tilde{\mathbf{c}}_{pre}[n]|_{opt} = \tilde{\mathbf{R}}_{apt}^{[t]-1}[n]\tilde{\mathbf{r}}_{apt}^{[t]}[n]. \tag{3.175}$$

Note that in terms of the computational complexity imposed the direct matrix inversion based solution of Equation 3.175 is proportional to the cube of the $N_{tap}^{[t]}$ number of predictor taps.

3.5.1.3 MSE Performance Assessment

In order to demonstrate the applicability of the RLS algorithm to the problem of CIR-related tap prediction in the context of DDCE we have portrayed in Figure 3.17 the evolution of the *a priori* channel estimation MSE versus the OFDM symbol index for an arbitrary time segment commencing with an initial vector of prediction coefficients given by $\tilde{\mathbf{c}}_{pre}[0,l] = (1,0,\ldots,0)^T$, where $l = 0,\ldots,K_0-1$. Here we have employed the sample-spaced indoor WATM channel model of Section 6.1.1, where the highest CIR tap delay is given by $11T_s$. Hence, the number of significant

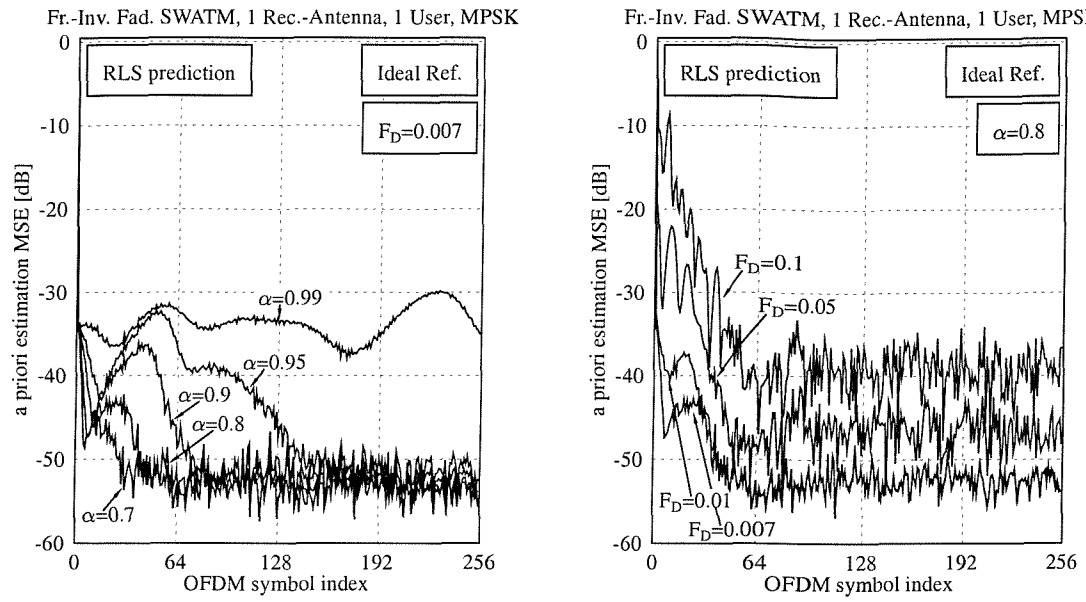

Figure 3.17: Evolution of the *a priori* channel estimation MSE observed with the aid of the RLS prediction assisted DDCE in the *single-reception antenna based single-user scenario* for a specific time-segment associated with the sample-spaced indoor WATM channel of Section 6.1.1, as a function of the OFDM symbol index; (left:) parameterized with the forgetting factor $\alpha = \alpha_{\text{RLS}}$, for a fixed OFDM symbol normalized Doppler frequency of $F_D = 0.007$; (right:) parameterized with the OFDM symbol normalized Doppler frequency F_D and for a fixed forgetting factor of $\alpha_{\text{RLS}} = 0.8$; in both cases the RLS predictor's startup constant was $\varepsilon_{\text{RLS},0} = 0.1$, the $N_{tap}^{[t]}$ number of CIR predictor taps was equal to four and the SNR at the reception antennas was assumed to be 40dB; furthermore the number of significant CIR-related taps was $K_0 = 12$ and the number of subcarriers was $K = 512$.

CIR-related taps was chosen as $K_0 = 12$. Furthermore, the CIR-related tap predictor's range was equal to $N_{tap}^{[t]} = 4$. Note that for different time segments the specific MSE evolution is potentially different from that of Figure 3.17, but obeys the same general trend. Here we have investigated the influence of the Kalman forgetting factor α_{RLS} and of the OFDM symbol normalized Doppler frequency on the *a priori* channel estimation MSE performance. Specifically, at the left-hand side of Figure 3.17 the OFDM symbol normalized Doppler frequency was set to $F_D = 0.007$, while the forgetting factor α_{RLS} was varied. We observe in Figure 3.17 that for lower values of α_{RLS} a faster adaptation is achieved, while the residual error after adaptation is potentially higher, than that achieved with the aid of a forgetting factor of a higher value, although the latter effect is not explicitly visible in Figure 3.17 due to the limited time span. By contrast, at the right-hand side of Figure 3.17 we have plotted the *a priori* channel estimation MSE for various OFDM symbol normalized Doppler frequencies, F_D, while keeping the forgetting factor α_{RLS} constant. As expected, the *a priori* estimation MSE is increased in scenarios having a higher OFDM symbol normalized Doppler frequency, while the speed of adaptation was almost identical for the different scenarios.

	$\mathbf{k}[n,l]$	$\tilde{\mathbf{R}}_{apt}^{[t]-1}[n,l]$	$\tilde{\mathbf{c}}_{pre}[n,l]$	$\sum$
$C_{\text{RLS},tap}^{(\mathbb{C}*\mathbb{C})}$	$N_{tap}^{[t]2}+N_{tap}^{[t]}$	$2N_{tap}^{[t]2}$	$N_{tap}^{[t]}$	$3N_{tap}^{[t]2}+2N_{tap}^{[t]}$
$C_{\text{RLS},tap}^{(\mathbb{C}+\mathbb{C})}$	$N_{tap}^{[t]2}+N_{tap}^{[t]}$	$N_{tap}^{[t]2}+N_{tap}^{[t]}$	$2N_{tap}^{[t]}$	$2N_{tap}^{[t]2}+4N_{tap}^{[t]}$
$C_{\text{RLS},tap}^{(\mathbb{R}*\mathbb{C})}$	$N_{tap}^{[t]}$	$N_{tap}^{[t]2}$	$N_{tap}^{[t]}$	$N_{tap}^{[t]2}+2N_{tap}^{[t]}$

Table 3.7: *Computational complexity per CIR-related tap* in terms of the $C_{\text{RLS},tap}^{(\mathbb{C}*\mathbb{C})}$ number of complex multiplications, the $C_{\text{RLS},tap}^{(\mathbb{C}+\mathbb{C})}$ number of complex additions and the $C_{\text{RLS},tap}^{(\mathbb{R}*\mathbb{C})}$ number of "mixed" multiplications (real/complex) associated with the different components of the **RLS-based adaptation** of the vector of predictor coefficients.

Note that for values of α_{RLS} that are significantly lower than those employed in Figure 3.17, the RLS predictor may potentially become unstable. Specifically in our experiments a value of $\alpha_{\text{RLS}} = 0.77$ was just acceptable, and yielded the highest speed of convergence while at the same time potentially the largest residual error after adaptation.

Curves similar to those seen in Figure 3.17 can also be generated for the lower-complexity ensemble averaging assisted adaptive DDCE, which was outlined in Section 3.5.1.2. Our simulation results, which are not explicitly portrayed here for reasons of space economy revealed that the MSE recorded after adaptation is potentially higher, than that of the RLS-assisted predictor, which adjusts the predictor coefficients on a CIR-related tap-by-tap basis. However, as it will be demonstrated in Section 3.5.1.4, an advantage of the ensemble averaging assisted adaptive DDCE is its potentially reduced complexity.

3.5.1.4 Complexity Study

In Table 3.7 we have summarized the implementational complexity associated with evaluating the Kalman gain vector $\mathbf{k}[n,l]$ according to Equation 3.169, that of updating the inverse auto-correlation matrix according to Equation 3.170 and that of updating the CIR-related tap predictor coefficient vector according to Equation 3.171. We observe that the complexity of this operation is proportional to the square of the $N_{tap}^{[t]}$ number of predictor coefficients. Note that the computational complexity could possibly be further reduced by exploiting that in the vector $\tilde{\mathbf{h}}_{apt}[n,l]$ associated with the n-th OFDM symbol period the last $(N_{tap}^{[t]}-1)$ elements are constituted by the first $(N_{tap}^{[t]}-1)$ elements of $\tilde{\mathbf{h}}_{apt}[n-1,l]$, while the first element is constituted by the estimated tap of $\tilde{h}_{apt}[n,l]$. For comparison we have summarized in Table 3.8 the computational complexity associated with updating the single vector of predictor coefficients based on the method outlined in Section 3.5.1.2, namely that of ensemble-averaging, rather than updating all the K_0 number of coefficients individually. Note that in Table 3.8 we have listed the total complexity imposed by updating K_0 number of CIR-related tap predictor coefficient vectors, while in Table 3.7 we have listed the complexity associated with

	$\tilde{\mathbf{R}}_{apt}^{[t]}[n]$	$\tilde{\mathbf{r}}_{apt}[n]$	$\tilde{\mathbf{c}}_{pre}[n]$	$\sum$
$C_{\text{RLS}}^{(\mathbb{C}*\mathbb{C})}$	$K_0 N_{tap}^{[t]2}$	$K_0 N_{tap}^{[t]}$	$\frac{1}{3} N_{tap}^{[t]3}$	$\frac{1}{3} N_{tap}^{[t]3} + K_0 N_{tap}^{[t]2} + K_0 N_{tap}^{[t]}$
$C_{\text{RLS}}^{(\mathbb{C}+\mathbb{C})}$	$K_0 N_{tap}^{[t]2}$	$K_0 N_{tap}^{[t]}$	$N_{tap}^{[t]2}$	$(K_0+1) N_{tap}^{[t]2} + K_0 N_{tap}^{[t]}$
$C_{\text{RLS}}^{(\mathbb{R}*\mathbb{C})}$	$2N_{tap}^{[t]2}$	$2N_{tap}^{[t]}$	–	$2N_{tap}^{[t]2} + 2N_{tap}^{[t]}$

Table 3.8: *Total computational complexity* in terms of the $C_{\text{RLS}}^{(\mathbb{C}*\mathbb{C})}$ number of complex multiplications, the $C_{\text{RLS}}^{(\mathbb{C}+\mathbb{C})}$ number of complex additions and the $C_{\text{RLS}}^{(\mathbb{R}*\mathbb{C})}$ number of "mixed" multiplications (real/complex) associated with the different components of the **ensemble-averaging assisted RLS-based adaptation** of the CIR-related taps' single vector of predictor coefficients.

the processing of a specific CIR-related tap. We emphasize that the standard RLS approach of Section 3.5.1.1 always imposes a higher complexity, than the ensemble-averaging assisted approach of Section 3.5.1.2 in terms of both the $C^{(\mathbb{C}+\mathbb{C})}$ number of complex additions and the $C^{(\mathbb{R}*\mathbb{C})}$ number of mixed multiplications.

By contrast, the $C^{(\mathbb{C}*\mathbb{C})}$ number of complex multiplications depends on the parameters K_0 and $N_{tap}^{[t]}$, which jointly determine, as to which of the above-mentioned two approaches exhibits a lower complexity. However, for a realistic choice of these parameters, for example for $K_0 \geq 3$ and $N_{tap}^{[t]} = \{4, 8, 16\}$, the ensemble-averaging assisted approach of Section 3.5.1.2 is always of a lower complexity. Again, this complexity reduction is achieved at the cost of an MSE performance degradation.

While in Section 3.5.1 the application of the RLS algorithm was discussed in the context of prediction-assisted DDCE for employment in single-user OFDM systems, in Section 3.5.1 we will portray its benefits in the context of the PIC-assisted DDCE for multi-user OFDM systems.

3.5.2 RLS-Adaptive PIC-Assisted DDCE for Multi-User OFDM

After having reviewed the theory of RLS-adaptive CIR-related tap-by-tap prediction for single-user OFDM systems in Section 3.5.1.1 we will directly embark here on an assessment of RLS-adaptive prediction based PIC-assisted DDCE for multi-user OFDM, or more generally, for OFDM systems which support multiple transmit antennas. Here we will concentrate on the idealistic scenario of a sample-spaced CIR, while investigations which take into account the specific properties of the more realistic non sample-spaced channels remain a potential part of our future work.

3.5.2.1 MSE Performance Assessment

Throughout our investigations in this section we will focus again on our standard multi-user OFDM scenario of four simultaneous users, each equipped with one transmit antenna, while at the base-station (BS) a four-element antenna array is employed. The channel between each transmit-receive

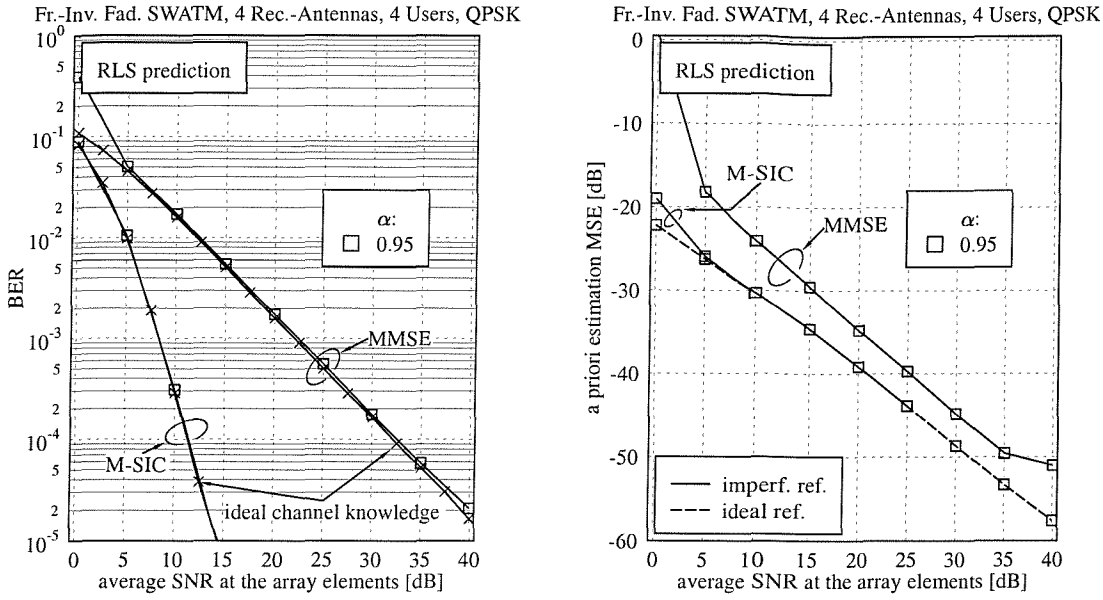

Figure 3.18: (Left:) BER versus SNR performance and (Right:) *a priori* channel estimation MSE versus SNR performance associated with the CIR-related tap-by-tap based RLS-adaptive PIC-assisted DDCE of Figure 3.3[18] in the context of a scenario of four receiver antennas at the BS and four simultaneous users, each equipped with one transmit antenna; the channel between each transmitter-receiver antenna pair is characterized in terms of its sample-spaced impulse response and OFDM parameters by the indoor WATM channel- and system parameters of Section 6.1.1; the OFDM symbol normalized Doppler frequency was $F_D = 0.007$; furthermore, the number of significant CIR-related taps was $K_0 = 12$ and the number of subcarriers was $K = 512$; MMSE- as well as M-SIC (M=2) detection was employed at the receiver and both an ideal, error-free reference and an imperfect, error-contaminated reference was invoked in the DDCE; the RLS-specific forgetting factor was set to $\alpha = \alpha_{\text{RLS}} = 0.95$.

antenna pair - characterized in terms of its sample-spaced impulse response - and the OFDM parameters are fixed to those used by the indoor WATM system of Section 6.1.1. Two detection techniques are invoked in our study, namely, the MMSE- and M-SIC detection techniques of Sections 4.2.3 and 4.3.1. The corresponding BER- and *a priori* channel estimation MSE simulation results - after the initial adaptation[19] of the predictor coefficients - are portrayed at the left- and right-hand side of Figure 3.18, respectively.

In the context of the BER performance assessment shown at the left-hand side of Figure 3.18 we observe that with the aid of the imperfect channel estimates produced by the RLS-adaptive PIC-assisted DDCE almost the same performance is achieved as when employing ideal channel knowledge. This is particularly true for the powerful M-SIC detection algorithm, which produces relatively reliable symbol decisions and hence also a reliable remodulated reference for the RLS-adaptive PIC-assisted DDCE. In contrast, a slight BER degradation is observed when using the less

[19]The initial adaptation of the predictor coefficients was observed e.g. in Figure 3.17. After the adaptation the *a priori* channel estimation MSE fluctuates around its specific mean value.

powerful MMSE detection scheme particularly for the range of SNRs up to 5dB, while for higher SNRs the BER performance is also almost identical to that when using perfect channel estimates.

The benefits of a more reliable remodulated reference used in the RLS-adaptive PIC-assisted DDCE become even more evident from the MSE performance results shown at the right-hand side of Figure 3.18. Here we observe a significant MSE reduction when employing the M-SIC assisted generation of the remodulated reference rather than that of the MMSE detector. In our specific example, which employs the sample-spaced three-path indoor WATM CIR, all of the channel's energy is concentrated in three CIR-related taps, namely those at zero, six and eleven sampling period delays, while at all other tap positions within the CIR window of the first $K_0 = 12$ taps, the RLS-based adaptive predictor succeeds in effectively reducing the noise without setting these taps by 'brute force' to zero. Hence the maximum noise reduction factor is about $3/512$. Note however again that in the more realistic scenario of a non-sample-spaced CIR in conjunction with employing the unitary DFT matrix $\mathbf{W}$ for transforming the least-squares channel transfer factor estimates from the frequency-domain to the CIR-related domain, the noise reduction is more moderate due to the effects of spectral leakage as it was discussed in Section 3.4.2.3. More explicitly, the energy conveyed by the channel is rather spread across the different CIR-related taps.

Finally, let us comment on the specific choice of the forgetting factor $\alpha_{\text{RLS}} = 0.95$. As suggested during our investigations of RLS based adaptive prediction-assisted DDCE employed in single-user OFDM systems in Section 3.5.1.3, for small values of α_{RLS}, the predictor may become unstable, as a result of which an excessive estimation MSE is observed. Our experiments conducted in the context of the PIC-assisted DDCE of Figure 3.3 further underlined that the appropriate range of α_{RLS} values has to be re-optimized when invoking an imperfect, potentially error-contaminated reference. Again, relatively small values of α_{RLS} yield a fast convergence, but also a high sensitivity to erroneous symbol decisions, while for higher values of α_{RLS} the opposite is true. A choice of $\alpha_{\text{RLS}} = 0.95$ was deemed reasonable in our application. However, for the robust RLS prediction approach outlined in Section 3.5.1.2, our results not included here for reasons of space economy suggested that the predictor's stability was less dependent on the specific choice of α_{RLS} due to the ensemble averaging carried out across the different CIR-related taps.

3.5.3 Conclusions

A drawback of the PIC-assisted DDCE of Figure 3.3 discussed in Section 3.4 was the relatively cumbersome procedure of the off-line optimization of the predictor coefficients by means of the iterative approach discussed in Section 3.4.1.6. As a prerequisite for its application, assumptions had to be made about the channel's spaced-time spaced-frequency correlation function, potentially inflicting a performance loss. In order to avoid these problems - but at the complexity-related disadvantage of an on-line optimization during the reception of the OFDM symbols - it was proposed

in Section 3.5 to render the CIR-related tap predictors adaptive by means of the RLS algorithm. This was motivated by the observation in the context of the iterative off-line optimization proposed in Section 3.4.1.6, that although in each iteration the adaptation of the different predictors' coefficients is performed independently, the average channel estimation MSE associated with the different users' channels converges to its minimum. In order to argue further, each iteration of the off-line optimization has its analogy in the predictor coefficient adjustment conducted by the RLS algorithm after the reception of each OFDM symbol.

Our more specific discussions commenced in Section 3.5.1 by considering a single-user scenario in Section 3.5.1.1. The philosophy of RLS-assisted CIR-related tap prediction was introduced, where the adaptation of the CIR-related tap predictor coefficients was carried out separately for each CIR-related tap. By contrast, in Section 3.5.1.2 a simplification was achieved in terms of the computational complexity by invoking ensemble averaging of the different CIR-related taps' auto-correlation matrices and cross-correlation vectors, according to Equations 3.173 and 3.174, respectively. However, the ensemble averaging prohibited the application of the Sherman-Morrison formula [87], which was invoked in the context of the standard RLS algorithm in an attempt to avoid an explicit solution of Equation 3.166 for the vector of optimum CIR-related tap predictor coefficients. Although the complexity of the direct solution of Equation 3.175 is proportional to the cube of the number of predictor coefficients, its application is in most cases significantly less complex than that of the RLS-assisted CIR-related tap-by-tap adaptation procedure of Section 3.5.1.1. This argument was supported by our complexity analysis provided in Section 3.5.1.4. The complexity reduction is achieved at the cost of an MSE performance degradation in conjunction with the ensemble-averaging assisted approach of Section 3.5.1.2, since the same vector of predictor coefficients is employed for the prediction of each of the different CIR-related taps, potentially exhibiting different variances. Our rudimentary *a priori* estimation MSE performance assessment in Section 3.5.1.3 focussed on the influence of the RLS-specific forgetting factor α_{RLS} and on that of the OFDM symbol normalized Doppler frequency F_D. For lower values of α_{RLS} the speed of convergence was faster, while at the same time the residual MSE after adaptation remained higher, than that recorded for higher values of α_{RLS}.

By contrast to our discussions in Section 3.5.1, in Section 3.5.2 we concentrated on the performance assessment of the RLS-adaptive PIC-assisted DDCE employed in the context of multi-user OFDM. From the BER- and MSE performance curves of Figure 3.18 presented in Section 3.5.2.1 the system's convergence was confirmed. In the context of an imperfect, potentially error contaminated DDCE-related reference we found that the RLS-related forgetting factor α_{RLS}, for which a stable operation is maintained even in the presence of sporadic subcarrier symbol errors, was required to be closer to unity, which implies slower loss of memory. A value of $\alpha_{\text{RLS}} = 0.95$ was deemed acceptable for this application. Simulation results generated for the ensemble-averaging based RLS-adaptive PIC-assisted DDCE were not presented here for reasons of space economy,

but our experiments revealed that as a positive side-effect of the ensemble averaging the specific choice of the forgetting factor α_{RLS} was deemed less critical. Part of our future research will be the assessment of the RLS-adaptive PIC-assisted DDCE in the context of channels exhibiting non-sample-spaced CIRs.

3.6 Chapter Conclusions

In Section 3 we have portrayed a range of decision-directed channel estimation (DDCE) approaches designed for multi-user OFDM scenarios, or more generally, for OFDM scenarios supporting multiple transmit antennas. While in Section 3.1 the motivation of the different channel estimation approaches was detailed, and in Section 3.2 the SDMA-MIMO channel scenario was outlined, our more specific discussions commenced in Section 3.3 with the portrayal of Li's least-squares error assisted estimator. Our detailed conclusions with respect to this approach were provided in Section 3.3.6. In the context of our discussions in Section 3.3 we provided a more general mathematical description of the estimator proposed by Li *et al.* [21], while at the same time providing expressions for the *a posteriori* channel transfer function estimation MSE in the context of both sample-spaced- as well as non-sample-spaced CIRs. Furthermore, the estimator's restriction in terms of supporting a maximum of $L = \frac{K}{K_0}$ number of simultaneous users was highlighted, where K is the number of subcarriers and K_0 is the number of significant CIR-related taps. Our discussions of the LS-assisted DDCE were concluded by a detailed complexity analysis, which motivated our quest for alternative channel transfer function estimation approaches. More specifically, the explicit solution for the vector of optimum CIR-related taps according to Equation 3.22 imposes a complexity, which is partially a cubical function of the product LK_0. Hence, depending on the specific choice of the L number of transmit antennas and the K_0 number of significant CIR-related taps, the complexity might become excessive.

In order to reduce this complexity it was proposed by Li [22] to perform a parallel cancellation of the interfering CIR contributions with the aim of avoiding a direct solution of the equation system seen in Equation 3.22. This was achieved on the basis of CIR-related *a posteriori* tap estimates generated during the previous OFDM symbol period by potentially invoking a linear CIR-related tap prediction filter. It was argued furthermore that from a mathematical point of view performing both the parallel interference cancellation and the CIR-related tap prediction in the CIR-related domain is equivalent to performing the PIC in the frequency-domain and the tap-prediction in the CIR-related domain, which was the topic of our in-depth discussions in Section 3.4. For detailed conclusions on this topic we refer to Section 3.4.4. As a result of our efforts in Section 3.4.1, expressions were derived for both the *a priori*- and *a posteriori* channel transfer function estimation MSE - taking into account the recursive nature of the estimator - and the conditions for its stability were presented. Furthermore, an iterative approach was proposed for the off-line optimization of the CIR-related tap

predictor coefficients. Our performance investigations in Section 3.4.2 were conducted with respect to both the estimator's MSE- and the system's BER performance, as a function of the various system parameters, namely that of the L number of simultaneous users, that of the K_0 number of significant CIR-related taps, the K number of subcarriers, the $N_{tap}^{[t]}$ number of predictor coefficients, and also that as a function of the OFDM symbol normalized Doppler frequency. Furthermore, the effects of non-sample-spaced CIRs were described. Our discussions were concluded by a complexity study in Section 3.4.3 by highlighting under which conditions it was more beneficial to perform the PIC in the frequency- or in the CIR-related domain, in order to minimize the associated complexity. It was found furthermore that the PIC-assisted DDCE's complexity is significantly lower, than that of the LS-assisted DDCE described in Section 3.3.

A disadvantage associated with the iterative off-line optimization of the CIR-related tap predictor coefficients is the requirement of having *a priori* knowledge concerning the channel's spaced-time spaced-frequency correlation function. Since this is normally not available, we argued in Section 3.4.1.7 that a standard procedure is to assume a uniform, ideally support-limited channel scattering function and its associated spaced-time spaced-frequency correlation function - with the consequence of a concomitant performance loss in comparison to the perfect knowledge of these parameters. In order to alleviate this problem, a viable approach is to render the PIC-assisted DDCE's prediction filter adaptive, which can be achieved with the aid of the RLS algorithm. This was the topic of Section 3.5. Again, for our detailed conclusions we refer to Section 3.5.3. Our strategy in this section was first to demonstrate the applicability of the RLS algorithm to the problem of adjusting the CIR-related tap predictor's coefficients in a DDCE-assisted single-user OFDM system, and then to demonstrate its applicability to the PIC-assisted DDCE of Figure 3.3 for multi-user OFDM. In order to further reduce the associated computational complexity of RLS-adaptive CIR-related tap-by-tap prediction it was proposed to employ the same vector of predictor coefficients for the prediction of each of the different CIR-related taps and hence to base its calculation on the ensemble average of the different CIR-related taps' auto-correlation matrices and cross-correlation vectors. As a side-effect, we expect a slight performance degradation compared to the higher-complexity case of CIR-related tap-by-tap prediction filtering having individual vectors of predictor coefficients. As our experiments showed, the choice of the RLS-specific forgetting factor α_{RLS} was also less critical, than for the standard RLS algorithm. Again, for more detailed conclusions on this topic we refer to Section 3.5.3.

Special Symbols - Decision-Directed Channel Estimation for Multi-User OFDM

Special Symbols - Common

$H_p^{(l)}[n,k]$: Channel transfer factor associated with the channel encountered between the l-th user's transmit antenna and the p-th receiver antenna-element in the k-th subcarrier of the n-th OFDM symbol period.

$\mathbf{H}_p^{(i)}[n]$: Vector of channel transfer factors $H_p^{(i)}[n,k]$, $k = 0,\ldots,K-1$ associated with the channel encountered between the i-th user's transmit antenna and the p-th receiver antenna element: $\mathbf{H}_p^{(i)}[n] \in \mathbb{C}^{K\times 1}$.

$\mathbf{I}_{K_0,p}^{(i)}$: Diagonal masking-matrix used for retaining the significant CIR-related taps: $\mathbf{I}_{K_0,p}^{(i)} = \mathbf{J}_{K_0,p}^{(i)}\mathbf{J}_{K_0,p}^{(i)H} \in \mathbb{R}^{K\times K}$.

$\mathbf{J}_{K_0,p}^{(i)}$: Matrix invoked for mapping the K_0 significant CIR-related taps' estimates contained in the vector $\hat{\mathbf{h}}_{K_0,p}^{(i)}[n]$ to their 'true' integer positions within the K-tap FFT window: $\mathbf{J}_{K_0,p}^{(i)} \in \mathbb{C}^{K\times K_0}$.

K_0: Number of significant CIR-related taps.

L: Number of simultaneous SDMA users, each equipped with a single transmit antenna.

$n_p[n,k]$: AWGN signal contribution of variance σ_n^2 associated with the p-th receiver antenna element.

$\mathbf{n}_p[n]$: Vector of AWGN signal contributions $n_p[n,k]$, $k = 0,\ldots,K-1$, associated with the p-th receiver antenna element in each of the K subcarriers: $\mathbf{n}_p[n] \in \mathbb{C}^{K\times 1}$.

P: Number of BS receiver antenna elements.

$s^{(l)}[n,k]$: Symbol transmitted by the l-th user.

$\mathbf{S}^{(i)}[n]$: Diagonal matrix of the i-th user's transmitted subcarrier symbols $s^{(i)}[n,k]$, $k = 0,\ldots,K-1$: $\mathbf{S}^{(i)}[n] \in \mathbb{C}^{K\times K}$.

$\check{\mathbf{S}}^{(i)}[n]$: Diagonal matrix of the i-th user's sliced subcarrier symbols $\check{s}^{(i)}[n,k]$, $k = 0,\ldots,K-1$: $\check{\mathbf{S}}^{(i)}[n] \in \mathbb{C}^{K\times K}$.

W_K: Complex Fourier kernel: $W_K = e^{-j\frac{2\pi}{K}}$.

$\mathbf{W}$:	DFT matrix hosting the complex exponentials $\mathbf{W}\|_{[i,j]} = \frac{1}{\sqrt{K}} W_K^{ij}$: $\mathbf{W} \in \mathbb{C}^{K \times K}$.
$x_p[n,k]$:	Signal received by the p-th receiver antenna element.
$\mathbf{x}_p[n]$:	Vector of signals $x_p[n,k]$, $k = 0, \ldots, K-1$ associated with the p-th receiver antenna element in the K subcarriers: $\mathbf{x}_p[n] \in \mathbb{C}^{K \times 1}$.
σ_s^2:	Variance of the l-th user's transmitted symbols.
$()[n,k]$:	Index employed for indicating that the signal in round brackets is associated with the k-th subcarrier of the n-th OFDM symbol period.
$()^{(i,j)}$:	Sub-matrix associated with the i-th 'row' and j-th 'column' of the block matrix in brackets.
$()\|_{[i,j]}$:	Element associated with the i-th row and j-th column of the matrix in brackets.

Special Symbols - LS-Assisted DDCE

$\mathbf{A}_p[n]$: Short-hand: $\mathbf{A}_p[n] = \check{\mathbf{S}}^T[n]\mathbf{W}_{J,p} \in \mathbb{C}^{K \times LK_0}$.

$\mathbb{C}^{(\mathbb{C}\{*,+\}\mathbb{C})}|_{\text{norm}}$: Normalized computational complexity quantified in terms of the number of complex multiplications or additions[20].

$\mathbb{C}^{(\mathbb{C}\{*,+\}\mathbb{C})}_{\text{MU-CE,LS}}|_{\text{norm}}$: Normalized total computational complexity quantified in terms of the number of complex multiplications or additions, associated with the LS-assisted DDCE designed for multi-user OFDM[21].

$\mathbb{C}^{(\mathbb{C}\{*,+\}\mathbb{C})}_{\text{MU-CE,PIC-LS}}|_{\text{norm}}$: Normalized total computational complexity in terms of the number of complex multiplications or additions, associated with the PIC-based LS-assisted DDCE designed for multi-user OFDM[22].

$\hat{\mathbf{h}}^{(i)}_{K_0,p}[n]$: Vector of K_0 significant CIR-related tap estimates associated with the channel encountered between the i-th user's transmit antenna and the p-th receiver antenna element: $\hat{\mathbf{h}}^{(i)}_{K_0,p}[n] \in \mathbb{C}^{K_0 \times 1}$.

$\hat{\mathbf{h}}_{K_0,p}[n]$: Block-vector hosting the L different users' vectors $\hat{\mathbf{h}}^{(i)}_{K_0,p}[n]$, $i = 1, \ldots, L$ of K_0 significant CIR-related tap estimates, associated with the p-th receiver antenna element: $\hat{\mathbf{h}}_{K_0,p}[n] = (\hat{h}^{(1)T}_{K_0,p}[n], \ldots, \hat{h}^{(L)T}_{K_0,p}[n])^T \in \mathbb{C}^{LK_0 \times 1}$.

$\tilde{\mathbf{h}}_{apt,K_0,p}[n]$: Block-vector hosting the L different users' vectors of least-squares error optimized significant CIR-related tap estimates, associated with the p-th receiver antenna element: $\tilde{\mathbf{h}}_{apt,K_0,p}[n] = \hat{\mathbf{h}}_{K_0,p}[n]|_{opt} \in \mathbb{C}^{LK_0 \times 1}$.

$\hat{\mathbf{H}}^{(i)}_p[n]$: Vector of channel transfer factor estimates associated with the channel encountered between the i-th user's transmit antenna and the p-th receiver antenna element, based on the vector $\hat{\mathbf{h}}^{(i)}_{K_0,p}[n]$ of significant CIR-related tap estimates: $\hat{\mathbf{H}}^{(i)}_p[n] = \mathbf{W}\mathbf{J}^{(i)}_{K_0,p}\hat{\mathbf{h}}^{(i)}_{K_0,p}[n] \in \mathbb{C}^{K \times 1}$.

$\mathbf{H}_p[n]$: Block-vector hosting the L different users' vectors $\mathbf{H}^{(i)}_p[n]$, $i = 1, \ldots, L$ of channel transfer factors, associated with the p-th receiver antenna element, which is given by: $\mathbf{H}_p[n] = (H^{(1)T}_p[n], \ldots, H^{(L)T}_p[n])^T \in \mathbb{C}^{LK \times 1}$.

$\hat{\mathbf{H}}_p[n]$: Block-vector hosting the L different users' vectors $\hat{\mathbf{H}}^{(i)}_p[n]$, $i = 1, \ldots, L$ of channel transfer factor estimates, associated with the p-th receiver antenna element: $\hat{\mathbf{H}}_p[n] = (\hat{\mathbf{H}}^{(1)T}_p[n], \ldots, \hat{\mathbf{H}}^{(L)T}_p[n])^T \in \mathbb{C}^{LK \times 1}$.

[20] The normalization was carried out with respect to the number of subcarriers K, number of users L and number of receiver antenna elements P.

[21] See Footnote 20.

[22] See Footnote 20.

$\tilde{\mathbf{H}}_{apt,p}[n]$: Block-vector of the L different users' vectors $\tilde{\mathbf{H}}^{(i)}_{apt,p}[n]$, $i = 1, \ldots, L$ of least-squares error optimized channel transfer factor estimates, associated with the p-th receiver antenna element: $\tilde{\mathbf{H}}_{apt,p}[n] \in \mathbb{C}^{LK \times 1}$.

$\mathbf{I}_A$: Unity matrix: $\mathbf{I}_A \in \mathbb{C}^{K_A \times K_A}$.

$\mathbf{I}_B$: Unity matrix: $\mathbf{I}_B \in \mathbb{C}^{K_B \times K_B}$.

$\mathbf{I}^{(i,j)}_{cyc}$: Matrix which performs the cyclic rotation of a matrix' rows, when multiplied from the left- or rotation of the matrix' columns, when multiplied from the right: $\mathbf{I}^{(i,j)}_{cyc} = \begin{pmatrix} 0 & \mathbf{I}_B \\ \mathbf{I}_A & 0 \end{pmatrix} \in \mathbb{C}^{K_0 \times K_0}$.

K_A: Short-hand: $K_A = [K - \overline{K}_0(i-j)] \bmod K$.

K_B: Short-hand: $K_B = [K - \overline{K}_0(j-i)] \bmod K$.

$\overline{K}_0$: Short-hand: $\overline{K}_0 = \lfloor \frac{K}{L} \rfloor$.

$\overline{\mathrm{MSE}}^{(i)}_{apt,p}[n]$: Subcarrier-averaged channel transfer factor estimation MSE associated with the channel encountered between the i-th user's single transmit antenna and the p-th receiver antenna element.

$\overline{\mathrm{MSE}}_{apt,p}[n]$: Subcarrier- and user-averaged estimation MSE associated with the channels encountered between the L users' single transmit antennas and the p-th receiver antenna element.

$\mathbf{p}_p[n]$: LS-related 'cross-correlation' vector: $\mathbf{p}_p[n] = \mathbf{A}^H_p[n]\mathbf{x}[n] \in \mathbb{C}^{LK_0 \times 1}$.

$\mathbf{P}_p[n]$: LS-related projection matrix- or Moore-Penrose pseudo inverse of the matrix $\mathbf{A}_p[n]$: $\mathbf{P}_p[n] \in \mathbb{C}^{LK_0 \times K}$.

$\mathbf{Q}_p[n]$: LS-related 'auto-correlation' matrix: $\mathbf{Q}_p[n] = \mathbf{A}^H_p[n]\mathbf{A}_p[n] \in \mathbb{C}^{LK_0 \times LK_0}$.

$\acute{\mathbf{Q}}^{(i,j)}_p[n]$: Short-hand: $\acute{\mathbf{Q}}^{(i,j)}_p[n] = \mathbf{W}^H \mathbf{S}^{(i)*}[n]\mathbf{S}^{(j)}[n]\mathbf{W}$.

$\mathbf{R}^{[f](i)}_p$: Spaced-frequency correlation matrix associated with the channel encountered between the i-th user's transmit antenna and the p-th receiver antenna element: $\mathbf{R}^{[f](i)}_p = E\{\mathbf{H}^{(i)}_p[n]\mathbf{H}^{(i)H}_p[n]\} \in \mathbb{C}^{K \times K}$.

$\mathbf{R}^{[f]}_p$: Block-diagonal auto-correlation matrix hosting the L spaced-frequency correlation matrices $\mathbf{R}^{[f](i)}_p, i = 1, \ldots, L$ associated with the channels encountered between the L users' single transmit antennas and the p-th receiver antenna element: $\mathbf{R}^{[f]}_p = E\{\mathbf{H}_p[n]\mathbf{H}^H_p[n]\} = diag(\mathbf{R}^{[f]1}_p \ldots \mathbf{R}^{[f]L}_p) \in \mathbb{C}^{LK \times LK}$.

$\mathbf{R}_{a,p}^{[f]}$: Auto-correlation matrix of the multi-user vector $\tilde{\mathbf{H}}_{apt,p}[n]$ hosting K subcarrier channel transfer factor estimates per user: $\mathbf{R}_{a,p}^{[f]} = E\{\tilde{\mathbf{H}}_{apt,p}[n]\tilde{\mathbf{H}}_{apt,p}^{H}[n]\} = \mathbf{R}_{a,\text{Channel,p}}^{[f]} + \mathbf{R}_{a,\text{AWGN,p}}^{[f]} \in \mathbb{C}^{LK\times LK}$.

$\mathbf{R}_{a,\text{AWGN},p}^{[f]}$: AWGN-related component of the auto-correlation matrix $\mathbf{R}_{a,p}^{[f]}$: $\mathbf{R}_{a,\text{AWGN},p}^{[f]} \in \mathbb{C}^{LK\times LK}$.

$\mathbf{R}_{a,\text{Channel},p}^{[f]}$: Channel-related component of the auto-correlation matrix $\mathbf{R}_{a,p}^{[f]}$: $\mathbf{R}_{a,\text{Channel},p}^{[f]} \in \mathbb{C}^{LK\times LK}$.

$\mathbf{R}_{c,p}^{[f]}$: Cross-correlation matrix between the L-user vector $\mathbf{H}_p[n]$ of the K subcarriers' 'true' channel transfer factors and the L-user vector $\tilde{\mathbf{H}}_{apt,p}[n]$ of the K subcarriers' transfer factor estimates: $\mathbf{R}_{c,p}^{[f]} = E\{\mathbf{H}_p[n]\tilde{\mathbf{H}}_{apt,p}^{H}[n]\} \in \mathbb{C}^{LK\times LK}$.

$\mathbf{R}_{\Delta\tilde{\mathbf{H}}_{apt,p}[n]}$: Auto-correlation matrix of the vector $\Delta\tilde{\mathbf{H}}_{apt,p}[n]$ of channel transfer factor estimation errors: $\mathbf{R}_{\Delta\tilde{\mathbf{H}}_{apt,p}[n]} = E\{\Delta\tilde{\mathbf{H}}_{apt,p}[n]\Delta\tilde{\mathbf{H}}_{apt,p}^{H}[n]\} = \mathbf{R}_{p}^{[f]} - 2\Re\mathfrak{e}\{\mathbf{R}_{c,p}^{[f]}\} + \mathbf{R}_{a,p}^{[f]} \in \mathbb{C}^{LK\times LK}$.

$\mathbf{S}[n]$: Block-matrix hosting the L different users' diagonal matrices $\mathbf{S}^{(i)}[n]$, $i = 1,\ldots,L$ of transmitted subcarrier symbols: $\mathbf{S}[n] = (\mathbf{S}^{(1)T}[n],\ldots,\mathbf{S}^{(L)T}[n])^{T} \in \mathbb{C}^{LK\times K}$.

$\check{\mathbf{S}}[n]$: Block-matrix hosting the L different users' diagonal matrices $\check{\mathbf{S}}^{(i)}[n]$, $i = 1,\ldots,L$ of sliced subcarrier symbols: $\check{\mathbf{S}}[n] \in \mathbb{C}^{LK\times K}$.

$t^{(i)}[n,k]$: k-th element of the optimum training subcarrier symbol sequence associated with the i-th user as proposed by Li [22]: $t^{(i)}[n,k] = \sigma_i t_p[n,k]W_K^{-\overline{K}_0(i-1)K}$

$t_p[n,k]$: k-th element of an arbitrary training subcarrier symbol sequence $t_p[n,k]$, $k = 0,\ldots,K-1$ having unit-variance elements.

$\mathbf{T}_{W,K_0,p}^{(i)}$: Short-hand: $\mathbf{T}_{W,K_0,p}^{(i)} = \mathbf{W}_{J,p}^{(i)}\mathbf{W}_{J,p}^{(i)H} \in \mathbb{C}^{K\times K}$.

$\mathbf{W}_{J,p}^{(i)}$: Combined DFT- and mapping matrix for transforming the vector $\hat{\mathbf{h}}_{K_0,p}^{(i)}[n]$ of K_0 significant CIR-related tap estimates to the vector $\hat{\mathbf{H}}_{p}^{(i)}[n]$ of K channel transfer factor estimates: $\mathbf{W}_{J,p}^{(i)} = \mathbf{W}\mathbf{J}_{K_0,p}^{(i)} \in \mathbb{C}^{K\times K_0}$.

$\mathbf{W}_{J,p}$: Block-diagonal matrix of the L different users' combined DFT- and mapping matrices $\mathbf{W}_{J,p}^{(i)}$, $i = 1,\ldots,K$ associated with the p-th receiver antenna element: $\mathbf{W}_{J,p} = diag(\mathbf{W}_{J,p}^{(1)},\ldots,\mathbf{W}_{J,p}^{(L)}) \in \mathbb{C}^{LK\times LK_0}$.

$\hat{\mathbf{x}}_p[n]$: Vector of estimated signals $\hat{x}_p[n,k]$, $k = 0,\ldots,K-1$ associated with the p-th receiver antenna element in each of the K subcarriers: $\hat{\mathbf{x}}_p[n] \in \mathbb{C}^{K\times 1}$.

$\Lambda_{W,p}^{[f](i)}$: Decomposition of the spaced-frequency correlation matrix $\mathbf{R}_p^{[f](i)}$ associated with the channel between the i-th user's transmit antenna and the p-th receiver antenna element, with respect to the DFT matrix $\mathbf{W}$: $\Lambda_{W,p}^{[f](i)} = (\mathbf{W}^H \mathbf{R}_p^{[f](i)} \mathbf{W}) \in \mathbb{C}^{K \times K}$.

$\Lambda_{W,J,p}^{[f](i)}$: Short-hand: $\Lambda_{W,J,p}^{[f](i)} = \mathbf{J}_{K_0,p}^{(i)H} \Lambda_{W,p}^{[f](i)} \mathbf{J}_{K_0,p}^{(i)} \in \mathbb{C}^{K_0 \times K_0}$.

$\Delta\tilde{\mathbf{H}}_{apt,p}[n]$: Vector of channel transfer factor estimation errors associated with the K subcarriers of each of the L users, with respect to the p-th receiver antenna element: $\Delta\tilde{\mathbf{H}}_{apt,p}[n] = \mathbf{H}_p[n] - \tilde{\mathbf{H}}_{apt,p}[n] \in \mathbb{C}^{LK \times 1}$.

$\Delta\hat{\mathbf{x}}[n]$: Vector of estimation errors between the received vector $\mathbf{x}[n]$- and the synthesized vector $\hat{\mathbf{x}}[n]$ of subcarrier signals: $\Delta\hat{\mathbf{x}}[n] = \mathbf{x}[n] - \hat{\mathbf{x}}[n] \in \mathbb{C}^{K \times 1}$.

Special Symbols - Decision-Directed Channel Estimation for Multi-User OFDM - PIC-assisted DDCE

$\tilde{c}_{pre,p}^{(i)}[\acute{n}]$: Predictor coefficient employed in the context of the CIR prediction process associated with the channel encountered between the i-th user's transmit antenna and the p-th receiver antenna element. Note that the $\acute{n}$-th predictor coefficient, where $\acute{n} \in \{0, \ldots, N_{tap}^{[t]} - 1\}$, is associated with the OFDM symbol having an offset of $-\acute{n}$ relative to the current OFDM symbol.

$\tilde{\mathbf{c}}_{pre,p}^{(i)}$: Vector of predictor coefficients employed in the context of the CIR prediction process associated with the channel encountered between the i-th user's transmit antenna and the p-th receiver antenna element: $\tilde{\mathbf{c}}_{pre,p}^{(i)} \in \mathbb{C}^{N_{tap}^{[t]} \times 1}$.

$\tilde{\mathbf{c}}_{pre,p}^{(j)}|_{opt}$: Vector of optimum predictor coefficients, based on the knowledge of the remaining users' average *a priori* estimation MSEs, namely on $\overline{\text{MSE}}_{apr}^{(i)}$, $i = 1, \ldots, L$, $i \neq j$: $\tilde{\mathbf{c}}_{pre,p}^{(j)}|_{opt} \in \mathbb{C}^{N_{tap}^{[t]} \times 1}$.

$\mathbf{C}_{pre}$: Diagonal matrix of the L different users' CIR-related tap prediction coefficient terms of $\frac{K_0}{K}\alpha_j \tilde{\mathbf{c}}_{pre,p}^{(j)H} \tilde{\mathbf{c}}_{pre,p}^{(j)}$, $j = 1, \ldots, L$: $\mathbf{C}_{pre} \in \mathbb{C}^{L \times L}$.

$\mathbb{C}_{\text{MU-CE,PIC}}^{(\mathbb{C}\{*,+\}\mathbb{C})}|_{\text{norm}}$: Normalized total computational complexity expressed in terms of the number of complex multiplications or additions, associated with the PIC-assisted DDCE designed for multi-user OFDM[23].

$\mathbb{C}_{\text{RLS}}^{\mathbb{C}\{*,+\}\mathbb{C}}$: Computational complexity of the CIR-related ensemble-averaging assisted RLS-based tap predictor, expressed in terms of the number of complex multiplications and additions, inflicted per channel and OFDM symbol.

$\mathbb{C}_{\text{RLS},tap}^{\mathbb{C}\{*,+\}\mathbb{C}}$: Computational complexity of the CIR-related RLS-based tap predictor, expressed in terms of the number of complex multiplications and additions, inflicted per CIR-related tap and OFDM symbol.

$\mathbf{F}$: Feedback matrix characterizing the PIC process. While the main-diagonal elements are zero, the side-diagonal elements are unity: $\mathbf{F} \in \mathbb{R}^{L \times L}$.

$\acute{\mathbf{F}}$: Short-hand: $\acute{\mathbf{F}} = \mathbf{C}_{pre} \cdot \mathbf{P}_s^{-1} \cdot \mathbf{F} \cdot \mathbf{P}_s \in \mathbb{R}^{L \times L}$.

$G(\acute{\mathbf{F}})$: Union of Gershgorin disks of $\acute{\mathbf{F}}$. With the aid of the Gershgorin circle theorem explicit bounds can be imposed on the regions in $\mathbb{C}$, which host the eigenvalues of the matrix $\acute{\mathbf{F}}$ [87].

[23] See Footnote 20.

$\hat{\mathbf{h}}^{(i)}_{apr,p}[n]$: Vector of the K CIR-related taps' *a priori* estimates $\hat{h}^{(i)}_{apr,p}[n,l]$, $l = 0,\ldots,K-1$: $\hat{\mathbf{h}}^{(i)}_{apr,p}[n] \in \mathbb{C}^{K\times 1}$.

$\tilde{\mathbf{h}}^{(i)}_{apt,p}[n]$: Vector of the K CIR-related taps' *a posteriori* estimates, namely $\tilde{h}^{(i)}_{apt,p}[n,l]$, $l = 0,\ldots,K-1$, which is given by: $\tilde{\mathbf{h}}^{(i)}_{apt,p}[n] \in \mathbb{C}^{K\times 1}$.

$\hat{\mathbf{H}}^{(i)}_{apr,p}[n]$: Vector of the K different subcarriers' *a posteriori*[24] channel transfer factor estimates $\hat{H}^{(i)}_{apr,p}[n,k]$, $k = 0,\ldots,K-1$: $\hat{\mathbf{H}}^{(i)}_{apr,p}[n] \in \mathbb{C}^{K\times 1}$.

$\tilde{\mathbf{H}}^{(i)}_{apt,p}[n]$: Vector of the K different subcarriers' *a priori* channel transfer factor estimates $\tilde{H}^{(i)}_{apt,p}[n,k]$, $k = 0,\ldots,K-1$: $\tilde{\mathbf{H}}^{(i)}_{apt,p}[n] \in \mathbb{C}^{K\times 1}$.

$\mathbf{k}^{(i)}_{p}[n,l]$: Kalman gain vector associated with the RLS-assisted prediction of the l-th CIR-related tap: $\mathbf{k}^{(i)}_{p}[n,l] \in \mathbb{C}^{N^{[t]}_{tap}\times 1}$.

$\overline{\mathrm{MSE}}^{(j)}_{apr,p}[n]$: Subcarrier-averaged *a priori* channel transfer factor estimation MSE, which is expressed as: $\overline{\mathrm{MSE}}^{(j)}_{apr,p}[n] = \frac{1}{K}\mathrm{Trace}(\mathbf{R}_{\Delta\hat{\mathbf{H}}^{(j)}_{apr,p}}[n])$.

$\overline{\mathrm{MSE}}^{(j)}_{apt,p}[n]$: Subcarrier-averaged *a posteriori* channel transfer factor estimation MSE, which is expressed as: $\overline{\mathrm{MSE}}^{(j)}_{apt,p}[n] = \frac{1}{K}\mathrm{Trace}(\mathbf{R}_{\Delta\tilde{\mathbf{H}}^{(j)}_{apt,p}}[n])$.

$\overline{\mathrm{MSE}}^{(j)}_{dec,p}[n]$: Subcarrier-averaged channel-decorrelation related MSE, which is expressed as: $\overline{\mathrm{MSE}}^{(j)}_{dec,p}[n] = \frac{1}{K}\mathrm{Trace}(\mathbf{R}_{\Delta\mathbf{H}^{(j)}_{dec,p}})$.

$\mathbf{MSE}_{apr,p}$: Vector of average *a priori* channel transfer factor estimation MSEs, namely $\overline{\mathrm{MSE}}^{(j)}_{apr,p}[n]$, $j = 1,\ldots,L$: $\mathbf{MSE}_{apr,p}[n] \in \mathbb{R}^{L\times 1}$.

$\mathbf{MSE}_{dec,p}$: Vector of average channel decorrelation related MSEs, namely $\overline{\mathrm{MSE}}^{(j)}_{dec,p}[n]$, $j = 1,\ldots,L$: $\mathbf{MSE}_{dec,p}[n] \in \mathbb{R}^{L\times 1}$.

$N^{[t]}_{tap}$: Number of filter taps associated with the CIR-related tap estimator- or predictor.

$\mathbf{P}_s$: Diagonal-matrix hosting the different users' signal variances σ^2_l, $l = 1,\ldots,L$: $\mathbf{P}_s \in \mathbb{R}^{L\times L}$.

r_{expo}: Amplitude quotient associated with the exponential multipath intensity profile $r_{h,\mathrm{expo}}(\tau)$: $r_{\mathrm{expo}} = \frac{r_{h,\mathrm{expo}}(T_m)}{r_{h,\mathrm{expo}}(0)}$.

$\mathbf{r}^{[t](j)}_{p}$: Spaced-time cross-correlation vector, whose elements are given by $\mathbf{r}^{[t](j)}|_{\acute{n}} = E\{H^{(j)*}[n+1,k]H^{(j)}[n-\acute{n},k]\}$: $\mathbf{r}^{[t](j)}_{p} \in \mathbb{C}^{N^{[t]}_{tap}\times 1}$.

[24]Note that the *a posteriori* channel transfer factor estimates for the n-th OFDM symbol were generated during the $(n-1)$-th OFDM symbol period by linear $N^{[t]}_{tap}$ filtering.

$\tilde{\mathbf{r}}_{apt,p}^{[t](j)}[n,l]$: l-th CIR-related tap's RLS-related spaced-time sample-cross-correlation vector associated with the n-th OFDM symbol period: $\tilde{\mathbf{r}}_{apt,p}^{[t](j)}[n,l] \in \mathbb{C}^{N_{tap}^{[t]} \times 1}$.

$\mathbf{R}_p^{[f](i)}$: Spaced-frequency correlation matrix: $\mathbf{R}_p^{[f](i)} = E\{\mathbf{H}_p^{(i)}[n]\mathbf{H}_p^{(i)H}[n]\} \in \mathbb{C}^{K \times K}$. The EigenValue Decomposition (EVD) of the matrix $\mathbf{R}_p^{[f](i)}$ is given by: $\mathbf{R}_p^{[f](i)} = \mathbf{U}_p^{[f](i)} \Lambda_p^{[f](i)} \mathbf{U}_p^{[f](i)H}$.

$\tilde{\mathbf{R}}_p^{[f](i)}$: Spaced-frequency correlation matrix invoked in the design of the predictor: $\tilde{\mathbf{R}}_p^{[f](i)} \in \mathbb{C}^{K \times K}$. The EigenValue Decomposition (EVD) of the matrix $\tilde{\mathbf{R}}_p^{[f](i)}$ is given by: $\tilde{\mathbf{R}}_p^{[f](i)} = \tilde{\mathbf{U}}_p^{[f](i)} \tilde{\Lambda}_p^{[f](i)} \tilde{\mathbf{U}}_p^{[f](i)H}$.

$\mathbf{R}_{apt,p}^{[f](i)}$: Spaced-frequency correlation matrix associated with the *a posteriori* transfer factor estimates of the channel: $\mathbf{R}_{apt,p}^{[f](i)} = E\{\tilde{\mathbf{H}}_{apt,p}^{(i)}[n]\tilde{\mathbf{H}}_{apt,p}^{(i)H}[n]\} \in \mathbb{C}^{K \times K}$. The EigenValue Decomposition (EVD) of the matrix $\mathbf{R}_{apt,p}^{[f](i)}$ is given by: $\mathbf{R}_{apt,p}^{[f](i)} = \mathbf{U}_{apt,p}^{[f](i)} \Lambda_{apt,p}^{[f](i)} \mathbf{U}_{apt,p}^{[f](i)H}$.

$\mathbf{R}_p^{[t](i)}$: Spaced-time correlation matrix, whose elements are given by $\mathbf{R}^{[t](j)}|_{\acute{n}_1,\acute{n}_2} = E\{H^{(j)}[n-\acute{n}_1,k]H^{(j)*}[n-\acute{n}_2,k]\}$: $\mathbf{R}_p^{[t](i)} \in \mathbb{C}^{N_{tap}^{[t]} \times N_{tap}^{[t]}}$.

$\tilde{\mathbf{R}}_{apt,p}^{[t](j)}[n,l]$: l-th CIR-related tap's RLS-related spaced-time sample-correlation matrix associated with the n-th OFDM symbol period: $\tilde{\mathbf{R}}_{apt,p}^{[t](j)}[n,l] \in \mathbb{C}^{N_{tap}^{[t]} \times N_{tap}^{[t]}}$.

$\mathbf{R}_{\mathbf{H}_{dec,p}^{(j)}}$: Channel transfer function decorrelation related matrix: $\mathbf{R}_{\mathbf{H}_{dec,p}^{(j)}} \in \mathbb{C}^{K \times K}$.

$\mathbf{R}_{\Delta\hat{\mathbf{H}}_{apr,p}^{(j)}}[n]$: Auto-correlation matrix of the vector $\Delta\hat{\mathbf{H}}_{apr,p}^{(j)}[n]$ of *a priori* channel transfer factor estimation errors: $\mathbf{R}_{\Delta\hat{\mathbf{H}}_{apr,p}^{(j)}}[n] = E\{\Delta\hat{\mathbf{H}}_{apr,p}^{(j)}[n]\Delta\hat{\mathbf{H}}_{apr,p}^{(j)H}[n]\} \in \mathbb{C}^{K \times K}$.

$\mathbf{R}_{\Delta\tilde{\mathbf{H}}_{apt,p}^{(j)}}[n]$: Auto-correlation matrix of the vector $\Delta\tilde{\mathbf{H}}_{apt,p}^{(j)}[n]$ of *a posteriori* channel transfer factor estimation errors: $\mathbf{R}_{\Delta\tilde{\mathbf{H}}_{apt,p}^{(j)}}[n] = E\{\Delta\tilde{\mathbf{H}}_{apt,p}^{(j)}[n]\Delta\tilde{\mathbf{H}}_{apt,p}^{(j)H}[n]\} \in \mathbb{C}^{K \times K}$.

$\mathbf{T}_{K_0,p}^{(i)}$: Short-hand: $\mathbf{T}_{K_0,p}^{(i)} = \tilde{\mathbf{U}}_p^{[f](i)} \mathbf{I}_{K_0,p}^{(i)} \tilde{\mathbf{U}}_p^{[f](i)H} \in \mathbb{C}^{K \times K}$.

$\mathbf{U}_p^{[f](i)}$: Unitary KLT matrix associated with the EVD of the spaced-frequency correlation matrix $\mathbf{R}_p^{[f](i)}$: $\mathbf{U}_p^{[f](i)} \in \mathbb{C}^{K \times K}$.

$\mathbf{U}_{apt,p}^{[f](i)}$: Unitary KLT matrix associated with the EVD of the *a posteriori* channel transfer factor estimates' spaced-frequency correlation matrix $\mathbf{R}_{apt,p}^{[f](i)}$: $\mathbf{U}_{apt,p}^{[f](i)} \in \mathbb{C}^{K \times K}$.

$\tilde{\mathbf{U}}_p^{[f](i)}$: Unitary KLT matrix associated with the EVD of the spaced-frequency correlation matrix $\tilde{\mathbf{R}}_p^{[f](i)}$ invoked in the design of the predictor: $\tilde{\mathbf{U}}_p^{[f](i)} \in \mathbb{C}^{K \times K}$.

α_{expo}: Decay factor associated with the exponentially decaying multipath intensity profile $r_{h,\text{expo}}(\tau)$.

α_j: Modulation-noise enhancement factor $\alpha_j = E\{\frac{1}{|s^{(j)}[n,k]|^2}\}$ associated with the j-th user's transmitted subcarrier symbols.

α_{RLS}: Forgetting factor employed in the context of RLS-assisted CIR-related tap prediction filtering: $\alpha_{\text{RLS}} \in \mathbb{R}$.

β_{expo}: Amplitude scaling factor associated with the exponentially decaying multipath intensity profile $r_{h,\text{expo}}(\tau)$.

$\varepsilon_{\text{RLS},0}$: Startup-constant employed in the context of RLS-assisted CIR-related tap prediction filtering: $\varepsilon_{\text{RLS},0} \in \mathbb{R}$.

$\lambda_{p,l}^{[f](i)}$: l-th eigenvalue associated with the EVD of the spaced-frequency correlation matrix $\mathbf{R}_p^{[f](i)}$: $\lambda_{p,l}^{[f](i)} = (\mathbf{U}_p^{[f](i)H}\mathbf{R}_p^{[f](i)}\mathbf{U}_p^{[f](i)})_{[l,l]}$.

$\lambda_{apt,p,l}^{[f](i)}$: l-th eigenvalue associated with the EVD of the *a posteriori* channel transfer factor estimates' spaced-frequency correlation matrix $\mathbf{R}_{apt,p}^{[f](i)}$, which is expressed as: $\lambda_{apt,p,l}^{[f](i)} = (\mathbf{U}_{apt,p}^{[f](i)H}\mathbf{R}_{apt,p}^{[f](i)}\mathbf{U}_{apt,p}^{[f](i)})_{[l,l]}$.

ν: Short-hand employed in the context of calculating the single coefficient of a CIR-related one-tap predictor.

$\rho(\acute{\mathbf{F}})$: Spectral radius of the matrix $\acute{\mathbf{F}}$. The spectral radius is the smallest radius of a circle centered around the origin of $\mathbb{C}$ that contains all the matrix' eigenvalues [87].

$\hat{\sigma}^2_{\tilde{h}_{apt}^{(j)}[n,l]}$: Estimated variance associated with the l-th CIR-related *a posteriori* tap estimate based upon the current and the $N_{tap} - 1$ number of previous CIR-related *a posteriori* tap estimates.

τ_{int}: Integer part of the delay τ normalized to the sampling period duration T_s, where we have: $\tau_{int} = \lfloor \frac{\tau}{T_s} \rfloor$.

τ_{frac}: Fractional part of the delay τ normalized to the sampling period duration T_s: $\tau_{frac} = \frac{\tau}{T_s} - \tau_{int}$.

$\upsilon_{p,l}^{[f](i)}$: l-th diagonal element associated with the decomposition of the spaced-frequency correlation matrix $\mathbf{R}_p^{[f](i)}$ with respect to the channel predictor's unitary transform matrix $\tilde{\mathbf{U}}_p^{[f](i)}$, where we have: $\upsilon_{p,l}^{[f](i)} = (\tilde{\mathbf{U}}_p^{[f](i)H}\mathbf{R}_p^{[f](i)}\tilde{\mathbf{U}}^{[f](i)})|_{[l,l]}$.

χ: Short-hand: $\chi = \frac{K_0}{K}\alpha$.

$\Lambda_p^{[f](i)}$: Diagonal matrix of eigenvalues $\lambda_{p,l}^{[f](i)}$, $l = 0, \ldots, K-1$ associated with the EVD of the spaced-frequency correlation matrix $\mathbf{R}_p^{[f](i)}$: $\Lambda_p^{[f](i)} \in \mathbb{R}^{K \times K}$.

$\Lambda_{apt,p}^{[f](i)}$: Diagonal matrix of eigenvalues $\lambda_{apt,p,l}^{[f](i)}$, $l = 0, \ldots, K-1$ associated with the EVD of the *a posteriori* channel transfer factor estimates' spaced-frequency correlation matrix $\mathbf{R}_{apt,p}^{[f](i)}$: $\Lambda_{apt,p}^{[f](i)} \in \mathbb{R}^{K \times K}$.

$\tilde{\Lambda}_{p}^{[f](i)}$: Diagonal matrix of eigenvalues $\tilde{\lambda}_{p,l}^{[f](i)}$, $l = 0, \ldots, K-1$ associated with the EVD of the spaced-frequency correlation matrix $\tilde{\mathbf{R}}_{p}^{[f](i)}$ invoked in the design of the channel predictor, where we have: $\tilde{\Lambda}_{p}^{[f](i)} \in \mathbb{R}^{K \times K}$.

$\Upsilon_{p}^{[f](i)}$: Decomposition of the spaced-frequency correlation matrix $\mathbf{R}_{p}^{[f](i)}$, with respect to the channel predictor's unitary transform matrix $\tilde{\mathbf{U}}_{p}^{[f](i)}$, which is given by: $\Upsilon_{p}^{[f](i)} = \tilde{\mathbf{U}}_{p}^{[f](i)H} \mathbf{R}_{p}^{[f](i)} \tilde{\mathbf{U}}_{p}^{[f](i)} \in \mathbb{C}^{K \times K}$.

$\Delta\hat{\mathbf{H}}_{apr,p}^{(i)}[n]$: Vector of the K different subcarriers' *a priori* channel transfer factor estimation errors: $\Delta\hat{\mathbf{H}}_{apr,p}^{(i)}[n,k] = \mathbf{H}_{p}^{(i)}[n] - \hat{\mathbf{H}}_{apr,p}^{(i)}[n] \in \mathbb{C}^{K \times 1}$.

$\Delta\tilde{\mathbf{H}}_{apt,p}^{(i)}[n]$: Vector of the K different subcarriers' *a posteriori* channel transfer factor estimation errors: $\Delta\tilde{\mathbf{H}}_{apt,p}^{(i)}[n,k] = \mathbf{H}_{p}^{(i)}[n] - \tilde{\mathbf{H}}_{apt,p}^{(i)}[n] \in \mathbb{C}^{K \times 1}$.

$\nabla_{p}^{(j)}$: Nabla operator with respect to the vector of predictor coefficients $\tilde{\mathbf{c}}_{pre,p}^{(j)*}$, which is expressed as: $\nabla_{p}^{(j)} = \frac{\partial}{\partial \tilde{\mathbf{c}}_{pre,p}^{(j)*}}$.

$()_{p}^{(j)}$: Notation used for indicating that the variable in round brackets is associated with the channel encountered between the j-th user's single transmit antenna and the p-th receiver antenna element.

$()|^{\text{SIMPLE}}$: Notation used for indicating that the variable in round brackets, which could either be the vector of optimum predictor coefficients, or the associated estimation MSE is employed in the context of the simplified scenario of different users having identical transmit powers, as well as identical modulation-mode noise enhancement factors and identical channel statistics.

$()_{\text{FIR}}$: Notation used in conjunction with the vector of optimum predictor coefficients in order to indicate that the $(L-1)$ number of interfering users' MSE contributions were neglected in the coefficients' calculation.

$()_{\text{spar}}$: Notation used for indicating a sparse multipath intensity profile $r_{h,\text{spar}}(\tau)$, a spaced-frequency correlation function $r_{H,\text{spar}}(\Delta f)$, a spaced-frequency correlation matrix $\mathbf{R}_{\text{spar}}^{[f]}$ and a decomposition $\Upsilon_{\text{spar}}^{[f]}$ of the spaced-frequency correlation matrix with respect to the DFT matrix $\mathbf{W}$.

$()_{\text{unif}}$: Notation used for specifying a uniform multipath intensity profile $r_{h,\text{unif}}(\tau)$, a spaced-frequency correlation function $r_{H,\text{unif}}(\Delta f)$, a spaced-frequency correlation matrix $\mathbf{R}_{\text{unif}}^{[f]}$ and a decomposition $\Upsilon_{\text{unif}}^{[f]}$ of the spaced-frequency correlation matrix with respect to the DFT matrix $\mathbf{W}$.

$()_{\text{expo}}$: Notation used for a negative exponentially decaying multipath intensity profile $r_{h,\text{expo}}(\tau)$, a spaced-frequency correlation function $r_{H,\text{expo}}(\Delta f)$, a spaced-frequency correlation matrix $\mathbf{R}_{\text{expo}}^{[f]}$ and a decomposition $\Upsilon_{\text{expo}}^{[f]}$ of the spaced-frequency correlation matrix with respect to the DFT matrix $\mathbf{W}$.

Chapter 4

Uplink Detection Techniques for Multi-User SDMA-OFDM

4.1 Introduction

Space-Division-Multiple-Access (SDMA) communication systems have recently drawn wide interests. In these systems the L different users' transmitted signals are separated at the base-station (BS) with the aid of their unique, user-specific spatial signature, which is constituted by the P-element vector of channel transfer factors between the users' single transmit antenna and the P different receiver antenna elements at the BS, upon assuming flat-fading channel conditions such as in each of the OFDM subcarriers. This will be further detailed during our portrayal of the SDMA-MIMO channel model in Section 4.1.3.

A whole host of multi-user detection (MUD) techniques known from Code-Division-Multiple-Access (CDMA) communications lend themselves also to an application in the context of SDMA-OFDM on a per-subcarrier basis. Some of these techniques are the Least-Squares (LS) [114, 118, 119, 140], Minimum Mean-Square Error (MMSE) [114, 123, 124, 125, 53, 126, 127, 128, 117, 118, 129], Successive Interference Cancellation (SIC) [114, 115, 116, 53, 117, 118, 119, 120, 121, 122], Parallel Interference Cancellation (PIC) [114, 139] and Maximum Likelihood (ML) detection [114, 53, 117, 131, 132, 133, 134, 135, 136, 138]. A comprehensive overview of recent publications on MUD techniques for MIMO systems is given in Tables 4.1 and 4.2.

The further structure of our introduction is as follows. In Section 4.1.1 a detailed classification of the different MUD techniques is provided. By contrast, a more simple classification is employed in Section 4.1.2, which reflects the structure of this chapter. Before we embark on the discussion of linear MUD techniques in Section 4.2, the SDMA-MIMO channel model, to be used in our further discussions will be introduced in Section 4.1.3

Year	Author	Contribution
'96	Foschini [115]	The concept of the BLAST architecture was introduced.
'98	Vook and Baum [126]	SMI-assisted MMSE combining was invoked on an OFDM subcarrier basis.
	Wang and Poor [124]	Robust sub-space based weight vector calculation and tracking was employed for co-channel interference suppression, as an improvement of the SMI-algorithm.
	Wong, Cheng, Letaief and Murch [127]	Optimization of an OFDM system was reported in the context of multiple transmit- and receive antennas upon invoking the maximum SINR criterion. The computational complexity was reduced by exploiting the channel's correlation in the frequency-direction.
	Li and Sollenberger [128]	Tracking of the channel correlation matrix' entries was suggested in the context of SMI-assisted MMSE combining for multiple receiver antenna assisted OFDM, by capitalizing on the principles of [17].
'99	Golden, Foschini, Valenzuela and Wolniansky [116]	The SIC detection assisted V-BLAST algorithm was introduced.
	Li and Sollenberger [125]	The system introduced in [128] was further detailed.
	Vandenameele, Van Der Perre, Engels and H. D. Man [130]	A comparative study of different SDMA detection techniques, namely that of MMSE, SIC and ML detection was provided. Further improvements of SIC detection were suggested by adaptively tracking multiple symbol decisions at each detection node.
	Speth and Senst [131]	Soft-bit generation techniques were proposed for MLSE in the context of a coded SDMA-OFDM system.
'00	Sweatman, Thompson, Mulgrew and Grant [118]	Comparisons of various detection algorithms including LS, MMSE, D-BLAST and V-BLAST (SIC detection) were carried out.
	van Nee, van Zelst and Awater [132, 133, 134]	The evaluation of ML detection in the context of a Space-Division Multiplexing (SDM) system was provided, considering various simplified ML detection techniques.
	Vandenameele, Van Der Perre, Engels, Gyselinckx and De Man [53]	More detailed discussions were provided on the topics of [130].

Table 4.1: Contributions on detection techniques for MIMO systems and more specifically multiple transmit antenna assisted OFDM systems.

Year	Author	Contribution
'00	Li, Huang, Lozano and Foschini [135]	Reduced complexity ML detection was proposed for multiple transmit antenna systems employing adaptive antenna grouping and multi-step reduced-complexity detection.
'01	Degen, Walke, Lecomte and Rembold [119]	An overview of various adaptive MIMO techniques was provided. Specifically, pre-distortion was employed at the transmitter, as well as LS- or BLAST detection were used at the receiver or balanced equalization was invoked at both the transmitter and receiver.
	Zhu and Murch [136]	A tight upper bound on the SER performance of ML detection was derived.
	Li, Letaief, Cheng and Cao [129]	Joint adaptive power control and detection was investigated in the context of an OFDM/SDMA system, based on the approach of Farrokhi *et al.* [137].
	van Zelst, van Nee and Awater [138]	Iterative decoding was proposed for the BLAST system following the turbo principle.
	Benjebbour, Murata and Yoshida [120]	The performance of V-BLAST or SIC detection was studied in the context of a backward iterative cancellation scheme employed after the conventional forward cancellation stage.
	Sellathurai and Haykin [139]	A simplified D-BLAST was proposed, which used iterative PIC capitalizing on the extrinsic soft-bit information provided by the FEC scheme employed.
	Bhargave, Figueiredo and Eltoft [121]	A detection algorithm was suggested, which followed the concepts of V-BLAST or SIC. However, multiple symbols states are tracked from each detection stage, where - in contrast to [53] - an intermediate decision is made at intermediate detection stages.
	Thoen, Deneire, Van Der Perre and Engels [140]	A constrained LS detector was proposed for OFDM/SDMA, which was based on exploiting the constant modulus property of PSK signals.
'02	Li and Luo [122]	The block error probability of optimally ordered V-BLAST was studied. Furthermore, the block error probability was also investigated for the case of tracking multiple parallel symbol decisions from the first detection stage, following an approach similar to that of [53].

Table 4.2: Contributions on detection techniques for MIMO systems and for multiple transmit antenna assisted OFDM systems.

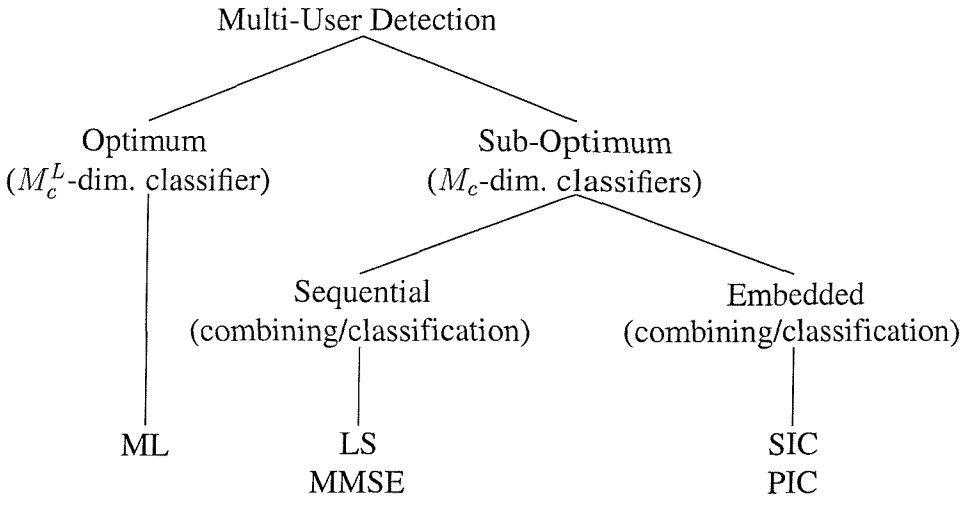

Figure 4.1: Classification of the various MUD techniques discussed in Chapter 4.

4.1.1 Classification of Multi-User Detection Techniques

The above techniques have been classified in Figure 4.1. Among the different techniques, the ML detection principle shown at the left-hand side of Figure 4.1 is known to exhibit the optimum performance, but also imposes the highest complexity. This is, because in ML detection the number of M_c^L trial symbol combinations, which are constituted by all possible combinations of the L different users' transmitted symbols belonging to an M_c-ary constellation, has to be evaluated in terms of the Euclidean distance between the vector of signals actually received by the P different antenna elements and the vector of trial signals, which are generated from all legitimate transmitted symbols, impaired according to the estimated channel.

In order to avoid the potentially excessive complexity of the optimum ML detection, a range of sub-optimum detection techniques have been devised, which are summarized at the right-hand side of Figure 4.1. The philosophy of the suboptimum detectors is to reduce the dimensionality of the classification problem associated with selecting the specific constellation point, which is most likely to have been transmitted by each user.

Specifically, in the context of the LS- and MMSE detection techniques to be detailed in Sections 4.2.2 and 4.2.3, first linear estimates of the different users' transmitted signals are provided with the aid of the weighted combining of the signals received by the different antenna elements at the BS. This is followed by separately demodulating each of the L different users' combiner output signals. Hence, the original M_c^L-dimensional classification problem associated with the optimum ML detection has been reduced to L number of individual classification steps, each having a dimensionality of M_c. This is achieved at the cost of a BER degradation, which is associated with ignoring the residual interference contaminating the linear combiner's output signals.

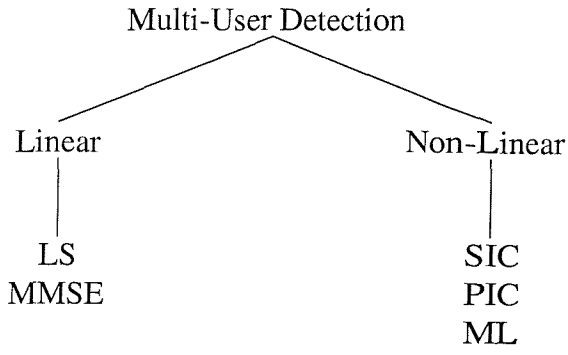

Figure 4.2: Classification of the various MUD techniques

We note again that in the context of LS- and MMSE detection the linear combining and classification steps are invoked in a sequential manner. However, a significant BER performance improvement can be achieved by embedding the classification process, which is a non-linear operation, into the linear combining process. Two of the most prominent representatives of this family of techniques are the SIC- and the PIC based detectors, which will be the topic of Sections 4.3.1 and 4.3.2, respectively.

4.1.2 Outline of Chapter 4

A possible classification of the various MUD techniques to be discussed in this chapter was presented in Figure 4.1. However, an alternative classification, which will serve as a guideline for our forthcoming discussions is portrayed in Figure 4.2. Here we have introduced the classes of linear- and non-linear detection techniques. The rationale of this classification is that in the context of linear detection techniques, such as LS- and MMSE detection, no *a priori* knowledge of the remaining users' transmitted symbols is required for the detection of a specific user. However, in the case of SIC, PIC and ML detection, *a priori* knowledge is involved, which must be provided by the non-linear classification operation involved in the demodulation process.

As shown in Figure 4.2, the further structure of this chapter 4 is as follows. In Section 4.2 the most salient linear detection techniques, namely LS- and MMSE detection will be discussed. These discussions include their MSE- and BER performance analysis in the context of both uncoded and turbo-coded scenarios, as well as the analysis of the computational complexity.

In Section 4.3 we will then embark on a detailed analysis of the family of non-linear detection techniques, namely that of SIC, PIC and ML detection, again, with respect to their BER performance in both uncoded and turbo-coded scenarios. Furthermore, a complexity analysis will be carried out. Specifically, in the context of our analysis of SIC detection and its derivatives, namely of M-SIC and partial M-SIC we will focus our efforts on the effects of error propagation across the

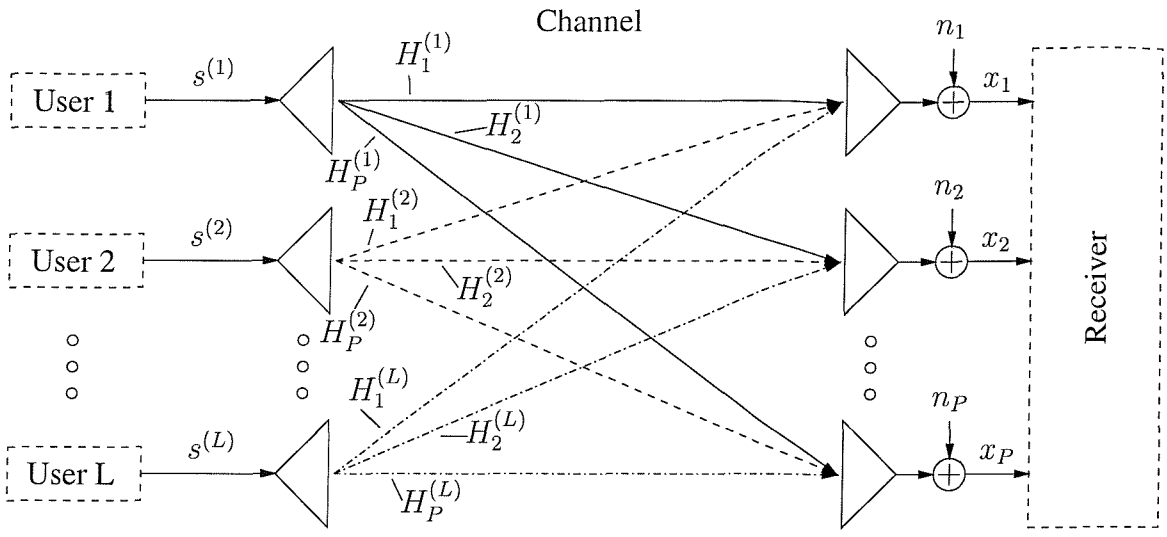

Figure 4.3: Schematic of an SDMA uplink MIMO channel scenario, where each of the L users is equipped with a single transmit antenna and the receiver is assisted by a P-element antenna front-end.

different detection stages. These investigations motivated the introduction of a weighted soft-bit metric to be employed in the context of turbo-decoding. Furthermore, in the context of PIC detection we proposed to embed turbo-decoding into the detection process, with the aim of increasing the reliability of the *a priori* symbol estimates employed in the PIC process. A final comparison between the different linear- and non-linear detection techniques in terms of their BER performance and computational complexity will be conducted at the end of Section 4.3.

In an effort to further enhance the performance of the different detection techniques without reducing their effective throughput, as in the case of turbo-coding, the applicability of adaptive modulation and Walsh-Hadamard Transform (WHT) based spreading will be investigated in Section 4.4. Our final conclusions for this chapter will then be offered in Section 4.5.

However, before we embark on the investigation of linear detection techniques in Section 4.2, the SDMA-MIMO channel model will be introduced in the next section.

4.1.3 SDMA-MIMO Channel Model

In Figure 4.3 we have portrayed a Space-Division-Multiple-Access (SDMA) uplink transmission scenario, where each of the L simultaneous users is equipped with a single transmission antenna, while the receiver capitalizes on a P-element antenna front-end. The vector of complex signals, $\mathbf{x}[n,k]$, received by the P-element antenna array in the k-th subcarrier of the n-th OFDM symbol is constituted by the superposition of the independently faded signals associated with the L users sharing the same space-frequency resource. The received signal was corrupted by the Gaussian noise at the array elements. The indices $[n,k]$ have been omitted for notational convenience during

our forthcoming discourse, yielding:

$$\mathbf{x} = \mathbf{Hs} + \mathbf{n}, \tag{4.1}$$

where the vector $\mathbf{x} \in \mathbb{C}^{P\times 1}$ of received signals, the vector $\mathbf{s} \in \mathbb{C}^{L\times 1}$ of transmitted signals and the array noise vector $\mathbf{n} \in \mathbb{C}^{P\times 1}$, respectively, are given by:

$$\mathbf{x} = (x_1, x_2, \ldots, x_P)^T, \tag{4.2}$$

$$\mathbf{s} = (s^{(1)}, s^{(2)}, \ldots, s^{(L)})^T, \tag{4.3}$$

$$\mathbf{n} = (n_1, n_2, \ldots, n_P)^T. \tag{4.4}$$

The frequency domain channel transfer factor matrix $\mathbf{H} \in \mathbb{C}^{P\times L}$ is constituted by the set of channel transfer factor vectors $\mathbf{H}^{(l)} \in \mathbb{C}^{P\times 1}$, $l = 1, \ldots, L$ of the L users:

$$\mathbf{H} = (\mathbf{H}^{(1)}, \mathbf{H}^{(2)}, \ldots, \mathbf{H}^{(L)}), \tag{4.5}$$

each of which hosts the frequency domain channel transfer factors between the single transmitter antenna associated with a particular user l and the reception antenna elements $p = 1, \ldots, P$:

$$\mathbf{H}^{(l)} = (H_1^{(l)}, H_2^{(l)}, \ldots, H_P^{(l)})^T, \tag{4.6}$$

with $l \in \{1, \ldots, L\}$. Regarding the statistical properties of the components associated with the vectors involved in Equation 4.1, we assume that the complex data signal $s^{(l)}$ transmitted by the l-th user has zero-mean and a variance of σ_l^2. The AWGN noise process n_p at any antenna array element p exhibits also zero-mean and a variance of σ_n^2. The frequency domain channel transfer factors $H_p^{(l)}$ of the different array elements $p \in \{1, \ldots, P\}$ or users $l \in \{1, \ldots, L\}$ are independent, stationary, complex Gaussian distributed processes with zero-mean and unit variance.

4.2 Linear Detection Techniques

The first class of detectors portrayed in this chapter belong to the family of the so-called linear detectors. Their employment is motivated by the observation that in the context of the optimum ML detector to be discussed in Section 4.3.3 a potentially excessive number of M_c^L trial symbol combinations has to be tested in terms of their associated trial signals' Euclidean distance measured from the vector of signals received by the different antenna elements. Recall that L represents the number of simultaneously transmitting users and M_c represents the number of legitimate transmitted symbols. Depending on the L number of simultaneous users supported and the M_c number of constellation points, a practical implementation of the ML detector may become unrealistic, as we will show during our complexity comparison in Section 4.3.4.2. A more practical approach is hence to generate estimates of the different users' transmitted signals with the aid of a linear

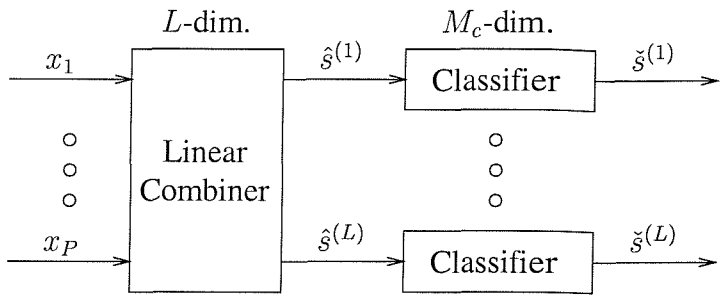

Figure 4.4: Illustration of the main signal paths associated with a linear detector such as LS or MMSE. The signals $x_p, p = 1, \ldots, P$ received by the different antenna elements are fed into the linear combiner, whose associated output vector $\hat{\mathbf{s}}$ of linear signal estimates with elements $\hat{s}^{(l)}, l = 1, \ldots, L$ is defined by Equation 4.7, and the LS- or MMSE-specific weight matrices are given by Equations 4.39 or 4.64 in its right-inverse related form and 4.68 in its left-inverse related form. The l-th user's signal, where $l = 1, \ldots, L$, is then conveyed to a separate classifier or demodulator, at the output of which the amplified constellation point $\check{s}^{(l)}$ most likely transmitted by the l-th user becomes available. The demodulator is described by Equation 4.94. Note that here we have omitted the signal paths associated with the channel transfer factor estimates required by the linear combiner.

combiner. These signal estimates would then be demodulated separately for each of the L users upon neglecting the residual interference caused by the remaining users in a specific user's combiner output signal. Hence the dimensionality of the receiver's classification task during demodulation is reduced from evaluating the multi-user Euclidean distance metric M_c^L times to the evaluation of the single-user Euclidean distance metric L times for all the M_c symbols. This reduces the total complexity to evaluating the Euclidean metric LM_c times. A simplified block diagram of the linear detector is also shown in Figure 4.4.

Our discussions commence in Section 4.2.1 with the characterization of the linear combiner's output signal and its components. By contrast, in Sections 4.2.2 and 4.2.3 we will focus our attention on two specific linear combiners, namely on the LS combiner and on the MMSE combiner, respectively[1]. These combiners constitute the basis for our discussions on non-linear detection techniques, such as SIC, PIC and transform-based ML detection in Sections 4.3.1, 4.3.2 and 4.3.3. Furthermore, in Section 4.2.4 the process of symbol classification or demodulation - as seen at the right-hand side of Figure 4.4 - is described while in Section 4.2.5 the generation of soft-bit values for turbo-decoding is outlined. The LS and MMSE detectors are characterized in terms of their associated combiner's MSE and SINR as well as the detector's BER performance in Section 4.2.6. This is followed by a detailed complexity analysis in Section 4.2.7. Finally, our conclusions on linear detection techniques will be offered in Section 4.2.8.

[1]Note that in the following the specific linear detector considered is referred to as the LS- or MMSE-detector, depending on whether LS- or MMSE combining is employed.

4.2.1 Characterization of the Linear Combiner's Output Signal

As the terminology suggests, an estimate $\hat{\mathbf{s}} \in \mathbb{C}^{L\times 1}$ of the vector of transmitted signals $\mathbf{s}$ of the L simultaneous users is generated by linearly combining the signals received by the P different receiver antenna elements with the aid of the weight matrix $\mathbf{W} \in \mathbb{C}^{P\times L}$, resulting in:

$$\hat{\mathbf{s}} = \mathbf{W}^H \mathbf{x}. \tag{4.7}$$

In order to gain a further insight into the specific structure of the combiner's output signal on a component basis, let us substitute Equation 4.1 into Equation 4.7 and consider the l-th user's associated vector component:

$$\begin{aligned} \hat{s}^{(l)} &= \mathbf{w}^{(l)H}\mathbf{x} && (4.8)\\ &= \mathbf{w}^{(l)H}(\mathbf{H}\mathbf{s}+\mathbf{n}) && (4.9)\\ &= \mathbf{w}^{(l)H}\mathbf{H}^{(l)}s^{(l)} + \mathbf{w}^{(l)H}\sum_{\substack{i=1\\ i\neq l}}^{L}\mathbf{H}^{(i)}s^{(i)} + \mathbf{w}^{(l)H}\mathbf{n}, && (4.10)\end{aligned}$$

where the weight vector $\mathbf{w}^{(l)} \in \mathbb{C}^{P\times 1}$ is the l-th column vector of the weight matrix $\mathbf{W}$. The further structure of Section 4.2.1 is as follows. While in Section 4.2.1.1 we briefly characterize the different additive components of the combiner's output signal, their statistical properties recorded in terms of the different contributions' variances are highlighted in Section 4.2.1.2. On the basis of these, the three most prominent performance measures used for assessing the quality of the combiner's output signal namely, the SINR, the SIR and the SNR will be introduced in Section 4.2.1.3.

4.2.1.1 Description of the Different Signal Components

We observe from Equation 4.10 that the combiner's output signal is constituted by three additive components. More specifically, in Equation 4.10 the first term, namely:

$$\hat{s}_S^{(l)} = \mathbf{w}^{(l)H}\mathbf{H}^{(l)}s^{(l)} \tag{4.11}$$

denotes the desired user's associated contribution, while the second term, namely:

$$\hat{s}_I^{(l)} = \mathbf{w}^{(l)H}\sum_{\substack{i=1\\ i\neq l}}^{L}\mathbf{H}^{(i)}s^{(i)} \tag{4.12}$$

denotes the interfering users' residual contribution. Finally, the last term, namely:

$$\hat{s}_N^{(l)} = \mathbf{w}^{(l)H}\mathbf{n} \tag{4.13}$$

is related to the AWGN. These components can be further characterized in terms of their variances, which will be further elaborated on in the next section.

4.2.1.2 Statistical Characterization

Specifically, the variance of the desired user's detected signal is given by:

$$\sigma_S^{(l)2} = E\{\hat{s}_S^{(l)H}\hat{s}_S^{(l)}\} \quad (4.14)$$

$$= \mathbf{w}^{(l)H}\mathbf{R}_{a,S}^{(l)}\mathbf{w}^{(l)}, \quad \text{where} \quad (4.15)$$

$$\mathbf{R}_{a,S}^{(l)} = \sigma_l^2\mathbf{H}^{(l)}\mathbf{H}^{(l)H} \in \mathbb{C}^{P\times P} \quad (4.16)$$

is the auto-correlation matrix of the desired user's signal. Following similar calculations, the variance of the interfering users' contribution is given as:

$$\sigma_I^{(l)2} = E\{\hat{s}_I^{(l)H}\hat{s}_I^{(l)}\} \quad (4.17)$$

$$= \mathbf{w}^{(l)H}\mathbf{R}_{a,I}^{(l)}\mathbf{w}^{(l)}, \quad \text{where} \quad (4.18)$$

$$\mathbf{R}_{a,I}^{(l)} = \sum_{\substack{i=1\\ i\neq l}}^{L}\sigma_i^2\mathbf{H}^{(i)}\mathbf{H}^{(i)H} \in \mathbb{C}^{P\times P} \quad (4.19)$$

is the auto-correlation matrix of the interfering users' signals. Finally, the residual AWGN related variance can be expressed as:

$$\sigma_N^{(l)2} = E\{\hat{s}_N^{(l)H}\hat{s}_N^{(l)}\} \quad (4.20)$$

$$= \mathbf{w}^{(l)H}\mathbf{R}_{a,N}\mathbf{w}^{(l)}, \quad \text{where} \quad (4.21)$$

$$\mathbf{R}_{a,N} = \sigma_n^2\mathbf{I} \in \mathbb{C}^{P\times P} \quad (4.22)$$

is the diagonal noise correlation matrix. Specifically, in the context of Equation 4.22 we have exploited again that the AWGN observed at different elements of the receiver antenna array is uncorrelated. For employment at a later stage we will additionally define here the undesired signal's auto-correlation matrix, which is related to the sum of the residual interference plus the AWGN expressed as:

$$\mathbf{R}_{a,I+N}^{(l)} = \mathbf{R}_{a,I}^{(l)} + \mathbf{R}_{a,N}, \quad (4.23)$$

where the matrices $\mathbf{R}_{a,I}^{(l)}$ and $\mathbf{R}_{a,N}$ were given by Equations 4.19 and 4.22, respectively.

4.2.1.3 Performance Measures

Three different performance measures can be defined on the basis of the desired signal's variance $\sigma_S^{(l)2}$, the interfering signal's variance $\sigma_I^{(l)2}$ and the noise variance $\sigma_N^{(l)2}$, which were given by Equations 4.14, 4.17 and 4.20. These measures can be employed for characterizing the quality of the linear combiner's output signal. These are the Signal-to-Interference-plus-Noise Ratio (SINR) at the combiner's output, defined as [123]:

$$\text{SINR}^{(l)} = \frac{\sigma_S^{(l)2}}{\sigma_I^{(l)2}+\sigma_N^{(l)2}} = \frac{\mathbf{w}^{(l)H}\mathbf{R}_{a,S}^{(l)}\mathbf{w}^{(l)}}{\mathbf{w}^{(l)H}\mathbf{R}_{a,I+N}^{(l)}\mathbf{w}^{(l)}}, \quad (4.24)$$

the Signal-to-Interference Ratio (SIR), defined as [123]:

$$\text{SIR}^{(l)} = \frac{\sigma_S^{(l)2}}{\sigma_I^{(l)2}} = \frac{\mathbf{w}^{(l)H}\mathbf{R}_{a,S}^{(l)}\mathbf{w}^{(l)}}{\mathbf{w}^{(l)H}\mathbf{R}_{a,I}^{(l)}\mathbf{w}^{(l)}}, \tag{4.25}$$

and the Signal-to-Noise Ratio (SNR) given by [123]:

$$\text{SNR}^{(l)} = \frac{\sigma_S^{(l)2}}{\sigma_N^{(l)2}} = \frac{\mathbf{w}^{(l)H}\mathbf{R}_{a,S}^{(l)}\mathbf{w}^{(l)}}{\mathbf{w}^{(l)H}\mathbf{R}_{a,N}^{(l)}\mathbf{w}^{(l)}}. \tag{4.26}$$

In the next section we will embark on the portrayal of least-squares error detection, in an effort to compare a number of different criteria that can be invoked for adjusting the detector's associated combiner weight matrix $\mathbf{W}$ introduced in Equation 4.7.

4.2.2 Least-Squares Error Detector

With reference to Figure 4.4, in this section we will derive the Least-Squares (LS) error- or Zero-Forcing (ZF) combiner [114, 118, 119, 140], which attempts to recover the vector $\mathbf{s}[n,k]$ of signals transmitted by the L different users in the k-th subcarrier of the n-th OFDM symbol period, regardless of the signal quality quantified in terms of the SNR at the reception antennas. For simplicity, we will again omit the index $[n,k]$ throughout our forthcoming discourse. Our description of the LS combiner is structured as follows. In Section 4.2.2.1 a simplified model $\hat{\mathbf{x}}$ of the vector $\mathbf{x}$ of signals received by the P different antenna elements is introduced as a function of the estimate $\hat{\mathbf{s}}$ of the vector of L number of transmitted signals. On the basis of this simplified model a cost-function is established in Section 4.2.2.2, which follows the philosophy of the squared model mismatch error. The estimate $\hat{\mathbf{s}}$ of the L different users' transmitted symbols is then determined in Section 4.2.2.3 with the aid of the conjugate-gradient method [87]. Alternatively, the so-called orthogonality principle [87] could be invoked. Furthermore, in Section 4.2.2.4 a condition is provided, which has to be satisfied in order to be able to identify the estimate $\hat{\mathbf{s}}$, while in Sections 4.2.2.5 and 4.2.2.6 expressions are presented for both the squared error measured in the received signal's domain and for the mean-square error evaluated in the transmitted signal's domain.

4.2.2.1 Simplified Model of the Received Signal

Upon assuming perfect knowledge of the channel transfer factor matrix $\mathbf{H}$ an estimate $\hat{\mathbf{x}} \in \mathbb{C}^{P\times 1}$ of the vector of signals received by the P different antenna elements in a specific subcarrier is given similarly to Equation 4.1 by:

$$\hat{\mathbf{x}} = \mathbf{H}\hat{\mathbf{s}}, \tag{4.27}$$

where $\hat{\mathbf{s}} \in \mathbb{C}^{L\times 1}$ is the estimate of the vector of signals transmitted by the L different users, which we are attempting to recover.

4.2.2.2 Least-Squares Error Cost-Function

The estimation error $\Delta\hat{\mathbf{x}} \in \mathbb{C}^{P\times 1}$ in the received signal's domain can hence be expressed as:

$$\Delta\hat{\mathbf{x}} = \mathbf{x} - \hat{\mathbf{x}} \tag{4.28}$$

$$= \mathbf{x} - \mathbf{H}\hat{\mathbf{s}}. \tag{4.29}$$

Correspondingly, the squared error $||\Delta\hat{\mathbf{x}}||_2^2 \in \mathbb{R}$ is given as the inner product of the vector of LS estimation errors formulated in Equation 4.28, namely as:

$$||\Delta\hat{\mathbf{x}}||_2^2 = \Delta\hat{\mathbf{x}}^H\Delta\hat{\mathbf{x}} \tag{4.30}$$

$$= \mathbf{x}^H\mathbf{x} - 2\Re\mathfrak{e}(\hat{\mathbf{s}}^H\mathbf{p}_{\text{LS}}) + \hat{\mathbf{s}}^H\mathbf{Q}_{\text{LS}}\hat{\mathbf{s}}, \tag{4.31}$$

where the 'cross-correlation' vector $\mathbf{p}_{\text{LS}} \in \mathbb{C}^{L\times 1}$ is given by:

$$\mathbf{p}_{\text{LS}} = \mathbf{H}^H\mathbf{x}, \tag{4.32}$$

while the 'auto-correlation' matrix $\mathbf{Q}_{\text{LS}} \in \mathbb{C}^{L\times L}$ is given by[2]:

$$\mathbf{Q}_{\text{LS}} = \mathbf{H}^H\mathbf{H}. \tag{4.33}$$

4.2.2.3 Recovery of the Transmitted Signals by the Gradient Approach

A standard approach designed for determining the desired vector $\hat{\mathbf{s}}$ representing the estimated transmitted signals of the L users is to minimize the squared error given by Equation 4.30. This can be achieved by noting that in the optimum point of operation, associated with the weight matrix having the optimum weights, the conjugate gradient $\nabla^* = \frac{\partial}{\partial\hat{\mathbf{s}}^*} \in \mathbb{C}^{L\times 1}$ of $||\Delta\hat{\mathbf{x}}||_2^2$ with respect to $\hat{\mathbf{s}}$ is equal to zero, which can be expressed as:

$$||\Delta\hat{\mathbf{x}}||_2^2 = \text{Min.} \quad \Longleftrightarrow \quad \nabla^*||\Delta\hat{\mathbf{x}}||_2^2 \stackrel{!}{=} 0. \tag{4.34}$$

Upon substituting Equation 4.31 into Equation 4.34, after some mathematical manipulations we obtain:

$$\mathbf{Q}_{\text{LS}}\hat{\mathbf{s}}_{\text{LS}} = \mathbf{p}_{\text{LS}} \quad \Longleftrightarrow \quad \hat{\mathbf{s}}_{\text{LS}} = \mathbf{Q}_{\text{LS}}^{-1}\mathbf{p}_{\text{LS}}. \tag{4.35}$$

Here we have specifically exploited that the gradient with respect to the first term of Equation 4.31 is equal to zero, while the gradient with respect to the second term was evaluated by capitalizing on $\frac{\partial}{\partial\mathbf{z}^*}\Re\mathfrak{e}(\mathbf{z}^H\mathbf{a}) = \frac{1}{2}\mathbf{a}$ [87] for complex valued vectors $\mathbf{z}$ and $\mathbf{a}$. Furthermore, in the context of evaluating the gradient of the last term in Equation 4.31 we have exploited that we have $\frac{\partial}{\partial\mathbf{z}^*}\mathbf{z}^H\mathbf{R}\mathbf{z} = \mathbf{R}\mathbf{z}$ [87] in conjunction with a Hermitian matrix $\mathbf{R}$.

[2]Note that $\mathbf{p}_{\text{LS}}$ and $\mathbf{Q}_{\text{LS}}$ have been intentionally termed 'cross-correlation' vector and 'auto-correlation' matrix, in order to highlight the similarities to the corresponding matrices in the context of MMSE combining, although the expectation operator is not invoked here.

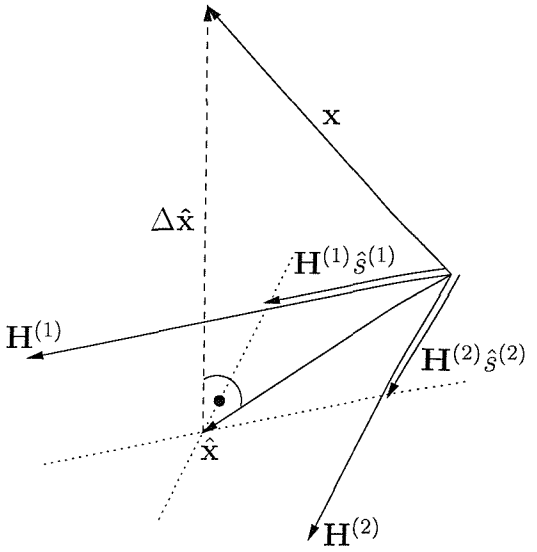

Figure 4.5: Illustration of the principle of LS detection for a scenario of $L = 2$ simultaneous users. The vector $\mathbf{x}$ of received signals is projected onto the vector space spanned by the column vectors $\mathbf{H}^{(1)}$, $\mathbf{H}^{(2)}$ hosted by the channel matrix $\mathbf{H}$.

Upon substituting Equations 4.32 and 4.33 into Equation 4.35 we obtain the following expression for the vector $\hat{\mathbf{s}}_{\text{LS}}$ of estimated transmitted signals of the L simultaneous users:

$$\hat{\mathbf{s}}_{\text{LS}} = \mathbf{P}_{\text{LS}}\mathbf{x}, \tag{4.36}$$

where the projection matrix $\mathbf{P}_{\text{LS}} \in \mathbb{C}^{L \times P}$ is given by:

$$\mathbf{P}_{\text{LS}} = (\mathbf{H}^H\mathbf{H})^{-1}\mathbf{H}^H. \tag{4.37}$$

More specifically, the matrix $\mathbf{P}_{\text{LS}}$ projects the vector $\mathbf{x}$ of the P different antenna elements' received signals onto the column space of the channel matrix $\mathbf{H}$ [87]. These principles are further illustrated in Figure 4.5. As a comparison between Equations 4.7 and 4.36 reveals, the least-squares estimation based weight matrix $\mathbf{W}_{\text{LS}} \in \mathbb{C}^{P \times L}$ is hence given by:

$$\mathbf{W}_{\text{LS}} = \mathbf{P}_{\text{LS}}^H \tag{4.38}$$

$$= \mathbf{H}(\mathbf{H}^H\mathbf{H})^{-1}, \tag{4.39}$$

while the l-th user's associated weight vector $\mathbf{w}_{\text{LS}}^{(l)}$, which is the l-th column vector of matrix $\mathbf{W}_{\text{LS}}$ can be expressed as:

$$\mathbf{w}_{\text{LS}}^{(l)} = \mathbf{H} \cdot \mathbf{col}^{(l)}\{(\mathbf{H}^H\mathbf{H})^{-1}\}, \tag{4.40}$$

where $\mathbf{col}^{(l)}\{\}$ denotes the l-th column vector of the matrix enclosed in curly brackets.

4.2.2.4 Condition for Identification

From the literature [87], the projection matrix $\mathbf{P}_{\text{LS}}$ of Equation 4.37 is also known as the Moore-Penrose pseudo-inverse or left-inverse of $\mathbf{H}$ [87], which is denoted by $\mathbf{H}^{\dagger}$. A sufficient condition for its existence is that the L number of columns of the matrix $\mathbf{H}$ are linearly independent, which implies that we have $rank(\mathbf{H}) = L$. A necessary condition for this is that the P number of rows of $\mathbf{H}$ is equal to or larger than its L number of columns, namely that $P \geq L$. This implies that the maximum number of simultaneous users or transmit antennas supported by the LS combiner must be lower or equal to the P number of receiver antennas.

4.2.2.5 Squared Estimation Error in the Received Signals' Domain

The squared estimation error formulated in the sense of Equation 4.30 and associated with the vector $\hat{\mathbf{s}}_{\text{LS}}$ of least-squares signal estimates is given upon substituting Equation 4.35 into Equation 4.31, resulting in:

$$(||\Delta\hat{\mathbf{x}}||_2^2)_{\text{LS}} = \mathbf{x}^H\mathbf{x} - \mathbf{p}_{\text{LS}}^H\hat{\mathbf{s}}_{\text{LS}}. \tag{4.41}$$

4.2.2.6 Mean-Square Estimation Error in the Transmitted Signals' Domain

By substituting the received signal's model of Equation 4.1 into Equation 4.36 we obtain:

$$\hat{\mathbf{s}}_{\text{LS}} = \mathbf{s} + \mathbf{P}_{\text{LS}}\mathbf{n}, \tag{4.42}$$

which indicates that the LS-estimate $\hat{\mathbf{s}}_{\text{LS}}$ of the transmitted signal vector $\mathbf{s}$ of the L simultaneous users is based on a noise-contaminated version of $\mathbf{s}$. We note that the vector $\mathbf{s}$ of transmitted signals is restored regardless of the potential noise amplification incurred, which coined the term Zero-Forcing (ZF) combiner. Since $E\{\hat{\mathbf{s}}_{\text{LS}}\} = \mathbf{s}$, the vector $\hat{\mathbf{s}}_{\text{LS}}$ is also called an unbiased estimate of $\mathbf{s}$ [87]. Furthermore, from the literature [87] the vector $\hat{\mathbf{s}}_{\text{LS}}$ is also known as the Maximum Likelihood (ML) estimate of $\mathbf{s}$. More specifically, the vector $\hat{\mathbf{s}}_{\text{LS}}$ is a sample of an L-dimensional multi-variate complex Gaussian distribution, namely, $\hat{\mathbf{s}}_{\text{LS}} \sim \mathcal{CN}(\mathbf{s}, \mathbf{R}_{\Delta\hat{\mathbf{s}}_{\text{LS}}})$ ([3]), with the mean vector $\mathbf{s}$ and the covariance matrix $\mathbf{R}_{\Delta\hat{\mathbf{s}}_{\text{LS}}} \in \mathbb{C}^{L\times L}$ ([4]), given by:

$$\begin{aligned} \mathbf{R}_{\Delta\hat{\mathbf{s}}_{\text{LS}}} &= E\{(\mathbf{P}_{\text{LS}}\mathbf{n})(\mathbf{P}_{\text{LS}}\mathbf{n})^H\} && (4.43)\\ &= \sigma_n^2(\mathbf{H}^H\mathbf{H})^{-1}, && (4.44) \end{aligned}$$

and where Equation 4.44 has been obtained by substituting Equation 4.37 into Equation 4.43, and by exploiting that $E\{\mathbf{n}\mathbf{n}^H\} = \sigma_n^2\mathbf{I}$. The average estimation Mean-Square Error (MSE) evaluated

[3]The complex Gaussian distribution function is denoted here as $\mathcal{CN}()$, in order to distinguish it from the Gaussian distribution function defined for real-valued random variables.

[4]Note that $\Delta\mathbf{s}_{\text{LS}} = \mathbf{s} - \hat{\mathbf{s}}_{\text{LS}}$.

in the transmitted signals' domain is hence given by:

$$\overline{\mathrm{MSE}}_{\mathrm{LS}} = \frac{1}{L}\mathrm{Trace}(\mathbf{R}_{\Delta\hat{\mathbf{s}}_{\mathrm{LS}}}) \quad (4.45)$$

$$= \frac{1}{L}\sigma_n^2\mathrm{Trace}((\mathbf{H}^H\mathbf{H})^{-1}), \quad (4.46)$$

while the l-th user's associated minimum MSE is given as the l-th diagonal element of the matrix $\mathbf{R}_{\Delta\hat{\mathbf{s}}_{\mathrm{LS}}}$ in Equation 4.43. Hence, according to Equations 4.43 and 4.44 we have:

$$\mathrm{MSE}_{\mathrm{LS}}^{(l)} = \sigma_n^2\mathbf{w}_{\mathrm{LS}}^{(l)H}\mathbf{w}_{\mathrm{LS}}^{(l)} \quad (4.47)$$

$$= \sigma_n^2((\mathbf{H}^H\mathbf{H})^{-1})_{[l,l]}. \quad (4.48)$$

In the next section the potentially more effective MMSE detection approach will be discussed.

4.2.3 Minimum Mean-Square Error Detector

With reference to Figure 4.4, in contrast to the LS combiner of Section 4.2.2 the Minimum Mean-Square Error (MMSE) detector's associated MMSE combiner [114, 123, 124, 125, 53, 126, 127, 128, 117, 118, 129] exploits the available statistical knowledge concerning the signals transmitted by the different users, as well as that related to the AWGN at the receiver antenna elements.

The specific structure of Section 4.2.3 is as follows. In Section 4.2.3.1 the mean-square error related cost-function is introduced, which is then employed in Section 4.2.3.2 for deriving the optimum weight matrix with the aid of the conjugate-gradient approach [87]. Furthermore, in Section 4.2.3.3 expressions are provided for the average MSE and the user-specific MSE, respectively, in the context of employing the optimum weight matrix. Our discussions of the MMSE combiner are concluded in Section 4.2.3.4 by reducing the expression derived for the optimum weight matrix to a standard form, which will be shown later in Section 4.2.3.4 to differ only by a scalar factor from the corresponding expressions associated with the Minimum Variance (MV) combiner and also from that of the maximum SINR combiner.

4.2.3.1 Mean-Square Error Cost-Function

In contrast to the derivation of the LS combiner in Section 4.2.2, the cost-function employed here directly reflects the quality of the combiner weights in the transmitted signals' domain. In order to elaborate further, the vector $\Delta\hat{s} \in \mathbb{C}^{L\times 1}$ of the L simultaneous users' estimation errors evaluated in the transmitted signals' domain can be defined as:

$$\Delta\hat{s} = \mathbf{s} - \hat{\mathbf{s}} \quad (4.49)$$

$$= \mathbf{s} - \mathbf{W}^H\mathbf{x}, \quad (4.50)$$

where Equation 4.50 has been obtained by substituting Equation 4.7 into Equation 4.49. Furthermore, the estimation error's auto-correlation matrix $\mathbf{R}_{\Delta\hat{s}} \in \mathbb{C}^{L\times L}$ is given by:

$$\begin{aligned}\mathbf{R}_{\Delta\hat{s}} &= E\{\Delta\hat{s}\Delta\hat{s}^H\} &(4.51)\\ &= \mathbf{P} - \mathbf{R}_c^H\mathbf{W} - \mathbf{W}^H\mathbf{R}_c + \mathbf{W}^H\mathbf{R}_a\mathbf{W}, &(4.52)\end{aligned}$$

where the cross-correlation matrix $\mathbf{R}_c \in \mathbb{C}^{P\times L}$ of the received and transmitted signals is defined as:

$$\begin{aligned}\mathbf{R}_c &= E\{\mathbf{x}\mathbf{s}^H\} &(4.53)\\ &= \mathbf{H}\mathbf{P}. &(4.54)\end{aligned}$$

Similarly, for the auto-correlation matrix $\mathbf{R}_a \in \mathbb{C}^{P\times P}$ of the received signals we obtain:

$$\begin{aligned}\mathbf{R}_a &= E\{\mathbf{x}\mathbf{x}^H\} &(4.55)\\ &= \mathbf{H}\mathbf{P}\mathbf{H}^H + \sigma_n^2\mathbf{I} &(4.56)\\ &= \sum_{l=1}^{L}\sigma_l^2\mathbf{H}^{(l)}\mathbf{H}^{(l)H} + \sigma_n^2\mathbf{I}. &(4.57)\end{aligned}$$

Note that clearly the sum of the auto-correlation matrices $\mathbf{R}_{a,S}$, $\mathbf{R}_{a,I}$ and $\mathbf{R}_{a,N}$ given by Equations 4.16, 4.19 and 4.22, respectively, constitutes the auto-correlation matrix $\mathbf{R}_a \in \mathbb{C}^{P\times P}$ of the different reception antennas' associated signals, which can be expressed as:

$$\mathbf{R}_a = \mathbf{R}_{a,S}^{(l)} + \mathbf{R}_{a,I+N}^{(l)}, \tag{4.58}$$

where $\mathbf{R}_{a,I+N}^{(l)} = \mathbf{R}_{a,I}^{(l)} + \mathbf{R}_{a,N}$ from Equation 4.23. Furthermore, in Equations 4.54 and 4.56 the matrix $\mathbf{P} \in \mathbb{R}^{L\times L}$ is the diagonal matrix of the different users' associated transmit powers- or signal variances, given by:

$$\mathbf{P} = Diag(\sigma_1^2, \sigma_2^2, \ldots, \sigma_L^2). \tag{4.59}$$

In the context of deriving Equations 4.54 and 4.56 we have also exploited that $E\{\mathbf{s}\mathbf{s}^H\} = \mathbf{P}$, as well as that $E\{\mathbf{n}\mathbf{n}^H\} = \sigma_n^2\mathbf{I}$ and that $E\{\mathbf{s}\mathbf{n}^H\} = 0$. On the basis of Equation 4.52, the *total* mean-square estimation error $E\{||\Delta\hat{s}||_2^2\} \in \mathbb{R}$ accumulated for the different users is given by:

$$\begin{aligned}E\{||\Delta\hat{s}||_2^2\} &= \text{Trace}(\mathbf{R}_{\Delta\hat{s}}) &(4.60)\\ &= \text{Trace}(\mathbf{P}) - \text{Trace}(\mathbf{R}_c^H\mathbf{W}) - \text{Trace}(\mathbf{W}^H\mathbf{R}_c) +\\ &\quad + \text{Trace}(\mathbf{W}^H\mathbf{R}_a\mathbf{W}). &(4.61)\end{aligned}$$

This equation will be employed in the next section in order to optimally adjust the matrix $\mathbf{W}$ of combiner coefficients.

4.2.3.2 Recovery of the Transmitted Signals by the Gradient Approach

Determining the weight matrix on the basis of evaluating the gradient with respect to the different users' total mean-square estimation error given by Equation 4.61 results in the standard form of the MMSE combiner, which is related to the right-inverse of the channel matrix $\mathbf{H}$. This will be further elaborated on in Section 4.2.3.2.1. Alternatively, the weight matrix can be represented in a form related to the left-inverse of the channel matrix $\mathbf{H}$, which had drawn our interest earlier in Section 4.2.2 in the context of the LS combiner characterized by Equations 4.36 and 4.37. The left-inverse related form of the MMSE combiner will be briefly addressed in Section 4.2.3.2.2.

4.2.3.2.1 Right-Inverse Related Form of the MMSE Combiner Similarly to our proceedings in Section 4.2.2.3, the matrix $\mathbf{W}$ of optimum weights can be determined by noting that when $E\{||\Delta\hat{s}||_2^2\}$ of Equation 4.60 is minimized, its conjugate gradient evaluated with respect to the weight matrix $\mathbf{W}$ is identical to the zero-matrix. Hence, we obtain the following equation for the matrix $\mathbf{W}_{\text{MMSE}} \in \mathbb{C}^{P\times L}$ of optimum weights:

$$\mathbf{R}_a\mathbf{W}_{\text{MMSE}} = \mathbf{R}_c \quad \Longleftrightarrow \quad \mathbf{W}_{\text{MMSE}} = \mathbf{R}_a^{-1}\mathbf{R}_c. \tag{4.62}$$

More specifically, upon substituting Equations 4.54 and 4.56 into Equation 4.62 we have:

$$\mathbf{W}_{\text{MMSE}} = (\mathbf{H}\mathbf{P}\mathbf{H}^H + \sigma_n^2\mathbf{I})^{-1}\mathbf{H}\mathbf{P}. \tag{4.63}$$

In the context of deriving the conjugate gradient of Equation 4.61 with respect to the weight matrix $\mathbf{W}$ we have exploited that the constant first term yields a zero contribution, while the remaining terms were evaluated upon noting that $\frac{\partial \text{Trace}(\mathbf{AXB})}{\partial \mathbf{X}^*} = \mathbf{0}$, as well as that $\frac{\partial \text{Trace}(\mathbf{AX}^H\mathbf{B})}{\partial \mathbf{X}^*} = \mathbf{BA}$ and $\frac{\partial \text{Trace}(\mathbf{X}^H\mathbf{AXB})}{\partial \mathbf{X}^*} = \mathbf{AXB}$ for the complex matrices $\mathbf{A}$, $\mathbf{B}$ and $\mathbf{X}$ [87]. Note that Equation 4.63 can be rewritten as:

$$\mathbf{W}_{\text{MMSE}} = (\mathbf{H}\mathbf{P}_{\text{SNR}}\mathbf{H}^H + \mathbf{I})^{-1}\mathbf{H}\mathbf{P}_{\text{SNR}}, \tag{4.64}$$

where similarly to Equation 4.59, the matrix $\mathbf{P}_{\text{SNR}} \in \mathbb{R}^{L\times L}$ is the diagonal matrix of the different users' associated SNRs at the receiver antennas, which can be written as:

$$\mathbf{P}_{\text{SNR}} = Diag(\text{SNR}^{(1)}, \text{SNR}^{(2)}, \ldots, \text{SNR}^{(L)}), \tag{4.65}$$

and where the l-th user's SNR is given by $\text{SNR}^{(l)} = \frac{\sigma_l^2}{\sigma_n^2}$. Furthermore, note from Equation 4.62 and 4.63 that the l-th user's associated weight vector $\mathbf{w}_{\text{MMSE}}^{(l)} \in \mathbb{C}^{P\times 1}$ is given by:

$$\mathbf{w}_{\text{MMSE}}^{(l)} = \mathbf{R}_a^{-1}\mathbf{H}^{(l)}\sigma_l^2 \tag{4.66}$$

$$= (\mathbf{H}\mathbf{P}\mathbf{H}^H + \sigma_n^2\mathbf{I})^{-1}\mathbf{H}^{(l)}\sigma_l^2. \tag{4.67}$$

4.2.3.2.2 Left-Inverse Related Form of the MMSE Combiner Recall that as demonstrated in Equation 4.22, the auto-correlation matrix of the AWGN is represented by a scaled identity matrix. Hence, it can be shown that an alternative expression with respect to Equation 4.63 for the MMSE combiner's weight matrix is given by:

$$\mathbf{W}_{\text{MMSE}} = \mathbf{H}\mathbf{P}_{\text{SNR}}(\mathbf{H}^H\mathbf{H}\mathbf{P}_{\text{SNR}} + \mathbf{I})^{-1}. \tag{4.68}$$

Upon substituting $\mathbf{R}_c = \mathbf{H}\mathbf{P}$ as defined in Equation 4.54([5]), as well as by substituting $\mathbf{R}_{\overline{a}} \in \mathbb{C}^{L\times L}$([6]) defined as:

$$\mathbf{R}_{\overline{a}} = \mathbf{H}^H\mathbf{H}\mathbf{P} + \sigma_n^2\mathbf{I}, \tag{4.69}$$

similarly to Equation 4.62 we obtain the following relation:

$$\mathbf{R}_{\overline{a}}^H\mathbf{W}_{\text{MMSE}}^H = \mathbf{R}_c^H \quad \Longleftrightarrow \quad \mathbf{W}_{\text{MMSE}}^H = \mathbf{R}_{\overline{a}}^{H-1}\mathbf{R}_c^H. \tag{4.70}$$

In terms of the required numerical accuracy, calculating the weight matrix $\mathbf{W}_{\text{MMSE}}$ by solving the system of equations as shown at the left-hand side of Equation 4.70 is more attractive, than a solution by the direct inversion of the auto-correlation matrix $\mathbf{R}_{\overline{a}}$, as shown at the right-hand side of Equation 4.70.

Note that in contrast to the auto-correlation matrix $\mathbf{R}_a$ defined in Equation 4.56, which is the core element of the right-inverse related representation of the weight matrix according to Equation 4.62, the correlation matrix $\mathbf{R}_{\overline{a}}$ defined in Equation 4.69, which was associated with the left-inverse related representation of the weight matrix in Equation 4.70 is not Hermitian. As a result, unfortunately the same computationally efficient methods which can be invoked for solving the system of equations associated with the right-inverse related representation of the weight matrix, namely the auto-correlation matrix's Toeplitz structure are not applicable here. However, a computational advantage is potentially achievable with the advent of the lower dimensionality of the matrix $\mathbf{R}_{\overline{a}} \in \mathbb{C}^{L\times L}$ compared to that of matrix $\mathbf{R}_a \in \mathbb{C}^{P\times P}$, provided that we have $P > L$. This property renders the left-inverse related form of the MMSE combiner particularly attractive for its repeated application in each cancellation stage of the SIC detector, which will be discussed in Section 4.3.1.

4.2.3.3 Mean-Square Estimation Error in the Transmitted Signals' Domain

Upon substituting the weight matrix $\mathbf{W}_{\text{MMSE}}$ defined in Equation 4.62 into Equation 4.52 we obtain for the auto-correlation matrix of the estimation errors associated with the different users' transmitted signals the following expression:

$$\mathbf{R}_{\Delta\hat{\mathbf{s}}_{\text{MMSE}}} = \mathbf{P} - \mathbf{R}_c^H\mathbf{R}_a^{-1}\mathbf{R}_c \tag{4.71}$$

$$= \mathbf{P} - \mathbf{R}_c^H\mathbf{W}_{\text{MMSE}}. \tag{4.72}$$

[5]Recall from Equations 4.59 and 4.65 that $\mathbf{P} = \sigma_n^2\mathbf{P}_{\text{SNR}}$.

[6]The left-inverse related form of the auto-correlation matrix is denoted here as $\mathbf{R}_{\overline{a}}$ in order to distinguish it from its right-inverse related form, namely $\mathbf{R}_a$, defined in Equation 4.56.

Hence, following the philosophy of Equation 4.60, the *average* minimum MSE (MMSE) of the L simultaneous users is given by:

$$\overline{\text{MMSE}}_{\text{MMSE}} = \frac{1}{L}\text{Trace}(\mathbf{R}_{\Delta\hat{\mathbf{s}}_{\text{MMSE}}}), \tag{4.73}$$

while the l-th user's MMSE is given as the l-th diagonal element of the estimation errors' auto-correlation matrix $\mathbf{R}_{\Delta\hat{\mathbf{s}}_{\text{MMSE}}}$ defined in Equation 4.71, namely as:

$$\text{MMSE}^{(l)}_{\text{MMSE}} = \sigma_l^2(1 - \mathbf{H}^{(l)H}\mathbf{R}_a^{-1}\mathbf{H}^{(l)}\sigma_l^2) \tag{4.74}$$

$$= \sigma_l^2(1 - \mathbf{H}^{(l)H}\mathbf{w}^{(l)}_{\text{MMSE}}). \tag{4.75}$$

4.2.3.4 Optimum Weight Vector in Standard Form

We recall from Equation 4.58 that the received signals' auto-correlation matrix $\mathbf{R}_a$ can be expressed as the sum of the desired- and undesired signals' contributions, namely as:

$$\mathbf{R}_a = \mathbf{R}^{(l)}_{a,S} + \mathbf{R}^{(l)}_{a,I+N}. \tag{4.76}$$

Upon invoking the well-known matrix-inversion lemma- or Sherman-Morrison formula [87], the inverse of the auto-correlation matrix, namely $\mathbf{R}_a^{-1}$, can be rewritten as:

$$\mathbf{R}_a^{-1} = \mathbf{R}^{(l)-1}_{a,I+N} - \frac{\mathbf{R}^{(l)-1}_{a,I+N}\sigma_l^2\mathbf{H}^{(l)}\mathbf{H}^{(l)H}\mathbf{R}^{(l)-1}_{a,I+N}}{1 + \sigma_l^2\mathbf{H}^{(l)H}\mathbf{R}^{(l)-1}_{a,I+N}\mathbf{H}^{(l)}}. \tag{4.77}$$

Upon further substituting Equation 4.77 into Equation 4.66 we obtain:

$$\mathbf{w}^{(l)}_{\text{MMSE}} = \beta_{\text{MMSE}}\mathbf{R}^{(l)-1}_{a,I+N}\mathbf{H}^{(l)}, \tag{4.78}$$

where:

$$\beta_{\text{MMSE}} = \frac{\sigma_l^2}{1 + \text{SINR}^{(l)}}, \tag{4.79}$$

and where the achievable SINR is given by:

$$\text{SINR}^{(l)} = \sigma_l^2\mathbf{H}^{(l)H}\mathbf{R}^{(l)-1}_{a,I+N}\mathbf{H}^{(l)}. \tag{4.80}$$

This is immediately seen by substituting Equation 4.78 into Equation 4.24. It is interesting to note that the SINR given by Equation 4.80 is independent from the factor β_{MMSE} related to the MMSE-criterion. As a consequence, different combining approaches result in achieving the same SINR at the combiner's output [123], provided that their weight vectors can be expressed in the form of Equation 4.78, despite having a constant β, which is potentially different from β_{MMSE} of the MMSE combiner. It was demonstrated in [123] that the most prominent combiners, which obey Equation 4.78 are the MMSE-, the Minimum Variance (MV) and the Maximum SINR combiners. As argued before, all three of these techniques exhibit the same SINR at the combiner's output, although they have different MSEs.

4.2.3.5 Relation between MMSE and MV combining

In order to motivate the employment of the Minimum Variance (MV) combiner let us recall from Section 4.2.2 that the LS combiner's philosophy was to fully recover the original signal transmitted - as illustrated by Equation 4.42 - without relying on any information concerning the AWGN process, which corrupts the signal received by the different antenna elements. By contrast, the philosophy of the MMSE combiner portrayed in Section 4.2.3 was to strike a balance between the recovery of the signals transmitted and the suppression of the AWGN. An attractive compromise is constituted by the MV approach, which aims for recovering the original signals transmitted whilst ensuring a partial suppression of the AWGN based on the knowledge of its statistics. In other words, the l-th user's associated weight vector $\mathbf{w}^{(l)}$ has to be adjusted such, that its transfer factor, which is seen from Equation 4.11 to be equal to $\mathbf{w}^{(l)H}\mathbf{H}^{(l)}$, assumes a specific predefined value of $g = \mathbf{w}^{(l)H}\mathbf{H}^{(l)}$. The corresponding interference and noise variances of $\sigma_I^{(l)2}$ and $\sigma_N^{(l)2}$ are given by Equations 4.17 and 4.20, respectively.

Usually the MV combiner is derived by minimizing a Lagrangian cost-function, which incorporates both a constraint on the desired user's effective transfer factor, as well as the undesired signal's variance [87, 123]. However, as argued in the previous section, the different combiners' associated weight vectors, namely those of the MMSE, MV and Maximum SINR combiners, differ only by a scalar multiplier. Hence, the MV-related weight vector $\mathbf{w}_{\text{MV}}^{(l)}$ of the l-th user can be directly inferred from the MMSE-related weight vector $\mathbf{w}_{\text{MMSE}}^{(l)}$ by simple normalization according to:

$$\mathbf{w}_{\text{MV}}^{(l)} = \frac{g}{\mathbf{w}_{\text{MMSE}}^{(l)H}\mathbf{H}^{(l)}}\mathbf{w}_{\text{MMSE}}^{(l)}. \tag{4.81}$$

Here the term in the nominator denotes the l-th user's gain factor valid in the context of MMSE combining. Upon substituting the MMSE-specific weight vector given by Equation 4.78 into Equation 4.81 we obtain:

$$\mathbf{w}_{\text{MV}}^{(l)} = \beta_{\text{MV}}\mathbf{R}_{a,I+N}^{(l)-1}\mathbf{H}^{(l)}, \tag{4.82}$$

where:

$$\beta_{\text{MV}} = \frac{g}{\mathbf{H}^{(l)H}\mathbf{R}_{a,I+N}^{(l)}\mathbf{H}^{(l)}}. \tag{4.83}$$

Specifically, for $g = 1$ this "normalized MMSE combiner" is also known as the Minimum Variance Distortionless Response (MVDR) combiner.

4.2.4 Demodulation of the Different Users' Combiner Output Signals

As observed at the left-hand side of Figure 4.4, the linear detector is constituted by the linear combiner, which produces estimates of the signals transmitted by the L different users. Based on these

linear estimates the task of the classifiers seen at the right-hand side of Figure 4.4 is to determine the complex symbols- or constellation points that are most likely to have been transmitted by the different users.

Our further proceedings are as follows. In Section 4.2.4.1 each user's combiner output signal is approximated as a sample of a complex Gaussian distribution function. This representation is then employed in Section 4.2.4.2 for determining the complex symbol- or constellation point that is most likely to have been transmitted by a specific user.

4.2.4.1 Approximation of a Specific User's Combiner Output Signal as a Sample of a Complex Gaussian Distribution

In Sections 4.2.2, 4.2.3 and 4.2.3.5 various methods of detecting the different users' transmitted signals were discussed namely, the LS- MMSE- and MV techniques, respectively. Common to these techniques was their linear structure, which was conveniently illustrated by Equation 4.10. Specifically, the l-th user's combiner output signal $x_{\text{eff}}^{(l)} = \hat{s}^{(l)}$ is constituted by a superposition of the desired user's signal $H_{\text{eff}}^{(l)} s^{(l)}$ and of the undesired signal $n_{\text{eff}}^{(l)}$, which is expressed as:

$$x_{\text{eff}}^{(l)} = H_{\text{eff}}^{(l)} s^{(l)} + n_{\text{eff}}^{(l)}. \tag{4.84}$$

Comparing Equation 4.84 with Equation 4.10 reveals that the desired user's effective transfer factor $H_{\text{eff}}^{(l)}$ is given by:

$$H_{\text{eff}}^{(l)} = \mathbf{w}^{(l)H} \mathbf{H}^{(l)}, \tag{4.85}$$

while the effective undesired signal $n_{\text{eff}}^{(l)}$, namely the sum of the $L-1$ interfering users' residual signals plus the residual AWGN, is given by:

$$n_{\text{eff}}^{(l)} = \hat{s}_I^{(l)} + \hat{s}_N^{(l)}. \tag{4.86}$$

The individual components were defined in Equations 4.12 and 4.13, while their associated variances $\sigma_I^{(l)2}$ and $\sigma_N^{(l)2}$ were given by Equations 4.18 and 4.21. The l-th user's combiner output signal can therefore be approximately modeled, as a sample of a complex Gaussian distribution having a mean value of $H_{\text{eff}}^{(l)} s^{(l)}$ and a variance of $\sigma_{n_{\text{eff}}}^{(l)2} = \sigma_I^{(l)2} + \sigma_N^{(l)2}$ which is formulated as, $x_{\text{eff}}^{(l)} \sim \mathcal{CN}(H_{\text{eff}}^{(l)} s^{(l)}, \sigma_{n_{\text{eff}}}^{(l)2})$ ([7]). We note however, that this relationship is only exactly true for an infinite number of interferers, as a result of the Central-Limit Theorem [141]. This complex Gaussian distribution can be expressed as [142]:

$$f\left(x_{\text{eff}}^{(l)} | s^{(l)}, H_{\text{eff}}^{(l)}\right) = \frac{1}{\pi \sigma_{n_{\text{eff}}}^{(l)2}} \exp\left(-\frac{1}{\sigma_{n_{\text{eff}}}^{(l)2}} \left| x_{\text{eff}}^{(l)} - H_{\text{eff}}^{(l)} s^{(l)} \right|^2\right). \tag{4.87}$$

[7] The complex Gaussian distribution function is denoted here as $\mathcal{CN}()$, in order to distinguish it from the Gaussian distribution function $\mathcal{N}()$ defined for real-valued random variables.

More explicitly, $P(x_{\text{eff}}^{(l)}|s^{(l)}, H_{\text{eff}}^{(l)}) = f(x_{\text{eff}}^{(l)}|s^{(l)}, H_{\text{eff}}^{(l)})$ denotes the *a priori* probability that $x_{\text{eff}}^{(l)}$ is observed at the l-th user's combiner output under the condition that the symbol $s^{(l)}$ is transmitted over a channel characterized by the effective transfer factor $H_{\text{eff}}^{(l)}$ of Equation 4.85.

4.2.4.2 Determination of a Specific User's Transmitted Symbol by Maximizing the *A Posteriori* Probability

The complex symbol $\check{s}_{\text{ML}\approx}^{(l)}$ [8] that is most likely to have been transmitted by the l-th user can be determined upon maximizing the *a posteriori* probability $P(\check{s}^{(l)}|x_{\text{eff}}^{(l)}, H_{\text{eff}}^{(l)})$, that the complex symbol $\check{s}$ was transmitted under the condition that the signal $x_{\text{eff}}^{(l)}$ is observed at the combiner output, for all symbols contained in the trial-set $\mathcal{M}^{(l)}$ given by:

$$\mathcal{M}^{(l)} = \left\{ \check{s}^{(l)} \middle| \frac{\check{s}^{(l)}}{\sigma_l} \in \mathcal{M}_c \right\}. \tag{4.88}$$

In Equation 4.88 $\mathcal{M}_c$ denotes the set of constellation points associated with the specific modulation scheme employed. In mathematical terms this can be formulated as:

$$\check{s}_{\text{ML}\approx}^{(l)} = arg \max_{\check{s}^{(l)} \in \mathcal{M}^{(l)}} P\left(\check{s}^{(l)}|x_{\text{eff}}^{(l)}, H_{\text{eff}}^{(l)}\right). \tag{4.89}$$

Upon invoking the definition of the conditional probability, the *a posteriori* probability $P(\check{s}^{(l)}|x_{\text{eff}}^{(l)}, H_{\text{eff}}^{(l)})$ seen in Equation 4.89 can be rewritten as:

$$P(\check{s}^{(l)}|x_{\text{eff}}^{(l)}, H_{\text{eff}}^{(l)}) = P(x_{\text{eff}}^{(l)}|\check{s}^{(l)}, H_{\text{eff}}^{(l)}) \frac{P(\check{s}^{(l)})}{P(x_{\text{eff}}^{(l)})}, \tag{4.90}$$

where the total probability $P(x_{\text{eff}}^{(l)})$ follows from the condition that:

$$\sum_{\check{s}^{(l)} \in \mathcal{M}^{(l)}} P(\check{s}^{(l)}|x_{\text{eff}}^{(l)}, H_{\text{eff}}^{(l)}) \stackrel{!}{=} 1, \tag{4.91}$$

which yields:

$$P(x_{\text{eff}}^{(l)}) = \sum_{\check{s}^{(l)} \in \mathcal{M}^{(l)}} P(x_{\text{eff}}^{(l)}|\check{s}^{(l)}, H_{\text{eff}}^{(l)}) P(\check{s}^{(l)}). \tag{4.92}$$

Note that Equation 4.90 in conjunction with Equation 4.92 is also known as Bayes' theorem [87].

Upon substituting Equation 4.90 into Equation 4.89 and by noting again that the *a priori* probability $P(x_{\text{eff}}^{(l)}|\check{s}^{(l)}, H_{\text{eff}}^{(l)})$ is given by the complex Gaussian distribution function of Equation 4.87, namely by $f(x_{\text{eff}}^{(l)}|\check{s}^{(l)}, H_{\text{eff}}^{(l)})$, we obtain for the ML symbol estimate $\check{s}_{\text{ML}\approx}^{(l)}$ the following expression:

$$\check{s}_{\text{ML}\approx}^{(l)} = arg \max_{\check{s}^{(l)} \in \mathcal{M}^{(l)}} P\left(x_{\text{eff}}^{(l)}|\check{s}^{(l)}, H_{\text{eff}}^{(l)}\right) \iff \check{s}_{\text{ML}\approx}^{(l)} = arg \min_{\check{s}^{(l)} \in \mathcal{M}^{(l)}} \left| x_{\text{eff}}^{(l)} - H_{\text{eff}}^{(l)} \check{s}^{(l)} \right|^2. \tag{4.93}$$

[8] Here we have denoted the most likely transmitted symbol as $\check{s}_{\text{ML}\approx}^{(l)}$, in order to emphasize that the Gaussian approximation was used for modelling the residual interference contaminating the combiner's output signal.

Note from Equation 4.93 that determining the ML symbol estimate implies minimizing the Euclidean distance in the argument of the exponential term associated with the Gaussian distribution function of Equation 4.87. In the context of our derivation we have also exploited that we have $P(\check{s}^{(l)}) = \frac{1}{M_c} = const.$, as well as that we have $P(x_{\text{eff}}^{(l)}) = const.$ as seen in Equation 4.91. Hence, these terms are irrelevant in the context of the minimization required by Equation 4.93.

In order to avoid the multiplication of each trial-symbol $\check{s}^{(l)}$ with the effective transfer factor $H_{\text{eff}}^{(l)}$, as required by Equation 4.93, it is legitimate to evaluate:

$$\check{s}_{\text{ML}\approx}^{(l)} = arg \min_{\check{s}^{(l)} \in \mathcal{M}^{(l)}} \left| \frac{1}{H_{\text{eff}}^{(l)}} x_{\text{eff}}^{(l)} - \check{s}^{(l)} \right|^2, \tag{4.94}$$

instead. Note again that if the estimate $x_{\text{eff}}^{(l)}$ at the l-th user's combiner output is generated with the aid of the MMSE criterion, then the normalized estimate $x_{\text{eff}}^{(l)}/H_{\text{eff}}^{(l)}$ is actually the complex symbol, which would be observed at the output of the MVDR combiner, as described in Section 4.2.3.5. Note however that in the context of MPSK modulation schemes the normalization by the real-valued factor of $H_{\text{eff}}^{(l)}$ is not necessary, since only the signal's phase is of importance to the detection process.

4.2.5 Generation of Soft-Bit Information for Turbo-Decoding

Employing turbo decoding at the receiver is a powerful means of further enhancing the system's BER. Naturally, this is achieved at the cost of a reduction of the system's effective throughput. A prerequisite for the employment of turbo codes is the availability of soft-bit information at the detector's output, whose generation will be discussed in this section.

Our discussions will be based on Equation 4.84, which described the l-th user's combiner output signal $x_{\text{eff}}^{(l)}$ as the superposition of the desired user's signal contribution $s^{(l)}$, which has a gain of $H_{\text{eff}}^{(l)}$, plus the effective noise contribution $n_{\text{eff}}^{(l)}$, which comprises the $L-1$ remaining users' residual interference and the residual AWGN. The residual interference was approximated by a Gaussian process and hence the total variance of the effective noise became $\sigma_{n_{\text{eff}}}^{(l)2} = \sigma_I^{(l)2} + \sigma_N^{(l)2}$.

With respect to Equation 4.84 the soft-bit value or log-likelihood ratio $L_{m\approx}^{(l)}$ associated with the l-th user at the m-th bit-position is given by [87]:

$$L_{m\approx}^{(l)} = \ln \frac{P(b_m^{(l)} = 1 | x_{\text{eff}}^{(l)}, H_{\text{eff}}^{(l)})}{P(b_m^{(l)} = 0 | x_{\text{eff}}^{(l)}, H_{\text{eff}}^{(l)})}, \tag{4.95}$$

which is the natural logarithm of the quotient of *a posteriori* probabilities that the m-th bit transmitted by the l-th user in the k-th subcarrier is associated with a logical value of $b_m^{(l)} = 1$ or $b_m^{(l)} = 0$. Note that here we have again omitted the index $[n,k]$ for the k-th subcarrier of the n-th OFDM symbol. Equation 4.95 can be further expanded by noting that the *a posteriori* probability that a bit of $b_m^{(l)} = 1$ was transmitted is given by the sum of the *a posteriori* probabilities of those symbols,

which are associated with a bit value of $b_m^{(l)} = 1$, again, at the m-th bit position. The *a posteriori* probability that a bit value of $b_m^{(l)} = 0$ was transmitted can be represented equivalently. Hence we obtain:

$$L_{m\approx}^{(l)} = \ln \frac{\sum_{(\check{s}^{(l)}/\sigma_l)\in\mathcal{M}_{cm}^{1}} P(\check{s}^{(l)}|x_{\text{eff}}^{(l)}, H_{\text{eff}}^{(l)})}{\sum_{(\check{s}^{(l)}/\sigma_l)\in\mathcal{M}_{cm}^{0}} P(\check{s}^{(l)}|x_{\text{eff}}^{(l)}, H_{\text{eff}}^{(l)})}, \tag{4.96}$$

where $\mathcal{M}_{cm}^{b}$ denotes the specific subset of the set $\mathcal{M}_c$ of constellation points of the modulation scheme employed, which are associated with a bit value of $b \in \{0,1\}$ at the m-th bit position. For notational convenience we can define the l-th user's associated set of trial-vectors employed for determining the probability that the m-th transmitted bit exhibits a value of $b \in \{0,1\}$ as follows:

$$\mathcal{M}_m^{b(l)} = \left\{ \check{s}^{(l)} \left| \frac{\check{s}^{(l)}}{\sigma_l} \in \mathcal{M}_{cm}^{b} \right. \right\}. \tag{4.97}$$

Substituting the Bayes theorem of Equation 4.90 into Equation 4.96 then yields for the l-th user's soft-bit value at the m-th bit position the following expression:

$$L_{m\approx}^{(l)} = \ln \frac{\sum_{\check{s}^{(l)}\in\mathcal{M}_m^{1(l)}} P(x_{\text{eff}}^{(l)}|\check{s}^{(l)}, H_{\text{eff}}^{(l)})}{\sum_{\check{s}^{(l)}\in\mathcal{M}_m^{0(l)}} P(x_{\text{eff}}^{(l)}|\check{s}^{(l)}, H_{\text{eff}}^{(l)})}. \tag{4.98}$$

Here we have exploited that the different trial-symbols $\check{s}^{(l)}$ have the same probability, namely $P(\check{s}^{(l)}) = const.$, $\check{s}^{(l)} \in \mathcal{M}^{(l)}$, where $\mathcal{M}^{(l)} = \mathcal{M}_m^{(0)(l)} \bigcup \mathcal{M}_m^{(1)(l)}$. Upon recalling from Section 4.2.4 that the *a priori* probability $P(x_{\text{eff}}^{(l)}|\check{s}^{(l)}, H_{\text{eff}}^{(l)})$ is given by the complex Gaussian distribution function $f(x_{\text{eff}}^{(l)}|\check{s}^{(l)}, H_{\text{eff}}^{(l)})$ defined in Equation 4.87, we obtain that:

$$L_{m\approx}^{(l)} = \ln \frac{\sum_{\check{s}^{(l)}\in\mathcal{M}_m^{1(l)}} \exp\left(-\frac{1}{\sigma_{n_{\text{eff}}}^2}|x_{\text{eff}}^{(l)} - H_{\text{eff}}^{(l)}\check{s}^{(l)}|^2\right)}{\sum_{\check{s}^{(l)}\in\mathcal{M}_m^{0(l)}} \exp\left(-\frac{1}{\sigma_{n_{\text{eff}}}^2}|x_{\text{eff}}^{(l)} - H_{\text{eff}}^{(l)}\check{s}^{(l)}|^2\right)}. \tag{4.99}$$

Observe that evaluating the l-th user's soft-bit value at the m-th bit position with the aid of Equation 4.99 involves the exponential function, which is computationally demanding.

4.2.5.1 Simplification by Maximum Approximation

In order to avoid the explicit evaluation of the exponential function, a common approach is constituted by the so-called maximum-approximation, which implies that only that specific additive term is retained in the calculation of the numerator and nominator of Equation 4.99, which yields the maximum contribution. It can be readily shown that as a result of this simplification we obtain instead of Equation 4.99 the following expression:

$$L_{m\approx}^{(l)} \approx \frac{1}{\sigma_{n_{\text{eff}}}^{(l)2}} \left[|x_{\text{eff}}^{(l)} - H_{\text{eff}}^{(l)}\check{s}_{m\approx}^{0(l)}|^2 - |x_{\text{eff}}^{(l)} - H_{\text{eff}}^{(l)}\check{s}_{m\approx}^{1(l)}|^2 \right], \tag{4.100}$$

system parameters	choice
CIR model	3-path indoor WATM of Section 6.1.1
CIR tap fading	OFDM symbol invariant
system model	indoor WATM of Section 6.1.1
channel estimation	ideal
transmit antennas per user	1

Table 4.3: Summary of the system setup; also note that the fading was assumed to be uncorrelated for the different CIR taps associated with the channel between a specific transmitter-receiver antenna pair, as well as uncorrelated for the same CIR tap of different transmitter-receiver antenna pairs.

turbo coding parameters	choice
coding rate R_c	1/2
constraint length K_c	3
generator polynomial	$(7,5)_8$
number of iterations	4

Table 4.4: Summary of the turbo-coding parameters.

where

$$\check{s}_{m\approx}^{b(l)} = arg \min_{\check{s}^{(l)} \in \mathcal{M}_m^{b(l)}} |x_{\text{eff}}^{(l)} - H_{\text{eff}}^{(l)} \check{s}^{(l)}|^2, \quad b \in \{0,1\}, \tag{4.101}$$

while the set $\mathcal{M}_m^{b(l)}$ was defined in Equation 4.97. We note that for each soft-bit to be determined, Equation 4.101 has to be invoked twice, namely, once for a bit value of $b = 1$ and once for $b = 0$.

A significant complexity reduction can be achieved by exploiting that $\mathcal{M}^{(l)} = \mathcal{M}_m^{0(l)} \bigcup \mathcal{M}_m^{1(l)}$. Hence, the calculation of the Euclidean distance metric $|x_{\text{eff}}^{(l)} - H_{\text{eff}}^{(l)} \check{s}^{(l)}|^2$ only has to be performed once for the different trial symbols $\check{s}^{(l)} \in \mathcal{M}^{(l)}$, followed by an appropriate selection in the context of the soft-bit generation assisted by Equation 4.101. Specifically half of the symbols $\check{s}_{m\approx}^{b(l)}$ for the different bit polarities $b \in \{0,1\}$ and bit positions m can be readily inferred by conducting an initial search of the entire set $\mathcal{M}^{(l)}$. This results in the ML estimate $\check{s}_{\text{ML}\approx}^{(l)}$ of the transmitted symbol according to Equation 4.94. The initial ML symbol estimate is constituted by a specific bit representation. The minimization obeying Equation 4.101 has to be conducted over the set of specific symbols, which contain the inverted versions of the bits identified during the previously mentioned initial ML symbol search.

4.2.6 Performance Analysis

In the context of our simulations the frame-invariant fading indoor WATM channel- and system model described in Section 6.1.1 will be employed. Furthermore, perfect knowledge of the channel

transfer functions associated with the different transmit-receive antenna pairs will be assumed. Note that as a result of performing the detection of the different users' transmitted symbols independently on an OFDM subcarrier-by-subcarrier basis, the performance results presented here for the uncoded system are independent from the indoor WATM channel's specific multipath intensity profile. The advantage of employing the idealistic model of an OFDM symbol invariant fading channel is that the performance results are not impaired by the obfuscating effects of Inter-subCarrier Interference (ICI). Again the general system setup has been summarized in Table 4.3, while in Table 4.4 we have summarized the turbo-coding parameters to be employed in the context of our investigation of turbo-coded systems.

The structure of our performance investigations is as follows. In Section 4.2.6.1 the different detectors, namely LS, MMSE and MV are compared to each other in terms of the achievable MSE at the associated combiner's output, as well as in terms of the BER. By contrast, in Sections 4.2.6.2 and 4.2.6.3 we concentrate on the assessment of the specific MMSE detector's performance in terms of the distribution of the SINR measured at the associated combiner's output, as well as that of the detector's BER performance, respectively. These investigations are conducted as a function of the number of users L and that of the number of reception antennas P. Our investigations are concluded upon evaluating the BER performance of turbo-coded MMSE detection-assisted SDMA-OFDM in Section 4.2.6.4.

4.2.6.1 MSE and BER Performance Comparison of LS, MMSE and MVDR Detection

At the left-hand side of Figure 4.6 we have portrayed the average MSE performance recorded at the different detectors' combiner outputs, as a function of the SNR at the reception antennas. More specifically, the MSE was evaluated as the squared error between the signal transmitted by a specific user and that observed at its associated combiner output, normalized to the user's signal variance. Here we have considered the scenario of two reception antennas and two simultaneous SDMA users, each equipped with one transmit antenna, which we denoted as (A2/U2). As expected, the best MSE performance is exhibited by the MMSE combiner, closely followed by the MVDR combiner, as seen in Figure 4.6. The worst MSE performance was exhibited by the LS combiner, which is also widely known as the zero-forcing combiner. Furthermore, observe that upon increasing the users' SNRs towards infinity, the different combiners' MSE curves merge. This is, because when increasing the SNR a Wiener filter based combiner effectively operates as an LS combiner, aiming for minimizing purely the interfering signals' variances, rather than that of the joint noise and interference contributions. Note that in the context of our simulations the LS combiner's correlation matrix given by Equation 4.33 was regularized [87] upon adding a value of 10^{-6} to its main diagonal elements. This contributed towards mitigating the problems associated with its inversion. By contrast, on the right-hand side of Figure 4.6 we have portrayed the system's BER associated with the different detectors

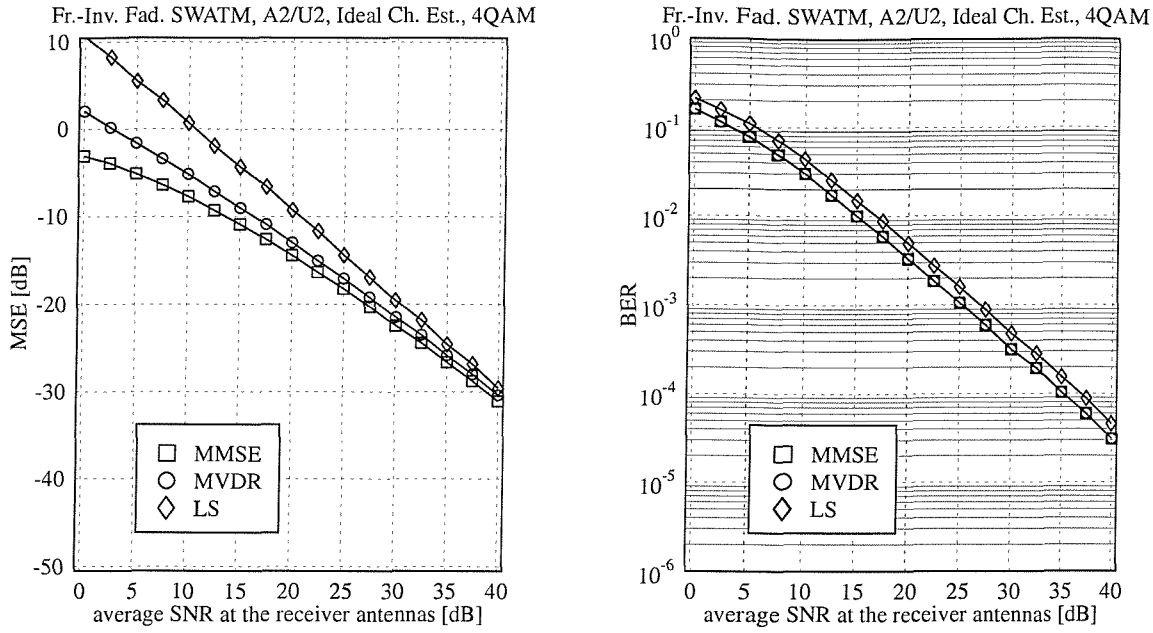

Figure 4.6: Comparison of the different linear detectors, namely, the LS, MMSE and MVDR techniques as a function of the SNR at the reception antennas, with respect to (left:) the MSE at the combiner's output and (right:) the detector's BER; here we have employed the configuration of $L = 2$ simultaneous users and $P = 2$ reception antennas at the BS $(A2/U2)$; for the basic simulation parameters we refer to Table 4.3

in the context of 4QAM modulation. We observe that both Wiener-filter based detectors, namely, the MMSE and MVDR schemes achieve the same BER performance, as a result of their identical SINR performance as it was highlighted in Sections 4.2.3.4 and 4.2.3.5. Note however that in the context of higher-order QAM modulation schemes, such as 16QAM for example, where also the constellation points' amplitude conveys information, a slight BER performance advantage was observed for the MVDR detector although the corresponding results are not included here for reasons of space economy. Furthermore, similarly to our observations with respect to the different detectors' associated combiner MSE performance, the LS detector performs significantly worse, than the MMSE and the MVDR detectors also in terms of the BER. Hence, in our following discussions we will focus on the MMSE detector, which will also be employed as the core element of SIC and PIC detectors to be discussed in Sections 4.3.1 and 4.3.2, respectively.

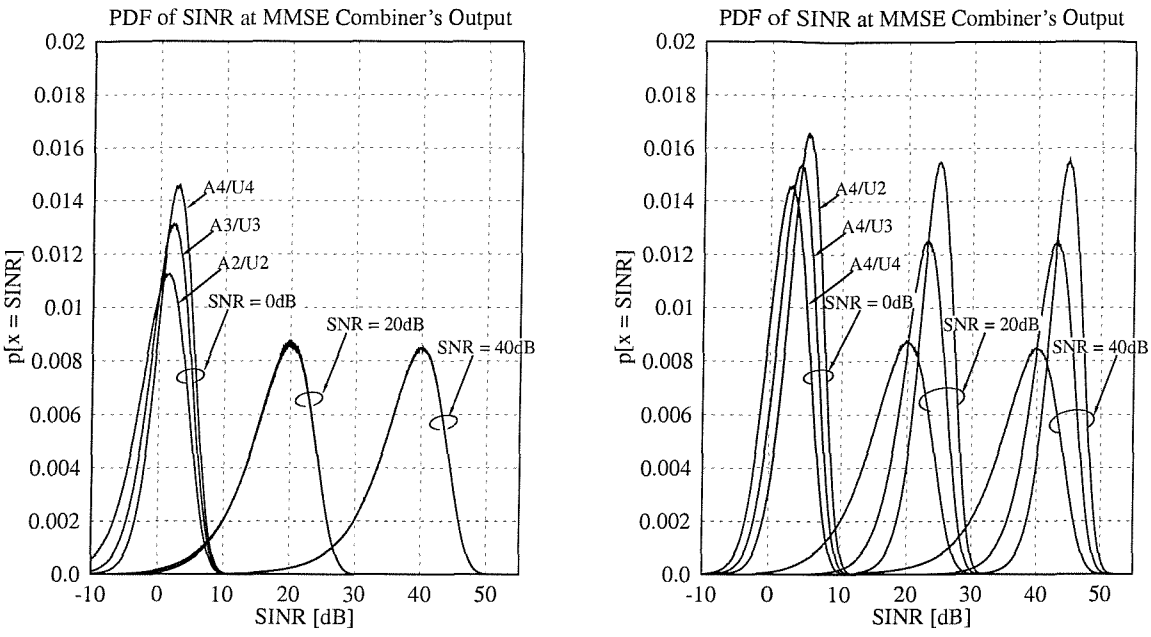

Figure 4.7: Characterization of the MMSE detector in terms of its associated SINR-PDF observed at the combiner's output; (left:) for each configuration the L number of users is identical to the P number of reception antennas, using the configurations of $A2/U2$, $A3/U3$ and $A4/U4$; (right:) the P number of reception antennas is equal to four, while the L number of users is varied, where we have the configurations of $A4/U2$, $A4/U3$ and $A4/U4$; for the basic simulation parameters we refer to Table 4.3.

4.2.6.2 SINR Performance of MMSE Detection for Different Numbers of Users and Reception Antennas

In order to further characterize the MMSE detector, in Figure 4.7 we have plotted the Probability Density Function (PDF) of the SINR at the combiner's output for different combinations of the number of simultaneous users L and the number of reception antennas P, as well as for SNRs of 0dB, 20dB and 40dB recorded at the reception antennas. Specifically, in the graph seen at the left-hand side of Figure 4.7 we have compared those PDFs against each other, which are associated with the particular configurations of $P = L \in \{2, 3, 4\}$. We observe that at sufficiently high SNRs the SINR distributions become *almost* identical, which is because the different arrangements have the same diversity order. Here we emphasize the expression "almost identical", since at higher SNRs - although visually they appear identical in Figure 4.7 - perceivable differences were found in terms of the corresponding average BER performance for the configurations of A2/U2, A3/U3 as well as A4/U4. More explicitly, upon increasing the MIMO system's order, the BER performance is

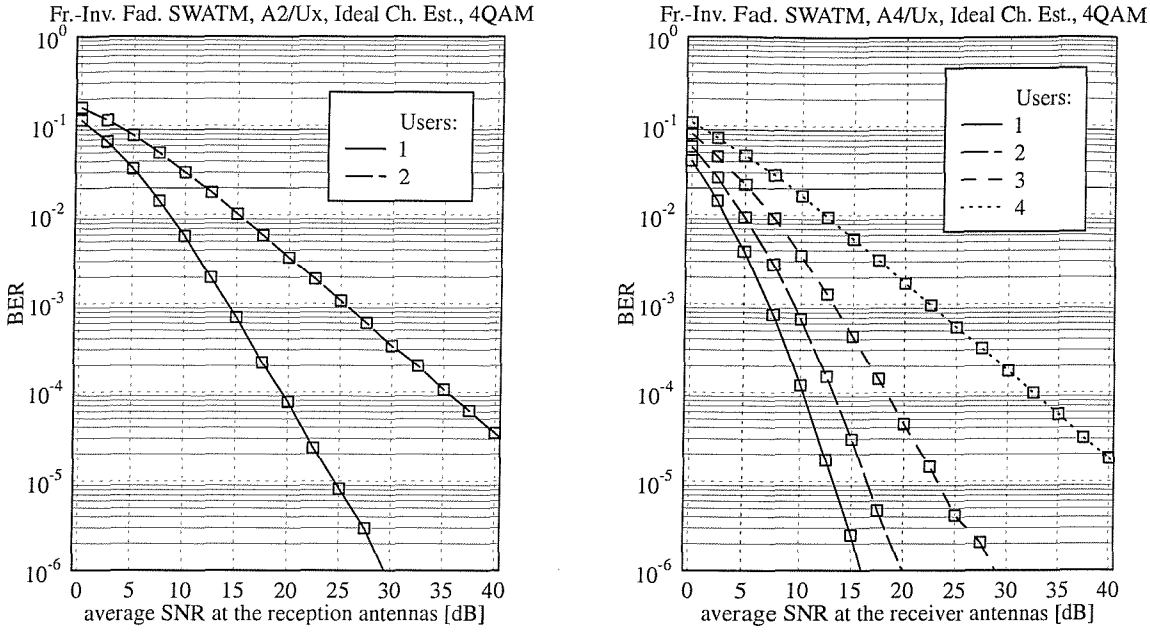

Figure 4.8: BER performance of 4QAM-modulated, MMSE detection-assisted SDMA-OFDM as a function of the SNR at the reception antennas; the curves are further parameterized with the number of simultaneous users L and the number of reception antennas P, where more specifically (left:) two reception antennas, (right:) four reception antennas were employed; for the basic simulation parameters we refer to Table 4.3.

improved.

By contrast, at the right-hand side of Figure 4.7 we have considered configurations of $P = 4$, $L \in \{2, 3, 4\}$. Here we observe that upon increasing the diversity order, namely by decreasing the L number of SDMA users, while keeping the P number of reception antennas constant, the probability of incurring higher SINRs is increased. The effects of these SINR improvements on the system's BER performance will be further investigated in the next section,

4.2.6.3 BER Performance of MMSE Detection for Different Numbers of Users and Reception Antennas

In Figure 4.8 we have portrayed the BER performance of a 4QAM-modulated MMSE detection-assisted SDMA-OFDM scheme as a function of the SNR at the reception antennas. The curves are further parameterized with the number of simultaneous users L and the number of reception antennas P. Upon decreasing the number of users L while keeping the number of reception antennas P constant, we observe that the BER performance is dramatically improved. This is because the

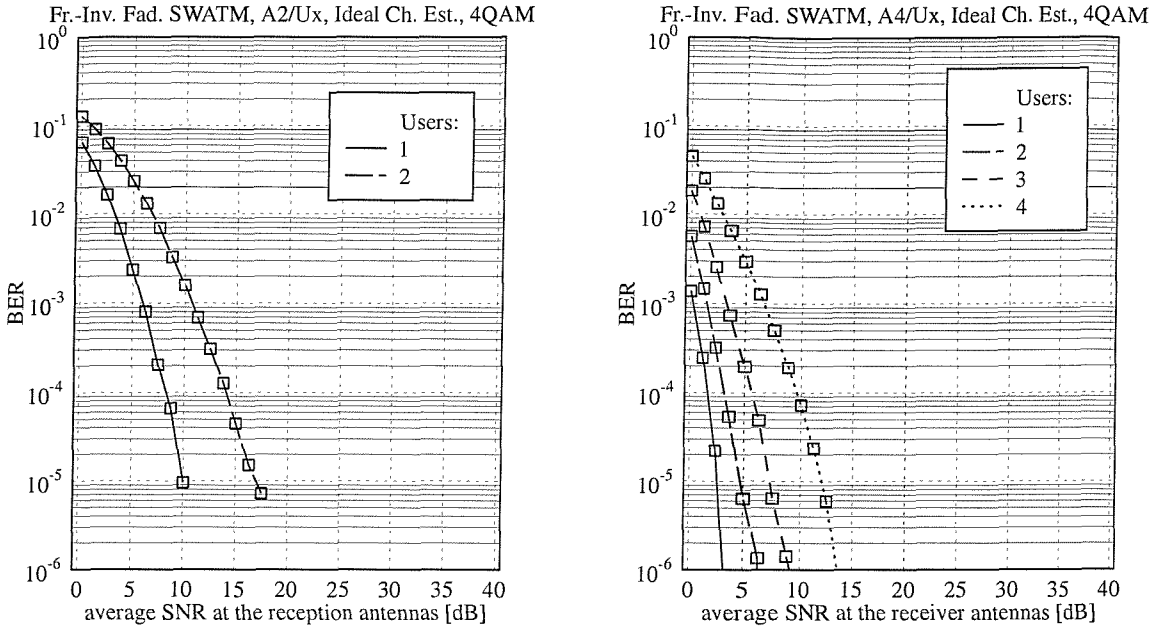

Figure 4.9: BER performance of turbo-coded, 4QAM-modulated, MMSE detection-assisted SDMA-OFDM as a function of the SNR at the reception antennas; the curves are further parameterized with the number of simultaneous users L and the number of reception antennas P, where (left:) two reception antennas, and (right:) four reception antennas were employed, respectively; for the basic simulation parameters and for the turbo-coding parameters we refer to Tables 4.3 and 4.4, respectively.

system's diversity order is increased and hence the detector benefits from a degree of freedom for adjusting its associated combiner weights in favour of a better exploitation of the channel's diversity, in favour of a reduction of the AWGN, rather than aiming for the mitigation of the remaining users' interference.

4.2.6.4 BER Performance of Turbo-Coded MMSE Detection-Assisted SDMA-OFDM

Turbo-decoding at the receiver is a powerful means of further enhancing the system's BER performance. This is achieved at the cost of reducing the system's effective throughput and by investing additional computational complexity. The turbo coding parameters were summarized in Table 4.4, but for the reader's convenience they are repeated here. Namely, the coding rate was $R_c = \frac{1}{2}$, the constraint length was $K_c = 3$, the octally represented generator polynomials of $(7, 5)_8$ were used and four iterations were performed. The generation of the soft-bits required for turbo-decoding was discussed earlier in Section 4.2.5.

Our BER simulation results are portrayed in Figure 4.9, at the left-hand side for $P = 2$ reception antennas, while at the right-hand side for $P = 4$ reception antennas, when supporting up to $L = P$ number of users. We observe that compared to the uncoded scenario, whose associated simulation results were shown in Figure 4.8 the BER is significantly reduced. To provide an example, for a so-called 'fully loaded' system associated with $L = P = 4$ the SNR at the reception antennas required for a BER of 10^{-5} was around 42dB, while in the context of turbo-decoding the same BER was reached at an SNR of around 13dB. Again, this performance improvement is achieved at the cost of halving the system's throughput and at an additional computational complexity imposed by the turbo-decoder. Furthermore, similarly to the uncoded scenario, upon removing one user from the 'fully loaded' system results in a significant reduction of the BER. This is, because the MMSE combiner has a higher degree of freedom in terms of the choice of the optimum weight matrix, with the beneficial effect of a better suppression of the undesired AWGN.

4.2.7 Complexity Analysis

In this section we will analyse the computational complexity inflicted per subcarrier when evaluating the vector of estimated transmitted signals, followed by hard-decision based demodulation carried out with the aid of minimizing the Euclidean distance metric of Equation 4.94. The structure of this section is as follows. While in Section 4.2.7.1 the LS combiner's complexity is quantified, in Section 4.2.7.2 we will concentrate on the portrayal of the MMSE combiner's complexity. Finally, the computational complexity related to the demodulation of the linear combiners' output signals will then be analysed in Section 4.2.7.3.

4.2.7.1 LS Combining

An expression for the LS combiner's associated weight vector was provided in Equation 4.35 for the case of $P \geq L$. First of all, the calculation of the 'auto-correlation' matrix $\mathbf{Q}_{\text{LS}}$ defined in Equation 4.33 requires L^2P number of complex multiplications and the same number of additions. By contrast, the evaluation of the 'cross-correlation' vector $\mathbf{p}_{\text{LS}}$ requires LP number of complex multiplications and additions. Due to the potentially high condition number [87] of the 'auto-correlation' matrix $\mathbf{Q}_{\text{LS}}$ it is disadvantageous to directly invert it, since it requires a high numerical accuracy. Recall that this direct solution for the vector $\hat{\mathbf{s}}_{\text{LS}}$ was shown at the right-hand side of Equation 4.35.

4.2.7.1.1 LS Combining without Generating the Weight Matrix In order to circumvent this problem, the preferred method is that of solving the equation system shown at the left-hand side of Equation 4.35. In order to ensure numerical stability, a matrix decomposition based approach such as the Cholesky-, LU- or QR decomposition [87] could be invoked. In the context of the LS solution the most prominent matrix factorization technique is the QR decomposition. However,

here we assume that the LU decomposition technique outlined in [87] is employed. Hence, in a first step the matrix $\mathbf{Q}_{\text{LS}}$ is LU decomposed, imposing a computational complexity of $\frac{1}{3}L^3$ complex multiplications and additions. Then, in a second step the desired vector $\hat{\mathbf{s}}_{\text{LS}}$ is determined with the aid of forward- and backward substitutions using the procedure outlined in [87], which imposes a complexity of L^2 complex multiplications and additions. Hence, the *total* computational complexity of solving Equation 4.35 per subcarrier is given by:

$$C_{\text{LS,direct}}^{(\mathbb{C}*\mathbb{C})} = C_{\text{LS,direct}}^{(\mathbb{C}+\mathbb{C})} = PL + (P+1)L^2 + \frac{1}{3}L^3. \tag{4.102}$$

Note however that as a result of this procedure the weight matrix $\mathbf{W}_{\text{LS}}$ defined in Equation 4.38 does not become explicitly available, although it might be required for determining the estimation MSE, the SNR or SINR on a subcarrier basis.

4.2.7.1.2 LS Combining Generating the Weight Matrix As an example, in the context of the SIC detection[9] procedure to be discussed in Section 4.3.1, explicit knowledge of the weight matrix is required for calculating the subcarrier based S(I)NR values employed for selecting the most dominant user to be cancelled next in a specific detection stage. A possible solution for determining $\mathbf{W}_{\text{LS}}$ is first to solve Equation 4.37 for obtaining the projection matrix $\mathbf{P}_{\text{LS}}$, which is related to the weight matrix $\mathbf{W}_{\text{LS}}$ by the Hermitian transpose as seen in Equation 4.38. This step is then followed by appropriately combining the output signals of the array elements according to Equation 4.36. As a consequence, the associated *total* computational complexity would be:

$$C_{\text{LS,W+cmb}}^{(\mathbb{C}*\mathbb{C})} = C_{\text{LS,W+cmb}}^{(\mathbb{C}+\mathbb{C})} = PL + 2PL^2 + \frac{1}{3}L^3. \tag{4.103}$$

The concomitant increase in computational complexity compared to that quantified by Equation 4.102 is, because in the process of evaluating $\mathbf{W}_{\text{LS}}$ the forward- and backward substitutions as outlined in [87] would have to be carried out for P different matrix right-hand sides.

Note that since the computational complexity is dominated in both cases by the third order as a function of the number of simultaneous users L, increasing this parameter will dramatically increase the associated complexity.

4.2.7.2 MMSE Combining

The second combiner which we will analyse in terms of its computational complexity is the MMSE combiner of Section 4.2.3. Here the relevant equations are the general combiner's formula, namely Equation 4.7, as well as the MMSE-specific expression that has to be evaluated for the determination of the optimum weight matrix, namely, Equation 4.64 or 4.68. Recall that both forms are equivalent to each other. Nonetheless, as argued in Section 4.2.3.2, there is a difference in the dimension of the

[9]The LS detector, or alternatively the MMSE detector could be employed as a baseline detector in each SIC detection stage.

auto-correlation matrices. Specifically, in the context of the left-inverse related form of the weight matrix given by Equation 4.68 an auto-correlation matrix $\mathbf{R}_{\overline{a}}$ of dimension $L \times L$ has to be inverted, while in conjunction with the right-inverse related form of Equation 4.64 the auto-correlation matrix $\mathbf{R}_a$ to be inverted is of dimension $P \times P$.

4.2.7.2.1 Left-Inverse Related Form of MMSE Combining without Generating the Weight Matrix As it was shown earlier in Section 4.2.7.1 for the LS combiner, if the weight matrix $\mathbf{W}_{\text{MMSE}}$ is not explicitly required, a complexity reduction can be achieved in conjunction with the left-inverse related representation of the MMSE combiner by directly solving Equation 4.70 for the vector of the transmitted symbols' estimates. The solution of Equation 4.70 imposes a complexity of:

$$C^{(\mathbb{C}*\mathbb{C})}_{\text{MMSE,direct}} = C^{(\mathbb{C}+\mathbb{C})}_{\text{MMSE,direct}} = PL + (P+1)L^2 + \frac{1}{3}L^3 \tag{4.104}$$

$$C^{(\mathbb{R}*\mathbb{C})}_{\text{MMSE,direct}} = PL \tag{4.105}$$

$$C^{(\mathbb{R}+\mathbb{C})}_{\text{MMSE,direct}} = L. \tag{4.106}$$

which implies a complexity reduction by a factor of $(P-1)L^2$ in terms of the number of complex multiplications and additions.

4.2.7.2.2 Left-Inverse Related Form of MMSE Combining Generating the Weight Matrix Upon following similar steps, as in the context of our analysis of the LS combiner's complexity, which was considered for the scenario of $P \geq L$ in Section 4.2.7.1, we found that the complexity of the MMSE combiner, as represented by Equation 4.68 in its left-inverse related form can be related to the complexity formula originally derived for the LS combiner namely, to Equation 4.103, which is repeated here for the reader's convenience:

$$C^{(\mathbb{C}*\mathbb{C})}_{\text{MMSE,W+cmb}} = C^{(\mathbb{C}+\mathbb{C})}_{\text{MMSE,W+cmb}} = PL + 2PL^2 + \frac{1}{3}L^3. \tag{4.107}$$

More explicitly, this LS combining related formula quantifies the number of complex multiplications and additions required by Equations 4.37 and 4.7, respectively. However, the MMSE combiner is somewhat more complex, since in Equation 4.68 an additional complexity contribution of mixed real-complex multiplications and additions is incurred due to incorporating the SNR matrix of $\mathbf{P}_{\text{SNR}}$. The number of these operations is given by:

$$C^{(\mathbb{R}*\mathbb{C})}_{\text{MMSE,W+cmb}} = PL \tag{4.108}$$

$$C^{(\mathbb{R}+\mathbb{C})}_{\text{MMSE,W+cmb}} = L. \tag{4.109}$$

4.2.7.3 Demodulation of the Linear Combiner's Output Signal

In addition to the computational complexity associated with the process of linear combining, we also have to account for the complexity imposed by demodulating the different users' associated

combiner output signals with the aid of Equation 4.94. More specifically, from Equation 4.94 we infer that evaluating the Euclidean distance metric for a single M_c-ary trial-symbol $\check{s}$ of a subcarrier requires one complex addition, as well as 'half' a complex multiplication, which is related to the operation of actually calculating the Euclidean norm[10] of the complex-valued difference between the received signal and the trial-symbol. Hence, in the context of M_c number of symbols per trial-set and for L number of simultaneous users to be demodulated, the total computational complexity related to the demodulation of Equation 4.94 is given by:

$$C_{\text{lin,dem}}^{(\mathbb{C}*\mathbb{C})} = \frac{1}{2}LM_c \tag{4.110}$$

$$C_{\text{lin,dem}}^{(\mathbb{C}+\mathbb{C})} = C_{\text{lin,dem}}^{(\mathbb{R}\lesseqgtr\mathbb{R})} = LM_c, \tag{4.111}$$

where we have introduced the number of real-valued comparisons $C_{\text{lin,dem}}^{(\mathbb{R}\lesseqgtr\mathbb{R})}$ between the Euclidean distance metric outcomes as a further index of complexity.

4.2.7.4 Simplified Complexity Formulae to be used in the Comparison of the Different Detectors

In Sections 4.2.7.1, 4.2.7.2 and 4.2.7.3 we elaborated on the individual computational complexity exhibited by the LS- and MMSE combiners described in Sections 4.2.2 and 4.2.3, respectively, as well as by the process of demodulating the combiner's output signal as outlined in Section 4.2.4. By contrast, in this section, we will present simplified complexity formulae for the LS- and MMSE detectors, which will be employed in our final comparison of the different detectors' complexities in Section 4.3.4.2. Our aim was to give a more compact representation of the complexity, in terms of the number of complex multiplications and additions, as well as real-valued comparisons. Specifically, in the context of the MMSE detector the number of mixed real-complex multiplications and additions has been expressed in terms of the number of complex multiplications and additions[11] upon weighting them by a factor of $\frac{1}{2}$. Here we assume that the weight matrix is not determined, which allows for a lower-complexity implementation, as argued in the previous sections. Hence, for the LS detector of Equation 4.35 and the associated process of demodulation in Equation 4.94 we obtain the following simplified complexity formulae:

$$C_{\text{LS}}^{\mathbb{C}*\mathbb{C}} = \frac{1}{2}LM_c + PL + (P+1)L^2 + \frac{1}{3}L^3 \tag{4.112}$$

$$C_{\text{LS}}^{\mathbb{C}+\mathbb{C}} = LM_c + PL + (P+1)L^2 + \frac{1}{3}L^3 \tag{4.113}$$

$$C_{\text{LS}}^{\mathbb{R}\lesseqgtr\mathbb{R}} = LM_c. \tag{4.114}$$

[10] $|a_x + ja_y|^2 = (a_x + ja_y) \cdot (a_x + ja_y)^* = a_x^2 + a_y^2$

[11] Here we have neglected the real-valued additions required for evaluating the product of two complex numbers and hence our complexity formulae provide an upper bound estimate.

By contrast, for the left-inverse related form of the MMSE detector in Equation 4.70 plus for the associated demodulation procedure of Equation 4.94 we obtain:

$$C_{\text{MMSE}}^{\mathbb{C}*\mathbb{C}} = \frac{1}{2}LM_c + \frac{3}{2}PL + (P+1)L^2 + \frac{1}{3}L^3 \quad (4.115)$$

$$C_{\text{MMSE}}^{\mathbb{C}+\mathbb{C}} = LM_c + \left(P + \frac{1}{2}\right)L + (P+1)L^2 + \frac{1}{3}L^3 \quad (4.116)$$

$$C_{\text{MMSE}}^{\mathbb{R}\lesssim\mathbb{R}} = LM_c. \quad (4.117)$$

Again, these simplified formulae will be employed in the context of Section 4.3.4.2 for comparing the different detectors' complexities.

4.2.8 Conclusions on Linear Detection Techniques

In Section 4.2 we have concentrated on the mathematical portrayal, performance- and complexity comparison of the most prominent linear detection techniques, namely on the LS and MMSE procedures of Sections 4.2.2 and 4.2.3, respectively. Our discussions commenced in Section 4.2.1 with the characterization of a linear combiner's output signal and its components, while our more specific discussions in Section 4.2.2 focussed on the LS detector, also known as the ZF detector- or decorrelating detector. Its associated combiner weight matrix was shown in Equation 4.38 to be given as the Hermitian transpose of the Moore-Penrose pseudo-inverse or left-inverse of the channel transfer factor matrix $\mathbf{H}$. In contrast to the calculation of the MMSE related weight matrix, its calculation outlined in Equation 4.38 does not require any statistical information. Although, as shown in Equation 4.42 the transmitted signal is recovered with unit-gain, it is contaminated by the residual AWGN, which is potentially boosted due to the effects of the actual channel matrix. In order to achieve a lower average MSE than that of Equation 4.46, derived for characterizing the LS combiner's output, the MMSE combiner of Section 4.2.3 can be invoked.

As suggested by the terminology, from the set of all linear combiners the MMSE combiner exhibits the lowest MSE at the output. As shown in Section 4.2.3, this is achieved upon incorporating statistical information concerning the transmitted signals' variances and the AWGN variance into the detection process, resulting in a Wiener filter-related weight matrix as evidenced by Equation 4.63 or 4.64. This representation of the weight matrix $\mathbf{W}_{\text{MMSE}}$ is related to the right-inverse of the channel matrix. If the auto-correlation matrix associated with the different antenna elements' AWGN is a scaled unity matrix, then an alternative representation, namely Equation 4.68, can be obtained, which is related to the channel matrix's left-inverse rather than its right-inverse. Depending on the dimensions of the channel transfer factor matrix $\mathbf{H}$ in terms of the L number of users and the P number of reception antenna elements, the left- or right-inverse related form may be preferred in terms of the computational complexity imposed. In the context of these discussions the relation between the MMSE- and MVDR combiner was briefly addressed. Similarly to the LS combiner of Section 4.2.2, the desired signal is recovered with unity gain, while at the same time

suppressing the AWGN, again, based upon knowledge of the different users' SNRs encountered at the reception antennas. Specifically, from Equations 4.78 and 4.82 we recall that both the l-th user's MMSE weight vector $\mathbf{w}_{\text{MMSE}}^{(l)}$ and the MVDR combiner's weight vector $\mathbf{w}_{\text{MV}}^{(l)}$ can be represented as the scaled product of the inverse interference-plus-noise correlation matrix $\mathbf{R}_{a,I+N}^{-1}$ and the desired user's channel vector $\mathbf{H}^{(l)}$. The difference between the two solutions resides in the choice of the scalar factor β, which for the specific case of MMSE detection was given by Equation 4.79, while for MV detection by Equation 4.83. As further argued in Section 4.2.3.4, both solutions exhibit the same SINR, which in turn is identical to that of the maximum SINR combiner [123, 87] not detailed here. The maximum SINR combiner can also be represented in a similar form as Equations 4.79 and 4.83, but with a different value of β. Hence, the Wiener filter-related linear combiners, namely the MMSE, MVDR and maximum SINR combiners maximise the SINR. Furthermore, in Section 4.2.5 the generation of soft-bit information for turbo-decoding was demonstrated.

Our performance assessment with respect to the MSE and SINR at the combiner's output, as well as with respect to the detector's BER was carried out in Section 4.2.6. The curves, which were shown on the left-hand side of Figure 4.6 supported that the MSE at the combiner's output is minimized by the MMSE weight matrix, while a slight MSE degradation was observed for the MVDR weight matrix of Equation 4.81 as a consequence of the requirement to recover the desired user's transmitted signal with a specific gain, which was assumed to be unity in our case. As expected, the worst MSE was exhibited by the LS combiner of Section 4.2.2. In terms of the system's 4QAM-related BER on the right-hand side of Figure 4.6 we observed an identical performance for both Wiener filter related detectors[12], namely for the MMSE and MV detector. Again, as argued in Section 4.2.3.5, their performance was identical, because the different Wiener filter-related detectors achieve the same SINR. However, for the LS detector of Section 4.2.2 a significant performance degradation was also observed in terms of the BER as shown at the right-hand side of Figure 4.6. Our further investigations concentrated on portraying the influence of the relation between the number of users L and the number of reception antennas P on the MMSE detector's SINR and on the associated BER performance. Specifically, from Figures namely, 4.7 and 4.8 we observed that upon decreasing the number of users L, while keeping the number of reception antennas P constant, the PDF of the SINR is shifted towards higher SINRs, while at the same time the system's BER is significantly improved. This is also a motivation for the employment of the successive interference cancellation approach, which will be discussed in Section 4.3.1.

Finally the BER performance of MMSE detection-assisted SDMA-OFDM was analysed in a turbo-coded scenario. The associated BER versus SNR performance curves were portrayed in Figure 4.9. Compared to the uncoded scenario the BER was significantly improved - although at the cost of halving the system's effective throughput. Our estimates of the computational complexity associated with the different linear detectors, namely LS and MMSE were presented in Section 4.2.7.

[12]Recall that the linear detector is constituted by the concatenation of the linear combiner and the classifier.

We found that the computational complexity is of third order, namely $\mathcal{O}(3)$ with respect to the number of users L, upon assuming the weight matrix's representation in its left-inverse related form.

4.3 Non-Linear Detection Techniques

In Section 4.2 the family of linear detection techniques was discussed. These detectors aimed at reducing the potentially excessive M_c^L number of evaluations of the multi-user Euclidean distance metric associated with the optimum ML detector to a significantly lower LM_c number of evaluations of the single-user Euclidean distance metric of Equation 4.94. This implies a substantial complexity reduction. Recall that the variable L represents the number of users supported, while M_c is the number of constellation points for the specific modulation scheme employed. As portrayed in the linear detector's block diagram shown in Figure 4.4, the strategy is first to provide linear estimates of the different users' transmitted signals and then to perform the non-linear classification- or demodulation separately for each user. This philosophy was based on the assumption that the different users' associated linear combiner output signals are corrupted only by the residual AWGN, which is however, only an approximation. In fact the linear combiners' output signals in Figure 4.4 also contain residual interference, which is not Gaussian distributed and hence represents an important source of further information.

Instead of sequentially performing the operations of linear combining and classification- or demodulation as in the linear detector's case of Figure 4.4, a more effective strategy is to embed the demodulation into the process of linear combining, which is known from the family of classic channel equalizers as decision-feedback. As a result, the residual multi-user interference observed at the classifier's inputs is reduced. Hence, the classifier's accuracy due to neglecting the residual interference is less impaired. Two of the most prominent multi-user detection techniques known from CDMA communications, which incorporate these ideas are the SIC and PIC detection techniques. These techniques are also applicable in the context of communicating over flat-fading channels as observed for example on an OFDM subcarrier basis. In the context of our portrayal of SIC detection in Section 4.3.1, apart from discussing various techniques for its improvement, a detailed analysis of the effects of error propagation occurring at the different detection stages will be provided. This error propagation analysis motivated the employment of weighted soft-bit metric assisted turbo-decoding. Furthermore, our discussions on PIC detection will be presented in Section 4.3.2. We will demonstrate that a significant enhancement of the PIC detector's performance can be achieved by embedding turbo-decoding into the PIC detection process, instead of simply serially concatenating the PIC detector with the turbo-decoder. Finally, the optimum ML detector will be analysed in Section 4.3.3.

4.3.1 SIC Detection

The philosophy of the Successive Interference Cancellation (SIC) assisted detector [114, 115, 116, 53, 117, 118, 119, 120, 121, 122] is motivated by two observations. First of all, we note that for a specific subcarrier the MSE and SINR at the output of the LS- or MMSE combiner might substantially differ for the different users, depending on their spatial signatures. Secondly, we recall from our investigations in Section 4.2.6.3 that upon increasing the MIMO system's diversity order, e.g. by decreasing the number of simultaneous users L while keeping the number of reception antennas P constant, the MSE performance of the LS- or MMSE combiner and correspondingly the system's BER performance is improved as a consequence of assigning a higher grade of diversity to mitigate the effects of fading. This was illustrated in Figure 4.8. Hence, an attractive strategy, which has recently drawn wide interests is to detect only the specific user having the highest SINR, SIR or SNR in each iteration at the output of the LS- or MMSE combiner. Having detected this user's signal, the corresponding remodulated signal is subtracted from the composite signal received by the different antenna elements. Furthermore, the channel transfer factor matrix - and the SNR matrix formulated in the context of the MMSE combiner characterized by Equation 4.68 in its left-inverse related form - are updated accordingly.

The further structure of this section is as follows. In Section 4.3.1.1 the standard SIC algorithm is portrayed, which allows only the most likely symbol decision to be retained in each detection stage. This section also includes a detailed analysis of the effects of error propagation, which occurs across the different detection stages. By contrast, in Section 4.3.1.2 M-SIC and its derivatives are discussed, where potentially the M most likely tentative symbol decisions are retained at each detection node of the detection process - as it will be further explained in Section 4.3.1.2.1 - rather than retaining only the most likely symbol decision. Note that each node is associated with a specific appropriately updated array output vector of the SIC-aided detection process. Furthermore, in Section 4.3.1.3 the various techniques of soft-bit generation will be discussed and a weighted soft-bit metric will be proposed for employment in turbo-decoding, which is capable of substantially enhancing the performance of turbo-coded SIC detection-assisted SDMA-OFDM systems. Finally, a detailed performance analysis of the standard SIC and that of the M-SIC is offered in terms of the associated system's BER and SER performance both in the context of uncoded and turbo-coded scenarios in Section 4.3.1.4. The complexity of the different detection schemes will be analysed in Section 4.3.1.5. Finally, the summary of Section 4.3.1 will be offered in Section 4.3.1.6 along with our conclusions.

4.3.1.1 Standard SIC

From now on we assume that the MMSE combiner in its specific left-inverse related form as given by Equation 4.68 is assumed to be employed for performing the detection of the most dominant

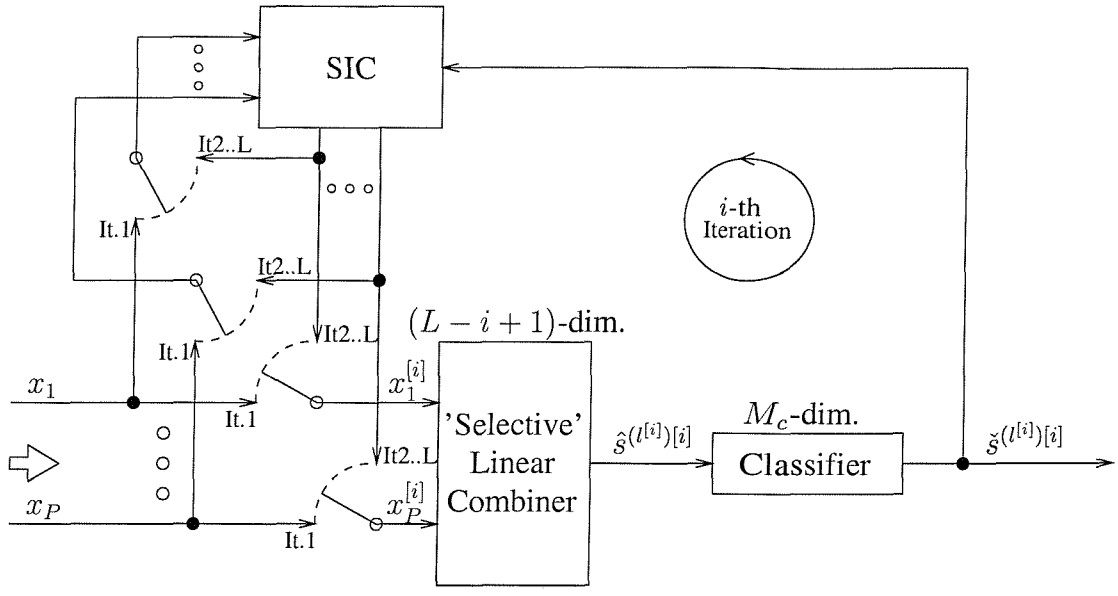

Figure 4.10: Illustration of the main signal paths associated with the standard SIC detector. During the first iteration the signals $x_p, p = 1, \ldots, P$ received by the different antenna elements are directly fed into the 'selective' linear combiner, where we have $\mathbf{x}^{[1]} = \mathbf{x}$ at the detection stage or iteration of $i = 1$. The task of the 'selective' linear combiner is to identify the most dominant remaining user in terms of its SINR at the combiner output - from the set of $(L - i + 1)$ remaining users during the i-th detection stage or iteration - and to provide its signal estimate $\hat{s}^{(l^{[i]})[i]}$ at the combiner's output. This is described by Equations 4.123 and 4.124. The selected $l^{[i]}$-th user's linear signal estimate $\hat{s}^{(l^{[i]})[i]}$ is then classified- or demodulated according to Equation 4.125, yielding the amplified constellation point $\check{s}^{(l^{[i]})[i]}$ that is most likely to have been transmitted by the $l^{[i]}$-th user. Now the corresponding modulated signal can be regenerated. The influence of the $l^{[i]}$-th user's modulated signal is then removed from the vector $\mathbf{x}^{[1]}$ of signals received by the different antenna elements with the aid of the SIC module. This cancellation operation is described by Equation 4.127. The first iteration $(i = 1)$ is deemed to have been completed, when the decontaminated signal appears at the output of the SIC stage. Hence, beginning with the second SIC iteration the 'selective' linear combiner's input, namely the 'decontaminated' vector $\mathbf{x}^{[i]}$ of signals received by the different antenna elements, which contains only the influence of the $(L-i+1)$ remaining users, is constituted by the output of the SIC module, provided that correct symbol decisions were conducted in the previous detection stages. Note that for the sake of visual clarity here we have omitted the signal paths associated with the channel transfer factor estimates required by the linear combiner and by the SIC module. The role of the switches is to indicate that at the first detection stage the SIC is directly fed with the signals received by the different array elements, while during the remaining iterations of $i = 2, \ldots, L$ with the partially 'decontaminated' composite signal of the remaining $(L - i + 1)$ users.

user in each cancellation stage. For the reader's convenience we have repeated here the formula describing the combiner's operation from Equation 4.70:

$$\mathbf{R}_{\overline{a}}^{H}\mathbf{W}_{\text{MMSE}}^{H} = \mathbf{R}_{c}^{H} \quad \Longleftrightarrow \quad \mathbf{W}_{\text{MMSE}}^{H} = \mathbf{R}_{\overline{a}}^{H-1}\mathbf{R}_{c}^{H}, \tag{4.118}$$

where the received signals' auto-correlation matrix $\mathbf{R}_{\overline{a}}$ was defined in Equation 4.69 as:

$$\mathbf{R}_{\overline{a}} = \mathbf{H}^{H}\mathbf{H}\mathbf{P} + \sigma_n^2\mathbf{I}, \tag{4.119}$$

while the cross-correlation matrix of the transmitted and received signals was given in Equation 4.54 namely:

$$\mathbf{R}_{c} = \mathbf{H}\mathbf{P}. \tag{4.120}$$

It is computationally efficient to refrain from recalculating the correlation matrix $\mathbf{R}_{\overline{a}}$ of Equation 4.119 and the cross-correlation matrix $\mathbf{R}_c$ of Equation 4.120 at each cancellation stage. This complexity reduction can be achieved by updating these matrices based on the specific index of the most recently detected user. Nonetheless, these matrices have to be calculated once at the beginning of the SIC detection procedure. The more detailed structure of the SIC detector will be portrayed below.

1. *Initialization*: Initialize the detector upon setting $\mathbf{x}^{[1]} = \mathbf{x} \in \mathbb{C}^{P\times 1}$, as well as upon evaluating $\mathbf{R}_{\overline{a}}^{[1]H} = \mathbf{P}\mathbf{H}^{H}\mathbf{H} + \sigma_n^2\mathbf{I}$ and $\mathbf{R}_{c}^{[1]H} = \mathbf{P}\mathbf{H}^{H}$. Here the index in the superscript, namely $()^{[i]}$ indicates the detection stage index, which is initially set to $i = 1$.

2. *i-th Detection Stage*: At the beginning of the i-th SIC detection stage, given correct symbol decisions in the previous detection stages, the updated vector $\mathbf{x}^{[i]}$ of received signals only contains the remaining $L^{[i]} = L - i + 1$ users' signal contributions plus the AWGN since the remodulated signals of the previously detected $(i-1)$ users have been deducted from the originally received composite signal of $\mathbf{x}$. Furthermore, the dimension of the auto-correlation matrix $\mathbf{R}_{\overline{a}}^{[i]H}$ - represented here in its Hermitian transposed form - has been reduced to $\mathbf{R}_{\overline{a}}^{[i]H} \in \mathbb{C}^{L^{[i]}\times L^{[i]}}$, while the dimension of the cross-correlation matrix $\mathbf{R}_{c}^{[1]H}$ also represented in its Hermitian transposed form has been reduced to $\mathbf{R}_{c}^{[i]H} \in \mathbb{C}^{L^{[i]}\times P}$ upon removing the previously cancelled users' associated entries. This matrix dimension reduction potentially facilitates the reduction of the system's overall complexity. Then the specific steps at the i-th detection stage are as follows:

   - *Calculation of the Remaining Users' Weight Matrix*: Generate the $L^{[i]}$ number of remaining users' associated weight matrix upon invoking the MMSE approach, which is represented in its left-inverse related form by:

$$\mathbf{R}_{\overline{a}}^{[i]H}\mathbf{W}_{\text{MMSE}}^{[i]H} = \mathbf{R}_{c}^{[i]H} \quad \Longleftrightarrow \quad \mathbf{W}_{\text{MMSE}}^{[i]H} = \mathbf{R}_{\overline{a}}^{[i]H-1}\mathbf{R}_{c}^{[i]H}. \tag{4.121}$$

Observe in Equation 4.121 that in contrast to Equation 4.119 and 4.120 we have substituted the matrices $\mathbf{R}_a^H$ and $\mathbf{R}_c^H$ by their reduced-dimensional counterparts associated with the i-th detection stage, namely by $\mathbf{R}_a^{[i]H}$ and $\mathbf{R}_c^{[i]H}$. The set of $L^{[i]}$ number of remaining users at the i-th detection stage is denoted here by $\mathcal{L}^{[i]}$.

- *Selection of the Most Dominant User*: Calculate the objective function, which could be the SINR, SIR or SNR at the MMSE combiner's output according to Equations 4.24, 4.25 or 4.26, respectively employing the different users' weight vectors. As an example, here we employ the SNR of Equation 4.26, since its calculation is significantly less complex than that of the SINR or SIR given by Equations 4.25 and 4.26. Based on Equation 4.26, the l-th user's associated SNR at the MMSE combiner's output during the i-th detection stage is given by:

$$\text{SNR}^{(l)[i]} = \frac{\mathbf{w}^{(l)[i]H}\mathbf{R}_{a,S}^{(l)}\mathbf{w}^{(l)[i]}}{\mathbf{w}^{(l)[i]H}\mathbf{R}_{a,N}\mathbf{w}^{(l)[i]}}, \tag{4.122}$$

  where the auto-correlation matrix $\mathbf{R}_{a,S}^{(l)}$ of the l-th user's channel transfer factors was defined in Equation 4.16, while the noise correlation matrix $\mathbf{R}_{a,N}$ recorded in case of encountering uncorrelated AWGN at the different reception antenna elements of the BS was given in Equation 4.22. Furthermore, the l-th user's weight vector $\mathbf{w}^{(l)[i]}$ is given here in form of the corresponding column vector of the weight matrix $\mathbf{W}_{\text{MMSE}}^{[i]}$, which has been obtained upon solving Equation 4.121.

  The selection of the most dominant user, which is assumed here to be the $l^{[i]}$-th user, can then be expressed as:

$$l^{[i]} = \underset{l \in \mathcal{L}^{[i]}}{argmax}(\text{SNR}^{(l)[i]}). \tag{4.123}$$

- *Detection of the Most Dominant User*: Under the assumption that the $l^{[i]}$-th user has been found to be the most dominant one among the $L^{[i]}$ remaining users at the i-th detection stage, detect the user's transmitted signal upon invoking Equation 4.8, namely:

$$\hat{\mathbf{s}}^{(l^{[i]})[i]} = \mathbf{w}^{(l^{[i]})[i]H}\mathbf{x}^{[i]}. \tag{4.124}$$

- *Demodulation of the Most Dominant User*: Carry out the demodulation by mapping the detected signal $\hat{\mathbf{s}}^{(l^{[i]})[i]}$[13] to one of the M_c number of constellation points contained in the set $\mathcal{M}_c$ associated with a particular modulation scheme. As shown in Equation 4.94, this involves minimizing the Euclidean distance metric, namely:

$$\check{\mathbf{s}}^{(l^{[i]})[i]} = arg \min_{\check{\mathbf{s}}/\sigma_{l^{[i]}} \in \mathcal{M}_c} \left| \frac{1}{H_{\text{eff}}^{(l^{[i]})[i]}} \hat{\mathbf{s}}^{(l^{[i]})[i]} - \check{\mathbf{s}} \right|^2, \tag{4.125}$$

[13]Note that while the superscript in round brackets denotes the user index, the superscript in squared brackets denotes the detection stage or iteration index.

where the detected user's transfer factor $H_{\text{eff}}^{(l^{[i]})[i]}$ is given by:

$$H_{\text{eff}}^{(l^{[i]})[i]} = \mathbf{w}^{(l^{[i]})[i]H}\mathbf{H}^{(l^{[i]})}. \tag{4.126}$$

Note however that for MPSK modulation schemes the normalization to $H_{\text{eff}}^{(l^{[i]})[i]}$ is not necessary, because the information transmitted is incorporated into the signal's phase. Furthermore, in the context of Equation 4.125 the variance of the $l^{[i]}$-th user's M_c number of legitimate trial symbols is given by $\sigma_{l^{[i]}}^2$. Alternatively the MMSE combiner's output signal $\hat{\mathbf{s}}^{(l^{[i]})[i]}$ can be normalized by $\sigma_{l^{[i]}} = \sqrt{\sigma_{l^{[i]}}^2}$ instead of amplifying the individual constellation points contained in the set $\mathcal{M}_c$.

- *Detector Update by Removing the Most Dominant User's Contribution*: Based on the demodulated signal $\check{\mathbf{s}}^{(l^{[i]})[i]}$, the $l^{[i]}$-th user's remodulated contribution is removed from the current vector of composite received signals, yielding:

$$\mathbf{x}^{[i+1]} = \mathbf{x}^{[i]} - \mathbf{H}^{(l^{[i]})}\check{\mathbf{s}}^{(l^{[i]})[i]}. \tag{4.127}$$

Furthermore, the influence of the $l^{[i]}$-th user's associated channel transfer factor vector $\mathbf{H}^{(l^{[i]})}$ is eliminated from the auto-correlation matrix $\mathbf{R}_a^{[i]H}$, yielding the reduced-dimensional matrix of:

$$\mathbf{R}_a^{[i]H} \longrightarrow \mathbf{R}_a^{[i+1]H} \in \mathbb{C}^{(L^{[i]}-1)\times(L^{[i]}-1)}, \tag{4.128}$$

as well as from the cross-correlation matrix $\mathbf{R}_c^{[i]H}$, yielding the reduced-dimensional matrix of:

$$\mathbf{R}_c^{[i]H} \longrightarrow \mathbf{R}_c^{[i+1]H} \in \mathbb{C}^{(L^{[i]}-1)\times P}. \tag{4.129}$$

More specifically, this is achieved by removing the $\acute{l}^{[i]}$-th row and column from the matrix $\mathbf{R}_a^{[i]H}$ as well as by eliminating the $\acute{l}^{[i]}$-th row from the matrix $\mathbf{R}_c^{[i]H}$, where the index $\acute{l}^{[i]}$ denotes the position of the column vector $\mathbf{H}^{(l^{[i]})}$ in the hypothetic reduced-size channel transfer factor matrix $\mathbf{H}^{[i]}$, which is associated with the i-th detection stage.

3. Commence the $(i+1)$-th iteration by returning to Step (2). Iterate, until all the L users have been detected.

We have summarized the standard SIC algorithm once again in Table 4.5. Furthermore, a simplified block diagram of the SIC detector was portrayed in Figure 4.10. Note that here we have omitted the signal paths associated with supplying of the channel transfer factor estimates to the linear combiner and to the SIC module. In the next section a higher-complexity strategy is proposed for further enhancing the standard SIC detector's performance.

Description	Instruction
Initialization	$\mathbf{x}^{[1]} = \mathbf{x}$; $\mathbf{R}_{\bar{a}}^{[1]H} = \mathbf{P}\mathbf{H}^H\mathbf{H} + \sigma_n^2\mathbf{I}$; $\mathbf{R}_c^{[1]H} = \mathbf{P}\mathbf{H}^H$; $L^{[1]} = L$
i-th iteration:	
Weight calc.	$\mathbf{R}_{\bar{a}}^{[i]H}\mathbf{W}_{\text{MMSE}}^{[i]H} = \mathbf{R}_c^{[i]H} \iff \mathbf{W}_{\text{MMSE}}^{[i]H} = \mathbf{R}_{\bar{a}}^{[i]H-1}\mathbf{R}_c^{[i]H}$
Selection	$\text{SNR}^{(l)[i]} = \frac{\mathbf{w}^{(l)[i]H}\mathbf{R}_{a,S}^{(l)}\mathbf{w}^{(l)[i]}}{\mathbf{w}^{(l)[i]H}\mathbf{R}_{a,N}\mathbf{w}^{(l)[i]}}$, $l \in \mathcal{L}^{[i]}$, $l^{[i]} = \underset{l\in\mathcal{L}^{[i]}}{argmax}(\text{SNR}^{(l)[i]})$
Combining	$\hat{\mathbf{s}}^{(l^{[i]})[i]} = \mathbf{w}^{(l^{[i]})[i]H}\mathbf{x}^{[i]}$
Demodulation	$\check{\mathbf{s}}^{(l^{[i]})[i]} = arg \underset{\check{\mathbf{s}}/\sigma_{l^{[i]}}\in\mathcal{M}_c}{min} \left\| \frac{1}{H_{\text{eff}}^{(l^{[i]})[i]}}\hat{\mathbf{s}}^{(l^{[i]})[i]} - \check{\mathbf{s}} \right\|^2$, $H_{\text{eff}}^{(l^{[i]})[i]} = \mathbf{w}^{(l^{[i]})[i]H}\mathbf{H}^{(l^{[i]})}$
Updating	$\mathbf{x}^{[i+1]} = \mathbf{x}^{[i]} - \mathbf{H}^{(l^{[i]})}\check{\mathbf{s}}^{(l^{[i]})[i]}$
	$\mathbf{R}_{\bar{a}}^{[i]H} \longrightarrow \mathbf{R}_{\bar{a}}^{[i+1]H} \in \mathbb{C}^{(L^{[i]}-1)\times(L^{[i]}-1)}$
	$\mathbf{R}_c^{[i]H} \longrightarrow \mathbf{R}_c^{[i+1]H} \in \mathbb{C}^{(L^{[i]}-1)\times P}$
	$L^{[i+1]} = L^{[i]} - 1$
Return	Start $(i+1)$-th iteration

Table 4.5: Summary of the standard SIC detector's operation in the context of employing MMSE combining and the SNR as an objective funtion for the selection of the most dominant user at each detection stage.

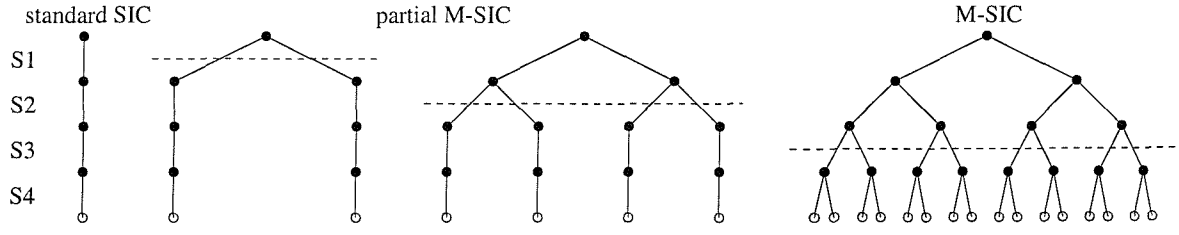

Figure 4.11: Illustration of the (left:) standard SIC, (middle:) partial M-SIC retaining multiple branches per detection node up to the first- and second detection stage, (right:) M-SIC with multiple tentative symbol decisions per detection node at all detection stages; here we have assumed that $M = 2$; in the graph each *detection node* represents an updated vector of signals received by the different antenna elements, for which also the linear combining - but not the array weight calculation has to be performed separately; furthermore, each *branch* represents a tentative symbol decision made at a given detection stage.

4.3.1.2 M-SIC and its Derivatives

As we will highlight in Section 4.3.1.4, the standard SIC detector's performance is impaired as a result of the error-propagation occuring between the different consecutive detection stages. Hence efficient countermeasures capable of significantly reducing these effects will be the topic of this section. Specifically in Section 4.3.1.2.1 M-SIC will be investigated, while partial M-SIC in Section 4.3.1.2.2 and Selective Decision Insertion (SDI) M-SIC in Section 4.3.1.2.3.

4.3.1.2.1 M-SIC A viable strategy of reducing the error propagation effects is to track from each detection stage not only the single most likely symbol decision, but an increased number of $M \leq M_c$ most likely tentative symbol decisions, where M_c denotes the number of constellation points associated with a specific modulation scheme. To provide an example, for $M = 2$ in the first detection stage we have a total of $M = 2$ possible symbol decisions, while in the second detection stage $M^2 = 4$ tentative symbol decisions and correspondingly, in the i-th detection stage we encounter M^i possible tentative symbol decisions. Following our description of the standard SIC detector in Table 4.5, associated with each tentative symbol decision there is a specific updated vector of signals, generated by cancelling the effects of the most dominant $L-i+1$ number of users from the P-dimensional vector of signals received by the P number of different antenna elements. Hence, in the following detection stage the MMSE combining has to be performed separately for the different updated P-dimensional vectors of received signals. Correspondingly, the number of parallel tentative symbol decisions to be tracked is increased by the factor of M compared to that of the current detection stage. This process can conveniently be portrayed with the aid of a tree-structure, as shown at the right-hand side of Figure 4.11, where again, we have assumed that $M = 2$ was used. Specifically, each detection node represents an updated P-dimensional vector of signals received by the P different antenna elements, while the branches are associated with the various tentative symbol decisions at the $i = 1, \ldots, L$ detection stages. Note that the first detection node at the top of the figure is associated with the original P-dimensional vector of signals received by the different antenna elements. In the final detection stage, after the subtraction of the least dominant user's estimated P-dimensional signal contribution, a decision must be made concerning which specific combination of L number of symbols - represented by the branches connecting the different detection nodes - has most likely been transmitted by the L different users in the specific subcarrier considered. A suitable criterion for performing this decision is given by the Euclidean distance between the original P-dimensional vector of signals received by the P different antenna elements and the estimated P-dimensional vector of received signals based on the tentative symbol decisions and upon taking into account the effects of the channel. The same decision metric is employed also by the ML detector, which will be discussed in Section 4.3.3. Note furthermore, that this distance measure is identical to the Euclidean norm of the P-dimensional vector of residual

signals after the subtraction of the last detected user's P-dimensional signal contribution vector.

The performance improvement potentially observed for the M-SIC scheme compared to the standard SIC arrangement is achieved at the cost of a significantly increased computational complexity. This is since the number of parallel tentative symbol decisions associated with a specific detection stage is a factor of M higher than that of the previous detection stage, and hence in the last detection stage we potentially have to consider M^L number of different tentative symbol decisions. Again, this implies that the approach of the M-SIC scheme resembles that of the ML detector to be discussed in Section 4.3.3.

4.3.1.2.2 Partial M-SIC A viable approach of further reducing the associated computational complexity is motivated by the observation that for sufficiently high SNRs the standard SIC detector's performance is predetermined by the bit- or symbol-error probabilities incurred during the first detection stage. This is, because if the most dominant user's associated symbol decision is erroneous, its effects potentially propagate to all other users' decisions conducted in the following detection stages. Furthermore, as observed previously in the context of our investigations of the MMSE detector's performance in Section 4.2.6.3 as a function of the number of simultaneous users L and the number of reception antennas P the highest performance gain in terms of the achievable SNR reduction at the reception antennas, whilst maintaining a specific BER is observed upon removing the first user from a fully loaded system. An example of such a fully loaded system is that supporting four simultaneous users with the aid of four reception antennas. Hence we conclude that the symbol error probability specifically of the first detection stage should be as low as possible, while the tentative symbol decisions carried out at later detection stages become automatically more reliable as a result of the system's increased diversity order due to removing the previously detected users.

Hence, our suggestion is to retain $M > 1$ number of tentative symbol decisions at each detection node, characterized by its associated updated P-dimensional vector of received signals only up to the specific $L_{\text{pM-SIC}}$-th stage in the detection process. By contrast, at later detection stages only one symbol decision is retained at each detection node, as in the standard SIC scheme. This philosophy is further highlighted with the aid of the two graphs at the centre of Figure 4.11. Specifically, in the illustration second from the left of Figure 4.11 we have portrayed the case of retaining two tentative symbol decisions per detection node only in the first detection stage, while in the illustration second from the right-hand side of Figure 4.11 two tentative symbol decisions per detection node are retained in both of the first two detection stages.

4.3.1.2.3 Selective-Decision-Insertion Aided M-SIC In order to even further reduce the computational complexity an improved strategy termed Selective-Decision-Insertion (SDI) can be applied, which was initially proposed in [53, 117]. The philosophy of the SDI technique is that of

tracking additional tentative symbol decisions only in those $N_{\text{SDI}}^{[1]}$ number of subcarriers, which exhibit the lowest SINR during the first detection stage, since these are most likely to cause symbol errors.

4.3.1.3 Generation of Soft-Bit Information for Turbo-Decoding

In Section 4.2.5 we elaborated on the process of soft-bit generation supporting the employment of turbo-decoding in the context of linear detection techniques, such as the LS and MMSE schemes. Specifically, we capitalized on the assumption that the residual interference at the combiner's output is Gaussian, which enabled us to employ the same strategies for generating the soft-bit values, as in a single-user scenario. In Section 4.3.1.3.1 we will demonstrate that the soft-bit generation process designed for the non-linear SIC detector can be based on that of the linear detection schemes, although, as shown in Section 4.3.1.3.2 a further performance enhancement can be achieved upon accounting for the effects of error propagation, which occur through the different detection stages, as it will be demonstrated in Section 4.3.1.4.2.

4.3.1.3.1 Generation of Rudimentary Soft-Bits As it was highlighted in Section 4.3.1.1, at each stage of the standard SIC-related detection process we generate estimates of the remaining users' transmitted signals with the aid of a linear combiner. Hence, a feasible approach employed for generating soft-bit values is to invoke the linear combiner's output signals of the most dominant user as it was demonstrated in Section 4.2.5. More specifically, the $l^{[i]}$-th user's soft-bit values - where the superscript i in $()^{[i]}$ indicates that this particular user was found to be the most dominant remaining user during the i-th detection stage - can be generated upon invoking the associated combiner output signal $x_{\text{eff}}^{(l^{[i]})[i]} = \hat{s}^{(l^{[i]})[i]}$ defined in the context of Equation 4.95 namely:

$$L_{m\approx}^{(l^{[i]})[i]} = \ln \frac{P(b_m^{(l^{[i]})[i]} = 1 | x_{\text{eff}}^{(l^{[i]})[i]}, H_{\text{eff}}^{(l^{[i]})[i]})}{P(b_m^{(l^{[i]})[i]} = 0 | x_{\text{eff}}^{(l^{[i]})[i]}, H_{\text{eff}}^{(l^{[i]})[i]})}, \tag{4.130}$$

where $H_{\text{eff}}^{(l^{[i]})[i]} = \mathbf{w}^{(l^{[i]})[i]H}\mathbf{H}^{(l^{[i]})[i]}$, as given by Equation 4.126 is the l-th detected user's effective channel transfer factor.

However, generating the soft-bit values of the $l^{[i]}$-th user - whose associated signal is linearly detected during the i-th detection stage - with the aid of Equation 4.130 inherently assumes that the signal components of those users, which have already been detected and demodulated during the previous SIC detection stages, have been correctly removed from the P-dimensional vector $\mathbf{x}^{[1]} = \mathbf{x}$ of signals received by the P different antenna elements for the successful employment of this principle. A necessary condition is that the associated symbol decisions were free of errors, namely that we had $s^{(l^{[j]})[j]} = \check{s}^{(l^{[j]})[j]}$, $j = 1, \ldots, i-1$. Naturally, this assumption only holds with a certain probability. In the sequel our aim will be to estimate this probability and draw our further conclusions.

4.3.1.3.2 Generation of Weighted Soft-Bits To elaborate a little further, during the first detection stage the probability that the $l^{[1]}$-th user, which was found to be the most dominant one, has been correctly demodulated is given by the *a posteriori* probability of $P(\check{s}^{(l^{[1]})[1]}|x_{\text{eff}}^{(l^{[1]})[1]}, H_{\text{eff}}^{(l^{[1]})[1]})$. Hence, by contrast during the second detection stage the probability that the $l^{[2]}$-th user, which was found to be the most dominant one among the $L-1$ remaining users, has been correctly demodulated is given by the *a posteriori* probability of $P(\check{s}^{(l^{[2]})[2]}|x_{\text{eff}}^{(l^{[2]})[2]}, H_{\text{eff}}^{(l^{[2]})[2]})$, conditioned on a correct symbol decision during the first detection stage.

Furthermore, since we have $P(x_{\text{eff}}^{(l^{[2]})[2]}|x_{\text{eff}}^{(l^{[1]})[1]}) = P(s^{(l^{[1]})[1]}|x_{\text{eff}}^{(l^{[1]})[1]})$, where we have exploited that $P(H_{\text{eff}}^{(l^{[1]})[1]}) = P(H_{\text{eff}}^{(l^{[2]})[2]}) = 1$, we obtain an estimate for the probability of the joint event that $\check{s}^{(l^{[1]})[1]}$ and $\check{s}^{(l^{[2]})[2]}$ are the correct symbol decisions at the first and second detection stages, respectively, which can be expressed as:

$$P(\check{s}^{(l^{[2]})[2]}, \check{s}^{(l^{[1]})[1]}|x_{\text{eff}}^{(l^{[1]})[1]}) = P(\check{s}^{(l^{[2]})[2]}|x_{\text{eff}}^{(l^{[2]})[2]})P(\check{s}^{(l^{[1]})[1]}|x_{\text{eff}}^{(l^{[1]})[1]}). \tag{4.131}$$

More generally, for the demodulated symbols of the first $(i-1)$ number of detection stages we have the joint probability:

$$P_{\text{joint}}^{[i-1]} = P(\check{s}^{(l^{[i-1]})[i-1]}, \ldots, \check{s}^{(l^{[1]})[1]}|x_{\text{eff}}^{(l^{[1]})[1]}) = \prod_{j=1}^{i-1} P(\check{s}^{(l^{[j]})[j]}|x_{\text{eff}}^{(l^{[j]})[j]}). \tag{4.132}$$

Note however that this is only an estimate of the true joint probability, since for a finite number of users the residual interference at a specific stage's combiner output is potentially non-Gaussian, which is particularly the case, if an error has occurred in one of the detection stages.

The estimated joint probability $P_{\text{joint}}^{[i-1]}$ of correct symbol decisions during the first $(i-1)$ number of detection stages, which was given by Equation 4.132, can be invoked as a measure of confidence for the soft-bit values generated during the i-th detection stage. Specifically, it is expected that if an error has occurred during one of the detection stages, then the soft-bit values produced with the aid of Equation 4.130 for the following detection stages will be relatively unreliable. Hence, a viable approach of mitigating these effects is the employment of weighting, namely by weighting of the *a posteriori* probabilities that a bit having a polarity of $b \in \{0, 1\}$ has been transmitted, as seen in the numerator and denominator of Equation 4.130, yielding:

$$L_{m\approx}^{(l^{[i]})[i]}|_{\text{weight}} = \ln \frac{P(b_m^{(l^{[i]})[i]} = 1|x_{\text{eff}}^{(l^{[i]})[i]}, H_{\text{eff}}^{(l^{[i]})[i]}) \cdot P_{\text{joint}}^{[i-1]} + \frac{1}{2}(1 - P_{\text{joint}}^{[i-1]})}{P(b_m^{(l^{[i]})[i]} = 0|x_{\text{eff}}^{(l^{[i]})[i]}, H_{\text{eff}}^{(l^{[i]})[i]}) \cdot P_{\text{joint}}^{[i-1]} + \frac{1}{2}(1 - P_{\text{joint}}^{[i-1]})}. \tag{4.133}$$

We observe that if $P_{\text{joint}}^{[i-1]}$ approaches unity, which reflects a high confidence in having no symbol errors during the previous $(i-1)$ number of detection stages, then the expression of Equation 4.133 transforms into that of Equation 4.130, which was based on the assumption of benefitting from the perfect removal of the previously detected users' signal contributions. By contrast, if $P_{\text{joint}}^{[i-1]}$ tends towards zero, which indicates a high probability of encountering symbol errors in the SIC process,

then the bit probabilities $P(b_m^{(l^{[i]})[i]}|x_{\text{eff}}^{(l^{[i]})[i]}, H_{\text{eff}}^{(l^{[i]})[i]})$, $b_m^{(l^{[i]})[i]} \in \{0,1\}$ are potentially unreliable and hence should be de-weighted. This has the effect that the L-value in Equation 4.133 tends to zero.

The advantage of weighted soft-bits will be demonstrated in the context of our investigations on turbo-coded SIC schemes in Section 4.3.1.4.7.

4.3.1.4 Performance Analysis

In this section the standard SIC algorithm and its derivative, namely the M-SIC scheme will be investigated in terms of their achievable Bit Error-Ratio (BER) and Symbol Error-Ratio (SER)[14] performance. Again, the frame-invariant fading indoor WATM channel model and its associated OFDM system model described in Section 6.1.1 were invoked and ideal knowledge of the channel transfer functions associated with the different transmit-receive antenna pairs was assumed. The aim of stipulating a frame-invariant fading channel was that of avoiding the obfuscating effects of Inter-subCarrier Interference (ICI). Note that as a result of this assumption in the uncoded scenario the different detectors' BER and SER performance curves are independent from the indoor SWATM channel's specific multipath intensity profile. For a summary of the basic simulation setup we refer to Table 4.3.

The structure of Section 4.3.1.4 is as follows. In Section 4.3.1.4.1 standard SIC and M-SIC are characterized in terms of their BER and SER performance for different numbers of communicating users and receiver antennas. Furthermore, in an effort to illustrate the effects of error-propagation across the different detection stages, in Section 4.3.1.4.2 more detailed investigations are conducted with respect to the associated system's SER performance, which is evaluated on a detection stage-by-stage basis. These investigations are further extended in Section 4.3.1.4.3 to the scenario, where an error-free remodulated reference signal is employed in the context of updating the vector of signals received by the different antenna elements in each detection stage. In order to further augment our understanding of the effects of error-propagation, in Section 4.3.1.4.4 the detection stages' symbol-error event probabilities are analysed. More specifically, each error-event is captured as the unique combination of the presence of a symbol error ("1") - or the absence of a symbol error ("0") at the different detection stages. Furthermore, in Section 4.3.1.4.5 the SER performance of the partial M-SIC scheme is analysed with respect to the detection stage $L_{\text{pM-SIC}}$ up to which the M most likely symbol decisions are retained at each detection node of the detection process. Finally, in Section 4.3.1.4.6 the technique of SDI-M-SIC is characterized briefly. Explicitly we will quantify the effect of the $N_{\text{SDI}}^{[1]}$ number of subcarriers for which $M = 2$ tentative symbol decisions are made during the first SIC detection stage. Our performance assessments will be concluded in Section 4.3.1.4.7 with the analysis of turbo-decoded, standard SIC detection-assisted SDMA-OFDM systems.

[14]Note that here we refer to the symbol transmitted on an OFDM subcarrier basis.

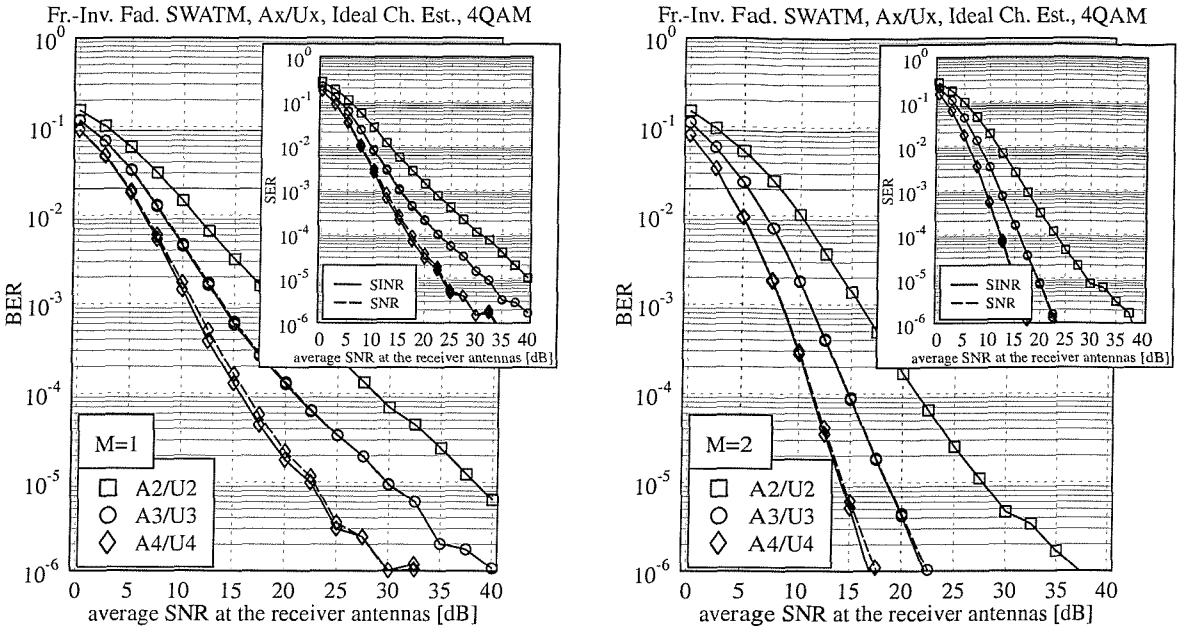

Figure 4.12: BER and SER performance of 4QAM-modulated (left:) standard SIC and (right:) M-SIC ($M = 2$) detection-assisted SDMA-OFDM as a function of the SNR recorded at the reception antennas and parameterized for the different system configurations in terms of the number of users L and the number of reception antennas P; two different measures, namely the SINR and the SNR at the combiner's output were employed for performing the selection of the most dominant user at each detection stage; for the basic simulation parameters we refer to Table 4.3.

4.3.1.4.1 BER and SER Performance of Standard SIC and M-SIC for Different Numbers of Users and Receiver Antennas In Figure 4.12 we have portrayed the BER- as well as the SER performance as a function of the SNR at the reception antennas. Specifically, at the left-hand side of Figure 4.12 we characterized the standard SIC, while at the right-hand side of Figure 4.12 the M-SIC scheme. The results of Figure 4.12 are also parameterized for the different configurations by the number of users L and by the number of reception antennas P, which were assumed here to be identical. Furthermore, both the SINR as well as the SNR recorded at the MMSE combiner's output are considered as potential alternatives for performing the selection of the most dominant user at each detection stage.

For both detectors, namely for the standard SIC and for the M-SIC scheme the general trend is that by increasing the MIMO system's order upon employing for example four reception antennas for supporting four simultaneous users (A4/U4) instead of two reception antennas for supporting two simultaneous users (A2/U2), the system's performance evaluated in terms of the achievable BER

and SER is significantly improved. This is, because in the context of encountering correct symbol decisions at the different stages of the detection process, the associated MIMO system's diversity order, namely the ratio between the number of transmit- and receive antennas, is increased. As argued in Sections 4.2.6.2 and 4.2.6.3, this has the effect of providing a higher degree of freedom at the MMSE combiner of each detection stage for adjusting the reception antennas' weights, which results in a more efficient suppression of the AWGN. Furthermore, for a MIMO system having a higher order, at a specific detection stage there is also the choice between a larger number of users to be selected as the most dominant user to be detected next, which also implies additional diversity. We also observe in Figure 4.12 that compared to standard SIC the M-SIC scheme retaining $M = 2$ tentative 4QAM symbol decisions out of the $M_c = 4$ legitimate symbols exhibits a significant performance advantage, which is achieved at the cost of an increased computational complexity. Hence, potential complexity reduction strategies, namely partial M-SIC and SDI-M-SIC will be characterized in Section 4.3.1.4.5 and 4.3.1.4.6.

With respect to the different objective measures, namely the SNR and SINR, employed for performing the selection of the most dominant user at each stage of the detection process a slight advantage is observed in favour of the SINR measure, although only for the system configurations of a higher order. In the context of these configurations the residual interference was apparently higher than for the system configurations supporting a lower number of users. In the next section we will focus our attention further on the effects of error propagation between the different detection stages.

4.3.1.4.2 SER Performance of Standard SIC and M-SIC on a Per-Detection Stage Basis In this section we will further investigate the effects of error propagation across the different detection stages. Hence at the left-hand side of Figure 4.13 we have portrayed the SER associated with the different detection stages for standard SIC, while at the right-hand side of Figure 4.13 for the M-SIC scheme. In the context of the simulation results presented in each of the larger graphs the SINR was invoked as the metric used for performing the selection of the most dominant user at each stage of the detection process. By contrast, in the smaller-sized sub-graphs of Figure 4.13, we have compared the SINR and SNR criteria against each other, at the first detection stage.

More specifically, for the standard SIC we observe at the left-hand side of Figure 4.13 that upon traversing through the different detection stages the SER is significantly increased at lower SNRs, while at higher SNRs the different detection stages' SERs become virtually identical. As it will be supported by our forthcoming analysis of the standard SIC detector's SER recorded in the context of an error-free reference signal, a viable explanation of this phenomenon is that the majority of symbol errors caused by the early detection stages propagates to the later stages. In other words, only a comparably small additional error contribution is caused by the later detection stages, which is a consequence of the increased diversity order associated with the gradually decreasing number

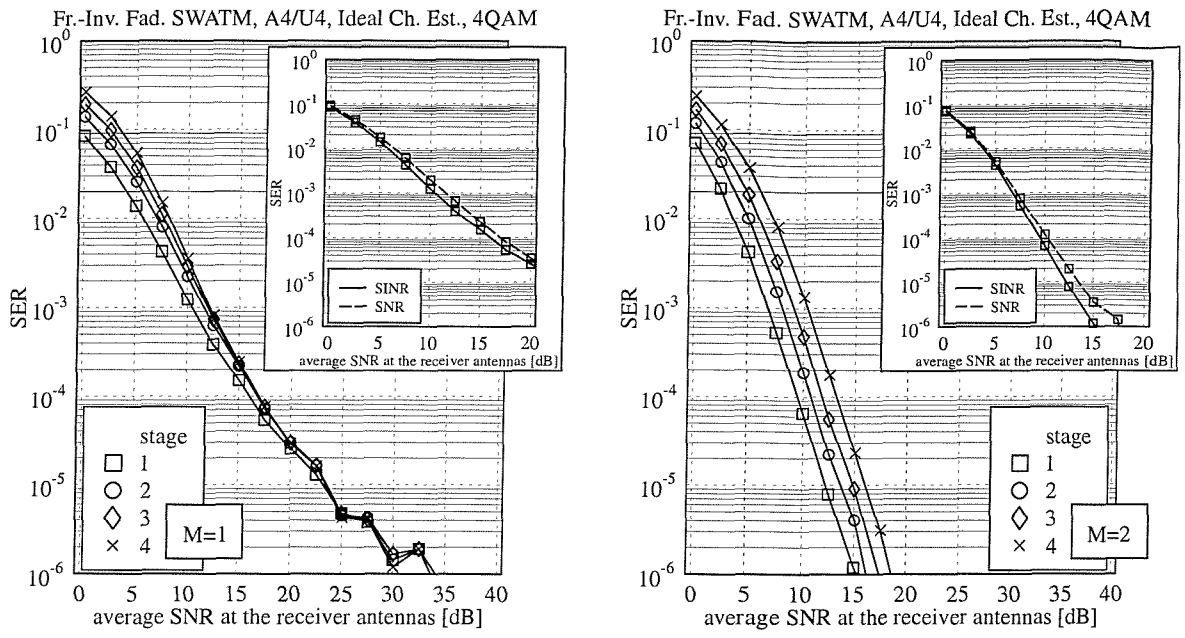

Figure 4.13: SER performance observed in different detection stages in the context of 4QAM-modulated (left:) standard SIC and (right:) M-SIC ($M = 2$) detection-assisted SDMA-OFDM as a function of the SNR at the reception antennas; here a system configuration of $L = 4$ simultaneous users and $P = 4$ reception antennas is considered; in the smaller-sized sub-figures two measures, namely the SINR and the SNR evaluated at the combiner's output are compared against each other in terms of performing the selection of the most dominant user at each detection stage; for the basic simulation parameters we refer to Table 4.3.

of undetected user symbols. For the M-SIC scheme at the right-hand side of Figure 4.13 a similar behaviour is observed, although, for higher SNRs the different detection stages' SER performance curves do not merge. This is, because at each detection stage the SER contribution induced by the error propagation from previous detection stages is of a similar significance as the additional contribution due to the AWGN.

4.3.1.4.3 SER Performance of Standard SIC and M-SIC on a Per-Detection Stage Basis for an Error-Free Reference In order to further highlight the associated error propagation effects, let us stipulate the availability of an ideal, error-free remodulated reference during the subtraction of the most recently detected user's contribution from the P-dimensional vector of signals received by the P different antenna elements. Corresponding to this scenario at the left-hand side of Figure 4.14 we have plotted the SER versus SNR performance of various system configurations parameterized again with the number of simultaneous users L, each equipped with one transmit antenna, which

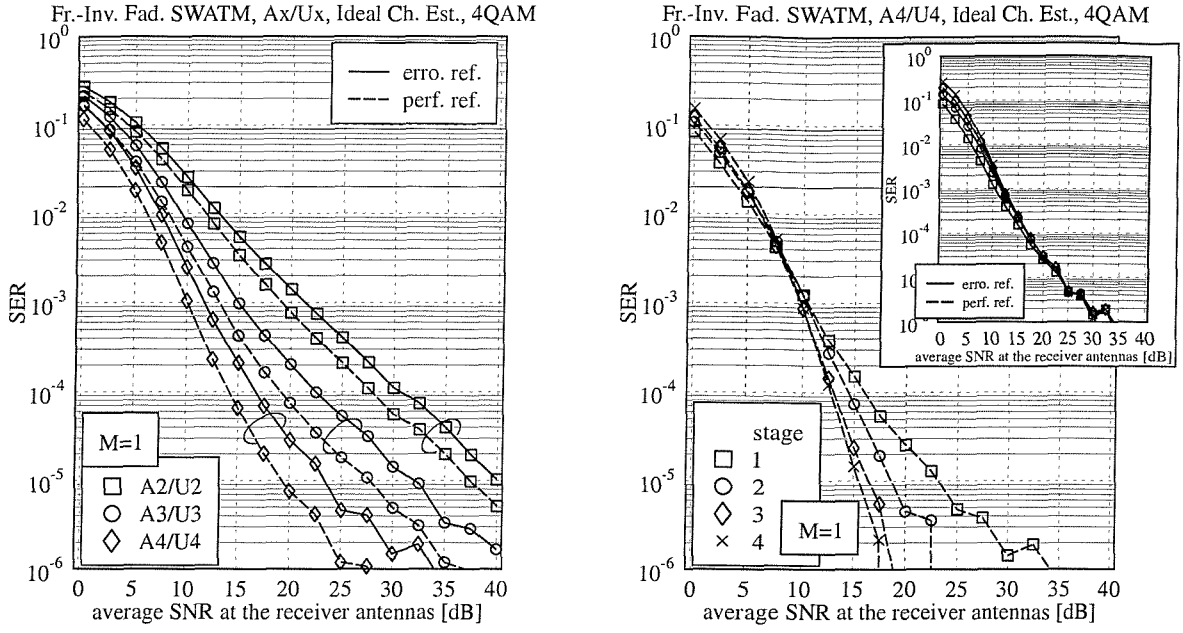

Figure 4.14: (left:) SER performance of 4QAM-modulated standard SIC detection-assisted SDMA-OFDM as a function of the SNR at the reception antennas, parameterized with the number of simultaneous users L and the number of reception antennas P, where $L = P$; (right:) SER performance of standard SIC recorded separately for each detection stage in the context of a scenario of $L = P = 4$; an ideal, error-free reference is employed in the subtractive interference cancellation process associated with each detection stage, while the curves associated with the more realistic error-contaminated reference have been plotted as a benchmarker; the SINR was invoked as the metric for the selection of the most dominant user at each detection stage; for the basic simulation parameters we refer to Table 4.3.

was assumed for each configuration to be identical to the number of reception antennas P, namely we had $L = P$. In contrast to the curves presented in Figure 4.12, which are repeated here as a benchmarker, the error propagation between the different detection stages was prevented due to the employment of an error-free remodulated reference. Again, the standard SIC detector with $M = 1$ is considered here. As a result of the idealistic nature of the reference, the system's SER performance is significantly improved compared to the more realistic case of an imperfect, potentially error-contaminated remodulated reference. The corresponding SER performance curves recorded during the different detection stages are shown at the right-hand side of Figure 4.14, where again, in the reduced-sized sub-figure we have plotted the curves associated with an imperfect remodulated reference. These curves were originally shown at the left-hand side of Figure 4.13. For the error-free remodulated reference related curves we observe at the higher-index detection stages that for

SNRs up to 7.5dB only a relatively modest SER degradation is encountered, when compared to the previous detection stages. This phenomenon is in contrast to the more distinct degradation observed in conjunction with the original curves generated in the context of a potentially error-contaminated remodulated reference. This was a result of the effects of error propagation. The residual SER degradation observed in Figure 4.14 for the SNR range up to 7.5dB is attributed to the process of ranking the remaining users' SINRs, where the most dominant remaining user is detected and consequently during the last detection stages only the weaker users are still to be detected. By contrast, at higher SNRs this trend is reversed. Specifically, the SER achieved during the last detection stages is far lower than that of the first detection stages, which is a result of the implicit increase of the system's diversity order. Again, as also supported by the BER curves of Figure 4.8, for a lower number of users the MMSE combiner employed at each detection stage is less restricted in terms of the specific choice of the receiver antenna weights, which results in a more efficient suppression of the AWGN.

4.3.1.4.4 Evaluation of the Error-Propagation-Related Event Probabilities In order to obtain an even further insight into the effects of error propagation across the different detection stages, we have measured the probabilities of the various symbol error events. More specifically, the error-event associated with index j can be defined as the following vector:

$$E_j = \mathbf{e}_j = (e_{L-1}, \ldots, e_i, \ldots, e_0), \quad e_i \in \{0, 1\}, \tag{4.134}$$

where the index j is given by interpreting the vector $\mathbf{e}_j$ as a binary number, yielding:

$$j = \sum_{i=0}^{L-1} \begin{cases} 2^i & \wedge\, e_i = 1 \\ 0 & \wedge\, e_i = 0 \end{cases} . \tag{4.135}$$

Explicitly, in case of an error at the i-th detection stage we have $e_i = 1$. In the context of our evaluations we have focussed on four specific symbol error events, which are suitable for further demonstrating the effects of error propagation through the different detection stages. These error events are $E_8 = (1, 0, 0, 0)$, $E_{12} = (1, 1, 0, 0)$, as well as $E_{14} = (1, 1, 1, 0)$ and $E_{15} = (1, 1, 1, 1)$, where E_8 indicates encountering an error event during the last detection stage. The corresponding probabilities of these events as a function of the SNR recorded at the reception antennas are portrayed at the left-hand side of Figure 4.15 for the standard SIC scheme. Here we observe that for SNRs below the cross-over point near 10dB the specific error propagation events, which extend from the first detection stage to the last stage are less likely than those events which commence in one of the last stages of the detection process.

This phenomenon can be explained as follows. Even for SNRs as low as 0dB, the probability of an AWGN-induced symbol error at a specific detection stage is far lower than the probability of incurring an error-free detection. Hence, the event having the highest probability is that of no

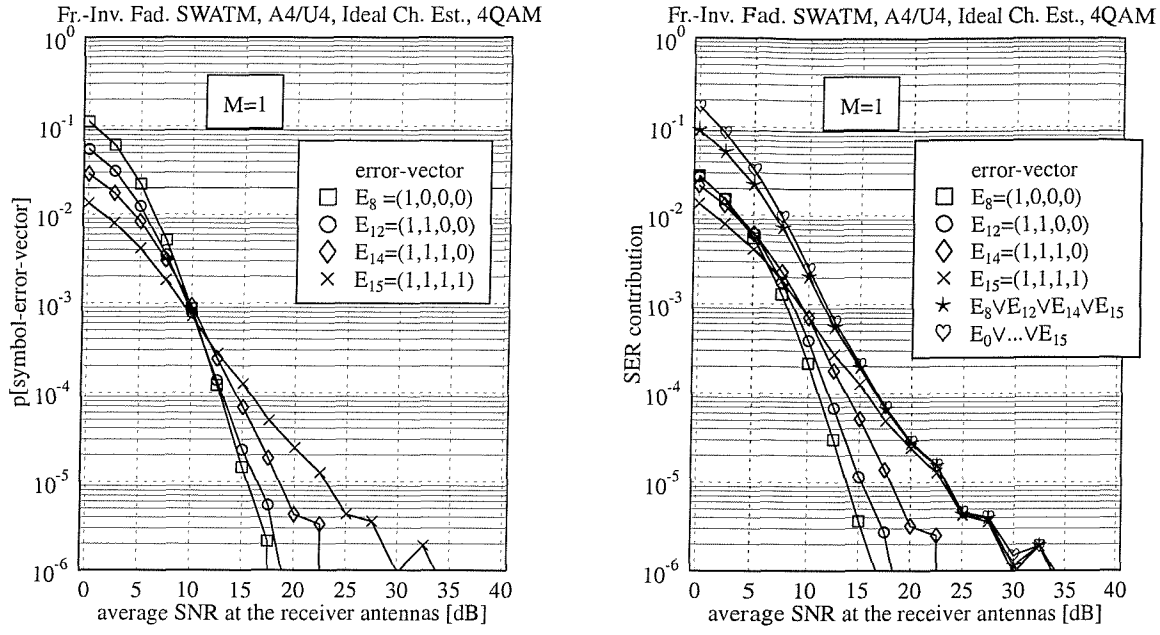

Figure 4.15: (left:) Probability- and (right:) SER contribution of the different significant error-vectors as a function of the SNR measured at the reception antennas; here 4QAM-modulated standard SIC detection-assisted SDMA-OFDM is considered in the context of a scenario of $L = 4$ simultaneous users and $P = 4$ reception antennas (A4/U4); the SINR was invoked as the metric for the selection of the most dominant user at each detection stage; for the basic simulation parameters we refer to Table 4.3.

symbol errors at all detection stages, which is denoted as E_0. The next most likely class of error events - assuming the independence of encountering decision errors at the different detection stages, as we also assumed in the case of an error-free reference - is constituted by those events which host a symbol error only in one of the detection stages. As highlighted earlier in the context of our description of the graph at the right-hand side of Figure 4.14, for relatively low SNRs it is more likely to incur symbol errors during the higher-index detection stages than in the lower-index stages, which was attributed to the process of ranking the users at the different detection stages. This effect is even further augmented here as a result of the associated error-propagation phenomenon. More explicitly, the probability of incurring an error event during the first detection stage only, which is indicated by $E_1 = (0, 0, 0, 1)$ is likely to be lower than the probability of encountering the error event of $E_{15} = (1, 1, 1, 1)$ due to the error-propagation effects, although in case of independent errors the probability of the latter would be expected to be significantly lower. Hence, following these argumentations, among the four different error events considered here, the event of $E_8 =$

$(1,0,0,0)$, which is associated with incurring a symbol error only in the last detection stage appears with the highest probability at low to medium SNRs of up to 10dB. By contrast, for higher SNRs the reverse behaviour is observed, namely that the event of incurring symbol errors in all detection stages occurs with the highest probability. This is because upon increasing the SNR, the probability of incurring a symbol error in the last detection stage decreases far more rapidly than the probability of incurring a symbol error in the first detection stage due to its interference-contaminated nature, despite detecting the highest-power user first. As argued earlier, this is also a consequence of the higher diversity order available for the MMSE combiner during the last detection stages, which is due to removing the interference imposed by other users during the previous detection stages.

On the right-hand side of Figure 4.15 we have related the different symbol error events to their SER contribution. For this purpose we have weighted the event probabilities presented at the left-hand side of Figure 4.15 by their relative contribution to the average SER. More specifically, for errors events which host a symbol error in a single detection stage only, the weighting factor is $1/L$, while correspondingly for two symbol errors we have $2/L$ and so on. Additionally, we have plotted here the joint contribution of the four most significant error events, as well as the total average SER, which is the joint contribution of all error events. While for lower SNRs some difference is observed between the SER predicted with the aid of the four most significant error events, namely $E_8 \vee E_{12} \vee E_{14} \vee E_{15}$ and the actual SER curves associated with $E_1 \vee \ldots \vee E_{15}$, at higher SNRs the former events of $E_8 \vee E_{12} \vee E_{14} \vee E_{15}$ closely predict the actual SER. A plausible interpretation of this phenomenon is that at higher SNRs the SER is constituted by error propagation events, which is even further augmented, since the MMSE combiner does not take into account the extra non-Gaussian "noise" caused by symbol errors encountered in previous detection stages. This problem results in a noise amplification, a phenomenon, which is also known from zero-forcing combiners.

4.3.1.4.5 SER Performance of the Partial M-SIC As observed in the previous sections, the M-SIC scheme described in Section 4.3.1.2.1 is capable of significantly outperforming the standard SIC arrangement, which was found to suffer from the consequences of error-propagation between the different detection stages. Furthermore, compared to the optimum ML detection scheme the performance degradation was observed to be less than 0.5dB in terms of the SNR at the receiver antennas required at a specific SER. This impressive performance was achieved at the cost of a significantly increased computational complexity compared to standard SIC. In order to reduce this potentially excessive complexity, it was proposed in Section 4.3.1.2.2 to retain $M > 1$ symbol decisions at each detection node, characterized by its associated updated vector of received signals up to the specific $L_{\text{pM-SIC}}$-th stage in the detection process, where the updating process implied cancelling the effects of the remodulated tentatively demodulated symbols from the composite multiuser signal. By contrast, at higher-index detection stages only one symbol decision would be tracked from each detection node, as in the standard SIC scheme. These principles were illustrated in Figure 4.11.

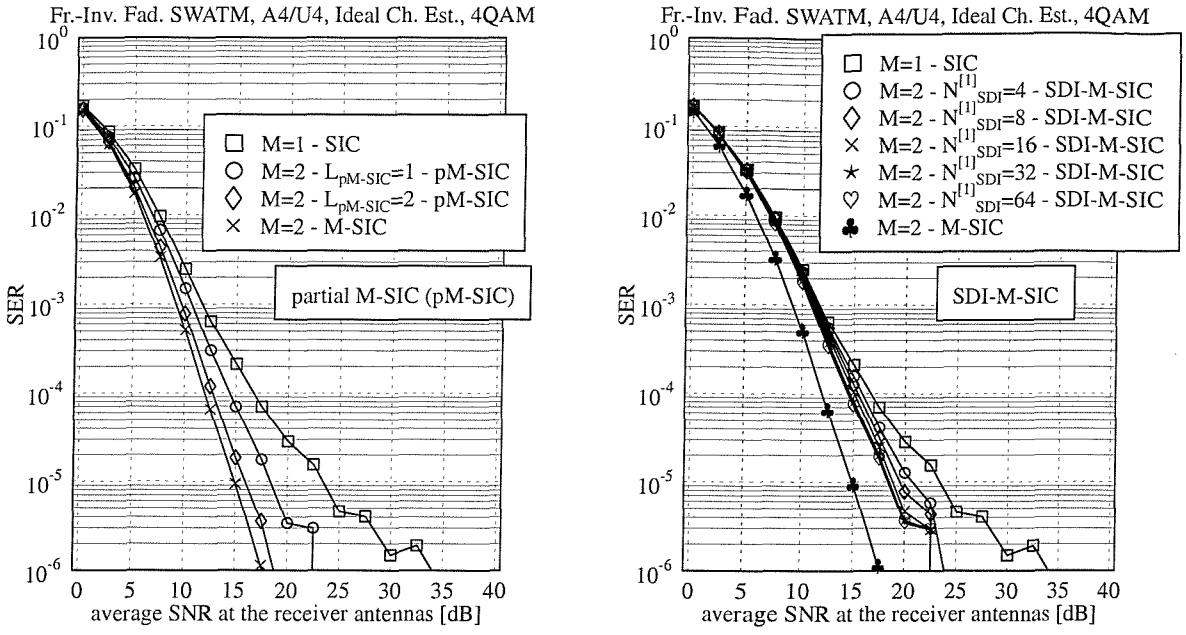

Figure 4.16: SER performance as a function of the SNR recorded at the reception antennas of 4QAM-modulated (left:) partial M-SIC ($M = 2$) detection-assisted SDMA-OFDM, parameterized with the index of the detection stage up to which multiple tentative symbol decisions are retained at each detection node of the detection process and (right:) SDI-M-SIC ($M = 2$) detection-assisted SDMA-OFDM, parameterized with the $N_{\text{SDI}}^{[1]}$ number of subcarriers associated with multiple tentative symbol decisions during the first detection stage; here a system configuration of $L = 4$ simultaneous users and $P = 4$ reception antennas (A4/U4) is considered; the SINR was employed as the metric for the selection of the most dominant user at each detection stage; for the basic simulation parameters we refer to Table 4.3.

The benefits of employing this strategy have again been verified here with the aid of simulations, as shown at the left-hand side of Figure 4.16. Again, we have plotted the performance of standard SIC ($M = 1$) as a benchmarker. Also note that the case of tracking multiple decisions per detection node in the first three detection stages is equivalent to the original M-SIC and hence it does not yield a complexity reduction. However, employing multiple tentative symbol decisions only at the first two detection stages will be shown to yield a significant complexity reduction in Section 4.3.1.5.2, which is achieved at the modest cost of increasing the SNR required for maintaining an SER of 10^{-5} by only about 1dB.

4.3.1.4.6 SER Performance of Selective-Decision-Insertion Aided M-SIC The philosophy of the SDI technique [53, 117] of Section 4.3.1.2 is that of tracking additional tentative symbol decisions only in those $N_{\text{SDI}}^{[1]}$ number of subcarriers, which exhibit the lowest SINR during the first detection stage, since these are most likely to cause symbol errors. As it was argued in the context of Figure 4.15, the employment of this approach is motivated by the observation that at higher SNRs symbol errors are mainly caused during the first detection stage because of the higher number of interfering users than at later stages. Again, we have evaluated the performance of this strategy with the aid of computer simulations. The associated SER performance results as a function of the SNR measured at the reception antennas and further parameterized with the number of low-quality subcarriers N_{SDI} where $M = 2$ tentative symbol decisions are retained during the first detection stage are shown at the right-hand side of Figure 4.16. By contrast, in all other subcarriers only one symbol decision is retained at each detection node for the sake of maintaining a low complexity. As a reference at the right-hand side of Figure 4.16 we have again plotted the SER performance curves associated with the partial M-SIC, as well as that of the original M-SIC, as shown at the left-hand side of Figure 4.16. We observe that when the $N_{\text{SDI}}^{[1]} = 64$ number of lowest-quality subcarriers classified in terms of the SINR experienced during the first detection stage are associated with $M = 2$ tentative symbol decisions during this specific detection stage, then a similar SER performance is observed, to the significantly more complex scenario, where all subcarriers are associated with $M = 2$ tentative symbol decisions during the first detection stage. This is because by retaining multiple tentative symbol decisions exclusively during the first detection stage, only the probability of those error propagation events is reduced, which are caused during the first detection stage and these are likely to be those associated with the $N_{\text{SDI}}^{[1]}$ number of lowest-SINR subcarriers.

However, compared to the SER performance of the M-SIC, the performance degradation incurred by the first-stage SDI-M-SIC characterized at the right-hand side of Figure 4.16 is substantial. In order to achieve further performance improvements, additional tentative symbol decisions could also be retained during the higher-index detection stages although naturally at the cost of a higher complexity.

4.3.1.4.7 BER Performance of Turbo-Coded SIC Detection-Assisted SDMA-OFDM As demonstrated in Section 4.2.6.4 in the context of MMSE detection-assisted SDMA-OFDM employing turbo-decoding at the receiver is a powerful means of further enhancing the system's BER performance. Naturally, this is achieved at the cost of reducing the system's effective throughput and by investing an additional amount of computational complexity. The relevant turbo coding parameters were summarized in Table 4.4, but for the reader's convenience they are repeated here: the coding rate was $R_c = \frac{1}{2}$, the constraint length was $K_c = 3$, the octally represented generator polynomials of $(7, 5)_8$ were used and four turbo decoding iterations were performed.

Our discussions will first of all concentrate on a comparison between the various methods of

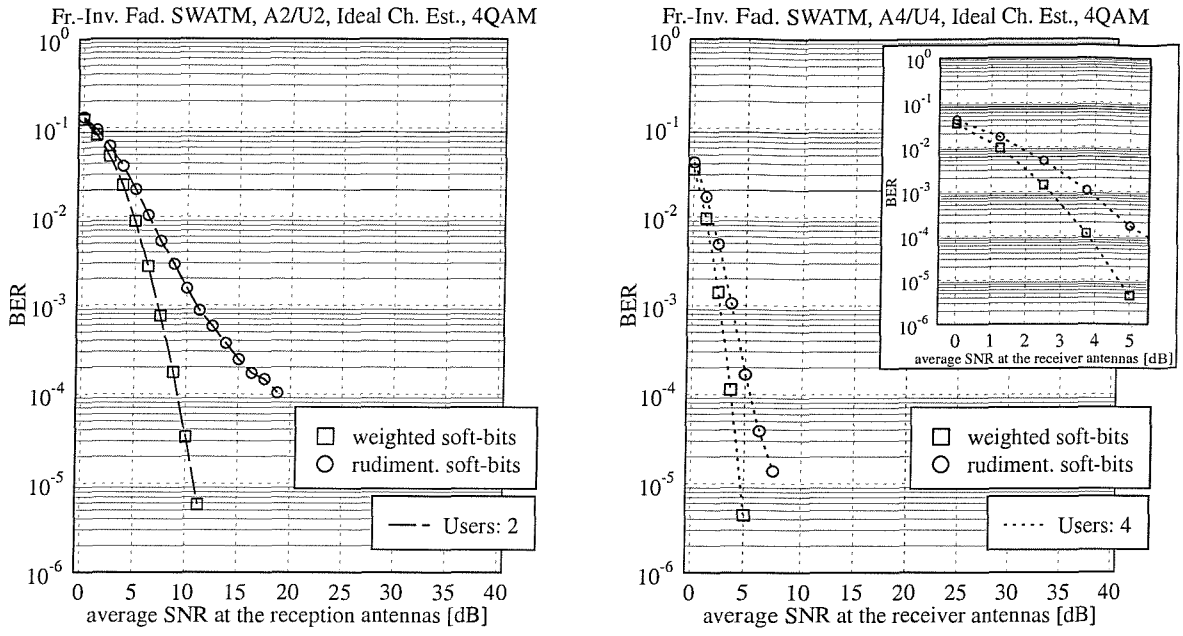

Figure 4.17: BER performance of turbo-coded, 4QAM-modulated, standard SIC detection-assisted SDMA-OFDM as a function of the SNR recorded at the reception antennas for the *rudimentary soft-bit generation* approach as suggested by Equation 4.130 and for the *weighted soft-bit generation* approach of Equation 4.133; the curves are further parameterized with the number of simultaneous users and reception antennas using $L = P$, where more specifically (left:) two reception antennas, and (right:) four reception antennas were employed; in the smaller-sized sub-figure we have magnified the range of SNRs between 0dB and 5dB; for the basic simulation parameters and the turbo-coding parameters we refer to Tables 4.3 and 4.4, respectively.

soft-bit generation, namely on the rudimentary approach of Equation 4.130 and on the weighted approach of Equation 4.133. The associated BER versus SNR simulation results valid for a scenario of $L = P = 2$ and $L = P = 4$ number of simultaneous users and reception antennas are portrayed at the left- and right-hand side of Figure 4.17, respectively. In both scenarios a significant performance advantage is observed for the weighted soft-bit generation approach, which attempts to take into account the effects of error propagation through the different SIC detection stages upon de-weighting potentially unreliable soft-bit values. For the lower-order SDMA scenario of $L = P = 2$ the performance improvement achieved by the weighted soft-bit generation is even more dramatic than for the scenario of $L = P = 4$. This is, because for the lower-order scenario the probability that a symbol error is incurred during the first detection stage is higher than for the higher-order scenario, since the latter system benefits more substantially from the increased grade of diversity experienced in conjunction with the higher number of users, supported by a higher number of antennas. Hence,

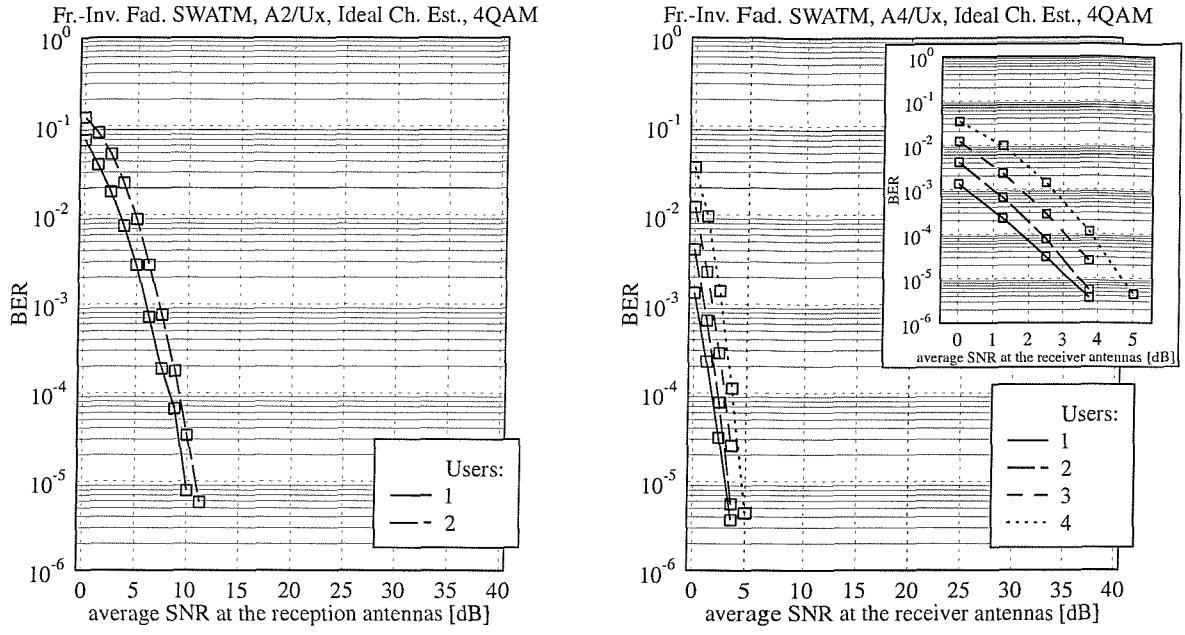

Figure 4.18: BER performance of turbo-coded, 4QAM-modulated, standard SIC detection-assisted SDMA-OFDM as a function of the SNR recorded at the reception antennas; the curves are further parameterized with the number of simultaneous users L and the number of reception antennas P, where more specifically (left:) two reception antennas, and (right:) four reception antennas were employed; in the smaller-sized sub-figure we have magnified the range of SNRs between 0dB and 5dB; for the basic simulation parameters and the turbo-coding parameters we refer to Tables 4.3 and 4.4, respectively.

weighting of the soft-bits is more effective in scenarios supporting a lower number of users with the aid of less antennas.

Having found that the weighted soft-bit metric of Equation 4.133 is the advantageous one in terms of the system's associated BER performance, further investigations were conducted with respect to different scenarios in terms of the number of simultaneous users L and the number of reception antennas P. The corresponding simulation results are shown in Figure 4.18 again, on the left-hand side for $P = 2$ reception antennas while at the right-hand side for $P = 4$ reception antennas. Similarly to our observations discussed in the context of turbo-coded MMSE detection-assisted SDMA-OFDM in Section 4.2.6.4, the system's BER performance is improved upon decreasing the number of simultaneous users L. Again, this is because, the associated MMSE combiner of each detection stage is less constrained with respect to the specific choice of the antenna array weights and hence more of the channel's diversity potential can be dedicated to mitigating the effects of

AWGN, rather than to suppressing the undesired co-channel users.

4.3.1.5 Complexity Analysis

In this section we will analyse the computational complexity exhibited by the various forms of the SIC algorithm on a per-subcarrier basis. The specific structure of this section is as follows. In Section 4.3.1.5.1 the computational complexity of the standard SIC algorithm will be investigated, while in Sections 4.3.1.5.2 and 4.3.1.5.3 the complexity of the M-SIC and partial M-SIC schemes will be analysed, respectively.

4.3.1.5.1 Complexity of Standard SIC Here we assume that at each stage of the detection process the MMSE combiner is employed in its specific left-inverse related representation as described in Section 4.2.3.2.2. As highlighted in Section 4.3.1.1, a prerequisite for the calculation of the weight matrix $\mathbf{W}_{\text{MMSE}}^{[i]H}$ according to Equation 4.118 in the i-th detection stage, is the availability of the left-inverse related correlation matrix $\mathbf{R}_{\overline{a}}^{[i]H}$ defined in Equation 4.119, and the knowledge of the cross-correlation matrix $\mathbf{R}_{c}^{[i]H}$ defined in Equation 4.120, which were employed in the context of our description of the SIC detector in Section 4.3.1.1 in their Hermitian transposed form. It was highlighted furthermore in the same section that instead of entirely recalculating these matrices at the beginning of each detection stage on the basis of the current reduced-size channel transfer factor matrix $\mathbf{H}^{[i]}$, it is computationally more advantageous to calculate them only once at the beginning of the detection process and then eliminate the most recently detected user's influence at the end of each detection stage. This is achieved by removing the $l'^{[i]}$-th row- and column from the matrix $\mathbf{R}_{\overline{a}}^{[i]H}$ and by eliminating the $l'^{[i]}$-th column from the matrix $\mathbf{R}_{c}^{[i]H}$, respectively, followed by appropriately rearranging these matrices with the result of a reduced dimensionality. Note that $l'^{[i]}$ is the column vector index of the reduced-size channel transfer factor matrix $\mathbf{H}^{[i]}$, which is associated with the most recently detected user, namely the $l^{[i]}$-th user. Let us now consider the individual steps one by one.

- *Initialization*: Specifically, the computational overhead incurred in terms of the number of complex - as well as mixed real-complex multiplications and additions at the beginning of the detection process required for the computation of the auto-correlation matrices $\mathbf{R}_{\overline{a}}^{[1]H}$ and $\mathbf{R}_{c}^{[1]H}$ is given by:

$$C_{\text{SIC,stp}}^{(\mathbb{C}*\mathbb{C})} = C_{\text{SIC,stp}}^{(\mathbb{C}+\mathbb{C})} = PL^2 \tag{4.136}$$

$$C_{\text{SIC,stp}}^{(\mathbb{R}*\mathbb{C})} = PL \tag{4.137}$$

$$C_{\text{SIC,stp}}^{(\mathbb{R}+\mathbb{C})} = L. \tag{4.138}$$

- *Weight Calculation*: Furthermore, during the i-th detection stage Equation 4.118 has to be solved for the weight matrix $\mathbf{W}_{\text{MMSE}}^{[i]H}$ with the aid of the LU-decomposition [87]. More

specifically, the LU decomposition implies factorizing the reduced-size correlation matrix $\mathbf{R}_{\bar{a}}^{[i]H} \in \mathbb{C}^{L^{[i]} \times L^{[i]}}$ into a lower (L) and upper (U) triangular matrix, followed by forward- and backward substitutions as outlined in [87]. The associated computational complexity becomes:

$$C_{\text{SIC,W}}^{(\mathbb{C}*\mathbb{C})[i]} = C_{\text{SIC,W}}^{(\mathbb{C}+\mathbb{C})[i]} = PL^{[i]2} + \frac{1}{3}L^{[i]3}. \tag{4.139}$$

Upon taking into account the reduction of the number of users to be detected and the corresponding reduction of the channel matrix' dimension across the different detection stages, the total complexity imposed by calculating the weight matrices defined in Equation 4.121 is given by:

$$C_{\text{SIC,W}}^{(\mathbb{C}*\mathbb{C})} = C_{\text{SIC,W}}^{(\mathbb{C}+\mathbb{C})} = P \sum_{L^{[i]}=1}^{L} (L^{[i]})^2 + \frac{1}{3} \sum_{L^{[i]}=1}^{L} (L^{[i]})^3 \tag{4.140}$$

$$= \frac{1}{3}P(2L+1)\alpha_{\text{SIC}} + \frac{1}{3}\alpha_{\text{SIC}}^2, \tag{4.141}$$

where the factor α_{SIC} is defined as:

$$\alpha_{\text{SIC}} = \sum_{i=1}^{L} i = \frac{1}{2}L(L+1). \tag{4.142}$$

Here we have exploited that [91] $\sum_{i=1}^{n} i = n(n+1)/2$ and $\sum_{i=1}^{n} i^2 = n(n+1)(2n+1)/6$ as well as $\sum_{i=1}^{n} i^3 = n^2(n+1)^2/4$.

- *Selection*: As the metric employed for the selection of the most dominant user we opted for the SNR at the combiner's output, as given by Equation 4.26. The rationale of this choice was that we demonstrated in Section 4.3.1.4.1 that the employment of the SNR only imposes a marginal performance loss compared to employing the SINR as the dominant user ranking metric. Here we have found that the number of complex multiplications and additions, as well as the number of real divisions and multiplications and the number of comparisons required is given by:

$$C_{\text{SIC,obj}}^{(\mathbb{C}*\mathbb{C})} = (\alpha_{\text{SIC}} - 1)(2P+1) \tag{4.143}$$

$$C_{\text{SIC,obj}}^{(\mathbb{C}+\mathbb{C})} = (\alpha_{\text{SIC}} - 1)(2P) \tag{4.144}$$

$$C_{\text{SIC,obj}}^{(\mathbb{R}/\mathbb{R})} = C_{\text{SIC,obj}}^{(\mathbb{R}*\mathbb{R})} = C_{\text{SIC,obj}}^{(\mathbb{R}\lesseqgtr\mathbb{R})} = (\alpha_{\text{SIC}} - 1). \tag{4.145}$$

In this context we implicitly assumed that the SNR calculation associated with the selection of the most dominant user is not required in the last detection stage, since only a single user remains to be detected.

- *Combining*: Furthermore, the linear combining at each stage of the successive cancellation process - carried out with the aid of Equation 4.124 - necessitates the following number of complex multiplications and additions as given by:

$$C_{\text{SIC,cmb}}^{(\mathbb{C}*\mathbb{C})} = C_{\text{SIC,cmb}}^{(\mathbb{C}+\mathbb{C})} = LP. \tag{4.146}$$

- *Demodulation*: In addition, the process of MPSK-related demodulation[15], which is realized with the aid of Equation 4.125, exhibits a total complexity of:

$$C_{\text{SIC,dem}}^{(\mathbb{C}*\mathbb{C})} = \frac{1}{2}LM_c \tag{4.147}$$

$$C_{\text{SIC,dem}}^{(\mathbb{C}+\mathbb{C})} = C_{\text{SIC,dem}}^{(\mathbb{R}\lesseqgtr\mathbb{R})} = LM_c, \tag{4.148}$$

  where again, we have included the number of comparisons between the outcomes of the Euclidean distance metric as an additional factor increasing the complexity.

- *Updating*: Finally, the process of updating the vector of signals received by the different antenna elements according to Equation 4.127 by cancelling the effects of the remodulated signal of a specific user from the composite multiuser signal imposes a total complexity of:

$$C_{\text{SIC,upd}}^{(\mathbb{C}*\mathbb{C})} = C_{\text{SIC,upd}}^{(\mathbb{C}+\mathbb{C})} = (L-1)P, \tag{4.149}$$

  where again, no updating or remodulated signal cancellation is required during the last detection stage. Here we have also taken into account the average number of explicit data transfers, which was quantified as:

$$C_{\text{SIC,upd}}^{\Rightarrow} = L\left[(L+1)\left[\frac{1}{9}(2L+1)-\frac{3}{4}\right]+\frac{5}{6}\right]+\frac{1}{4}PL(L-1). \tag{4.150}$$

  More explicitly, the first term corresponds to rearranging the auto-correlation matrix $\mathbf{R}_{\overline{a}}^{[i]H}$, while the second terms is associated with rearranging the cross-correlation matrix $\mathbf{R}_{c}^{[i]H}$ at the end of each detection stage, $i = 1, \ldots, L$.

Upon combining the different contributions given in the previous equations, we obtain for the total complexity of the standard SIC detector as a function of the number of users L, the number of reception antennas P and the number of constellation points M_c the following expressions:

$$C_{\text{SIC}}^{(\mathbb{C}*\mathbb{C})} = \frac{1}{2}LM_c + [P(L-3)-1] + \frac{1}{3}[3+P(2L+13)]\,\alpha_{\text{SIC}} + \frac{1}{3}\alpha_{\text{SIC}}^2 \tag{4.151}$$

$$C_{\text{SIC}}^{(\mathbb{C}+\mathbb{C})} = LM_c + [P(L-3)-1] + \frac{1}{3}[3+P(2L+13)]\,\alpha_{\text{SIC}} + \frac{1}{3}\alpha_{\text{SIC}}^2 \tag{4.152}$$

$$C_{\text{SIC}}^{(\mathbb{R}\lesseqgtr\mathbb{R})} = (\alpha_{\text{SIC}}-1) + LM_c \tag{4.153}$$

$$C_{\text{SIC}}^{(\mathbb{R}*\mathbb{C})} = PL \tag{4.154}$$

$$C_{\text{SIC}}^{(\mathbb{R}+\mathbb{C})} = L \tag{4.155}$$

$$C_{\text{SIC}}^{(\mathbb{R}/\mathbb{R})} = C_{\text{SIC}}^{(\mathbb{R}*\mathbb{R})} = (\alpha_{\text{SIC}}-1) \tag{4.156}$$

[15] In the context of the MPSK modulation scheme the normalization of the MMSE combiner's output signal is avoided.

where again, $\alpha_{\text{SIC}} = \frac{1}{2}L(L+1)$ was defined in Equation 4.142. In order to further simplify the complexity analysis, it is reasonable to assume that mixed real-complex multiplications[16] and additions are only half as complex as those performed on two complex variables, while the multiplication of two real-valued variables exhibits only one fourth of the complexity. Hence, a slightly simplified characterization of the standard SIC detector's complexity is given by:

$$C_{\text{SIC}}^{(\mathbb{C}*\mathbb{C})} = \frac{1}{2}LM_c + \left[P\left(\frac{3}{2}L-3\right) - \frac{5}{4}\right] + \frac{1}{3}\left[\frac{15}{4} + P\left(2L+13\right)\right]\alpha_{\text{SIC}} + \frac{1}{3}\alpha_{\text{SIC}}^2 \quad (4.157)$$

$$C_{\text{SIC}}^{(\mathbb{C}+\mathbb{C})} = L\left(M_c + \frac{1}{2}\right) + P(L-3) + \frac{1}{3}P(2L+13)\alpha_{\text{SIC}} + \frac{1}{3}\alpha_{\text{SIC}}^2 \quad (4.158)$$

$$C_{\text{SIC}}^{(\mathbb{R}\lessgtr\mathbb{R})} = (\alpha_{\text{SIC}} - 1) + LM_c \quad (4.159)$$

$$C_{\text{SIC}}^{(\mathbb{R}/\mathbb{R})} = (\alpha_{\text{SIC}} - 1). \quad (4.160)$$

4.3.1.5.2 Complexity of M-SIC As argued in Section 4.3.1.4.2, the standard SIC algorithm suffers from error propagation, especially in those subcarriers, where the S(I)NR observed at the selected user's associated combiner output during the first detection stage is relatively low. A viable strategy of improving the achievable performance and of further reducing the BER/SER is that of allowing not only the single most likely constellation point to be selected from the constellation during a specific detection stage's demodulation process, but rather to retain the $M > 1$ number of most likely constellation points. As a result, in the i-th stage $M^{(i-1)}$ number of detection and demodulation operations has to be performed. This also requires M^i number of updating or interference cancellation operations with respect to the local vector $\mathbf{x}^{[i]}$ of received signals. The complexity contribution required for evaluating the weight matrices and SNR estimates, namely 'Initialization', 'Weight Calculation' and 'Selection' of Section 4.3.1.5.1 remains unchanged.

- *Combining*: More specifically, the computational complexity associated with the operation of combining hence becomes:

$$C_{\text{M-SIC,cmb}}^{(\mathbb{C}*\mathbb{C})} = C_{\text{M-SIC,cmb}}^{(\mathbb{C}+\mathbb{C})} = \beta_{\text{M-SIC}}P, \quad (4.161)$$

  where the factor $\beta_{\text{M-SIC}}$, which corresponds to the total number of different detection nodes in the detection process is given by:

$$\beta_{\text{M-SIC}} = \sum_{i=0}^{L-1} M^i = \begin{cases} L & \wedge M = 1 \\ \frac{M^L-1}{M-1} & \wedge M > 1. \end{cases} \quad (4.162)$$

  This is the formula characterizing a geometrical series [91].

[16]Here we neglect that the multiplication of two complex numbers involves real-valued additions as well. Hence our simplified formulae are to be understood as best-case estimates of the complexity.

- *Demodulation*: For the MPSK-related demodulation operation we have:

$$C_{\text{M-SIC,dem}}^{(\mathbb{C}*\mathbb{C})} = \frac{1}{2}\beta_{\text{M-SIC}}M_c \tag{4.163}$$

$$C_{\text{M-SIC,dem}}^{(\mathbb{C}+\mathbb{C})} = \beta_{\text{M-SIC}}M_c, \tag{4.164}$$

where the factor $\beta_{\text{M-SIC}}$ was given by Equation 4.162. Additionally, it is also useful to take into account the number of comparisons to be carried out in the context of the demodulation process invoked at the different detection stages. Here we have to differentiate between the first $L-1$ detection stages and the last detection stage. Specifically, during the first $L-1$ stages of Figure 4.11 there are:

$$\gamma_{\text{M-SIC,i}} = \sum_{i=0}^{L-2} M^i = \begin{cases} L-1 & \wedge\, M=1 \\ \frac{M^{(L-1)}-1}{M-1} & \wedge\, M>1, \end{cases} \tag{4.165}$$

number of different detection nodes, each of which is associated with selecting the M number of most likely tentative symbol decisions out of the M_c number of possible symbol decisions associated with the specific modulation scheme employed. The number of comparisons per detection node required by this operation is given by:

$$\delta_{\text{M-SIC,i}} = \sum_{i=M_c-(M-1)}^{M_c} i = \frac{1}{2}M(1+2M_c-M), \tag{4.166}$$

which could potentially be further reduced with the aid of more effective binary tree-based search methods[17]. By contrast, during the last detection stage we incur:

$$\gamma_{\text{M-SIC,ii}} = \begin{cases} 1 & \wedge\, M=1 \\ M^{(L-1)} & \wedge\, M>1 \end{cases} \tag{4.167}$$

number of different detection nodes, each of which is associated with the selection of the single most likely symbol decision. This imposes a total number of comparisons per detection node, which is given by:

$$\delta_{\text{M-SIC,ii}} = M_c. \tag{4.168}$$

The final operation in the M-SIC detection process is to select the specific symbol vector from the various possible symbol vectors defined by the different tentative symbol decisions retained at each detection node, whose associated Euclidean distance metric is the lowest during the last detection stage. This requires an additional $M^{(L-1)}-1$ number of comparisons. Hence, the total number of demodulation-related comparisons during the entire detection process is given by:

$$C_{\text{M-SIC,dem}}^{(\mathbb{R}\lesseqgtr\mathbb{R})} = \epsilon_{\text{M-SIC}}, \tag{4.169}$$

[17]From the literature it is well-known that recursive search algorithms, such as 'quick-sort' require a potentially lower number of comparisons than those based on the principles of 'sorting by selection'.

where:

$$\epsilon_{\text{M-SIC}} = \gamma_{\text{M-SIC,i}}\delta_{\text{M-SIC,i}} + \gamma_{\text{M-SIC,ii}}\delta_{\text{M-SIC,ii}} + M^{(L-1)} - 1. \tag{4.170}$$

- *Updating*: Furthermore, for the total number of updating operations with respect to the vector of signals received by the different antenna elements which implies cancelling the effects of the remodulated signal from the composite multiuser signal as seen in Equation 4.127 we obtain:

$$C_{\text{M-SIC,upd}}^{(\mathbb{C}*\mathbb{C})} = C_{\text{M-SIC,upd}}^{(\mathbb{C}+\mathbb{C})} = \zeta_{\text{M-SIC}}P, \tag{4.171}$$

where $\zeta_{\text{M-SIC}}$ is defined here as:

$$\zeta_{\text{M-SIC}} = \sum_{i=1}^{L-1} M^i = \begin{cases} L-1 & \wedge M = 1 \\ M\frac{M^{(L-1)}-1}{M-1} & \wedge M > 1. \end{cases} \tag{4.172}$$

Upon additionally recalling the complexity-related contributions corresponding to the initialization, weight calculation and selection from Section 4.3.1.5.1, the M-SIC detector's complexity is characterized by the following equations:

$$\begin{aligned} C_{\text{M-SIC}}^{(\mathbb{C}*\mathbb{C})} &= \frac{1}{2}\beta_{\text{M-SIC}}M_c + \left[P\left(\beta_{\text{M-SIC}} + \zeta_{\text{M-SIC}} - \frac{1}{2}L - 2\right) - \frac{5}{4}\right] + \\ &\quad + \frac{1}{3}\left[\frac{15}{4} + P\left(2L + 13\right)\right]\alpha_{\text{SIC}} + \frac{1}{3}\alpha_{\text{SIC}}^2 \qquad (4.173) \\ C_{\text{M-SIC}}^{(\mathbb{C}+\mathbb{C})} &= \beta_{\text{M-SIC}}M_c + L\left(\frac{1}{2} - P\right) + P(\beta_{\text{M-SIC}} + \zeta_{\text{M-SIC}} - 2) + \\ &\quad + \frac{1}{3}P(2L + 13)\alpha_{\text{SIC}} + \frac{1}{3}\alpha_{\text{SIC}}^2 \qquad (4.174) \\ C_{\text{M-SIC}}^{(\mathbb{R}/\mathbb{R})} &= (\alpha_{\text{SIC}} - 1) \qquad (4.175) \\ C_{\text{M-SIC}}^{(\mathbb{R}\lessgtr\mathbb{R})} &= (\alpha_{\text{SIC}} - 1) + \epsilon_{\text{M-SIC}}, \qquad (4.176) \end{aligned}$$

where again, α_{SIC}, $\beta_{\text{M-SIC}}$, as well as $\gamma_{\text{M-SIC,i}}$, $\delta_{\text{M-SIC,i}}$ and $\gamma_{\text{M-SIC,ii}}$, $\delta_{\text{M-SIC,ii}}$ and additionally $\epsilon_{\text{M-SIC}}$, $\zeta_{\text{M-SIC}}$ were given by Equations 4.142, 4.162, as well as 4.165, 4.166 and 4.167, 4.168 and also Equations 4.170, 4.172, respectively. In the context of these equations we have once again taken into account that mixed real-complex multiplications and additions are only half as complex as the corresponding operations associated with two complex numbers[18].

4.3.1.5.3 Complexity of Partial M-SIC In this section we will briefly assess the computational complexity of partial M-SIC. We recall from Section 4.3.1.2.2 that in contrast to the M-SIC described in Section 4.3.1.2.1, the M most likely symbol decisions per detection node are only retained up to the specific $L' = L_{\text{pM-SIC}}$-th detection stage. By contrast, for the higher-index detection

[18]Again, this neglects that the multiplication of two complex numbers also involves real-valued additions.

stages only the single most likely symbol decision per detection node is retained, as in the case of the standard SIC scheme, which was described in Section 4.3.1.1. This implies that for $L' = 1$ the partial M-SIC detector is identical to the standard SIC detector, while for $L' = L$ the M-SIC detector is obtained. The analysis of the partial M-SIC's complexity follows a similar procedure to that applied in Section 4.3.1.5.2 in the case of the M-SIC scheme. The difference resides in the specific composition of the factors $\beta_{\text{M-SIC}}$ and $\gamma_{\text{pM-SIC,i}}$, $\gamma_{\text{pM-SIC,ii}}$, as well as $\epsilon_{\text{pM-SIC}}$ and $\zeta_{\text{pM-SIC}}$, which were defined for M-SIC in Equations 4.162 and 4.165, 4.167 as well as 4.170, 4.172. By contrast, here we have:

$$\beta_{\text{pM-SIC}} = \sum_{i=0}^{L'-1} M^i + \sum_{i=L'}^{L-1} M^{L'-1} = \begin{cases} L & \wedge M = 1 \\ \frac{M^{L'}-1}{M-1} + (L-L')M^{L'-1} & \wedge M > 1, \end{cases} \tag{4.177}$$

as well as:

$$\gamma_{\text{pM-SIC,i}} = \sum_{i=0}^{L'-2} M^i = \begin{cases} L'-1 & \wedge M = 1 \\ \frac{M^{L'-1}-1}{M-1} & \wedge M > 1, \end{cases} \tag{4.178}$$

and:

$$\gamma_{\text{pM-SIC,ii}} = \sum_{i=L'-1}^{L-1} M^{(L'-1)} = (L-L'+1)M^{(L'-1)}. \tag{4.179}$$

Hence, similarly to Equation 4.169 the total number of demodulation-related comparisons during the entire detection process is given by:

$$C_{\text{pM-SIC,dem}}^{(\mathbb{R}\lessgtr\mathbb{R})} = \epsilon_{\text{pM-SIC}}, \tag{4.180}$$

where we have:

$$\epsilon_{\text{pM-SIC}} = \gamma_{\text{pM-SIC,i}}\delta_{\text{pM-SIC,i}} + \gamma_{\text{pM-SIC,ii}}\delta_{\text{pM-SIC,ii}} + M^{(L'-1)} - 1, \tag{4.181}$$

and $\delta_{\text{pM-SIC,i}} = \delta_{\text{M-SIC,i}}$ as well as $\delta_{\text{pM-SIC,ii}} = \delta_{\text{M-SIC,ii}}$. Furthermore, the interference-cancellation based updating-related factor $\zeta_{\text{pM-SIC}}$ is given by:

$$\zeta_{\text{pM-SIC}} = \sum_{i=1}^{L'-1} M^i + \sum_{i=L'}^{L-1} M^{L'-1} = \begin{cases} L-1 & \wedge M = 1 \\ M\frac{M^{L'-1}-1}{M-1} + (L-L')M^{(L'-1)} & \wedge M > 1. \end{cases} \tag{4.182}$$

In order to obtain the expressions for the total complexity associated with partial M-SIC, the variables $\beta_{\text{M-SIC}}$, $\gamma_{\text{M-SIC,i}}$, $\gamma_{\text{M-SIC,ii}}$, $\epsilon_{\text{M-SIC}}$ and $\zeta_{\text{pM-SIC}}$ employed in the context of Equations 4.173, 4.174, 4.175, 4.176 have to be substituted against the corresponding partial M-SIC-specific expressions defined in this section.

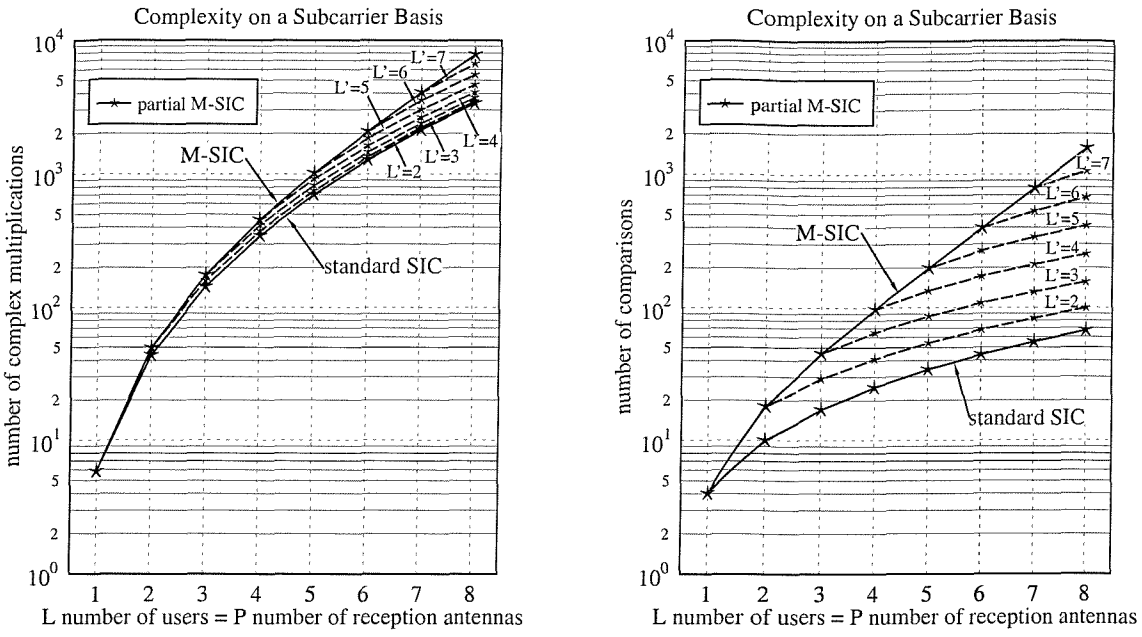

Figure 4.19: Complexity of standard SIC, M-SIC and partial M-SIC in terms of (left:) the number of complex multiplications $C^{(\mathbb{C}*\mathbb{C})}$ and (right:) the number of real-valued comparisons $C^{(\mathbb{R}\lesseqgtr\mathbb{R})}$ recorded on a subcarrier basis, as a function of the number of simultaneous users L, which was assumed to be equal to the number of reception antennas P; the curves related to partial M-SIC are further parameterized with the index of the detection stage namely, $L' = L_{\text{pM-SIC}}$, up to which M number of tentative symbol decisions per detection node were retained; specifically for M-SIC and partial M-SIC the number of retained tentative symbol decisions per detection node was equal to $M = 2$, while in all scenarios $M_c = 4$ constellation points were assumed, which is for example the case in the context of 4QAM modulation.

4.3.1.5.4 Complexity Comparison of the Different SIC Detectors In this section the different SIC-related detection techniques, namely standard SIC, M-SIC and partial M-SIC will be compared against each other on the basis of the complexity formulae developed in the previous sections. In the context of our evaluations the M_c number of constellation points associated with the modulation scheme employed was assumed to be $M_c = 4$, which is the case for example for 4QAM modulation. The M-SIC retained $M = 2$ number of symbol decisions at each detection node. In the context of the 4QAM modulation scheme we found that further increasing the M number of tentative symbol decisions per detection node retained does not yield a significant additional performance improvement.

Specifically, on the left-hand side of Figure 4.19 we have compared standard SIC against the M-SIC scheme as well as to the partial M-SIC arrangement in terms of the number of complex

multiplications imposed on a subcarrier basis, as a function of the number of simultaneous users L, which was assumed here to be equal to the number of reception antennas P. Furthermore, the curves associated with the partial M-SIC scheme are additionally parameterized with the index of the detection stage, namely $L' = L_{\text{pM-SIC}}$, up to which the M most likely tentative symbol decisions per detection node were retained. By contrast, for the higher-index detection stages only one symbol decision per detection node was retained. The curves associated with the different detection techniques in Figure 4.19 were generated with the aid of the complexity formulae given by Equations 4.157 as well as 4.173. For the partial M-SIC scheme furthermore the specific variables have to be substituted into Equation 4.173. The number of complex additions associated with the different detectors has not been illustrated here, since these values were found only to differ slightly from those of the number of complex multiplications. As expected, it is evidenced by Figure 4.19 that the M-SIC detector may become significantly more complex than standard SIC, depending on the number of simultaneous users L. While for a scenario of $L = P = 4$ the complexity of the M-SIC scheme is observed in Figure 4.19 to be higher than that of standard SIC by about 32%, for a scenario of $L = P = 8$ the M-SIC is by a factor of about 2.32 or equivalently, by about 132% more complex. This is a result of the exponential growth of the number of demodulation and updating operations associated with the M-SIC scheme, when increasing the number of users L as seen in Figure 4.19. As expected, the complexity of partial M-SIC is shown in Figure 4.19 to be between that of standard SIC and M-SIC for $1 < L' < L$.

Similar observations can also be inferred for the computational complexity in terms of the number of comparisons between real-valued numbers, as portrayed at the right-hand side of Figure 4.19. Here the complexity difference between standard SIC and M-SIC is even more dramatic. While for a scenario of $L = P = 4$ the M-SIC is a factor 3.88 more complex than standard SIC, for a scenario of $L = P = 8$ this factor is as high as 23.32. Again, the partial M-SIC is capable of significantly reducing the complexity - also depending on the cut-off level L' - although this is achieved at the cost of a performance degradation, as it was observed in Section 4.3.1.4.5.

In order to further characterize the complexity of the standard SIC- and that of the M-SIC detector, in Table 4.6 we have listed the complexity-related contribution of the different components involved in the detection process for a scenario of $L = P = 4$. Note that the process of initialization, weight calculation and selection - as described in Section 4.3.1.1 - is identical for both the standard- and the M-SIC detector, which is indicated by "%" in the corresponding entries of Table 4.6. However, as argued earlier in this section, the computational complexity related to the operations of demodulation, combining and updating is significantly increased for the M-SIC scheme compared to standard SIC due to the higher number of detection nodes.

description	$C_{\text{SIC}}^{(\mathbb{C}*\mathbb{C})}$	$C_{\text{SIC}}^{(\mathbb{C}+\mathbb{C})}$	$C_{\text{SIC}}^{(\mathbb{R}\lesseqgtr\mathbb{R})}$	$C_{\text{M-SIC}}^{(\mathbb{C}*\mathbb{C})}$	$C_{\text{M-SIC}}^{(\mathbb{C}+\mathbb{C})}$	$C_{\text{M-SIC}}^{(\mathbb{R}\lesseqgtr\mathbb{R})}$
initialization:	72	66	-	%	%	%
weight calc.	153.33	153.33	-	%	%	%
selection	83.25	72	9	%	%	%
combining	16	16	-	60	60	-
demodulation	8	16	16	30	60	88
updating	12	12	-	56	56	-
$\rightarrow$ total	345	335.33	25	454.58	467.33	97

Table 4.6: Computational complexity of the different processing steps involved in standard SIC (columns 1...3) and M-SIC (columns 4...6) for a scenario of $L = P = 4$ simultaneous users- and reception antennas; specifically for M-SIC the number of tentative symbol decisions per detection node was equal to $M = 2$, while in all scenarios $M_c = 4$ constellation points were assumed, which is for example the case with 4QAM modulation.

4.3.1.6 Summary and Conclusions on SIC Detection Techniques

Our discussions commenced in Section 4.3.1 with a portrayal and characterization of standard SIC based detection and its derivatives, namely the M-SIC and partial M-SIC detection schemes in the context of both uncoded and turbo-coded scenarios. More specifically, standard SIC detection was detailed in Section 4.3.1.1. Its associated block diagram was portrayed in Figure 4.10 and the most significant equations were summarized in Table 4.5. As a result of the SIC detector's strategy of detecting only the most dominant user having the highest SINR, SIR or SNR at its associated linear combiner's output, the dimensionality of the associated symbol classification- or demodulation was reduced to evaluating the single-user Euclidean distance metric of Equation 4.125 LM_c times in contrast to calculating the multi-user Euclidean distance metric of Equation 4.223 M_c^L-times, as in the case of joint optimum ML detection.

The performance of the SIC detector critically relies on correct symbol decisions at the different detection stages, otherwise potentially catastrophic error propagation is encountered. An attractive strategy of reducing these effects is that of tracking multiple symbols decisions from each detection node. The philosophy of this technique was addressed in Section 4.3.1.2. Specifically in Section 4.3.1.2.1 we considered M-SIC, where the M number of most likely tentative symbol decisions were tracked from all detection nodes in the detection 'tree' of Figure 4.11.

In an effort to reduce the potentially high computational complexity of M-SIC compared to that of standard SIC and motivated by the observation that the highest symbol error probabilities are associated with the 'early' or low-index detection stages, in Section 4.3.1.2.2 the partial M-SIC was briefly characterized. Recall that at higher SNRs for the detection stages encountered towards the end of the detection process the symbol error probability is lower than for the detection process at the beginning, provided that error-free symbol decisions were encountered in the previous detection

stages. This is because towards the end of the detection process the MIMO system's effective diversity order is increased. More specifically, the principle of partial M-SIC was to track the $M > 1$ number of most likely tentative symbol decisions per detection node only during the first few detection stages. By contrast, for the later detection stages only one symbol decision per detection node was made, as in the case of standard SIC. The philosophy of these techniques was further augmented with the aid of Figure 4.11, which illustrates the associated detection trees for the specific scenario of $L = 4$ users and for retaining $M = 2$ number of tentative symbol decisions per detection node in case of M-SIC and partial M-SIC. Specifically, the graph at the left-hand side of Figure 4.11 was associated with standard SIC, while that at the right-hand side of Figure 4.11 with M-SIC. Finally, in the centre of Figure 4.11 the various partial M-SIC related detection 'trees' were portrayed. A further reduction of the computational complexity could potentially be achieved with the aid of the SDI-M-SIC technique [53, 117], which was briefly addressed in Section 4.3.1.2.3.

Our further deliberations in Section 4.3.1.3 then addressed the problem of SIC-specific soft-bit generation required for turbo-decoding. Based on our observation of the effects of error propagation through the different SIC detection stages the weighted soft-bit metric of Equation 4.133 was proposed. It was demonstrated later in Section 4.3.1.4.7 that the employment of this weighted soft-bit metric resulted in a significant BER performance improvement in scenarios, where the number of users L is of similar value to the number of BS reception antenna elements P.

Our performance analysis of the various SIC-related detection techniques was conducted in Section 4.3.1.4. Specifically, in Section 4.3.1.4.1 our discussions commenced with the analysis of the BER and SER performance of standard SIC and M-SIC, parameterized with the number of users L and the number of reception antennas P. A significant performance improvement was observed in Figure 4.12 upon increasing the SDMA-MIMO system's order under the constraint of $L = P$. This was a result of the higher 'diversity' of users in terms of their different received signal quality observed at each detection stage. Furthermore, we found that using the SINR instead of the SNR at the linear combiner's output for selecting the most dominant user from the set of remaining users at each SIC detection stage had a modest, but noticeable beneficial effect at low BERs in conjunction with more than three users.

Our further investigations conducted in Section 4.3.1.4.2 then focused on the analysis of the SER encountered at each detection stage, again for both the standard SIC and the M-SIC. As it was shown for the standard SIC scheme at the left-hand side of Figure 4.13, the SER monotonously increases upon approaching the last detection stage. Our explanation of this phenomenon was that the symbol error probability encountered at a specific detection stage is composed of the symbol error probability of the previous stage plus an 'additional' error probability, which is related to the effects of the residual AWGN at the specific stage considered under the assumption that no symbol errors have occurred in the previous detection stages. For higher SNRs we observed that the different detection stages' SER curves merge, since the 'AWGN'-related symbol error contribution

is decreased for the higher-index detection stages, which is a result of the system's increased grade of diversity. For M-SIC similar SER curves were shown at the right-hand side of Figure 4.13.

In order to further highlight the effects of error propagation through the different SIC detection stages, in Section 4.3.1.4.3 the standard SIC detector's SER performance was portrayed in the context employing error-free symbol decisions in the SIC module of Figure 4.10. Specifically at the left-hand side of Figure 4.14 the SER results were averaged over the different detection stages, while at the right-hand side of Figure 4.14 the SER results were portrayed on a per-detection stage basis. Compared to the more realistic case of employing an imperfect, potentially error-contaminated re-modulated reference the SER improvement is substantial, which provided a further motivation for mitigating the effects of error-propagation for example with the aid of the M-SIC scheme of Section 4.3.1.2.

In an effort to further characterize the effects of error-propagation, in Section 4.3.1.4.4 we have analysed the probability of the various symbol error events, namely that a symbol error has occurred in the first detection stage, while the symbol decisions carried out during the higher-index detection stages were error-free. The associated probabilities of the various error-events at the reception antennas were shown at the left-hand side of Figure 4.15 as a function of the SNR, while at the right-hand side their contribution to the total SER was portrayed. From these curves we inferred that for higher SNRs the SER is governed by specific error-events, which originated from the first detection-stage, followed by those events, which commenced in the second stage and so on.

This was the main motivation for employing partial M-SIC, which was characterized in terms of its SER in Section 4.3.1.4.5, specifically at the left-hand side of Figure 4.16. Here we observed that in a scenario of $L = P = 4$ users and reception antennas as well as at an SER of 10^{-5} achieved by the partial M-SIC scheme up to and including the second detection stage, the SNR must be only a modest 1dB higher than that required by the M-SIC arrangement, while at the same time halving the complexity.

Furthermore, in Section 4.3.1.4.6 SDI-M-SIC was discussed and compared to both standard SIC and M-SIC at the right-hand side of Figure 4.16. The philosophy of SDI-M-SIC was to allow the employment of M-SIC or partial M-SIC only in a limited number of low-quality OFDM subcarriers, namely in those, which exhibit the lowest SINR during the first detection stage, while using standard SIC in all other subcarriers. In our specific example we employed partial M-SIC, where multiple tentative symbol decisions per detection node were permitted only during the first detection stage. In the context of the indoor WATM channel model of Section 6.1.1 it was shown at the right-hand side of Figure 4.16 that a modest number of $N_{\text{SDI}}^{[1]} = 64$ decision-insertion related subcarriers is sufficient for closely approximating the performance of the partial M-SIC scheme. This corresponded to $1/8$-th of the total subcarriers.

Finally, in Section 4.3.1.4.7 the BER performance of turbo-coded standard SIC detection-assisted

SDMA-OFDM was analysed. Specifically, in the context of Figure 4.17 we have compared the benefits of employing the rudimentary soft-bit metric of Equation 4.130 against those of the improved soft-bit metric of Equation 4.133, which accounted for the effects of error-propagation through the different detection stages. The employment of the weighted soft-bit metric of Equation 4.133 was found to be particularly beneficial in the context of a 'fully-loaded' SDMA-OFDM system, where the number of users L equals the number of reception antennas P. Further BER performance results related to the weighted soft-bit metric were presented in Figure 4.18, which characterized the influence of the number of users L on the SDMA-OFDM system's BER performance. Here we observed that the BER curves associated with different numbers of users were within an SNR range of 2dB at a BER of 10^{-5}. This is an indication of the higher quality of the soft-bit estimates.

Our discussions in Section 4.3.1 were concluded in Section 4.3.1.5 with the aid of a complexity analysis of standard SIC, M-SIC and partial M-SIC, which were the topics of Sections 4.3.1.5.1, 4.3.1.5.2 and 4.3.1.5.3. Specifically, the associated complexity formulae of standard SIC, which reflect the number of complex multiplications and additions as well as real-valued comparisons and divisions were given by Equations 4.157, 4.158, 4.159 and 4.160, respectively. Furthermore, the corresponding complexity formulae of M-SIC were given by Equations 4.173, 4.174, 4.175 and 4.176, respectively. Based on these equations the different SIC detectors' complexities were graphically compared in Figure 4.19. Specifically at the left-hand side of Figure 4.19 we have plotted the number of complex multiplications, while at the right-hand side the number of real-valued comparisons required. We observed that standard SIC exhibits the lowest complexity, while M-SIC the highest complexity. A compromise in terms of both the achievable BER performance and the complexity imposed is achieved with the aid of the partial M-SIC scheme. In order to support our analysis, the corresponding numerical complexity values were provided in Table 4.5 for the standard SIC and the M-SIC.

4.3.2 PIC Detection

One of the key justifications for proposing SIC was that upon decreasing the number of users during the successive detection stages a higher grade of antenna array diversity potential can be dedicated by the MMSE combiner to the mitigation of the serious channel transfer factor fades, rather than to suppressing the interfering signal sources. Hence the highest array noise mitigation is achieved during the last SIC iteration, when after correct detection and subtraction of all the co-channel users' remodulated signals, the interference-free array output vector is constituted by the transmitted signal of the least dominant user plus an array noise contribution. The above interference cancellation principle - which was portrayed in the context of SIC in Section 4.3.1 - can be invoked also in form of a PIC scheme [114, 139].

The outline of this section is as follows. Our discussions commence in Section 4.3.2.1 with the

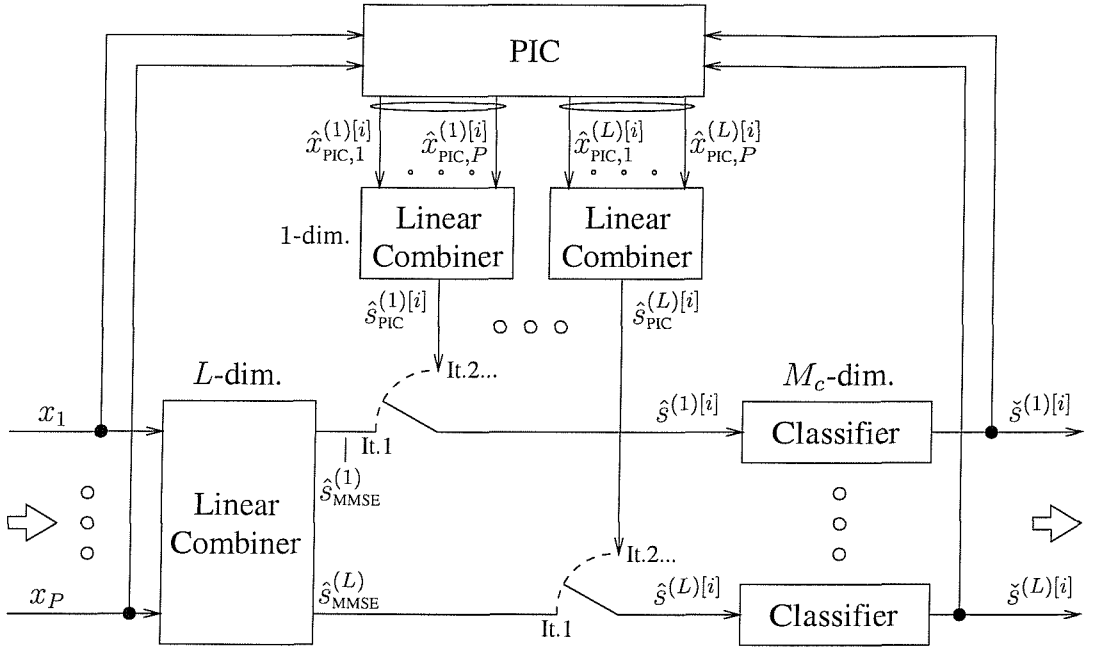

Figure 4.20: Illustration of the main signal paths associated with the hard-decision based PIC detector. The signals $x_p, p = 1, \ldots, P$ received by the different antenna elements are fed into the MMSE linear combiner described by Equations 4.185 and 4.186, which is active only during the first PIC detection stage. Furthermore, the signals $x_p, p = 1, \ldots, P$ are fed into the PIC module described by Equation 4.189, which is active for all PIC iterations associated with $i \geq 2$. The outputs $\check{s}^{(l)[i]}, l = 1, \ldots, L$ of the bank of M_c-ary symbol classifiers or demodulators obeying Equations 4.187 and 4.193 are then fed back to the PIC module seen at the top of the figure. According to Equation 4.189, P different signals $\hat{x}^{(l)[i]}_{\text{PIC},p}, p = 1, \ldots, P$, namely the potentially interference-free i.e. 'decontaminated' antenna output signals are available for the l-th user at the output of the PIC module, which are again linearly combined with the aid of Equations 4.191 and 4.192, in order to form the estimate $\hat{s}^{(l)[i]}_{\text{PIC}}$ of the signal transmitted by the l-th user, where $l = 1, \ldots, L$. Note that for the sake of visual clarity here we have omitted the signal paths associated with the channel transfer factor estimates required by the linear combiners and the PIC module. Also note than in our specific case the linear combiner employed is the MMSE combiner of Section 4.2.3

description of the PIC detector's structure in the context of an uncoded scenario, while in Section 4.3.2.2 the principles of turbo-coded PIC are discussed. This is followed in Section 4.3.2.3 by the analysis of its performance in both an uncoded- and a turbo-coded scenario, while in Section 4.3.2.4 the analysis of the detector's complexity is carried out. A summary and conclusions will be offered in Section 4.3.2.5.

4.3.2.1 Uncoded PIC

In this section we will highlight the PIC detector's structure, which is depicted in Figure 4.20. Let us commence our discussions upon recalling from Equation 4.1 the specific structure of the vector $\mathbf{x} \in \mathbb{C}^{P\times 1}$ of signals received by the different antenna elements, namely that we have:

$$\mathbf{x} = \mathbf{H}\mathbf{s} + \mathbf{n} \tag{4.183}$$

$$= \mathbf{H}^{(l)}s^{(l)} + \sum_{\substack{i=1 \\ i\neq l}}^{L} \mathbf{H}^{(i)}s^{(i)} + \mathbf{n}, \tag{4.184}$$

where again, $\mathbf{H} \in \mathbb{C}^{P\times L}$ is the channel transfer factor matrix, $\mathbf{s} \in \mathbb{C}^{L\times 1}$ is the composite multiuser vector of signals transmitted by the L different users and $\mathbf{n} \in \mathbb{C}^{P\times 1}$ is the vector of AWGN contributions encountered at the P different antenna elements. Specifically, from the component representation given by Equation 4.184 we observe that the array output vector $\mathbf{x}$ is composed of the l-th user's signal contribution vector and the $L-1$ interfering users' signal contribution vectors plus the AWGN vector. Hence, if initial estimates $\check{s}^{(i)}, i \in \{1,\ldots,L\} \setminus \{l\}$ of the interfering users' transmitted signals would be available, a noisy estimate $\hat{\mathbf{x}}^{(l)}$ of the l-th user's signal contribution could be obtained upon removing the $L-1$ interfering users' estimated signal contributions given by $\mathbf{H}^{(i)}\check{s}^{(i)}, i \in \{1,\ldots,L\} \setminus \{l\}$ from the vector $\mathbf{x}$ of signals received by the different antenna elements. An estimate $\hat{s}^{(l)}$ of the l-th user's transmitted signal could then be inferred by linear antenna diversity combining. The more specific processing steps of the PIC detector proposed here will be further detailed in the following sections with reference to Figure 4.20.

First-Stage - MMSE Detection

- *Combining*: During the first PIC iteration seen in Figure 4.20 each user is detected by means of the MMSE combiner, where the linear combiner's output vector $\hat{\mathbf{s}}_{\text{MMSE}} \in \mathbb{C}^{L\times 1}$ is given according to Equation 4.50 by:

$$\hat{\mathbf{s}}_{\text{MMSE}} = \mathbf{W}_{\text{MMSE}}^{[1]H}\mathbf{x}, \tag{4.185}$$

and the weight matrix $\mathbf{W}_{\text{MMSE}}^{[1]} \in \mathbb{C}^{L\times L}$ is given in its left-inverse related form according to Equation 4.68 as:

$$\mathbf{W}_{\text{MMSE}}^{[1]} = \mathbf{H}\mathbf{P}_{\text{SNR}}(\mathbf{H}^H\mathbf{H}\mathbf{P}_{\text{SNR}} + \mathbf{I})^{-1}, \tag{4.186}$$

where $\mathbf{P}_{\text{SNR}} \in \mathbb{C}^{L \times L}$ is the diagonal-shaped SNR matrix.

- *Classification/Demodulation*: Then the linear combiner's output vector $\hat{\mathbf{s}}^{[1]} = \hat{\mathbf{s}}_{\text{MMSE}}$ is demodulated, with the aid of the blocks seen at the bottom right-hand corner of Figure 4.20, resulting in the vector $\check{\mathbf{s}}^{[1]} \in \mathbb{C}^{L \times 1}$ of symbols that are most likely to have been transmitted by the L different users. More specifically, as shown in Section 4.2.4, the demodulation is carried out upon evaluating Equation 4.94, namely:

$$\check{s}^{(l)[1]} = arg \min_{\check{s}/\sigma_l \in \mathcal{M}_c} \left| \frac{1}{H_{\text{eff}}^{(l)[1]}} \hat{s}^{(l)[1]} - \check{s} \right|^2, \; l = 1, \ldots, L, \tag{4.187}$$

where the l-th user's effective channel transfer factor $H_{\text{eff}}^{(l)[1]}$ is given by:

$$H_{\text{eff}}^{(l)[1]} = \mathbf{w}_{\text{MMSE}}^{(l)[1]} \mathbf{H}^{(l)}, \tag{4.188}$$

and the l-th user's weight vector $\mathbf{w}_{\text{MMSE}}^{(l)[1]}$ is the l-th column vector of the weight matrix $\mathbf{W}_{\text{MMSE}}^{[1]}$. Equation 4.187 implies calculating the Euclidean distance between each of the normalized elements[19] of the combiner's output vector $\hat{\mathbf{s}}^{[i]}$ namely, $\hat{s}^{(l)[i]}, l = 1, \ldots, L$, and all of the legitimate trial-symbols, which are the amplified constellation points contained in the set $\mathcal{M}_c$, associated with the specific modulation scheme employed. According to the ML principle that specific trial-symbol is retained as the most likely transmitted one for the l-th user, which exhibits the smallest Euclidean distance from the combiner's normalized output signal $\hat{s}^{(l)}$. However, as argued in Section 4.2.4, this decision principle is based on the assumption, that the residual interference contaminating the combiner's output signal is also Gaussian, which in general is not the case. Hence the demodulation principle formulated according to Equation 4.187 is sub-optimum.

i-th Stage: PIC Detection

- *Parallel Interference Cancellation*: During the i-th PIC iteration seen in Figure 4.20, where $i \geq 2$ a potentially improved estimate $\hat{s}_{\text{PIC}}^{(l)[i]}$ of the complex symbol $s^{(l)}$ transmitted by the l-th user is obtained upon subtracting in a first step the $L-1$ interfering users' estimated signal contributions, from the original vector $\mathbf{x}$ of signals received by the different antenna elements, which can be expressed as:

$$\hat{\mathbf{x}}_{\text{PIC}}^{(l)[i]} = \mathbf{x} - \sum_{\substack{j=1 \\ j \neq l}}^{L} \mathbf{H}^{(j)} \check{s}^{(j)[i-1]}. \tag{4.189}$$

This operation takes place within the PIC block shown at the top of Figure 4.20. Provided that correct tentative symbol decisions were made during the previous detection stage, namely we

[19]The normalization is not necessary in the context of employing MPSK modulation schemes in the absence of turbo-decoding.

have $\check{s}^{(j)[i-1]} = s^{(j)}, j \in \{1, \ldots, L\} \setminus \{l\}$ for the $L-1$ interfering users, the estimated array output vector $\hat{\mathbf{x}}_{\text{PIC}}^{(l)[i]} \in \mathbb{C}^{P \times 1}$ will only consist of the l-th user's namely the desired user's signal contribution vector $\mathbf{H}^{(l)} s^{(l)}$ plus the AWGN vector $\mathbf{n}$, which is expressed as:

$$\hat{\mathbf{x}}_{\text{PIC}}^{(l)[i]} = \mathbf{H}^{(l)} s^{(l)} + \mathbf{n} \quad \wedge \check{s}^{(j)[i-1]} = s^{(j)}, j \in \{1, \ldots, L\} \setminus \{l\}. \tag{4.190}$$

- *Combining*: The final task is hence to extract an estimate $\hat{s}_{\text{PIC}}^{(l)[i]}$ of the signal $s^{(l)}$ transmitted by the l-th user from the l-th user's PIC-related array output vector $\hat{\mathbf{x}}_{\text{PIC}}^{(l)[i]}$. This can be achieved upon invoking once again the left-inverse related MMSE combiner, seen below the PIC block at the top of Figure 4.20, whose associated weight matrix was given by Equation 4.186 for the more general case of detecting L users. As observed in Equation 4.190, the signal vector $\hat{\mathbf{x}}_{\text{PIC}}^{(l)[i]}$ at the output of the PIC block at the top of Figure 4.20 is now potentially free of interference. Hence the channel transfer factor matrix $\mathbf{H}$ and the SNR matrix $\mathbf{P}_{\text{SNR}}$ defined in Equation 4.65, which are integral parts of the MMSE-related weight matrix according to Equation 4.186, have to be substituted by the l-th user's related components namely, by $\mathbf{H}^{(l)}$ and $\text{SNR}^{(l)} = \frac{\sigma_l^2}{\sigma_n^2}$. This results in the weight vector $\mathbf{w}_{\text{MMSE}}^{(l)[i]}$, given by:

$$\mathbf{w}_{\text{MMSE}}^{(l)[i]} = \frac{\mathbf{H}^{(l)}}{||\mathbf{H}^{(l)}||_2^2 + \frac{1}{\text{SNR}^{(l)}}}. \tag{4.191}$$

With the aid of the weight vector of Equation 4.191 an estimate $\hat{s}^{(l)[i]} = \hat{s}_{\text{PIC}}^{(l)[i]}$ of the l-th user's transmitted signal $s^{(l)}$ can then be extracted from the vector $\hat{\mathbf{x}}_{\text{PIC}}^{(l)[i]}$ seen at the output of the linear MMSE combiner in the centre of Figure 4.20 - similarly to Equation 4.185 - as follows:

$$\hat{s}_{\text{PIC}}^{(l)[i]} = \mathbf{w}_{\text{MMSE}}^{(l)[i]H} \hat{\mathbf{x}}_{\text{PIC}}^{(l)[i]}. \tag{4.192}$$

- *Classification/Demodulation*: The above PIC and MMSE-combining steps are again followed by the classification, demodulation stage seen at the right of Figure 4.20, which obeys:

$$\check{s}^{(l)[i]} = arg \min_{\check{s}/\sigma_l \in \mathcal{M}_c} \left| \frac{1}{H_{\text{eff}}^{(l)[i]}} \hat{s}^{(l)[i]} - \check{s} \right|^2, \; l = 1, \ldots, L, \tag{4.193}$$

where the l-th user's effective channel transfer factor $H_{\text{eff}}^{(l)[i]}$ is given by:

$$H_{\text{eff}}^{(l)[i]} = \mathbf{w}_{\text{MMSE}}^{(l)[i]} \mathbf{H}^{(l)}. \tag{4.194}$$

In other words, Equation 4.193 delivers the symbol $\check{s}^{(l)[i]}$ that is most likely to have been transmitted by the l-th user. The i-th PIC iteration described above potentially has to be performed for all the different SDMA users namely, for $l = 1, \ldots, L$.

description	instruction
First-Stage - MMSE Det.	
Calc. MMSE weight matrix	$\mathbf{W}_{\text{MMSE}}^{[1]} = \mathbf{H}\mathbf{P}_{\text{SNR}}(\mathbf{H}^H\mathbf{H}\mathbf{P}_{\text{SNR}} + \mathbf{I})^{-1} \in \mathbb{C}^{P\times L}$
Detection	$\hat{\mathbf{s}}_{\text{MMSE}} = \mathbf{W}_{\text{MMSE}}^{[1]H}\mathbf{x} \in \mathbb{C}^{L\times 1}, \quad \hat{s}^{(l)[1]} = \hat{s}_{\text{MMSE}},\ l = 1,\ldots,L$
Demodulation, $l = 1,\ldots,L$	$\check{s}^{(l)[1]} = arg \min_{\check{s}/\sigma_l\in\mathcal{M}_c} \left\lvert \frac{1}{H_{\text{eff}}^{(l)[1]}}\hat{s}^{(l)[1]} - \check{s}\right\rvert^2, H_{\text{eff}}^{(l)[1]} = \mathbf{w}_{\text{MMSE}}^{(l)[1]}\mathbf{H}^{(l)}$
i-th Stage - PIC ($l = 1,..,L$)	
Subtraction	$\hat{\mathbf{x}}_{\text{PIC}}^{(l)[i]} = \mathbf{x} - \sum_{\substack{j=1\\ j\neq l}}^{L} \mathbf{H}^{(j)}\check{s}^{(j)[i-1]} \in \mathbb{C}^{P\times 1}$
Calc. MMSE weight vectors	$\mathbf{w}_{\text{MMSE}}^{(l)[i]} = \frac{\mathbf{H}^{(l)}}{\lvert\lvert\mathbf{H}^{(l)}\rvert\rvert_2^2 + \frac{1}{\text{SNR}^{(l)}}} \in \mathbb{C}^{P\times 1}$
Detection	$\hat{s}_{\text{PIC}}^{(l)[i]} = \mathbf{w}_{\text{MMSE}}^{(l)[i]H}\hat{\mathbf{x}}_{\text{PIC}}^{(l)[i]}, \quad \hat{s}^{(l)[i]} = \hat{s}_{\text{PIC}}^{(l)[i]}$
Demodulation	$\check{s}^{(l)[i]} = arg \min_{\check{s}/\sigma_l\in\mathcal{M}_c} \left\lvert \frac{1}{H_{\text{eff}}^{(l)[i]}}\hat{s}^{(l)[i]} - \check{s}\right\rvert^2, H_{\text{eff}}^{(l)[i]} = \mathbf{w}_{\text{MMSE}}^{(l)[i]H}\mathbf{H}^{(l)}$

Table 4.7: Summary of the standard hard-decision based PIC detector.

We have summarized the steps of the PIC algorithm once again in Table 4.7, while the schematic of the PIC detector was provided in Figure 4.20. Note however that for the sake of visual clarity in the context of this simplified schematic we have omitted the signal paths associated with the channel transfer factor estimates required by the linear combiners and within the PIC module.

4.3.2.2 Turbo-Coded PIC

In the context of our investigations concerning uncoded PIC detection assisted SDMA-OFDM in Section 4.3.2.3.1 we will highlight that the system's relatively poor performance compared to that of uncoded SIC detection-assisted SDMA-OFDM, discussed in Section 4.3.1.4.1, is related to the effects of 'error propagation' *between the different users' symbol estimates* during the second PIC detection stage. This is, because if amongst the L different users' tentative symbol decisions made during the first PIC stage there is a specific subcarrier, which has an unreliable tentative symbol decision while all the $L-1$ remaining users' tentative symbol decisions are relatively reliable, then after the second PIC detection stage all of these $L-1$ users' symbol decisions will become potentially unreliable. By contrast, the single user's tentative symbol decision, which was unreliable after the first detection stage is expected to become more reliable.

In Sections 4.2.6.4 and 4.3.1.4.7 we demonstrated in the context of both MMSE- and SIC detection-assisted SDMA-OFDM that turbo-decoding at the receiver is a powerful means of further enhancing the system's BER performance. Specifically, the turbo-decoder was incorporated into the system by simply feeding the demodulator's soft-bit output into the turbo-decoder. Recall that the generation of the soft-bits required for turbo-decoding was discussed earlier in Section 4.2.5 and 4.3.1.3, respectively. In the context of the associated simulations four turbo decoding iterations were performed

by the turbo-decoder, followed by slicing or hard-decision of the turbo-decoder's 'source'-related soft-output bits. Here we note explicitly that the turbo-iterations were entirely performed within the turbo-decoder, without invoking again the system's remaining components. The turbo coding parameters were summarized in Table 4.4.

Similarly to the MMSE and SIC schemes, in order to enhance the BER performance of PIC detection-assisted SDMA-OFDM a trivial approach would be to feed the turbo-decoder with the demodulator's soft-bit output after the PIC detection process and again, to perform a number of iterations within the turbo-decoder, followed by slicing the turbo-decoder's 'source'-related soft-output bits. However, recall our observation that for some users the reliability of the second PIC detection stage's symbol decisions might be degraded compared to that of the first PIC detection stage due to feeding potentially unreliable tentative symbol decisions into the second PIC detection stage. Hence it is potentially beneficial to embed the turbo-decoding into the PIC detection process. To be more specific, after the first detection stage - based on the different users' soft-bit values derived from the associated MMSE combiner's output signals, as it was demonstrated in Section 4.2.5, only a fraction of the total number of turbo-decoding iterations is performed. A reference signal is then generated upon slicing and remodulating the turbo-decoder's 'source- plus parity'-related *a posteriori* soft-output bits for the following second PIC detection stage. Our experiments revealed that it is less effective to slice, *reencode* and remodulate only the 'source'-related *a posteriori* soft-output bits. After the second PIC detection stage, again, soft-bits would again be generated, which are fed into the turbo-decoder, followed by a number of turbo-iterations and a final slicing of the 'source'-related soft-output bits. These constitute the PIC receiver's output bits. Alternatively, further PIC iterations could be performed, but in the context of the hard-decision- or slicing based PIC scheme employed here no additional performance gain was observed.

A further BER performance improvement can potentially be achieved upon feeding soft-bit values, rather than sliced bits, into the second PIC detection stage following the concepts of turbo-equalization [139] instead of the hard-decision based remodulated reference signals.

4.3.2.3 Performance Analysis

In this section the PIC algorithm will be investigated with respect to its BER performance in both a scenario without channel coding, as well as a scenario where turbo-coding is employed. Specifically, the interference cancellation process carried out during the PIC detector's second stage will be shown to benefit from the less error-contaminated first stage tentative symbol decisions. Again, the frame-invariant fading indoor WATM channel model and its associated OFDM system model described in Section 6.1.1 were invoked and ideal knowledge of the channel transfer functions associated with the different transmit-receive antenna pairs was assumed. For a summary of the basic simulation setup we refer again to Table 4.3.

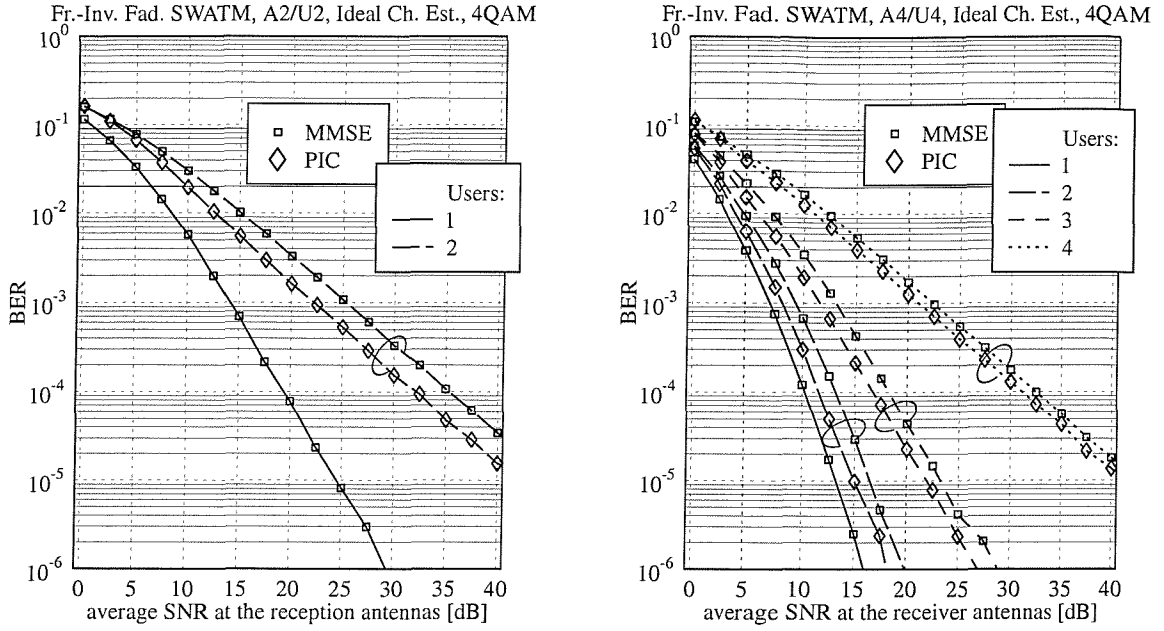

Figure 4.21: BER performance of 4QAM-modulated, PIC detection-assisted SDMA-OFDM as a function of the SNR encountered at the reception antennas for (left:) $P = 2$ reception antennas and up to $L = 2$ simultaneous users and (right:) $P = 4$ reception antennas and up to $L = 4$ simultaneous users; additionally, we have plotted the BER performance of MMSE detection-assisted SDMA-OFDM; for the basic simulation parameters we refer to Table 4.3.

The further structure of Section 4.3.2.3 is as follows. While in Section 4.3.2.3.1 the PIC detection assisted SDMA-OFDM system's BER performance is considered without employing channel coding, our simulation results for the turbo-coded scenario will be discussed in Section 4.3.2.3.2.

4.3.2.3.1 BER Performance of Uncoded PIC Detection-Assisted SDMA-OFDM for Different Numbers of Users and Receiver Antennas In Figure 4.21 we have portrayed the BER- as well as the SER performance of 4QAM-modulated PIC detection-assisted SDMA-OFDM as a function of the SNR encountered at the reception antennas. Specifically, in the context of the curves shown at the left-hand side of Figure 4.21 $P = 2$ reception antennas and up to $L = 2$ simultaneous users were assumed. By contrast, the curves at the right-hand side of Figure 4.21 characterize the scenario of $P = 4$ reception antennas supporting up to $L = 4$ simultaneous users. The MMSE detection-related BER performance curves, which were shown earlier in Figure 4.8 have again been plotted as a reference. We observe that upon increasing the SNR, the PIC detection-assisted system's BER performance exhibits the same trends as that of the MMSE detector, although a specific BER

performance is achieved at consistently lower SNRs. The highest SNR gain achievable with the advent of employing PIC detection compared to MMSE detection is approximately 3.03dB at a BER of 10^{-4}, which was observed here for the basic SDMA scenario of $P = 2$ reception antennas and $L = 2$ simultaneous users (A2/U2). By contrast, for the higher-order SDMA scenario of $P = 4$ reception antennas the highest SNR gain of 1.61dB is observed for $L = 2$ simultaneous users namely, while for $L = 3$ and $L = 4$ users the SNR gains are approximately 1.43dB and 1.25dB, again, at a BER of 10^{-4}. The reason for the reduction of the SNR gain along with increasing the number of simultaneous users L is, because upon supporting more users the probability of an erroneous first-stage tentative symbol decision among one of the users is increased. Hence also the users benefitting from correct tentative symbol decisions during the first detection stage are more likely to be corrupted. As mentioned before, in an effort to render the first-stage tentative symbol decisions more reliable, channel coding can be employed. Hence, in the next section we will concentrate our attention on characterizing the PIC detection-assisted system's BER performance in a turbo-coded scenario.

4.3.2.3.2 BER Performance of Turbo-Coded PIC Detection-Assisted SDMA-OFDM for Different Numbers of Users and Receiver Antennas As demonstrated in Sections 4.2.6.4 and 4.3.1.4.7 in the context of turbo-coded MMSE- and SIC detection-assisted SDMA-OFDM, employing turbo-decoding at the receiver is a powerful means of further enhancing the system's BER performance. Again, this is achieved at the cost of reducing the system's effective throughput and by imposing additional computational complexity.

In the context of PIC detection-assisted SDMA-OFDM we conjectured in Section 4.3.2.2 that instead of simply concatenating PIC detection and turbo-decoding as we did in the case of turbo-coded MMSE- or SIC detection-assisted SDMA-OFDM, it is potentially more beneficial to embed the turbo-decoding into the PIC detection process. As a result, a set of more accurate remodulated reference signals can be obtained for the second PIC detection stage.

More explicitly, a fraction of the total number of affordable turbo-decoding iterations would be performed after the first PIC detection stage, while the rest of the turbo iterations is carried out during the second PIC detection stage. More explicitly, in order to render the associated BER performance results comparable to those of turbo-coded MMSE-, SIC and ML detection-assisted SDMA-OFDM presented in Sections 4.2.6.4, 4.3.1.4.7 and 4.3.3.4.2, respectively, it is useful to split the total number of turbo iterations available between the turbo-decoding conducted after the first- and the second PIC detection stage. Since four turbo iterations were employed in our previous investigations, a plausible choice is to assign two iterations to both the first- and the second PIC detection stage. An equal splitting of the number of turbo iterations is also motivated by the observation that the most significant BER improvement due to turbo decoding is achieved during the first few turbo-decoding iterations.

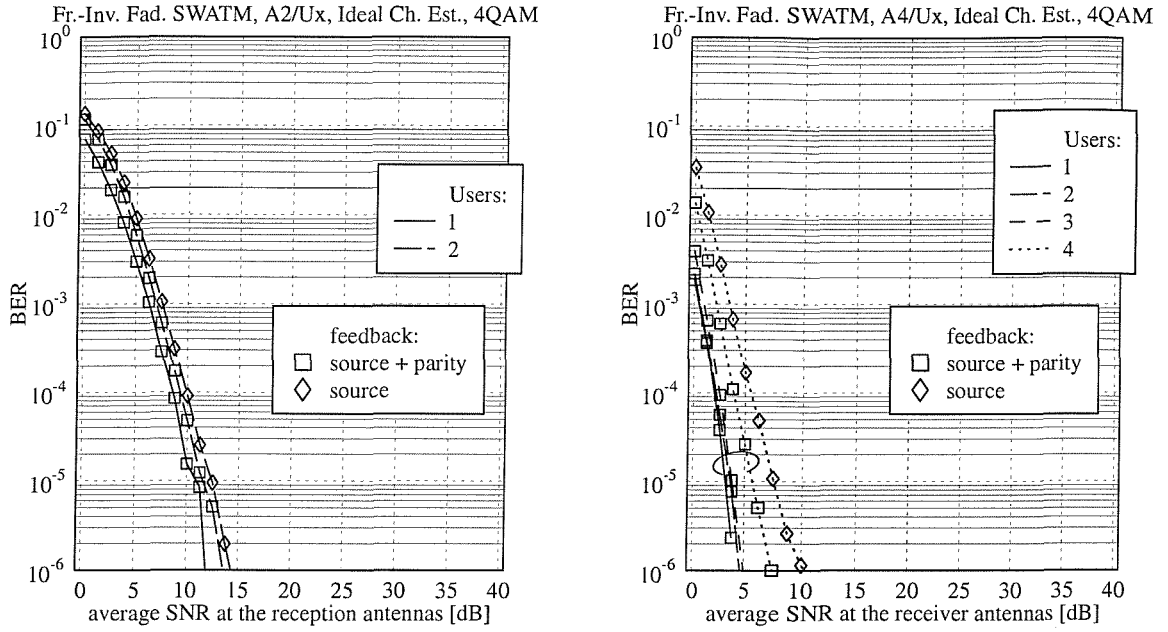

Figure 4.22: BER performance of turbo-coded, 4QAM-modulated, PIC detection-assisted SDMA-OFDM as a function of the SNR recorded at the reception antennas for (left:) $P = 2$ reception antennas and up to $L = 2$ simultaneous users and (right:) $P = 4$ reception antennas and up to $L = 4$ simultaneous users. Two methods of generating the remodulated reference signal were employed by the PIC module of Figure 4.20, namely a 'source'- related *a posteriori* soft-output based reference and a 'source- plus parity'-related *a posteriori* soft-output based reference. For the list of basic simulation parameters we refer to Table 4.3.

The other relevant turbo coding parameters were summarized in Table 4.4, but for the reader's convenience they are repeated: the coding rate was $R_c = \frac{1}{2}$, the constraint length was $K_c = 3$, and octally represented generator polynomials of $(7, 5)_8$ were used. Again, a total of four turbo iterations was performed.

Our BER simulation results are portrayed in Figure 4.22 at the left-hand side for $P = 2$ reception antennas, while at the right-hand side for $P = 4$ reception antennas, when supporting up to $L = P$ number of users. Two methods of generating the remodulated reference- or reconstructed received signal used in the PIC module of Figure 4.20 are compared against each other. Specifically in the first case we used slicing, reencoding, interleaving and remodulating only for the 'source'-related *a posteriori* soft-output bits, while in the second scenario we employed slicing, interleaving and remodulating for the 'source- plus parity'-related *a posteriori* soft-output bits of the turbo-decoder. As expected, compared to the uncoded scenario, whose associated simulation results were shown

in Figure 4.21, the BER is significantly reduced for both methods of generating the remodulated reference signal. However, for the 'source- plus parity' related remodulated reference signal of the second scenario a performance advantage of about 1.8dB was observed in Figure 4.22 at a BER of 10^{-5} compared to the 'source'-related reference based scenario. In general, note the significant BER performance difference in favour of the scenario of four reception antennas and three simultaneous users, compared to supporting four simultaneous users. The explanation of this phenomenon is that in the scenario supporting a lower number of users the tentative symbol decisions provided by the first PIC detection stage are more reliable. This is a result of the higher relative diversity order encountered by the MMSE combiner, which constitutes the first detection stage of the PIC process, as argued in Section 4.3.2.1. Hence the effects of 'error propagation' between the different users' signals during the second PIC detection stage are reduced.

4.3.2.4 Complexity Analysis

In this section we will analyse the complexity exhibited by the PIC detector described in Section 4.3.2.1, which was also summarized in Table 4.7. We will consider each step of Section 4.3.2.1 and Table 4.7 in terms of the associated complexity.

First-Stage - MMSE Detection:

- *Combining*: In the standard PIC algorithm of Section 4.3.2.1 the MMSE-related weight matrix $\mathbf{W}_{\text{MMSE}}^{[1]}$ to be employed for detection during the first PIC iteration does not explicitly have to be made available. Hence, according to Equations 4.104, 4.105 and 4.106 an initial estimate $\hat{\mathbf{s}}^{[1]}$ of the vector $\mathbf{s}$ of signals transmitted by the different users can be obtained, which imposes a computational complexity quantified in terms of the number of complex multiplications and additions, as follows:

$$C_{\text{PIC,direct}}^{[1](\mathbb{C}*\mathbb{C})} = C_{\text{PIC,direct}}^{[1](\mathbb{C}+\mathbb{C})} = PL + (P+1)L^2 + \frac{1}{3}L^3 \tag{4.195}$$

$$C_{\text{PIC,direct}}^{[1](\mathbb{R}*\mathbb{C})} = PL \tag{4.196}$$

$$C_{\text{PIC,direct}}^{[1](\mathbb{R}+\mathbb{C})} = L. \tag{4.197}$$

- *Demodulation*: Furthermore, the demodulation operation carried out during the first PIC iteration, which follows the philosophy of Equation 4.187, imposes a computational complexity of:

$$C_{\text{PIC,dem}}^{[1](\mathbb{C}*\mathbb{C})} = \frac{1}{2}LM_c \tag{4.198}$$

$$C_{\text{PIC,dem}}^{[1](\mathbb{C}+\mathbb{C})} = C_{\text{PIC,dem}}^{[1](\mathbb{R}\lesseqgtr\mathbb{R})} = LM_c, \tag{4.199}$$

where M_c is the number of constellation points contained in the set $\mathcal{M}_c$. Note that the number of complex multiplications has been weighted by a factor of $\frac{1}{2}$ in order to account for the

reduced complexity associated with calculating the product between a complex number and its conjugate complex value in the context of the Euclidean distance metric evaluation of Equation 4.187.

Second-Stage - PIC Detection:

- *Parallel Interference Cancellation*: As observed in Table 4.7 the second PIC iteration commences by the operation of parallel interference cancellation, described by Equation 4.189, which is associated with a complexity of:

$$C_{\text{PIC,sub}}^{[2](\mathbb{C}*\mathbb{C})} = LP \tag{4.200}$$

$$C_{\text{PIC,sub}}^{[2](\mathbb{C}+\mathbb{C})} = L(\log_2 L)P. \tag{4.201}$$

Here we have assumed that the parallel subtraction based interference cancellation is organized in form of a binary tree. This reduces the complexity $C_{\text{PIC,sub}}^{[2](\mathbb{C}+\mathbb{C})}$ from originally $L(L-1)P$ complex additions associated with a linear implementation to that of $L(\log_2 L)P$.

- *Combining*: The operation of combining was described by Equations 4.191 and 4.192. A complexity reduction is achieved, when employing constant-modulus M-PSK modulation schemes. Then it is sufficient to perform the combining of the different users' associated signals by multiplying them with the Hermitian transpose of their associated channel vectors, which results in:

$$C_{\text{PIC,cmb-MPSK}}^{[2](\mathbb{C}*\mathbb{C})} = C_{\text{PIC,cmb-MPSK}}^{[2](\mathbb{C}+\mathbb{C})} = PL. \tag{4.202}$$

By contrast, in the more general case of QAM modulation schemes it can be shown that we have:

$$C_{\text{PIC,cmb-QAM}}^{[2](\mathbb{C}*\mathbb{C})} = \frac{3}{2}LP \tag{4.203}$$

$$C_{\text{PIC,cmb-QAM}}^{[2](\mathbb{C}+\mathbb{C})} = 2LP \tag{4.204}$$

$$C_{\text{PIC,cmb-QAM}}^{[2](\mathbb{R}/\mathbb{C})} = C_{\text{PIC,cmb-QAM}}^{[2](\mathbb{R}+\mathbb{R})} = L, \tag{4.205}$$

where the number of complex multiplications inflicted by calculating the Euclidean norm $||\mathbf{H}^{(l)}||_2^2$ has, again, been weighted by a factor of $\frac{1}{2}$ in order to account for the reduced complexity of calculating the product of a complex number with its conjugate complex value.

- *Demodulation*: In a final step, the different users' estimated signals are again demodulated according to Equation 4.193, which requires a computational complexity of:

$$C_{\text{PIC,dem}}^{[2](\mathbb{C}*\mathbb{C})} = \frac{1}{2}LM_c \tag{4.206}$$

$$C_{\text{PIC,dem}}^{[2](\mathbb{C}+\mathbb{C})} = C_{\text{PIC,dem}}^{[2](\mathbb{R}\lesseqgtr\mathbb{R})} = LM_c. \tag{4.207}$$

Hence, upon combining the different implementational complexity contributions we obtain the following expression for the total computational complexity:

$$C_{\text{PIC}}^{\mathbb{C}*\mathbb{C}} = LM_c + 5PL + (P+1)L^2 + \frac{1}{3}L^3 \quad (4.208)$$

$$C_{\text{PIC}}^{\mathbb{C}+\mathbb{C}} = 2L(M_c + \frac{1}{2}) + (4 + \log_2 L)PL + (P+1)L^2 + \frac{1}{3}L^3 \quad (4.209)$$

$$C_{\text{PIC}}^{\mathbb{R}\lessgtr\mathbb{R}} = 2LM_c \quad (4.210)$$

$$C_{\text{PIC}}^{\mathbb{R}/\mathbb{C}} = L, \quad (4.211)$$

where again, mixed real-complex multiplications and additions as well as real additions were assumed to have half the complexity of those, which involve complex numbers[20].

4.3.2.5 Summary and Conclusions on PIC Detection

In Section 4.3.2.5 PIC assisted detection of SDMA-OFDM was introduced and characterized with respect to its BER performance in the context of both uncoded and turbo-coded scenarios. Furthermore, its complexity was analysed.

The employment of PIC detection was motivated by two observations. In Section 4.3.1.6 we found that SIC based detection is capable of significantly outperforming MMSE detection in terms of the system's BER performance. This was a result of increasing the system's diversity order by successively removing the already detected users' remodulated signal contributions from the vector $\mathbf{x}$ of composite multiuser signals received by the different BS antenna elements. A substantial computational complexity was associated with the calculation of the linear combiner's weight matrix at each detection stage according to Equation 4.121, and with the calculation of the remaining users' SINRs according to Equation 4.122, which was followed by the selection of the most dominant user according to Equation 4.123. Hence, in our quest for alternative, potentially less complex detection techniques, PIC detection was considered.

As shown in the PIC detector's block diagram of Figure 4.20 and as described in Section 4.3.2.1, during the first PIC iteration linear MMSE estimates of the different users' transmitted signals were generated with the aid of a linear combiner, obeying Equations 4.185 and 4.186. These linear estimates seen in Figure 4.20 were demodulated, as shown in Equation 4.187, and employed in the context of the PIC module seen at the bottom left corner of Figure 4.20 as a reference for reconstructing the different users' transmitted signal contributions. A potentially more accurate estimate of the l-th user's transmitted signal, where $l = 1, \ldots, L$, was then generated during the next PIC iteration by subtracting the $L-1$ remaining users' reconstructed signal contributions from the vector $\mathbf{x}$ of received composite multiuser signals as suggested by Equation 4.189. These operations were followed by diversity combining, obeying Equations 4.191 and 4.192 and demodulation, described

[20]Here we have again neglected that no real-valued additions are required in the context of real-complex multiplications and hence our calculation produces an upper-bound estimate of the complexity imposed

by Equation 4.193, in order to obtain the specific constellation point that is most likely to have been transmitted. Provided that correct tentative symbol decisions were made for all the $L-1$ remaining users in the previous PIC iteration, an improved linear MMSE estimate of the l-th user's transmitted signal would become available at the associated demodulator's input. This procedure has to be invoked for all the L different users. These processing steps were also summarized in Table 4.7 and in Figure 4.20.

Motivated by the PIC detector's relatively limited BER improvement compared to MMSE detection in the context of an uncoded scenario, in Section 4.3.2.2 we proposed to embed turbo-decoding into the PIC iteration, instead of simply concatenating the PIC detector and the turbo-decoder. As a result of this embedded turbo-decoding operation we expected to reduce the effects of 'error-propagation' in the PIC module of Figure 4.20. In these experiments soft-bits were generated for turbo-decoding as it was described in Section 4.2.5 in the context of MMSE detection. This procedure was similar to the single-user scenario. Hence, there still remains some potential for further further improvement. In the context of turbo-decoding a sliced reference was generated for employment in the PIC module, which was the result of performing hard-decisions on the turbo-decoder's 'source'-related soft-output bits followed by reencoding. An alternative strategy was that of performing hard-decisions on both the 'source'- and the 'parity'-related soft-output bits, which was shown in our performance investigations in Section 4.3.2.3.2 to be advantageous.

Our BER performance studies were conducted in Section 4.3.2.3. Specifically, Figure 4.21 characterized an uncoded scenario, while Figure 4.22 was recorded in the context of a turbo-coded scenario, again upon portraying the influence of the number of users L and the number of reception antennas P. For the uncoded scenario the SNR performance improvement compared to a system employing MMSE detection was at most 3.03dB, in a scenario of $L = P = 2$, while for a scenario of $L = P = 4$ the corresponding gain was at least 1.25dB. For a turbo-coded scenario the SNR improvement was more substantial. This will be further detailed in the context of our final comparison of all the different detectors in Section 4.3.4.1.

In order to conclude our discussions, the computational complexity imposed by PIC detection was analysed in Section 4.3.2.4, which resulted in Equations 4.208, 4.209 and 4.210, describing the number of complex multiplications and additions, as well as real-valued comparisons. These equations were invoked in our graphical portrayal of the different detectors' implementational complexities in Section 4.3.4.2.

4.3.3 ML Detection

In this section we will outline the philosophy of the Maximum Likelihood (ML) detector [114, 53, 117, 131, 132, 133, 134, 135, 136, 138], which is optimum from a statistical point of view. An associated disadvantage is its potentially excessive computational complexity, which results from

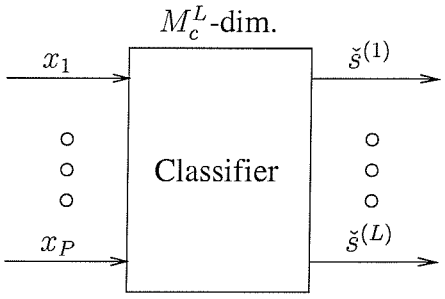

Figure 4.23: Representation of the optimum ML detector. In contrast to the sub-optimum linear- and non-linear detectors, namely LS and MMSE discussed in Sections 4.2.2 and 4.2.3, respectively, as well as SIC and PIC discussed in Sections 4.3.1 and 4.3.2, respectively, the L different users' complex symbols most likely transmitted are *jointly* detected. This is achieved upon evaluating the M_c^L number of trial-symbols in terms of their multi-user Euclidean distance metric with respect to the vector $\mathbf{x}$ of the signals received by the different antenna elements, namely Equation 4.223. A disadvantage is the associated computational complexity, which might be excessive.

the strategy of jointly detecting the L different users. This implies assessing the M_c^L possible combinations of symbols transmitted by the L different users by evaluating their Euclidean distance from the received signal, upon taking into account the effects of the channel. The stylized ML detector has once again been portrayed in Figure 4.23.

The structure of this section is as follows. In Section 4.3.3.1 the philosophy of standard ML detection will be portrayed. In scenarios, where the number of users L is lower than the number of reception antennas P, a complexity reduction can be achieved by transforming the vector of composite multiuser signals received by the different antenna elements first to the so-called 'trial-space' with the aid of a linear transform, as it will be discussed in Section 4.3.3.2. In an attempt to further enhance the system's BER performance turbo-coding can be invoked. The generation of the soft-bit information required will be discussed in Section 4.3.3.3, where a further reduction of the computational complexity can be achieved by applying the well-known maximum approximation. Our BER performance investigation will be conducted in Section 4.3.3.4 for both uncoded as well as turbo-coded scenarios. Furthermore, estimates of the computational complexity imposed will be provided in Section 4.3.3.5. A summary and conclusions will be offered in Section 4.3.3.6

4.3.3.1 Standard ML Detection

The structure of our discussions on the ML detector is as follows. In Section 4.3.3.1.1 the vector $\mathbf{x}$ of received signals is interpreted as a manifestation of a multi-variate complex Gaussian distribution function $f(\mathbf{x}|\check{\mathbf{s}}, \mathbf{H})$, which reflects the *a priori* probability that the vector $\mathbf{x}$ was received. Furthermore, in Section 4.3.3.1.2 it will be shown that determining the desired vector of symbols $\check{\mathbf{s}}_{\text{ML}}$ that is most likely to have been transmitted by the L different users is equivalent to maximizing

the transmitted symbols' *a posteriori* probability. However, it will be demonstrated with the aid of the Bayes theorem [87] that this is equivalent to maximizing the *a priori* probability, which again, is available in terms of the Gaussian distribution function.

4.3.3.1.1 Representation of the Vector of Received Signals as a Sample of a Multi-Variate Complex Gaussian Distribution Function In order to commence our discussions, let us recall from Equation 4.1 the definition of the vector $\mathbf{x}$ of signals received by the P different antenna elements, namely that we have:

$$\mathbf{x} = \mathbf{Hs} + \mathbf{n}, \tag{4.212}$$

where again, we have omitted the index $[n, k]$, which denotes the k-th subcarrier of the n-th OFDM symbol. We observe that $\mathbf{x} \sim \mathcal{CN}(\mathbf{Hs}, \mathbf{R_n})$, namely $\mathbf{x}$ is a sample of an L-dimensional multi-variate complex Gaussian distribution, having a vector of mean values given by $\mathbf{Hs}$ and a covariance matrix of $\mathbf{R_n} \in \mathbb{C}^{P \times P}$, where the latter is given by:

$$\begin{aligned} \mathbf{R_n} &= E\{\mathbf{n}\mathbf{n}^H\} && (4.213) \\ &= \sigma_n^2 \mathbf{I}, && (4.214) \end{aligned}$$

implying that the different noise contributions are assumed to be uncorrelated. This multi-variate complex Gaussian distribution function can be expressed as [142]:

$$\begin{aligned} f(\mathbf{x}|\mathbf{s}, \mathbf{H}) &= \frac{1}{\pi^P |\mathbf{R_n}|} \exp\left(-(\mathbf{x} - \mathbf{Hs})^H \mathbf{R_n}^{-1} (\mathbf{x} - \mathbf{Hs})\right) && (4.215) \\ &= \frac{1}{\pi^P (\sigma_n^2)^P} \exp\left(-\frac{1}{\sigma_n^2} ||\mathbf{x} - \mathbf{Hs}||_2^2\right), && (4.216) \end{aligned}$$

where Equation 4.216 was obtained by substituting Equation 4.214 into Equation 4.215. The representation of the complex Gaussian distribution function is legitimate, since again, the noise at the different receiver antenna elements is assumed to be uncorrelated. More explicitly, $P(\mathbf{x}|\mathbf{s}, \mathbf{H}) = f(\mathbf{x}|\mathbf{s}, \mathbf{H})$ denotes the *a priori* probability that the vector $\mathbf{x}$ has been received by the BS antenna elements under the condition that the vector $\mathbf{s}$ was transmitted by the different users over a channel characterized by the matrix $\mathbf{H}$.

4.3.3.1.2 Determination of the Vector of Transmitted Symbols by Maximizing the *A Posteriori* Probability In simple verbal terms the ML detector finds the specific L-dimensional vector of M_c-ary symbols, which is most likely to have been transmitted. In more formal terms ML detection is based on the idea of maximizing the *a posteriori* probability $P(\check{\mathbf{s}}|\mathbf{x}, \mathbf{H})$ that the specific vector $\check{\mathbf{s}} \in \mathbb{C}^{L \times 1}$ of the different users' symbols - which is an element of the set $\mathcal{M}^L$ of trial-vectors - was transmitted over the SDMA-MIMO channel characterized by the channel transfer factor matrix

$\mathbf{H} \in \mathbb{C}^{P \times L}$ under the condition that the vector $\mathbf{x} \in \mathbb{C}^{P \times 1}$ was received by the different BS receiver antenna elements. This maximization procedure can be expressed as:

$$\check{\mathbf{s}}_{\text{ML}} = \underset{\check{\mathbf{s}} \in \mathcal{M}^L}{arg\,max}\, P(\check{\mathbf{s}}|\mathbf{x}, \mathbf{H}), \tag{4.217}$$

where the set $\mathcal{M}^L$ of trial-vectors is given by:

$$\mathcal{M}^L = \left\{ \check{\mathbf{s}} = \begin{pmatrix} \check{s}^{(1)} \\ \vdots \\ \check{s}^{(L)} \end{pmatrix} \middle| \frac{\check{s}^{(1)}}{\sigma_1}, \ldots, \frac{\check{s}^{(L)}}{\sigma_L} \in \mathcal{M}_c \right\}, \tag{4.218}$$

and where $\sigma_l = \sqrt{\sigma_l^2}$ denotes the l-th user's standard deviation, while $\mathcal{M}_c$ denotes the set of complex constellations points associated with the specific modulation scheme employed.

The maximization procedure obeying Equation 4.217 involves knowledge of the *a posteriori* probabilities $P(\check{\mathbf{s}}|\mathbf{x}, \mathbf{H})$, $\check{\mathbf{s}} \in \mathcal{M}^L$, which can be obtained from the *a priori* probabilities $P(\mathbf{x}|\check{\mathbf{s}}, \mathbf{H})$ with the aid of the Bayes' theorem [87], namely:

$$P(\check{\mathbf{s}}|\mathbf{x}, \mathbf{H}) = P(\mathbf{x}|\check{\mathbf{s}}, \mathbf{H}) \frac{P(\check{\mathbf{s}})}{P(\mathbf{x})}, \tag{4.219}$$

where all symbol vector probabilities are assumed to be identical, i.e. we have $P(\check{\mathbf{s}}) = \frac{1}{M_c^L} = const.$, and for the total probability $P(\mathbf{x})$ we have:

$$P(\mathbf{x}) = \sum_{\check{\mathbf{s}} \in \mathcal{M}^L} P(\mathbf{x}|\check{\mathbf{s}}, \mathbf{H}) P(\check{\mathbf{s}}) = const., \tag{4.220}$$

which follows from the simple fact that all probabilities have to sum to unity, i.e. that:

$$\sum_{\check{\mathbf{s}} \in \mathcal{M}^L} P(\check{\mathbf{s}}|\mathbf{x}, \mathbf{H}) \stackrel{!}{=} 1. \tag{4.221}$$

Hence, upon substituting Equation 4.219 into Equation 4.217 and exploiting that we have $P(\check{\mathbf{s}}) = const.$ as well as that $P(\mathbf{x}) = const.$ for all $\check{\mathbf{s}} \in \mathcal{M}^L$, we obtain:

$$\check{\mathbf{s}}_{\text{ML}} = \underset{\check{\mathbf{s}} \in \mathcal{M}^L}{arg\,max}\, P(\check{\mathbf{s}}|\mathbf{x}, \mathbf{H}) \quad \Longleftrightarrow \quad \check{\mathbf{s}}_{\text{ML}} = \underset{\check{\mathbf{s}} \in \mathcal{M}^L}{arg\,max}\, P(\mathbf{x}|\check{\mathbf{s}}, \mathbf{H}), \tag{4.222}$$

where $P(\mathbf{x}|\check{\mathbf{s}}, \mathbf{H}) = f(\mathbf{x}|\check{\mathbf{s}}, \mathbf{H})$ was given by Equation 4.216. Note from Equation 4.216 that maximizing $f(\mathbf{x}|\check{\mathbf{s}}, \mathbf{H})$ is equivalent to minimizing the Euclidean distance metric $||\mathbf{x} - \mathbf{H}\check{\mathbf{s}}||_2^2 \, \forall \, \check{\mathbf{s}} \in \mathcal{M}^L$, and hence we have:

$$\check{\mathbf{s}}_{\text{ML}} = \underset{\check{\mathbf{s}} \in \mathcal{M}^L}{arg\,max}\, P(\check{\mathbf{s}}|\mathbf{x}, \mathbf{H}) \quad \Longleftrightarrow \quad \check{\mathbf{s}}_{\text{ML}} = \underset{\check{\mathbf{s}} \in \mathcal{M}^L}{arg\,min}\, ||\mathbf{x} - \mathbf{H}\check{\mathbf{s}}||_2^2. \tag{4.223}$$

Note however that the complexity associated with evaluating Equation 4.223 might potentially be excessive, depending on the M_c^L number of vectors contained in the trial-set $\mathcal{M}^L$. An attractive strategy of reducing the complexity in the context of scenarios, where the L number of users is lower than the P number of BS reception antenna elements will be outlined in the next section.

4.3.3.2 Transform-Based ML Detection

As observed in Equation 4.223, determining the ML symbol estimate requires comparing the Euclidean distance between the vector $\mathbf{x}$ of signals actually received by the different antenna elements and the vector $\mathbf{H}\check{\mathbf{s}}$ of signals, which would be received in the absence of AWGN, for all the different vectors $\check{\mathbf{s}}$ of symbol combinations contained in the set $\mathcal{M}^L$. In order to potentially reduce the computational complexity in a specific scenario, where the L number of users is lower than the P number of reception antenna elements, it was proposed in [131] to transform the vector $\mathbf{x}$ of received signals first to the trial-domain[21] with the aid of a linear transform and then to perform the calculation of the Euclidean distance directly in the trial-domain. More explicitly applying this transform-based approach results in a potentially lower complexity than that associated with evaluating Equation 4.223. A linear transform which yields a particularly simple form of the Euclidean distance metric to be evaluated is based on the left-inverse- or Moore-Penrose pseudo-inverse of the channel matrix $\mathbf{H}$, which was discussed in Section 4.2.2. The resultant vector is also known as the LS estimate or ML estimate of the vector $\mathbf{s}$ of transmitted signals. More specifically, the LS estimate $\hat{\mathbf{s}}_{\text{LS}}$ was given by Equation 4.36, namely by:

$$\hat{\mathbf{s}}_{\text{LS}} = \mathbf{P}_{\text{LS}}\mathbf{x}, \tag{4.224}$$

with the associated projection matrix $\mathbf{P}_{\text{LS}}$ defined in Equation 4.37 as:

$$\mathbf{P}_{\text{LS}} = (\mathbf{H}^H\mathbf{H})^{-1}\mathbf{H}^H. \tag{4.225}$$

Furthermore, it was shown in Equation 4.42 that the LS combiner's output vector $\mathbf{s}_{\text{LS}}$ is composed of the vector $\mathbf{s}$ of transmitted signals plus an additional contribution due to the AWGN encountered at the array elements, which is formulated as:

$$\hat{\mathbf{s}}_{\text{LS}} = \mathbf{s} + \mathbf{P}_{\text{LS}}\mathbf{n}. \tag{4.226}$$

Recall from Equation 4.44 that the noise at the LS combiner's output is correlated, having a covariance matrix $\mathbf{R}_{\Delta\hat{\mathbf{s}}_{\text{LS}}}$ expressed in the form of:

$$\mathbf{R}_{\Delta\hat{\mathbf{s}}_{\text{LS}}} = \frac{1}{\sigma_n^2}(\mathbf{H}^H\mathbf{H})^{-1}. \tag{4.227}$$

Hence, in equivalence to Equation 4.215, the multi-variate complex Gaussian distribution function, which reflects the probability that the vector $\hat{\mathbf{s}}_{\text{LS}}$ is observed at the output of the linear combiner under the condition that the vector $\mathbf{s}$ was transmitted over a channel characterized by the channel transfer factor matrix $\mathbf{H}$ is given by:

$$f(\hat{\mathbf{s}}_{\text{LS}}|\mathbf{s},\mathbf{H}) = \frac{1}{\pi^P|\mathbf{R}_{\Delta\hat{\mathbf{s}}_{\text{LS}}}|}\exp\left(-(\hat{\mathbf{s}}_{\text{LS}}-\mathbf{s})^H\mathbf{R}^{-1}_{\Delta\hat{\mathbf{s}}_{\text{LS}}}(\hat{\mathbf{s}}_{\text{LS}}-\mathbf{s})\right). \tag{4.228}$$

[21] The trial-domain is equal to the transmitted signal's domain.

Upon following the steps outlined in the context of Section 4.3.3.1, the vector $\check{\mathbf{s}}_{\text{ML}}$ of symbols that is most likely to have been transmitted is then given by:

$$\check{\mathbf{s}}_{\text{ML}} = \underset{\check{\mathbf{s}} \in \mathcal{M}^L}{arg\,max}\, P(\check{\mathbf{s}}|\mathbf{x}, \mathbf{H}) \quad \Longleftrightarrow \quad \check{\mathbf{s}}_{\text{ML}} = \underset{\check{\mathbf{s}} \in \mathcal{M}^L}{arg\,min}\, (\hat{\mathbf{s}}_{\text{LS}} - \check{\mathbf{s}})^H \mathbf{R}^{-1}_{\Delta\hat{\mathbf{s}}_{\text{LS}}} (\hat{\mathbf{s}}_{\text{LS}} - \check{\mathbf{s}}). \tag{4.229}$$

As a result of the linear properties of the transform applied in Equation 4.224 to the vector $\mathbf{x}$ of signals received by the different antenna elements, the same symbol detection error probability is achieved as with the aid of the standard approach of Equation 4.223, however at a potentially lower complexity. Note however, that a necessary condition for the existence of the projection matrix $\mathbf{P}_{\text{LS}}$ is that the number of users L must be lower than or equal to the number of reception antenna elements P, which imposes a limitation compared to the standard ML detector of Section 4.3.3.1.

4.3.3.3 ML-Assisted Soft-Bit Generation for Turbo-Decoding

Turbo coding based error protection of the different subcarriers hosted by an OFDM symbol is a powerful means of further enhancing the system's BER performance. This is achieved at the cost of reducing the system's effective throughput and increasing the system's complexity. A prerequisite for performing turbo decoding at the receiver is the availability of soft-bit information. As suggested in [131], it is desirable in terms of keeping the computational complexity as low as possible to perform the turbo trellis-decoding separately for the different users. This is, because the joint trellis-decoding of the different users' transmitted signals would potentially require an excessive number of trellis decisions and hence impose a high complexity.

4.3.3.3.1 Standard ML-Assisted Soft-Bit Generation Following the concepts of Equation 4.95 the soft-bit value or log-likelihood ratio- or LLR-value associated with the l-th user at the m-th bit-position is given by:

$$L_m^{(l)} = \ln \frac{P(b_m^{(l)} = 1|\mathbf{x}, \mathbf{H})}{P(b_m^{(l)} = 0|\mathbf{x}, \mathbf{H})}, \tag{4.230}$$

which is the natural logarithm of the quotient of probabilities that the bit considered assumes either a value of $b_m^{(l)} = 1$ or $b_m^{(l)} = 0$. Note that here we have again omitted the index $[n, k]$ for the k-th subcarrier of the n-th OFDM symbol, which is associated with the different variables. Equation 4.230 can be further expanded by noting that the probability that a binary bit value of $b_m^{(l)} = 1$ was transmitted at the m-th bit position associated with the l-th user in the k-th subcarrier is given by the sum of the probabilities of those symbol combinations, where the l-th user's transmitted symbol is associated with a bit value of $b_m^{(l)} = 1$. The probability that a bit value of $b_m^{(l)} = 0$ was transmitted can be expanded equivalently. Hence we obtain:

$$L_m^{(l)} = \ln \frac{\sum_{\check{s}^{(1)}/\sigma_1 \in \mathcal{M}_c} \cdots \sum_{\check{s}^{(l)}/\sigma_l \in \mathcal{M}_{cm}^1} \cdots \sum_{\check{s}^{(L)}/\sigma_L \in \mathcal{M}_c} P(\check{\mathbf{s}}|\mathbf{x}, \mathbf{H})}{\sum_{\check{s}^{(1)}/\sigma_1 \in \mathcal{M}_c} \cdots \sum_{\check{s}^{(l)}/\sigma_l \in \mathcal{M}_{cm}^0} \cdots \sum_{\check{s}^{(L)}/\sigma_L \in \mathcal{M}_c} P(\check{\mathbf{s}}|\mathbf{x}, \mathbf{H})}, \tag{4.231}$$

where $\mathcal{M}_{cm}^{b}$ denotes the specific subset of the set $\mathcal{M}_c$ of constellation points of the modulation scheme employed, which are associated with a bit value of $b \in \{0,1\}$ at the m-th bit position. For notational convenience we can define the l-th user's associated set of trial-vectors employed for determining the probability that the m-th transmitted bit exhibits a value of $b \in \{0,1\}$ as follows:

$$\mathcal{M}_m^{b(l)L} = \left\{ \check{\mathbf{s}} = \begin{pmatrix} \check{s}^{(1)} \\ \vdots \\ \check{s}^{(L)} \end{pmatrix} \middle| \frac{\check{s}^{(1)}}{\sigma_1} \in \mathcal{M}_c, \ldots, \frac{\check{s}^{(l)}}{\sigma_l} \in \mathcal{M}_{cm}^{b}, \ldots, \frac{\check{s}^{(L)}}{\sigma_L} \in \mathcal{M}_c \right\}. \tag{4.232}$$

Upon invoking again Bayes' theorem given by Equation 4.219, namely that:

$$P(\check{\mathbf{s}}|\mathbf{x},\mathbf{H}) = P(\mathbf{x}|\check{\mathbf{s}},\mathbf{H})\frac{P(\check{\mathbf{s}})}{P(\mathbf{x})}, \tag{4.233}$$

and re-substituting Equation 4.233 into Equation 4.231 we obtain the following expression for the l-th user's soft-bit value at the m-th bit position:

$$L_m^{(l)} = \ln \frac{\sum_{\check{\mathbf{s}} \in \mathcal{M}_m^{1(l)L}} P(\mathbf{x}|\check{\mathbf{s}},\mathbf{H})}{\sum_{\check{\mathbf{s}} \in \mathcal{M}_m^{0(l)L}} P(\mathbf{x}|\check{\mathbf{s}},\mathbf{H})}. \tag{4.234}$$

Here we have exploited that the different symbol combination vectors $\check{\mathbf{s}}$ have the same probability namely that $P(\check{\mathbf{s}}) = const.$, $\check{\mathbf{s}} \in \mathcal{M}^L$. Upon recalling from Section 4.3.3.1 that the probability $P(\mathbf{x}|\check{\mathbf{s}},\mathbf{H})$ is given by the multi-variate complex Gaussian distribution function $f(\mathbf{x}|\check{\mathbf{s}},\mathbf{H})$ defined in Equation 4.216, we obtain:

$$L_m^{(l)} = \ln \frac{\sum_{\check{\mathbf{s}} \in \mathcal{M}_m^{1(l)L}} \exp\left(-\frac{1}{\sigma_n^2}||\mathbf{x}-\mathbf{H}\check{\mathbf{s}}||_2^2\right)}{\sum_{\check{\mathbf{s}} \in \mathcal{M}_m^{0(l)L}} \exp\left(-\frac{1}{\sigma_n^2}||\mathbf{x}-\mathbf{H}\check{\mathbf{s}}||_2^2\right)}. \tag{4.235}$$

Observe that evaluating the l-th user's soft-bit value based on its LLR at the m-th bit position with the aid of Equation 4.235 involves the exponential function, which might be computationally expensive.

4.3.3.3.2 Simplification by Maximum Approximation In order to avoid the explicit evaluation of the exponential function in Equation 4.235, a common approach is the employment of the so-called maximum-approximation, which implies that only that specific additive term is retained in the calculation of the numerator and nominator of Equation 4.235, which yields the maximum contribution. It can be readily shown that as a result of this simplification we obtain instead of Equation 4.235 the following expression:

$$L_m^{(l)} \approx \frac{1}{\sigma_n^2}\left[||\mathbf{x}-\mathbf{H}\check{\mathbf{s}}_m^{0(l)}||_2^2 - ||\mathbf{x}-\mathbf{H}\check{\mathbf{s}}_m^{1(l)}||_2^2\right], \tag{4.236}$$

where

$$\check{\mathbf{s}}_m^{b(l)} = arg \min_{\check{\mathbf{s}} \in \mathcal{M}_m^{b(l)L}} ||\mathbf{x}-\mathbf{H}\check{\mathbf{s}}||_2^2, \quad b \in \{0,1\}, \tag{4.237}$$

while the set $\mathcal{M}_m^{b(l)L}$ was defined in Equation 4.232. We note that for each soft-bit to be determined, Equation 4.237 has to be invoked twice, once for a bit status of $b = 1$ and once for $b = 0$.

Observe however, that a significant complexity reduction can be achieved by exploiting that the union of the two subspaces associated with the binary bit values of 0 and 1 of the L users at bit position m constitutes the entire trial space, namely that $\mathcal{M}^L = \mathcal{M}_m^{0(l)L} \bigcup \mathcal{M}_m^{1(l)L}$. Hence, the calculation of the Euclidean distance metric $||\mathbf{x} - \mathbf{H}\check{\mathbf{s}}||_2^2$ has to be performed only once for the different trial vectors $\check{\mathbf{s}} \in \mathcal{M}^L$, followed by an appropriate selection in the context of the soft-bit generation assisted by Equation 4.237. Specifically, in a first step the Euclidean distance metric can be determined for half of the vectors $\check{\mathbf{s}}_m^{b(l)}$ associated with the different bit polarities $b \in \{0, 1\}$ and bit positions m by searching the entire set $\mathcal{M}^L$, which results in the ML estimate $\check{\mathbf{s}}_{\text{ML}}$ of the vectors of transmitted symbols according to Equation 4.223. This initial L-dimensional, M_c-ary ML symbol estimate is given by a specific bit vector. The inverse of this ML bit vector contains the specific bit polarities, for which the further minimization according to Equation 4.237 still has to be conducted.

4.3.3.4 Performance Analysis

In this section the BER performance of ML detection-assisted SDMA-OFDM will be investigated in both a lower-complexity, higher effective throughput scenario using no channel coding, as well as in a higher-complexity, lower throughput scenario where turbo-coding is employed. Again, the frame-invariant fading indoor WATM channel model and its associated OFDM system model described in Section 6.1.1 were invoked and ideal knowledge of the channel transfer functions associated with the different transmit-receive antenna pairs was assumed. For a summary of the basic simulation setup we refer again to Table 4.3. The further structure of Section 4.3.3.4 is as follows. While in Section 4.3.3.4.1 the ML detection-assisted SDMA-OFDM system's BER performance is considered in the uncoded scenario, our simulation results characterizing the turbo-coded scheme will be discussed in Section 4.3.3.4.2.

4.3.3.4.1 BER Performance of ML Detection-Assisted SDMA-OFDM for Different Numbers of Users and Reception Antennas In Figure 4.24 we have portrayed the BER performance of ML detection-assisted OFDM as a function of the SNR encountered at the reception antennas. Specifically, the curves at the left-hand side of Figure 4.24 are parameterized with both the number of users L and the number of reception antennas P, where only scenarios associated with $L \leq P$ are considered. We observe that upon increasing the MIMO system's order, namely by considering a system of four reception antennas and four simultaneous users compared to a system of two reception antennas and two simultaneous users, the system's BER performance is significantly improved. This is in contrast to the behaviour observed for the MMSE detector in Figure 4.8, where a more

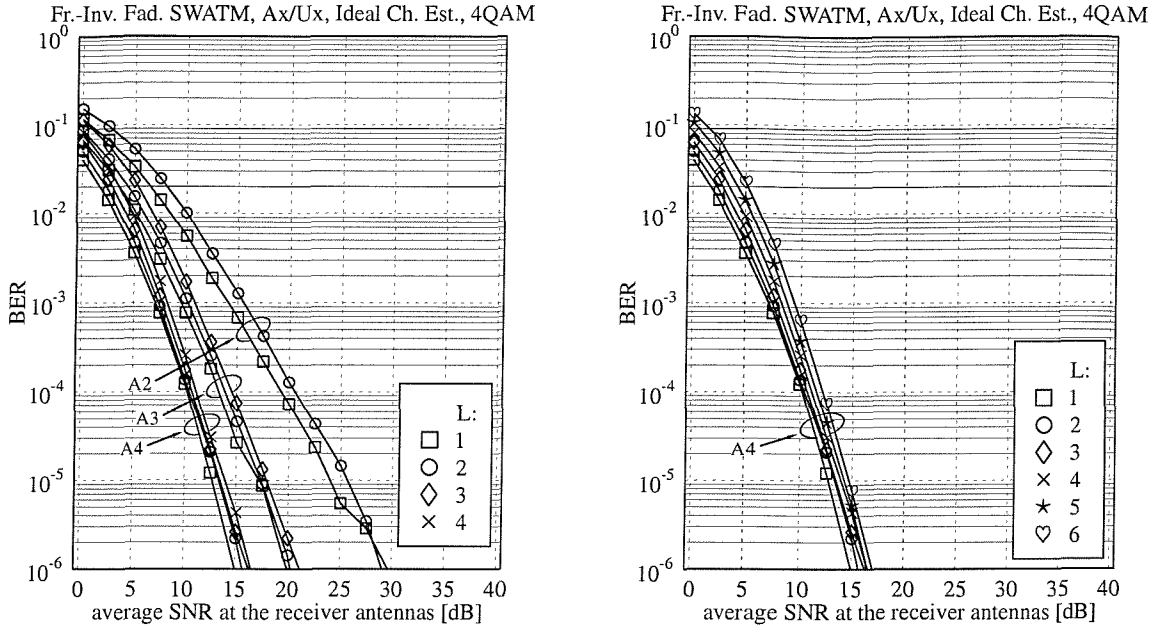

Figure 4.24: BER performance of 4QAM-modulated, ML detection-assisted SDMA-OFDM as a function of the SNR encountered at the reception antennas; (left:) the curves are further parameterized with the number of simultaneous users L and the number of reception antennas P, using the configurations of A2/U1..2, A3/U1..3 and A4/U1..4; (right:) the curves are parameterized with the L number of users for a fixed number of $P = 4$ reception antennas, namely using configurations of A4/U1..6; for the basic simulation parameters we refer to Table 4.3.

modest improvement was observed, but it follows similar trends to those exhibited by the SIC detector characterized in Figure 4.12. More specifically, the ML detector benefits from the higher grade of diversity provided by a higher-order MIMO system. Also observe that by increasing the number of users L at a fixed number of reception antennas P, the system's performance degrades gracefully. More explicitly, the performance difference between the lowest-complexity system supporting one user and that of a "fully loaded" system associated with $L = P$ users is less than 2dB, which is in contrast to the significant degradation observed for the MMSE detector in Figure 4.8.

Our further investigations were conducted with respect to supporting L number of users, which was higher than the P number of reception antennas. By contrast, employing a configuration, where $L > P$ was prohibited in the context of the linear detectors, such as the LS or MMSE as well as the MMSE-based SIC and PIC schemes. The associated simulation results are portrayed at the right-hand side of Figure 4.24 for a scenario of $P = 4$ reception antennas, supporting up to $L = 6$ simultaneous users. Here we observe again that the performance degradation incurred

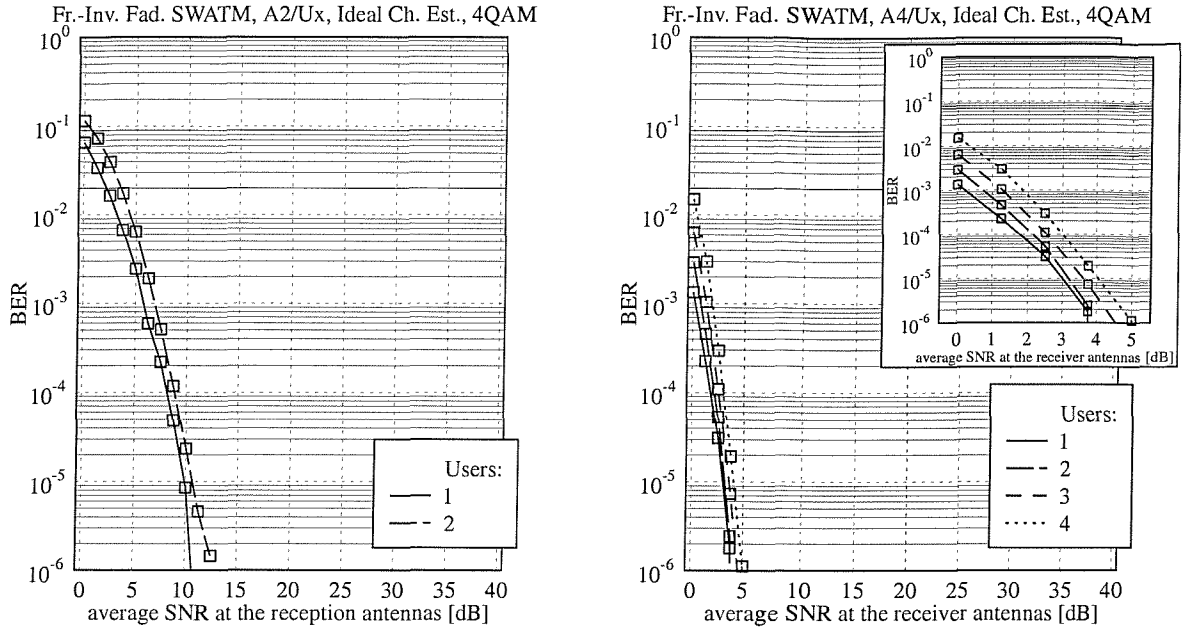

Figure 4.25: BER performance of turbo-coded, 4QAM-modulated, ML detection-assisted SDMA-OFDM as a function of the SNR recorded at the reception antennas; the curves are further parameterized with the number of simultaneous users L and the number of reception antennas P, where more specifically (left:) two reception antennas and (right:) four reception antennas were employed; for the basic simulation- and turbo-coding parameters we refer to Tables 4.3 and 4.4, respectively.

upon increasing the number of users L beyond the number of reception antennas P is gradual. This is in contrast to the more abrupt degradation, which would potentially be observed in conjunction with MMSE-based detection schemes, when allowing for example five simultaneous users instead of four users in a scenario of four reception antennas.

4.3.3.4.2 BER Performance of Turbo-Coded ML Detection-Assisted SDMA-OFDM for Different Numbers of Users and Reception Antennas As it was shown in Sections 4.2.6.4, 4.3.1.4.7 and 4.3.2.3.2 for MMSE, SIC and PIC detection-assisted SDMA-OFDM systems, respectively, the employment of turbo-decoding at the receiver is a powerful means of further enhancing the system's BER performance. This is achieved at the cost of a reduction of the system's effective throughput and by investing additional computational complexity. The associated turbo coding parameters were summarized in Table 4.4, but for the reader's convenience they will be repeated here: the coding rate was $R_c = \frac{1}{2}$, the constraint length was $K_c = 3$, the octally represented generator polynomials

of $(7,5)_8$ were used and 4 iterations were performed. The generation of the soft-bits required for turbo-decoding in the context of ML detection was discussed earlier in Section 4.3.3.3.

Our BER simulation results are portrayed in Figure 4.25, at the left-hand side for $P = 2$ reception antennas, while at the right-hand side for $P = 4$ reception antennas and up to $L = P$ number of simultaneous users. Again, we observe that compared to the uncoded scenario, whose associated BER simulation results were shown in Figure 4.24, the SNR at the reception antennas required for maintaining a specific BER is significantly reduced. In order to provide an example, in the context of a scenario associated with $L = P = 2$ and in the absence of channel coding an SNR of about 25.7dB is required for maintaining a target BER of 10^{-5}, while with the assistance of turbo-coding this target BER is reached at a reduced SNR of about 10.6dB. Similarly, for a scenario of $L = P = 4$ the corresponding SNRs for the uncoded and coded case are given by 13.9dB and 4dB, respectively.

4.3.3.5 Complexity Analysis

The structure of our complexity analysis of the ML-related detection techniques is as follows. While in Section 4.3.3.5.1 the complexity of standard ML detection is discussed, we will focus our attention in Section 4.3.3.5.2 on the analysis of transform-based ML detection. Our discussions will be concluded in Section 4.3.3.5.3 by elaborating on the complexity associated with the generation of soft-bits to be used in the context of turbo-coded ML detection-assisted SDMA-OFDM.

4.3.3.5.1 Complexity of Standard ML Detection As observed in Equation 4.223, an M_c^L number of symbol combinations has to be compared in terms of the Euclidean distance metric for the detection of the different users' transmitted symbols in a specific OFDM subcarrier. This imposes a computational complexity quantified in terms of the number of complex multiplications, additions as well as real-valued comparisons, which is given by:

$$C_{\text{ML}}^{(\mathbb{C}*\mathbb{C})} = M_c^L P \left(\frac{1}{2} + L\right) \quad (4.238)$$

$$C_{\text{ML}}^{(\mathbb{C}+\mathbb{C})} = M_c^L P \left(\frac{3}{2} + L\right) \quad (4.239)$$

$$C_{\text{ML}}^{(\mathbb{R}\lesseqgtr\mathbb{R})} = M_c^L, \quad (4.240)$$

where again, the number of complex multiplications and additions involved in actually calculating the Euclidean norm $||.||_2^2$ has been weighted with a factor of $\frac{1}{2}$, because the multiplication of a complex number with its conjugate complex value inflicts two real-valued multiplications[22]. Note however that the number of multiplications $M_c^L PL$ required in the context of evaluating the term $\mathbf{H}\check{\mathbf{s}}$ in Equation 4.223 for the M_c^L number of different trial vectors can be reduced to $M_c PL$ by evaluating $\mathbf{H}^{(l)}\check{s}^{(l)}$, $\check{s}^{(l)} \in \mathcal{M}_c$, $l = 1, \ldots, L$ and storing the resultant vectors in a lookup table. A

[22] $(a_x + ja_y) \cdot (a_x - ja_y) = a_x^2 + a_y^2$

similar technique could also be applied for reducing the number of complex multiplications in the context of the transform-based ML detection technique of Section 4.3.3.2, as it will be discussed in the next section.

4.3.3.5.2 Complexity of Transform-Based ML Detection The transform-based ML detection technique of Equation 4.229 capitalized on the LS estimate $\hat{\mathbf{s}}_{\text{LS}}$ of the vector $\mathbf{x}$ of signals received by the different antenna elements. This estimate was provided with the aid of Equation 4.224 which employs the projection matrix $\mathbf{P}_{\text{LS}}$ given by Equation 4.225. Furthermore, in the transform-based ML detection process obeying Equation 4.229 explicit knowledge of the error- or noise covariance matrix $\mathbf{R}_{\Delta\hat{\mathbf{s}}_{\text{LS}}}$ given by Equation 4.213, was required for describing the statistical properties of the LS combiner's vector of output signals.

Hence, it is a reasonable strategy to determine the error covariance matrix $\mathbf{R}_{\Delta\hat{\mathbf{s}}_{\text{LS}}}$ first with the aid of Equation 4.213. This imposes a computational complexity given by:

$$C^{(\mathbb{C}*\mathbb{C})}_{\text{ML-trf,err-cov}} = C^{(\mathbb{C}+\mathbb{C})}_{\text{ML-trf,err-cov}} = PL^2 + \frac{4}{3}L^3, \tag{4.241}$$

where the second term accounts for performing the direct inversion in Equation 4.213 with the aid of the LU decomposition [87]. Specifically, the LU decomposition [87] itself requires a complexity of $\frac{1}{3}L^3$ complex multiplications and additions, while the ensuing forward- and backward substitutions as outlined in [87] contribute another $L \cdot L^2$ number of complex multiplications and additions. The LU decomposition technique is only used here for a base-line comparison - more efficient techniques of performing the matrix inversion are known from the literature. Common to most of these matrix inversion techniques is that they are associated with a complexity order of $\mathcal{O}(m^3)$, where m is the dimension of the square matrix to be inverted.

Generating the LS estimate $\hat{\mathbf{s}}_{\text{LS}}$ of the vector $\mathbf{s}$ of transmitted signals with the aid of Equations 4.224 and 4.225, where the latter can be simplified upon substituting the expression of Equation 4.213 derived for the error covariance matrix $\mathbf{R}_{\Delta\hat{\mathbf{s}}_{\text{LS}}}$ imposes an additional complexity of:

$$C^{(\mathbb{C}*\mathbb{C})}_{\text{ML-trf,LS-est}} = C^{(\mathbb{C}+\mathbb{C})}_{\text{ML-trf,LS-est}} = PL + L^2. \tag{4.242}$$

The major part of the computational complexity, however, is imposed - similarly to standard ML detection - by evaluating the M_c^L number of possible trial vectors $\check{\mathbf{s}} \in \mathcal{M}^L$ with the aid of Equation 4.229. This inflicts an additional number of operations given by:

$$C^{(\mathbb{C}*\mathbb{C})}_{\text{ML-trf,trial}} = M_c^L L\left(\frac{1}{2} + L\right) \tag{4.243}$$

$$C^{(\mathbb{C}+\mathbb{C})}_{\text{ML-trf,trial}} = M_c^L L\left(\frac{3}{2} + L\right) \tag{4.244}$$

$$C^{(\mathbb{R}\lessgtr\mathbb{R})}_{\text{ML-trf,trial}} = M_c^L. \tag{4.245}$$

Upon combining the different contributions quantified in this section, the total complexity of the transform-based ML detector becomes:

$$C_{\text{ML-trf}}^{(\mathbb{C}*\mathbb{C})} = PL + (P+1)L^2 + \frac{4}{3}L^3 + M_c^L L\left(\frac{1}{2} + L\right) \quad (4.246)$$

$$C_{\text{ML-trf}}^{(\mathbb{C}+\mathbb{C})} = PL + (P+1)L^2 + \frac{4}{3}L^3 + M_c^L L\left(\frac{3}{2} + L\right) \quad (4.247)$$

$$C_{\text{ML-trf}}^{(\mathbb{R}\lesseqgtr\mathbb{R})} = M_c^L. \quad (4.248)$$

A comparison between the equations associated with the standard ML detector and the transform-based ML detector reveals that employing the latter is only recommended, when the number of users L is smaller than the number of reception antenna elements P, but even then it still depends on the particular scenario, whether the latter is really advantageous.

In conclusion, particularly in the context of the higher-order QAM modulation schemes, such as for example 16QAM and in conjunction with a relatively high number of simultaneous users the computational complexity might become prohibitive for the application of the ML detector.

4.3.3.5.3 Complexity of ML-Assisted Maximum Approximation Based Soft-Bit Generation

In this section the complexity of maximum approximation based soft-bit generation will be analysed which was discussed in Section 4.3.3.3.2. We argued that the soft-bit generation procedure commences by evaluating the Euclidean distance metric, which is part of Equations 4.223 and 4.237, for all the different vectors of symbols contained in the set $\mathcal{M}^L$. The computational complexity of this processing step expressed in terms of the number of complex multiplications and additions was already quantified in Equations 4.238 and 4.239. Additionally, a substantial number of comparisons has to be carried out between the real-valued metric values, which constitute an integral part of the search across the different subsets of symbols denoted by $\mathcal{M}_m^{b(l)L}$ according to Equation 4.237. As argued in Section 4.3.3.3.2, this complexity can be halved by determining in a first step the ML symbol estimate and its associated bit vector with the aid of Equation 4.223. This complexity is quantified in terms of the number of comparisons between real-valued metric values, as given by Equation 4.240, namely M_c^L. Furthermore, in the second step a $L\log_2 M_c$ number of search steps - where $\log_2 M_c$ is the number of bits per symbol - has to be conducted across a set of dimension $M_c^L/2$ each. Hence the total complexity is given by:

$$C_{\text{ML-soft}}^{(\mathbb{C}*\mathbb{C})} = C_{\text{ML}}^{(\mathbb{C}*\mathbb{C})} = M_c^L P\left(\frac{1}{2} + L\right) \quad (4.249)$$

$$C_{\text{ML-soft}}^{(\mathbb{C}+\mathbb{C})} = C_{\text{ML}}^{(\mathbb{C}+\mathbb{C})} = M_c^L P\left(\frac{3}{2} + L\right) \quad (4.250)$$

$$C_{\text{ML-soft}}^{(\mathbb{R}\lesseqgtr\mathbb{R})} = C_{\text{ML}}^{(\mathbb{R}\lesseqgtr\mathbb{R})}\left(1 + \frac{1}{2}L\log_2 M_c\right) \quad (4.251)$$

$$= M_c^L\left(1 + \frac{1}{2}L\log_2 M_c\right) \quad (4.252)$$

$$C_{\text{ML-soft}}^{(\mathbb{R}+\mathbb{R})} = L\log_2 M_c, \quad (4.253)$$

where the contribution $C_{\text{ML-soft}}^{(\mathbb{R}+\mathbb{R})}$ accounts for performing the subtraction of the metric values as shown in Equation 4.236.

4.3.3.6 Summary and Conclusions on ML Detection

In Section 4.3.3 the ML detector was discussed, which is optimum from a statistical point of view. That specific vector $\check{\mathbf{s}}_{\text{ML}}$ of the different users' symbols is deemed to be optimum at the output of the ML detector, which exhibits the highest *a posteriori* probability of $P(\check{\mathbf{s}}_{\text{ML}}|\mathbf{x}, \mathbf{H})$ amongst the M_c^L number of trial-vectors contained in the set $\mathcal{M}^L$ defined by Equation 4.218. Recall from Section 4.3.3.1.2 that the *a posteriori* probability $P(\check{\mathbf{s}}_{\text{ML}}|\mathbf{x}, \mathbf{H})$ can be expressed with the aid of the Bayesian theorem of Equation 4.219, in terms of the *a priori* probability $P(\mathbf{x}|\check{\mathbf{s}}_{\text{ML}}, \mathbf{H})$, which is given by the multi-variate complex Gaussian distribution function, of Equation 4.216. Identifying the optimum trial-vector $\check{s}_{\text{ML}}$ is equivalent to minimizing the Euclidean distance between the vector $\mathbf{x}$ of received signals and the trial-vector $\check{\mathbf{s}}$ transmitted over the MIMO channel described by the channel transfer factor matrix $\mathbf{H}$ for all trial-vectors contained in the set $\mathcal{M}^L$ as it was highlighted in Equation 4.223.

The computational complexity associated with this minimization process is potentially excessive, since all the number of M_c^L trial-vectors contained in the set $\mathcal{M}^L$ have to be compared to each other in terms of the Euclidean distance metric of Equation 4.223. Provided that the number of users L is lower than the number of BS reception antenna elements P, a reduction of the complexity can be achieved by transforming the vector $\mathbf{x}$ of received signals first to the trial-space with the aid of the linear transform of Equation 4.224, instead of transforming each trial-vector $\check{\mathbf{s}} \in \mathcal{M}^L$ separately to the received signal's space upon multiplication with the channel transfer factor matrix $\mathbf{H}$. These discussions were conducted in the context of Section 4.3.3.2.

Furthermore, in Section 4.3.3.3 the principles of ML detection-assisted soft-bit generation for employment in turbo-decoding were discussed, where a complexity reduction was achieved by applying the maximum approximation.

The ML detector's associated BER performance evaluated in the context of both a low-complexity, higher effective throughput uncoded- and a higher-complexity, lower-throughput turbo-coded scenario was the topic of Section 4.3.3.4. Specifically, in Section 4.3.3.4.1 the influence of the number of users L and the number of BS reception antennas P on the BER performance of 4QAM-modulated ML detection-assisted SDMA-OFDM was analysed. We found that as shown at the left-hand side of Figure 4.24 - regardless of the number of users L - upon increasing the number of reception antennas P, the ML detector's associated BER performance was significantly improved. This was a result of the increased grade of channel diversity available. Furthermore, as shown at the right-hand side of Figure 4.24 the ML detector also exhibited a high resilience against the increase of the number of users L. Specifically, for a scenario of $P = 4$ reception antennas the BER curves

of one to six users were confined to a narrow interval of about 2.5dB. This performance trend is in contrast to that observed for the linear combining based detectors, such as the LS and MMSE as well as SIC and PIC schemes, where a necessary condition of high integrity detection is that $L \leq P$. Furthermore, our BER performance results recorded for the turbo-coding based system were presented in Figure 4.25, as part of Section 4.3.3.4.2.

Finally our analysis of the ML detector's computational complexity was conducted in Section 4.3.3.5. Specifically, in Section 4.3.3.5.1 we analysed the complexity of standard ML detection, where the number of complex multiplications and additions as well as real-valued comparisons was given by Equations 4.238, 4.239 and 4.240, respectively. As expected, these complexities were proportional to the number of vectors M_c^L contained in the trial-set $\mathcal{M}^L$. Furthermore, in Section 4.3.3.5.2 the complexity of transform-based ML detection was evaluated. The associated complexity formulae were given by Equations 4.246, 4.247 and 4.248. It was clear from these equations that the transform based ML detection may only be preferred against standard ML detection, if the number of users L is lower than the number of reception antennas P. Our analysis of the complexity of ML-assisted maximum approximation based soft-bit generation in Section 4.3.3.5.3 revealed that compared to standard ML detection the complexity quantified in terms of the number of real-valued comparisons due to comparing the values of the Euclidean distance metric across subsets of the set $\mathcal{M}^L$ of trial-vectors is significantly increased.

4.3.4 Final Comparison of the Different Detection Techniques

In this section a final comparison of the different linear- and non-linear detection techniques namely, that of the MMSE, standard SIC, M-SIC, PIC and ML schemes will be carried out, which were described and characterized in Sections 4.2.3, 4.3.1.1, 4.3.1.2, 4.3.2 and 4.3.3, respectively. Again, as in previous sections, our comparison will focus on the system's BER performance in both an uncoded- and a turbo-coded scenario, which will be the topic of Section 4.3.4.1. By contrast in Section 4.3.4.2 a comparison between the different detectors' complexities will be carried out.

4.3.4.1 BER Performance Comparison of the Different Detection Techniques in Uncoded and Turbo-Coded Scenarios

In Figure 4.26 we have compared the different detectors' SDMA-OFDM related BER performance, at the left-hand side for the uncoded scenario and at the right-hand side for the turbo-coded scenario.

Let us first of all focus our attention on the uncoded scenario. As expected, the best performance is exhibited by the most complex ML detector, closely followed by the M-SIC scheme, where $M = 2$. By contrast, a significant BER degradation is observed for the standard SIC scheme potentially as a result of the effects of error propagation through the different detection stages, a phenomenon which was analysed in Section 4.3.1.4.2. The second worst performance is exhibited

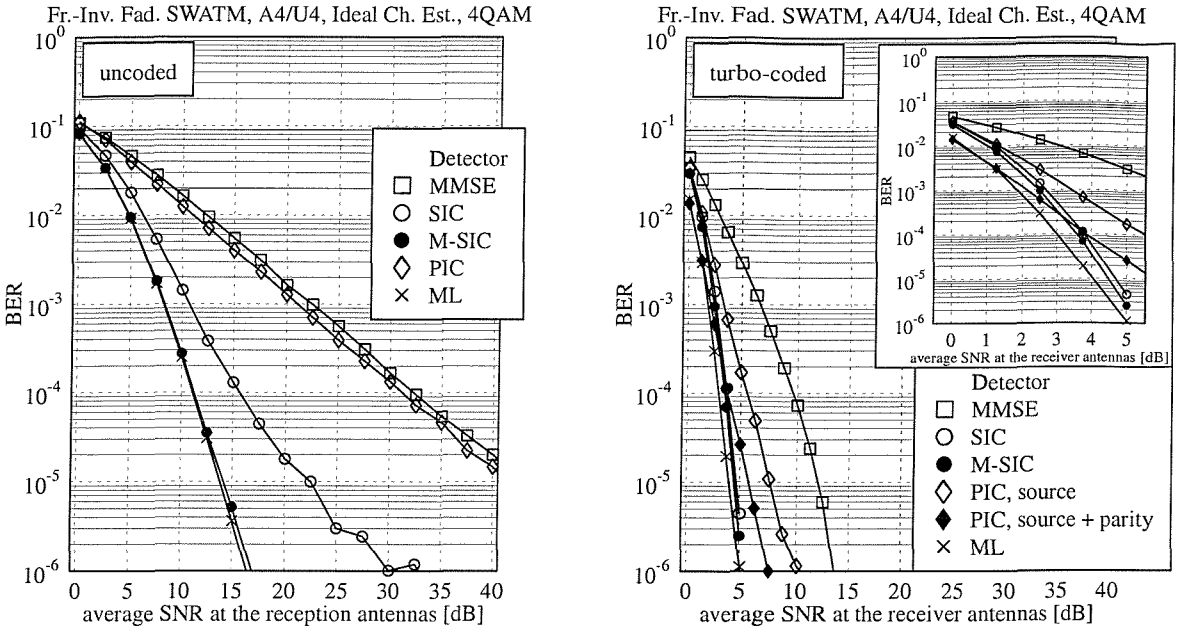

Figure 4.26: BER performance of (left): uncoded and (right:) turbo-coded, 4QAM-modulated, MMSE, standard SIC, M-SIC (M=2), PIC and ML detection assisted SDMA-OFDM as a function of the SNR at the reception antennas; in the context of the turbo-coded scenario both a PIC scheme capitalizing on a 'source'-related reference and a 'source- plus parity'-related reference are compared against each other; $L = P = 4$ simultaneous users and reception antennas were employed; for the list of basic simulation- and turbo-coding parameters we refer to Tables 4.3 and 4.4, respectively.

by the PIC arrangement, while a further degradation by about 1.25dB is incurred upon employing the rudimentary MMSE detection, as argued earlier in Section 4.3.2.3.1. Specifically, the PIC detector's performance was impaired by the lower-power users, potentially propagating errors to those users, which benefitted from a relatively high SNR at the first-stage combiner output. An attractive approach of significantly improving the PIC detector's performance in the context of an SDMA-OFDM system is that of employing channel decoding after the first detection stage, as it was suggested in Section 4.3.2.2.

Let us now summarize our observations inferred in the context of the turbo-coded scenario, portrayed at the right-hand side of Figure 4.26. Again, the SDMA-OFDM system exhibits the best BER performance in the context of employing soft-bit values, which are generated with the aid of the ML-related metric of Section 4.3.3.3. Note that here we employed the simplified, maximum-approximation based formula of Equation 4.236. By contrast, a modest SNR degradation of only

around 0.6dB is observed for the M-SIC (M=2) and of about 0.8dB for the standard SIC scheme, both recorded at a BER of 10^{-4}. Again, the SIC detector's soft-bit values were generated with the aid of the weighted soft-bit metric of Equation 4.133. These performance trends are closely followed by the BER performance evaluated in the context of PIC aided soft-bit generation, where we have compared two different approaches of generating the PIC-related remodulated reference- or feedback signals against each other. Recall from Section 4.3.2.3.2 that the 'source'-related reference generation implied slicing, reencoding, interleaving and remodulating the 'source'-related *a posteriori* soft-output bits of the turbo-decoder. By contrast, the 'source- plus parity'-related remodulated reference implied slicing, interleaving and remodulating the 'source- plus parity'-related *a posteriori* soft-output bits of the turbo-decoder. The performance degradation of the 'source- plus parity'-related reference assisted PIC scheme compared to standard SIC is observed in Figure 4.26 to be about 1dB, while for the 'source'-related reference assisted PIC scheme an SNR degradation of 2.8dB is observed compared to standard SIC. Again, for MMSE detection-assisted SDMA-OFDM the worst performance is observed, namely an additional SNR degradation of about 4.3dB, compared to the 'source'-related reference assisted PIC arrangement.

4.3.4.2 Complexity Comparison of the Different Detection Techniques

Having compared the various detection techniques, namely MMSE, SIC, M-SIC, PIC and ML in terms of the associated system's BER performance, in this section we will compare them with respect to their computational complexity. Here we will concentrate on the previously introduced two measures of complexity namely, the number of complex multiplications, as well as the number of comparisons between real-valued variables, which occur in the process of demodulation and during the selection of the most dominant user in each of the SIC's detection stages. In the context of our evaluations the number of constellation points associated with the modulation scheme employed was assumed to be $M_c = 4$, which is the case for example in 4QAM modulation, while for the M-SIC the number of symbols retained at each detection node was $M = 2$.

Specifically, at the left-hand side of Figure 4.19 we have compared the MMSE[23], standard SIC, M-SIC, PIC and the ML detection schemes in terms of the number of complex multiplications $C^{\mathbb{C}*\mathbb{C}}$ incurred on a subcarrier basis, as a function of the number of simultaneous users L, which was assumed here to be equal to the number of reception antennas P. The curves associated with the different detection techniques were generated with the aid of the complexity formulae given by Equations 4.115, 4.157, 4.173, 4.208 and 4.238, respectively. As expected, the lowest computational complexity expressed in terms of the number of multiplications is exhibited by the MMSE detector, followed by PIC, standard SIC and M-SIC, while the highest complexity is exhibited by the optimum ML detector.

[23]The LS detector's complexity has not been portrayed here explicitly, since it is only marginally less complex than the MMSE detector.

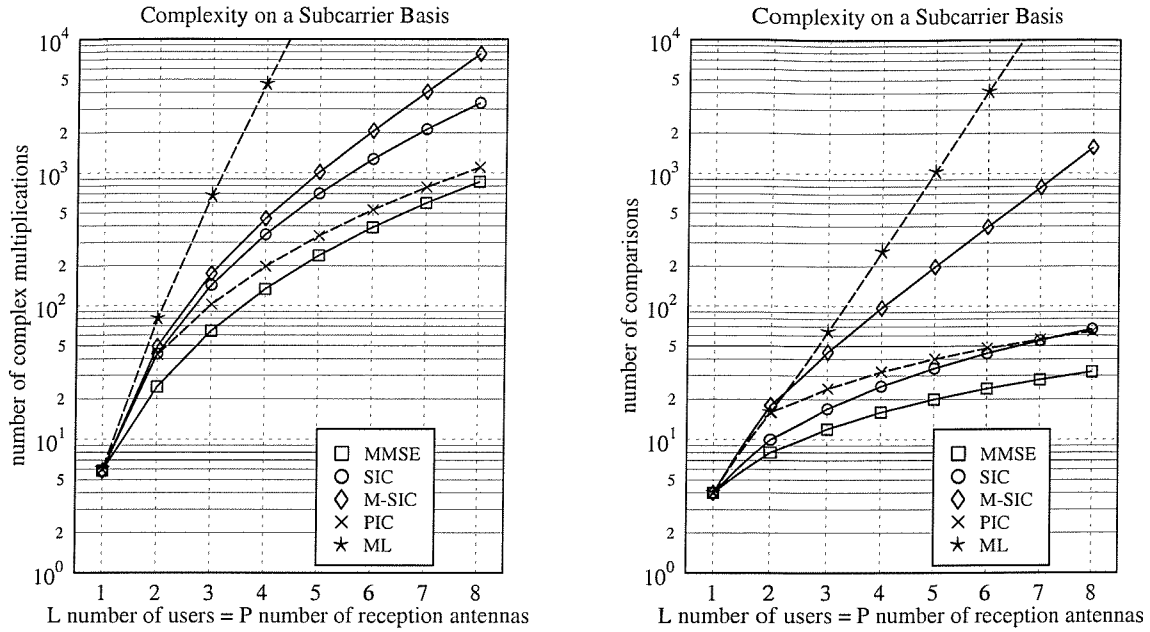

Figure 4.27: Complexity of the MMSE, standard SIC, M-SIC, PIC and ML detection schemes in terms of (left:) the $C^{(\mathbb{C}*\mathbb{C})}$ number of complex multiplications and (right:) the $C^{(\mathbb{R}\lessgtr\mathbb{R})}$ number of real-valued comparisons on a subcarrier basis, as a function of the number of simultaneous users L, which was assumed here to be equal to the number of reception antennas P; specifically for M-SIC the number of tentative symbol decisions per detection node was equal to $M = 2$, while in all scenarios $M_c = 4$ constellation points were assumed, which is for example the case in the context of 4QAM modulation.

Similar observations can also be made for the computational complexity quantified in terms of the number of comparisons between real-valued numbers $C^{(\mathbb{R}\lessgtr\mathbb{R})}$, as portrayed at the right-hand side of Figure 4.27. Here the associated complexity formulae were given for the MMSE, standard SIC, M-SIC, PIC and ML detection schemes by Equations 4.117, 4.159, 4.176, 4.210 and 4.240, respectively. We observe a similar ranking of the different detectors in terms of their associated complexity, as previously seen at the left-hand side of Figure 4.27 in terms of the associated performance. An exception is given by the number of comparisons associated with the PIC detector, which was found to be higher in the context of lower-order SDMA scenarios than for the standard SIC detector. The reason for this trend is that the PIC detector's complexity is increased compared to that of the MMSE detector, since the demodulation of each user's signal has to be performed twice, namely during the first- and the second detection stage. By contrast, the complexity of the standard SIC is increased compared to MMSE, since in each detection stage the most dominant user

	MMSE	std. SIC	M-SIC	PIC	ML
$C^{\mathbb{C}*\mathbb{C}}$	133.33	344.58	454.58	197.33	4608
$C^{\mathbb{C}+\mathbb{C}}$	135.33	335.33	467.33	233.33	5632
$C^{\mathbb{C}\lesseqgtr\mathbb{C}}$	16	25	97	32	256

Table 4.8: Computational complexity of the different detection schemes, namely MMSE, standard SIC, M-SIC, PIC and ML detection quantified in terms of the number of complex multiplications and additions $C^{\mathbb{C}*\mathbb{C}}$, $C^{\mathbb{C}+\mathbb{C}}$ as well as the number of real-valued comparisons $C^{\mathbb{R}\lesseqgtr\mathbb{R}}$ for a scenario of $L = P = 4$ simultaneous users- and reception antennas; specifically for M-SIC the number of tentative symbol decisions per detection node was equal to $M = 2$, while in all scenarios $M_c = 4$ constellation points were assumed, which is for example the case in conjunction with 4QAM modulation.

has to be selected from the set of remaining users.

The number of complex additions associated with the different detectors has not been illustrated here, since these values were found only to differ slightly from those characterizing the number of complex multiplications.

In order to further support our comparison of the different detectors in terms of their associated computational complexity, we have summarized in Table 4.8 the number of complex multiplications and additions, as well as real-valued comparisons imposed in a scenario of $L = 4$ simultaneous users and $P = 4$ reception antenna elements.

4.4 Performance Enhancement

The BER reduction observed in the context of turbo-coded SDMA-OFDM in conjunction with various detection techniques, namely MMSE, SIC, PIC and ML detection in Sections 4.2.6.4, 4.3.1.4.7, 4.3.2.3.2 and 4.3.3.4.2 was achieved at the cost of a substantial reduction of the system's effective throughput, namely by 50% upon employing half-rate turbo-coding. This loss in throughput could have however been compensated upon employing a higher-order modulation scheme, namely 16QAM instead of 4QAM, thus further increasing the computational complexity. Obviously there is a trade-off between the BER performance, the throughput and the computational complexity.

In this section we will study potential techniques for further enhancing the BER performance of SDMA-OFDM on the uplink channel to the basestation, *without* reducing the system's effective throughput. The techniques envisaged are constant throughput adaptive modulation as well as Walsh-Hadamard Transform (WHT) spreading across the different subcarriers. Both of these techniques have been recognized as being effective for exploiting the diversity offered by a wideband channel. Specifically adaptive modulation has widely been discussed in the context of single-user OFDM systems, namely in [98], and furthermore it was also successfully employed in conjunction

with decision-directed channel prediction in Section 2.4. On the other hand, spreading the transmitted signal by means of orthogonal codes has been extensively discussed in the context of single- and multi-carrier CDMA systems, potentially supporting multiple simultaneous users. In our contribution however, spreading is employed for further exploiting the channel's diversity potential, while multiple users are supported with the aid of the multiple BS receiver antennas.

The further structure of this section is as follows. In Section 4.4.1 adaptive modulation assisted SDMA-OFDM- or in short form SDMA-AOFDM will be discussed. We will then embark in Section 4.4.2 on a discussion of WHT spreading assisted SDMA-OFDM- or again, in short form SDMA-WHTS-OFDM.

4.4.1 Adaptive Modulation Assisted SDMA-OFDM

In order to commence our discussions, let us briefly review in the next section the concepts of adaptive modulation as employed in the context of a single-user OFDM scenario.

4.4.1.1 Outline of the Adaptive Single-User Receiver

Adaptive modulation employed in single-user OFDM systems has previously been discussed in Section 2.4 in the context of our assessment of channel transfer function prediction techniques. Recall that invoking adaptive modulation was motivated by the observation that the BER performance of an OFDM modem, which employs a fixed-mode modulation scheme is severely degraded due to the deep frequency-domain channel transfer function fades experienced. This deficiency of the fixed-mode modems may be mitigated by assigning a more robust, but lower throughput modulation mode to those subcarriers, which are severely affected by the deep fades. By contrast, a potentially less robust, but higher throughput modulation mode may be assigned to the higher quality subcarriers.

A prerequisite of performing the modulation mode assignment during the n-th uplink[24] OFDM symbol period for employment during the $(n+1)$-th OFDM symbol period is the availability of a reliable estimate of the channel transfer function to be experienced by the OFDM symbol received during $(n+1)$-th OFDM symbol period. The simplest approach to subcarrier channel quality estimation would be to employ the pilot-based- or decision-directed channel estimate[25] for the n-th OFDM symbol period as an *a priori* estimate of the channel experienced during the $(n+1)$-th OFDM symbol period. However, as shown in Section 2.4 depending on the OFDM symbol normalized Doppler frequency of the channel this *a priori* estimate may result in an inaccurate assignment of the modulation modes to the different subcarriers, which is a consequence of the channel variations incurred between the two OFDM symbol periods.

A significant improvement leading to a more accurate *a priori* channel estimate for the $(n+1)$-th

[24]Unless otherwise stated, we refer to 'uplink OFDM symbol period' simply as 'OFDM symbol period'.

[25]Again, we synonymously use the expressions 'channel estimate' and 'channel transfer function estimate'.

OFDM symbol period could however be achieved with the aid of the decision-directed Wiener-filter based channel prediction techniques discussed in Section 2. As a result of the modulation mode adaptation portrayed the BER performance of the AOFDM modem was observed in Figure 2.19 to be significantly improved compared to that of an OFDM modem having the same throughput, but using a fixed modulation mode. At the same time, relatively rapidly varying channels having a high OFDM symbol normalized Doppler frequency could be supported.

Motivated by the successful employment of constant throughput adaptive modulation techniques in the context of single-user OFDM systems, we will now investigate their potential for employment in multi-user SDMA-OFDM systems. We will focus our attention on employing a linear detector at the receiver, which exhibits the highest potential of achieving a significant BER performance improvement with the aid of adaptive modulation techniques.

The further structure of this section is as follows. Our discussions commence in Section 4.4.1.2 with the outline of the adaptive multi-user receiver's structure. This is followed in Section 4.4.1.3 by an assessment of the system's BER performance. Our summary and conclusions will be offered in Section 4.4.1.4.

4.4.1.2 Outline of the Adaptive Multi-User SDMA-OFDM Receiver

In Figure 4.28 we have portrayed the basic block diagram of the adaptive multi-user SDMA-OFDM receiver employed at the BS. During the n-th OFDM symbol period, after removing the cyclic OFDM prefix- or guard interval, which is not shown here, the complex time-domain signals received by the P different BS antenna elements are independently subjected to the FFT, which delivers the frequency-domain- or subcarrier based representation of the signals received, namely $x_p[n,k]$, where $p = 1,\ldots,P$ and $k = 0,\ldots,K-1$. Note that for notational convenience the subcarrier index k has been omitted in Figure 4.28.

The various signals $x_p[n,k]$ are then conveyed to the linear combiner, represented by Equation 4.7, which produces linear estimates $\hat{s}^{(l)}[n,k]$ of the signals transmitted by the L different users, namely $l = 1,\ldots,L$, separately for each subcarrier. The combiner weights were already generated during the $(n-1)$-th OFDM symbol period for employment during the n-th OFDM symbol period.

The linear signal estimates $\hat{s}^{(l)}[n,k]$ are then conveyed to the adaptive classifiers, which deliver the sliced symbols $\check{s}^{(l)}[n,k]$ that are most likely to have been transmitted according to the Euclidean distance metric of Equation 4.94. Again, this classification takes place separately for the different users $l = 1,\ldots,L$ and subcarriers $k = 0,\ldots,K-1$. Note that the classifiers of the adaptive OFDM modem require side information concerning the subcarrier- or subband modulation mode assignment employed, which was generated during the previous OFDM symbol period and was locally stored at the receiver. The sliced symbols are then demapped to their bit-representation not

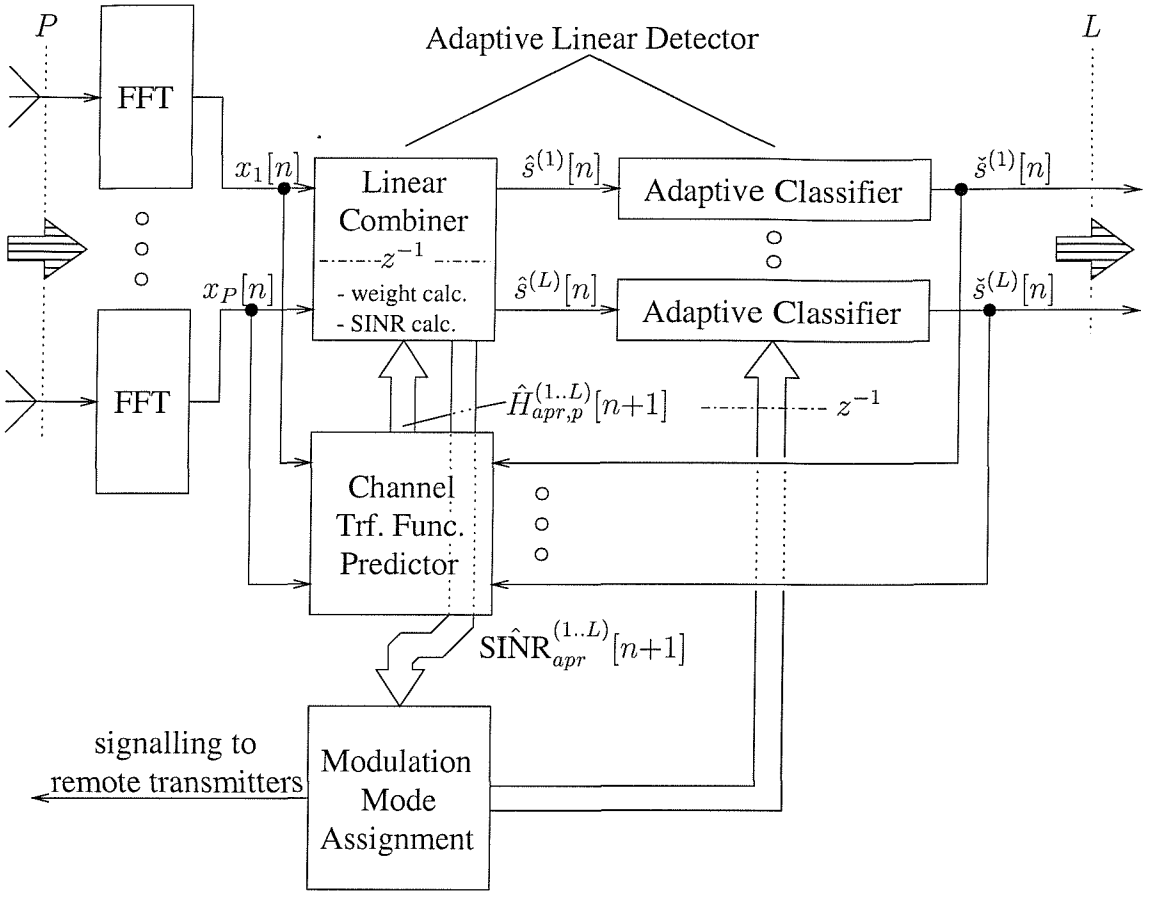

Figure 4.28: Block diagram of the adaptive multi-user SDMA-OFDM receiver, which is supported by a P-element antenna front-end in order to facilitate the separation of the L number of simultaneous users' associated signals at the BS's receiver. The subcarrier index k, where $k = 0, \ldots, K-1$ has been omitted for reasons of simplicity.

shown in Figure 4.28, in order to obtain the bits transmitted.

Furthermore, the sliced symbols $\check{s}^{(l)}[n,k]$ of Figure 4.28 are conveyed together with the received subcarrier symbols $x_p[n,k]$ to the channel transfer function predictor, which generates the *a priori* estimates $\hat{H}^{(l)}_{apr,p}[n+1,k]$ of the channel transfer factors $H^{(l)}_p[n+1,k]$, associated with the $L \cdot P$ number of SDMA-MIMO channels portrayed in Figure 4.3 during the $(n+1)$-th OFDM symbol period. However, these *a priori* channel transfer factor estimates $\hat{H}^{(l)}_{apr,p}[n+1,k]$ have already been employed during the n-th OFDM symbol period for generating the matrices $\hat{\mathbf{W}}_{apr}[n+1,k]$, $k = 0, \ldots, K-1$ of the combiner weights associated with the $(n+1)$-th OFDM symbol period, upon invoking Equations 4.64 or 4.68[26].

Furthermore, the combiner weights are then employed in conjunction with Equation 4.24 for

[26]Here the combiner weight matrix for a specific subcarrier is represented by $\hat{\mathbf{W}}_{apr}$ instead of $\mathbf{W}$ as in Equations 4.64 and 4.68, in order to indicate that its calculation is based on the imperfect estimates delivered by the *a priori* channel transfer function predictor.

obtaining *a priori* estimates of the subcarrier-based SINRs, namely of $\hat{\text{SINR}}_{apr}^{(l)}[n+1,k]$, potentially observed by the L different users at the linear combiner's output during the $(n+1)$-th OFDM symbol period. These *a priori* subcarrier SINR estimates are required for computing the different users' modulation mode assignments to be employed during the $(n+1)$-th uplink OFDM symbol period. The algorithm used for performing the modem mode assignment was summarized earlier in Section 2.4.1.1. Note that the updated modulation mode assignment is conveyed to the remote transmitters during the next downlink OFDM symbol period.

4.4.1.3 Performance Assessment

In this section we will briefly assess the BER performance of MMSE detection-assisted SDMA-AOFDM. Again, we employed the indoor WATM system- and channel model of Section 6.1.1, where the fading was OFDM symbol invariant in order to avoid the obfuscating effects of inter-subcarrier interference.

Furthermore, perfect channel prediction was invoked, namely perfect knowledge of the channel transfer functions experienced during $(n+1)$-th OFDM symbol period was made available during the n-th OFDM symbol period for calculating the MMSE combiner's weights to be employed during the $(n+1)$-th OFDM symbol period. The number of BS receiver antennas P was equal to four. A total of 32 subbands each hosting 16 subcarriers was employed in the context of AOFDM, which capitalized on four modulation modes, namely 'no transmission', BPSK, 4QAM and 16QAM.

Our simulation results are portrayed in Figure 4.29. On the left-hand side of Figure 4.29 we have compared SDMA-OFDM using fixed 4QAM modulation against 32 Subband (Sb)-SDMA-AOFDM having the same throughput, namely 1024 Bit per OFDM Symbol (BPOS). Note that here we have neglected the signalling overhead required for transmitting side information related to the modulation mode assignment to be employed during the next downlink OFDM symbol period. The BER curves are parameterized with the number of users L. The highest beneficial impact of adaptive modulation is observed for a 'fully loaded' SDMA-AOFDM system, where the number of users equals the number of BS receiver antennas. The is because for a lower number of users the effective channel - namely the SDMA-MIMO channel concatenated with the linear combiner - experienced by the different users across the various subcarriers fluctuates less dramatically. The justification of this observation is that the linear combiner is capable of dedicating more of the channel's diversity potential to mitigating the serious frequency-domain channel fades, rather than to suppressing the interference imposed by the undesired co-channel users. As a result, the benefits of adaptive modulation are eroded.

Having found that adaptive modulation is rendered attractive only in the context of an almost fully loaded SDMA-OFDM scenario, we will now focus our attention further on the BER performance of 32Sb-SDMA-AOFDM in the context of a scenario of four simultaneous users and reception

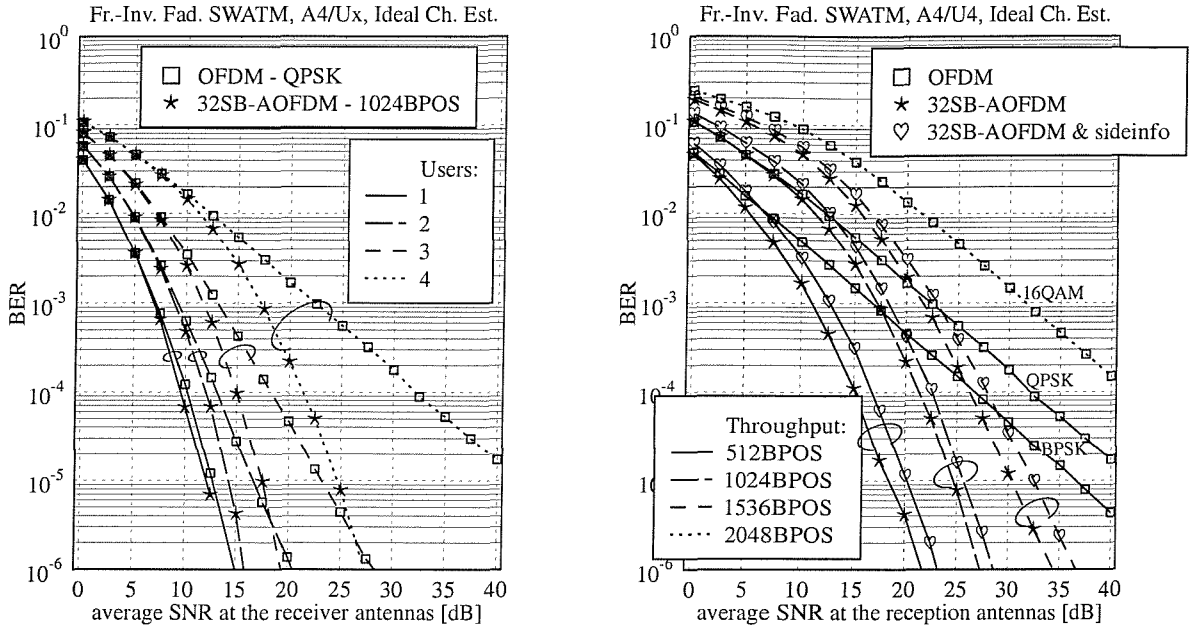

Figure 4.29: BER performance of MMSE detection-assisted SDMA-AOFDM as a function of the SNR recorded at the reception antennas. The curves are further parameterized with the number of simultaneous users L while the number of reception antennas P was fixed to four. Specifically, on the (left:) we have compared SDMA-OFDM using fixed 4QAM modulation to 32 Subband (Sb) AOFDM having the same throughput. Furthermore, on the (right:) we have compared SDMA-OFDM using fixed BPSK, 4QAM or 16QAM modulation to 32Sb-AOFDM having equivalent throughputs, upon once neglecting ('32Sb-AOFDM')- and once incorporating ('32Sb-AOFDM & sideinfo') the additional overhead required for transmitting side-information for the reverse link. Note that in the context of the 512-subcarrier indoor WATM system model of Section 6.1.1 employed here, fixed BPSK-, 4QAM- or 16QAM modulation assisted OFDM is associated with throughputs of 512, 1024 or 2048 Bit per OFDM Symbol (BPOS). Perfect channel transfer function prediction was employed.

antennas. Here we have considered both cases, namely that where no side-information is transmitted as in the context of the results presented on the left-hand side of Figure 4.29, and that, where explicit side-information related to the modulation mode assignment to be used on the next downlink OFDM symbol period is received from the remote transmitters. Upon assuming that the AOFDM modem supports four modulation modes, namely 'no transmission', BPSK, 4QAM and 16QAM, a total number of two bits per subband are required. This number is increased to four bits upon assuming the employment of half-rate error-correction coding. Hence, in the context of 32Sb-SDMA-AOFDM the transmission overhead required for signalling the modulation mode assignment to be used on the reverse link is equal to 128 bit per OFDM symbol and user. Hence, for the effective system throughputs of 512, 1024 and 1536 BPOS the total target throughputs of the AOFDM modem are 640, 1152 and 1664 BPOS, respectively. From the BER curves shown at the right-hand side of Figure 4.29 we infer that in the context of the more realistic arrangement of transmitting explicit side-information the SNR required for attaining a specific BER is increased by a maximum of about 2dB, compared to the rather idealistic scenario, which neglects the transmission of side-information. Note furthermore that compared to the SDMA-OFDM schemes using fixed BPSK and 4QAM modulation modes, which support throughputs of 512 and 1024 BPOS the BER reduction achieved by AOFDM at a fixed SNR or equivalently, the SNR reduction attained at a specific BER is substantial. To provide an example, for a throughput of 1024 BPOS the SNR reduction due to employing SDMA-AOFDM compared to SDMA-OFDM using fixed 4QAM modulation is around 16dB at a BER of 10^{-5}, upon considering explicit side-information in the AOFDM transmissions.

4.4.1.4 Summary and Conclusions

In summary, in Section 4.4.1 we have described and characterized adaptive modulation assisted SDMA-OFDM. More specifically, in Section 4.4.1.1 adaptive modulation employed in single-user scenarios such as those described in Section 2.4 was briefly revisited. Furthermore, in Section 4.4.1.2 the architecture of multi-user SDMA-AOFDM receiver was detailed in the context of employing linear detection techniques, such as MMSE. Its simplified block diagram was shown in Figure 4.28. Our BER performance assessment was then conducted in Section 4.4.1.3. We found that the employment of adaptive modulation in SDMA-OFDM is useful only in the context of an almost fully-loaded SDMA-OFDM scenario, where the number of users L approaches the number of receiver antennas P. Using the indoor WATM system- and channel parameters as described in Section 6.1.1, the SNR advantage owing to employing 32Sb-SDMA-AOFDM having an effective throughput of 1024 BPOS compared to SDMA-OFDM using fixed 4QAM modulation was around 16dB at a BER of 10^{-5} in the context of assuming perfect channel transfer function prediction.

In our further experiments, which are not explicitly described here for reasons of space economy, we found that PIC detection, which was discussed in Section 4.3.2 is also amenable to employment

in conjunction with adaptive modulation techniques, resulting in a similar BER improvement as recorded in the context of MMSE detection. The modulation mode assignment to be used would be based on the SNR or SINR observed at the output of the linear combiner, which constitutes the first PIC stage, as it was shown in Figure 4.20. By contrast, in the context of the SIC detection scheme investigated in Section 4.3.1 the employment of adaptive modulation techniques turned out to be less attractive. This is because the effects of deep channel transfer function fades experienced by some of the subcarriers have already been mitigated by detecting in each SIC stage only the most dominant remaining user. Similarly, the advantages of adaptive modulation are also expected to erode in the context of ML detection. In the next section we consider an alternative frequency-domain fading counter measure, namely that of averaging the effects of fading, rather than accommodating them.

4.4.2 Walsh-Hadamard Transform Spreading Assisted SDMA-OFDM

Spreading the information symbols to be transmitted with the aid of orthogonal codes is the basis of supporting multiple-access capabilities in the context of single- and multicarrier CDMA (MC-CDMA) systems [143]. Instead of transmitting each complex symbol delivered by the modulator separately on a specific subcarrier in the context of multi-carrier OFDM modems, its influence is spread over several subcarriers with the aid of orthogonal multi-chip spreading codes. The advantage of employing orthogonal codes for performing the spreading is related to the resultant simple receiver design. A prominent class of orthogonal codes, which have been often used in CDMA systems is constituted by the family of orthogonal Walsh codes [143], which are particularly attractive, since the operation of spreading with the aid of these codes can be implemented in form of a 'fast' transform, which takes advantage of the codes' recursive structure, similarly to the FFT.

Note however, that in the context of our discussions presented in this section, we are more interested in spreading as a means of exploiting the wideband channel's diversity potential, rather than in its ability of supporting multiple users, since multiple users are supported in the context of the SDMA-OFDM receiver with the aid of the P-element antenna array and the associated detection techniques.

Due to the operations of spreading and despreading combined with MMSE based frequency-domain equalization the adverse effects of the low-SNR subcarriers on the average BER performance is potentially improved. This is a direct consequence of spreading, because even if the signal corresponding to a specific chip is obliterated by a deep frequency-domain channel fade, after despreading its effects are spread over the Walsh-Hadamard Transform (WHT) length. Hence there is a high chance of still recovering all the partially affected subcarrier symbols without errors.

The further structure of this section is as follows. In Section 4.4.2.1 the structure of the WHT

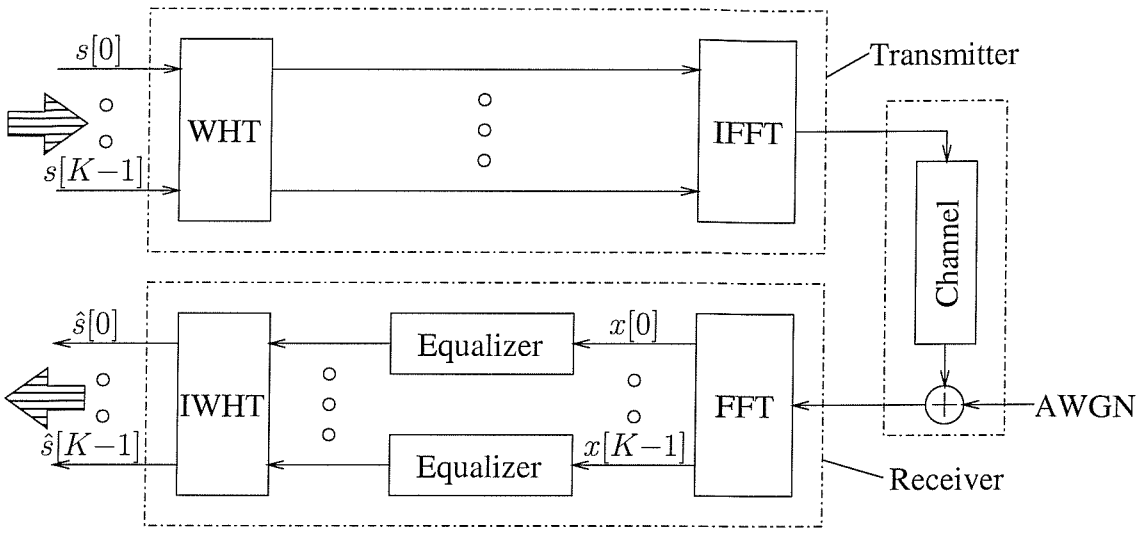

Figure 4.30: Simplified block diagram of the single-user WHTS-OFDM scenario. For reasons of notational simplicity the OFDM symbol index n and the static index $()_{MC}$ have been removed from the different variables.

spreading assisted single-user OFDM receiver is outlined. Specifically, we will demonstrate the separability of the operations of frequency-domain channel transfer factor equalization and despreading in the context of orthogonal codes. In Section 4.4.2.2 we will then describe the WHT spreading (WHTS) assisted multi-user SDMA-OFDM (SDMA-WHTS-OFDM) receiver's specific structure. The BER performance assessment of SDMA-WHTS-OFDM cast in the context of employing either MMSE- or PIC detection at the receiver will then be conducted in Section 4.4.2.3. Our conclusions will be offered in Section 4.4.2.4.

4.4.2.1 Outline of WHTS Assisted Single-User OFDM Receiver

In Figure 4.30 we have portrayed the simplified block diagram of the single-user WHTS-OFDM transmission scenario. More specifically, at the top of Figure 4.30 the WHTS-OFDM transmitter is shown, which consists of WHT-assisted spreading, followed by the OFDM-related IFFT based modulator. The IFFT assisted modulator's output samples are then conveyed - upon neglecting here the further OFDM transmitter processing steps - through the stylized AWGN contaminated transmission channel, as shown at the right-hand side of Figure 4.30. The WHTS-OFDM receiver shown at the bottom of Figure 4.30 then performs the OFDM-related FFT-aided demodulation of the incoming signal samples, followed by subcarrier-based channel transfer factor equalization and despreading with the aid of the inverse WHT (IWHT). As we will show in the context of the forthcoming derivations, the separation of the WHTS-OFDM receiver into subcarrier-based equalization and despreading is a consequence of the orthogonality of the Walsh codes employed.

The further structure of this section is as follows. Our discussions commence in Section 4.4.2.1.1 with an outline of the WHT matrix's specific properties, namely its unitary nature. Furthermore, in Section 4.4.2.1.2 the WHTS-OFDM receiver's design will be outlined. We will highlight that due to the WHT matrix's unitary nature the processes of channel transfer function equalization and despreading can be conducted separately.

4.4.2.1.1 Properties of the Walsh-Hadamard Transform The lowest-dimensional WHT from which the higher dimensional WHTs can be recursively derived, is given by the WHT_2 transform, which is described by the following unitary matrix:

$$\mathbf{U}_{\text{WHT}_2} = \frac{1}{\sqrt{2}} \begin{pmatrix} 1 & 1 \\ 1 & -1 \end{pmatrix}. \tag{4.254}$$

More generally, the N-th order WHT is given by the following recursive expression:

$$\mathbf{U}_{\text{WHT}_N} = \frac{1}{\sqrt{2}} \begin{pmatrix} 1 \cdot \mathbf{U}_{\text{WHT}_{N-1}} & 1 \cdot \mathbf{U}_{\text{WHT}_{N-1}} \\ 1 \cdot \mathbf{U}_{\text{WHT}_{N-1}} & -1 \cdot \mathbf{U}_{\text{WHT}_{N-1}} \end{pmatrix}, \tag{4.255}$$

as a function of the $(N-1)$-th order WHT matrix, namely $\mathbf{U}_{\text{WHT}_{N-1}}$. Note that the column vectors of matrix $\mathbf{U}_{\text{WHT}_N}$ represent the orthogonal Walsh code vectors, for which we have:

$$col_i^H\{\mathbf{U}_{\text{WHT}_N}\} \cdot col_j\{\mathbf{U}_{\text{WHT}_N}\} = \begin{cases} 1 & i = j \\ 0 & i \neq j \end{cases}. \tag{4.256}$$

This implies that $\mathbf{U}_{\text{WHT}_N}$ is an orthogonal matrix, namely that we have [87]:

$$\mathbf{U}_{\text{WHT}_N}^T \mathbf{U}_{\text{WHT}_N} = \mathbf{I}, \tag{4.257}$$

which therefore allows us to conclude that $\mathbf{U}_{\text{WHT}_N}$ is also unitary, satisfying [87]:

$$\mathbf{U}_{\text{WHT}_N}^H \mathbf{U}_{\text{WHT}_N} = \mathbf{I}. \tag{4.258}$$

The unitary property allows us to separate the signal processing at the receiver into the operations of subcarrier-based channel transfer factor equalization followed by despreading, as it will be demonstrated in the next section.

4.4.2.1.2 Receiver Design The vector $\mathbf{x}[n] \in \mathbb{C}^{K \times 1}$ of complex signals observed in the K different subcarriers at the output of the receiver's FFT-based demodulation is given for the WHT-OFDM system portrayed in Figure 4.30 by:

$$\mathbf{x}[n] = \mathbf{H}[n]\mathbf{U}_{\text{WHT}}\mathbf{s}[n] + \mathbf{n}[n], \tag{4.259}$$

where $\mathbf{H}[n] \in \mathbb{C}^{K \times K}$ is the diagonal matrix of subcarrier channel transfer factors, namely:

$$\mathbf{H}[n] = diag\left(H[0], H[1], \ldots, H[K-1]\right), \tag{4.260}$$

and $\mathbf{U}_{\text{WHT}} \in \mathbb{C}^{K \times K}$ is the unitary WHT matrix[27] of K-th order, which was defined by Equation 4.255. Furthermore, in Equation 4.259 $\mathbf{s}[n] \in \mathbb{C}^{K \times 1}$ denotes the vector of transmitted subcarrier symbols, namely:

$$\mathbf{s}[n] = \left(s[0], s[1], \ldots, s[K-1]\right)^T, \tag{4.261}$$

and $\mathbf{n}[n] \in \mathbb{C}^{K \times 1}$ is the vector of subcarrier-related AWGN samples, namely:

$$\mathbf{n}[n] = \left(n[0], n[1], \ldots, n[K-1]\right)^T. \tag{4.262}$$

Note that in the context of the above definitions we have omitted the OFDM symbol index $[n]$ for reasons of notational simplicity.

Equation 4.259 can be transferred into standard form, namely to:

$$\mathbf{x}[n] = \mathbf{H}_{\text{WHT}}[n]\mathbf{s}[n] + \mathbf{n}[n], \tag{4.263}$$

by considering the product of the diagonal channel matrix $\mathbf{H}[n]$ and the WHT matrix $\mathbf{U}_{\text{WHT}}$ as the effective channel matrix $\mathbf{H}_{\text{WHT}}[n] \in \mathbb{C}^{K \times K}$, namely by introducing:

$$\mathbf{H}_{\text{WHT}}[n] = \mathbf{H}[n]\mathbf{U}_{\text{WHT}}. \tag{4.264}$$

Note that Equation 4.263 exhibits the same structure as Equation 4.1, describing the SDMA-MIMO channel scenario on a subcarrier basis. Hence the same techniques can be invoked for recovering the vector $\mathbf{s}[n]$ of symbols transmitted over the K different OFDM subcarriers. These detection techniques were investigated in Sections 4.2 and 4.3 for recovering the symbols transmitted by the L different users on a subcarrier basis in the context of SDMA-OFDM.

Here we will focus our attention on the case of linear equalization, namely where an estimate $\hat{\mathbf{s}}[n] \in \mathbb{C}^{K \times 1}$ of the vector of transmitted subcarrier symbols $\mathbf{s}[n]$ is obtained by linearly combining the complex signals received in the different subcarriers, which are represented by the vector $\mathbf{x}[n]$. The combining can be achieved with the aid of the weight matrix $\mathbf{W}[n] \in \mathbb{C}^{K \times K}$, as shown in Equation 4.7, namely:

$$\hat{\mathbf{s}}[n] = \mathbf{W}^H[n]\mathbf{x}[n]. \tag{4.265}$$

In the context of the MMSE criterion we obtain - as demonstrated earlier in Equation 4.63 - the weight matrix $\mathbf{W}_{\text{MMSE}}[n] \in \mathbb{C}^{K \times K}$, which is given in its right-inverse related form as follows:

$$\mathbf{W}_{\text{MMSE}}[n] = \left(\mathbf{H}_{\text{WHT}}[n]\mathbf{P}_{\text{MC}}\mathbf{H}^H_{\text{WHT}}[n] + \sigma_n^2\mathbf{I}\right)^{-1}\mathbf{H}_{\text{WHT}}[n]\mathbf{P}_{\text{MC}}. \tag{4.266}$$

[27] Note that here we have omitted the lower case index, which indicates the order of the WHT.

In Equation 4.266 the diagonal matrix $\mathbf{P}_{\text{MC}} \in \mathbb{R}^{K \times K}$ of transmit powers associated with the different subcarriers is given for an equal power allocation by:

$$\mathbf{P}_{\text{MC}} = \sigma_s^2 \mathbf{I}, \tag{4.267}$$

where σ_s^2 denotes the signal variance, and σ_n^2 is the AWGN variance. Upon substituting Equations 4.264 and 4.267 into Equation 4.266 we obtain the following equation for the weight matrix $\mathbf{W}_{\text{MMSE}}[n]$:

$$\mathbf{W}_{\text{MMSE}}[n] = \mathbf{E}_{\text{MMSE}}[n]\mathbf{U}_{\text{WHT}}, \tag{4.268}$$

where the *channel-related equalizer matrix* $\mathbf{E}_{\text{MMSE}}[n] \in \mathbb{C}^{K \times K}$ is given by:

$$\mathbf{E}_{\text{MMSE}}[n] = (\mathbf{H}[n]\mathbf{H}^H[n] + \frac{\sigma_n^2}{\sigma_s^2}\mathbf{I})^{-1}\mathbf{H}[n]. \tag{4.269}$$

This matrix describes the operation of the equalizer seen in Figure 4.30. Here we have capitalized on the unitary nature of the matrix $\mathbf{U}_{\text{WHT}}$, as reflected by Equation 4.258. Note that $\mathbf{E}_{\text{MMSE}}[n]$ given by Equation 4.269 is a diagonal matrix, where the k-th diagonal element is given by:

$$\mathbf{E}_{\text{MMSE}}[n]|_{(k,k)} = \frac{H[n,k]}{|H[n,k]|^2 + \frac{\sigma_n^2}{\sigma_s^2}}, \tag{4.270}$$

and where $H[n,k]$ is the k-th subcarrier's channel transfer factor. Upon substituting Equation 4.268 into Equation 4.265 the MMSE combining related vector $\hat{\mathbf{s}}_{\text{MMSE}}[n] \in \mathbb{C}^{K \times 1}$ of the transmitted subcarrier symbols' estimates is given by:

$$\hat{\mathbf{s}}_{\text{MMSE}}[n] = \mathbf{U}_{\text{WHT}}^H \mathbf{E}_{\text{MMSE}}^H[n]\mathbf{x}[n]. \tag{4.271}$$

Note in Equation 4.271 that the receiver's operation is separated into two steps. The first step is the subcarrier-based one-tap equalization, which is carried out by multiplying the FFT-based OFDM demodulator's output vector $\mathbf{x}[n]$ in Figure 4.30 by the Hermitian transpose of the diagonal matrix $\mathbf{E}_{\text{MMSE}}[n]$ of Equation 4.269. The second step is the IWHT assisted despreading based on multiplying with the unitary matrix $\mathbf{U}_{\text{WHT}}^H = \mathbf{U}_{\text{WHT}}$, which was also shown in Figure 4.30.

Following the philosophy of Equation 4.73 it can be demonstrated furthermore that the signal estimation MSE averaged over the different subcarrier-related components of $\hat{\mathbf{s}}_{\text{MMSE}}[n]$ is given by:

$$\overline{\text{MMSE}}_{\text{MMSE}}[n] = \sigma_s^2 \left(1 - \frac{1}{K}\sum_{k=0}^{K-1} H_{\text{MMSE}}[n,k]\right), \tag{4.272}$$

where the k-th subcarrier's effective 'channel' transfer factor $H_{\text{MMSE}}[n,k]$, includes both the effects of the channel and that of the one-tap equalization at the receiver, namely:

$$H_{\text{MMSE}}[n,k] = \frac{|H[n,k]|^2}{|H[n,k]|^2 + \frac{\sigma_n^2}{\sigma_s^2}}. \tag{4.273}$$

In the context of deriving Equation 4.272 we have exploited only that $\text{Trace}(\mathbf{U}^H\mathbf{A}\mathbf{U}) = \text{Trace}(\mathbf{A})$ for a unitary matrix $\mathbf{U}$ and for an arbitrary matrix $\mathbf{A}$ [94]. Note however that in the specific case of employing the WHT as the unitary transform, an estimation MSE identical to that averaged over an OFDM symbol, namely that quantified by Equation 4.272 is also observed for each individual subcarrier. This could be shown by following the philosophy of Equation 4.74. Furthermore, it can be demonstrated that after IWHT assisted despreading, as seen in Figure 4.30 the subcarrier based SINR is identical for all the different subcarriers, which is given by:

$$\text{SINR}_{\text{WHT,MMSE}}[n] = \frac{\sigma^2_{S,\text{WHT,MMSE}}[n]}{\sigma^2_{I,\text{WHT,MMSE}}[n] + \sigma^2_{N,\text{WHT,MMSE}}[n]}, \tag{4.274}$$

where we have:

$$\sigma^2_{S,\text{WHT,MMSE}}[n] = \frac{\sigma_s^2}{K^2}\left(\sum_{k=1}^{K} H_{\text{MMSE}}[n,k]\right)^2 \tag{4.275}$$

$$\sigma^2_{I,\text{WHT,MMSE}}[n] = \frac{\sigma_s^2}{K^2}\left(\sum_{k=0}^{K-1}\left[(K-1)H_{\text{MMSE}}[n,k] - \sum_{\substack{k'=0\\k'\neq k}}^{K-1} H_{\text{MMSE}}[n,k']\right]H_{\text{MMSE}}[n,k]\right) \tag{4.276}$$

$$\sigma^2_{N,\text{WHT,MMSE}}[n] = \frac{\sigma_n^2}{K}\left(\sum_{k=1}^{K}\frac{H_{\text{MMSE}}[n,k]}{\left(|H[n,k]|^2 + \frac{\sigma_n^2}{\sigma_s^2}\right)^2}\right). \tag{4.277}$$

In the next section we will embark on describing the multi-user SDMA-WHTS-OFDM receiver.

4.4.2.2 Outline of the WHTS Assisted Multi-User SDMA-OFDM Receiver

In the previous section we have demonstrated in the context of a single-user WHTS-OFDM receiver that the operations of linear frequency-domain channel transfer factor equalization and despreading can be sequentially performed. Similar derivations can also be conducted in the context of the multi-user SDMA-WHTS-OFDM scenario, resulting in the receiver design shown in Figure 4.31. Following the design concepts of the multi-user SDMA-AOFDM receiver, shown in Figure 4.28, we have included a decision-directed channel transfer function predictor in Figure 4.31 for providing the channel estimates required by the linear combiner.

Again, as seen in Figure 4.31, blocks of K consecutive samples of the signals received by the P number of BS antenna elements are independently subjected to a K-point FFT, which yields the signal samples' frequency-domain representation, namely $x_p[n,k]$, $p = 1,\ldots,P$, $k = 0,\ldots,K-1$. Following this step linear combining is performed on a per subcarrier basis with the aid of Equation 4.7 in order obtain estimates $\hat{s}^{(l)}[n,k]$ of the signals $s^{(l)}[n,k]$ transmitted by the L different users, where $l = 1,\ldots,L$. Recall that the combiner matrix associated with the MMSE criterion was given in its right-inverse related form by Equation 4.63. Following the design concepts of the single-user WHTS-OFDM receiver shown in Figure 4.30, the linear signal estimates associated with the

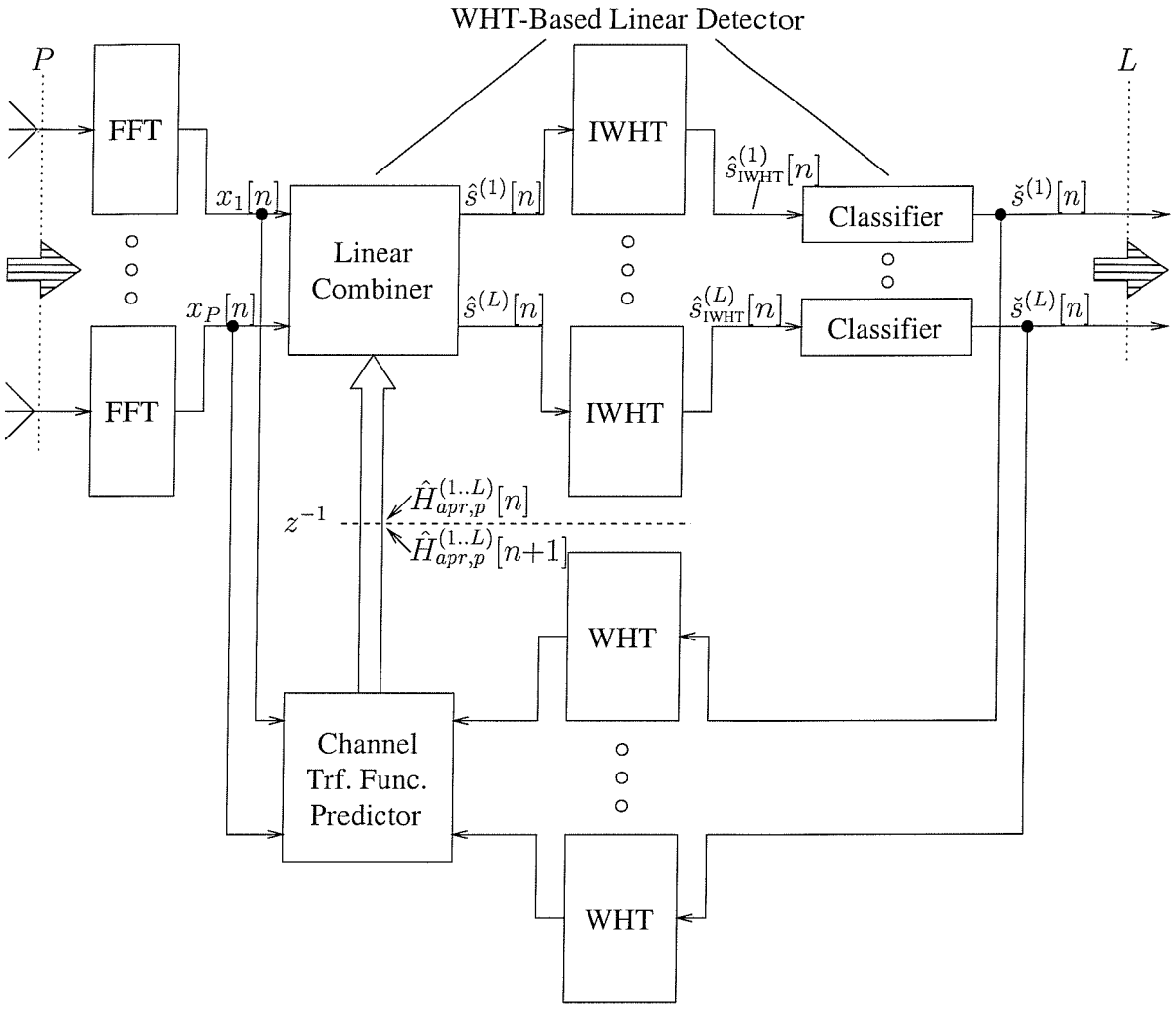

Figure 4.31: Block diagram of the linear combining assisted multi-user SDMA-WHTS-OFDM receiver, which is supported by a P-element antenna front-end in order to facilitate the separation of the L number of simultaneous users' associated signals at the receiver. Decision-directed channel transfer function prediction is performed in order to facilitate the separation of the different users' transmitted signals with the aid of the linear combiner. The subcarrier index k, where $k = 0, \ldots, K-1$ has been omitted for reasons of notational simplicity.

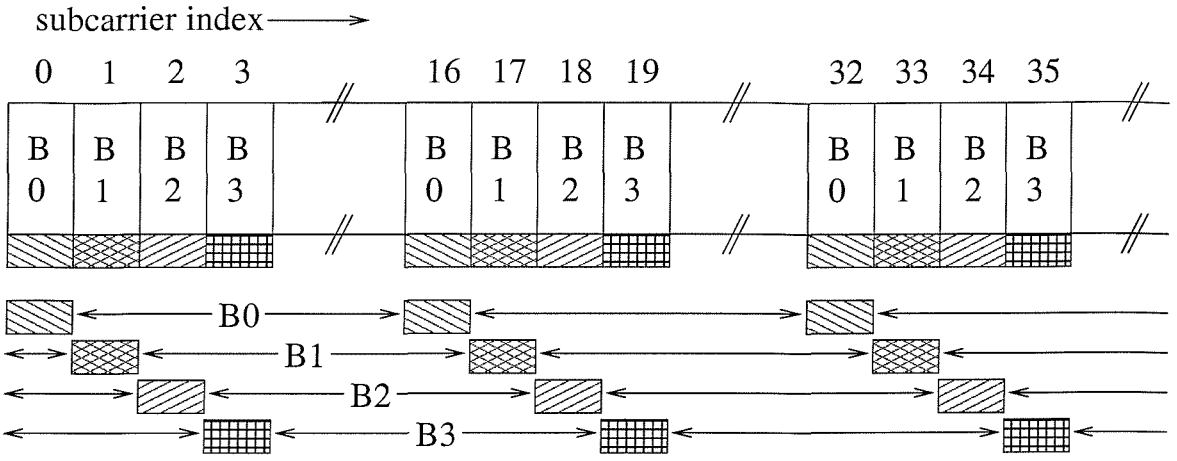

Figure 4.32: Illustration of WHT based subcarrier spreading using a limited WHT blocksize M_{WHT}, which is typically a fraction of the total number of subcarriers K hosted by the OFDM symbol for the sake of low implementational complexity.

L different users are independently subjected to despreading by means of a K-point IWHT, which results in the despread signal estimates $\hat{s}^{(l)}_{\text{IWHT}}[n,k]$ of Figure 4.31. These are classified separately for each subcarrier and each user with the aid of Equation 4.94 in order to obtain the complex symbols $\check{s}^{(l)}[n,k]$ that are most likely to have been transmitted. In the context of the receiver design proposed here and depicted in Figure 4.31, *a priori* estimates of the channel transfer factors $H_p^{(l)}[n,k]$ employed in the calculation of the different subcarriers' weight matrices according to Equation 4.63 are again generated upon feeding back the current OFDM symbol's subcarrier symbol decisions, which are subjected to WHT based spreading in order to regenerate the complex symbols transmitted by the L different users in each subcarrier.

Since the employment of WHTs having a high transform length, such as for example 512, as required in case of the indoor WATM system model employed in our investigations in Section 4.4.2.3 would impose a high computational complexity, we partition the OFDM symbol into several WHTs as seen in Figure 4.32. This is also justified by the observation that most of the channel's frequency-domain diversity potential can be exploited with the aid of a relatively short spreading length, as illustrated in Figure 4.33. Furthermore, depending on the particular power delay profile of the channel, the OFDM symbol bandwidth of K subcarriers can be divided into K/M_{WHT} interleaved blocks of size M_{WHT} each, which are separately subjected to the WHT. More specifically, the i-th WHT block of an OFDM symbol contains subcarriers having indices j given by:

$$j = i + r\frac{K}{M_{\text{WHT}}}, \qquad 0 \leq r \leq M_{\text{WHT}} - 1, \tag{4.278}$$

where according to our definition both the first WHT block and the first OFDM subcarrier are represented by an index of zero. In Figure 4.32 we have further illustrated the operation of WHT

based spreading applied to blocks of an identical size, where each block hosts only a fraction of the total number of subcarriers K associated with the OFDM symbol. More specifically, in this particular example the OFDM symbol is composed of 16 interleaved WHT blocks and the specific subcarriers, which are 16 frequency positions apart from each other belong to the same WHT block.

4.4.2.3 Performance Assessment

Our performance investigations of WHTS-OFDM are conducted separately for single- and multi-user OFDM scenarios. Specifically in Section 4.4.2.3.1 we will demonstrate the influence of the spreading code length on the WHTS-OFDM system's performance. Furthermore, a comparison between WHTS-OFDM and AOFDM is also carried out. Our investigations of multi-user SDMA-WHTS-OFDM cast in the context of MMSE- and PIC detection will then be conducted in Section 4.4.2.3.2.

4.4.2.3.1 Single-User WHTS-OFDM Simulation results have been obtained for the indoor WATM system- and channel model of Section 6.1.1. We commenced our investigations by assessing the impact of Walsh-Hadamard spreading using different spreading code lengths on the BER performance of a 4QAM single reception antenna, single user OFDM system in the indoor WATM channel environment. MMSE-based frequency domain channel equalization, as described in Section 4.4.2.1.2, was performed at the receiver. The corresponding results are portrayed at the left-hand side of Figure 4.33. We observe that as a consequence of the residual 'multiple-access' interference imposed by the spread signals of the different subcarriers hosted by each WHT block, the BER performance is not particularly sensitive to the WHT block length, provided that it is in excess of 32 subcarriers for the SNRs of our interest. It should be noted that the benefit of spreading is directly related to the frequency-domain diversity potential offered by a specific dispersive channel. More specifically, the higher the channel's delay spread, the less separated are the frequency-domain fades, hence tolerating a higher WHT length, while achieving as high a randomization of the frequency-domain fading effects as possible.

In our next investigations we compared the BER performance of the WHT assisted OFDM system to a non-spread OFDM system and to an OFDM system employing adaptive modulation [98], under the constraint of having a target throughput equivalent to that of the fixed mode 4QAM modulated OFDM system. The modulation mode adaptation regime employed a total of four modes, namely 'no transmission', BPSK, 4QAM and 16QAM transmission. In order to reduce the signalling overhead required, the modulation modes were assigned on a subband basis, where each subband hosted either one or a number of subcarriers. Specifically, using one subcarrier per subband allowed us to determine the upperbound performance of the system. Furthermore, the best-case scenario of perfect channel transfer function knowledge was invoked in the process of determining the optimum modulation mode assignment. The corresponding simulation results are illustrated at the right-hand

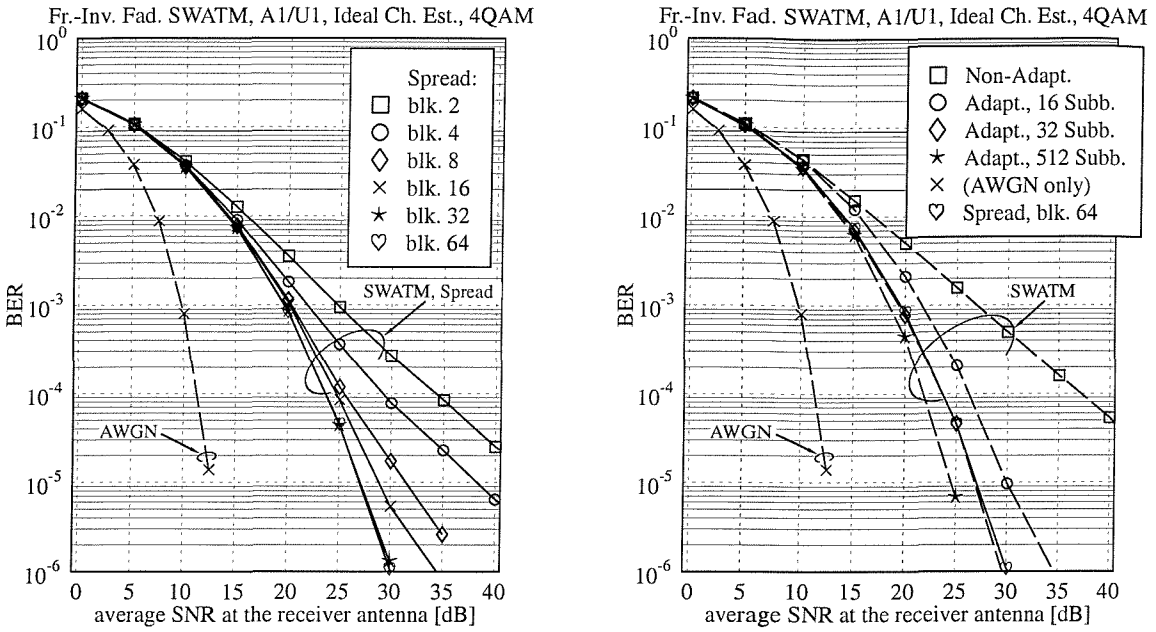

Figure 4.33: (Left:) BER performance of a WHT spreading assisted 4QAM modulated single reception antenna, single user OFDM system parameterised with the spreading blocksize. (Right:) BER performance comparison between a 4QAM modulated single reception antenna, single user standard OFDM system, an OFDM system employing four-mode ('no transmission', BPSK, 4QAM, 16QAM), constant-throughput, zero-delay signalling based adaptive modulation using 16 or 512 subbands, and a Walsh-Hadamard spreading assisted OFDM system. The simulations were conducted in the context of the 'frame-invariant' fading indoor WATM system- and channel model of Section 6.1.1. Ideal channel transfer function knowledge was assumed. The BER performance of 4QAM signalling over an AWGN channel has been plotted as a reference.

side of Figure 4.33. We observe that in the specific indoor WATM channel environment, assuming the separation of the total bandwidth into 32 equal-sized subbands, each hosting 16 subcarriers, the OFDM system employing adaptive modulation exhibits a similar performance to that of the spread OFDM system for a WHT blocksize of 64 subcarriers. By contrast, a hypothetic system assigning the best-matching individual modulation mode to each subcarrier outperformed the WHT OFDM scheme by about 2dB in terms of the required SNR. Hence, taking also into account the signalling overhead required by the adaptive modulation scheme, as well as its limited applicability restricted to relatively slowly varying channels in the absence of channel transfer function prediction techniques, we conclude that subcarrier spreading is a more convenient approach to exploiting the wideband channel's diversity potential.

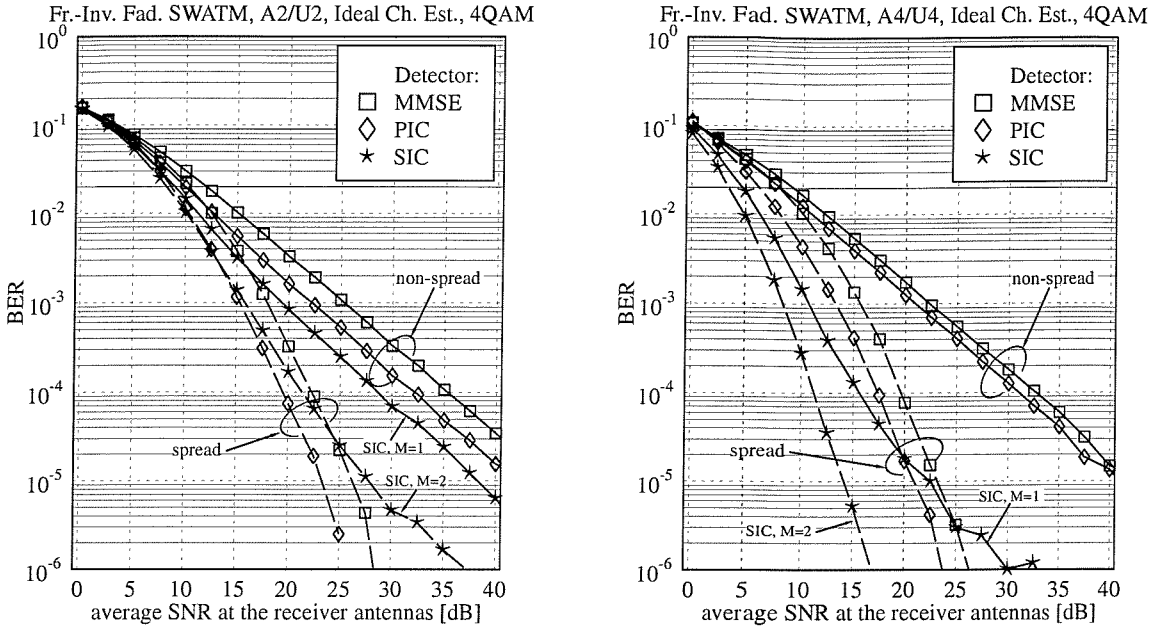

Figure 4.34: BER performance comparison between 4QAM modulated MMSE, PIC or SIC detection-assisted SDMA-OFDM systems as a function of the SNR at the reception antennas, (left:) for a $L = P = 2$ number of simultaneous users and reception antennas, while (right:) for a $L = P = 4$ number of simultaneous users and reception antennas. The systems employing MMSE and PIC multi-user detection were further assisted by Walsh-Hadamard spreading using a blocksize of 16 subcarriers. Ideal channel transfer function knowledge was assumed. The simulations were conducted in the context of the frame-invariant fading indoor WATM system- and channel model described in Section 6.1.1.

4.4.2.3.2 Multi-User SDMA-WHTS-OFDM Our further aim was to investigate the applicability of WHT based spreading in the context of an SDMA-OFDM system, where the signals of L simultaneous users each equipped with one transmission antenna are separated at the BS with the aid of a P-element antenna array. The design of the corresponding receiver was outlined in Section 4.4.2.2. In our investigations we invoked the MMSE- and PIC based multi-user detection approaches of Sections 4.2.3 and 4.3.2, while SIC described in Section 4.3.1 was not directly applicable to a spread OFDM system. This is because in a specific subcarrier or subband in each iteration the highest-power user is detected first, followed by the subtraction of its sliced and remodulated signal from the residual composite multi-user signal received by each antenna. Since the WHT based spreading is performed across subcarriers spaced apart from each other as far as possible for the sake of maximising the achievable frequency-domain diversity effect, these subcarriers would potentially require a different SIC detection order. Hence not all the symbols of a specific user

contained in a WHT block are available at the same time for demodulation. Simulation results have been obtained for a two reception antenna, two user SDMA scenario. The results are portrayed at the left-hand side of Figure 4.34. We observe that both the MMSE and the PIC detector using WHT based spreading outperform the M-SIC detector in the non-spread case, which tracked $M = 1$ or $M = 2$ tentative symbol decisions from each detection node as shown in Figure 4.11. Note that the least complex multi-user receiver, namely the MMSE detector performed about 2.5dB worse on average, than PIC, which was also observed in the non-spread scenario. Again, by contrast, in case of a four reception antenna, four user SDMA scenario characterized at the right-hand side of Figure 4.34, the $(M = 2)$-SIC detector applied in the non-spread scenario outperforms both spreading assisted arrangements, namely those employing MMSE and PIC based detection. However, compared to the standard $(M = 1)$-SIC detector, at sufficiently high SNRs both the MMSE and PIC detection assisted SDMA-OFDM systems exhibit a better BER performance. This is achieved at a significantly lower complexity than that of the SIC scheme, upon assuming that a 'fast' implementation of the WHT is employed for performing the spreading.

4.4.2.4 Summary and Conclusions

In Section 4.4.2 WHT spreading assisted OFDM was discussed in the context of both single- and multi-user OFDM scenarios. Our discussions commenced in Section 4.4.2.1 with an outline of the WHTS-OFDM receiver's structure in the context of the single-user scenario. Specifically, in Section 4.4.2.1.1 the WHT's properties, namely its recursive structure, as reflected by Equation 4.255, which allows for a 'fast' implementation, similarly to the FFT, were described. Of further interest was the WHT matrix' unitary nature, as described by Equation 4.258, which follows from the orthogonality of the different Walsh code vectors. Next we highlighted in Section 4.4.2.1.2 that the unitary nature of the WHT matrix facilitates a particularly simple receiver design in the context of linear channel transfer function equalization. The block diagram of the single-user WHTS-OFDM receiver was shown at the bottom of Figure 4.30. Specifically, the IWHT based despreading was shown to be decoupled from the channel transfer factor equalization. This was also demonstrated in the context of the formal derivation of a linear estimate $\hat{\mathbf{s}}_{\mathrm{MC,MMSE}}$ of the vector $\mathbf{s}_{\mathrm{MC}}$ of signals transmitted in the K different subcarriers, which was formulated in Equation 4.271. Furthermore, we found that the signal estimation MSE at the receiver's output is identical for the different subcarriers, which was given by Equation 4.272. We also found that the SINR at the receiver's output, which is given by Equation 4.274, is identical for the different subcarriers.

In Section 4.4.2.2 we then embarked on the description of the multi-user SDMA-WHTS-OFDM receiver's structure shown in Figure 4.31, which followed the same design concepts as the single-user WHTS-OFDM receiver. Specifically the multi-user SDMA scheme employed a sequential equalization- or combining scheme, followed by WHT despreading, implemented separately for the

different users. In order to reduce the computational complexity, we found that it was attractive to perform the spreading separately for K/M_{WHT} number of 'interleaved' blocks of size M_{WHT} subcarriers each, as it was shown in Figure 4.32, instead of implementing it for a single larger-size block of K subcarriers, without incurring a noticeable increase of the BER.

The evaluation of the single-user WHTS-OFDM and multi-user SDMA-WHTS-OFDM systems' BER performance was then carried out in Section 4.4.2.3. Specifically, in Figure 4.33 of Section 4.4.2.3.1 we found that already for relatively small spreading block lengths, namely 64 subcarriers per block employed in the context of the indoor WATM channel of Figure 6.1.1, the wideband channel's diversity can be exploited, while a further increase of the spreading length did not yield a significant BER improvement, as shown at the left-hand side of Figure 4.33. This was because by increasing the spreading block length, the channel transfer factors associated with neighbouring subcarriers contained in a block became more similar. Furthermore, our BER comparisons portrayed at the right-hand side of Figure 4.33 revealed that WHTS-OFDM is also more attractive than AOFDM. More explicitly, AOFDM is capable of slightly outperforming WHTS-OFDM, but only for an unrealistically high number of subbands, namely in excess of 64, when neglecting the transmission of side-information and by assuming perfect channel transfer function knowledge in the modulation mode assignment, the AOFDM is capable of slightly outperforming WHTS-AOFDM.

Our BER performance assessment of multi-user WHTS-OFDM was then conducted in the context of Figure 4.34 for scenarios of two BS reception antennas and two simultaneous users as well as for four reception antennas and four simultaneous users, as shown at the left-hand- and right-hand side of Figure 4.34, respectively. Various detection techniques were compared against each other, namely MMSE, PIC and SIC detection, noting that in the context of the latter WHTS was not directly applicable. We found that in the lower-dimensional SDMA-OFDM scenario of two users both PIC- as well as MMSE detection-assisted SDMA-WHTS-OFDM are capable of outperforming $(M = 1)$- and $(M = 2)$-aided SIC detection-assisted SDMA-OFDM, while in the higher-dimensional SDMA-OFDM scenario $(M = 2)$-SIC detection-assisted SDMA-OFDM performed best, while at the same time exhibiting by far the highest complexity. By contrast, at sufficiently high SNRs $(M = 1)$-SIC detection-assisted SDMA-OFDM was outperformed by both PIC- as well as MMSE detection-assisted SDMA-WHTS-OFDM, while at the same time exhibiting a potentially far lower computational complexity, than the SIC detection-assisted systems.

4.5 Summary and Conclusions

In this section our summary and conclusions will be provided for this chapter, where we discussed a range of uplink detection techniques designed for multi-user SDMA-OFDM. The specific structure of this section is as follows. In Section 4.5.1 the motivation of employing multiple reception antenna assisted SDMA receivers is reviewed, which is followed in Section 4.5.2 by a summary of the

family of linear detection schemes. Our summary and conclusions related to the set of non-linear detection schemes will be offered in Section 4.5.3. Finally our overall comparison between the different detection schemes investigated will then be offered in Section 4.5.3.4. This is followed in Section 4.5.3.5 by our conclusions on the suite of performance enhancement techniques studied.

4.5.1 Review of the Motivation for Multiple Reception Antenna SDMA Receivers

During the past few decades a variety of Multiple Access (MA) techniques, such as Time Division Multiple Access (TDMA), Frequency Division Multiple Access (FDMA), Code Division Multiple Access (CDMA) have found favour in the various wireless communications systems. More recently Space Division Multiple Access (SDMA) has been proposed for supporting multiple users in OFDM-based communications system. In the context of the more conventional techniques, namely TDMA, FDMA and CDMA, both the mobiles as well as the basestation are typically equipped with a single transmit- and receive antenna, respectively. The access of the different users to the finite capacity transmission channel is then facilitated in TDMA by allowing each user to access the channel's entire bandwidth for a finite time duration, namely for the duration of a time-slot. By contrast, in FDMA we assign each user a frequency slot. Finally, in CDMA all users share the same frequency band and we facilitate the separation of the different users' transmitted signals with the aid of unique, user-specific spreading codes.

Alternatively, all users could potentially share the same frequency band, as in CDMA, and we could exploit for their separation that the different users' transmitted signals experience different channel transfer functions. The separation of the different users based on their unique channel transfer function constitutes the principle of a minimalistic SDMA scheme. More specifically, in the context of each of the flat-fading OFDM subcarriers, the channel matrix $\mathbf{H}$ associated with the scenario of $L > 1$ different users and $P = 1$ receiver antenna is of unity rank. Hence, only the ML detector is capable of separating the different users' transmitted signals, upon inflicting a potentially large complexity.

In order to render SDMA amenable to employment of lower complexity linear combining-based multi-user detection techniques, such as the LS, MMSE, SIC and PIC detection arrangements discussed in Sections 4.2.2, 4.2.3, 4.3.1 and 4.3.2, respectively, a viable strategy is to increase the P number of receiver antennas, such that we have $P \geq L$. Hence the channel matrix $\mathbf{H}$ is potentially of 'full rank' with respect to the number of users L. In other words, we have $L = rank(\mathbf{H})$, which facilitates the linear separation of the different users' transmitted signals based on their spatial signature. More specifically, the spatial signature of a particular user is constituted by the set of channel transfer factors between the user's single transmit antenna and the P number of different receiver antennas, again, upon assuming flat-fading channel conditions for each of the OFDM subcarriers. This Multiple-Input Multiple-Output (MIMO) channel scenario was further detailed in

Section 4.1.3, where for simplicity we assumed that the fading experienced by each of the MIMO sub-channels associated with a specific transmitter-receiver antenna pair is independent from that of the other MIMO sub-channels.

Our more specific discussions of multi-user detection techniques applicable to SDMA-OFDM were separated into the subclasses of linear- and non-linear detection techniques of Sections 4.2 and 4.3, respectively. As argued in Sections 4.1.1 and 4.1.2 the rationale of this classification was that in the context of linear detection techniques, such as the LS- and MMSE detection schemes discussed in Section 4.2, no *a priori* knowledge of the remaining users' transmitted symbols is required for the detection of a specific user. However, in the case of the SIC, PIC and ML detection techniques discussed in Section 4.3, *a priori* knowledge of the likely values of the symbol is involved, which must be provided by the non-linear classification or decision operation involved in the demodulation process.

4.5.2 Summary and Conclusions Related to Linear Detectors

The typical structure of a linear detector was highlighted in Figure 4.4. More specifically, in a first step linear estimates of the L different users' transmitted signals are obtained by appropriately combining the signals received by the P different antenna elements. In a next step these signal estimates are classified- or demodulated in order to determine the complex symbol- or constellation point that is most likely to have been transmitted by each user. As a result of the user signal separation facilitated with the aid of the linear combiner, the process of classification is substantially simplified compared to that of the multi-user ML detector discussed in Section 4.3.3. Instead of evaluating the multi-user Euclidean distance metric associated with the multi-user ML detector M_c^L number of times, in case of the linear detector the single-user Euclidean distance metric has to be evaluated LM_c number of times, which constitutes a complexity reduction. However, this complexity reduction is achieved at the cost of a significant performance degradation in the context of the linear detector compared to that of the optimum ML detector, since the effects of the residual interference contaminating the linear combiner's output signals are neglected by the former.

The linear combiner's associated weight matrix can be adjusted according to a number of different criteria. Explicitly, the Least-Squares (LS) error- and the Minimum Mean-Square Error (MMSE) criteria were investigated in Sections 4.2.2 and 4.2.3, respectively. More specifically, as it was detailed in Section 4.2.2, the LS detector's associated LS combiner generates linear estimates of the signals transmitted by the different users based solely on the knowledge of the channel's frequency-domain transfer factors. In contrast to the LS combiner, the MMSE detector's associated MMSE combiner, which belongs to the class of Wiener-filter related combiners, as argued in Section 4.2.3.4, additionally capitalizes on statistical knowledge of the AWGN process, which contaminates the signals received by the P number of different antenna elements. As the terminology suggests, the

MMSE combiner achieves the minimum signal estimation MSE. However, the transmitted signals to be estimated cannot be recovered with a unity gain, which is in contrast to the LS combiner. As argued in Section 4.2.3.5, this non-unity gain may be compensated by normalizing the MMSE combiner's output signals, at the cost of increasing the estimation MSE. The resultant normalized combiner weight vectors were identical to those of the MV combiner.

Our analysis of the LS- and MMSE detector's MSE and BER performance characterized in Section 4.2.6 underlined the MMSE detector's advantage compared to the LS detector in terms of achieving a lower signal estimation MSE and BER, as it was shown in Figure 4.6. Furthermore, we found that upon decreasing the number of simultaneous SDMA users L, while keeping the number of reception antennas P constant, the MMSE detector's performance quantified in terms of the SINR and BER was significantly improved, as it was shown in Figures 4.7 and 4.8. A further BER reduction was achieved with the aid of turbo-coding, as it was shown in Figure 4.9, although as usual, this was achieved at the cost of reducing each SDMA user's effective throughput, while also imposing further additional computational complexity.

Our detailed analysis of the different linear detectors' computational complexity provided in Section 4.2.7 revealed that the MMSE detector is slightly more complex than the LS detector. However, the general trend is that the complexity is proportional to the cube of the number of users L, as in case of LS detection or MMSE detection implemented in its left-inverse related form. A similar cubically proportional complexity dependence is valid also with respect to the number of reception antennas P, as in case of the MMSE detection implemented in its right-inverse related form.

For a more detailed summary and conclusions related to the family of linear detection techniques we refer to Section 4.2.8.

4.5.3 Summary and Conclusions Related to Non-Linear Detectors

Our summary and conclusions on non-linear detectors are separated into Sections 4.5.3.1, 4.5.3.2 and 4.5.3.3, considering SIC, PIC and ML detection, respectively.

4.5.3.1 SIC Detection

The employment of SIC detection was motivated earlier in the context of our performance analysis of MMSE detection in Section 4.2.6.3 by the specific observation that upon decreasing the number of simultaneous users L, while keeping the number of reception antennas P constant, the MMSE detector's BER performance was improved. This was because for a lower number of SDMA users the associated MMSE combiner was less constrained with respect to the specific choice of the combiner weights optimized for suppressing the interfering users' signal contributions. This allowed for a more effective noise mitigation. The same principle can be invoked in the context of an iterative detector, namely the standard SIC detector of Figure 4.10, where in each iteration- or cancellation

stage only the most dominant user having for example the highest SNR, SIR or SINR at the linear combiner's output was detected. The detected user's influence is eliminated from the partially decontaminated vector of signals received by the different antenna elements, upon invoking the detected user's remodulated signal. This principle was further detailed in Section 4.3.1.1.

In the context of the BER and SER performance results of Section 4.3.1.4 we found that the standard SIC detector suffers from the effects of error propagation across the different detection stages. In fact, it was observed that if a symbol error occurred in one of the lower-index detection stages, then there was a relatively high probability that symbol errors also occurred in the higher-index detection stages. By contrast, if correct symbol decisions were made in the lower-index detection stages, then the probability that an error occurred in one of the higher-index detection stages was lower, than for the lower-index detection stages. This was a consequence of the MIMO channel's increased diversity order in the context of the higher-index detection stages, following the removal of the signal contributions of those users, which had already been detected. In order to mitigate the effects of error propagation across the different detection stages, the standard SIC detector was appropriately modified.

More specifically, in the context of the M-SIC scheme discussed in Section 4.3.1.2 an $M > 1$ number of tentative symbol decisions are tracked from each detection node. Consequently, after the detection of the last user a decision has to be made as to which of the $M^{(i-1)}$ number of vectors of the different users' tentative symbols is most likely to have been transmitted. The significant performance advantage offered by M-SIC compared to standard SIC is achieved at the cost of an increased computational complexity, which is related to the additional number of 'decontamination'- and demodulation operations associated with the increased number of detection nodes involved.

Based on the observation that symbol error propagation events are predominantly triggered by the lower-index detection stages, as it was evidenced by Figure 4.16, a viable strategy of reducing the complexity of M-SIC is to restrict the employment of $M > 1$ number of tentative symbol decision per detection node to the lower-index detection stages, while at the higher-index detection stages employing $M = 1$. This strategy was discussed in Section 4.3.1.2.2 and it was termed partial M-SIC- or pM-SIC.

A further complexity reduction was achieved in Section 4.3.1.2.3 by restricting the employment of M-SIC- or partial M-SIC to those specific OFDM subcarriers, which exhibited a relatively low SINR during the first detection stage, while using standard SIC in conjunction with $M = 1$ in the subcarriers exhibiting a higher SINR. This strategy, which was initially proposed in [53, 117] was termed as Selective-Decision-Insertion M-SIC (SDI-M-SIC).

Our further discussions presented in Section 4.3.1.3 addressed the task of soft-bit generation in the context of standard SIC. While our rudimentary approach in Section 4.3.1.3.1 followed the philosophy of soft-bit generation contrived for the MMSE detection technique, as discussed in Section 4.2.5, the improved 'weighted' soft-bit metric of Section 4.3.1.3.2 additionally accounted for

the effects of error-propagation across the different SIC stages. More specifically, in case of relatively unreliable symbol decisions generated during the previous SIC detection stages a viable strategy is to de-emphasize the soft-bits generated for the current detection stage by appropriately decreasing their value and thus indicating a low associated confidence.

The assessment of the BER and SER performance exhibited by the standard SIC, M-SIC, pM-SIC and SDI-M-SIC schemes was conducted in Section 4.3.1.4. Specifically, we found in Figure 4.12 that the BER and SER performance of SIC- and M-SIC detection was significantly improved upon increasing the $L = P$ number of users and reception antennas of the 'fully loaded' SDMA-OFDM system. This is, because for a higher number of users, the SIC detector benefits from selecting the most dominant user from a larger 'pool' of different users at a specific detection stage, with the desirable effect of reducing the probability of incurring a low-SINR user as the most dominant user. Furthermore, in Figure 4.12 we found that upon employing M-SIC instead of standard SIC, a further substantial reduction of the BER or SER can be achieved. Using the SINR instead of the SNR recorded at the linear combiner's output in each detection stage for identifying the most dominant user yielded a noticeable BER or SER reduction, although only for SDMA scenarios, where the number of users and reception antennas was in excess of four. The effects of error propagation were detailed in Sections 4.3.1.4.2, 4.3.1.4.3 and 4.3.1.4.4. Furthermore, the SER performance of both pM-SIC and SDI-M-SIC was evaluated in Sections 4.3.1.4.5 and 4.3.1.4.6 with associated Figure 4.16. These schemes were employed for reducing the potentially substantial computational complexity associated with M-SIC. Specifically, in the context of an SDMA scenario supporting $L = 4$ simultaneous users with the aid of $P = 4$ reception antennas we found that employing $M = 2$ tentative symbol decisions per detection node during the first two detection stages ($L_{\text{pM-SIC}} = 2$) of pM-SIC, which was reduced to $M = 1$ symbol decision per detection node during the higher-index detection stages, results in an SNR degradation of approximately 1dB at an SER of 10^{-5}. This 1dB SNR degradation was the price of halving the computational complexity quantified in terms of the number of comparisons to be conducted, as it was shown with the aid of Figure 4.19. Our performance assessment of SDI-pM-SIC was the topic of Section 4.16, which demonstrated that in the context of the specific indoor WATM channel model of Section 6.1.1, SDI-pM-SIC yields the same SER performance as pM-SIC ($L_{\text{pM-SIC}} = 1$)[28], provided that in the context of SDI-pM-SIC pM-SIC is employed in the $N_{\text{SDI}}^{[1]} = 64$ number of lowest-SINR subcarriers recorded during the first detection stage, while using standard SIC in the remaining subcarriers. The performance assessment of the various SIC schemes was concluded with the evaluation of the BER performance exhibited by turbo-coded standard SIC detection-assisted SDMA-OFDM in Figures 4.17 and 4.18, which conveniently highlighted the benefits of the weighted soft-bit metric in comparison to the standard soft-bit metric, both of which were outlined in Section 4.3.1.3.

[28]This implied using $M = 2$ tentative symbol decisions at the first detection stage, which was reduced to employing $M = 1$ symbol decision during the remaining detection stages.

Finally, an analysis of the computational complexity exhibited by the various SIC schemes was carried out in Section 4.3.1.5. Specifically, in Figure 4.19 it was demonstrated that amongst the various successive interference cancellation based detectors the standard SIC detector is the least complex one, while M-SIC exhibits the highest complexity. A compromise between performance and complexity is constituted by the partial M-SIC scheme. For a more detailed summary and conclusions we refer to Section 4.3.1.6.

4.5.3.2 PIC Detection

The employment of the PIC detection scheme discussed in Section 4.3.2 was partially motivated by the SIC detector's potentially high complexity, which is related to the requirement of identifying the most dominant user - as well as recalculating the selected user's weight vector - in each detection stage, as outlined in Section 4.3.1. Furthermore, we found in the context of SIC detection that the highest AWGN mitigation was achieved by the linear combiner employed in each of the SIC detection stages, during its last detection stage, following the successful removal of all interfering co-channel users' contributions.

As a consequence, the PIC scheme portrayed in Figure 4.20 was investigated. In the context of this arrangement tentative estimates of the different users' transmitted signals were generated with the aid of a linear combiner, which was the MMSE combiner of Section 4.2.3 in our specific case. These signal estimates were then demodulated in order to obtain tentative symbol decisions, which were remodulated and subtracted from the vector of signals received by the different antenna elements, upon taking into account the effects of the channel. As a result, a potentially interference-free vector of received signals was obtained for each user, provided that correct symbol decisions were made for the remaining users. Hence, the MMSE combiners, which were employed for obtaining improved signal estimates from the decontaminated array output vectors became then capable of more effectively suppressing the AWGN. This principle was further detailed in Section 4.3.2.1.

However, in the context of our performance study provided in Section 4.3.2.3 we found that in the absence of channel coding the detector performs only slightly better, than the MMSE detector. Specifically, in the context of the 'fully loaded' SDMA scenario of four reception antennas supporting four simultaneous SDMA users, as characterized in Figure 4.21, the SNR advantage of PIC detection over MMSE detection when aiming for maintaining a BER of 10^{-4} was as low as 1.25dB, while for a 'minimalistic' SDMA scenario of two reception antennas and two simultaneous users an SNR advantage of 3.03dB was observed at the same BER. The relatively modest SNR improvement of 1.25dB was related to the effect that if the symbol decisions obtained during the first detection stage were erroneous even for a single user, then during the PIC process of Figure 4.20 the remaining users' received signals were imperfectly decontaminated. This phenomenon had the effect of potentially incurring erroneous symbol decisions for all the other users as well during the following

demodulation process.

In order to combat these effects it was proposed in Section 4.3.2.2 to combine the PIC detection scheme with turbo-decoding, incorporated into the classification module of Figure 4.20. A remodulated reference signal to be used in the PIC process may be generated based on the original information bit-positions or 'source'-related soft-output bits of the turbo-decoder, requiring the slicing, re-encoding and remodulation of these bits. Alternatively, the 'source- plus parity'-related soft-output bits may be sliced and remodulated, which exhibited a slight advantage in Figure 4.22 in terms of the system's BER performance. In order to render the associated BER simulation results presented in Figure 4.22 comparable to those of the other detectors we decided to equally split the total affordable number of PIC iterations into those employed during the first- and the second PIC stage. Compared to turbo-coded MMSE detection-assisted SDMA-OFDM a dramatic performance advantage was achieved with the aid of this arrangement, as it was shown in our final performance comparison of the different detection schemes portrayed in Figure 4.26.

A detailed complexity analysis of the PIC detector was conducted in Section 4.3.2.4 and based on these equations it became obvious in our final comparison of the different detectors' complexities quantified in Figure 4.27 that the PIC detector constitutes an attractive design compromise between the MMSE- and standard SIC detectors. For a more detailed summary and conclusions on PIC detection we refer to Section 4.3.2.5.

4.5.3.3 ML Detection

In Section 4.3.3 the optimum ML detector was described and characterized. As argued in Section 4.3.3.1, ML detection is based on the strategy of maximizing the *a posteriori* probability $P(\check{\mathbf{s}}|\mathbf{x}, \mathbf{H})$ that a hypothetic 'L-user' vector of symbols $\check{\mathbf{s}}$ was composed of the individual symbols transmitted by the L different users over a channel characterized by the matrix $\mathbf{H}$ defined in Equation 4.212, conditioned on the vector $\mathbf{x}$ of signals received by the P different antenna elements. The maximization of the likelihood metric was carried out over the entire set $\mathcal{M}^L$ of M_c^L number of hypothetic 'L-user' symbol vectors constituted by the L different users' M_c-ary constellations. With the aid of Bayes' theorem [87] and upon exploiting that the different symbol combination vectors were transmitted with equal probability, it was furthermore shown that maximizing the *a posteriori* probability $P(\check{\mathbf{s}}|\mathbf{x}, \mathbf{H})$ is equivalent to maximizing the *a priori* probability $P(\mathbf{x}|\check{\mathbf{s}}, \mathbf{H})$, which is the probability that the signal vector $\mathbf{x}$ was received by the different antenna elements, conditioned on transmitting the hypothetic 'L-user' symbol vector $\check{\mathbf{s}}$. It was furthermore shown that the *a priori* probability $P(\mathbf{x}|\check{\mathbf{s}}, \mathbf{H})$ is given by the multi-variate complex Gaussian distribution function $f(\mathbf{x}|\check{\mathbf{s}}, \mathbf{H})$, which is defined by its vector of mean values and by its covariance matrix. Hence, it was argued that maximization of the *a priori* probability $P(\mathbf{x}|\check{\mathbf{s}}, \mathbf{H})$ is equivalent to minimizing the argument of the exponential function of Equation 4.216 constituting the multi-variate complex

Gaussian distribution function. This involved minimizing the Euclidean distance between the vector $\mathbf{x}$ of received signals and the hypothetic 'L-user' vector of transmitted signals $\check{\mathbf{s}}$, upon taking into account the effects of the MIMO channel described by the channel matrix $\mathbf{H}$ of Equation 4.212, again for all trial-vectors contained in the set $\mathcal{M}^L$ of M_c^L number of 'L-user' symbol vectors.

As part of minimizing the multi-user Euclidean distance metric, each of the M_c^L different hypothetic trial-vectors $\check{\mathbf{s}} \in \mathcal{M}^L$ has to be transformed to the received signal's space upon multiplication with the channel matrix $\mathbf{H}$ of Equation 4.212. It was demonstrated in Section 4.3.3.1 that if the number of simultaneous users L is significantly lower than the number of receiver antennas P, the associated complexity can potentially be reduced upon transforming each trial-vector first to the transmitted signal's space with the aid of a linear transform, followed by evaluating a modified Euclidean distance metric. It was shown in Section 4.3.3.2 that a particularly suitable transform is the LS-related transform matrix of Equation 4.225, which delivers a noise-contaminated unity-gain estimate of the 'L-user' vector of transmitted signals, simplifying the Euclidean distance metric employed.

Furthermore, the generation of soft-bit values for turbo-decoding at the receiver was alluded to in Section 4.3.3.3 based on the assumption of employing a separate trellis decoding of the different users' signals.

The BER performance of both the uncoded and turbo-coded scenarios was then characterized in Section 4.3.3.4. Specifically, in Figure 4.24 we found for the uncoded scenario that the ML detector's performance is relatively insensitive to the number of users L, given a fixed number of reception antennas P. In contrast to the linear combining based detectors discussed in this chapter, even when increasing the number of users beyond the number of reception antennas, the performance degradation is graceful. Furthermore, we found that similarly to the SIC detector's behaviour recorded when increasing the number of reception antennas, the ML detector's BER performance was significantly improved owing to the higher degree of diversity provided by a MIMO system of a higher order. Again, for the turbo-coded scenario we observed in Figure 4.25 a substantially improved BER performance compared to that of the uncoded scenario. For example, for the 'fully loaded' system of four reception antennas supporting four simultaneous users the BER at an SNR of 5dB was as low as 10^{-6}.

Our complexity analysis documented in Section 4.3.3.5 revealed that the ML detector's complexity is proportional to the M_c^L number of symbol combinations constituted by the L different users' M_c-ary trial symbols. For a more detailed summary and conclusions were refer to Section 4.3.3.6.

4.5.3.4 Overall Comparison of the Different Detection Techniques

Our final comparison of the different linear- and non-linear detection techniques in both uncoded- and turbo-coded scenarios was documented in Section 4.3.4. Specifically the achievable BER performance was documented in Figure 4.26, while the associated computational complexity, in Figure 4.27.

The essence of this comparison was that in all investigated scenarios - as expected - the ML detector constituted the best performing, but highest complexity solution, while the MMSE detector was the worst-performing, lowest-complexity solution.

A compromise in terms of performance and complexity was provided by the class of SIC detectors and its derivatives as documented in Section 4.3.1. While in the uncoded scenario of Figure 4.26 the M-SIC (M=2) scheme performed almost identically to the ML detector, a substantial performance degradation was observed in Figure 4.26 for the lower-complexity standard SIC detector. A trade-off between the performance and the complexity associated with the standard SIC and M-SIC schemes of Sections 4.3.1.1 and 4.3.1.2.1 was achievable with the aid of the partial M-SIC or SDI-M-SIC arrangements of Sections 4.3.1.2.2 and 4.3.1.2.3. The associated performance results were, however, not repeated in Figure 4.26. By contrast, in the turbo-coded scenario, both detectors, namely the standard SIC and M-SIC (M=2) schemes of Sections 4.3.1.1 and 4.3.1.2.1 performed within a range of 1dB in excess of the SNR required by turbo-coded ML detection-assisted SDMA-OFDM, when maintaining a specific BER.

While PIC detection was unattractive in the uncoded scenario, owing to its relatively modest BER improvement compared to MMSE detection, in the turbo-coded scenario a significant BER improvement was achieved. However, for the range of BERs of our interest, namely below 10^{-4}, the PIC detector's performance was worse than that of turbo-coded standard SIC. This was related to the imperfections of the soft-bit estimates employed and hence there is still some potential for its improvement. Note that this performance improvement was achieved, while exhibiting a lower complexity, than that of standard SIC.

4.5.3.5 Summary and Conclusions Related to Performance Enhancement Techniques

In order to render the less complex, but also less powerful detection techniques, such as MMSE and PIC also more attractive for employment in uncoded scenarios, the performance enhancement techniques of Section 4.4.1 may be invoked, which are well-known from the field of single reception antenna based communications systems. Specifically, constant throughput adaptive modulation as well as Walsh-Hadamard spreading using orthogonal spreading codes may be employed. While AOFDM capitalizes on the difference of the different subcarriers' channel quality offered by the wide-band channel, spreading aims for averaging the subcarriers' quality differences.

4.5.3.5.1 Adaptive Modulation Assisted SDMA-OFDM Adaptive modulation employed in the context of OFDM - which we termed as AOFDM - is based on the idea of assigning a more robust, lower-throughput modulation mode to those subcarriers, which are likely to cause symbol errors in the context of a fixed-mode transceiver as a result of their associated low SNR. By contrast, a less robust, higher throughput modulation mode is assigned to the higher-quality subcarriers. These concepts were further elaborated on in Section 4.4.1. In the context of our associated BER performance investigations conducted in Section 4.4.1.3 we found that as shown in Figure 4.29, the employment of adaptive modulation in an MMSE detection-assisted SDMA-OFDM system is only advantageous in terms of further reducing the BER in specific scenarios, where the number of simultaneous users L approaches the number of reception antennas P. This is because in this specific scenario the effective channel transfer function experienced by the different users is 'sufficiently non-flat' across the different subcarriers, with the result of exhibiting sufficient difference in terms of the associated channel quality for AOFDM to excel.

However, there are two aspects of adaptive modulation, which render its employment less convenient. First of all, it is necessary to provide an estimate of the subcarrier channel quality for the next transmission timeslot, which could be generated on the basis of the channel estimates available for the current transmission timeslot, upon assuming time-invariance of the channel. However, under time-variant channel conditions, the more elaborate, potentially decision-directed channel prediction techniques as seen in Figure 4.28 have to be invoked, in order to obtain accurate estimates of the channel transfer function for the next transmission timeslot. Secondly, the employment of adaptive modulation requires the signalling of the requested modulation mode assignment to be used during the next transmission time-slot to the remote users, which requires the existence of a reverse-link and hence its applicability is mainly confined to Time-Division Duplexing (TDD) systems, where every uplink transmission time-slot is followed by a down-link time-slot and vice-versa. Furthermore, the transmission of channel-quality related side-information reduces the AOFDM modem's effective throughput, which has to be compensated for by appropriately increasing the target throughput of the AOFDM modem.

4.5.3.5.2 Walsh-Hadamard Transform Spreading Assisted SDMA-OFDM The above-mentioned deficiencies of AOFDM constituted the motivation for the alternative technique of employing spreading with the aid of orthogonal spreading codes across the various subcarriers, which was the topic of Section 4.4.2. We argued that as a result of the spreading codes' orthogonality the operations to be carried out at the receiver - also in the multi-user SDMA-WHTS-OFDM scenario - can be separated into that of channel transfer function equalization and WHT despreading, which substantially simplifies the receiver's design. This was illustrated in Figures 4.30 and 4.31 for the single- and multi-user OFDM scenarios, respectively.

The initial BER performance results portrayed in Figure 4.32 in the context of the single user

WHTS-OFDM scenario demonstrated that with the aid of spreading almost the same BER performance can be achieved, as in conjunction with employing adaptive modulation capitalizing on perfect channel transfer function predictions used for estimating the subcarrier channel quality during the modulation mode assignment. Furthermore, in contrast to AOFDM, there is no need for transmitting side-information to the remote transmitters. Hence, the employment of WHTS-OFDM is amenable to a wider range of transmission scenarios. As shown in [144] the WHT spreading employed at the transmitter can be efficiently combined with the OFDM-related IFFT. As for the receiver, we can argue that the additional complexity imposed by performing the despreading operation is marginal, compared to that owing to multi-user detection.

However, the main essence of our investigations was that as portrayed in Figure 4.34, with the aid of spreading the performance of the MMSE- or PIC detection assisted SDMA-OFDM systems can be significantly improved, again, provided that the effective transmission channel is strongly frequency selective. As outlined in the previous section, this is the case in almost fully-loaded SDMA-OFDM scenarios, where the number of simultaneous users L approaches the number of reception antennas P. For sufficiently high SNRs the MMSE- or PIC detection-assisted WHTS-OFDM systems of Section 4.4.2.2 were capable of outperforming standard SIC detection-assisted SDMA-OFDM of Section 4.3.1.1.

Special Symbols - MUD Techniques for SDMA-OFDM

$b_m^{(l)}[n,k]$: Bit polarity associated with the l-th user at the m-th bit position.

$\mathcal{C}_{\text{lin,dem}}$: Computational complexity associated with the operation of received symbol classification or synonymously demodulation in the context of the linear detectors.

$\mathcal{C}_{\text{LS,direct}}$: Computational complexity associated with the LS solution $\hat{\mathbf{s}}_{\text{LS}}[n,k]$ found for a specific subcarrier, without explicitly generating the weight matrix.

$\mathcal{C}_{\text{LS,W+cmb}}$: Computational complexity associated with the LS solution $\hat{\mathbf{s}}_{\text{LS}}[n,k]$ found for a specific subcarrier, upon explicitly generating the weight matrix, followed by combining the different antennas' received signals.

$\mathcal{C}_{\text{LS}}$: Total computational complexity associated with LS detection invoked for a specific subcarrier, without explicitly generating the weight matrix.

$\mathcal{C}_{\text{ML}}$: Computational complexity associated with the joint ML detection of the different users' transmitted symbols.

$\mathcal{C}_{\text{ML-trf,x}}$: Computational complexity associated with the transform-based joint ML detection-related (x=err-cov:) error-covariance matrix calculation, (x=LS-est:) calculation of the LS estimates and (x=trial:) evaluation of the trial-symbol-vectors.

$\mathcal{C}_{\text{ML-trf}}$: Total computational complex associated with the transform-based joint ML detection of the different users' transmitted symbols for a specific subcarrier.

$\mathcal{C}_{\text{MLSE}}$: Computational complexity associated with the joint ML detection assisted soft-bit generation for a specific subcarrier.

$\mathcal{C}_{\text{MMSE,direct}}$: Computational complexity associated with the MMSE solution $\hat{\mathbf{s}}_{\text{MMSE}}[n,k]$ for a specific subcarrier, without explicitly generating the weight matrix.

$\mathcal{C}_{\text{MMSE,W+cmb}}$: Computational complexity associated with the MMSE solution for a specific subcarrier, upon explicitly generating the weight matrix, followed by combining the different antennas received signals.

$\mathcal{C}_{\text{MMSE}}$: Total computational complexity associated with the MMSE detection for a specific subcarrier, without explicitly generating the weight matrix.

$\mathcal{C}_{\text{PIC,x}}^{[1]}$: Computational complexity associated with the PIC-related (x=MMSE,direct:) and MMSE-assisted generation of linear signal estimates and (x=dem:) with the

demodulation process during the first PIC detection stage for a specific subcarrier.

$\mathcal{C}^{[2]}_{\text{PIC,x}}$: Computational complexity associated with the PIC-related (x=sub:) subtraction, (x=cmb:) diversity combining and (x=dem:) demodulation during the second PIC detection stage for a specific subcarrier.

$\mathcal{C}_{\text{PIC}}$: Total computational complexity associated with the PIC detection for a specific subcarrier.

$\mathcal{C}_{\text{SIC,x}}$: Computational complexity associated with the SIC-related (x=stp:) startup, (x=W:) weight vector calculation, (x=obj:) objective function calculation, (x=cmb:) combining, (x=dem:) demodulation and (x=upd:) updating for a specific subcarrier.

$\mathcal{C}_{\text{SIC}}$: Total computational complexity of standard SIC detection for a specific subcarrier.

$\mathcal{C}_{\text{p/M-SIC,x}}$: Computational complexity associated with the M-SIC- or pM-SIC -related (x=cmb:) combining, (x=dem) demodulation and (x=upd:) updating for a specific subcarrier.

$\mathcal{C}_{\text{p/M-SIC}}$: Total computational complexity of M-SIC- or pM-SIC detection for a subcarrier.

E_j: j-th error-event employed for characterizing the effects of SIC-related error propagation. The index j is generated by interpreting the different detection stages' conditions of an error-free detection ('0') or an erroneous detection ('1') as a binary number.

$\mathbf{E}_{\text{MMSE}}[n]$: Diagonal-shaped MMSE-based equalizer matrix employed in the context of the single-user WHTS-OFDM system: $\mathbf{E}_{\text{MMSE}}[n] \in \mathbb{C}^{K \times K}$.

$f(x^{(l)}_{\text{eff}}|s^{(l)}, H^{(l)}_{\text{eff}})$: Complex Gaussian distribution function of the signal $x^{(l)}_{\text{eff}}[n,k]$ observed at the l-th combiner's output, conditioned on transmitting the symbol $s^{(l)}[n,k]$ over a channel characterized by the effective transfer factor $H^{(l)}_{\text{eff}}[n,k]$.

$f(\mathbf{x}|\mathbf{s},\mathbf{H})$: Multi-variate complex Gaussian distribution function of the vector $\mathbf{x}[n,k]$ of signals observed at the different BS receiver antenna elements conditioned on transmitting the vector $\mathbf{s}[n,k]$ of symbols over a channel characterized by the matrix $\mathbf{H}[n,k]$.

$H_{\text{MMSE}}[n,k]$: Effective joint transfer factor of the equalizer and the channel in the context of single-user WHTS-OFDM.

$H_{\text{eff}}^{(l)}[n,k]$: Effective transfer factor associated with the l-th user's signal contribution to the l-th user's linear combiner output signal $x_{\text{eff}}^{(l)}[n,k]$, which is given by: $H_{\text{eff}}^{(l)}[n,k] = \mathbf{w}^{(l)H}[n,k]\mathbf{H}^{(l)}[n,k]$.

$H_p^{(l)}[n,k]$: Channel transfer factor associated with the channel encountered between the l-th user's single transmit antenna and the p-th receiver antenna element in the k-th subcarrier of the n-th OFDM symbol period: $H_p^{(l)}[n,k] \in \mathbb{C}$.

$\mathbf{H}^{(l)}[n,k]$: Vector of channel transfer factors $H_p^{(l)}[n,k]$, $p = 1,\ldots,P$ encountered between the l-th user's transmit antenna and the P receiver antenna elements: $\mathbf{H}^{(l)}[n,k] \in \mathbb{C}^{P\times 1}$.

$\mathbf{H}[n,k]$: Matrix constituted by the vectors of channel transfer factors $\mathbf{H}^{(l)}[n,k]$, $l = 1,\ldots,L$, each hosting the channel transfer factors between a specific user's single transmit antenna and the L receiver antenna elements: $\mathbf{H}[n,k] \in \mathbb{C}^{P\times L}$.

$\mathbf{H}_{\text{WHT}}$: Short-hand: $\mathbf{H}_{\text{WHT}}[n] = \mathbf{H}[n]\mathbf{U}_{\text{WHT}}$.

$l^{[i]}$: Index of the user selected during the i-th SIC detection stage from the set of remaining users with indices contained in $\mathcal{L}^{[i]}$.

L: Number of simultaneous users.

$\mathcal{L}^{[i]}$: Set of indices associated with the $L-i+1$ number of remaining users during the i-th SIC detection stage.

$L_m^{(l)}[n,k]$: Soft-bit value or log-likelihood ratio associated with the l-th user at the m-th bit position in the context of the joint ML detection of the different users' symbols.

$L_{m,\approx}^{(l)}[n,k]$: Soft-bit value or log-likelihood ratio associated with the l-th user at the m-th bit position. The index $()_{\approx}$ serves to distinguish the soft-bit value from the optimum soft-bit value generated in the context of the joint ML detection of the different users' symbols.

$L_{\text{pM-SIC}}$: Index of the detection stage up to which $M > 1$ number of tentative symbol decisions are tracked in the context of pM-SIC.

M: Number of tentative symbol decisions per detection node in the context of M-SIC, where we have $M \leq M_c$.

M_c: Number of constellation points associated with the modulation scheme employed.

M_{WHT}: Number of subcarriers contained in a WHT block.

$\text{MSE}^{(l)}[n,k]$: MSE of the l-th user's linear symbol estimate in the context of linear detection techniques.

$\overline{\text{MSE}}[n,k]$: Average estimation MSE of the L different users' transmitted symbols, which is given by: $\overline{\text{MSE}}[n,k] = \frac{1}{L}\text{Trace}(\mathbf{R}_{\Delta\hat{\mathbf{s}}}[n,k])$.

$\overline{\text{MMSE}}_{\text{MMSE}}[n]$: Estimation MSE averaged over the different subcarriers, which is identical for all linear subcarrier symbol estimates $\hat{s}[n,k],\ k = 0,\ldots,K-1$ after equalization and despreading in the context of the single-user WHTS-OFDM system.

$\mathcal{M}_c$: Set of the M_c number of constellation points associated with the modulation scheme employed.

$\mathcal{M}_{cm}^{b}$: Subset of the set $\mathcal{M}_c$ of constellation points, associated with a bit polarity of $b \in \{0,1\}$ at the m-th bit position.

$\mathcal{M}^{(l)}$: Set of the M_c number of trial-symbols associated with the modulation scheme employed by the l-th user. The trial-symbols are the appropriately amplified constellation points.

$\mathcal{M}_{cm}^{b(l)}$: Subset of the set $\mathcal{M}^{(l)}$ of the l-th user's trial symbols, associated with a bit polarity of $b \in \{0,1\}$ at the m-th bit position.

$\mathcal{M}^{L}$: Set of the M_c^L number of trial-symbol-vectors $\check{\mathbf{s}}$.

$\mathcal{M}_{m}^{b(l)L}$: Subset of the set $\mathcal{M}^{L}$ of the L users' trial-symbol-vectors, associated with a bit polarity of $b \in \{0,1\}$ at the l-th user's m-th bit position.

$n_{\text{eff}}^{(l)}[n,k]$: Effective interference- plus noise contribution associated with the l-th user's linear combiner output signal $x_{\text{eff}}^{(l)}[n,k] = \hat{s}^{(l)}[n,k]$, which is given by: $n_{\text{eff}}^{(l)}[n,k] = \hat{s}_I^{(l)}[n,k] + \hat{s}_N^{(l)}[n,k]$.

$n_p[n,k]$: AWGN signal contribution associated with the p-th receiver antenna element.

$\mathbf{n}[n,k]$: Vector of AWGN signal contributions $n_p[n,k],\ p = 1,\ldots,P$ associated with the P different receiver antenna elements: $\mathbf{n}[n,k] \in \mathbb{C}^{P\times 1}$.

$N_{\text{SDI}}^{[1]}$: Number of subcarriers for which more than one symbol decision is tracked from the first detection stage in the context of SDI-M-SIC.

$\mathbf{p}_{\text{LS}}[n,k]$: LS-related 'cross-correlation' vector: $\mathbf{p}_{\text{LS}}[n,k] = \mathbf{H}^H[n,k]\mathbf{x}[n,k] \in \mathbb{C}^{L\times 1}$.

P: Number of BS receiver antenna elements.

$P(x_{\text{eff}}^{(l)}[n,k])$: Probability of the signal $x_{\text{eff}}^{(l)}[n,k]$, which is given by the total probability, namely by $P(x_{\text{eff}}^{(l)}) = \sum_{\check{s}\in\mathcal{M}^{(l)}} P(x_{\text{eff}}^{(l)}|\check{s}, H_{\text{eff}}^{(l)}) \cdot P(\check{s})$.

$P(x_{\text{eff}}^{(l)}|s^{(l)}, H_{\text{eff}}^{(l)})$: *A priori* probability that $x_{\text{eff}}^{(l)}[n,k]$ is observed at the l-th user's combiner output under the condition, that $s^{(l)}[n,k]$ was transmitted, which is given by: $P(x_{\text{eff}}^{(l)}|s^{(l)}, H_{\text{eff}}^{(l)}) = f(x_{\text{eff}}^{(l)}|s^{(l)}, H_{\text{eff}}^{(l)})$.

$P(\check{s}^{(l)}[n,k])$: Probability of the symbol $\check{s}^{(l)}[n,k]$. When no *a priori* probability is available about the transmitted symbols, it is assumed that all symbols $\check{s}^{(l)}[n,k] \in \mathcal{M}^{(l)}$ appear with the same probability $P(\check{s}^{(l)}[n,k]) = \frac{1}{M_c}$.

$P(\check{s}^{(l)}|x_{\text{eff}}^{(l)}, H_{\text{eff}}^{(l)})$: *A posteriori* probability that the symbol $\check{s}^{(l)}[n,k]$ was transmitted by the l-th user under the condition that the signal $x_{\text{eff}}^{(l)}[n,k]$ has been received, which can be expressed with the aid of the Bayes' rule as: $P(\check{s}^{(l)}|x_{\text{eff}}^{(l)}, H_{\text{eff}}^{(l)}) = P(x_{\text{eff}}^{(l)}|\check{s}^{(l)}, H_{\text{eff}}^{(l)}) \frac{P(\check{s}^{(l)})}{P(x_{\text{eff}}^{(l)})}$.

$P(b_m^{(l)}|x_{\text{eff}}^{(l)}, H_{\text{eff}}^{(l)})$: *A posteriori* probability that a bit having a polarity of $b_m^{(l)}[n,k]$ was transmitted by the l-th user at the m-th bit position, under the condition that the signal $x_{\text{eff}}^{(l)}[n,k]$ has been received.

$P_{\text{joint}}^{[i]}[n,k]$: Joint probability of the symbol decisions up to- and including the i-th SIC detection stage, employed in the context of the weighted soft-bit generation for the $(i+1)$-th detection stage.

$P(\check{\mathbf{s}}[n,k])$: Probability of the vector $\check{\mathbf{s}}[n,k]$ of symbols. When no *a priori* probability is available about the transmitted symbols, it is assumed that all symbols $\check{\mathbf{s}}[n,k] \in \mathcal{M}^L$ appear with the same probability $P(\check{\mathbf{s}}[n,k]) = \frac{1}{M_c^L}$.

$P(\mathbf{x}[n,k])$: Probability of the vector $\mathbf{x}[n,k]$ of signals, which is given as the total probability, namely: $P(\mathbf{x}) = \sum_{\check{\mathbf{s}}\in\mathcal{M}^L} P(\mathbf{x}|\check{\mathbf{s}}, \mathbf{H})P(\check{\mathbf{s}})$.

$P(\mathbf{x}|\mathbf{s}, \mathbf{H})$: *A priori* probability that the vector $\mathbf{x}[n,k]$ of signals is observed at the BS receiver antenna elements under the condition that the vector $\mathbf{s}[n,k]$ of symbols has been transmitted: $P(\mathbf{x}|\mathbf{s}, \mathbf{H}) = f(\mathbf{x}|\mathbf{s}, \mathbf{H})$.

$P(\check{\mathbf{s}}|\mathbf{x}, \mathbf{H})$: *A posteriori* probability that the vector $\check{\mathbf{s}}[n,k]$ of symbols was transmitted under the condition that the vector $\mathbf{x}[n,k]$ of signals has been received, which can be expressed according to Bayes' rule as: $P(\check{\mathbf{s}}|\mathbf{x}, \mathbf{H}) = P(\mathbf{x}|\mathbf{s}, \mathbf{H}) \frac{P(\check{\mathbf{s}})}{P(\mathbf{x})}$.

$\mathbf{P}$: Diagonal matrix of the L different users' transmit powers σ_l^2, $l = 1, \ldots, L$: $\mathbf{P} \in \mathbb{C}^{L\times L}$.

$\mathbf{P}_{\text{MC}}$: Diagonal matrix of the K subcarriers' transmit powers in the context of the single-user WHTS-OFDM system: $\mathbf{P}_{\text{MC}} = \sigma_s^2\mathbf{I} \in \mathbb{C}^{K\times K}$.

$\mathbf{P}_{\text{SNR}}$: Diagonal matrix of the L different users' SNR values given by $\text{SNR}^{(l)} = \frac{\sigma_l^2}{\sigma_n^2}$, $l = 1,\ldots,L$ at the receiver antenna elements: $\mathbf{P}_{\text{SNR}} \in \mathbb{C}^{L\times L}$.

$\mathbf{P}_{\text{LS}}[n,k]$: LS-related projection matrix: $\mathbf{P}_{\text{LS}}[n,k] = (\mathbf{H}^H[n,k]\mathbf{H}[n,k])^{-1}\mathbf{H}[n,k] \in \mathbb{C}^{L\times P}$.

$\mathbf{Q}_{\text{LS}}[n,k]$: LS-related 'auto-correlation' matrix: $\mathbf{Q}_{\text{LS}}[n,k] = \mathbf{H}^H[n,k]\mathbf{H}[n,k] \in \mathbb{C}^{L\times L}$.

$\mathbf{R}_{a,S}^{(l)}[n,k]$: Auto-correlation matrix of the l-th user's signal contribution to the vector $\mathbf{x}[n]$ of received signals: $\mathbf{R}_{a,S}^{(l)}[n,k] \in \mathbb{C}^{P\times P}$.

$\mathbf{R}_{a,I}^{(l)}[n,k]$: Auto-correlation matrix of the $(L-1)$ interfering users' signal contributions to the vector $\mathbf{x}[n]$ of received signals, when regarding the l-th user as the desired user: $\mathbf{R}_{a,I}^{(l)}[n,k] \in \mathbb{C}^{P\times P}$.

$\mathbf{R}_{a,N}[n,k]$: Auto-correlation matrix of the AWGN signal contribution to the vector $\mathbf{x}[n]$ of received signals: $\mathbf{R}_{a,N}[n,k] \in \mathbb{C}^{P\times P}$.

$\mathbf{R}_{a,I+N}^{(l)}[n,k]$: Short-hand: $\mathbf{R}_{a,I+N}^{(l)}[n,k] = \mathbf{R}_{a,I}^{(l)}[n,k] + \mathbf{R}_{a,N}[n,k] \in \mathbb{C}^{P\times P}$.

$\mathbf{R}_a[n,k]$: Auto-correlation matrix of the vector of received signals $\mathbf{x}[n,k]$: $\mathbf{R}_a[n,k] = E\{\mathbf{x}[n,k]\mathbf{x}^H[n,k]\} = \mathbf{H}\mathbf{P}\mathbf{H}^H + \sigma_n^2\mathbf{I} \in \mathbb{C}^{P\times P}$.

$\mathbf{R}_{\overline{a}}[n,k]$: Left-inverse related form of the auto-correlation matrix: $\mathbf{R}_{\overline{a}}[n,k] = \mathbf{H}^H\mathbf{H}\mathbf{P} + \sigma_n^2\mathbf{I} \in \mathbb{C}^{L\times L}$.

$\mathbf{R}_c[n,k]$: Cross-correlation matrix of the vectors of received signals $\mathbf{x}[n,k]$ and transmitted symbols $\mathbf{s}[n,k]$: $\mathbf{R}_c[n,k] = E\{\mathbf{x}[n,k]\mathbf{s}^H[n,k]\} = \mathbf{H}[n,k]\mathbf{P} \in \mathbb{C}^{P\times L}$.

$\mathbf{R}_{\Delta\hat{\mathbf{s}}}[n,k]$: Auto-correlation matrix of the vector $\Delta\hat{\mathbf{s}}[n,k]$ constituted by the transmitted symbols' estimation errors: $\mathbf{R}_{\Delta\hat{\mathbf{s}}}[n,k] = E\{\Delta\hat{\mathbf{s}}[n,k]\Delta\hat{\mathbf{s}}^H[n,k]\} \in \mathbb{C}^{L\times L}$.

$\mathbf{R}_{\mathbf{n}}$: Auto-correlation matrix of the AWGN at the receiver antenna elements: $\mathbf{R}_{\mathbf{n}} = \sigma_n^2\mathbf{I} \in \mathbb{C}^{P\times P}$.

$s^{(l)}[n,k]$: Symbol transmitted by the l-th user.

$\hat{s}^{(l)}[n,k]$: Linear estimate of the symbol transmitted by the l-th user, which is given by: $\hat{s}^{(l)}[n,k] = \mathbf{w}^{(l)H}[n,k]\mathbf{x}[n,k]$.

$\hat{s}_S^{(l)}[n,k]$: Desired l-th user's contribution to the linear estimate $\hat{s}^{(l)}[n,k]$ of the symbol transmitted by the l-th user, based on using the weight vector $\mathbf{w}^{(l)}[n,k]$.

$\hat{s}_I^{(l)}[n,k]$: Undesired interfering users' contribution to the linear estimate $\hat{s}^{(l)}[n,k]$ of the symbol transmitted by the l-th user, based on using the weight vector $\mathbf{w}^{(l)}[n,k]$.

$\hat{s}_N^{(l)}[n,k]$: Undesired noise-related contribution to the linear estimate $\hat{s}^{(l)}[n,k]$ of the symbol transmitted by the l-th user, based on using the weight vector $\mathbf{w}^{(l)}[n,k]$.

$\hat{s}^{(l)}[n,k]$: Linear estimate of the symbol transmitted by the l-th user after despreading in the context of the multi-user WHTS-OFDM system.

$\check{s}^{(l)}[n,k]$: Classified linear estimate of the symbol transmitted by the l-th user.

$\check{s}_{\text{ML}\approx}^{(l)}[n,k]$: The symbol that is most likely to have been transmitted by the l-th user, found upon maximizing the *a posteriori* probability $P(\check{s}^{(l)}|x_{\text{eff}}^{(l)}, H_{\text{eff}}^{(l)})$ across the set of trial-symbols $\mathcal{M}^{(l)}$. The index $()_{\approx}$ is employed in order to distinguish this solution from the optimum solution $\check{s}_{\text{ML}}[n,k]$ found by joint ML detection of the L different users' transmitted symbols.

$\check{s}_{m\approx}^{b(l)}[n,k]$: The symbol that is most likely to have been transmitted by the l-th user, found upon maximizing the *a posteriori* probability $P(\check{s}^{(l)}|x_{\text{eff}}^{(l)}, H_{\text{eff}}^{(l)})$ across the subset of trial-symbols $\mathcal{M}_m^{b(l)}$.

$\hat{\mathbf{s}}[n]$: Vector of the K subcarriers' linear symbol estimates in the context of the single-user WHTS-OFDM system: $\hat{\mathbf{s}}[n] \in \mathbb{C}^{K\times 1}$.

$\hat{\mathbf{s}}_{\text{MMSE}}[n]$: Vector of the K subcarriers' MMSE-based linear symbol estimates in the context of the single-user WHTS-OFDM system: $\hat{\mathbf{s}}_{\text{MMSE}}[n] \in \mathbb{C}^{K\times 1}$.

$\mathbf{s}[n,k]$: Vector of symbols $s^{(l)}[n,k]$, $l = 1,\ldots,L$ transmitted by the L different users: $\mathbf{s}[n,k] \in \mathbb{C}^{L\times 1}$.

$\hat{\mathbf{s}}[n,k]$: Vector of linear symbol estimates $\hat{s}^{(l)}[n,k]$, $l = 1,\ldots,L$, which is given by: $\hat{\mathbf{s}}[n,k] = \mathbf{W}^H[n,k]\mathbf{x}[n,k] \in \mathbb{C}^{L\times 1}$.

$\hat{\mathbf{s}}_{\text{LS}}[n,k]$: LS-assisted vector of linear symbol estimates: $\hat{\mathbf{s}}_{\text{LS}}[n,k] = \mathbf{Q}_{\text{LS}}^{-1}[n,k]\mathbf{p}_{\text{LS}}[n,k] = \mathbf{P}_{\text{LS}}[n,k]\mathbf{x}[n,k] = \mathbf{W}_{\text{LS}}^H[n,k]\mathbf{x}[n,k] \in \mathbb{C}^{L\times 1}$.

$\check{\mathbf{s}}[n,k]$: Vector of classified linear symbol estimates $\check{s}^{(l)}[n,k]$, $l = 1,\ldots,L$, which is given by: $\check{\mathbf{s}}[n,k] \in \mathbb{C}^{L\times 1}$.

$\check{\mathbf{s}}_{\text{ML}}[n,k]$: Vector of symbols that are most likely to have been transmitted by the L different users, found upon maximizing the *a posteriori* probability $P(\check{\mathbf{s}}|\mathbf{x},\mathbf{H})$ across the set of trial-symbol-vectors $\mathcal{M}^L$.

$\check{\mathbf{s}}_m^{b(l)}$: Vector of symbols that are most likely to have been transmitted by the L different users found upon maximizing the *a posteriori* probability $P(\check{\mathbf{s}}|\mathbf{x}, \mathbf{H})$ across the subset of trial-symbol-vectors $\mathcal{M}_m^{b(l)L}$.

$\text{SINR}_{\text{WHT,MMSE}}[n]$: Subcarrier-averaged SINR associated with the linear subcarrier symbol estimates $\hat{s}[n,k]$, $k = 0, \ldots, K-1$ in the context of the single-user WHTS-OFDM system: $\text{SINR}_{\text{WHT,MMSE}}[n] = \frac{\sigma^2_{S,\text{WHT,MMSE}}}{\sigma^2_{I,\text{WHT,MMSE}} + \sigma^2_{N,\text{WHT,MMSE}}}$.

$\text{SINR}^{(l)}[n,k]$: SINR at the l-th user's associated combiner output, which is expressed as: $\text{SINR}^{(l)}[n,k] = \frac{\sigma_S^{(l)2}[n,k]}{\sigma_I^{(l)2}[n,k] + \sigma_N^{(l)2}[n,k]}$.

$\text{SIR}^{(l)}[n,k]$: SIR at the l-th user's associated combiner output: $\text{SIR}^{(l)}[n,k] = \frac{\sigma_S^{(l)2}[n,k]}{\sigma_I^{(l)2}[n,k]}$.

$\text{SNR}^{(l)}[n,k]$: SNR at the l-th user's associated combiner output: $\text{SNR}^{(l)}[n,k] = \frac{\sigma_S^{(l)2}[n,k]}{\sigma_N^{(l)2}[n,k]}$.

$\mathbf{U}_{\text{WHT}_N}$: N-th order Walsh-Hadamard Transform (WHT) matrix.

$\mathbf{w}^{(l)}[n,k]$: Weight vector used for estimating the l-th user's transmitted symbol: $\mathbf{w}^{(l)}[n,k] \in \mathbb{C}^{P\times 1}$.

$\mathbf{W}[n,k]$: Matrix of weight vectors $\mathbf{w}^{(l)}[n,k]$, $l = 1, \ldots, L$ used for estimating the L different users' transmitted symbols: $\mathbf{W}[n,k] \in \mathbb{C}^{P\times L}$.

$\mathbf{W}_{\text{LS}}[n,k]$: LS-optimized weight matrix: $\mathbf{W}_{\text{LS}}[n,k] = \mathbf{P}_{\text{LS}}^H \in \mathbb{C}^{P\times L}$.

$\mathbf{W}_{\text{MMSE}}[n,k]$: MMSE-optimized weight matrix: $\mathbf{W}_{\text{MMSE}}[n,k] = \mathbf{R}_a^{-1}[n,k]\mathbf{R}_c[n,k] \in \mathbb{C}^{P\times L}$ in its right-inverse related form, or $\mathbf{W}_{\text{MMSE}}[n,k] = \mathbf{R}_c[n,k]\mathbf{R}_a^{-1}[n,k]$ in its left-inverse related form.

$\mathbf{W}[n]$: Weight matrix in the context of the single-user WHTS-OFDM system: $\mathbf{W}[n] \in \mathbb{C}^{K\times K}$.

$\mathbf{W}_{\text{MMSE}}[n]$: MMSE-based weight matrix employed in the context of the single-user WHTS-OFDM system: $\mathbf{W}_{\text{MMSE}}[n] = \mathbf{E}_{\text{MMSE}}[n]\mathbf{U}_{\text{WHT}} \in \mathbb{C}^{K\times K}$.

$x_{\text{eff}}^{(l)}[n,k]$: Model of the l-th user's combiner output signal: $x_{\text{eff}}^{(l)}[n,k] = H_{\text{eff}}^{(l)}[n,k]s^{(l)}[n,k] + n_{\text{eff}}^{(l)}[n,k] = \hat{s}^{(l)}[n,k]$.

$x_p[n,k]$: Signal recorded at the p-th receiver antenna element.

$\mathbf{x}[n,k]$: Vector of signals $x_p[n,k]$, $p = 1, \ldots, P$ recorded at the P receiver antenna elements: $\mathbf{x}[n,k] \in \mathbb{C}^{P\times 1}$.

$\hat{\mathbf{x}}[n,k]$: Vector of linear estimates of the signals $x_p[n,k],\ p=1,\ldots,P$ recorded at the P receiver antenna elements: $\hat{\mathbf{x}}[n,k] \in \mathbb{C}^{P\times 1}$.

α_{SIC}: Constant employed in the context of quantifying the SIC detector's computational complexity: $\alpha_{\text{SIC}} = \sum_{i=1}^{L} i = \frac{1}{2}L(L+1)$.

β_{MMSE}: Proportionality constant associated with the MMSE combiner' weight vector in the context of its representation in standard form.

β_{MV}: Proportionality constant associated with the MV combiner's weight vector in the context of its representation in standard form.

$\beta_{\text{p/M-SIC}}$: Constants employed in the context of quantifying the M-SIC- or pM-SIC detector's computational complexity.

$\gamma_{\text{p/M-SIC,\{i/ii\}}}$: Constants employed in the context of quantifying the M-SIC- or pM-SIC detector's computational complexity.

$\delta_{\text{p/M-SIC,\{i/ii\}}}$: Constants employed in the context of quantifying the M-SIC- or pM-SIC detector's computational complexity.

$\epsilon_{\text{p/M-SIC}}$: Constant employed in the context of quantifying the M-SIC- or pM-SIC detector's computational complexity.

ζ_{PIC}: Constant employed in the context of quantifying the M-SIC- or pM-SIC detector's computational complexity.

σ_l^2: Variance of the l-th user's transmitted subcarrier symbols.

$\sigma^2_{x,\text{WHT,MMSE}}[n]$: Average (x=S:) desired signal variance, (x=I:) undesired interference signal variance and (x=N:) undesired AWGN variance associated with the linear subcarrier symbols estimates $\hat{s}[n,k],\ k=0,\ldots,K-1$ after equalization and despreading in the context of single-user WHTS-OFDM.

$\sigma_x^{(l)2}[n,k]$: Variance of the signal $\hat{s}_x^{(l)}[n,k]$, where (x=S:) desired signal, (x=I:) undesired interference signal, (x=N:) AWGN noise.

σ_n^2: Variance of the AWGN.

$\sigma_{\text{eff}}^{(l)2}[n,k]$: Variance of the effective interference- plus noise contribution $n_{\text{eff}}^{(l)}[n,k]$, which is given by: $\sigma_{\text{eff}}^{(l)2}[n,k] = \sigma_I^{(l)2} + \sigma_N^{(l)2}$.

$\Delta\hat{\mathbf{s}}[n,k]$: Vector of the transmitted symbols' estimation errors: $\Delta\hat{\mathbf{s}}[n,k] = \mathbf{s}[n,k] - \hat{\mathbf{s}}[n,k] \in \mathbb{C}^{L\times 1}$.

$\Delta\hat{\mathbf{x}}[n,k]$: Vector of the received signals' estimation errors: $\Delta\hat{\mathbf{x}}[n,k] = \mathbf{x}[n,k] - \hat{\mathbf{x}}[n,k] \in \mathbb{C}^{P\times 1}$.

$()[n,k]$: Signal associated with the k-th subcarrier of the n-th OFDM symbol.

$()_{\text{LS}}$: Variables associated with the LS combiner.

$()_{\text{MMSE}}$: Variables associated with the MMSE combiner.

$()_{\text{MV}}$: Variables associated with the MV combiner.

$()_{\text{p/M-/SIC}}$: Variables associated with the standard SIC, M-SIC- or pM-SIC detectors.

$()_{\text{PIC}}$: Variables associated with the PIC detector.

$()^{[i]}$: Notation used in the context of SIC detection in order to indicate that the variable enclosed in round brackets is associated with the i-th detection stage, where $i = 1, \ldots, L$.

$()^{(l^{[i]})[i]}$: Notation used in the context of SIC detection in order to indicate that the variable enclosed in round brackets is associated with the i-th detection stage, conditioned on regarding the $l^{[i]}$-th user as the strongest user to be detected during the i-th stage.

$()^{(l)[i]}$: Notation used in the context of PIC detection in order to indicate that the variable enclosed in round brackets is associated with the l-th user during the i-th detection stage.

Chapter 5

Conclusions and Future Work

5.1 Decision-Directed Channel Estimation for Single-User OFDM

In the context of our portrayal of single-user OFDM in Section 1.3.1 we highlighted that a prerequisite for performing coherent detection of the different subcarriers' symbols at the receiver is the availability of an estimate of the subcarriers' channel transfer factors.

An initial *a posteriori* estimate of the channel transfer factor associated with a specific subcarrier can be generated upon dividing the received subcarrier signal by the remodulated symbol decision obtained for this subcarrier. The initial *a posteriori* channel transfer factor estimates can then be further enhanced with the aid of generating smoothed estimates using filtering between neighbouring estimates based on exploiting the channel transfer factors' correlation in both the frequency- and the time-direction.

Depending on the origin of the sliced and remodulated symbol employed as a reference for deriving the initial *a posteriori* channel transfer factor estimates, the channel estimators can be divided into two categories, namely pilot-assisted and decision-directed approaches.

More specifically, in the context of pilot-assisted channel estimation the initial *a posteriori* channel transfer factor estimates are calculated only for a number of so-called pilot subcarriers, for which the complex transmitted symbol is known *a priori* at the receiver. This is followed by an interpolation between the different pilot subcarriers' *a posteriori* channel transfer factor estimates, in order to obtain channel transfer factor estimates for all subcarriers.

By contrast, the philosophy of the decision-directed channel estimation discussed in Chapter 2 was based on the idea of employing the remodulated subcarrier symbol decisions as "pilots", or in other words as a reference signal for generating the set of K initial *a posteriori* channel transfer factor estimates for the current OFDM symbol. These initial estimates could then be further enhanced by MMSE-based 1D-FIR Wiener filtering across the K subcarriers exploiting also the channel transfer factors' correlation in the frequency-direction, as suggested by Edfors *et al.* [13, 14, 15]. An

even further MSE enhancement was achieved by Li *et al.* [17] with the aid of MMSE-based 2D-FIR Wiener filtering upon also exploiting the channel's correlation in the time-direction, namely with the aid of employing also a number of previous OFDM symbols' initial *a posteriori* channel transfer factor estimates in the filtering process. These enhanced *a posteriori* channel transfer factor estimates derived for the current OFDM symbol would then be employed as *a priori* channel transfer factor estimates for frequency-domain equalization conducted during the next OFDM symbol period upon neglecting the channel's decorrelation between the two OFDM symbol periods.

5.1.1 Complexity Reduction by CIR-Related Domain Filtering

However, the complexity imposed upon performing the filtering across all the K different subcarriers in the frequency-domain may potentially become excessive. To be more specific, a computational complexity of K^2 number of complex multiplications and the same number of complex additions would be inflicted. In order to reduce the associated computational complexity, it was suggested by Edfors *et al.* [13, 14, 15] to transform the initial *a posteriori* channel transfer factor estimates to the CIR-related domain with the aid of the Karhunen Loeve Transform (KLT), followed by CIR-related one-tap filtering of only the first K_0 number of uncorrelated CIR-related taps, which are assumed to be the most significant taps in terms of their variance. Finally, the remaining filtered CIR-related taps are transformed back to the frequency-domain. In this case the computational complexity would be quantified in terms of $2K_0K$ complex multiplications and additions. While the KLT achieves a perfect decorrelation and hence the best possible energy compaction in the CIR-related domain, a disadvantage is that for its calculation explicit knowledge of the channel's statistics, namely the spaced-frequency correlation matrix is required, which is not known *a priori*. Hence, as suggested by van de Beek *et al.* [66], Edfors *et al.* [15] and Li *et al.* [17], the channel-independent DFT matrix could be employed instead of the optimum KLT matrix for transforming the initial *a posteriori* channel transfer factor estimates to the CIR-related domain. In the context of a sample-spaced CIR the DFT matrix is identical to the KLT matrix and hence the CIR-related taps are uncorrelated. By contrast, in the context of a non-sample-spaced CIR the DFT matrix is sub-optimum in the sense that the CIR-related taps are not perfectly decorrelated and hence the energy compaction becomes sub-optimum. As a result of windowing, the CIR-related taps generated upon retaining only a limited number of $K_0 \ll K$ taps with the aim of reducing the estimator's complexity, the DFT based estimator's MSE is significantly degraded compared to that of the KLT-based estimator. This is because significant signal components are removed. Note that windowing is particularly effective in terms of complexity reduction, when the CIR-related taps are also filtered in the time-direction, as in case of the 2D-MMSE based estimator proposed by Li *et al.* [17]. A attractive compromise between the optimum KLT and the channel-independent DFT was found by Li and Sollenberger [69] upon employing the unitary matrix, which is related to the KLT of the

uniform multipath intensity profile's spaced-frequency correlation matrix as the transform matrix required for transforming the initial *a posteriori* channel transfer factor estimates to the CIR-related domain. Thus attractive energy compaction properties, similar to those of the optimum KLT, are achieved without having exact knowledge of the channel's statistics. As a result, only a slight MSE degradation compared to that of the optimum KLT-based estimator is incurred.

5.1.2 Compensation of the Channel's Time-Variance by CIR-Related Tap Prediction Filtering

Our more detailed investigations of Chapter 2 concentrated on the effects of the channel's decorrelation incurred between consecutive OFDM symbols. Li *et al.* [17] proposed to employ 2D-MMSE based estimation filtering for deriving improved *a posteriori* channel transfer factor estimates for the current OFDM symbol based on the current- and a number of previous OFDM symbols' initial *a posteriori* channel transfer factor estimates. These channel estimates could then been employed as *a priori* channel transfer factor estimates for demodulation during the next OFDM symbol period. However, in the context of rapidly time-variant channels, associated with a potentially high OFDM symbol normalized Doppler frequency, it is more effective to directly predict the channel transfer factors for the next OFDM symbol period. This can be achieved by substituting the Wiener filter based CIR-related tap estimation filters of Li's 2D-MMSE based channel estimator design [17] by Wiener filter-based CIR-related tap prediction filters. Our investigations demonstrated that with the aid of CIR-related tap prediction filtering even channel scenarios having OFDM symbol normalized Doppler frequency as high as $F_D = 0.1$ can be supported, while capitalizing on relatively short prediction filters. Employing four predictor taps seemed to be sufficient for compensating most of the channel's variation, while further increasing the predictor's length resulted in additional modest MSE reduction due to averaging over a higher number of noisy samples. However, our experiments demonstrated that at lower SNRs and for higher-order modulation schemes the channel estimation MSE is potentially high, which is the result of employing erroneous subcarrier symbol decisions in the DDCE process. As a consequence, error propagation effects occur, which have to be curtailed by regularly transmitting training OFDM symbols. In order to further reduce the system's BER, the employment of turbo-coding was considered as a viable option. However, generating the DDCE's reference signal by slicing, reencoding, interleaving and remodulating the turbo-decoder's 'source'-related soft-output bits only exhibited no significant advantage compared to slicing and remodulating the turbo-decoder's soft-input bits. By contrast, generating the DDCE's reference from the turbo-decoder's 'source- plus parity'-related soft-output bits proved to be more effective.

5.1.3 Subject for Future Research: Successive Adaptivity of KLT and CIR-Related Tap Prediction Filtering

In the context of the 2D-MMSE based channel prediction the concepts of "robustness" with respect to the channel's true scattering function can be applied, as it was originally proposed by Li *et al.* [17] for the 2D-MMSE based channel estimator. However, in order to further improve the 2D-MMSE based channel predictor's MSE performance, the channel predictor could be rendered adaptive with respect to two components, namely the transform, which conveys the initial *a posteriori* channel transfer factor estimates to the CIR-related domain and secondly, with respect to the CIR-related tap predictors.

Recall that the optimum transform is known to be the Karhunen-Loeve transform with respect to the channel's spaced-frequency correlation matrix. An estimate of the channel's spaced-frequency correlation matrix is given by the auto-correlation matrix of the initial *a posteriori* channel transfer factor estimates. Although this matrix differs from the channel's spaced-frequency correlation matrix by an additive weighted identity matrix, which is associated with the noise contributions, the eigenvectors of both matrices are identical [14, 87]. Also recall that these eigenvectors constitute the optimum transform in terms of achieving a perfect decorrelation of the frequency-domain channel transfer factors. The auto-correlation matrix of the initial *a posteriori* channel transfer factor estimates can be estimated with the aid of the sample-correlation method [87]. Based on the current OFDM symbol's *a posteriori* channel transfer factor estimates the sample-correlation matrix can be regularly updated. Instead of entirely recomputing the KLT matrix in every OFDM symbol period, an iterative update- or tracking method proposed by Davila [145] as well as Rezayee and Gazor [146] in the context of speech coding is expected to be computationally more effective.

Apart from the above-mentioned adaptive transform, the second component of the 2D-MMSE based channel predictor, which can be rendered adaptive, are the CIR-related tap predictors. In the context of our investigations we compared the block-based Burg algorithm assisted CIR-related tap prediction approach proposed by Al-Susa and Ormondroyd [18] against the non-adaptive robust approach proposed by Li *et al.* [17]. Although these investigations demonstrated that an adaptive predictor is capable of outperforming the robust predictor, a disadvantage of the block-based adaptation was constituted by the extra storage requirements imposed. In order to avoid these disadvantages, an OFDM symbol-by-symbol adaptation technique relying on the LMS- or RLS algorithms is expected to be more attractive. We have further illustrated the concepts of the fully adaptive 2D-MMSE based channel predictor in Figure 5.1. Besides the potentially reduced estimation MSE, an additional advantage of the adaptive predictor compared to a robust predictor is its ability to better compensate for the effects of erroneous subcarrier symbol decisions, which manifest themselves similarly to the effects of impulsive noise in the DDCE process. However, the advantages of the adaptive predictor have to be viewed in the light of the disadvantage of a higher complexity compared to the robust

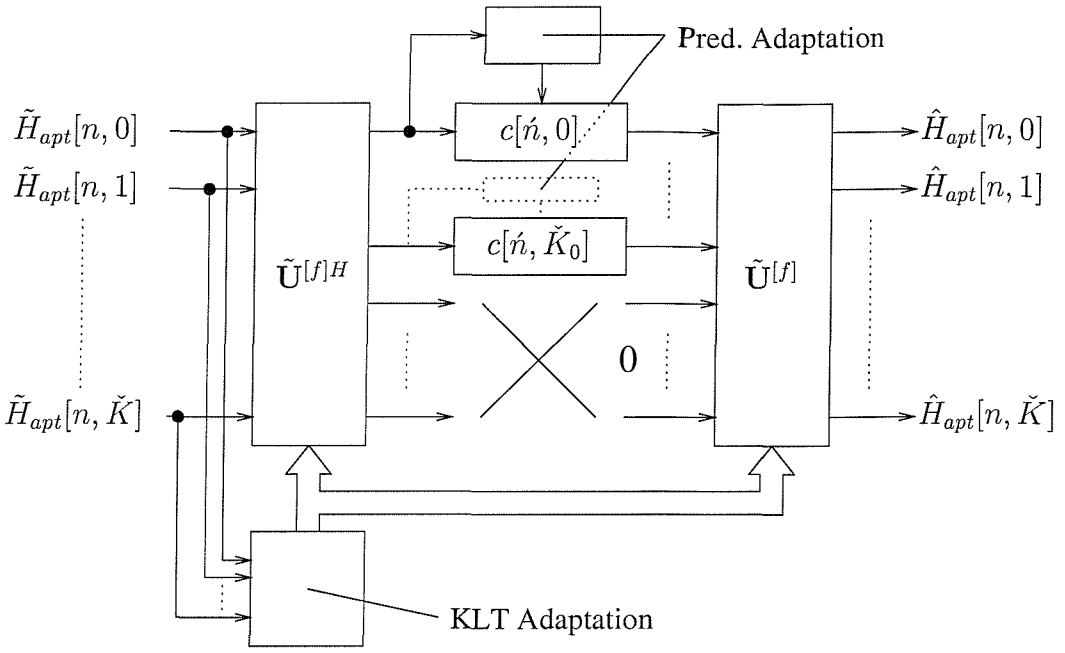

Figure 5.1: Stylized illustration of a fully adaptive 2D-MMSE based channel predictor. The KLT coefficients are adapted for the sake of transforming the initial *a posteriori* channel transfer factor estimates to the CIR-related domain and for transforming the filtered CIR-related tap predictions back to the frequency-domain. Furthermore, also the CIR-related tap predictor coefficients are subjected to adaptation, potentially invoking the RLS algorithm. Note that we have defined $\check{K} = K - 1$.

predictor.

Our further investigations in Chapter 2 were cast in the context of employing 2D-MMSE based channel prediction in an OFDM system, which employs adaptive modulation. This was motivated by the observation that as a result of the channel's variation versus time, the modulation mode assignment computed during the current OFDM symbol period - based on the current OFDM symbol's channel transfer factor estimates - for application during the next OFDM symbol period becomes inaccurate. Hence the AOFDM modem's performance is limited. A significant performance improvement was hence achieved by computing the modulation mode assignment based on the *a priori* channel transfer factor estimates generated for the following OFDM symbol period with the aid of the 2D-MMSE based channel predictor. Note that the benefits of combining decision-directed channel prediction and adaptive modulation are twofold. On the one hand, the modulation mode assignment profits from the accurate channel predictions and on the other hand the channel predictions benefit from the more reliable remodulated reference signal invoked in the DDCE process in the light of employing adaptive modulation.

5.2 Channel Estimation for Multi-User SDMA-OFDM

In the context of a single-user, single-transmit antenna assisted scenario the task of acquiring a set of K initial *a posteriori* channel transfer factor estimates was accomplished by simply dividing the signal received in each subcarrier by the subcarrier's complex transmitted symbol. These initial *a posteriori* channel transfer factor estimates were then employed for deriving improved *a posteriori* channel transfer factor estimates for the current OFDM symbol period or for generating *a priori* channel transfer factor estimates for employment during the next OFDM symbol period upon invoking CIR-related tap estimation- or prediction filtering, respectively.

By contrast, in the context of a multi-user SDMA-OFDM scenario considered in Chapter 3, the signal received by each antenna element at the basestation is constituted by the superposition of the L different users' transmitted and independently faded signals.

5.2.1 LS-Assisted DDCE

Based on the observation that the channel's multipath spread T_m - normalized to the OFDM sampling period duration T_s - is typically only a fraction of the number of subcarriers K, a subspace-based approach was proposed by Li *et al.* [21] for recovering the L sets of K-subcarrier channel transfer factors associated with a specific BS receiver antenna. Based on the Least-Squares (LS) error criterion the vector of received subcarrier signals is projected onto the sub-space spanned by the first K_0 number of column vectors associated with the K-th order DFT matrix upon taking into account the different users' unique transmitted subcarrier symbol sequences. As a result, for each of the L users a set of K_0 CIR-related tap estimates is obtained, which are then subjected to the DFT in order to obtain the desired L number of sets of channel transfer factor estimates.

Our mathematical portrayal of this estimation problem capitalized on a more compact matrix notation than that of [21], which further motivated the employment of the LS error criterion as proposed by Li *et al.* [21]. Based on this notation a necessary condition was provided for the identification of the different users' CIR-related taps. More explicitly, the product of the L number of users and the K_0 number of CIR-related taps to be estimated was required to be lower than or equal to the K number of OFDM subcarriers, namely we required that the condition of $LK_0 \leq K$ was satisfied. While this constitutes a necessary condition, it was observed that if the L number of users was close to the tolerable limit, the estimation MSE was potentially degraded depending on the specific subcarrier symbol sequences transmitted by the different users. This provided an additional motivation for devising alternative multiuser channel estimation approaches.

Furthermore, the computational complexity of the LS-assisted DDCE was found to be substantial, because a system of equations associated with a left-hand matrix of dimension $LK_0 \times LK_0$ and a right-hand matrix of dimension $LK_0 \times P$ had to be solved for estimating the CIR-related taps of the MIMO system's channels between the L users' single transmit antennas and the base-station's P

receiver antennas. However, an advantage of the LS-assisted DDCE is that its MSE can be further improved by invoking pure transversal CIR-related tap filtering.

5.2.2 PIC-Assisted DDCE

In order to address the LS-assisted DDCE's deficiency of supporting only a limited number of users and imposing a potentially excessive computational complexity, the idea of Parallel Interference Cancellation (PIC)-assisted DDCE, which was originally suggested for the CIR-related domain by Li [22] and for the frequency-domain by Jeon *et al.* [23] was significantly further developed. We argued above that since in a multi-user SDMA-OFDM scenario the signal received by a specific antenna element is given by the superposition of the different users' transmitted signals, the low-complexity single-user techniques for deriving initial *a posteriori* channel transfer factor estimates cannot be directly applied. However, a viable approach for the estimation of a specific user's channel transfer factors is constituted by first removing the remaining users' interference from the received composite multi-user signal, and then performing the channel estimation with the aid of the same techniques as in the single transmit-antenna assisted scenario. This involves generating the initial *a posteriori* channel transfer factor estimates, followed by CIR-related domain filtering. We found that from a mathematical point of view, performing the PIC in the frequency-domain- or in the time-domain are identical. However, performing the PIC in the frequency-domain, while the filtering in the CIR-related domain seems to be the least complex solution. Note that in the context of the PIC process the remaining users' interfering signal components are reconstructed based on the sliced symbols generated at the multi-user detector's output, and upon invoking furthermore the associated *a priori* channel transfer factor estimates generated during the previous OFDM symbol period for the current OFDM symbol period.

However, compared to the single-user single-transmit antenna assisted scenario, the prediction filters to be potentially employed in the CIR-related domain for further enhancing the estimator's MSE were shown not to be transversal, but recursive. In the context of our discussions, mathematical expressions were derived for the current OFDM symbol's *a posteriori* channel transfer factor estimates' MSE and for the next OFDM symbol's predicted *a priori* channel transfer factor estimates' MSE. Furthermore, conditions for the estimator's stability were provided. Based on the system equations' contractive properties [87] an iterative algorithm was devised for the off-line optimization of the CIR-related tap predictor's coefficients with the aim of minimizing the *a priori* estimator's average MSE. Our simulation results demonstrated that the number of users each having a single transmit antenna is not limited by K/K_0, as it is the case for the LS-assisted DDCE. Furthermore we found that also the principles of "robustness" with respect to the channel's actual scattering function as invoked in the single-user scenario were also applicable for the multi-user scenario, which renders the off-line optimization of the CIR-related tap predictor coefficients an

attractive option. In the context of our investigations we also illustrated the effects of a non-sampled spaced CIR on the estimator's MSE, based on using the DFT matrix as the unitary transform matrix for conveying the inital *a posteriori* channel transfer factor estimates to the CIR-related domain. We found that as a result of retaining only the K_0 most significant CIR-related taps with the aim of reducing the estimator's complexity, in the frequency-domain the channel transfer factors' estimation MSE significantly increased towards the edges of the OFDM symbol. This problem can be addressed by using the "robust" transform basis' as proposed by Li and Sollenberger [69] instead of the unitary DFT matrix.

In order to potentially further improve the estimator's MSE and for rendering the estimator capable of appropriately reacting to impulsive noise as caused for example by erroneous subcarrier symbol decisions, we demonstrated that the adaptation of the CIR-related tap predictor coefficients could also be performed with the aid of the RLS algorithm. It is interesting to note that although the different predictors associated with the CIR-related taps of a specific channel- or with different channels perform their coefficient adaptation independently, the estimators' average MSE is minimized.

5.3 Uplink Detection Techniques for SDMA-OFDM

Finally, in Chapter 4 we discussed a range of uplink multi-user detection techniques, which - in addition to multi-user channel estimation - constitute one of the pivotal components of the SDMA-OFDM receiver. The detection techniques investigated were separated into the sub-classes of linear- and non-linear detection. Specifically, in the context of linear detection techniques, such as the Least-Squares (LS)- and Minimum Mean-Square Error (MMSE) approaches no *a priori* knowledge about any of the other users' transmitted symbols is required for the detection of a specific user's transmitted symbol. This in contrast to the family of non-linear detectors, namely to the Successive Interference Cancellation (SIC), Parallel Interference Cancellation (PIC) and Maximum Likelihood (ML) detection based approaches. Explicitly, in the context of these schemes *a priori* knowledge about one or more of the remaining users' transmitted symbols is required for the detection of a specific user's transmitted symbol. An exception is the first cancellation stage of the SIC detector.

For the different multi-user detectors investigated a mathematical analysis as well as a performance- and complexity analysis was conducted. We found that the linear detectors, which perform the operations of linear combining and classification sequentially, constitute the lowest-complexity, but also the least powerful solutions in terms of the achievable BER. By contrast, the ML detector is associated with the highest computational complexity due to evaluating M_c^L number of L-dimensional trial-vectors in each subcarrier in terms of their Euclidean distance from the vector of received signals upon taking into account the effects of the channel. As a benefit, the ML detector's BER performance is optimum. Recall in this context that L denotes the number of simultaneous SDMA

users and M_c is the number of constellation points associated with the specific modulation scheme employed. A compromise between the achievable performance and complexity imposed is given by the SIC- and PIC detectors.

5.3.1 SIC Detection

The philosophy of the SIC scheme is based on linearly detecting and cancelling successively in each stage of the detection process the strongest remaining user in terms of an objective measure, which could either be the SNR, SIR or SINR at the linear combiner's output of each detection stage. Thus, the minimum occuring value of the objective function is maximized. The potential of various schemes was assessed for further enhancing the SIC detector's performance, namely that of the M-SIC, partial M-SIC and SDI-M-SIC schemes, which were contrived based on the idea of tracking multiple tentative symbol decisions from each detection stage, while performing a decision as regards to which symbols were transmitted, after the cancellation of the last user. Our analysis of SIC also considered the effects of error propagation potentially occuring between the different detection stages. Based on these observations an improved metric was developed for soft-bit generation to be employed in the context of a system using turbo-decoding at the receiver. While the SIC and M-SIC schemes potentially perform close to ML detection, this is achieved at the cost of a significantly increased computational complexity compared to the MMSE detection.

5.3.2 PIC Detection

We found that a further enhancement of the performance versus complexity tradeoffs is constituted by the PIC detector. Recall that the signal received by the different BS antenna elements is constituted by the superposition of the different users' transmitted signals. Hence, a linear estimate of a specific user's transmitted signal can be generated upon removing the remaining users' transmitted signals, followed by single-user diversity combining. In the context of PIC detection, initial symbol decisions are generated with the aid of the MMSE detector for reconstructing the channel-impaired transmitted signals to be used in the actual cancellation process. While in the context of an uncoded scenario the PIC detector was found to perform only marginally better, than the MMSE detector, in the turbo-coded scenario a significant performance improvement was observed when using the sliced, interleaved and remodulated "source- plus parity"-related soft-output bits of the turbo-decoder obtained during the first detection stage as a reference for the PIC process of the second stage. A further performance improvement can potentially be achieved with the aid of a soft-bit based PIC process instead of a hard-decision based PIC.

5.3.3 Improvement of MMSE- and PIC-Detection by Adaptive Modulation or WHT Spreading

In order to render the employment of MMSE- and PIC detection more attractive also in an uncoded scenario, investigations were conducted with respect to additional employing either adaptive modulation or Walsh-Hadamard Transform (WHT) based spreading in the multi-user SDMA-OFDM scenario. We found that these techniques are most effective in the context of a fully-loaded system, namely where the number of simultaneous users - and hence the number of transmit antennas - equals the number of BS receiver antenna elements. Given the restriction of employing AOFDM only in Time-Division Duplexing (TDD) scenarios and the requirement of employing prediction filtering for compensating for the channel's variations with time, a more straightforward solution is constituted by WHT spreading across the different subcarriers. While at the transmitters the Walsh Hadamard Transform can be combined with the OFDM-related IFFT, at the receiver the computational complexity is increased, since the despreading has to be performed separately for each user. In the context of our investigations we highlighted that both in the single-user- and in the multi-user SDMA-OFDM system, the equalization- or linear combining at the receiver and the despreading can be performed sequentially as a result of the WHT matrix's unitary nature. Our simulation results demonstrated that with the aid of adaptive modulation or WHT spreading the performance of the MMSE- or PIC detection assisted systems can be significantly improved. Hence these schemes constitute an attractive compromise in comparison to the significantly more complex SIC-assisted SDMA-OFDM schemes. For further reading on related topics we refer to [147, 148, 149, 150, 151, 152, 153, 154, 155].

5.4 Closing Remarks

This thesis considered a range of OFDM-related topics. However, a whole host of further advances in the field of communications research are applicable also to OFDM. Specifically the family of classification and learning based neural network assisted receivers investigated in the context of conventional single-carrier systems provides a rich set of further research topics. Partial response modulation techniques also have the promise of advantages in OFDM schemes. The joint optimization of adaptive bit-allocation and crest-factor reduction techniques constitutes a further research challange. All the above-mentioned techniques have the potential of improving the complexity versus performance balance of the system. Finally, the employment of OFDM in ultra-wide band systems invoking various frequency-hopping and multiple access techniques is likely to grow in popularity as an exciting research area.

Chapter 6

Appendix

6.1 Channel Model for Monte-Carlo Simulations

The simulation results presented throughout our discussions based on Monte-Carlo simulations were generated with the aid of the indoor WATM system- and channel model, which will be outlined in the following.

6.1.1 The Indoor WATM Model

The WATM system's parameters used in our investigations follow closely a proposal of the Pan-European Advanced Communications Technologies (ACTS) Median system, which constitutes a wireless extension of wire-line based ATM-type networks [98]. These parameters are listed in Table 6.1. More specifically, the number of OFDM sub-carriers is $K = 512$ and the cyclic prefix exhibits a length of $K_g = 64$ samples. The transmitted signal, which is centered at a carrier frequency of $f_c = 60$GHz is sampled by the receiver at a rate of $f_s = 225$ Msamples/s. Assuming a worst-case vehicular speed of $v = 50$km/h or equivalently $v = 13.9$m/s, the received signal exhibits a maximum Doppler frequency deviation of $f_D = 2778$Hz from the transmitted carrier frequency [98], which is defined by $f_D = \frac{vf_c}{c}$ [98]. This equals to an OFDM-symbol-normalized Doppler frequency of $F_D = 0.0071$, defined by $F_D = (K + K_g)\frac{f_D}{f_s}$, which is a more adequate metric for characterising the channel's variation versus time. It should be noted that our definition

ind. WATM **system**	K	K_g	f_s	f_c
	512	64	225MHz	60GHz
ind. WATM **channel**	N_{path}	$RMS(\tau)$	f_D	F_D
	3	16.9ns	2778Hz	0.0071

Table 6.1: Parameters of the indoor WATM system model [98, 77]

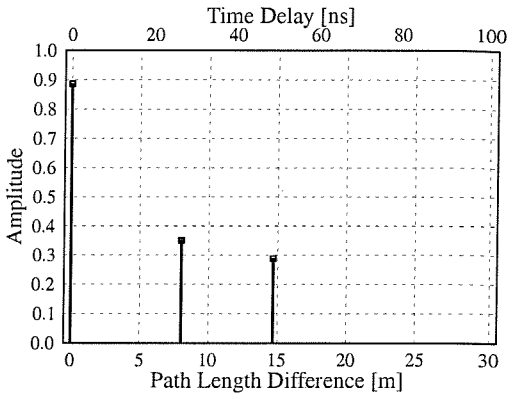

Figure 6.1: Channel impulse response (CIR) of the indoor WATM channel [98, 77]

of the OFDM symbol-normalized Doppler frequency F_D is different from the definition presented in [98, 156] in the sense that here the number of guard samples K_g is incorporated as well. Associated with the WATM system model is a three-path Channel Impulse Response (CIR) which exhibits an RMS delay spread of $RMS(\tau) = 0.109\mu s$. The CIR is illustrated in Figure 6.1 [98]. Each of the three paths is independently Rayleigh-faded. In comparison to the original five-path CIR of [98] only the three paths associated with the lowest-delay taps have been retained. This helps to avoid Inter-Symbol Interference (ISI), since the two highest path delays of the original channel model are in excess of the duration of the OFDM symbol's cyclic prefix. Hence, in the following sections we will refer to the three-path CIR as the **indoor WATM channel's**- or, synonymously, the **shortened WATM (SWATM) channel's** CIR.

6.2 The Stochastic Channel Model

In this section the stochastic channel model employed in our investigations is outlined. The further structure of this section is as follows. In Section 6.2.1 the model of the time-variant Channel Impulse Response (CIR) is outlined. Its further characterization is then conducted with reference to Figure 6.2 in terms of the CIR's Auto-Correlation Function (ACF) denoted as $r_h(\Delta t, \tau)$ in Section 6.2.2. Furthermore, the Fourier Transform (FT) of the CIR's ACF with respect to the multipath delay variable τ, namely $r_H(\Delta t, \Delta f)$ - also known as the *spaced-time spaced-frequency correlation function* - is considered in Section 6.2.3. Further Fourier transforming with respect to the spaced-time variable Δt yields the function $S_H(f_d, \Delta f)$, which is addressed in Section 6.2.4. Finally, the *scattering function* $S_h(f_d, \tau)$ is obtained by Fourier transforming the CIR's ACF with respect to the spaced-time variable Δt, which is the topic of Section 6.2.5. Our portrayal of the channel model we be concluded in Section 6.2.6 by highlighting the conditions for *separability* of the channel's

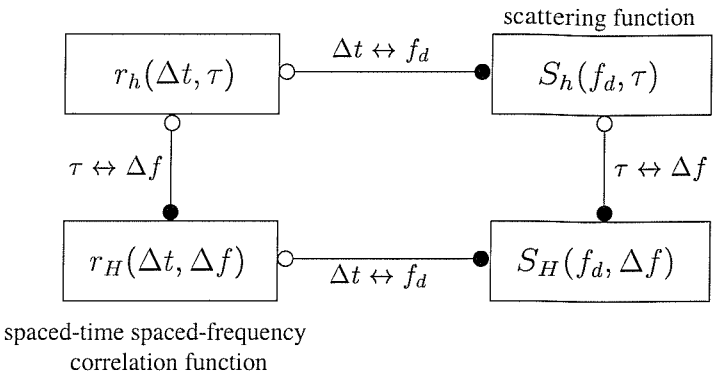

Figure 6.2: Illustration of the Fourier transform relationships between the stochastic channel model's associated correlation functions. Upon setting $\Delta t = 0$, the CIR's auto-correlation function $r_h(\Delta t, \tau)$ is simplified to $r_h(\tau)$, which is known as the multipath intensity profile of the channel. In contrast, when setting $\Delta f = 0$, the Fourier transform of the CIR's auto-correlation function $r_h(\Delta t, \tau)$ with respect to Δt and τ, denoted by $S_H(f_d, \Delta f)$, is simplified to $S_H(f_d)$, which is known as the channel's Doppler power spectrum.

spaced-time spaced-frequency correlation function $r_H(\Delta t, \Delta f)$.

6.2.1 Model of the Channel Impulse Response

The time-variant channel impulse response CIR is given in terms of its lowpass representation by [157, 141]:

$$h(t, \tau) = \sum_n \alpha_n(t) e^{-j\theta_n(t)} \delta(\tau - \tau_n(t)), \tag{6.1}$$

where $\theta_n(t) = 2\pi f_c \tau_n(t)$ and f_c is the carrier frequency. Furthermore, in Equation 6.1 $\alpha_n(t)$ denotes the time-variant attenuation factor, while $\tau_n(t)$ represents the time-variant delay associated with the n-th CIR path. Please note that since in state-of-the-art communication systems f_c is usually high, relatively small variations of $\tau_n(t)$ result in large changes in the value of the phase $\theta_n(t)$, which in turn impose significant changes on the CIR $h(t, \tau)$. Since the paths' delays are expected to vary randomly as a result of the scatterers' random motion, the CIR tap magnitudes of $h(t, \tau)$ versus time can also be modeled as random processes. More specifically, under these assumptions and for a sufficiently large number of different paths, according to the central limit theorem, each tap of $h(t, \tau)$ can be modeled as a zero-mean complex Gaussian random process with respect to the variable t. Hence, the envelope $|h(t, \tau)|$ is Rayleigh distributed. By contrast, in the presence of static scatterers in addition to the randomly varying scatterers, the mean value of $h(t, \tau)$ is different from zero and hence the envelope $|h(t, \tau)|$ is Ricean distributed [157, 141].

In order to further characterize the above stochastic channel model the associated Fourier transforms can be defined which are known in the literature as Bello's system functions [158, 157, 141].

Instead of using the Bello functions for characterizing the channel, due to their relevance for the different channel transfer function estimation methods, here we will rather employ the related correlation functions and their associated Fourier transforms. The corresponding relationships are further illustrated in Figure 6.2.

6.2.2 Auto-Correlation Function of the CIR: $r_h(\Delta t, \tau)$

Upon assuming that the process modelling $h(t, \tau)$ is wide-sense-stationary, which implies that the process' mean value is time-invariant and its auto-correlation is only a function of the time-difference, but not of the absolute time instants, the Auto-Correlation Function (ACF) $r_h(\Delta t, \tau_1, \tau_2)$[1] of $h(t, \tau)$ can be defined as [157, 141]:

$$r_h(\Delta t, \tau_1, \tau_2) = E\{h(t, \tau_1)h^*(t - \Delta t, \tau_2)\} \quad (6.2)$$

$$= r_h(\Delta t, \tau_1)\delta(\tau_1 - \tau_2), \quad (6.3)$$

where in the context of Equation 6.3 the assumption of *uncorrelated scattering* [157, 141] has been invoked. This implies that the amplitudes and phase shifts associated with the different CIR delays of $\tau_1 \neq \tau_2$ are uncorrelated. For $\Delta t = 0$, the function $r_h(\Delta t, \tau_1)$ simplifies to $r_h(0, \tau) \equiv r_h(\tau)$, with $\tau = \tau_1$, which is known as the *multipath intensity profile* or *delay power spectrum* [157, 141] of the channel. More explicitly, $r_h(\tau)$ is the average power output of the channel for a given multipath delay τ. The delay range $0 \leq \tau \leq T_m$ across which $r_h(\tau)$ exhibits significant values is referred to as the *multipath spread* [157, 141] of the channel.

6.2.3 Spaced-Time Spaced-Frequency Correlation Function $\hat{=}$ Fourier Transform of the CIR's ACF with Respect to the Multipath Delay Variable: $r_H(\Delta t, \Delta f)$

Let us denote the time-variant channel transfer function by $H(t, f)$, which is the Fourier Transform (FT) of the channel impulse response $h(t, \tau)$ with respect to the variable τ, formulated as:

$$H(t, f) = \underset{\tau \to f}{\mathcal{FT}}\{h(t, \tau)\} \quad (6.4)$$

$$= \int_{-\infty}^{\infty} h(t, \tau)e^{-j2\pi f\tau}d\tau. \quad (6.5)$$

Then the auto-correlation of $H(t, f)$, namely $r_H(\Delta t, f_1, f_2)$[2] is given as the Fourier transform of the auto-correlation function $r_h(\Delta t, \tau_1, \tau_2)$ of the CIR $h(t, \tau)$ taken also with respect to the variable

[1]Note that the definition of the auto-correlation function of $h(t, \tau)$ is different from that of [157, 141], where an arbitrary normalization factor of $1/2$ was employed, yielding: $r_h(\Delta t, \tau_1, \tau_2) = \frac{1}{2}E\{h(t, \tau_1)h^*(t - \Delta t, \tau_2)\}$.

[2]Note that the definition of the auto-correlation function of $H(t, f)$ is different from that of [157, 141], where an arbitrary normalization factor of $1/2$ is employed: $r_H(\Delta t, f_1, f_2) = \frac{1}{2}E\{H(t, f_1)H^*(t - \Delta t, f_2)\}$.

τ [157, 141], which is given by:

$$r_H(\Delta t, f_1, f_2) = E\{H(t, f_1)H^*(t - \Delta t, f_2)\} \quad (6.6)$$

$$= \underset{\tau \to \Delta f}{\mathcal{FT}}\{r_h(\Delta t, \tau)\} \quad (6.7)$$

$$\equiv r_H(\Delta t, \Delta f). \quad (6.8)$$

This relationship is also shown in Figure 6.2. The auto-correlation function $r_H(\Delta t, \Delta f)$ is known as the *spaced-time, spaced-frequency correlation function* [157, 141] of the channel. Its dependence on the frequency difference $\Delta f = f_1 - f_2$, rather than on the individual frequency values f_1, f_2 is related to the assumption of uncorrelated scattering. For $\Delta t = 0$, which corresponds to considering the channel transfer factors associated with a specific OFDM symbol, the ACF $r_H(\Delta t, \Delta f)$ simplifies to $r_H(0, \Delta f) \equiv r_H(\Delta f)$. Since we have $r_H(\Delta f) = \underset{\tau \to \Delta f}{\mathcal{FT}}\{r_h(\tau)\}$, the reciprocal of the channel's multipath spread T_m can be employed for defining the *coherence bandwidth* $(\Delta f)_c$ [157, 141] of the channel, which is the range $-(\Delta f)_c/2 \leq \Delta f \leq (\Delta f)_c/2$ of frequencies over which the channel transfer function exhibits a significant correlation [157, 141], namely:

$$(\Delta f)_c \approx \frac{1}{T_m}. \quad (6.9)$$

6.2.4 Fourier Transform of the CIR's ACF with Respect to the Multipath Delay- and Spaced-Time Variables: $S_H(f_d, \Delta f)$

In order to further characterize the channel, the Fourier transform of $r_H(\Delta t, \Delta f)$ with respect to the difference in time, namely Δt, can be obtained as [157, 141]:

$$S_H(f_d, \Delta f) = \underset{\Delta t \to f_d}{\mathcal{FT}}\{r_H(\Delta t, \Delta f)\}. \quad (6.10)$$

This relationship is also shown in Figure 6.2. More specifically, for $\Delta f = 0$ which corresponds to considering a specific subcarrier of consecutive OFDM symbols, each of which fades according to a certain Doppler frequency in the time-direction, the function $S_H(f_d, \Delta f)$ simplifies to $S_H(f_d, 0) \equiv S_H(f_d)$, which is known as the *Doppler power spectrum* of the channel. In analogy to the definition of the coherence bandwidth and the related multipath spread, which characterize the correlation properties of the channel for a specific time instant associated with a given OFDM symbol, similar definitions apply to the characterization of the channel variations as a function of time. More specifically, the frequency range of $-B_D/2 \leq f_d \leq B_D/2$, over which $S_H(f_d)$ exhibits significant values is referred to as the *Doppler spread* B_D [157, 141] of the channel, while its inverse is known as the *coherence time* [157, 141], which is expressed as:

$$(\Delta t)_c \approx \frac{1}{B_D}. \quad (6.11)$$

More explicitly, $(\Delta t)_c$ quantifies the time-domain displacement range of $-(\Delta t)_c/2 \leq \Delta t \leq (\Delta t)_c/2$, over which $r_H(\Delta t, \Delta f)$ exhibits significant correlation for $\Delta f = 0$. In this case $r_H(\Delta t, \Delta f)$ simplifies to $r_H(\Delta t, 0) \equiv r_H(\Delta t)$.

6.2.5 Scattering Function $\hat{=}$ Fourier Transform of the CIR's ACF with Respect to the Time-Delay: $S_h(f_d, \tau)$

A further transform pair can be defined by applying the Fourier transform to $r_h(\Delta t, \tau)$ of Equation 6.3 with respect to the variable Δt [157, 141], yielding:

$$S_h(f_d, \tau) = \underset{\Delta t \to f_d}{\mathcal{FT}}\{r_h(\Delta t, \tau)\}, \tag{6.12}$$

which is referred to as the *scattering function* [157, 141] of the channel. Furthermore, it follows that $S_H(f_d, \Delta f)$ and $S_h(f_d, \tau)$ also form a Fourier transform pair [157, 141], which is expressed as:

$$S_H(f_d, \Delta f) = \underset{\tau \to \Delta f}{\mathcal{FT}}\{S_h(f_d, \tau)\}, \tag{6.13}$$

as seen in Figure 6.2.

6.2.6 Separability of the Channel's Spaced-Time Spaced-Frequency Correlation Function

In this section we will comment on the conditions that have to be satisfied for the sake of maintaining the *separability* [17] of the channel's spaced-time spaced-frequency correlation function $r_H(\Delta t, \Delta f)$. This property will be employed, for example, in the context of our discussions on decision-directed channel estimation (DDCE) invoked in single-user OFDM systems in Section 2. Finally, the separability will be also exploited in parallel interference cancellation (PIC) assisted DDCE characterized in the context of multi-user OFDM systems in Section 3.4.

Based on Equation 6.1 and following the arguments of Section 6.2.1, a simplified model of the CIR is given by:

$$h(t, \tau) = \sum_n \gamma_n(t)\delta(\tau - \tau_n), \tag{6.14}$$

where in the absence of static scatterers the time-variant fading factor $\gamma_n(t) \in \mathbb{C}$ obeys a complex Gaussian distribution function. For simplicity we also assume that we have $\tau_{n_1} \neq \tau_{n_2}\ \forall\, n_1 \neq n_2$.

Upon substituting Equation 6.14 describing the time-variant CIR $h(t, \tau)$ into Equation 6.5, the channel's time-variant transfer function $H(t, f)$ is given by:

$$H(t, f) = \sum_n \gamma_n(t)e^{-j2\pi f \tau_n}. \tag{6.15}$$

By further substituting the expression of Equation 6.15 into Equation 6.6 the channel's spaced-time spaced-frequency correlation function $r_H(\Delta t, \Delta f)$ is obtained in the following form:

$$\begin{aligned} r_H(\Delta t, \Delta f) &= E\{H(t_1, f_1)H^*(t_2, f_2)\} && (6.16)\\ &= E\left\{\sum_{n_1} \gamma_{n_1}(t_1)e^{-j2\pi f_1 \tau_{n_1}} \sum_{n_2} \gamma^*_{n_2}(t_2)e^{j2\pi f_2 \tau_{n_2}}\right\} && (6.17)\\ &= \sum_n E\{\gamma_n(t_1)\gamma^*_n(t_2)\}e^{-j2\pi\tau_n(f_1 - f_2)}. && (6.18) \end{aligned}$$

In the context of Equation 6.18 we have exploited that $E\{\gamma_{n_1}(t_1)\gamma^*_{n_2}(t_2)\} = 0 \; \forall \; n_1 \neq n_2$ is satisfied, which follows from the assumption of uncorrelated scattering. Furthermore, in Equation 6.18 the n-th CIR tap's spaced-time correlation function is given by:

$$r_{h,n}(\Delta t) = E\{\gamma_n(t_1)\gamma^*_n(t_2)\} \tag{6.19}$$

$$= \sigma^2_{h,n} r_{\bar{h},n}(\Delta t), \tag{6.20}$$

where $\sigma^2_{h,n}$ is the n-th CIR tap's variance and $r_{\bar{h},n}(\Delta t)$ is the n-th CIR tap's normalized spaced-time correlation function, which obeys $r_{\bar{h},n}(0) = 1$. Note furthermore that we have $\Delta t = t_1 - t_2$. Upon substituting Equation 6.20 into Equation 6.18 we obtain the following equation for the channel's spaced-time spaced-frequency correlation function:

$$r_H(\Delta t, \Delta f) = \sum_n \sigma^2_{h,n} r_{\bar{h},n}(\Delta t) e^{-j2\pi\tau_n \Delta f}, \tag{6.21}$$

where we have $\Delta f = f_1 - f_2$. For $\Delta t = \Delta f = 0$ the channel transfer factor's variance is obtained, namely $\sigma^2_H = r_H(0,0) = \sum_n \sigma^2_{h,n}$, which is assumed to be unity [17] in the context of our discussions.

Upon stipulating that the same normalized spaced-time correlation function $r_{\bar{h}}(\Delta t)$ is associated with the different CIR taps [17], the spaced-time spaced-frequency correlation function of Equation 6.21 simplifies to:

$$r_H(\Delta t, \Delta f) = r_H(\Delta t) \cdot r_H(\Delta f), \tag{6.22}$$

where:

$$r_H(\Delta t) = r_{\bar{h}}(\Delta t), \tag{6.23}$$

and:

$$r_H(\Delta f) = \sum_n \sigma^2_{h,n} e^{-j2\pi\tau_n \Delta f}. \tag{6.24}$$

Equation 6.22 reflects the *separability* of the channel's spaced-time spaced-frequency correlation function into the product of the spaced-time correlation function and the spaced-frequency correlation function.

Glossary

ACF	Auto-Correlation Function
ACTS	Advanced Communications Technologies and Services - a European research programme
ADSL	Asynchronous Digital Subscriber Loop
AOFDM	Adaptive Orthogonal Frequency Division Multiplexing
APR	A Priori
APT	A Posteriori
AWGN	Additive White Gaussian Noise
BER	Bit-Error Ratio
BLAST	Bell Labs Space-Time architecture
BPOS	Bit Per OFDM Symbol
BPSK	Binary Phase-Shift Keying
BS	Basestation
CDF	Cumulative Distribution Function
CDMA	Code-Division Multiple Access
CE	Channel Estimation
CIR	Channel Impulse Response
DAB	Digital Audio Broadcasting

DDCE	Decision-Directed Channel Estimation
DDCP	Decision-Directed Channel Prediction
DFT	Discrete Fourier Transform
DMUX	Demultiplexer
DTTB	Digital Terrestrial Television Broadcast
D-BLAST	Diagonal BLAST
EM	Expectation Maximization
EVD	EigenValue Decomposition
FDM	Frequency Division Multiplexing
FDMA	Frequency Division Multiple Access
FEC	Forward Error Correction
FFT	Fast Fourier Transform
FIR	Finite Impulse Response
HF	High-Frequency
ICI	Inter-subCarrier Interference
IDFT	Inverse Discrete Fourier Transform
IFFT	Inverse Fast Fourier Transform
IIR	Infinite Impulse Response
ISI	Inter-Symbol Interference
IWHT	Inverse Walsh Hadamard Transform
KLT	Karhunen-Loeve Transform
LLR	Log-Likelihood Ratio
LS	Least-Squares
LSE	Least-Squares Error
MA	Multiple Access

MC	Multi-Carrier
MIMO	Multiple-Input Multiple-Output
ML	Maximum Likelihood
MLSE	Maximum Likelihood Sequence Estimation
MMSE	Minimum Mean-Square Error
MSE	Mean-Square Error
MU	Multi-User
MUD	Multi-User Detection
MUI	Multi-User Interference
MUX	Multiplexer
MV	Minimum Variance
MVDR	Minimum Variance Distortionless Response
OFDM	Orthogonal Frequency Division Multiplexing
PAPR	Peak-to-Average Power Ratio
PDF	Probability Density Function
PIC	Parallel Interference Cancellation
PSAM	Pilot Symbol Aided Modulation
PSD	Power Spectral Density
PSK	Phase-Shift Keying
QAM	Quadrature Amplitude Modulation
QPSK	Quadrature Phase-Shift Keying
RLS	Recursive Least-Squares
RNS	Residue Number System
SB	Subband
SDM	Space-Division Multiplexing

SDMA	Space-Division Multiple Access
SDI	Selective Decision Insertion
SER	Symbol Error Ratio
SIC	Successive Interference Cancellation
SINR	Signal-to-Interference-plus-Noise Ratio
SIR	Signal-to-Interference Ratio
SMI	Sample Matrix Inversion
SNR	Signal-to-Noise Ratio
STC	Space-Time Coding
SVD	Singular-Value Decomposition
TCM	Trellis-Coded Modulation
TDD	Time-Division Duplexing
TDMA	Time-Division Multiple Access
TTCM	Turbo-Trellis Coded Modulation
V-BLAST	Vertical BLAST
WATM	Wireless Asynchronous Transfer Mode
WHT	Walsh-Hadamard Transform
WHTS	Walsh-Hadamard Transform Spreading
ZF	Zero-Forcing
1D	One-Dimensional
2D	Two-Dimensional

Bibliography

[1] R. W. Chang, "Synthesis of Band-Limited Orthogonal Signals for Multichannel Data Transmission," *Bell System Technical Journal*, vol. 46, pp. 1775–1796, December 1966.

[2] W. Webb and L. Hanzo, *Modern Quadrature Amplitude Modulation: Principles and Applications for Wireless Communications*. IEEE Press-Pentech Pressm, 1994.

[3] I. Kalet, "The multitone channel," *IEEE Transactions on Communications*, vol. 37, pp. 119–124, February 1989.

[4] F. Mueller-Roemer, "Directions in audio broadcasting," *Journal of Audio Engineering Society*, vol. 41, pp. 158–173, March 1993.

[5] I. J. H. Sari and G. Karam, "Transmission Techniques for Digital Terrestrial Television Broadcasting," *IEEE Communications Magazine*, February 1995.

[6] B. Hirosaki, "An Orthogonally Multiplexed QAM System Using the Discrete Fourier Transform," *IEEE Transactions on Communications*, vol. 29, pp. 983–989, July 1981.

[7] H. J. Kolb, "Untersuchungen über ein digitales Mehrfrequenzverfahren zur Datenübertragung," *Ausgewählte Arbeiten über Nachrichtensysteme, Universität Erlangen-Nürnberg*, no. 50, 1982.

[8] R. Rückriem, "Realisierung und messtechnische Untersuchung an einem digitalen Parallelverfahren zur Datenübertragung im Fernsprechkanal," *Ausgewählte Arbeiten über Nachrichtensysteme, Universität Erlangen-Nürnberg*, no. 59, 1985.

[9] J. Cimini, "Analysis and Simulation of a Digital Mobile Channel Using Orthogonal Frequency Division Multiplexing," *IEEE Transactions on Communications*, vol. 33, pp. 665–675, July 1985.

[10] K. Fazel and G. Fettweis, *Multi-carrier Spread Spectrum, ISBN 0-7923-9973-0.* Kluwer, 1997.

[11] F. Classen and H. Meyr, "Synchronisation algorithms for an OFDM system for mobile communications," in *Codierung für Quelle, Kanal und Übertragung*, (Berlin), pp. 105–113, VDE-Verlag, 1994.

[12] F. Classen and H. Meyr, "Frequency synchronisation algorithms for OFDM systems suitable for communication over frequency selective fading channels," in *Proceedings of Vehicular Technology Conference*, (Stockholm, Sweden), pp. 1655–1659, IEEE, 1994.

[13] O. Edfors, M. Sandell, J. J. v. .d. Beek, S. K. Wilson, and P. O. Börjesson, "OFDM Channel Estimation by Singular Value Decomposition," in *Proceedings of Vehicular Technology Conference*, vol. 2, (Atlanta, GA USA), pp. 923–927, IEEE, April 28 - May 1 1996.

[14] O. Edfors, *Low-Complexity Algorithms in Digital Receivers*. Lulea University of Technology, 1996.

[15] O. Edfors, M. Sandell, J.-J. v. d. Beek, S. K. Wilson, and P. O. Börjesson, "OFDM Channel Estimation by Singular Value Decomposition," *IEEE Transactions on Communications*, vol. 46, pp. 931–939, April 1998.

[16] M. Sandell, *Design and analysis of estimators for multicarrier modulation and ultrasonic imaging*. Lulea University of Technology, 1996.

[17] Y. Li, L. J. Cimini, and N. R. Sollenberger, "Robust Channel Estimation for OFDM Systems with Rapid Dispersive Fading Channels," *IEEE Transactions on Communications*, vol. 46, pp. 902–915, April 1998.

[18] E. Al-Susa and R. F. Ormondroyd, "A Predictor-Based Decision Feedback Channel Estimation Method for COFDM with High Resilience to Rapid Time-Variations," in *Proceedings of Vehicular Technology Conference*, vol. 1, (Amsterdam, Netherlands), pp. 273–278, IEEE, September 19-22 1999.

[19] M. Münster and L. Hanzo, "MMSE Channel Prediction For Symbol-by-symbol Adaptive OFDM Systems," in 5^{th} *International OFDM-Workshop 2000*, pp. 35/1–35/6, Technische Universität Hamburg-Harburg, September 2000.

[20] M. Münster and L. Hanzo, "MMSE Channel Prediction Assisted Symbol-by-Symbol Adaptive OFDM," in *Proceedings of International Conference on Communications*, (Birmingham, Alabama), IEEE, April 28 - May 2 2002.

[21] Y. Li, N. Seshadri, and S. Ariyavisitakul, "Channel Estimation for OFDM Systems with Transmitter Diversity in Mobile Wireless Channels," *IEEE Journal on Selected Areas in Communications*, vol. 17, pp. 461–471, March 1999.

[22] Y. Li, "Optimum Training Sequences for OFDM Systems with Multiple Transmit Antennas," in *Proc. of Global Telecommunications Conference*, vol. 3, (San Francisco, United States), pp. 1478–1482, IEEE, November 27 - December 1 2000.

[23] W. G. Jeon, K. H. Paik, and Y. S. Cho, "An Efficient Channel Estimation Technique for OFDM Systems with Transmitter Diversity," in *Proceedings of International Symposium on Personal, Indoor and Mobile Radio Communications*, vol. 2, (Hilton London Metropole Hotel, London, UK), pp. 1246–1250, IEEE, September 18-21 2000.

[24] M. Münster and L. Hanzo, "Parallel Interference Cancellation Assisted Decision-Directed Channel Estimation for Multi-User OFDM," in 6^{th} *International OFDM-Workshop 2000*, (Hotel Hafen Hamburg, Germany), pp. 35/1–35/5, Technische Universität Hamburg-Harburg, September 18-19 2001.

[25] M. Münster and L. Hanzo, "PIC-Assisted Decision-Directed Channel Estimation for Multi-User OFDM Environments," in *accepted for publication in Proceedings of Vehicular Technology Conference*, IEEE, September 2002.

[26] M. Münster and L. Hanzo, "Co-Channel Interference Cancellation Techniques for Antenna Array Assisted Multiuser OFDM Systems," in *Proceedings of 3G-'2000 Conference*, vol. 1, (London, Great Britain), pp. 256–260, IEE, IEE, March 27-29 2000.

[27] M. Münster, T. Keller, and L. Hanzo, "Co–Channel Interference Suppression Assisted Adaptive OFDM in Interference Limited Environments," in *Proceedings of Vehicular Technology Conference*, (Amsterdam, Netherlands), pp. 284–288, IEEE, September 19-22 1999.

[28] S. Kaiser, *Multi-Carrier CDMA Mobile Radio Systems - Analysis and Optimization of Detection, Decoding and Channel Estimation*. VDI Verlag GmbH, 1998.

[29] F. Tufvesson, *Design of Wireless Communication Systems - Issues on Synchronization, Channel Estimation and Multi-Carrier Systems*. Department of Applied Electronics, Lund University, Sweden, 2000.

[30] P. Frenger, *Multirate Codes and Multicarrier Modulation for Future Communication Systems*. Department of Signals and Systems, Chalmers University of Technology, Göteborg, Sweden, 1999.

[31] S. Müller-Weinfurtner, *OFDM for Wireless Communications: Nyquist Windowing, Peak-Power Reduction and Synchronization*. Shaker Verlag, 2000.

[32] M. Flament, *On 60GHz Wireless Communication Channels, Technical Report No. 365L*. Department of Signals and Systems, Chalmers University of Technology, Göteborg, Sweden, 2000.

[33] R. van Nee and R. Prasad, *OFDM for Wireless Multimedia Communications*. Artech House Publishers, Boston, London, 2000.

[34] K. Witrisal, *OFDM air-interface design for multimedia communications, ISBN 90-76928-03-7.* , 2002.

[35] T. Keller and L. Hanzo, "Orthogonal frequency division multiplex synchronisation techniques for wireless local area networks," in *Proceedings of IEEE International Symposium on Personal, Indoor, and Mobile Radio Communications (PIMRC'96)*, vol. 3, (Taipei, Taiwan), pp. 963–967, IEEE, 15–18 October 1996.

[36] L. Hanzo, W. Webb, and T. Keller, *Single- and Multi-Carrier Quadrature Amplitude Modulation: Principles and Applications for Personal Communications, WLANs and Broadcasting*. IEEE Press, 2000.

[37] J. Davis and J. Jedwab, "Peak-to-mean power control in OFDM, Golay complementary sequences, and reed-muller codes," *IEEE Transactions on Information Theory*, vol. 45, pp. 2397–2417, November 1999.

[38] S. J. Shepherd, J. Oriss, and S. K. Barton, "Asymptotic limits in peak envelope power reduction by redundant coding in orthogonal frequency-division multiplex modulation," *IEEE Transactions on Communications*, vol. 46, no. 1, pp. 5–10, 1998.

[39] A. E. Jones, T. A. Wilkinson, and S. K. Barton, "Block coding scheme for reduction of peak to mean envelope power ratio of multicarrier transmission schemes," *Electronics Letters*, vol. 30, pp. 2098–2099, December 1994.

[40] P. V. Eetvelt, G. Wade, and M. Tomlinson, "Peak to average power reduction for OFDM schemes by selective scrambling," *Electronics Letters*, vol. 32, pp. 1963–1964, October 1996.

[41] M. Friese, "Multicarrier modulation with low peak-to-average power ratio," *Electronics Letters*, vol. 32, pp. 713–714, April 1996.

[42] R. W. Bäuml, R. F. H. Fischer, and J. B. Huber, "Reducing the peak-to-average power ratio of multicarrier modulation by selected mapping," *Electronics Letters*, vol. 32, pp. 2056–2057, October 1996.

[43] J. A. Davis and J. Jedwab, "Peak-to-mean power control and error correction for OFDM transmission using Golay sequences and Reed-Muller codes," *Electronics Letters*, vol. 33, no. 4, pp. 267–268, 1997.

[44] S. H. Müller and J. B. Huber, "OFDM with reduced peak-to-mean power ratio by optimum combination of partial transmit sequences," *Electronics Letters*, vol. 33, pp. 368–369, February 1997.

[45] X. Li and J. A. Ritcey, "M-sequences for OFDM peak-to-average power ratio reduction and error correction," *Electronics Letters*, vol. 33, pp. 554–555, March 1997.

[46] J. Jedwab, "Comment : M-sequences for OFDM peak-to-average power ratio reduction and error correction," *Electronics Letters*, vol. 33, pp. 1293–1294, July 1997.

[47] C. Tellambura, "Use of m-sequences for OFDM peak-to-average power ratio reduction," *Electronics Letters*, vol. 33, pp. 1300–1301, July 1997.

[48] C. Tellambura, "Upper bound on peak factor of n-multiple carriers," *Electronics Letters*, vol. 33, pp. 1608–1609, September 1997.

[49] C. Tellambura, "Phase optimisation criterion for reducing peak-to-average power ratio in OFDM," *Electronics Letters*, vol. 34, pp. 169–170, January 1998.

[50] E. V. der Ouderaa, J. Schoukens, and J. Renneboog, "Peak factor minimization using a time-frequency domain swapping algorithm," *IEEE Transactions on Instrumentation and Measurement*, vol. 37, pp. 145–147, March 1988.

[51] R. Steele and L. Hanzo, eds., *Mobile Radio Communications*, ch. 4.4.4, pp. 425–428. IEEE Press, 445 Hoes Lane, Piscataway, NJ, 08855, USA: IEEE Press and Pentech Press, 1999.

[52] A. Viterbi, *CDMA: Principles of Spread Spectrum Communication.* Reading MA, USA: Addison-Wesley, June 1995. ISBN 0201633744.

[53] P. Vandenameele, L. V. D. Perre, M. G. E. Engels, B. Gyselinckx, and H. J. D. Man, "A Combined OFDM/SDMA Approach," *IEEE Journal on Selected Areas in Communications*, vol. 18, pp. 2312–2321, November 2000.

[54] P. Höher, "TCM on frequency-selective land-mobile fading channels," in *International Workshop on Digital Communications*, (Tirrenia, Italy), pp. 317–328, September 1991.

[55] F. Tufvesson and T. Maseng, "Pilot Assisted Channel Estimation for OFDM in Mobile Cellular Systems," in *Proceedings of Vehicular Technology Conference*, vol. 3, (Phoenix, Arizona), pp. 1639–1643, IEEE, May 4-7 1997.

[56] P. Höher, S. Kaiser, and P. Robertson, "Two-dimensional pilot-symbol-aided channel estimation by Wiener filtering," in *International Conference on Acoustics, Speech and Signal Processing*, (Munich, Germany), pp. 1845–1848, IEEE, April 1997.

[57] P. Höher, S. Kaiser, and P. Robertson, "Pilot–symbol–aided channel estimation in time and frequency," in *Proceedings of Global Telecommunications Conference: The Mini–Conf.*, (Phoenix, AZ), pp. 90–96, IEEE, November 1997.

[58] M. Itami, M. Kuwabara, M. Yamashita, H. Ohta, and K. Itoh, "Equalization of Orthogonal Frequency Division Multiplexed Signal by Pilot Symbol Assisted Multipath Estimation," in *Proceedings of Global Telecommunications Conference*, vol. 1, (Sydney, Australia), pp. 225–230, IEEE, November 8-12 1998.

[59] B. Yang, K. B. Letaief, R. S. Cheng, and Z. Cao, "Robust and Improved Channel Estimation for OFDM Systems in Frequency Selective Fading Channels," in *Proceedings of Global Telecommunications Conference*, vol. 5, (Rio de Janeiro, Brazil), pp. 2499–2503, IEEE, December 5-9 1999.

[60] Y. Li, "Pilot-Symbol-Aided Channel Estimation for OFDM in Wireless Systems," *IEEE Transactions on Vehicular Technology*, vol. 49, pp. 1207–1215, July 2000.

[61] B. Yang, Z. Cao, and K. B. Letaief, "Low Complexity Channel Estimator Based on Windowed DFT and Scalar Wiener Filter for OFDM Systems," in *Proceedings of International Conference on Communications*, vol. 6, (Helsinki, Finnland), pp. 1643–1647, IEEE, June 11-14 2001.

[62] X. Wang and K. J. R. Liu, "OFDM Channel Estimation Based on Time-Frequency Polynomial Model of Fading Multipath Channel," in *Proceedings of Vehicular Technology Conference*, vol. 1, (Atlantic City, NJ USA), pp. 460–464, IEEE, October 7-11 2001.

[63] B. Yang, Z. Cao, and K. B. Letaief, "Analysis of Low-Complexity Windowed DFT-Based MMSE Channel Estimator for OFDM Systems," *IEEE Transactions on Communications*, vol. 49, pp. 1977–1987, November 2001.

[64] M.-X. Chang and Y. T. Su, "Model-Based Channel Estimation for OFDM Signals in Rayleigh Fading," *IEEE Transactions on Communications*, vol. 50, pp. 540–544, April 2002.

[65] S. K. Wilson, R. E. Khayata, and J. M. Cioffi, "16QAM Modulation with Orthogonal Frequency Division Multiplexing in a Rayleigh-Fading Environment," in *Vehicular Technology Conference*, vol. 3, (Stockholm, Sweden), pp. 1660–1664, IEEE, June 1994.

[66] J.-J. van de Beek, O. Edfors, M. Sandell, S. K. Wilson, and P. O. Börjesson, "On channel estimation in OFDM systems," in *Proceedings of Vehicular Technology Conference*, vol. 2, (Chicago, IL USA), pp. 815–819, IEEE, July 1995.

[67] P. Frenger and A. Svensson, "A Decision Directed Coherent Detector for OFDM," in *Proceedings of Vehicular Technology Conference*, vol. 3, (Atlanta, GA USA), pp. 1584–1588, IEEE, Apr 28 - May 1 1996.

[68] V. Mignone and A. Morello, "CD3-OFDM: A Novel Demodulation Scheme for Fixed and Mobile Receivers," *IEEE Transactions on Communications*, vol. 44, pp. 1144–1151, September 1996.

[69] Y. Li and N. R. Sollenberger, "Clustered OFDM with Channel Estimation for High Rate Wireless Data," *IEEE Transactions on Communications*, vol. 49, pp. 2071–2076, December 2001.

[70] S. Zhou and G. B. Giannakis, "Finite-Alphabet Based Channel Estimation for OFDM and Related Multicarrier Systems," *IEEE Transactions on Communications*, vol. 49, pp. 1402–1414, August 2001.

[71] B. Lu and X. Wang, "Bayesian Blind Turbo Receiver for Coded OFDM Systems with Frequency Offset and Frequency-Selective Fading," *IEEE Journal on Selected Areas in Communications*, vol. 19, pp. 2516–2527, December 2001.

[72] Bölcskei, J. R. W. Heath, and A. J. Paulray, "Blind Channel Identification and Equalization in OFDM-Based Multi-Antenna Systems," *IEEE Transactions on Signal Processing*, vol. 50, pp. 96–109, January 2002.

[73] M. C. Necker and G. L. Stüber, "Totally Blind Channel Estimation for OFDM over Fast Varying Mobile Channels," in *Proceedings of International Conference on Communications*, (New York, NY. USA), IEEE, April 28 - May 2 2002.

[74] T. Keller, J. Woodard, and L. Hanzo, "Turbo-coded parallel modem techniques for personal communications," in *Proceedings of IEEE VTC'97*, (Phoenix, AZ, USA), pp. 2158–2162, IEEE, 4–7 May 1997.

[75] T. Keller, T. Liew, and L. Hanzo, "Adaptive redundant residue number system coded multi-carrier modulation," *IEEE Journal on Selected Areas in Communications*, vol. 18, pp. 2292–2301, November 2000.

[76] T. Keller, T. Liew, and L. Hanzo, "Adaptive rate RRNS coded OFDM transmission for mobile communication channels," in *Proceedings of VTC 2000 Spring*, (Tokyo, Japan), pp. 230–234, 15-18 May 2000.

[77] T. Keller and L. Hanzo, "Adaptive Orthogonal Frequency Division Multiplexing Schemes," in *Proceedings of ACTS'98 Summit*, (Rhodos, Greece), pp. 794–799, June 1998.

[78] T. Keller and L. Hanzo, "Adaptive modulation technique for duplex OFDM transmission," *IEEE Transactions on Vehicular Technology*, vol. 49, pp. 1893–1906, September 2000.

[79] J. S. Chow, J. M. Cioffi, and J. A. C. Bingham, "Equalizer training algorithms for multicarrier modulation systems.," in *International Conference on Communications*, (Geneva, Switzerland), pp. 761–765, IEEE, May 1993.

[80] F. Tufvesson, M. Faulkner, and T. Maseng, "Pre-Compensation for Rayleigh Fading Channels in Time Division Duplex OFDM Systems," in *Proceedings of 6th International Workshop on Intelligent Signal Processing and Communications Systems*, (Melbourne, Australia), pp. 57–33, IEEE, November 5-6 1998.

[81] B. Yang, K. B. Letaief, R. S. Cheng, and Z. Cao, "Channel Estimation for OFDM Transmission in Multipath Fading Channels Based on Parametric Channel Modeling," *IEEE Transactions on Communications*, vol. 49, pp. 467–479, March 2001.

[82] M. Morelli and U. Mengali, "A Comparison of Pilot-Aided Channel Estimation Methods for OFDM Systems," *IEEE Transactions on Signal Processing*, vol. 49, pp. 3065–3073, December 2001.

[83] J. R. Deller, J. G. Proakis, and J. H. L. Hansen, *Discrete-Time Processing of Speech Signals*. Macmillan Publishing Company, 1993.

[84] L. Hanzo, F. C. A. Somerville, and J. P. Woodard, *Voice Compression and Communications*. IEEE Press Wiley Inter-Science, 2001.

[85] A. Duel-Hallen, S. Hu, and H. Hallen, "Long Range Prediction of Fading Signals," *IEEE Signal Processing Magazine*, vol. 17, pp. 62–75, May 2000.

[86] W. H. Press, S. A. Teukolshy, W. T. Vetterling, and B. P. Flannery, *Numerical Recipes in C*. Cambridge University Press, 1992.

[87] T. K. Moon and W. C. Stirling, *Mathematical Methods and Algorithms for Signal Processing*. Prentice Hall, 2000.

[88] M. Münster and L. Hanzo, "First-Order Channel Parameter Estimation Assisted Cancellation of Channel Variation-Induced Inter-Subcarrier Interference in OFDM Systems," in *Proceedings of EUROCON '2001*, vol. 1, (Bratislava, Czech), pp. 1–5, IEEE, July 2001.

[89] A. Chini, Y. Wu, M. El-Tanany, and S. Mahmoud, "Filtered Decision Feedback Channel Estimation for OFDM Based DTV Terrestrial Broadcasting System," *IEEE Transactions on Broadcasting*, vol. 44, pp. 2–11, Mar 1998.

[90] J. W. C. Jakes, *Mobile Microwave Communications*. John Wiley & Sons, New York, 1974.

[91] G. Grosche, V. Ziegler, and D. Ziegler, *Taschenbuch der Mathematik*. BSB B. G. Teubner Verlagsgesellschaft, Leipzig, 1989.

[92] S. Haykin, *Adaptive Filter Theory*. Prentice Hall, Inc., 1996.

[93] S. Weiss and R. W. Stewart, *On Adaptive Filtering in Oversampled Subbands*. Shaker Verlag GmbH, Aachen, Germany, 1998.

[94] G. Strang, *Linear Algebra and Its Applications, 2nd edition*. Academic Press, 1980.

[95] "EN 300 744, V1.1.2, Digital Video Broadcasting (DVB); Framing structure, channel coding and modulation for digital terrestrial television," in *European Standard (Telecommunications Series)*, pp. 26–28, ETSI, ETSI, 1997.

[96] C. Berrou, A. Glavieux, and P. Thitimajshima, "Near shannon limit error-correcting coding and decoding: Turbo codes," in *Proc. of International Conference on Communications*, (Geneva, Switzerland), pp. 1064–1070, IEEE, May 1993.

[97] C. Berrou and A. Glavieux, "Near optimum error correcting coding and decoding: turbo codes," *IEEE Transactions on Communications*, vol. 44, pp. 1261–1271, October 1996.

[98] L. Hanzo, W. Webb, and T. Keller, *Single- and Multi-carrier Quadrature Amplitude Modulation*. IEEE Press- John Wiley, April 2000.

[99] H. Rohling and R. Gruenheid, "Adaptive Coding and Modulation in an OFDM-TDMA Communication System," in *Proceedings of Vehicular Technology Conference*, vol. 2, (Ottawa, Canada), pp. 773–776, IEEE, May 18-21 1998.

[100] D. Hughes-Hartogs, "Ensemble modem structure for imperfect transmission media," *U.S. Patents Nos. 4,679,222 (July 1987), 4,731,816 (March 1988) and 4,833,796 (May 1989).*

[101] T. Keller and L. Hanzo, " Blind-detection Assisted Sub-band Adaptive Turbo-Coded OFDM Schemes," in *Proc. of Vehicular Technology Conference*, (Houston, USA), pp. 489–493, IEEE, May 1999.

[102] A. N. Mody and G. L. Stüber, "Parameter Estimation for OFDM with Transmit Receive Diversity," in *Proceedings of Vehicular Technology Conference*, vol. 2, (Rhodes, Greece), pp. 820–824, IEEE, May 6-9 2001.

[103] Y. Gong and K. B. Letaief, "Low Rank Channel Estimation for Space-Time Coded Wideband OFDM Systems," in *Proceedings of Vehicular Technology Conference*, vol. 2, (Atlantic City Convention Center, Atlantic City, NJ USA), pp. 772–776, IEEE, October 7-11 2001.

[104] W. Jeon, K. H. Paik, and Y. S. Cho, "Two-Dimensional MMSE Channel Estimation for OFDM Systems with Transmitter Diversity," in *Proceedings of Vehicular Technology Conference*, vol. 3, (Atlantic City Convention Center, Atlantic City, NJ USA), pp. 1682–1685, IEEE, October 7-11 2001.

[105] F. W. Vook and T. A. Thomas, "MMSE Multi-User Channel Estimation for Broadband Wireless Communications," in *Proceedings of Global Telecommunications Conference*, vol. 1, (San Antonio, Texas, USA), pp. 470–474, IEEE, November 25-29 2001.

[106] Y. Xie and C. N. Georghiades, "An EM-based Channel Estimation Algorithm for OFDM with Transmitter Diversity," in *Proceedings of Global Telecommunications Conference*, vol. 2, (San Antonio, Texas, USA), pp. 871–875, IEEE, November 25-29 2001.

[107] Y. Li, "Simplified Channel Estimation for OFDM Systems with Multiple Transmit Antennas," *IEEE Transactions on Wireless Communications*, vol. 1, pp. 67–75, January 2002.

[108] H. Minn, D. I. Kim, and V. K. Bhargava, "A Reduced Complexity Channel Estimation for OFDM Systems with Transmit Diversity in Mobile Wireless Channels," *IEEE Transactions on Wireless Communications*, vol. 50, pp. 799–807, May 2002.

[109] S. B. Slimane, "Channel Estimation for HIPERLAN/2 with Transmitter Diversity," in *International Conference on Communications*, (New York, NY USA), IEEE, April 28 - May 2 2002.

[110] C. Komninakis, C. Fragouli, A. H. Sayed, and R. D. Wesel, "Multi-Input Multi-Output Fading Channel Tracking and Equalization Using Kalman Estimation," *IEEE Transactions on Signal Processing*, vol. 50, pp. 1065–1076, May 2002.

[111] F. Rashid-Farrokhi, L. Tassiulas, and K. J. R. Liu, "Joint Optimal Power Control and Beamforming in Wireless Networks Using Antenna Arrays," *IEEE Transactions on Communications*, vol. 46, pp. 1313–1324, October 1998.

[112] F. R. Gantmacher, *The Theory of Matrices*, vol. 2. New York: Chelsea, 1990.

[113] W. Fischer and I. Lieb, *Funktionentheorie*. Vieweg Verlag, Braunschweig, Germany, 1983.

[114] S. Verdu, *Multiuser Detection*. Cambridge University Press, 1998.

[115] G. J. Foschini, "Layered Space-Time Architecture for Wireless Communication in a Fading Environment when using Multi-Element Antennas"," *Bell Labs Technical Journal*, vol. Autumn, pp. 41–59, 1996.

[116] G. D. Golden, G. J. Foschini, R. A. Valenzuela, and P. W. Wolniansky, "Detection Algorithms and Initial Laboratory Results using V-BLAST Space-Time Communication Architecture," *IEE Electronics Letters*, vol. 35, pp. 14–16, January 1999.

[117] P. Vandenameele, L. V. der Perre, M. Engels, B. Gyselinckx, and H. D. Man, "A Novel Class of Uplink OFDM/SDMA Algorithms: A Statistical Performance Analysis," in *Proceedings of Vehicular Technology Conference*, vol. 1, (Amsterdam, Netherlands), pp. 324–328, IEEE, September 19-22 1999.

[118] C. Z. W. H. Sweatman, J. S. Thompson, B. Mulgrew, and P. M. Grant, "A Comparison of Detection Algorithms including BLAST for Wireless Communication using Multiple Antennas," in *Proceedings of International Symposium on Personal, Indoor and Mobile Radio Communications*, vol. 1, (Hilton London Metropole Hotel, London, UK), pp. 698–703, IEEE, September 18-21 2000.

[119] C. M. Degen, C. M. Walke, A. Lecomte, and B. Rembold, "Adaptive MIMO Techniques for the UTRA-TDD Mode," in *Proceedings of Vehicular Technology Conference*, vol. 1, (Rhodes, Greece), pp. 108–112, IEEE, May 6-9 2001.

[120] A. Benjebbour, H. Murata, and S. Yoshida, "Performance of Iterative Successive Detection Algorithm with Space-Time Transmission," in *Proceedings of Vehicular Technology Conference*, vol. 2, (Rhodes, Greece), pp. 1287–1291, IEEE, May 6-9 2001.

[121] A. Bhargave, R. J. P. Figueiredo, and T. Eltoft, "A Detection Algorithm for the V-BLAST System," in *Proceedings of Global Telecommunications Conference*, vol. 1, (San Antonio, Texas, USA), pp. 494–498, IEEE, November 25-29 2001.

[122] Y. Li and Z.-Q. Luo, "Parallel Detection for V-BLAST System," in *Proceedings of International Conference on Communications*, (New York, NY USA), IEEE, April 28 - May 2 2002.

[123] J. Litva and T. K.-Y. Lo, *Digital Beamforming in Wireless Communications*. Artech House Publishers, Inc., Boston, London, 1996.

[124] X. Wang and H. V. Poor, "Robust Adaptive Array for Wireless Communications," *IEEE Transactions on Communications*, vol. 16, pp. 1352–1366, October 1998.

[125] Y. Li and N. R. Sollenberger, "Adaptive Antenna Arrays for OFDM Systems with Cochannel Interference," *IEEE Transactions on Communications*, vol. 47, pp. 217–229, February 1999.

[126] F. W. Vook and K. L. Baum, "Adaptive Antennas for OFDM," in *Proceedings of Vehicular Technology Conference*, vol. 2, (Ottawa, Canada), pp. 606–610, IEEE, May 18-21 1998.

[127] K.-K. Wong, R. S.-K. Cheng, K. B. Letaief, and R. D. Murch, "Adaptive Antennas at the Mobile and Base Station in an OFDM/TDMA System," in *Proceedings of Global Telecommunications Conference*, vol. 1, (Sydney, Australia), pp. 183–190, IEEE, November 8-12 1998.

[128] Y. Li and N. R. Sollenberger, "Interference Suppression in OFDM Systems using Adaptive Antenna Arrays," in *Proceedings of Global Telecommunications Conference*, vol. 1, (Sydney, Australia), pp. 213–218, IEEE, November 8-12 1998.

[129] J. Li, K. B. Letaief, R. S. Cheng, and Z. Cao, "Joint Adaptive Power Control and Detection in OFDM/SDMA Wireless LANs," in *Proceedings of Vehicular Technology Conference*, vol. 1, (Rhodes, Greece), pp. 746–750, IEEE, May 6-9 2001.

[130] P. Vandenameele, L. V. der Perre, M. Engels, and H. D. Man, "A Novel Class of Uplink OFDM/SDMA Algorithms for WLAN," in *Proceedings of Global Telecommunications Conference*, vol. 1, (Rio de Janeiro, Brazil), pp. 6–10, IEEE, December 5-9 1999.

[131] M. Speth, A. Senst, and H. Meyr, "Low Complexity Space-Frequency MLSE for Multi-User COFDM," in *Proceedings of Global Telecommunications Conference*, (Rio de Janeiro, Brazil), pp. 2395–2399, IEEE, December 5-9 1999.

[132] R. van Nee, A. van Zelst, and G. Awater, "Maximum Likelihood Decoding in a Space-Division Multiplexing System," in *Proceedings of Vehicular Technology Conference*, vol. 1, (Tokyo, Japan), pp. 6–10, IEEE, May 15-18 2000.

[133] G. Awater, A. van Zelst, and R. van Nee, "Reduced Complexity Space Division Multiplexing Receivers," in *Proceedings of Vehicular Technology Conference*, vol. 1, (Tokyo, Japan), pp. 11–15, IEEE, May 15-18 2000.

[134] A. van Zelst, R. van Nee, and G. A. Awater, "Space Division Multiplexing (SDM) for OFDM systems," in *Proceedings of Vehicular Technology Conference*, vol. 2, (Tokyo, Japan), pp. 1070–1074, IEEE, May 15-18 2000.

[135] X. Li, H. C. Huang, A. Lozano, and G. J. Foschini, "Reduced-Complexity Detection Algorithms for Systems Using Multi-Element Arrays," in *Proc. of Global Telecommunications Conference*, vol. 2, (San Francisco, United States), pp. 1072–1076, IEEE, November 27 - December 1 2000.

[136] X. Zhu and R. D. Murch, "Multi-Input Multi-Output Maximum Likelihood Detection for a Wireless System," in *Proceedings of Vehicular Technology Conference*, vol. 1, (Rhodes, Greece), pp. 137–141, IEEE, May 6-9 2001.

[137] F. Rashid-Farrokhi, K. J. R. Liu, and L. Tassiulas, "Transmit Beamforming and Power Control for Cellular Wireless Systems," *IEEE Journal on Selected Areas in Communications*, vol. 16, pp. 1437–1450, October 1998.

[138] A. van Zelst, R. van Nee, and G. A. Awater, "Turbo-BLAST and its Performance," in *Proceedings of Vehicular Technology Conference*, vol. 2, (Rhodes, Greece), pp. 1282–1286, IEEE, May 6-9 2001.

[139] M. Sellathurai and S. Haykin, "A Simplified Diagonal BLAST Architecture with Iterative Parallel-Interference Cancellation Receivers," in *Proceedings of International Conference on Communications*, vol. 10, (Helsinki, Finnland), pp. 3067–3071, IEEE, June 11-14 2001.

[140] S. Thoen, L. Deneire, L. V. D. Perre, and M. Engels, "Constrained Least Squares Detector for OFDM/SDMA-based Wireless Networks," in *Proceedings of Global Telecommunications Conference*, vol. 2, (San Antonio, Texas, USA), pp. 866–870, IEEE, November 25-29 2001.

[141] J. G. Proakis, *Digital Communications*. McGraw-Hill, Inc., 1995.

[142] S. M. Kay, *Fundamentals of Statistical Signal Processing, Estimation Theory*. Prentice Hall, New Jersey, 1993.

[143] K. Fazel and G. Fettweis, *Multi-carrier Spread Spectrum & Related Topics, ISBN 0-7923-7740-0*. Kluwer, 2000.

[144] H. Bogucka, "Application of the New Joint Complex Hadamard Transform - Inverse Fourier Transform in a OFDM/CDMA Wireless Communication System," in *Proceedings of Vehicular Technology Conference*, vol. 5, (Amsterdam, Netherlands), pp. 2929–2933, IEEE, September 19-22 1999.

[145] C. E. Davila, "Blind Adaptive Estimation of KLT Basis Vectors," *IEEE Transactions on Signal Processing*, vol. 49, pp. 1364–1369, July 2001.

[146] A. Rezayee and S. Gazor, "An Adaptive KLT Approach for Speech Enhancement," *IEEE Transactions on Speech and Audio Processing*, vol. 9, pp. 87–95, February 2001.

[147] Y. Li, J. C. Chuang, and N. R. Sollenberger, "Transmitter Diversity for OFDM Systems and Its Impact on High-Rate Data Wireless Networks," *IEEE Journal on Selected Areas in Communications*, vol. 17, pp. 1233–1243, July 1999.

[148] B. Lu and X. Wang, "Iterative Receivers for Multi-User Space-Time Coding Systems," *IEEE Journal on Selected Areas in Communications*, vol. 18, pp. 2322–2335, November 2000.

[149] M. L. Honig and W. X. Xiao, "Performance of Reduced-Rank Linear Interference Cancellation," *IEEE Transactions on Information Theory*, vol. 47, pp. 1928–1946, July 2001.

[150] D. R. Brown, M. Motani, V. V. Veeravalli, H. V. Poor, and J. C. R. Johnson, "On the Performance of Linear Parallel Interference Cancellation," *IEEE Transactions on Information Theory*, vol. 47, pp. 1957–1970, July 2001.

[151] A. Grant and C. Schlegel, "Convergence of Linear Interference Cancellation Multiuser Receivers," *IEEE Transactions on Communications*, vol. 49, pp. 1824–1834, October 2001.

[152] H. Dai and H. V. Poor, "Turbo Multiuser Detection for Coded DMT VDSL Systems," *IEEE Journal on Selected Areas in Communications*, vol. 20, pp. 351–362, February 2002.

[153] K.-W. Cheong, W.-J. Choi, and J. M. Cioffi, "Multiuser Soft Interference Canceler via Iterative Decoding for DSL Applications," *IEEE Journal on Selected Areas in Communications*, vol. 20, pp. 363–371, February 2002.

[154] A. Lampe, R. Schober, W. Gerstacker, and J. Huber, "A Novel Iterative Multiuser Detector for Complex Modulation Schemes," *IEEE Journal on Selected Areas in Communications*, vol. 20, pp. 339–350, February 2002.

[155] B. Lu, X. Wang, and Y. Li, "Iterative Receivers for Space-Time Block-Coded OFDM Systems in Dispersive Fading Channels," *IEEE Transactions on Wireless Communications*, vol. 1, pp. 213–225, April 2002.

[156] T. Keller, *Adaptive OFDM techniques for personal communications systems and local area networks*. PhD Thesis, Department of Electronics and Computer Science, University of Southampton, United Kingdom, 1999.

[157] R. Steele and L. Hanzo, *Mobile Radio Communications*. John Wiley & Sons, LTD, Chichester, 1999.

[158] P. A. Bello, "Time-frequency duality," *IEEE Transactions on Information Theory*, vol. 10, pp. 18–33, January 1964.